



U.S. DEPARTMENT OF  
**ENERGY**

Office of  
Science

**Preliminary Conceptual Design Report  
for the  
FACET-II Project  
at  
SLAC National Accelerator Laboratory**

**SLAC Site Office**

**Office of High Energy Physics  
Office of Science  
U.S. Department of Energy**

**SLAC-R-1067**



*This material is based upon work supported by the U.S. Department of Energy, Office of Science,  
Office of Basic Energy Sciences, under Contract No. DE-AC02-76SF00515 and HEP.*

## CDR Outline

- 1 Executive Summary
- 2 Overview
- 3 Scientific Objectives
- 4 Parameters & Performance
- 5 Electron Injector
  - 5.1 Accelerator Intro & Overview
  - 5.2 Drive Laser
  - 5.3 Electron Gun & Injector
  - 5.4 Instrumentation, Diagnostics, Feedback, Collimation
- 6 Bunch Compressors & Linac
  - 6.1 Main FACET-II Linac
  - 6.2 Bunch Compression
  - 6.3 The First Electron Bunch Compressor (BC1)
  - 6.4 Bunch Compression System for e+ and e- in Sector 14 (BC2)
  - 6.5 Sector 20 Chicanes
  - 6.6 RF Systems
  - 6.7 Particle Tracking
  - 6.8 Instrumentation, Diagnostics, Feedback, Collimation
- 7 Experimental Area & Infrastructure
  - 7.1 Introduction and Overview
  - 7.2 Sector 10 Shielding Wall
  - 7.3 Experimental Area
  - 7.3 Personnel Protection and Other Safety Systems
  - 7.5 Controls System recovery
- 8 Positron System
  - 8.1 Positron System - Introduction & Overview
  - 8.2 PRLTR – Positron Return Line to Damping Ring
  - 8.3 Positron Damping Ring
  - 8.4 Positron Extraction and Compression
  - 8.5 Instrumentation, Diagnostics and Feedback
- 9 Sector 20 Sailboat and W Chicanes
  - 9.1 Overview
  - 9.2 Beam Parameters
  - 9.3 Layout and Optics Design
  - 9.4 Beam Dynamics
  - 9.5 Path Length Tuning Chicanes
  - 9.6 New Magnets
  - 9.7 Instrumentation, Diagnostics and Feedback
- 10 Future Upgrades
  - 10.1 Future Upgrades - Introduction & Overview
  - 10.2 High Electron Charge Operation Mode

- 10.3 Witness Bunch Injector
- 10.4 Differential Pumping
- 10.5 Compton Source
- 10.6 Photon-Photon Collider Option

# 1 Executive Summary

The discovery of the Higgs boson, a subatomic particle responsible for endowing all other particles with mass, is one of the major discoveries of the last decade. To unlock the mysteries of the subatomic world, physicists use the worlds' most powerful microscopes – particle accelerators. The resolving power of these microscopes is proportional to the energy of the beams they produce. Since their inception nearly 80 years ago, the energy reach of accelerators has grown exponentially due to continued breakthroughs in accelerator physics and engineering. The highest energy beams in the world are currently at the 27km circumference Large Hadron Collider (LHC) in Europe. Although it is a monument to human engineering, scientists are approaching a practical limit to the size and cost of such collider facilities. Innovation is essential for continued progress.

Electrons can “surf ” on waves of plasma – a hot gas of charged particles – gaining very high energies in very short distances. This approach, called plasma wakefield acceleration, has the potential to dramatically shrink the size and cost of particle accelerators. Research at the SLAC National Accelerator Laboratory has demonstrated that plasmas can provide 1,000 times the acceleration in a given distance compared with current technologies. Developing revolutionary and more efficient acceleration techniques that allow for an affordable high-energy collider is the focus of FACET, a National User Facility at SLAC.

FACET uses part of SLAC's two-mile-long linear accelerator to generate high-density beams of electrons and their antimatter counterparts, positrons. These beams are so intense, they are equivalent to focusing all the power of the sun onto a surface 10 meters square. This produces large electric and magnetic fields over a very short span of time – ideal for creating exotic states of matter and researching advanced accelerator technologies.

Near the end of the first year of FACET operation, the plasma wakefield acceleration program laid out a 4-year plan of milestones to be accomplished during the FACET runs in 2013 to 2016. The goals for 2013 were commission both the high power laser and two-beam generation and with those, demonstrate mono-energetic acceleration for the first time. The goals for 2014 were to refine the mono-energetic acceleration parameters, demonstrate acceleration with positrons, and first experiments using plasma wakefields for a high-brightness injector. The goals for 2015 were to refine the positron acceleration experiments, demonstrate high efficiency and further explore the high-brightness injector. Each of these goals was successfully accomplished as planned. For the last year of the program in 2016, the goals will be demonstration of a single stage with narrow energy spread, low emittance and high efficiency.

High-energy particle beams also provide unparalleled tools for studying the building blocks of life at the molecular level using powerful beams of x-rays. With the recent success of the world's first hard x-ray laser, the Linac Coherent Light Source (LCLS) at SLAC, scientists can image the smallest structures with intense pulses lasting only a millionth of a billionth of a second – like an ultimate high speed camera. FACET also produces unprecedented intensities of

terahertz or “sub-millimeter” electromagnetic radiation, which has many applications in material science, semiconductor research, chemical imaging and more.

Scientists from all over the world come to FACET to do experiments aimed at improving the power and efficiency of particle accelerators used in basic research, medicine, industry and other areas important to society. Experimental proposals are peer-reviewed by the SLAC Accelerator Research Experiment Committee (SAREC), which would also review FACET-II proposals. There has been extensive outreach to the user community through three FACET User Meetings at SLAC, satellite FACET informational meetings at IPAC and other conferences, and direct involvement of the users in the FACET-II proposal.

In 2016, the second phase of SLAC’s x-ray laser, the LCLS-II, will begin to use part of the tunnel occupied by FACET, and the world’s only multi-GeV facility for advanced accelerator research will cease operation. FACET-II is a new test facility to provide DOE with the unique capability to develop advanced acceleration and coherent radiation techniques with high-energy electron and positron beams. FACET-II is an opportunity to build on the decades-long experience developed conducting advanced accelerator R&D at the FFTB and FACET and re-deploy HEP infrastructure in continued service of its mission.

FACET-II provides a major upgrade over current FACET capabilities and the breadth of the potential research program makes it truly unique. It will synergistically pursue accelerator science that is vital to the future of both advanced acceleration techniques for High Energy Physics, ultra-high brightness beams for Basic Energy Science, and novel radiation sources for a wide variety of applications. An international group of high energy physicists are interested in using it as a foundation for the world’s first photon collider. Nuclear physicists have proposed using the unprecedentedly high intensity gamma beams to study the structure of nuclei and as a novel particle source for future colliders. No other test facility has attracted such broad interest across so many branches of the Office of Science.

## 2 Overview

The existing FACET National User Facility uses part of SLAC's two-mile-long linear accelerator to generate high-density beams of electrons and positrons. These beams are so intense, they are ideal for creating exotic states of matter and researching advanced accelerator technologies. Scientists from all over the world come to FACET to do experiments and there has been extensive outreach to the user community in the FACET-II proposal.

In 2016, the second phase of SLAC's x-ray laser, the LCLS-II, will begin to use part of the tunnel occupied by FACET, and the world's only multi-GeV facility for advanced accelerator research will cease operation. FACET-II is a new test facility to develop advanced acceleration and coherent radiation techniques with high-energy electron and positron beams. It is the only facility in the world with high energy positron beams and it offers an opportunity to build on the decades-long experience developed conducting advanced accelerator R&D at SLAC. FACET-II provides a major upgrade over current FACET capabilities and the breadth of the potential research program makes it truly unique. No other test facility has attracted such broad interest across so many branches of the Office of Science.

The design parameters for FACET-II are set by the requirements of the plasma wakefield experimental program. To drive the plasma wakefield requires a high peak current, in excess of 10kA. To reach this peak current, the electron and positron design bunch size is  $10\mu$  by  $10\mu$  transversely with a bunch length of  $10\mu$ . This is more than 200 times better than what has been achieved at the existing FACET. The beam energy is 10 GeV, set by the Linac length available and the repetition rate is up to 30 Hz.

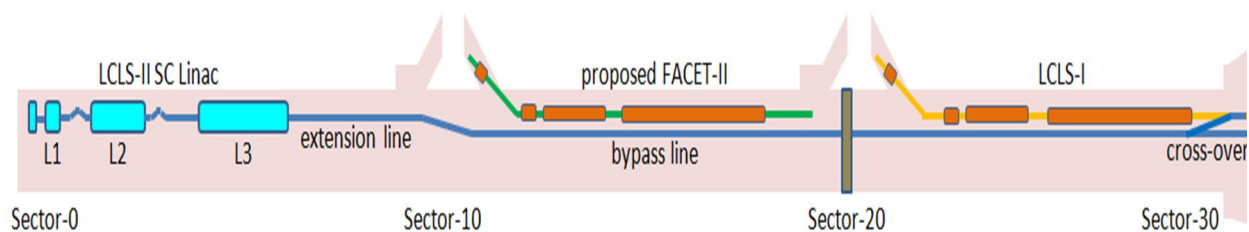


Figure 2.1. Schematic layout of FACET-II in the middle third of the SLAC linac, downstream of LCLS-II and upstream of LCLS-I.

The FACET-II project is scheduled to be constructed in three major stages: 1) a new photoinjector at Sector 10 and two bunch compressors in the Linac will restore operation with electrons; 2) a new positron damping ring located in the Sector 10 tunnel with injection and extraction lines will restore operation with positrons; 3) a new final chicane in Sector 20 will provide for simultaneous delivery of positrons and electrons to the experimental area. A schematic of the full set of FACET-II beamlines is shown in figure 2.1.

For stage one, FACET-II will complete the original LCLS-II installation of the photoinjector and its auxiliary systems at Linac Sector 10. This will include installation of a gun and injector beamline

in the Linac tunnel and power sources and control electronics in the gallery. These systems will connect the new injector at Sector 10 with the Linac, where the beam can then be accelerated and transported to the existing FACET experimental area in Sector 20. Two bunch compressor chicanes will be installed in Sector 11 and Sector 14 to provide the first two of three stages of bunch compression needed to produce the required high energy density beams at the FACET experimental area in Sector 20. The third stage of compression is in Sector 20. A shield wall, similar to the existing one in Sector 20, will be constructed in Sector 10 to separate the LCLS-II and FACET-II accelerator areas.

In stage two for positron operation, FACET-II will reuse the existing positron target at Sector 19. A new small damping ring, which fits inside of the accelerator tunnel, will be installed at Sector 10. In addition to the beamline in the tunnel, there will be power sources and control electronics in the gallery. Two new beamlines in Sector 10 will bring the positrons from the existing Positron Return Line into the new Damping Ring and from the Damping Ring back into the main linac.

In stage three for the simultaneous delivery of positrons and electrons to the user area, a second arm of the final chicane will be installed in S-20. This beamline in the tunnel will be connected to power supplies and control electronics in the gallery.

## 2.1 Staged Approach and Level of Maturity of the Conceptual Design

Because the project is to be completed in sequential stages, the Design Report and the Work Breakdown Structure both reflect this staged approach. Chapters 5, 6 and 7 on the Electron Injector, Linac and Bunch Compressors, and Experimental Area and Infrastructure describe the aspects of the project to be completed in stage one. Chapter 8 on Positron Systems describes the aspects of the project to be completed in stage two. Chapter 9 on the Sector 20 W and Sailboat Chicanes describes the existing electron arm of the 3<sup>rd</sup> bunch compressor, which remains unchanged in stage one and two, and the new positron arm of the 3<sup>rd</sup> bunch compressor which is to be built in stage three.

In this document, the description of the first stage of the FACET-II project, which will restore electron operation, is based on the existing injector built and operated for LCLS-I and the original design of a copy of that injector for LCLS-II. Since the injector and 1<sup>st</sup> two bunch compressors in the Linac, are essentially identical to what was built for LCLS, the design is very mature and more at the level of a Technical Design Report. Because the positron systems are new, their designs are much less mature and more at the level of a Conceptual Design Report. They do not yet have the same level of engineering design. Detailed specifications for items such as power supplies, controls and vacuum systems will be prepared for the next release of the Conceptual Design Report at CD-2.

## 2.2 Electron Injector

In order to achieve the scientific goals of the experimental program at FACET-II, a high electron peak current with small transverse core beam size at the experimental IP waist, ~10 $\mu$ m, and a small longitudinal emittance are required. FACET-II will operate with an electron energy up to 10 GeV. The most challenging parameters are for the plasma wakefield acceleration (PWFA)

experiments which require peak currents in excess of 10 kA. The RF photocathode gun and injection system is similar to that used in LCLS. This injector is capable of producing a charge of up to 5 nC in a bunch length of <5.4 ps, corresponding to a peak current of >120 A with a transverse emittance of less than 5 $\mu$ m. This implies a required compression ratio in excess of 100 to achieve the desired beam characteristics at the IP waist in sector 20. The acceleration and compression is done in the 2nd kilometer of the SLAC linac in 3 compression stages. A schematic of the electron injector, linac and bunch compressors is shown in Figure 2.2.

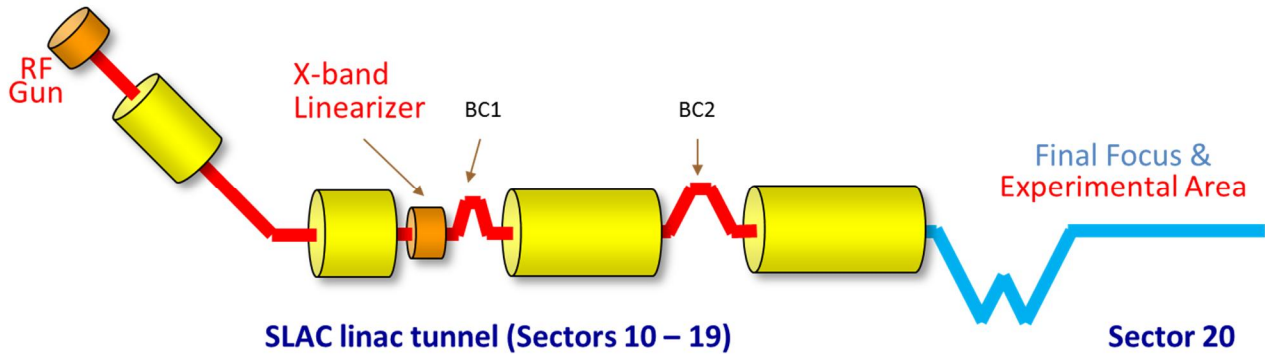


Figure 2.2. Schematic showing injector, linac, bunch compressors, and experimental area for stage one of the FACET-II project. The blue sections depict the electron specific and common e-/e+ areas.

The capabilities of FACET-II vary in a non-trivial way depending on the choice of initial charge from the RF gun. The baseline design is for a 2nC electron bunch charge from the electron gun, operating together with a 2nC positron bunch from the positron damping ring once positrons have been reestablished. To demonstrate design flexibility and characterize the extremes of the possible parameter space, a second configuration option is considered in chapter 10 corresponding to a 5 nC pulse from the electron gun. The conceptual design here represents a parameter set to demonstrate the highest deliverable peak currents to the sector 20 user area within various parameter constraints set by later operation modes. In particular, the design is constrained by the requirements for operation with positrons. For single sign particle operation, the compression scheme can be tailored towards higher electron-only peak current.

### 2.3 Bunch Compressors and Linac

Both electrons and positrons undergo three stages of bunch compression, the first two stages in Linac Sectors 11 and 14 and the final compression stage in Sector 20. The Sector 20 chicanes are described in Chapter 9. For positron operation, positrons produced in sector 19 are returned to the beginning of the linac in a ceiling-mounted transfer line and injected into a damping ring in Sector 10 at an energy of 335 MeV. The initial stage of positron compression takes place in the transfer line from the damping ring before injection into the main linac in the final bend of BC1 (in Sector 11). The design of the compression scheme addresses the most challenging option which requires the positron beam to be co-accelerated along with the electron beam through the main linac, separated by ~5cm, i.e.  $\frac{1}{2}$  of an S-band RF bucket. This requires a common RF chirp and BC2 compression configuration for both electron and positron bunches. Hence, the configuration of the linac-based compression scheme must take into

account the compression requirements of both particle species simultaneously. The details of the positron systems are mainly described in chapters 8 and 9.

The bunch compression is accomplished by a series of magnetic chicanes arranged and located such that non-linearities in the compression and acceleration process (longitudinal wakefields, RF curvature, and second order momentum compaction) are all approximately compensated. A short section of X-band deceleration (3.3 MeV, 11.424 GHz) ahead of the first compressor is used to linearize the compression for the electron beam. The goal for the linac design is to a) achieve design peak current requirements for both positron and electron bunches, b) cancel the correlated energy spread after the final compression and c) minimize sensitivities to RF phase and amplitude variations and also to bunch charge variations. The electron energy at the first compressor is 335 MeV. This choice avoids space charge effects, while the bunch compression is still early enough in the linac to ease the effects of transverse wakefields. In the first compressor (BC1), the electron bunch length is reduced from 0.8 mm to 287  $\mu\text{m}$  (rms). For operation with positrons, the positron beam is injected into the linac at the final BC1 bend. The injection energy of 335 MeV is also most suitable for the design of the compact positron damping ring. The bunch length of the positrons, upon extraction from the damping ring, is 4 mm (rms). To match well into the linac compression scheme, an additional bunch compressor (2.1m S-band RF section and 4-bend chicane) is included in the damping ring-to-linac beamline section. The positron bunch length is compressed to 308  $\mu\text{m}$  (rms) before being injected into the shared linac through a horizontal dogleg section

The second compressor (BC2 in Sector 14) produces a 23.6/28.9  $\mu\text{m}$  rms bunch length for electrons/positrons. The energy of the second compressor, 4.5 GeV, is chosen as a balance between the conflicting requirements of longitudinal emittance dilution due to synchrotron radiation, and the need to cancel the final correlated energy spread when including the final compression stage in sector 20. The design of the compressors is dominated by the need to reduce Coherent Synchrotron Radiation (CSR) effects, which are most pronounced for short bunches. The most significant effect of CSR is to generate a time-dependent energy variation along the bunch. Designs utilizing relatively weak chicanes and larger initial correlated energy spreads for the various compression stages help control the effect CSR has on transverse emittance dilution. Additionally, adjustable collimators in the center of BC1 and BC2 are used to cut high-energy, non-linear tails and also allow for fine-tuning the positron and electron bunch populations to help with balancing relative beam-loading energy losses in the linacs. The final compression stage in sector 20 using the electron (BC3E) and positron (BC3P) chicanes at 10 GeV is described in Chapter 9.

## 2.4 Experimental Area and Infrastructure

In addition to construction of the FACET-II injector and bunch compressors, several modifications are needed in the Linac infrastructure before electron beams can be restored. A concrete shielding wall must be constructed in Sector 10 to separate the LCLS-II and FACET-II sections of the Linac tunnel. This allows access to the LCLS-II tunnel while there is beam in the FACET-II area. It does not permit access to the FACET-II area during LCLS-II beam operation. In addition to the wall, the Personnel Protection System (PPS) for the two areas must be separated to allow independent access. A separate PPS zone with Controlled Access is planned

for Sector 20 to facilitate efficient entry to that region. Other infrastructure tasks include modifications to the control system network to restore the legacy control system post LCLS-II modifications in the first 10 sectors and a new Beam Containment System for the injector and chicanes.

The experimental area in Sector 20 will also be modified to support a range of expected experiments which can be prepared in advance and run sequentially without the need for access. This is necessary because access to the experimental area will be much more limited once LCLS-II is operating.

## 2.5 Positron Systems

The positrons are produced by sending an electron bunch onto the existing positron target and capture section in Sector 19. The positron bunch is transported back to Sector 11 in the existing Positron Return Line. A new beamline that starts in Sector 11 takes the positrons from the Return Line and injects them into a new Damping Ring in the Sector 10 Linac tunnel. The energy of the beam from the positron production system is 210 MeV and the Damping Ring energy is 335 MeV, so 125 MeV of energy must be provided by S-band accelerating structures to be located in Sector 14. The accelerating structures will replace a section of the existing return line. A schematic of the positron systems for stage two of the FACET-II project is shown in Figure 2.3.

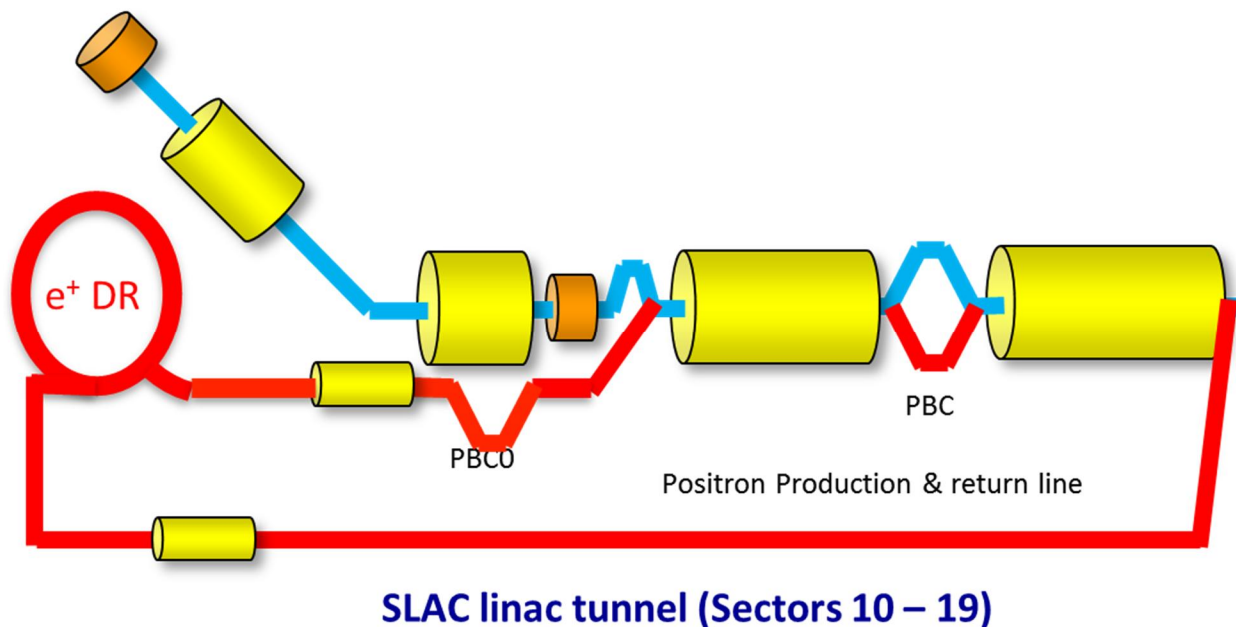


Figure 2.3. Schematic showing positron production, return line with acceleration section, damping ring, extraction line and bunch compressors for stage two of the FACET-II project. The blue sections depict the electron specific areas. The red sections are for positrons.

The positron beam into the damping ring has a very large transverse emittance that must be reduced by three orders of magnitude in a few milliseconds. Because the damping ring is located in the existing Linac tunnel, the diameter of the ring must be smaller than 3 meters.

This constraint dictates a compact design with minimal gaps between the magnets in the arcs. The large injected beam size also dictates that the acceptance of the ring be large enough to accommodate on-axis injection. The proposed design incorporates many aspects of recent developments for diffraction-limited light sources. The beam energy is chosen to be 335 MeV which is as high as possible given the space constraints.

Given the compact dimensions, the magnet design for the damping ring arcs is particularly challenging. As proposed, the three dipole magnets in each arc cell are wound on a single block of steel, the arc quadrupoles have a very compact and innovative design, and the arc sextupoles are very thin permanent magnets. Conceptual designs for these magnets are described in Section 8.3.6. The straight sections contain both the injection and extraction and the RF cavities. Vacuum requirements are not particularly challenging because of the single bunch operation.

A second new positron beamline in Sector 10 takes the beam from the damping ring extraction point, performs a 1st stage of bunch compression and injects it into the last dipole magnet of the 1st electron bunch compressor (BC1) in Sector 11. All of the components of the injection and extraction lines are conventional. Once the positrons are injected into the Linac, they are accelerated to 10 GeV in the second and third Linac sections. The second stage of bunch compression is performed in a second arm of the bunch compressor in Sector 14 (BC2) and the 3rd stage in a second arm of the chicane in Sector 20, which is described in Chapter 9. They are focused to a transverse size of about 10 microns at the FACET Interaction Point and dumped at the end of Sector 20.

## 2.6 Sector 20 Sailboat and **W** Chicanes

In order to achieve the full scientific goals of the plasma wakefield experimental program at FACET-II, it is necessary to bring both the electron and positron bunches to the FACET Interaction Point (IP) on the same pulse within about 100  $\mu\text{m}$ . The chicanes in Sector 20 provide the 3rd and final stage of bunch compression for both bunches. The existing **W** chicane can compress and transport either type of particle, depending on the polarity of the magnets. When both chicanes are implemented, the **W** chicane will serve as the electron chicane so it is referred to as BC3E (3rd bunch compressor for electrons). BC3E compresses the beam to final high peak-currents  $>10$  kA and demagnifies the transverse spot sizes to  $\sim 10$   $\mu\text{m}$  at selectable locations in the experimental region. A schematic of the new positron chicane for stage three of the FACET-II project is shown in Figure 2.4.

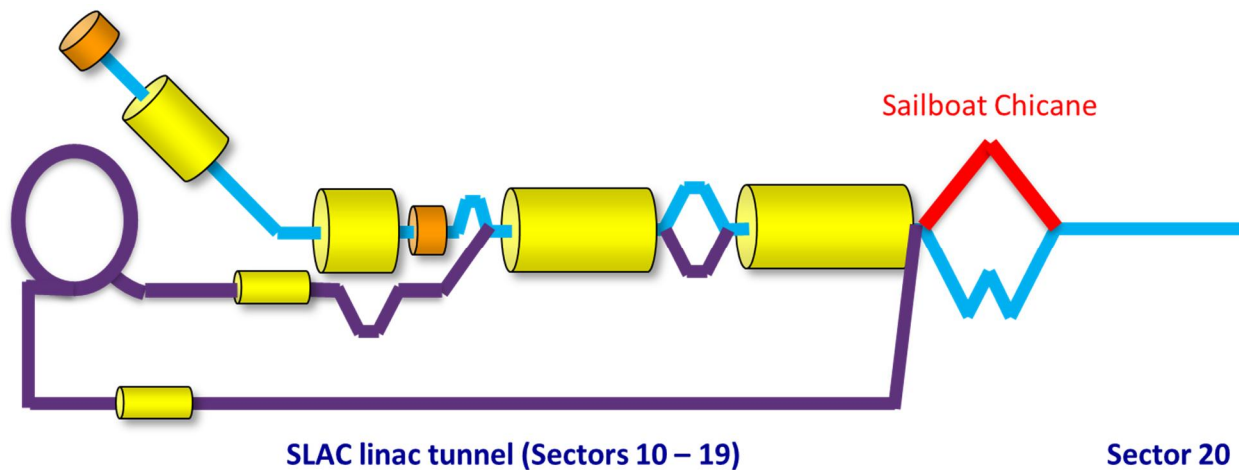


Figure 2.4. Schematic showing the second positron arm of the Sector 20 chicane for stage three of the FACET-II project. The blue sections depict the electron specific areas. The purple and red sections are for positrons.

In order to bring both types of particle to the experiments on the same pulse, the positron bunch is co-accelerated through the main linac with the electron bunch, which follows the positrons by  $\sim 5\text{cm}$ , i.e.  $\frac{1}{2}$  of an S-band RF bucket. The 3rd stage of compression for positrons requires a second arm of the chicane in Sector 20 (BC3P -3rd bunch compressor for positrons). The positron chicane has a path length which is  $5.27\text{ cm}$  longer than the electron chicane, reversing the order of the bunches when they arrive at the IP. The positron (witness) bunch arrives at the experimental plasma acceleration chamber  $\sim 215\ \mu\text{m}$  behind the driving electron beam. A pair of short 4-bend adjustable chicanes in each half of BC3P provide for fine adjustments to the electron-positron longitudinal spacing at the IP ( $\pm 100\ \mu\text{m}$ ).

Both chicanes share the first and last bend magnets. Sextupole magnets placed in dispersive locations of each main sector 20 chicane also control chromaticity and second-order dispersion caused by the chicanes and the final focus magnets.

## 2.7 Beam Tracking and Simulations

6D tracking simulations have been made to model the beam transport through the FACET-II complex, including the non-linear compression and final beam focus process. The simulations include the effects of longitudinal wakefields in the  $1\text{km}$  linac as well as incoherent and coherent synchrotron radiation effects in the various bending magnets. Longitudinal space charge effects are also simulated throughout the beam transport. Simulations have also been made which calculate emittance dilution in the linac due to transverse wakefields and anomalous momentum dispersion, each of which arises from a variety of considered error sources such as component misalignment and magnetic field errors. Diagnostics, correction techniques, and feedback systems have also been incorporated into the design. For operation with positrons, the electron bunch is preceded by a positron bunch separated by  $\frac{1}{2}$  an S-band RF wavelength ( $5.25\text{ cm}$ ). The coupling of trajectory errors through transverse wakefields in the two-bunch system required for simultaneous operation with both electrons and positrons is also included in the tracking simulations.

For the positron complex, simulations have been performed to demonstrate the performance of the transport lines and damping ring. Collective effects have been estimated analytically and appear to be controllable.

## 2.8 Future Upgrades

To support the full breadth of the experimental program outlined in Chapter 3, several additions or upgrades will be required to expand future capabilities. These are described briefly in this chapter. They could be funded as Accelerator Improvement Projects during the operation of the FACET-II facility, but they are also available as possible scope additions should project funds be available.

The Plasma Wakefield Acceleration experimental program will eventually desire a higher current electron bunch than provided in the baseline configuration. As one possible implementation, we have designed the linac and bunch compression to be compatible with a 1nC/5nC configuration of the positron /electron beams respectively. The 1nC/5nC configuration has a large imbalance in the wakefield loading in the linac between electron and positron bunches as well as CSR effects. This configuration would require installation of new 2nd or 4th harmonic (C- or X-band) acceleration sections in the Linac for energy equalization.

This upgrade represents a highly “pushed” parameter set to demonstrate the highest deliverable peak currents to the Sector 20 user area. This requires pushing the limits of the bunch compressor systems while operating the beams with high energy spread which leads to highly non-Gaussian beam distributions in all 6 degrees of freedom. This leads to standard statistical measures of beam quality such as emittance being a poor choice for describing the desirable beam characteristics. Typically, where projected beam sizes are referred to in the text, this refers to a Gaussian fit to the core of the projection which de-weights smaller charge distributions at high relative offsets.

Other upgrades are described briefly. 1) installation of a witness injector to provide an independent bunch to sample the plasma wakefields. This allows complete freedom to tailor the drive bunch shape for maximum transfer efficiency. 2) installation of a differential pumping system to isolate the vacuum in the experimental region from the Linac vacuum. This provides flexibility with the plasma chamber experiments and avoids the need for beryllium windows. 3) installation of a Compton source for a variety of proposed experiments. 4) operation of Compton sources in the Sector 20 chicanes to form a photon-photon collider in the final bend of BC3E & BC3P.

# 3 Scientific Objectives

We need to push the properties of accelerators beyond the present limits of performance and create innovative ways of applying accelerator technologies in order to advance science and further the goals of High Energy Physics and Basic Energy Science. Reaching well beyond the trillion-electron-volt (TeV) energy scale with an electron/positron collider will not be affordable without a marked improvement in accelerating gradient. Techniques developed to enable a TeV collider will also make GeV-scale light sources smaller and less expensive. Providing the luminosity required to support precision science will require significant gains in beam brightness and accelerator power efficiency. Such gains will improve the source quality and reduce the operating cost of light sources.

Developing the accelerator science necessary to make game-changing performance improvements requires significant experimentation and refinement. Such work requires a suitable test facility where machine changes can be made and significant beam time assigned to experiments without adversely impacting a scientific user community.

Decades of experience in advanced accelerator research have shown that some basic facility features are needed to support the work:

- A stable, well-diagnosed beam with broadly adjustable properties
- An extensive user-configurable beam area with a wealth of diagnostics
- An external diagnostic hutch where both electrical and optical signals can be gathered and processed
- A laser hutch, providing coherent radiation for excitation and diagnostics

Facilities at Argonne, Brookhaven, SLAC, UCLA and elsewhere cover the energy range below 1 GeV, but there is currently no planned national user beam facility above the 1 GeV range after FACET. Wakefield acceleration and coherent radiation generation are fundamentally collective effects that grow stronger with beam density and energy, and consequently the science and potential applications grow more compelling with beam energy and brightness. The wealth of attosecond-scale manipulation techniques being developed for the photon sciences (e.g. iSASE, ESASE, HGHG, and seeding) all become more robust at higher energies, where path length slippage and space charge effects can be mitigated.

An additional consideration for an advanced accelerator research facility is the pulse format. Many advanced accelerator experiments are inherently single-pulse (or single drive-witness pair) experiments because the physical process is single pass (non-resonant), or because the experiment relies on single-shot diagnostics (such as cameras), or both. Short pulse trains of <10 bunches are useful to probe long-range wakefield effects, as are pulses with widely variable spacing (perhaps out to 100 ns).

The FACET-II science program has three principle thrusts:

- High gradient acceleration techniques for the next e<sup>+</sup>/e<sup>-</sup> collider
- Radiation generation and enhancement techniques for photon science
- Physics of very high field interactions with materials

The high energy and high brightness characteristics of the FACET-II beam enables a broad class of coherent radiation and beam/matter interaction science at field strengths and energy densities not available anywhere else. While an experimental program is defined below that focuses on key challenges for discovery science, we will also seek out new opportunities to apply the unique capabilities of FACET-II to solve problems in other scientific areas, drawing in university and industrial researchers in the process.

The FACET-II scientific program will make orders of magnitude advancements in three primary areas: accelerating gradient, beam quality and photon flux. Wakefield acceleration—whether in plasma or in dielectric waveguides—is a cornerstone of the program, building on a more than 20 year history of performing groundbreaking work in GeV-scale beam-driven wakefield acceleration at SLAC. A major goal of FACET-II is to utilize gradients 1,000 times higher than current technology in a meter scale prototype plasma accelerator. The existence of such ultra-high gradients also makes it possible to trap particles and produce a beam with 1,000 times the brightness currently achievable. The combination of uniquely high energy, high density beams and the short pulse, high power FACET laser enables the generation of very high flux photon beams. In principle, 100-1000 times higher gamma flux from 10 MeV to 5 GeV and 10,000 times higher total gamma flux up to 5 GeV should be deliverable.

By offering pulse charge from pC to a nC, emittance from nm to microns, electrons and positrons, single and double bunches, tailored current profiles of up to nearly 100kA and energy up to 10GeV FACET-II provides experimental capabilities unparalleled anywhere in the world. By leveraging the additional infrastructure afforded by SLAC's laser group, the FACET laser systems provide multi-terawatt peak powers with state of the art synchronization approaching 10fs. These capabilities will draw in additional experimental programs that exploit these capabilities to their fullest generating orders of magnitude improvements in electron and photon beam brightness. The initial vision for the FACET-II science programs is described in this section, but this will certainly evolve to reflect the most pressing science issues of the time as guided by the SAREC committee.

## 3.1 Plasma Wakefield Acceleration (PWFA) Program at FACET-II

### 3.1.1 Introduction

The first phase of our beam driven plasma wakefield accelerator (PWFA) program began with the experiments in the SLAC FFTB between 1998 and 2006. These experiments demonstrated, among many other things, that a plasma can accelerate electrons with a gradient of 50GeV/m over nearly a meter. By April 2016, the FACET scientific program will complete the second phase of our plasma wakefield acceleration program. Upon successful conclusion we will have demonstrated several ambitious goals including a meter-scale plasma accelerator module for electrons and the first tests to identify the optimal technique to accelerate positrons in a

plasma. For electrons the acceleration will be meter scale, multi-GeV/m, produce a beam with 100's pC of charge and a narrow energy spread (<10%) while preserving the incoming emittance. For positrons, The SLAC FFTB program was the first experimental investigation of the issues of accelerating and focusing positrons in a plasma. With relatively long positron bunches and low density plasmas accelerating gradients of 100MeV/m were demonstrated but the aberrations in focusing in the positron driven wake resulted in halo formation and emittance growth. FACET will make the first experimental investigation with more compressed positron bunches in tailored high-density hollow-channel plasma cells. Hollow channel plasmas are predicted to achieve an order of magnitude larger accelerating gradient compared to the FFTB experiments while being free of the focusing aberrations for positrons in uniform plasmas.

FACET-II will restart the science programs in 2019 and begin the third phase of plasma wakefield accelerator development. FACET-II will build directly on the results from FACET and investigate the issues of staging, positron acceleration, efficiency and beam quality. The first experiments will take advantage of the high-brightness beams available from the FACET-II LCLS-style photoinjector. When operated in a low charge mode, the large phase space density of these pico-coulomb beams allows them to be compressed to a few femtoseconds and to be focused to a few microns in size. In this extreme it is possible to generate TV/m fields in high-density plasmas that will break new ground for wakefield accelerators, study the threshold for ion-motion in PWFA and allow the properties of materials to be tested under extreme conditions (see Section 3.14). When operated in high-charge mode with bunch charges of 5nC or more, the compressed pulses will have peak currents approaching 100kA opening the door to new forms of plasma injectors and beam-ionized plasma sources. Harnessing the large fields and small spatial extent of the plasma wake, plasma injectors have already produced beams with state of the art micron level emittance and brightness. By controlling the injection using laser pulses and tailored plasma profiles, we will harness the flexibility of the photoinjector drive beam to produce high-energy beams from the plasma with a normalized emittance approaching a nanometer. By demonstrating the ability of compact plasma sources to function as both an energy and brightness transformer, producing multi-GeV beams with unprecedented brightness from a plasma only a meter long, we will pave the way for the first applications such as compact plasma driven XFELs.

By 2020 we will commission the new positron damping ring (see Section 8. Error! Reference source not found.) and renew experiments comparing and contrasting wakefield acceleration of single species bunch(es) of either electrons or positrons in hollow channel plasmas. Using the notch collimator we will optimize the accelerating wakefield in hollow channels for an electron witness beam in an electron driven wake and for a positron witness in a positron driven wake. In 2022 the sailboat chicane (Chapter 9) will allow us to overcome the single species limitations of FFTB and FACET to demonstrate high-gradient acceleration of a positron beam in a plasma wake driven by an electron beam. This is a critical step in assessing the viability of the staged approach to a compact energy frontier electron-positron collider as exemplified in our concept recently developed prior to the 2013 Community Summer Study [i]. Staging issues common to accelerating both electrons and positron such as timing, alignment, beam combining and separation will be studied in detail using an independent witness bunch injector as described in

Section 10.3. The flexibility of independent drive and witness beams will allow us to optimize the current profile of the individual pulses to maximize the energy gain and efficiency of the PWFA process.

Answering these important questions through experiments will be the main goal of the plasma wakefield accelerator research program at FACET-II.

### 3.1.2 The High Transformer Ratio Problem

The E200 experiment currently underway at FACET relies on significant beam loading to flatten the accelerating field, [ii] thereby ensuring that the particles in the trailing beam gain energy uniformly. This results in a narrow energy spread. Beam loading causes local damping of the wake such that the energy of the drive beam is efficiently transferred to the trailing beam via the wake. However beam loading leads to an effective reduction of the transformer ratio, [iii] which is defined as  $T = E^+/E^-$ , where  $E^+$  and  $E^-$  are the magnitudes of the accelerating and the decelerating fields, respectively.

In the linear regime of the PWFA, the unloaded wake produced by a symmetric beam has a transformer ratio of 2. In the blowout or the bubble regime shown in Figure 2-1, for particles in the tail of the one-bunch case (blue curve)  $T$  is much greater than 1. When the wake is loaded by the trailing bunch, however,  $T$  can be reduced to 1 or less (red and green curves) as shown in Figure 2-1b. This means that with the current 20 GeV FACET drive beam we expect the energy gain of electrons to be equal to or less than 20 GeV.

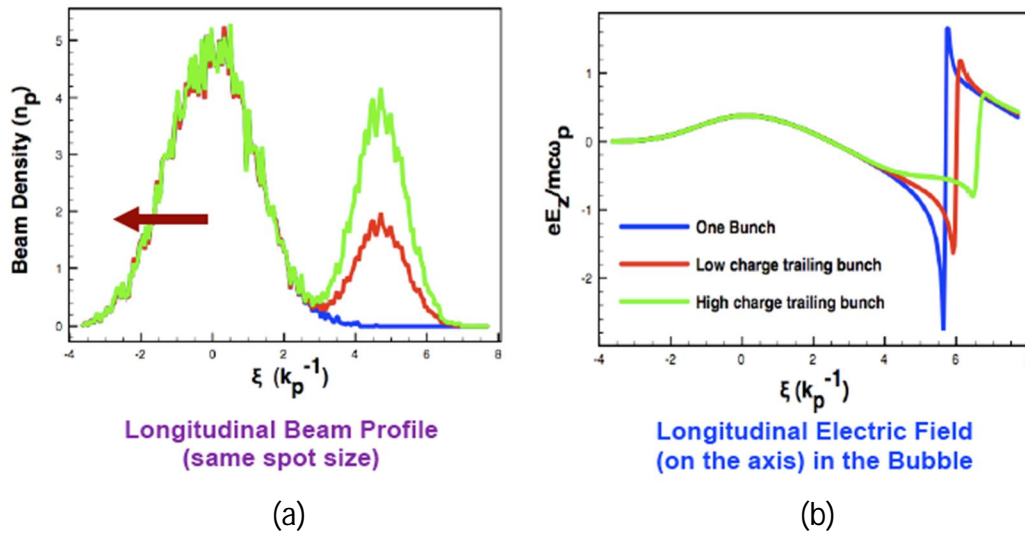


Figure 2-1: The wakes produced in plasma can have a dramatically different transformer ratio depending on the extent of the beam loading by the trailing bunch. (a) Shows the three pulse shapes used to produce the wakes and (b) shows the line out of the longitudinal electric field of the excited wake. The transformer ratio is the ratio of the peak decelerating (peak of the positive green curve) to the peak accelerating (peak of the spiky negative curves) field. (Courtesy Weiming An, UCLA)

Cost considerations of a future PWFA-based linear collider indicate that the primary beam should have a charge of several nC and a beam energy of several GeV. [iv] This allows us to design a single PWFA stage with a beam-loaded transformer ratio of at least 3. This means that the drive linac for a future PWFA-based linear collider needs to deliver 5 or 10 GeV drive pulses with 4 or 8 nC of charge while adding 15 to 30 GeV per stage to the beam that is being accelerated. This concept requires about 20 stages to reach an energy of 1 TeV. We can accomplish this using one of two approaches.

In the first approach we break the assumption of a symmetric drive beam as shown in Figure 2-2(a). If, instead of using a temporally Gaussian current profile, we shape the beam so that it is bi-Gaussian with a longer rise and a sudden fall, then the unloaded transformer ratio can be increased to a value much greater than 2. As can be seen in Figure 2-2, if the drive beam has a linear rise over 100  $\mu\text{m}$  followed by a sharp drop over 1  $\mu\text{m}$  the fully loaded transformer ratio can be as high as 8. With a more gradual fall time, T becomes smaller but even for a 5- $\mu\text{m}$  fall time, a T of 4 appears feasible. It is therefore possible that a 10 GeV drive beam could add up to 40 GeV per electron to the trailing beam.

There are of course many challenges to realizing such a result in practice. We need to understand how to precisely craft the drive beam pulse shape and how to produce such a high charge and transversely compact trailing beam and load it in the wake with sub-micron accuracy. We do not know whether the drive and trailing beams will be stable or if the beams will be susceptible to the hosing instability.[v] Answering these questions will be the prime goal of exploring this idea.

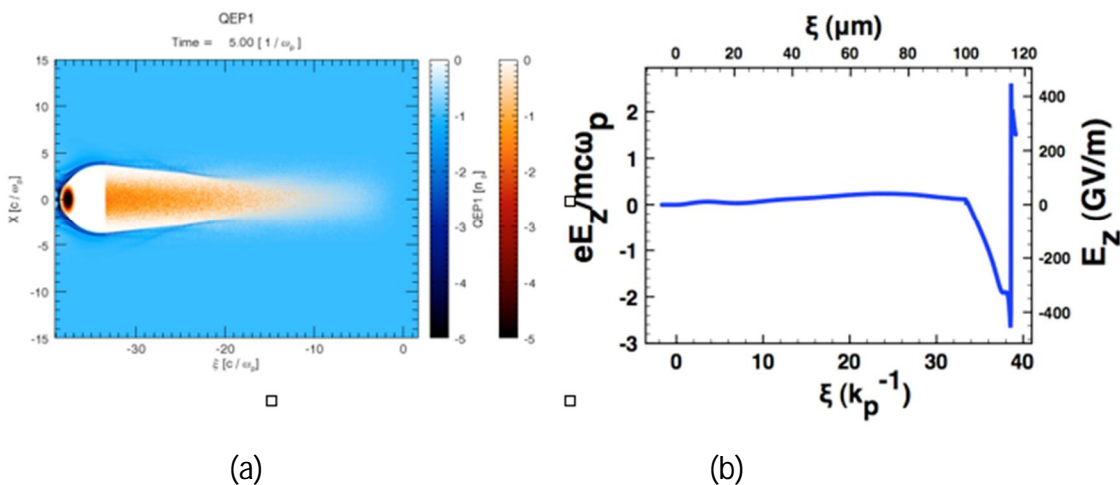


Figure 2-2: The idea behind generating high transformer ratio wakes using a shaped drive beam. (a) beams with the wake structure and (b) the on axis electric field showing a near uniform decelerating field and a highly nonlinear accelerating spike soon after the beam has entered the plasma. In this case  $T=8$ . Drive Beam Parameters:  $Q = 6 \text{ nC}$ ,  $\sigma_r = 5 \mu\text{m}$ ,  $L_z = 100 \mu\text{m}$ ,  $\epsilon_N = 5 \text{ mm mrad}$ ,  $E = 10.0 \text{ GeV}$ . Trailing Beam Parameters:  $Q = 0.288 \text{ nC}$ ,  $\sigma_r = 2 \mu\text{m}$ ,  $\sigma_z = 1 \mu\text{m}$ ,  $\epsilon_N = 1.0 \text{ mm mrad}$ ,  $E = 100 \text{ MeV}$ . Distance between two beams:  $12.5 \mu\text{m}$ . Plasma Density  $n_p = 3.17 \times 10^{18} \text{ cm}^{-3}$ . The beams propagate in a pre-ionized plasma and  $k_p^{-1} = 3 \mu\text{m}$ . (Courtesy Weiming An, UCLA)

Although for linear wakes that are excited by symmetric bunches  $T$  is less than equal to 2, it can be shown that in a certain regime [vi] of the fully blown-out wake,  $T = k_p \sigma_z / \Lambda^{1/2} > 2$ . Here  $k_p$ ,  $\sigma_z$  and  $\Lambda$  are wake wave number, rms bunch length and charge per unit length, respectively. Thus by appropriately optimizing the plasma density for a given charge and bunch length it is possible to achieve unloaded  $T \gg 2$  and a loaded  $T$  of  $>2$ . The goal here would be to use the 10 GeV FACET-II beam to add 30 GeV per particle to the electrons in the trailing beam over a distance of less than a meter while extracting more than 90% of the drive beam's energy. Figure 2-3 shows such a case where the loaded  $T$  is about 3. The FWHM energy spread of the trailing bunch is still a only few percent.

To load these wakes we need trailing beams to be much shorter than the drive beam and these must contain a significant amount of charge to flatten the wake so that the energy spread is narrow. The current approach to getting such a drive beam/trailing beam structure is to collimate a portion of an appropriately chirped beam in the dispersive plane and then to partially recompress the beam. [vii] In this process, however, a significant amount of original beam charge is lost and the drive beam/trailing beams are tens of  $\mu\text{m}$  long. These lower charge, longer bunches require a longer and lower density preformed plasma in the current E200 experiment.

However, FACET-II would be able to supply electron bunches that contain up to 5 nC of charge. This opens the possibility of producing a drive beam/trailing beam configuration with an adequate amount of peak current in each to self-ionize the gas. We will therefore be able to produce the wake with the drive pulse and beam-load the wake with the trailing pulse. An example of such a case is discussed in detail in Ref. (2) and will in fact be one of the first experiments to do at FACET-II when the witness injector is complete. The drive beam will have an rms bunch length of  $30\mu\text{m}$  and contain  $3 \times 10^{10}$  electrons, while the trailing bunch will have a bunch length of  $10\mu\text{m}$  and contain  $1 \times 10^{10}$  electrons. The separation between the two bunches will be  $115\mu\text{m}$  and both bunches will be focused to a spot size of  $3.3\mu\text{m}$  in a  $1 \times 10^{17}\text{cm}^{-3}$  Li vapor. In this case, the energy should double from 10 to 20 GeV in just 30 cm.

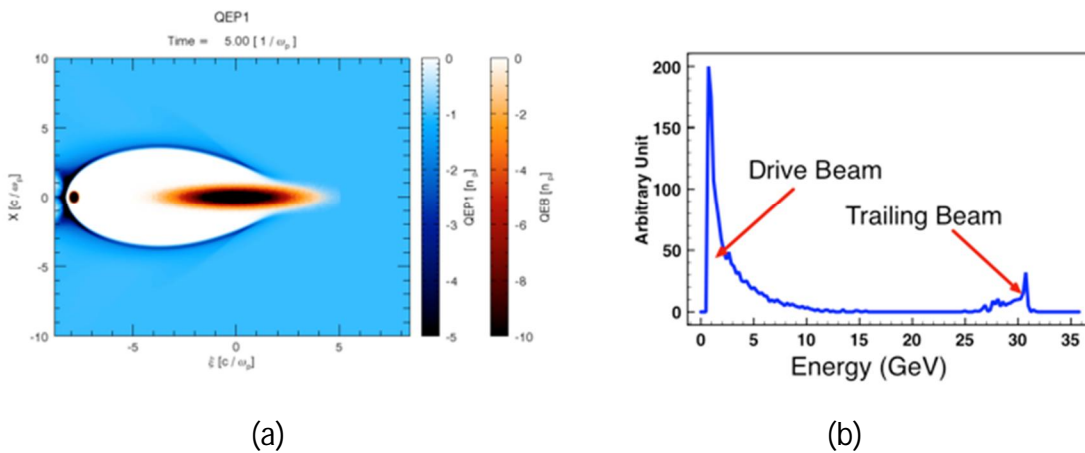


Figure 2-3: Generation of fully loaded transformer ratio wakes of 3 using the FACET-II beam. (a) shows the beams and the wake and (b) shows the energy spectrum of the two beams after just 26 cm. Drive Beam

Parameters:  $Q = 4 \text{ nC}$ ,  $\sigma_r = 5 \text{ }\mu\text{m}$ ,  $\sigma_z = 20 \text{ }\mu\text{m}$ ,  $\epsilon_N = 5 \text{ mm mrad}$ ,  $E = 10.0 \text{ GeV}$ . Trailing Beam Parameters:  $Q = 0.288 \text{ nC}$ ,  $\sigma_r = 2 \text{ }\mu\text{m}$ ,  $\sigma_z = 2 \text{ }\mu\text{m}$ ,  $\epsilon_N = 1.0 \text{ mm mrad}$ ,  $E = 100 \text{ MeV}$ . Distance between two beams:  $93.5 \text{ }\mu\text{m}$ . Plasma Density  $n_p = 2.0 \times 10^{17} \text{ cm}^{-3}$ . The beams propagate in a pre-ionized plasma. (Courtesy Weiming An, UCLA)

The higher transformer ratio experiments need trailing bunches on the order of  $2 \text{ }\mu\text{m}$  rms with sub 100 nanometer emittance and a significant amount of charge. It is not easy to achieve all these requirements with a few femtosecond jitter between the drive and the trailing beam. Fortunately, there are other possible methods for generating such a trailing beam in situ without any loss of charge in the drive beam that can be developed at FACET-II. Below we discuss two different methods that we would like to explore on FACET-II for generating suitable beams for injection into a PWFA that is operating in the high transformer ratio mode.

### 3.1.3 Generation of super- high brightness beams

#### 3.1.3.1 Density down-ramp injection using beam parameters at FACET-II

A sudden density transition from a high-to-low-density region traps plasma electrons in the wake. [viii] Even a relatively gradual density transition can trap electrons as the wavelength of the wake adiabatically increases. [ix] We have examined this so-called down-ramp injection, via 3D particle-in-cell (PIC) code simulations, using the FACET-II beam driver with a charge of  $5 \text{ nC}$ , a transverse emittance of  $5 \times 5 \text{ }\mu\text{m}$ , an energy of  $10 \text{ GeV}$  and a spatial size of  $10 \times 10 \times 10 \text{ }\mu\text{m}$ . Plasma density is varied from  $2 \times 10^{18} \text{ cm}^{-3}$  to  $1.5 \times 10^{18} \text{ cm}^{-3}$  with a down-ramp length of  $115 \text{ }\mu\text{m}$ .

Figure 2-4(a) shows the wake excited in the down-ramp and the trapped beam in this wake. The density distribution shows that the injected particles have a “head” with a relatively larger emittance that forms a halo around a beam core with a smaller emittance. To eliminate the particles of the beam halo, we just take the 95% electrons into account. The emittance of the beam core is  $\epsilon_{n,0.95} 70 \times 100 \text{ nm}$  as shown in Figure 2-4(b). The beam charge, peak current and brightness are  $580 \text{ pC}$ ,  $47 \text{ kA}$  and  $1.4 \times 10^{19} \text{ A/rad}^2\text{m}^2$  respectively. The emittance of the beam head is much larger, i.e.  $\epsilon_{n,0.95}$  are  $630 \times 590 \text{ nm}$ . The beam charge, peak current and brightness of the particles in the beam head are  $610 \text{ pC}$ ,  $107 \text{ kA}$  and  $2.9 \times 10^{17} \text{ A/rad}^2\text{m}^2$  respectively. Clearly for these parameters, there is a trade-off between current and brightness of the core and head.

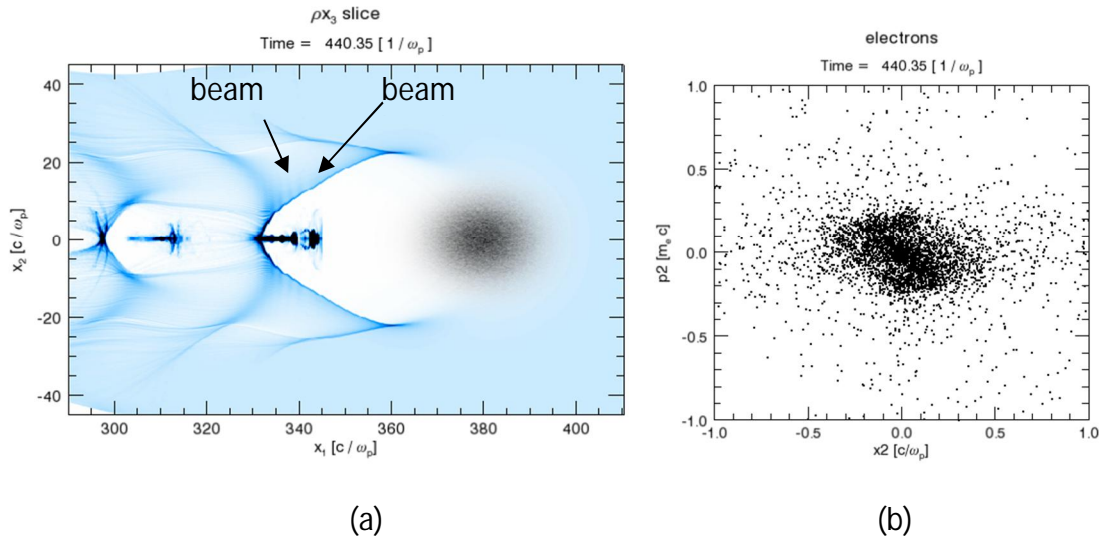


Figure 2-4: Simulation results of density down ramp injection with a 5 nC,  $10 \times 10 \times 10 \mu\text{m}$  beam driver. (a) electron density distribution (b)  $x_2$ - $p_2$  phase space of the beam core. The unit simulation length in this figure is 1 micron. (Courtesy Fei Li and Wei Lu Tsinghua University & UCLA)

The total emittance of the beam can be further reduced if the drive beam charge is lower. We next use a drive beam with spatial size  $10 \times 10 \times 10 \mu\text{m}$ , but with a lower charge of 1 nC. The plasma density is varied from  $2.9 \times 10^{17} \text{cm}^{-3}$  down to  $2.2 \times 10^{17} \text{cm}^{-3}$  and the down ramp length is  $260 \mu\text{m}$ . The results of this simulation are shown in Figure 2-5. The emittance of the total beam is now  $120 \times 120 \text{nm}$ . The beam charge, peak current and brightness are 230 pC, 27 kA and  $3.8 \times 10^{18} \text{A rad}^2\text{m}^{-2}$ , respectively. Thus there appears to be a trade-off between the drive beam charge and the trailing beam brightness that is counter-intuitive and calls for experimental investigation.

How can such an experiment be realized at FACET-II? The 5 nC beam used in the first simulation is capable of field-ionizing hydrogen gas, but a 1 nC beam requires a laser-ionized column of hydrogen. At the upstream end of a tube of hydrogen at the appropriate pressure we place a thin gas cell containing higher pressure gas with an approximately 200 micron entrance and exit holes to create the necessary density ramp. [x, xi] Such cells have been successfully used in injector- accelerator experiments done with intense laser pulses. The beam trapping preferentially occurs in the down-ramp and the electrons are then accelerated in the accelerator portion of the wake excited in the approximately 30 cm long ionized gas column in the downstream tube. The attraction of this method is that it is simple and in principle jitter free. The emittance, energy and charge of the accelerated beam can be measured by changing the length of the tube and the scale-length of the density ramp. If this technique can be perfected, it will give beam emittances that are smaller than those achieved by state-of-the art methods.

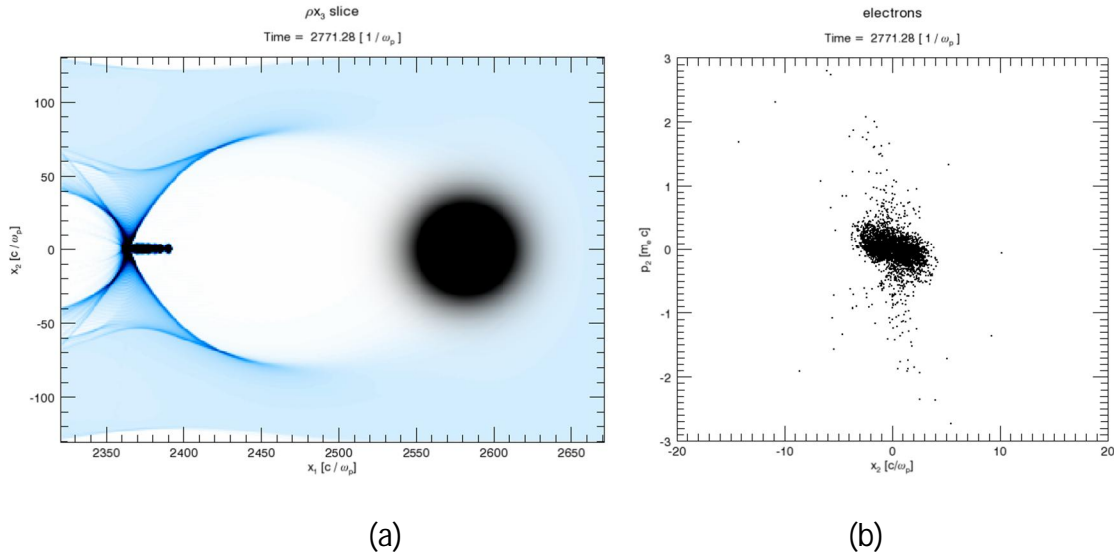


Figure 2-5: Simulation results of density down ramp injection with a 1.1 nC,  $10 \times 10 \times 10 \mu\text{m}$  beam driver. (a) electron density distribution (b)  $x_2$ - $p_2$  phase space of the total bunch. The unit simulation length in this figure is 1/3 micron. (Courtesy Fei Li and Wei Lu, Tsinghua University & UCLA)

### 3.1.3.2 Electron Injection by Transversely Colliding Laser Pulses

Generation of low emittance electron bunches will be tested at FACET using the so-called Trojan Horse scheme, [xii] wherein a longitudinally co-propagating laser pulse ionizes and injects electrons inside an electron beam driven wake. At FACET-II we propose to test a variation of this scheme that has the potential to generate the highest brightness beams to-date. [xiii] We call this the transversely colliding laser injection method. Here ultra-bright electron bunches are produced using ionization injection triggered by two transversely colliding laser pulses inside a beam-driven wake. The relatively low intensity lasers are polarized along the wake axis and overlap with the wake for a very short time. The result is that the residual momentum of the ionized electrons in the transverse plane of the wake is much reduced and the injection is localized along the propagation axis of the wake. This minimizes both the initial “thermal” emittance and the emittance growth due to longitudinal phase mixing. This concept can be successfully tested through 3D particle-in-cell (PIC) simulations. In Figure 2-6 we show the injection process of helium electrons by two colliding laser pulses in a wake formed in a partially ionized He plasma by an electron beam. We show that ultra-short ( $\sim 8\text{fs}$ ) high-current (0.4kA) electron bunches with normalized emittance of 8 and 6 nm in the two planes and brightness greater than  $1.7\text{e}19 \text{ Amp rad}^{-2} \text{ m}^{-2}$  can be obtained for realistic parameters.

The transverse colliding pulse is inherently more complex than the density down ramp injection. We now have to deal with femtosecond synchronization of two laser ultra-short laser pulses that must overlap with one another within a micron inside the wake. In either scheme, electrons are accelerated to multi-GeV levels within roughly 10 centimeters. How does one measure the emittance of such a beam? Perhaps the most conclusive demonstration that the beam has a brightness exceeding  $10^{19} \text{ Amp rad}^{-2} \text{ m}^{-2}$  is to send this beam through a section of

the LCLS undulator and measure SASE gain. This is currently being studied through integrated PIC and FEL simulations.

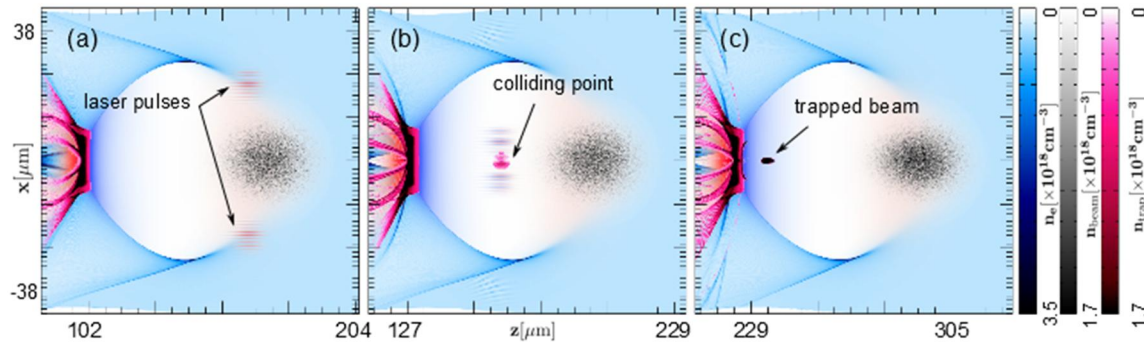


Figure 2-6: Snapshots from PIC code simulations illustrating the transverse colliding pulse injection of helium electrons into the ion cavity. Snapshots (a) to (c) show the charge density distribution of driver beam, wake electrons and helium electrons at three different times (a)  $\sim 80$ fs before laser pulses collision (b) around laser pulses' collision time (c)  $\sim 200$ fs after collision when the injected electrons become trapped in the wake. (Courtesy Fei Li and Wei Lu Tsinghua University & UCLA)

### 3.1.4 Determining the repetition rate of a single module for stable operation and staging of two PWFA modules.

The repetition rate requirements of a future PWFA depend on the application. [xiv] For instance a PWFA-based X-FEL may operate at one kHz whereas a future linear collider may need to operate at 10 kHz with a CLIC-like drive bunch structure. Different drive beam train formats can be tested at FACET-II to see what ultimate repetition rates are acceptable. FACET-II has high charge bunches compared to FACET which means that we can probably operate with field-ionized plasmas of noble gases which can be flowed and replenished in between shots. This could be tested at FACET-II.

The staging of two PWFA modules is a far more challenging problem. Any misalignment between the drive beam in the second stage and the accelerating beam from the first stage leads to strong radiation loss and emittance growth. [xv] This problem has to be addressed at some point and engineering solutions have to be developed.

### 3.1.5 Summary

The PWFA program on FACET-II seeks to demonstrate a high efficiency, high transformer ratio PWFA stage that gives a 20-30 GeV energy gain while generating an electron beam with high charge, low energy spread and low transverse emittance. While working towards this goal, we will develop new beam injection and diagnostic techniques. We have considered two new injection schemes that allow for the full use of the FACET-II drive beam, as opposed to current experiments that require spoiling the FACET drive beam. One is to use the natural injection that occurs in a density down ramp and the other is to use active injection via counter-propagating laser pulses. Repetition-rate limitations have not yet been addressed in any plasma wakefield

experiments. High-efficiency transfer of drive-beam energy to the trailing beam will likely be necessary for high luminosity colliders. Additionally, particle-beam-ionized plasmas can be rapidly replenished via laminar flow of fresh gas on a tens of kHz time scale. FACET-II possesses unique capabilities that enable these studies.

## 3.2 Physics of positively charged drive beams for PD-PWFA

### 3.2.1 Motivation for CERN Experiments with Protons

LHC proton bunches are the only plasma wakefield drivers that carry enough energy to produce an ILC type electron or positron bunch in a one or few plasma stage. Existing laser pulses and electron particle beams do not carry enough energy. ILC bunches of  $2 \times 10^{10}$  particles at 1TeV carry about 2 kJ. For reference, an LHC bunch at 7TeV and with  $10^{11}$  protons carries over 100kJ. Protons also have a large mass, can have a very high energy ( $\sim$ TeV/ $p^+$ ) and are so “stiff” that bunches can propagate over many meters of plasma without significant transverse size change. Therefore, a large average accelerating gradient (1GeV/m or more) could be sustained over the entire acceleration length without suffering from the gradient dilution arising when staging is required [xvi]. Gradient dilution occurs because of the drift distance necessary between stages to seed the next drive bunch into the next plasma section and to capture and re-focus the witness bunch. It can vastly exceed the length of each stage and drastically decrease the average accelerating gradient.

Operating at lower peak gradient also means at lower plasma density since the maximum accelerating field increases with the square root of electron density (that is,  $E_{\max} \sim n_e^{1/2}$ ). This also means that the size of the accelerating structure or plasma density perturbation is larger, as both scale with the inverse square root of electron density (in 3D,  $\sim \lambda_{pe}^3 \sim (n_e^{-1/2})^3$ ). This reduces the requirements in bunch longitudinal and transverse (focusing) compression ( $\sigma_r, \sigma_z < \lambda_{pe}$ ) and in temporal and spatial alignment. Matching of the bunch transverse size to the weaker plasma focusing field ( $E_r$ ), which scales with the plasma density is easier since the matched size also increases with decreasing density ( $\sigma_r \sim n_e^{1/4}$ ). This is true even for very low emittance bunches.

### 3.2.2 PD-PWFA Physics experiments at SLAC with electron and positron bunches

Short proton bunches, on the order of 100  $\mu$ m, are suitable for driving wakefields with large amplitude (1GV/m or more), but these are not currently available. Initial experiments will be performed around 2015 at CERN with longer bunches in the self-modulation instability regime. [xvii] These experiments use bunches of length  $\sigma_z = 12$ cm with plasma wavelength  $\lambda_{pe} = 1.5$ mm.

High energy ( $\sim 20$  GeV) positron bunches are much less “stiff” and can self-modulate in only a few cm whereas CERN SPS proton bunches ( $\sim 450$  GeV) need meters of plasma.

In addition, it is well known that plasmas respond very differently to negatively and positively charged particle bunches. This was clearly demonstrated in the PWFA experiment performed at

the SLAC FFTB. [xviii, xix,xx] Even in the self-modulation regime, plasma behavior is quite different as soon as the nonlinear, high-gradient regime is reached, as was demonstrated in numerical simulations (see Figure 2-7). [xxi]

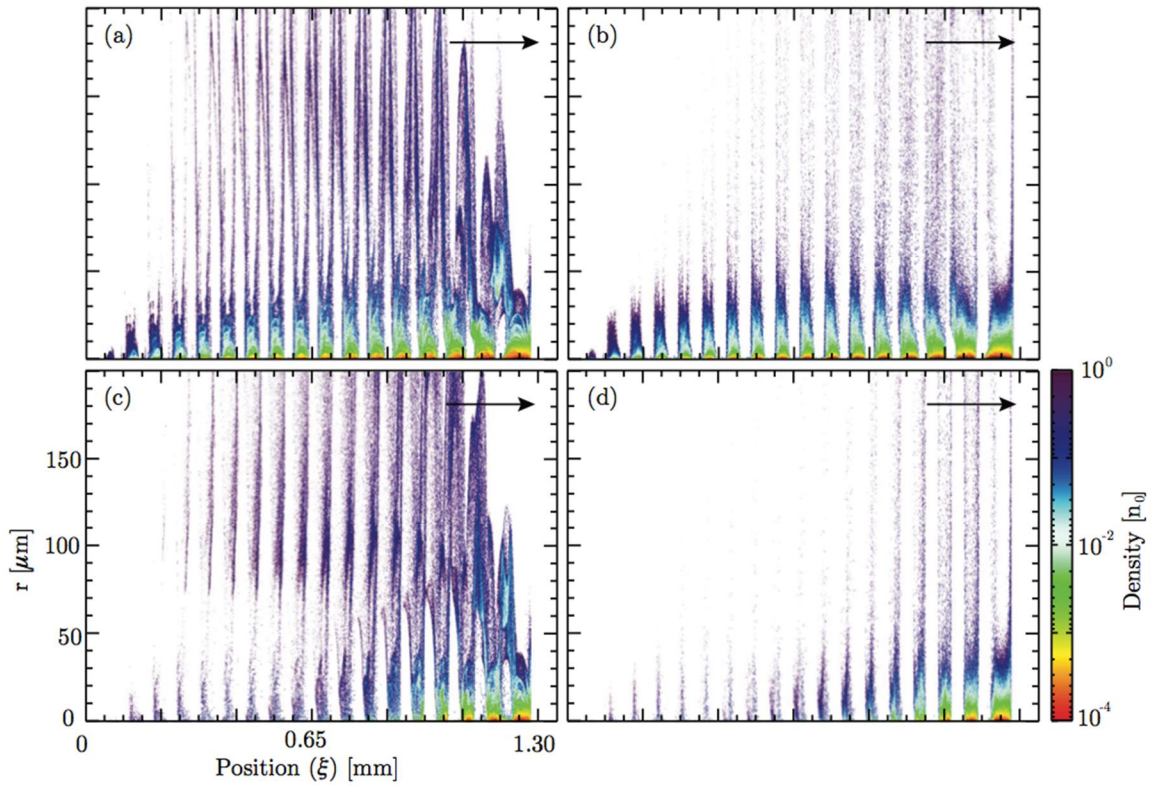


Figure 2-7: Electron (top) and positron (bottom) bunch density after propagation of 10 cm (left) and 1 m (right) plasma with a density of  $2.3 \times 10^{17} \text{ cm}^{-3}$ .

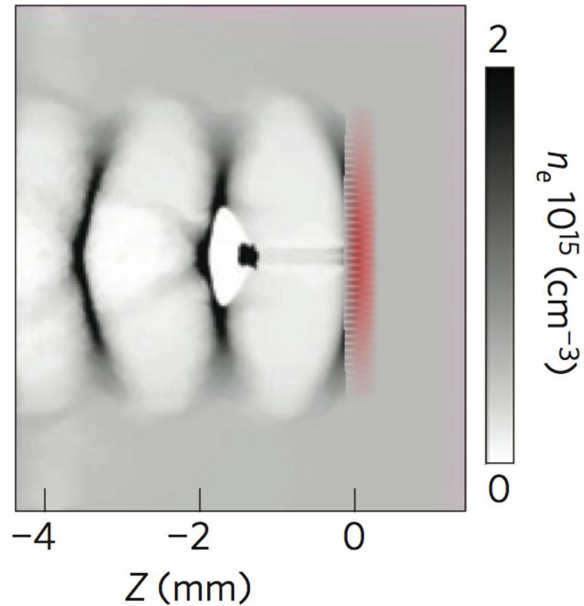


Figure 2-8: Plasma density perturbation driven by a short ( $\sigma_z=100 \mu\text{m}$ ) and wide ( $\sigma_r=430 \mu\text{m}$ ) proton bunch. The proton bunch density is indicated in red while the witness electron bunch to be accelerated is shown in black.

Short positron bunches can be produced at SLAC and are therefore the ideal candidate to test the concept of a PWFA stage driven by a , positively charged bunch shorter than the plasma period. In particular, the transverse evolution of the drive bunch along the plasma is a concern since there is no equivalent of the bubble regime that exists for negatively charged particle bunches. Simulations indicate that positively charged bunches need to be shaped like pancakes, in contrast to the pencil shape of electron bunches, in order to drive wakefields towards the blowout regime (see Figure 2-8). [xxii] In addition these simulations also indicate the real blowout is difficult to reach. This could lead to emittance growth of the accelerated witness bunch. The conditions appear to be much less favorable for positively charged bunches than for negatively charged bunches in the self-modulated PWFA regime (see Figure 2-7). Simulations clearly show that the loss of drive particles along the plasma is significantly larger with positively charged bunches. This leads to lower wakefield amplitudes and larger dephasing between the wakefield structure and the drive bunch and thus also with the accelerated bunch. The situation seems worse when approaching the nonlinear PWFA regime.

One to one comparisons between the case of an electron and a positron bunch could clearly show these differences and help in determining an optimum regime of operation with short, positively and negatively charged bunches. This difference will be evidenced by measuring the energy loss and gain by drive bunch particles, as well as by measuring the drive bunch self-modulation. In addition, the availability of a short, trailing electron bunch to witness the wakefields with a variable delay with respect to the drive bunch is a great asset.

Simulation of the self-modulation PWFA regime is much more challenging than that of the short bunch PWFA regime and numerical codes have not been benchmarked against experimental results.

The availability both electron and positron bunches long and short would definitely give access to a number of PWFA regimes that have never been accessed before, which will drive new discoveries in PWFA physics. Existing plasma-based PWFA designs (see section 3) use electron beams to drive the wakefields. In order to create a next-generation electron/positron collider we need to be able to accelerate the positron bunch directly.

Therefore the availability of a witness bunch, whether electron or positron, with independently controllable parameters, would greatly enhance the relevance of the results to advanced accelerators. The actual acceleration of a witness bunch with a bunch length well below the plasma wavelength could be directly tested, both in the self-modulated and in the short bunch PWFA regime. In particular, we could test the acceleration of a positron bunch in the wakefields driven by an electron bunch. This is the favored scheme for the acceleration of a positron at high-gradient in a plasma. However, no clear parameter set that can produce a high quality positron bunch exists. The availability of a facility to test this scheme would no doubt generate the new and original ideas needed.

The availability of an electron witness bunch produced by an RF photo-injector gun would allow for exquisite and independent control of the witness bunch parameters (charge, length, timing, and transverse size), a required condition for the demonstration of beam loading producing narrow final energy spread and for optimization of the energy transfer efficiency.

Results with a positron drive bunch would bring early and important results relevant to the longer-term plans with a proton bunch as a driver. Producing suitable, short proton bunches requires very significant efforts and maybe even the design of a dedicated circular machine. Therefore, establishing the physics of this scheme with positron bunches will provide important validation.

### 3.3 PWFA Based on High Brightness Photoinjector-derived Electron Beams

In this section, we summarize the new physics that is made possible by the introduction of very high brightness electron drivers in PWFA experiments. The scenarios presented take advantage of the improved compressibility of photoinjector beams, particularly at low charge, as well as superior focusability of low emittance systems. These attributes permit three new experimental initiatives in FACET-II: teravolt-per-meter plasma wakes with ultra-short beams; ion motion experiments (with associated implications for fusion physics); and exploration of the quasi-nonlinear regime of the PWFA. We now recount briefly the case for investigating each of these topics at FACET-II.

#### 3.3.1 TV/m PWFA Using Femtosecond Beams

Scientists have recently proposed using low charge ( $Q$ ), in the pC range, as a path to achieving GeV-class beams that may be compressed down to hundreds of attoseconds. [xxiii] Further, these beams are predicted to have very low transverse emittance, and thus unprecedented brightness. This proposal [xxiv] addresses two challenges in the x-ray SASE FEL. It breaches the fs frontier in x-ray pulse length, and should also allow single-spike x-ray SASE FEL. [xxv] Both

features are critical for resolving properties of atomic and molecular systems at the spatial and temporal scales relevant to electronic motion. Low charge operation is therefore important for advancing both FEL capabilities and fundamental beam physics.

Recent experimental work at the SLAC Linear Coherent Light Source (LCLS) focused on generating compressed beams with short pulses. In initial tests, 20 pC beams were compressed to rms duration  $\sigma_t \cong 2$  fs, while achieving transverse normalized emittances of  $\varepsilon_{n,x} = 0.14 \mu\text{m}$  and  $\varepsilon_{n,y} = 0.4 \mu\text{m}$  at an energy  $U_b = 14$  GeV. This beam, having high peak current,  $I \sim 8$  kA, and low emittance is predicted to produce nm-wavelength FEL pulses in the single-spike regime. [xxvi] We propose to use similar beams at FACET-II to generate an extremely high field PWFA.

Beams having short duration can produce coherent excitations with frequency components up to a cut-off of  $\omega_m \sim \sigma_t^{-1}$ . Further, in the context of PWFA, as with all Cerenkov-class interactions, the amplitude  $E$  of the radiated field scales as  $\propto N_b \omega_m^2 \cong N_b / \sigma_t^2$ , where  $N_b$  is the number of particles in the beam. To maximize the wake amplitude, the maximum excitation frequency must equal the plasma frequency,  $\omega_m = \omega_p$ , giving the optimization condition  $\omega_p \sigma_t \cong 1$ . This scaling has been investigated experimentally, [xxvii,xxviii] theoretically and computationally, [xxix, xxx] and its validity in application even in the nonlinear “blowout” regime [xxxii] is well understood. PWFA operation in the blowout regime is desired, as the plasma electrons are all evacuated from the beam channel, producing acceleration dependent only on longitudinal position  $\xi = z - v_b t$  in the beam channel, where  $v_b \cong c$  is the beam  $z$ -directed velocity. Further, the nominally uniform ion density makes focusing linearly dependent on radial position  $r$  relative to the beam axis. Both of these attributes of the wake forces are deemed necessary for producing high quality beams with the phase space density demanded by advanced applications in high-energy physics and at x-ray FELs.

For the LCLS 20 pC beam scenario,  $\omega_p \sigma_t \cong 1$  yields a plasma electron density  $n_0 = [4\pi r_e (c\sigma_t)^2]^{-1} \cong 7.8 \times 10^{19} \text{ cm}^{-3}$  corresponding to a gas density of several atm. We can estimate whether this case accesses the blowout regime by evaluating the ratio of beam electrons to plasma electrons found within a volume of a cubic plasma skin-depth ( $k_p^{-1} = c/\omega_p$ ),  $\tilde{Q} \equiv N_b k_p^3 / n_0 = 4\pi k_p r_e N_b$ . [xxix] In our case we have  $\tilde{Q} \cong 7.4$ ; a value exceeding unity indicates the blowout regime may be achieved. To access the blowout regime we must also focus the beam to a rms size  $\sigma_x$  smaller than a skin-depth,  $k_p \sigma_x < 1$ . The self-consistent equilibrium beam size in the plasma arising from PWFA ion focusing is a function of the equilibrium  $\beta$ -function,  $\beta_{eq} = \sqrt{2\gamma} / k_p$  as  $\sigma_{x,eq} = \sqrt{\beta_{eq} \varepsilon_{nx} / \gamma}$ . For our current parameters,  $\beta_{eq} = 140 \mu\text{m}$  and  $\sigma_{x,eq} = 45 \text{ nm}$ , and thus  $k_p \sigma_x \approx 0.075$ . The beam density associated with this extremely bright beam in the dense plasma is  $n_b = 6.5 \times 10^{21} \text{ cm}^{-3}$ , giving  $n_b / n_0 \approx 84$ , a highly nonlinear blowout scenario. To gauge the strength of the plasma wakes in initial particle-in-cell (PIC) simulations we use a slightly initially mismatched injected beam, to  $\sigma_x \cong 77 \text{ nm}$  ( $n_b / n_0 \approx 28$ ). These simulations were carried out using the 2D EM PIC code OOPIC, [xxxii] with the predictions for the longitudinal plasma wake  $E_z(r, \xi)$  shown in Figure 2-9. This simulation produces

unprecedented large fields, in excess of 1.3 TV/m. This field amplitude is also remarkable in that it is enormous even by internal atomic physics standards. Indeed, the collective field such beams can readily ionized matter, thus allowing both plasma formation, and a unique probe of atomic physics in an extreme field limit. The size of  $E_z$  is not surprising, however, in that the fields at the beam edge before the plasma entrance is estimated as  $E_{r,\max} \cong eN_b / 2(4\pi)^{1/2} \epsilon_0 \sigma_x \sigma_z = 1.5 \text{ TV/m}$ ; the maximum transverse field is roughly transformed to longitudinal field amplitude by the plasma response.

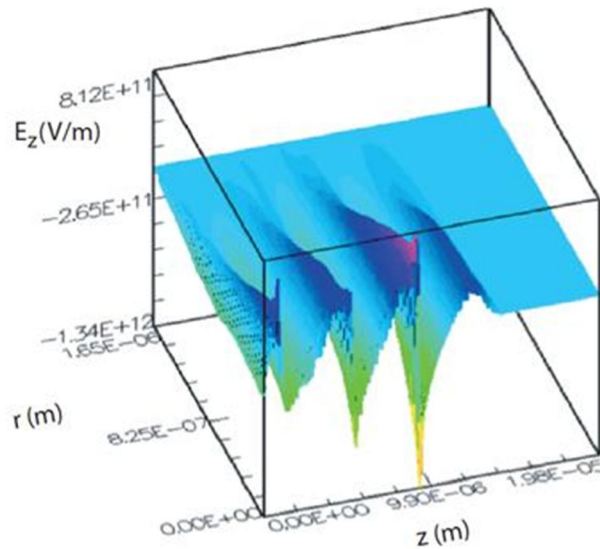


Figure 2-9: OOPIC simulation of PWFA, 20 pC, 2 fs beam case, showing TV/m wakes.

To produce the conditions for plasma creation and optimum plasma wake formation, we must implement an appropriate focusing scheme. Further, in order to consider implementing this experiment in a spatially-limited region such as FACET-II, we should make the focusing system as compact and easily implemented as possible. We may base the mini- $\beta$  optics on an ultra-high field gradient system based on permanent magnet quadrupoles (PMQs), similar to that developed for previous UCLA experiments on inverse Compton scattering. [xxxiii] This system, tunable by repositioning of quadrupoles, can achieve quadrupole gradients of over 700 T/m and has the further advantage of evading restrictions on performance due to geometric and chromatic aberrations without requiring complex sextupole correction schemes. With the PMQs arranged in a modified triplet configuration, [xxxiii]. ELEGANT simulations [xxxiv] indicate that we can focus the beam to  $\sigma_x = 130 \text{ nm}$ . This size is well suited for injection into the plasma, with a final  $\beta$  function of 1.2 mm. While this beam size is not matched to the plasma focusing, it is small enough to ionize the gas, and enter into an adiabatic focus, as shown in Figure 2-10.

The bare (no plasma) beam is compelling, as this beam allows electric field levels possibly as high as  $100 \text{ V/\AA}$ , into the range that accesses the barrier suppression ionization (BSI) regime [xxxv] in a wide variety of atomic species. This implies that the field strength at FACET-II makes it easier to create the desired plasma using the electron beam. In previous experiments at FACET that employed over an order of magnitude smaller fields, plasma formation was

attributed to tunneling ionization [xxxvi, xxxvii, xxxii]. Accessing BSI is an exciting possibility — a highly focused, multi-kA beam in and of itself is new instrument for performing fundamental atomic physics investigations. We will be able to use the very intense beams at FACET-II to expand upon existing research programs, such as the ultra-fast magnetic switching studies currently active at FACET, and study phenomena that have thus far been inaccessible.

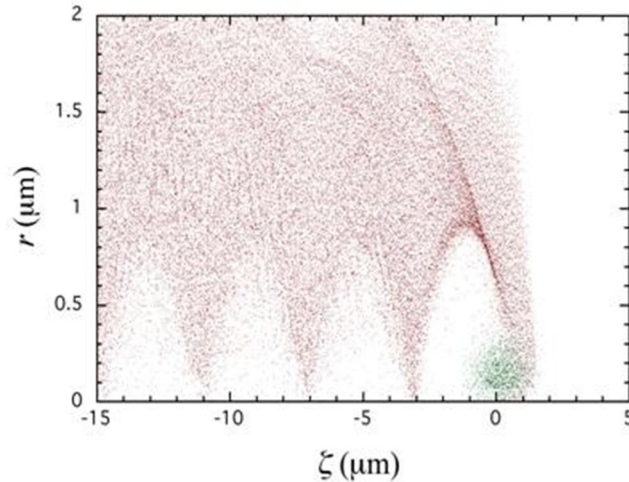


Figure 2-10: Beam (green) and plasma (red) electrons in simulation of LCLS 20 pC beam initially focused to  $\sigma_x=130$  nm passage through 3.15 atm  $H_2$  gas.

As a practical rather than fundamental concern, the self-consistent ionization of a high pressure gas by the beam fields must occur within hundreds of attoseconds to create the plasma within the appropriate time scale to allow the full amplitude plasma wakefields to develop. The UCLA PBPL team studied this computationally and theoretically and found it to be practical with the final focus discussed above. The method is straightforward using Li gas, and is possible even in hydrogen. [xxxviii]. It should be noted that with beams well below optical wavelengths in dimension, all signals from beam profile monitors are coherent, and coherent imaging techniques should be embraced .

### 3.3.2 Ion Motion in High Brightness Beam Drivers

The condition  $n_b > n_0$  is a defining characteristic of the blowout regime. Indeed, as seen above, the density of the high brightness driving beam in a PWFA may exceed  $n_0$  by several orders of magnitude. Under these circumstances, the beam’s electric field can produce relativistic plasma electron motion. [xxxix,xl] Additionally, this electric field is high enough that the ions may move significantly during the beam passage. For the parameters given by S. Lee, et al.,[xli] and quoted by Raubenheimer in his discussion of the implementation of a PWFA “afterburner” to boost the energy of a linear collider (LC) by at least a factor of two, [xlii]the ions can collapse towards the beam axis, causing a large, non-uniform ion density spike within the beam. This *ion collapse* has disastrous implications for preserving the transverse emittance of the accelerating beam, effectively negating the oft-claimed advantage of linear transport in the blowout regime. Thus the issue of ion motion is of critical importance in evaluating the viability of using the PWFA in a collider and other high brightness beam applications. [xliii]

The theoretical and computational analysis of the ion collapse problem has been performed at UCLA PBPL. [xliv] The phenomenon of ion collapse in the PWFA can be viewed in several useful ways. First, it is a form of wakefield, with as direct as possible coupling between the beam and its environment, in this case plasma electrons and ions that lie in the beam path. The fact that linear collider beams are of unprecedented density (similar to solid matter) means that they act as a *high energy density* driver of plasma motion. As such, the study of physical effects associated with plasma wakefields in such extreme scenarios represents an unprecedented opportunity in high field plasma physics. This frontier opens up a new application to an unrelated field, as the ions are simultaneously heated and confined by the application of the beam focusing fields. Thus, with appropriate choice of ionized species (i.e. deuterium and tritium), we may envision an alternate scenario for creating fusion-relevant plasma conditions.

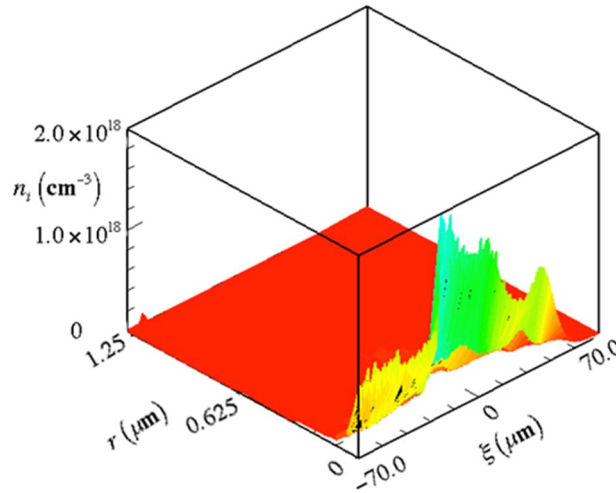


Figure 2-11: Surface plot of ion density distribution, as simulated by OOPIC showing increase in  $n_i > 200$  due to ion collapse (from Ref. 20)

To create the conditions for ion collapse at FACET-II, we concentrate on a large-charge scenario with the following beam parameters:  $Q = 3 \text{ nC}$ ,  $\epsilon_{n,x} = 3 \text{ } \mu\text{m}$ , with moderate compression to  $\sigma_t = 0.2 \text{ ps}$  ( $\sigma_z = 60 \text{ } \mu\text{m}$ ). Using  $\omega_p \sigma_t \cong 1$  we have a relatively low plasma density,  $n_0 \cong 8 \times 10^{15} \text{ cm}^{-3}$ , and a total phase advance for small amplitude ion oscillation in the beam's potential well of

$$\Delta\phi = \sqrt{\frac{Zr_a N_b \sqrt{2\pi\gamma}}{A\epsilon_{n,x}}} = \sqrt{\frac{Zr_a N_b}{A\epsilon_{n,x}}} (2\pi\gamma)^{1/4} \cong \frac{\pi}{2}$$

This phase advance indicates that the ions indeed *focus* inside of the driving beam. The first observable consequence of this ion collapse, which is illustrated in Figure 2-11, is that the transverse emittance of the trailing part of the drive beam increases dramatically.

Ion focusing not only may concentrate the ions, it may impart to them a large kinetic energy, thus providing temperatures similar to those in fusion plasmas. The maximum energy may be estimated from the potential at the beam's edge to be

$$q\Phi_{\max} = \frac{Zr_a N_b m_a c^2}{2\sqrt{2\pi\sigma_z\sigma_r}} r^2 \Big|_{\text{beam edge}} \cong \frac{Zr_a N_b m_a c^2}{2\sqrt{2\pi\sigma_z}}$$

For our parameters, this indicates that we may achieve energies near to 100 keV in a deuterium plasma, which is adequate for achieving D-T fusion. We may observe these particles in fusion events by allowing them to collide with a tritiated wall, for example, or by using an electrostatic energy analyzer. If we wish to confine the ions for a longer time ( $\Delta\phi \gg 1$ ) we can utilize a higher density gas, with density on the order of TV/m. Then, by increasing  $n_0$  by a factor of 10,000, the phase advance for ion oscillations is augmented by a factor of 100. In this case, the ion temperature achieved is expected to be nearly the same, in the range of 100 keV, as can be deduced from the expression for the potential given above.

### 3.3.3 The Quasi-Nonlinear Regime of the PWFA

The original form of PWFA proposed exciting wakefields through the use of relativistic electron bunches, which induce a small density perturbation in the plasma. Using the linearized equations of motion, continuity and Maxwell's equations, one can readily discern the basic dynamics of PWFA in the linear regime. While the simple harmonic plasma response allows the wakefields to be driven resonantly, a small density perturbation implies that plasma electrons persist both within the volume of the driving bunch and in the beam (driving and accelerating) region. Consequently, the fields experienced by the beams are non-ideal in both the radial and longitudinal directions. In the blowout regime of PWFA, as noted above, a high intensity beam excites nonlinear plasma oscillations, having amplitude-dependent period, and thoroughly evacuates a bubble of its plasma electrons leaving behind only the ions, with associated (up to the onset of ion motion) excellent quality transverse and longitudinal fields. These distinct advantages, however, come at the expense of a nonlinear plasma response that does not permit, for example, the use of pulse trains in future linear colliders [xxvii].

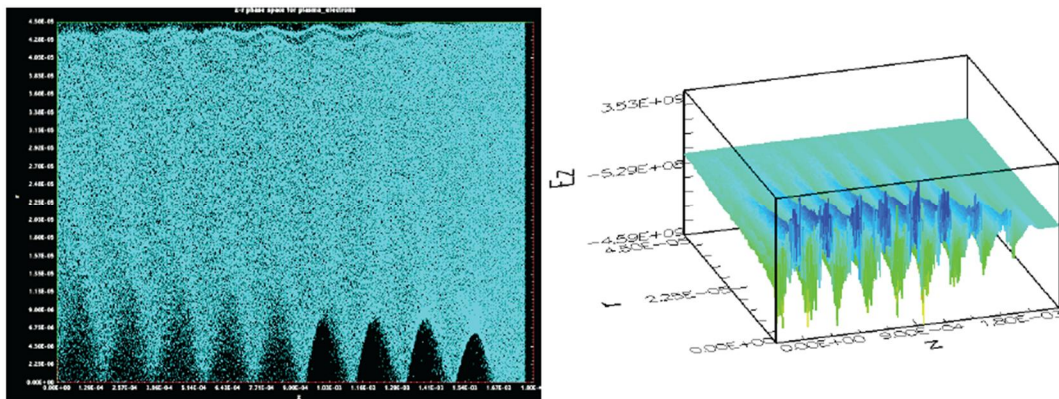


Figure 2-12 (Left) Plasma electron spatial ( $r, z$ ) response to a 4-beam pulse train with each beam having  $Q^- = 0.11$ , separated by  $\sigma_p = 190 \mu\text{m}$ , and (right) the associated longitudinal electric fields.

In order to envision large total charge acceleration needed for linear colliders, we must consider how to achieve blow-out while maintaining a resonant plasma response. Such a regime is accessed with high brightness beams, by restricting pulse trains to a total charge where  $\tilde{Q} < 1$ . With very low emittance beams, the beam density may permit blow-out conditions to be accessed even with low  $\tilde{Q}$ . This scenario is termed the *quasi-nonlinear regime*, and is the subject of large theoretical [xlv] and experimental [xlvi] interest, with first experiments now commencing at the Accelerator Test Facility (ATF) at Brookhaven National Laboratory. We show an example of quasi-nonlinear operation in Figure 2-12, in which a 4-pulse train with a periodicity equal to the linear plasma period resonantly excites a wave. This mode produces total plasma electron rarefaction in the region around the beam, similar to the blowout regime. In this case the normalized charge is 0.44, we have a constant plasma period of 190  $\mu\text{m}$  and beam charge per pulse is 16 pC. This is indeed an experimental design regime of interest to FACET-II. We can apply pulse-train chopping techniques to a photoinjector-enabled FACET-II (see Section Error! Reference source not found.) to create these high brightness, low emittance, and relatively low charge beams [xlvii]. The additional energy in the beam, and the ability to access shorter beam dimensions give FACET-II a large advantage over the present ATF configuration.

## 3.4 Trojan Horse Under dense Photocathode PWFA and follow-up applications

### 3.4.1 Introduction

Plasma acceleration at FACET aims for both maximized energy gain (e.g., in the E-200 experiment) as well as for dramatically increased beam quality, stability and tunability (E-210 experiment). These experiments and other advanced hybrid LWFA/PWFA strategies require a high-power laser system capable of ultra short, high-intensity pulses for preionization of the plasma, and highly controllable electron release in the wakefield to enable pump-probe measurements and many other applications.

At FACET, therefore, a ~10 TW, ~50 fs laser system is currently being installed. However, the synchronization obtainable at FACET at the interaction point between electron bunch and laser pulse is several hundreds of femtoseconds, mainly because of the thermal cathode and the large compression factor of the electron bunch. Such a jitter is unacceptable for many advanced experiments.

Installing a photoinjector and a high-power laser system at FACET-II would improve the expected jitter between electron bunch and laser pulse to probably less than 50 fs. Many experiments would profit greatly from such a reduced jitter, and others would become feasible in the first place. The proposed system would have potentially much higher maximum beam density and connected radial fields, allowing for extended self-ionization studies and extended acceleration lengths.

### 3.4.2 Advantages of excellent synchronization between electron beam driver from photocathode and low-energy Ti:Sapphire laser beam (~100 μJ)

One experiment that would profit massively from improved synchronization would be E-210, “Trojan Horse Plasma Wakefield Acceleration”, whose name alludes to the ancient tale where the Greek soldiers are hidden in the horse’s belly. This experiment depends on the strongly localized release of electrons inside a beam-driven plasma blowout. This localized release is done by focusing a co-propagating laser pulse to an intensity slightly above the ionization threshold of an additional gaseous component (for example, helium in a lithium plasma oven or the second ionization level of rubidium in a rubidium oven). Therefore the electrons would be released only in the arbitrarily small focal region of the laser pulse. Since this laser pulse only needs a maximum density of the order of  $10^{14-15}$  W/cm<sup>2</sup> in order to ionize this component, the electrons receive a very limited transverse kick by the transversely oscillating laser fields. At the same time, the electrons are accelerated in GV/m electric plasma fields in the forward direction, which results in transversally extremely cold electrons with minimized transverse emittance down to the unprecedented level of  $10^{-4}$  μm. This would constitute a breakthrough in plasma acceleration, for the first time providing electron bunches with much *better* beam quality when compared to state-of-the-art accelerators based on conventional technology.

The release position of electrons by the photoionization laser relative to the plasma wave determines the trapping point inside the plasma wave and therefore the electron witness bunch parameters after the acceleration. Therefore, the synchronization between the driver electron bunch and the release laser pulse should be as good as possible. It is expected that with a photoinjector and smaller compression factor, the jitter between laser pulse and driver electron bunch will be much better at FACET-II as compared to FACET. At the same time, the duration of the witness electron bunch, and consequently the energy spread of the witness bunch electrons, is strongly dependent on the laser pulse duration. Therefore, the laser pulse should be as short as possible. Fortunately, the controlled release of electrons requires a laser pulse energy of only ~100 μJ. At such energy levels, laser pulse compression to the sub-10-fs level (e.g., in a gas-filled hollow fiber via group velocity dispersion) is relatively easy.

### 3.4.3 Advantages of high-density electron beam driver from photocathode

In addition to laser pulse duration and synchronization, the characteristics of the driving electron beam are important for the Trojan horse scheme. At FACET, the electric self-fields of the electron bunch are barely high enough to self-ionize low-alkali metal vapor media such as rubidium and lithium. The parameters eventually obtainable at FACET-II at the interaction point (i.e. 5 nC, 10x10x20 μm beam size) allow the maximum radial self-fields of the driver bunch to approach an estimated 100 GV/m. Such unprecedented values would be enough to overcome not only the first ionization thresholds of alkali metal vapors (~5 eV), but also those of a variety of other gases such as hydrogen, nitrogen, oxygen, CO<sub>2</sub>, etc. Therefore, independent of the specific requirements for the Trojan horse scenario, self-ionization and other phenomena could be studied in an unprecedented parameter range. For the specific Trojan horse scenario, such large electric self-fields of the driver beam would allow for testing and optimizing the Trojan horse scheme in a fully gaseous environment at ambient conditions. For example, instead of

having to use alkali metal vapors, we could use hydrogen as the beam-ionized, beam-driven plasma wave medium, and helium as the gas to be released by the injection laser pulse. Working with species that are gaseous at ambient conditions would be highly beneficial from an engineering point of view, since the optical access is easy. The gas may be contained in a glass container at room temperature, whereas alkali metal ovens need a temperature of many hundreds of Kelvin, water cooling, and a buffer gas, which prohibits easy optical access. These studies are directly relevant to future scenarios where electron bunches from laser-wakefield accelerators would be used as driver electron beams, and a small split-off fraction of the main laser pulse would be used to release the electrons in the electron beam driven wakefield. Such future systems have the inherent advantage of synchronization to the femtosecond level.

#### 3.4.4 Advantages in case of a Joule-class (>10 TW) Ti:Sapphire laser beam

A high-power (> 10 TW) laser system would further allow for preionization of the low-ionization threshold component. This would decouple the acceleration process from the ability of the driver bunch to self-ionize the plasma medium. We could preionize not only alkali metal vapors, which are hard to access due to the geometry of the plasma oven, but also media which are gaseous at ambient conditions. For example, we could preionize hydrogen with the preionization laser pulse, and ionize helium with the release laser pulse. The mixture of hydrogen and helium could be stored in a glass vessel, which allows for easy access by the laser pulses, and for probing and diagnostics. In this configuration, the preionization laser pulse would ionize the helium gas a few ps before the electron beam arrives, and the release laser pulse would hit and ionize the helium gas a couple of tens of fs after the electron beam. In this configuration, it would be possible to study the Trojan horse process when the electron beam density is much weaker than in the self-ionization case. Also, it is possible to extend the total acceleration length (and thus the energy gain) by having the electron beam self-ionize during the first part of acceleration, and then have the laser pulse take over ionization in the latter part of the acceleration, where the electron beam may drop below the self-ionization threshold due to head erosion, pulse scalloping and other effects.

A high-power laser pulse capable of driving a plasma wave by itself could further be used to boost the energy of the electron beam coming from the photocathode. Such an external injection and energy boost process would be most effective at lower electron energies (i.e., at a couple of hundreds of MeV instead of 10 GeV).

Further, a high-power laser pulse could be used for Thomson scattering. The ultralow emittance of the witness beam generated by the Trojan horse process would allow for extremely large beam brightness, which could be exploited in Thomson scattering schemes, where the high-power laser pulse would scatter with the electron witness beam.

#### 3.4.5 Further scenarios and light source experiments

A currently discussed scenario for FACET-II is to ramp up the energy of the electron beam in several major radiofrequency-cavity based stages.[xlvi] The first would accelerate to 200 to 250 MeV, the second to 4 GeV, and the final to above 7 GeV and possibly as high as 10 GeV. In any case, studies on Trojan horse acceleration could potentially be done after each of these

stages, shown in Figure 2-13. Note that while in reality ,the facility setup has to be strictly linear, in the figure the three stages are drawn next to each other to indicate that in principle we may be able to insert R&D sections after each stage.

A 200-250 MeV, high-density electron bunch would be sufficient to drive a plasma wave in a low-ionization threshold medium over a limited distance, and a low-energy laser pulse could then release electrons in that plasma wave. However, since the electron energy of 250 MeV is moderate, a 10 TW+ LWFA stage could be used to substantially boost this energy to the ~1 GeV level. Then, the boosted bunch could be used as a PWFA driver in the Trojan horse stage (see 250 MeV arm of Figure 2-13). Since such a bunch with relatively high charge would be produced to generate a Trojan horse witness electron bunch with much lower charge, this witness bunch may gain several GeV of energy. The witness bunch could then be used to power a cryogenic undulator, such as the one which is currently used at the NLCTA in order to directly make use of the expected excellent witness bunch's emittance. [xlix] In turn, the output of the undulator could be used to definitively measure such unprecedented emittance. There may be space limitations after the first accelerator stage in the final version of the facility which would not allow us to implement a Trojan horse/LWFA booster/undulator stage. On the other hand, in case of limited funding to build FACET-II up to the 10 GeV level, we would still be able to do substantial R&D on Trojan horse E-210 follow-up experiments at 250 MeV.

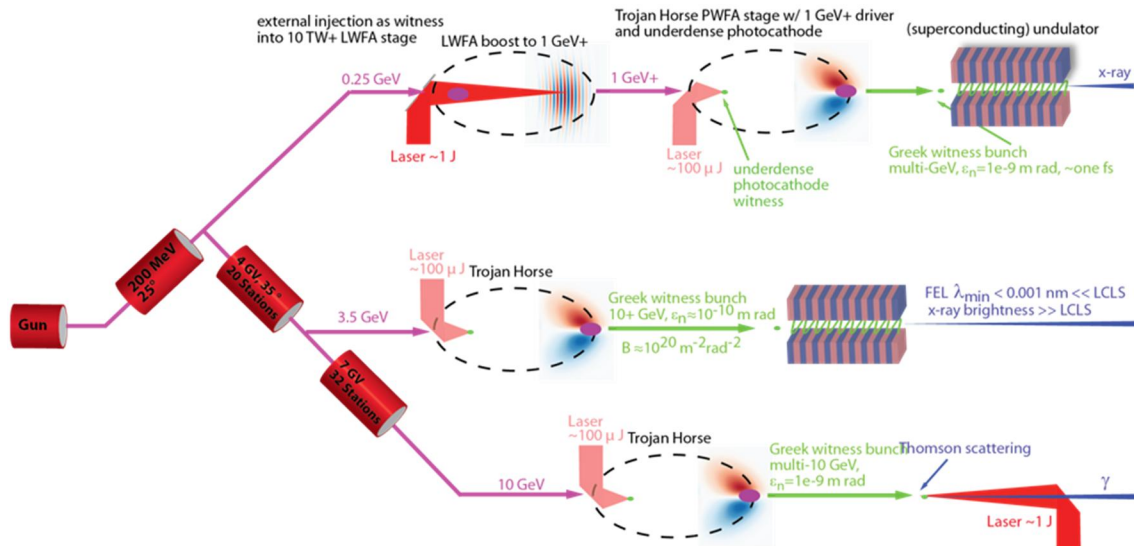


Figure 2-13: Sketch of potential Trojan horse R&D at FACET-II

At around 4 GeV, there would be no need to implement an LWFA booster stage. We would directly be able to conduct E-210 follow-up R&D with a beam at this energy level. While it is not shown in the figure, this stage is also attractive for Thomson scattering with a high-power laser pulse.

Note that the figure, for reasons of simplicity, does not depict the preionization laser beam, which would be highly desirable to preionize PWFA stages.

At the highest driver beam energies of 10 GeV, potentially the electron energy and flux of the driver beam and the witness beam may already be too high to use an undulator for free-electron-laser x-ray generation due to potential material damage in the undulator. A Thomson scattering light source, however, could be realized here after the Trojan horse stage.

### 3.4.6 Summary

The combination of photoinjector gun and accelerator, synchronized with a Ti:Sapphire short-pulse laser beam (30 fs, ideally less) will be ideally suited to do extended research in the context of follow-up experiments to the E-210 Trojan Horse Underdense Photocathode Plasma Wakefield Acceleration experiments. Such research at FACET-II is highly promising, since the scheme may enable the production of electron beams with highest tunability and stability, bunch durations down to the sub-fs regime and normalized emittance down to  $\epsilon_n \approx 10^{-4} \mu\text{m}$ . One of the most intriguing applications of such a hybrid accelerator system would be to power a free-electron-laser, potentially allowing for a performance much better than at the LCLS.

The following requirements are *Essential* for such research: an electron beam driver generated by a photoinjector, an electron energy of  $> 200$  MeV, a beam density after compression such that the electric self-fields exceed 10 GV/m, and a synchronized laser pulse at the 30 fs, 100  $\mu\text{J}$  level.

Other features are *Highly Desirable*. These include an electron energy up to 10 GeV, a beam density with self-fields up to 100 GV/m, and excellent synchronization between the electron driver beam and the laser pulse. This laser pulse would be used for preionization and/or for electron witness bunch production, and therefore should have the smallest possible pulse duration, at least for the low-energy mJ-level arm. It could also be used for laser wakefield acceleration to boost the incoming electron beam energy from the photo gun prior to Trojan horse stages, which would further connect the FACET-II to laser wakefield acceleration groups worldwide.

## 3.5 Dielectric Wakefield Acceleration at FACET-II

Recent studies at Argonne, Brookhaven and SLAC have focused on large amplitude wakefields driven in dielectric structures. The primary applications focus on high-gradient dielectric wakefield acceleration (DWA) with other applications in. beam energy chirp mitigation for future FEL application, and developing high-power, narrowband, tunable sources of THz radiation. Relevant, outstanding issues in DWA research include the determination of a working parameter space for this technology such as structure material and geometry optimization, effects of transverse modes and beam-break up, 1D- and 3D-periodic structures for enhanced mode confinement, and, ultimately, demonstration of high gain in acceleration through a passive dielectric lined structure.

The UCLA-led E-201 collaboration (2011-) at SLAC FACET is pursuing studies covering several of these key issues. The experimental program includes a careful parameter optimization of materials (e.g.  $\text{SiO}_2$ , sapphire, diamond, alumina) to explore and identify the limits and causes of dielectric breakdown at high fields. These materials exhibit low loss tangents in THz frequencies and can thus accommodate large fields before the onset of breakdown effects. We

are studying other geometries such as 1D-periodic claddings (i.e. Bragg-like alternating dielectric materials) and fully 3D photonic-like structures for enhanced mode confinement and higher breakdown thresholds compared to purely metallic boundaries. Finally, we have developed advanced autocorrelation techniques to fully characterize the modal content of the structures using the emitted coherent Cherenkov radiation (CCR) as a diagnostic. The emitted CCR also has proven useful as a powerful, tunable THz source.

The E201 experimental program has a well-defined scope of goals to address issues in ultrahigh-gradient DWA studies today, but there are a number of open questions in the field that are not readily addressable given current electron beam limitations at FACET. These include the demonstration of high gain in acceleration, the investigation of shaped drive bunches for enhanced transformer ratios, and the exploration of beam breakup and acceleration in long structures. In order to begin to address these issues in detail, the current beam constraints, notably in beam emittance and lack of drive beam parameter flexibility, must be overcome.

The viability of a dielectric structure as a future driver for compact free-electron lasers (FEL) or colliders lies in the ability to demonstrate high-gradient DWA. The proposed parameter space of FACET-II allows such investigation of high-gradient fields. First, the ability to create a drive-witness beam pair with variable chirp and delay will allow the clear observation of acceleration. Second, the ability to shape the drive bunch (e.g. triangular ramp or multi-pulse) with a readily adaptable beam will allow the exploration of enhanced transformer ratios. Third, the photoinjector quality beam with low emittance and small spot sizes will permit the use of long structures. The effects of beam breakup due to transverse mode excitation in long structures can be investigated. Long structures also allow achieving higher energies in acceleration. Finally, the improved beam quality will permit the study of advanced 3D-photonic bandgap-like structures which have smaller beam gaps and tighter tolerances on input beams. The accelerating gradients benefit from the scalability of the wakefields with smaller dimensions of the beam. The fields are proportional to the beam charge divided by the wavelength squared, and the wavelength of the mode scales with beam dimensions. This will also allow the exploration of low emittance, low charge regimes where GV/m are more readily achieved. This exploration is also synergistic with laser-fed accelerator structures, which also demand low emittance, low charge drive beams.

### 3.5.1 Introduction to DWA

The DWA typically consists of a dielectric lined waveguide and a relativistic electron beam (drive beam) that generates a wakefield in the medium (Figure 2-14 shows a cylindrically symmetric configuration of a DWA structure). A trailing particle bunch (witness beam) can sample the wakefield and gain or lose energy depending on its phase (or delay) relative to the drive beam. The peak accelerating gradient is determined by the bunch charge, bunch length, bunch size and properties of the dielectric lined waveguide, such as the dielectric constant, and waveguide dimensions (e.g. inner/outer radii).

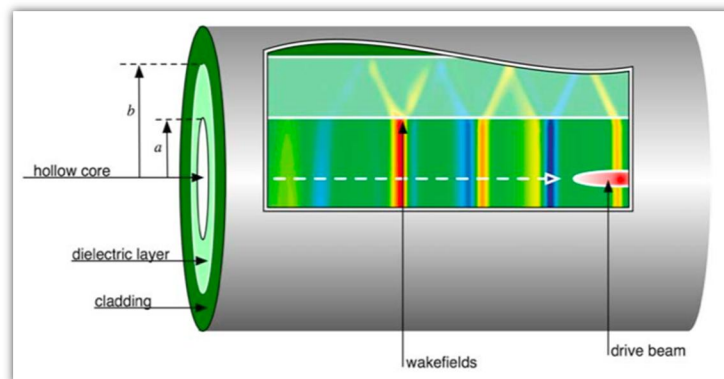


Figure 2-14: Conceptual schematic of a generic dielectric lined cylindrical waveguide.

### 3.5.2 E-201 at SLAC FACET

One of the flagship experiments at the SLAC FACET facility is E-201, which aims at the direct testing of DWA structures. The main goals of the experiment are the characterization of the emitted CCR and the determination of achievable field gradients. The DWA samples (cylindrical, slab, and Bragg array) are mounted on a monolithic block incorporated on a remote control 5-axis precision stage (Figure 2-15, right). A gold coated off-axis parabolic mirror is mounted coaxially at 90° to collimate and extract the CCR to a Michelson interferometer with pyroelectric detectors (Figure 2-15, left). The mirror also has a 3mm hole to allow the electron beam to propagate to a beam dump for future energy modulation measurements. A high-magnification imaging system allows for the observation of the face plane of the structures for signs of damage due to breakdown (signified by a violent flash and subsequent reduced transmission of laser light through the structure). The FACET facility has nominal parameters of  $E=28\text{GeV}$ ,  $\sigma_z=20\mu\text{m}$ ,  $\sigma_x = \sigma_y = 20\mu\text{m}$ , and  $Q=3\text{nC}$ , which allows the excitation of fields in excess of 1 GV/m in the THz scale DWA structures.

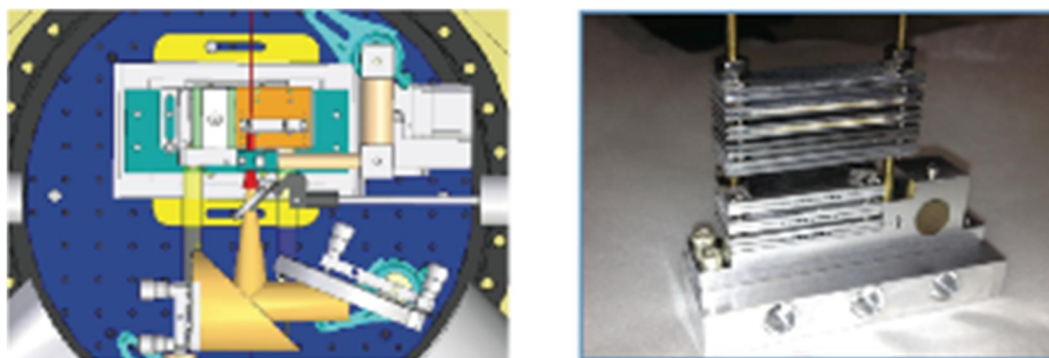


Figure 2-15: The experimental chamber at FACET (left). Photograph of the sample holder mounting block (right).

Preliminary results, from the experimental runs in 2012, show signs of breakdown in certain structures. In Figure 2-16, an alignment laser illuminates the inner dielectric of the cylindrical structure before the beam passes (Figure 2-16a), then again after it passes (Figure 2-16b). The cladding is not intact after the beam passes, presumably due to the heating caused by the

>GV/m fields produced in the dielectric. A photograph of the sample mounting block shows clear signs of vaporization (Figure 2-16c). The cylindrical structures were characterized as darkened and brittle after exposure to the beam and the high fields. In addition, the first CCR measurements showed a weak signal at the expected fundamental mode for the cylindrical structures. The studies will continue through the next experimental runs with additional efforts placed on drive beam preparation and improved signal-to-noise in the diagnostics.

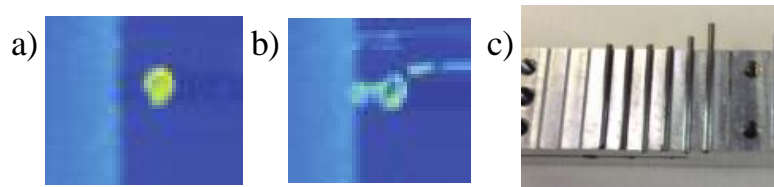


Figure 2-16: (a) In-vacuum image of a cylindrical DWA with a laser shining through the end. (b) Image of the structure after exposure to high-fields of the beam; the cladding is no longer intact and the laser light seeps out of the side of the structure. (c) Photograph of the various cylindrical DWA structures exposed at the experiment

### 3.5.3 DWA studies at FACET-II

The FACET-II parameter space has the potential to expose DWA research to the low emittance drive beam regime, which enables wakefields above 1 GV/m in smaller structures. Here we present several possibilities opened up by the FACET-II studies.

#### 3.5.3.1 Drive + Witness beam

The proposed photoinjector would improve the quality of the beam, allowing the further characterization of DWA structures and the ability to unambiguously observe acceleration using a drive-witness pair. Recent experiments in THz scale slab-symmetric structures at the BNL ATF show acceleration using a chirped beam but with very modest fields (<10MV/m). The fields scale with charge and emittance, which determines the structure's dimensions and fundamental accelerating mode. With expected fields surpassing the GV/m range, FACET-II will allow the observation of near-GeV acceleration.

#### 3.5.3.2 Long structures

The improved emittance due to the photoinjector would enhance the delivery of small spot size beams (<20 $\mu$ m) with low emittance and longer collimation, allowing the use of long structures. In the current FACET setup, the structures are limited to 2.5cm in length. This is mainly due to the beam beta functions for a given beam spot size, since the gap of the structures must be five to six times the rms spot size to ensure full transport through the structure. At FACET-II, structures over ten times longer (e.g. 50cm) can be studied due to the improved emittance from the photoinjector. This allows the study of similar gap DWA structures with small beam sizes, yet much larger beta functions. Long structures are important for observing gain in acceleration and studies of beam breakup, and also will provide insight on the maximum length of the structures as it relates to multi-staged accelerating systems.

### 3.5.3.3 Beam breakup

One of the limiting issues with long DWA structures is the undesirable effect of beam breakup within the structure. The beam dynamics due to interaction with the higher order mode excitation leads to stability issues caused by off-axis or off-angle operation. Such operation can lead to coupling to transverse modes that have adverse effects, including emittance growth, increased energy spread, and head-tail instabilities (see Figure 2-17). Beam breakup effects resulting from parasitic wakefield excitation may limit the efficacy of DWA structures as next generation drivers. Therefore these issues must be studied in detail experimentally. The FACET-II photoinjector will allow unprecedented control of a high-energy beam to purposefully excite transverse modes and develop a fundamental understanding of suppression methods and the limits of the harmful behavior of beam breakup.

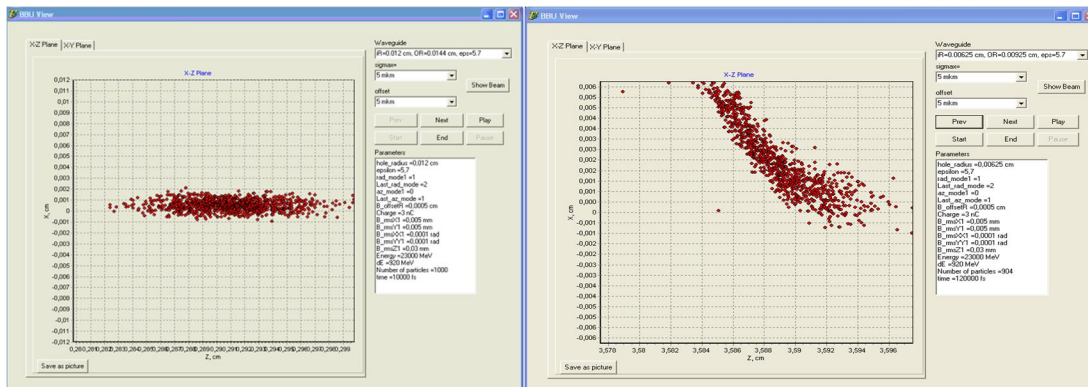


Figure 2-17: Effects of beam breakup due to excitation of transverse modes.

### 3.5.3.4 Shaped bunches

For Gaussian beams, the transformer ratio (TR), the ratio of accelerated field to decelerated field, is limited  $<2$ . The viability of a DWA as a future driver for advanced applications and light source lies in the ability to overcome this TR limitation. Studies have shown that triangular longitudinal profiles, or ramped beams, have the potential to demonstrate  $TR > 2$ . In the FACET-II scenario, jaw collimators may be used to longitudinally shape the drive bunch while maintaining small transverse emittance. For example, in the current FACET scenario, structures of inner diameter (ID)  $200\mu\text{m}$ , and a ramped bunch produce a TR of 1.5 for a 1nC beam. However, with reduced spot size,  $ID=30\mu\text{m}$ , the TR increase to  $>5$  with the same ramp and charge (Figure 2-18).. This is a dramatic improvement and a necessary step to demonstrate the viability of the DWA as a future compact high-brightness driver.

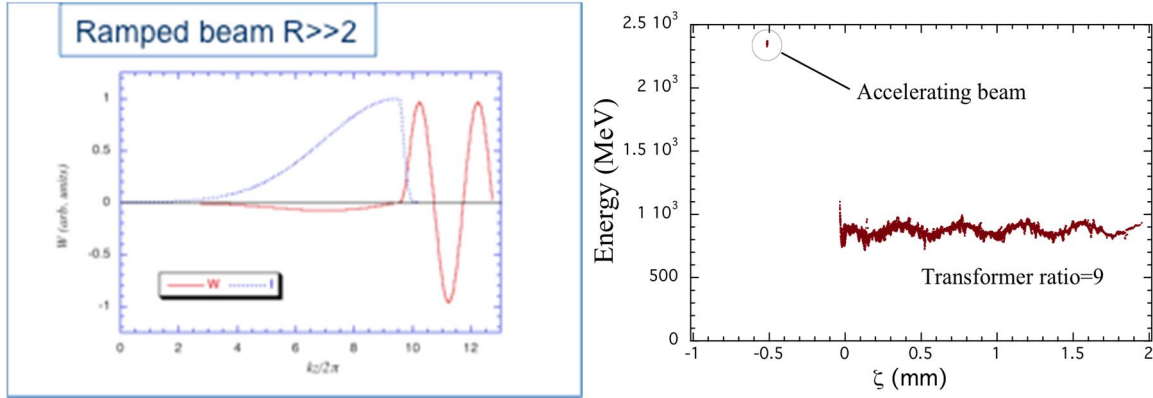


Figure 2-18: Concept of shaped drive beam (left) and witness beam acceleration with high transformer ratio (right).

### 3.5.3.5 Longitudinally periodic structures

With advances in nano- and micro-fabrication technology of dielectrics (e.g. ceramics and diamond) the development of 1D-periodic structures is feasible. In FACET, transversely periodic structures are being investigated for mode confinement and damage threshold measurements. However, with the introduction of multi-pulse beams, longitudinally periodic structures can be studied as well. By exploiting the position-time correlation and using a notch or rigid-mask collimator, FACET-II will be able to produce a multi-pulse drive beam.

The longitudinal DWA structures are analogous to “slow-wave” structures where the group velocity of the wakefield can be controlled by appropriate selection of dielectric constants and periodicity. One scenario under theoretical and numerical investigation is the “zero group velocity” structure, which is composed of quartz and diamond. Figure 2-19 shows the mode confinement of the structure and the field within the structure once the beam has left, where a near-standing wave is produced and confined to the structure.

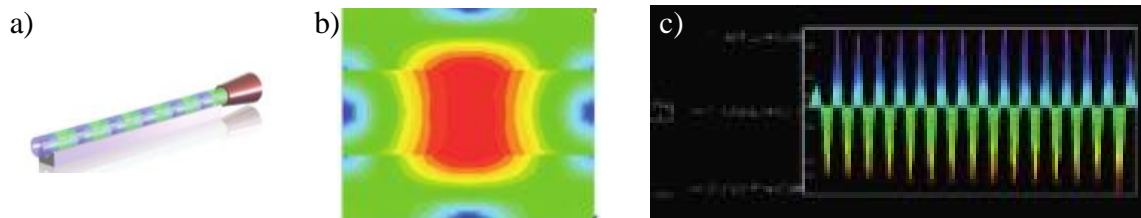


Figure 2-19: Rendering of periodic structure (a), mode confinement of structure (b) and field (c).

### 3.5.3.6 Photonic structures

Motivated by the need to abandon the use of metals in the presence of high fields, we have looked at a few examples of simple beam-driven all-dielectric wakefield accelerators from the perspective of bandgap photonics in 1D. However, we also gain design advantages in the ability to manipulate the modes' characteristics by examining fully 3D photonic-like structures, such as the woodpile in Figure 2-20. Control and manipulation of properties — such as modal confinement, spatial harmonic content, phase velocity, and group velocity — are reasons why an all-dielectric beam-driven accelerator would be expected to benefit by borrowing from the

field of optical bandgap photonics. The smaller beams and low charge operating regime afforded by FACET-II would allow further studies of these structures.

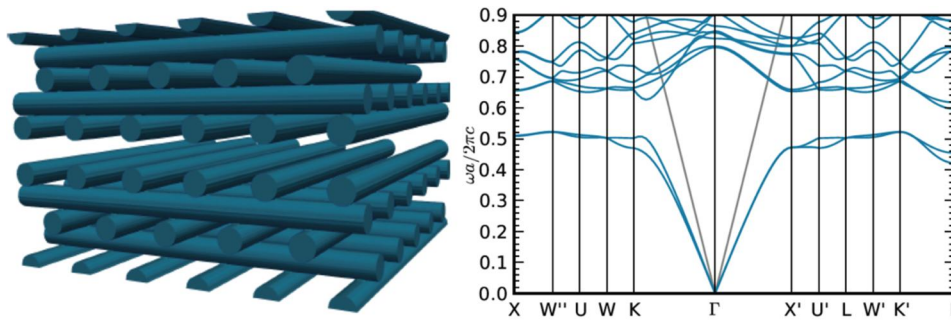


Figure 2-20: Concept of the sapphire ( $\epsilon = 9.3$ ) woodpile (left) and simulated bandgap diagram (right).

### 3.5.4 Conclusion

The proposed FACET-II parameter set opens up the possibilities for novel and exciting research into dielectric wakefield acceleration that is currently inaccessible due to constraints on drive beam generation and transport. These pertinent studies and demonstrations are necessary to ascertain the feasibility of the DWA as a next generation, compact accelerator for FEL and collider applications.

## 3.6 BIG: Beams of Intense Gamma-rays at FACET-II

### 3.6.1 Introduction.

Richard Feynman once wrote:

One very powerful way of experimentally investigating the strongly interacting particles (hadrons) is to look at them, to probe them with a known particle; in particular the photon (no other is known as well). This permits a much finer control of variables, and probably decreases the theoretical complexity of the interactions [1].

Indeed,  $\gamma$ -ray sources are intensely used in quantum chromodynamics (QCD) research to study structure of nuclei and nucleons. Controllable linear and circular polarization of the Compton back-scattering  $\gamma$ -ray sources opens the window of spin and parity observables in this research.

Polarized Compton back-scattering  $\gamma$ -ray sources, pioneered at ADONE and SLAC in the 1960s, [1i] remain an important research and application tool. Presently there are four operational facilities covering  $\gamma$ -ray energy range from 1 MeV to 2.4 GeV.

The area of research is roughly split into low, medium and high energy ranges. Low energies,  $E_\gamma = 1-15$  MeV, are well-suited to studying the resonant structure and states in nuclei below the giant dipole resonance. Nuclear resonant fluorescence (NRF) is the primary method for these studies. In addition, direct photon excitation and disintegration of nuclei gives access to a

number important processes in astrophysics, such as  $^{16}\text{O}(\gamma,\alpha)$ . [lii] Figure 2-21 indicates the richness of the nuclear structure.

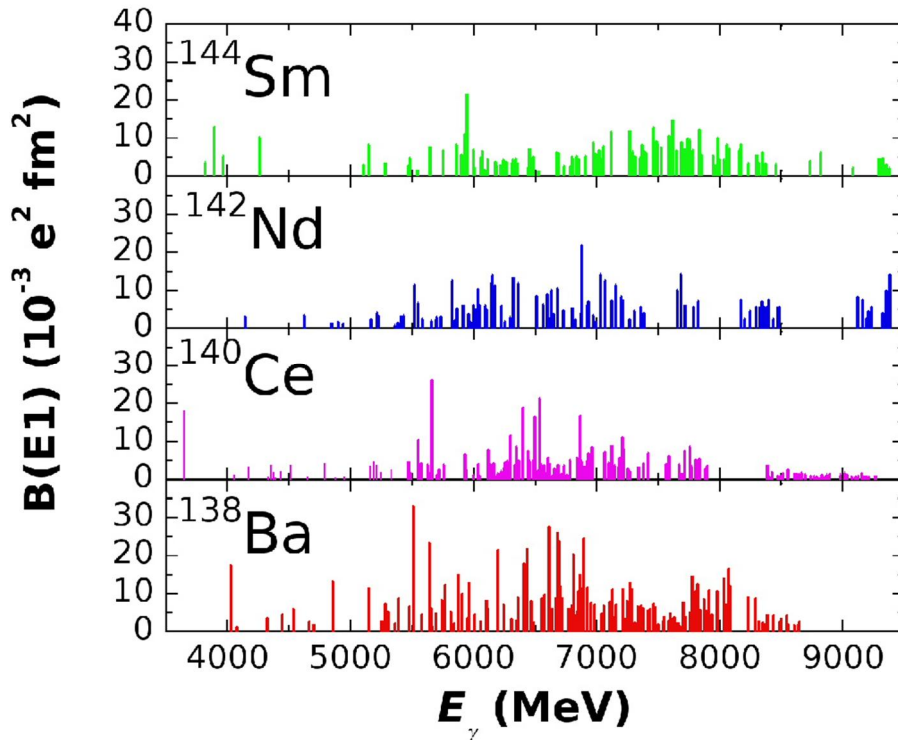


Figure 2-21: E1 dipole strength distribution in  $N = 82$  isotones. [Courtesy of A. Tonchev, LLNL].

Intermediate energies,  $E_\gamma = 100\text{-}200 \text{ MeV}$ , are optimal for studying spontaneous breaking of QCD chiral symmetry. The main areas of interest are near threshold of pion photo-production, [liii] measuring nucleon spin polarizabilities [liv] and measuring the integrand of the Drell-Hearn-Gerasimov integral for the deuteron. [lv].

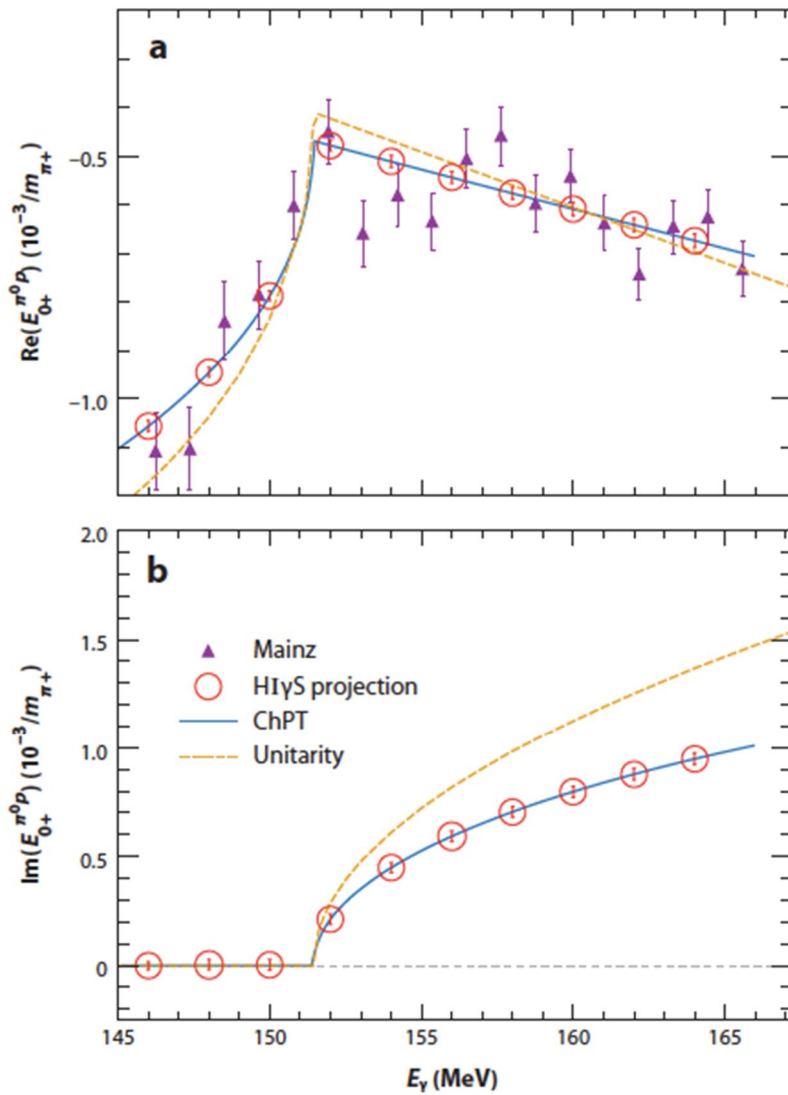


Figure 2-22: The  $\gamma + p \rightarrow \pi_0 + p$  reaction: (a)  $\text{Re}(E_{0+})$ , the solid blue curves represent chiral perturbation theory (ChPT) calculations, and the dashed orange curves represent the unitarity fit; (b)  $\text{Im}(E_{0+})$  [Courtesy of A.M. Bernstein, MIT].

High energies,  $E_{\gamma} > 200 \text{ MeV}$ , are needed for studying the resonant structure and states in nucleons. The high energy reach of BIG opens the possibility of searching for light-quark + glue hybrid baryons and, probably, heavy-quark baryons. This research requires meson photo-production and direct access to gluons. These experiments are focused on a high precision extraction of pseudoscalar meson photo-production amplitudes. The most general analytic form of the cross section involves 16 spin-dependent observables, which can be reached using the flexibility of BIG in combination with a sophisticated detector. [Ivi]. Potential discoveries include a hypothetical glue-ball [Ivii].

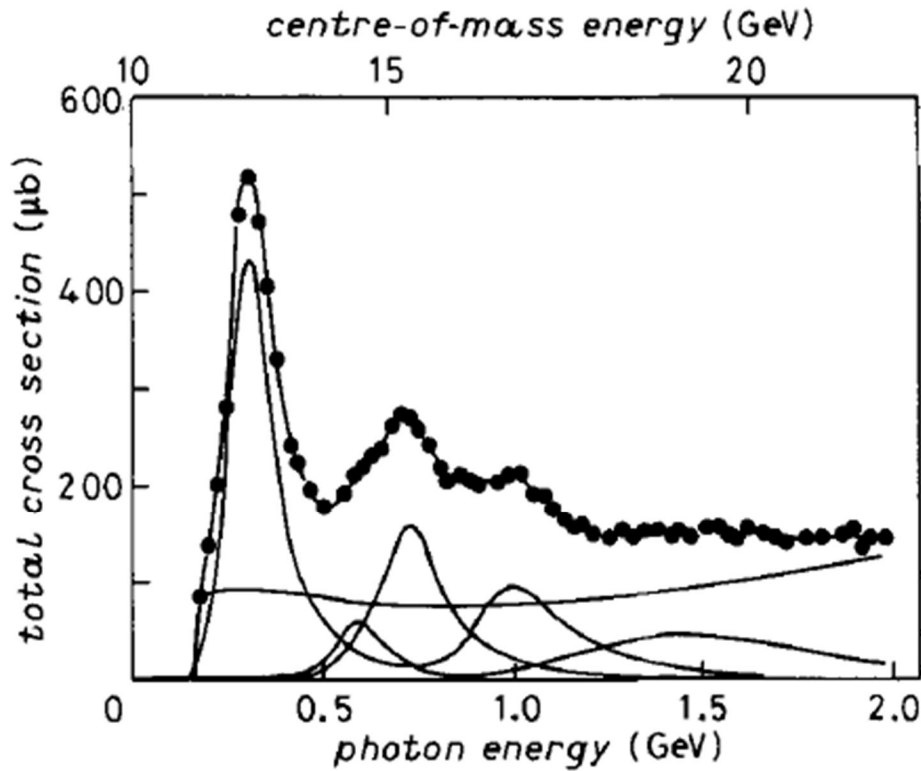


Figure 2-23: Reach energy spectrum and structure of nucleons. Shown is the total photo-absorption cross-section on the proton: the curves beneath the three peaks show a fit to the resonance cross-section corresponding to the M1, E1 and E2 proton excitation, respectively. The flat curve is the background; the other curves come from states with lower excitation probability. [lviii]

In addition to QCD experiments, the BIG can be used for R&D in generating polarized lepton (positron and muon) beams for future linear lepton and linac-ting lepton-hadron colliders. Furthermore, it can act as a test-bed for a  $\gamma\text{-}\gamma$  collider. The time structure of BIG may allow us to create a textbook experiment – generating an electron-positron pair in vacuum by colliding two  $\gamma$ -ray beams.

All existing Compton back-scattering sources create  $\gamma$ -rays with a similar overall energy spectrum. The energy spread of  $\gamma$ -rays can be limited by geometrical collimation, with about 1.5% of the flux per 1% energy spread in the region near the top energy of the photons:

$$E_{\gamma\text{max}} = \hbar\omega \cdot \frac{1 + \beta}{1 - \beta + 2\hbar\omega / \gamma mc^2} \sim \frac{4\gamma^2 \hbar\omega}{1 + 4\gamma\hbar\omega / mc^2};$$

$$\gamma = 1 / \sqrt{1 - \beta^2}.$$

Hence, the spectral (energy) density of the beam is determined by its total flux  $\dot{N}_\gamma$  and the maximum energy of the photons in the beam:

$$\frac{d\dot{N}_\gamma}{dE_\gamma} \sim 1.5 \frac{\dot{N}_\gamma}{E_{\gamma\max}}$$

The  $\gamma$ -ray energy resolution can be obtained either by tagging the energy of scattered electrons or by collimating the beam. The tagging approach does not create high fluxes, since only one  $\gamma$ -ray per collision can be effectively used. Collimation does not impose such restrictions. The resolution obtained by collimation depends on the quality of the electron beam.

Table 2-1 compares main parameters of existing polarized Compton  $\gamma$ -ray sources. A number of bremsstrahlung  $\gamma$ -ray sources exist as well, but these are unpolarized and in a large background of low energy photons, and are therefore not suitable for QCD experiments.

Table 2-1: Main parameters of operational polarized Compton back-scattering  $\gamma$ -ray sources and the BIG.

Name	ROKK	GRAAL	LEPS	H $\gamma$ S	BIG
Location	Novosibirsk, Russia	Grenoble, France	Harima, Japan	Durham, NC, USA	Palo Alto, CA, USA
Accelerator	VEPP-4M	ESRF	SPRING-8	Duke SR	SLAC
e-beam, GeV	1.4 - 6	6	8	0.24 – 1.2	1-10
$\gamma$ -beam, GeV	0.1-1.6	0.55-1.5	1.5-2.4	0.001-0.095	0.001-2 (5)
best $\gamma$ -energy resolution, %	1-3	1.1	1.25	0.8-10	0.1

Note: not all parameters in the table can be obtained simultaneously

It is clear from Table 2-1 that the BIG is a superior source when compared with the other existing sources. It has a  $\gamma$ -ray energy span of more than three orders of magnitude, from MeV to GeV, about 10-fold better energy resolution than competing sources, and two to four orders of magnitude larger flux. BIG's unprecedented intensities and unique time structure open unprecedented opportunities for its utilization in fundamental and applied research.

In addition to existing Compton back-scattering  $\gamma$ -ray sources, there are a number of recent proposals for new sources. Two of them are in the USA: one is proposed at LLNL [lix] and the other is the recently proposed ASTA facility at FNAL [Ix]. While both of these proposals promise to deliver very high fluxes of  $\gamma$ -rays, their energy reach and coverage do not match that of the BIG. The LLNL source, with its 200 MeV linac, will generate  $\gamma$ -rays with a maximum energy near 1MeV. The ASTA facility, with its proposed 800 MeV SRF linac, would be capable of generating high intensity  $\gamma$ -ray beams with a maximum energy of 15 MeV.

Hence, a large number of ground breaking experiments requiring high flux, excellent energy resolution and detailed energy scans will become possible at BIG. In short, the BIG is the dream facility for polarized photo-production and photon scattering experiments.

2007 Nuclear Physics Long Range Plan "The Frontiers of Nuclear Science" Effective Field Theory clearly indicate importance of intense polarized  $\gamma$ -ray sources for frontier QCD research. It reads:

*Effective field theories provide a powerful framework for solving physical problems that are characterized by a natural separation of distance scales. They are particularly important tools in QCD, where the relevant degrees of freedom are quarks and gluons at short distances and hadrons and nuclei at longer distances. Indeed, at energies below the proton mass, the most notable features of QCD are the confinement of quarks and the spontaneous breaking of QCD's chiral symmetry. Chiral perturbation theory is an effective field theory that incorporates both; when applied to mesons it is a mature theory. Perhaps the most striking advances in chiral effective field theory have come in its application to few-nucleon systems. This has yielded precise results for nucleon-nucleon forces and also produced consistent three-nucleon forces. This opens the way for precision analyses of electromagnetic reactions on light nuclei, e.g., the Compton scattering reactions on systems having two or three nucleons.*

The BIG would be perfectly suited for the research described above. Its energy range is ideal and its intensity is sufficient for the challenges presented by the experiments.

Another challenge where BIG may excel is studying the spontaneous breaking of chiral symmetry due to the finite quark masses. This study requires polarized photon energies between the thresholds of neutral and charged pion production (e.g. between the  $\pi^0$  threshold of 144.7 MeV and the  $\pi^+$  threshold of 151.4 MeV). As a result of the vanishing of the threshold amplitudes in the chiral limit, the experiments are difficult to perform because the cross sections are small. Furthermore, an energy scan with very narrow energy spread of the  $\gamma$ -ray (well below 1% FWHM) is needed to map this energy range. This is the reason why experts in the field call it a "dream experiment" [ix]. Existing and proposed polarized  $\gamma$ -ray sources either do not have energy reach (HI $\gamma$ S) or have very low flux: with GRAAL or LEPS it would take about 10,000 years to collect necessary statistics. The BIG's intensity and energy resolution would allow us to perform this experiment in under one year.

The BIG's energy reach and unprecedented intensity (~ 10,000-fold increase in the energy of interest) opens a window for studying critical details of chiral dynamics in meson photo-production. Excellent energy spread down to 0.1% FWHM in the BIG's collimated  $\gamma$ -ray beam opens a new window into nuclear structure studies.

### 3.6.2 Nuclear Structure Studies: Nuclear Resonant Fluorescence (NRF), including pigmy resonances

Studies of nuclear structure, some of which also have an astrophysical context, would strongly benefit from the high intensity and high quality of  $\gamma$ -ray beams at the BIG source at FACET-II. The most important parameter in any NRF or photo-induced experiment is the number of

photons per eV, or the flux energy density. This is dictated by the fact that the width of nuclear states below the neutron separation energy ranges from few meV to eV depending on the nucleus and structure involved. BIG's tunability and flux energy-density exceed any operating sources by orders of magnitude, making it a perfect choice for this application. We anticipate that dozens of scientists from the U.S. and Europe will want to take advantage of BIG for research into nuclear structure.

Studies of nuclear structure are on the forefront of low energy nuclear physics and astrophysics. The neutrino flavor transformation in the star explosions determine charged- and neutral-current interactions of supernova neutrinos. Mapping the M1 strength distributions for isotopes ranging from  $^{40}\text{Ar}$  to isotopes of Mo have been proposed for neutral-current detectors. The stable isotopes of Mo are likely to be sensitive to both  $n_e$  and anti- $n_e$  interactions [Ixii].

The electric dipole (E1) response is a fundamental property of atomic nuclei. As with other collective multipole responses it is directly connected to the bulk properties of nuclei and nuclear matter. Recently, the E1 response (especially its low-lying part) has been shown [Ixiii, Ixiv, Ixv] to provide a constraint on the isovector properties of nuclear matter, e.g., the symmetry energy, which are key ingredients in the description of exotic astrophysical objects like neutron stars. [Ixvi] Furthermore, the E1 response builds up the major part of the photo-absorption cross section and represents the dominant  $\gamma$ -ray strength function, an important quantity in determining reaction rates in different astrophysical scenarios. [Ixvii, Ixviii] Photon induced reactions are an ideal tool to investigate the dipole strength below and above thresholds in a model independent way. However, data are so far available only for a few nuclei mainly at or close to the magic shell closures. Measurements of  $(\gamma, \gamma')$  reactions at BIG will extend these studies to a wider range of masses including highly deformed nuclei.

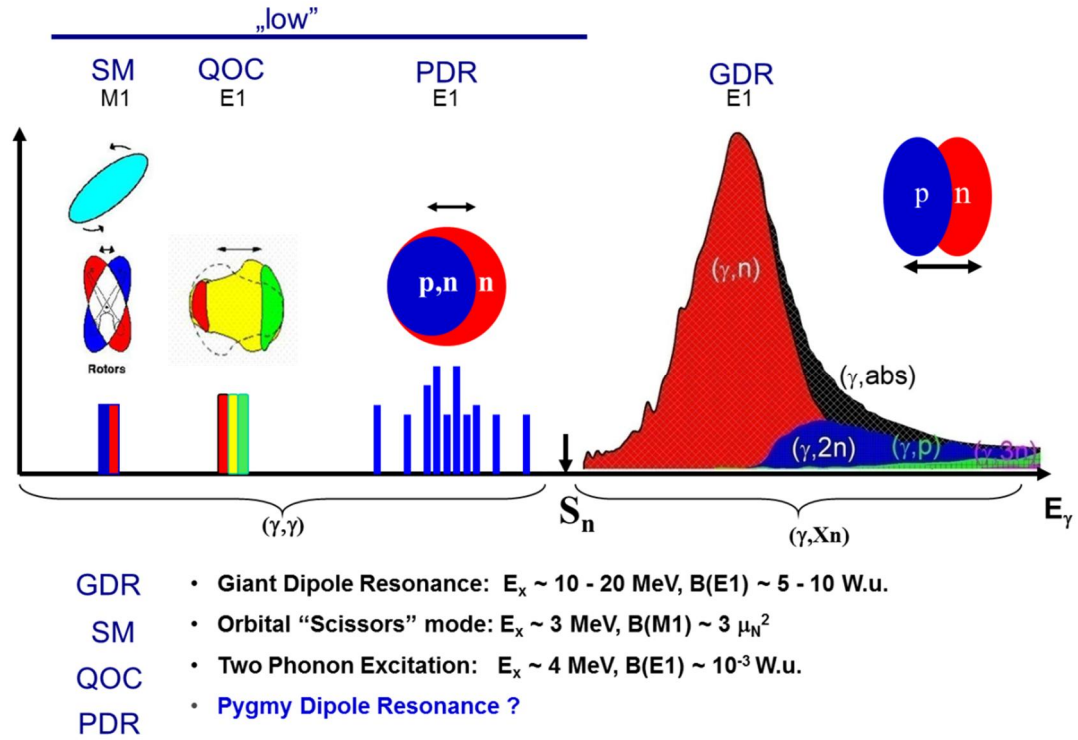


Figure 2-24: Schematic of the dipole response over a broad range of energies, up to 10's of MeV, and related structural phenomena

The nuclear dipole response covers a range of structural phenomena, as shown in Figure 2-24. Physics themes involving electric and magnetic dipole distributions, which can easily be separated making use of the polarization of the photon beams, range from the study of isospin purity of states, to the emergence and evolution of nuclear quadrupole and octupole collectivity, and the build-up of nucleon skins. The best-known dipole excitation is the giant dipole resonance (GDR), which is typically found at energies around 15 MeV, well above the neutron-separation threshold. On the low-energy tail of the GDR another structure has been identified in a small set of nuclei, as mentioned above. This enhancement of strength around or below the neutron-separation threshold, referred to as Pygmy dipole resonance (PDR), is typically interpreted as the effect of a neutron skin building up around a proton-neutron symmetric core. The lowest part of the electric dipole response, at few MeV excitation energy, is dominated by multi-phonon excitations involving the octupole degree of freedom. The latter requires a short bursts of  $\gamma$ -rays natural for BIG's time structure. In either case, the enhanced, collective electric dipole strengths at low energies are a challenge to nuclear theory, since they can usually only occur due to particle-hole excitations across a major shell.

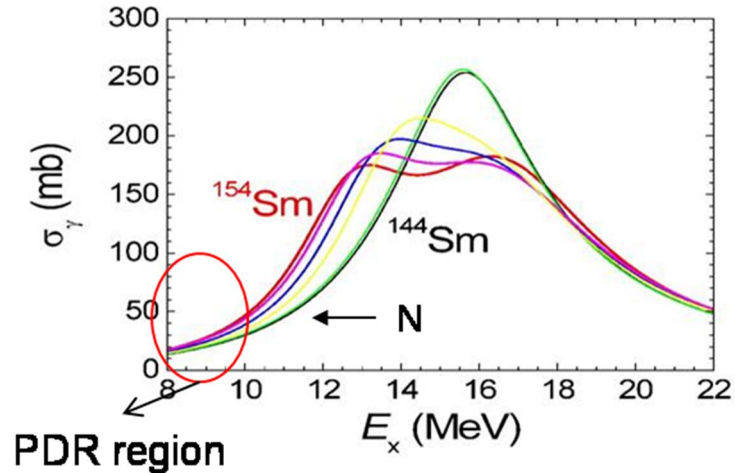


Figure 2-25: Evolution of the GDR for all Sm isotopes calculated by the QRPA model [Ixix]

Figure 2-25 depicts calculated GDR distributions for Sm isotopes across the onset of deformation. For spherical isotopes the resonance has a Lorentzian-type shape, whereas the GDR splits into two Lorentzians in deformed isotopes, corresponding to vibrations with respect to the two major axes. A similar behavior can be expected for the PDR, but has so far not been observed due to the lack of data in deformed regions. An additional complication is the disentanglements of PDR and GDR strengths, since - as indicated in Figure 2-25 - the PDR lies on the low-energy tail of the GDR.

Dipole excited states, particularly, the PDR, are at the intersection of nuclear structure and nuclear astrophysics. They are of interest to nuclear structure because they represent a weak collective mode that remains to be understood in a systematic way. The astrophysics context is clearer, since these states directly influence the rates for stellar photodisintegration reactions. Nuclear resonance fluorescence studies of the PDR show that we are missing significant (maybe most) of its excitation strength because cascades through lower-lying excited states have thus far escaped detection. Coincidence measurements, which will isolate cascades from the PDR, require the intensity and energy resolution of BIG. In addition, coincidences provide a unique way to excite other collective dipole structures, such as quadrupole-octupole coupled (QOC) states or the nuclear M1 scissors mode, and simultaneously observe their detailed decay behavior, which is the smoking gun of their nature. Such fingerprints are, for example, the one-phonon decays of QOC states corresponding to the annihilation of a quadrupole phonon, as depicted in Figure 2-26.

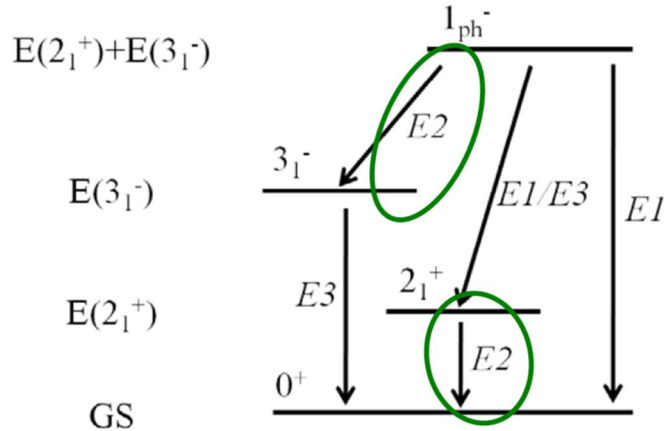


Figure 2-26: The  $J=1$  member of the negative-parity multiplet from coupling a quadrupole phonon to an octupole phonon is characterized by its  $E2$  transition to the octupole state, which must have the same transition probability as the quadrupole phonon to ground state decay.

Background suppression is a very big problem for this kind of experiments. Very low background to signal ratio is one of the unique aspects of BIG. BIG's geometry, e.g. a short chicane where  $\gamma$ -rays are generated, provides for bremsstrahlung-free environment. In addition, the time structure with short bursts of  $\gamma$ -rays creates an additional 30,000 fold suppression of the background to signal ratio, compared with near-CW storage ring sources, such as H $\gamma$ S. Finally, a 10-fold narrower energy spread in the  $\gamma$ -ray energies provides for removing the beam-related background. Hence, BIG would open opportunities to perform experiments which are currently impossible because of the signal to background ratio being low.

In contrast to existing facilities, the very high brilliance of the beam will allow to excite specific states and study their detailed decay behavior, even in regions of high level densities. High-resolution charged particle spectroscopy has been used to map out the fission barrier landscape of many of the light actinides. [lxx,lxxi] As a result, a new picture of the triple-humped fission barrier was established with an unexpected, rather deep, third hyper-deformed minimum. New photo-fission experiments could significantly improve our present knowledge on the fission resonance structure and on the potential energy landscape of the actinides, which has very important astrophysical relevance as well: the fission barrier controls the fission losses at the end of the r-process path and also the population of long-lived uranium and thorium nuclei. The improved beam energy resolution of the BIG will allow for the search and study of narrow fission resonances near the barrier.

### 3.6.3 Nuclear Physics near pion threshold

Intense beams of medium energy polarized  $\gamma$ -rays are of great interest for a variety of QCD and nuclear physics experiments. Below we describe some of new physics which can be studied with the BIG.

### 3.6.3.1 Isospin Breaking Due to the Light Quark Masses

Chiral symmetry in QCD is both spontaneously [lxxii] and explicitly broken due to the non-zero values of the light quark masses. Since the up and down quark masses differ by almost a factor of two, isospin symmetry is also violated. [lxxiii] Strong isospin violation is usually predicted when  $(m_d - m_u)/\Lambda_{QCD} \cong 2\%$ . However, there is one case where strong isospin breaking is predicted when  $(m_d - m_u)/(m_d + m_u) \cong 25\%$ . [lxxiv] The quantity of interest is  $a(\pi^0 p)$ , the s-wave scattering length on the proton. [lxxv]

Clearly this quantity cannot be directly measured since  $\pi^0$  beams cannot be constructed. Our present knowledge comes from data involving charged pions and constructing the isospin even s wave scattering length,  $a^+ = (a_{\pi^- p} + a_{\pi^+ p})/2$ , measured from pionic hydrogen and deuterium, with the Coulomb contributions removed. [lxxvi, lxxvii] If isospin symmetry holds, then  $a^+ = a(\pi^0 p)$ . To test this it is essential to measure  $a(\pi^0 p)$ . This is difficult since  $\pi^0$  beams cannot be made. However it can be measured as a final state interaction in the  $\gamma p \rightarrow \pi^0 p$  reaction with transversely polarized protons in the energy region between the  $\pi^0$  threshold of 144.7 MeV and the  $\pi^+$  threshold of 151.4 MeV. [lxxviii, lxxix] This experiment requires a beam of  $\sim 10^9$  photons/sec with  $\approx 1\%$  energy resolution. [lxxx] This beam is possible with the proposed FACET-II facility at SLAC. The experiment requires a time structure in which each beam burst is divided into 1000 short beam bursts. It requires an  $a \cong 4\pi$  photon detector with good energy and time resolution to observe the  $\pi \rightarrow \gamma\gamma$  decay mode, a transverse polarized proton target (butanol) and state of the art electronics due to the low duty cycle. Even with this intense beam the experiment requires  $\sim 2000$  hours of running time to measure  $a(\pi^0 p)$  with a statistical accuracy of  $\cong 10^{-3}/m_\pi$ , which is comparable with the present determination of  $a^+$ . A comparison of  $a(\pi^0 p)$  and  $a^+$  will test the predicted violation of isospin symmetry. [lxxxi] This is an ambitious and difficult experiment to test a fundamental consequence of explicit chiral symmetry and isospin breaking due to the non-zero up and down quark masses first pointed out by Weinberg over half a century ago, and will test a firm confinement scale QCD prediction.

### 3.6.3.2 Measurements of the Drell-Hearn-Gerasimov Integrand for the Deuteron

We propose measuring the integrand of the Drell-Hearn-Gerasimov integral for the deuteron from as close as possible to the maximum photon energy of 160 MeV. S. B. Gerasimov [lxxxii] and, independently, S. D. Drell and A. C. Hearn [lxxxiii] showed that, using reasonable assumptions,

$$\int_{\omega_0}^{\infty} \frac{\sigma_{1/2} - \sigma_{3/2}}{\omega} d\omega = -4S\alpha\pi^2 \left( \frac{\kappa}{M} \right)^2$$

where  $\sigma_{1/2}, \sigma_{3/2}$  are total inelastic cross section when the target nucleon spin and the incident photon helicity are anti-parallel (parallel),  $\omega_0$  is the threshold photon energy for inelastic processes,  $M, \kappa$  are the mass and anomalous magnetic moment of the target, and S is the spin of the target. The equation above applies to protons, but Hosada and Yamamoto [lxxxiv] and

Gerasimov pointed out that these arguments could be applied equally well to the deuteron. That is, the deuteron could be treated as the object of the sum rule rather than simply as a source of neutrons. The resultant "GDH" sum rule is given by

$$\int_{\omega_2}^{\infty} \frac{\sigma_{1/2}^d - \sigma_{3/2}^d}{\omega} d\omega = -4\alpha\pi^2 \left( \frac{\kappa_d}{m_d} \right)^2$$

where  $\omega_2$  is the threshold not for pion production ( $\approx 145$  MeV) but for photo-disintegration ( $\approx 2.2$  MeV), and  $m_d$  and  $\kappa_d$  are the mass and anomalous magnetic moment of the deuteron, respectively. The sum rule values for the proton, neutron, and deuteron are given in Table 2-2.

Table 2-2: Sum rule values for particles

Target	$\kappa$	$\int GDH, \mu b$
p	1.79	-204.0
n	-1.91	-232.0
d	-0.14	-0.6

The GDH integral for the deuteron can be separated into three terms:

$$\int_{\omega_2}^{\infty} \frac{\sigma_{1/2}^d - \sigma_{3/2}^d}{\omega} d\omega = \int_{\omega_2}^{\omega_\pi} \frac{\sigma_{1/2}^d - \sigma_{3/2}^d}{\omega} d\omega + \int_{\omega_\pi}^{\omega_{\max}} \frac{\sigma_{1/2}^d - \sigma_{3/2}^d}{\omega} d\omega + \int_{\omega_{\max}}^{\infty} \frac{\sigma_{1/2}^d - \sigma_{3/2}^d}{\omega} d\omega = -0.6 \mu b$$

The second term, which also can be measured at BIG, has been measured at Brookhaven's Laser Electron Gamma Source and elsewhere. For the high photon energies relevant to the third (unmeasured) term we note that to the order of 0.1% the deuteron can be treated as the sum of a neutron plus a proton plus trivial corrections. The first term remains unknown. Currently there is no available source for such measurement, but BIG will be the perfect source to fill in this gap.

If the sum rule is valid then the sum of the unmeasured terms of the GDH integral for the neutron and proton must equal the unmeasured term of the deuteron. Adding these to the measured terms of the deuteron, the GDH integral should yield a value in agreement with the sum rule prediction.

If the GDH rule holds, then we can conclude that the sum rule is valid and calculating the "unmeasured" terms of the neutron and proton integrals will be a test of nucleon models. If no

agreement is observed, then something is wrong with the sum rule. Perhaps the assumption of unsubtracted dispersion relations?

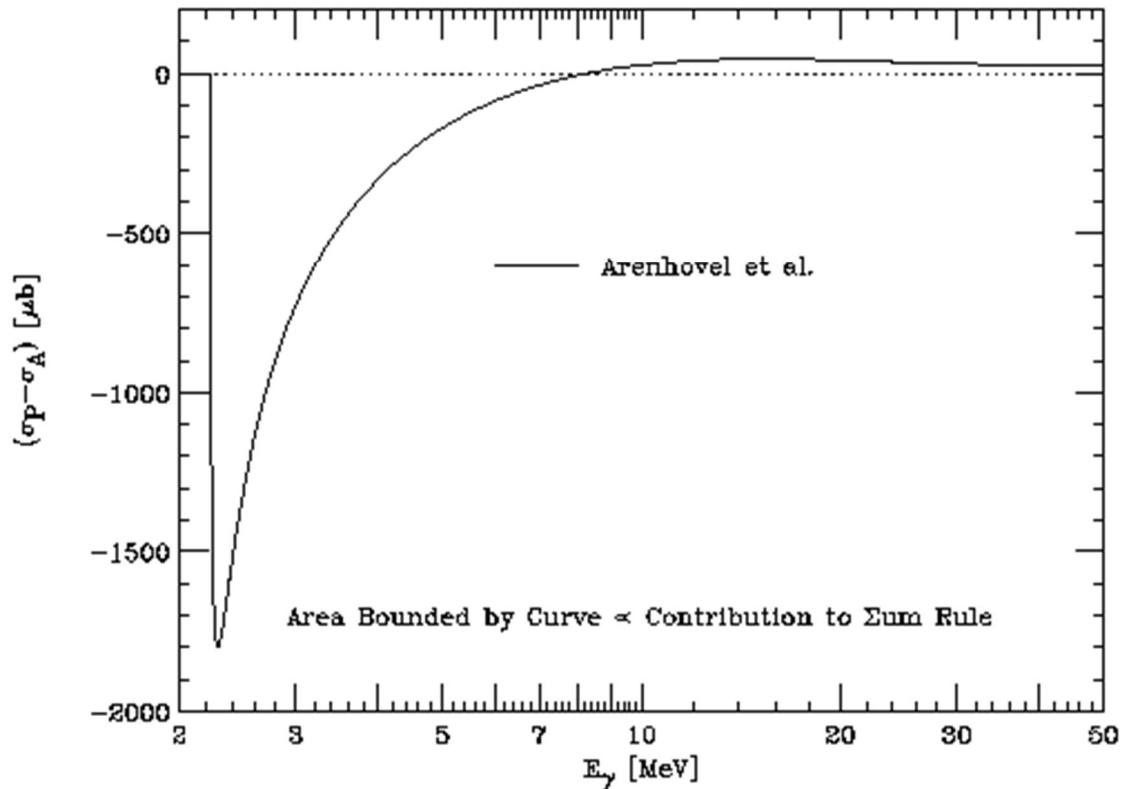


Figure 2-27: The cross section difference entering the GDH Sum Rule integral. Note that the abscissa scale is logarithmic so the area under the curve is proportional to the contribution to the sum rule integral.

The Blowfish detector, [lxxxv] with its associated electronics and data acquisition system, is ready for use for these measurements. The measurements require a detailed energy scan, where both the energy reach, the energy resolution and the intensity of the BIG makes it uniquely suited for this important measurement.

The experiment will involve photon energy scans from 2 MeV to about 200 MeV. The helicity of the photons should be switchable. The difference in energy between charged and neutral pion threshold is about 4.5 MeV so the energy resolution should be less than 2%. The required flux is at least  $10^7$  per MeV. BIG can achieve the required polarization, energy range, energy resolution and intensity. We expect to complete this experiment in about 2000 hours of beam-time.

### 3.6.3.3 Compton Scattering from a High Pressure Polarized $^3\text{He}$ Target

Experimental and theoretical investigation of the nucleon structure has grown more intense in the last two decades, resulting in breakthroughs in both experiment and theory. Nucleon

polarizabilities, describing the response of the nucleon in external electromagnetic fields, have attracted more attention. Significant efforts have been devoted in the last two decades to unpolarized Compton scattering measurements from the proton and deuteron to extract the nucleon electric and magnetic polarizabilities. However, very little is known about nucleon spin polarizabilities, which are fundamental quantities related to the structure of the nucleon. For a spin 1/2 target, there exist four independent spin polarizabilities. Due to the lack of free neutron targets in nature, our knowledge of the neutron polarizabilities is poor.. A theoretical calculation shows that double-polarization asymmetries from circularly polarized photons Compton-scattering off a polarized  $^3\text{He}$  target elastically are expected to be sensitive to the neutron spin polarizabilities. [lxxxvi]

We propose a double polarization Compton scattering experiment of circularly polarized photons from a polarized  $^3\text{He}$  target at the elastic kinematics. The experiment will be carried out with a photon energy of 120 MeV at a minimum photon flux of  $5 \times 10^8/\text{sec}$ . The polarized  $^3\text{He}$  target is a high pressure target based on the spin-exchange optical pumping technique, and the scattered photons can be detected by using a detection system such as the NaI Detector Array (HINDA). During the experiment, the double polarization asymmetry will be formed by flipping the target spin direction or the beam helicity. The proposed layout of the experiment using HINDA system is shown in Figure 2-28.

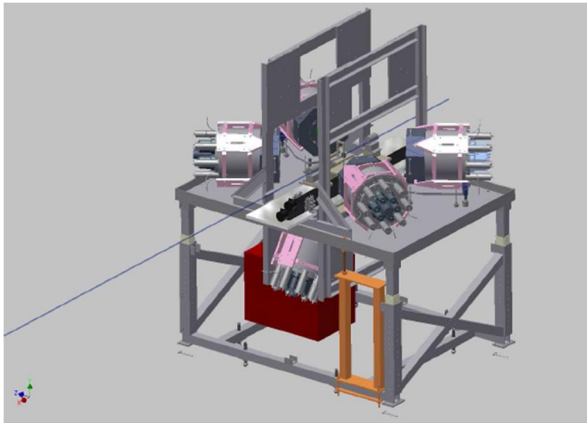


Figure 2-28: The proposed experimental setup for Compton scattering using NaI Detector Array (HINDA) system

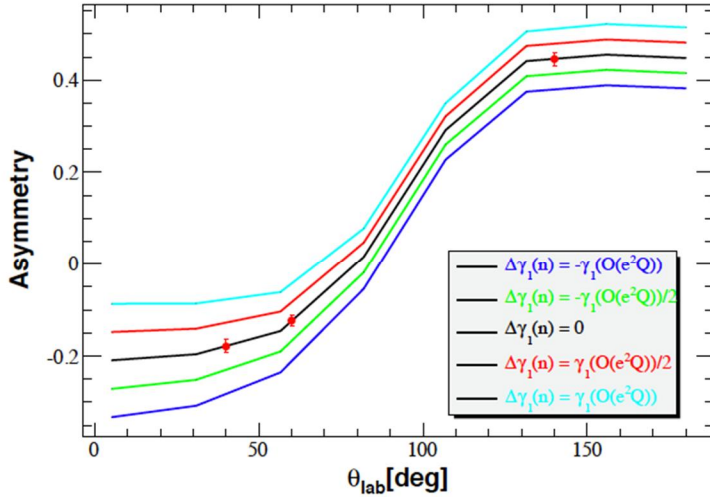


Figure 2-29: The projected sensitivity to the neutron spin polarizability  $\gamma_1$  from double polarization asymmetry measurement from a polarized  $^3\text{He}$  target as a function of photon scattering angle in the laboratory frame. The simulated results for Compton scattering (red points) are plotted along with theoretical calculations using different  $\gamma_1$  values

We propose a total beam time of 900 hours with 100% polarized photon beam and a 50% polarized  $^3\text{He}$  target with a target thickness of  $1.1 \times 10^{22}$  atoms/cm<sup>2</sup> and have considered possible physics backgrounds and detection efficiency. The spin-dependent asymmetry difference can be formed from the simulated events, and compared with different neutron spin polarizabilities. For example, the projected sensitivity to the neutron spin polarizability  $\gamma_1$  is shown in Figure 2-29.

### 3.6.3.4 Deuteron photodisintegration and Bethe-Heitler processes

There is added interest in measurements of both single and double polarization observables in deuteron photodisintegration based on the discrepancy that Nath observed in the reaction  $d(\gamma \bar{n})n$ . [lxxxvii] The break between theory and experiment occurs at just the energy at which measurements of other reactions suggest the existence of a narrow two-nucleon state/resonance, making the experiment especially compelling. The present indications must be treated very carefully since such a state, usually referred to as a dibaryon, has been sought for decades, and its existence has been announced and then refuted.

BIG can resolve this controversy. The  $d(\gamma \bar{n})n$  measurements involve a secondary scattering of the emitted neutron, making the high flux of the BIG essential. If the Nath data are confirmed, then a program of follow-on measurements is anticipated. These will not only expand the energy range but also address the related polarization of the neutron in the orthogonal

direction. In addition, measurements of the reaction  ${}^3\text{He}(\gamma\bar{n})(np)$  would be very interesting - the presence of a narrow two-nucleon resonance should show up in this reaction. While this specific possibility is very speculative, it has discovery potential and therefore is very exciting.

Another set of experiments that can be pioneered at BIG are the Bethe-Heitler processes. [lxxxviii] For low-Z nuclei which, arguably, may be the most interesting, the question of flux is paramount, as the effect is small. The energy asymmetry in wide- and medium-angle electron/positron pair production off protons (and other targets) is caused by the interference between the first- and second-order Born diagrams and the Compton scattering diagram. It directly probes aspects of quantum electrodynamics, as well as providing a direct measurement of the real part of the Compton amplitude. The two-photon Bethe-Heitler amplitude is closely related to the two-photon exchange amplitude in  $ep \rightarrow ep'$  which is believed to cause the breakdown of the Rosenbluth separation in electron scattering. [lxxxix, xc] It may be much easier to measure two photon exchange effects to high precision in  $\gamma p \rightarrow e^+ e^- p'$  than to measure the electron-positron asymmetry in  $e^\pm p \rightarrow e^\pm p'$  elastic scattering.

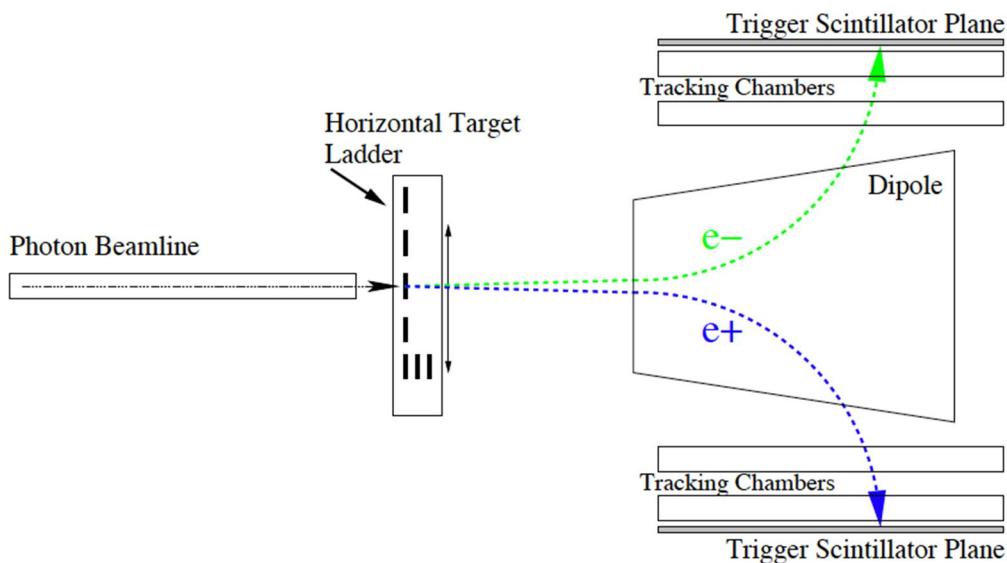


Figure 2-30: A schematic top-view of the proposed experimental layout showing the photon beam, the horizontal target ladder, the pair spectrometer dipole, and the tracking packages (not to scale).

### 3.6.4 QCD with real photons: Nucleon structure

The spectra of baryon resonances have been a focus of experimental and theoretical studies, both for particles composed of the light u and d quarks, and those containing one or more of the heavy c and b quarks. In the energy region available at BIG (from 300 MeV to 5 GeV) the nucleons exhibit many major and minor resonance states. There is increasing activity aimed at

understanding the spectra of particles containing one or more  $s$  quarks, so-called hyperon physics. [xcj] At present the knowledge of the  $\Xi$  and  $\Omega$  families is particularly limited with only a few states experimentally studied, and scant knowledge as to their properties. [xcii] The 5 GeV energy reach of the BIG allows us to search for light-quark + glue hybrid baryons as well as for heavy-quark baryons. Figure 2-31 shows some of the recent lattice QCD predictions, showing the bands of states with alternating parities and increasing energies. [xciii] Each state has a well-defined spin and generally a dominant flavor content. The number of non-hybrid states of each spin and flavor in the lowest-energy bands is in agreement with the expectations based on weakly broken  $SU(6)O(3)$  symmetry. These states correspond to the quantum numbers of the quark model.

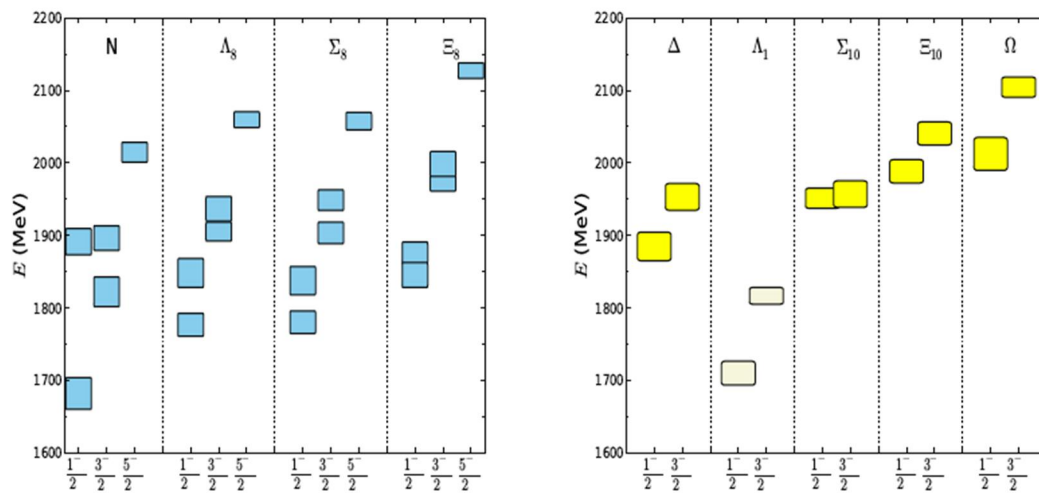


Figure 2-31: Lattice QCD predictions: Left, the lowest negative-parity states (flavor-octet); Right, the lowest negative-parity states that are flavor-singlet (beige) and decuplet (yellow). [xciii]

It would be very important to find some of these predicted states experimentally, but the experiments would be very complicated. To convincingly extract such states we would need to measure almost all polarization observables. This would require  $a \sim 4\pi$  detector to analyze recoil polarization for some channel like  $K\Lambda$  or  $K\Xi^+$ , and both linear and circular photons and one target polarization. [xciv] High flux  $\gamma$ -rays from the BIG and its fully controllable polarization are well suited for such studies. The extremely high intensity of the BIG, exceeding all existing Compton  $\gamma$ -ray sources by four orders of magnitude, is the key for making these experiments possible.

In addition, a precise measurements of  $d\sigma/dt$  and the meson helicity in the  $\phi$  photo-production in the energy region of 2 to 3 GeV may reveal the existence of a  $0^{++}$  glueball, whose contribution falls off rapidly at high energies because of a negative value for  $\alpha(t=0)$ . [xcv] Furthermore, the study of the strangeness quark content in nucleon - which is of great relevance for modern particle physics - can be extracted from the spin observables in  $\phi$ -photo-

production. Also, photo-production of a  $\Lambda$  in  $\gamma p \rightarrow \Lambda K^+$  reactions is of great importance for a microscopic understanding of hypernuclei.

### 3.7 Gamma-gamma collider

Gamma-gamma colliders have recently attracted much interest because they would, thanks to s-channel production, probably provide the cheapest option to construct a dedicated Higgs factory. [xcvi, xcvi] Such a project would require a recirculating linac and possibly energy recovery. The crucial issues for gamma-gamma Higgs factories are the realization of Compton collisions with high repetition rate, the intensity and properties of the Compton- backscattered photons, the stability and the efficiency of the Gamma-gamma Compton process.

A recent proposal for a Higgs factory gamma-gamma collider, called “SAPPHiRE” is based on a recirculating superconducting linac in possible synergy with the Large Hadron-Electron Collider [xcvi]. Pertinent parameters are compiled in Table 2-3.

Table 2-3: Example parameters for SAPPHiRE.

SAPPHiRE	Symbol	Value
total electric power	P	100 MW
e <sup>-</sup> beam energy	E	80 GeV
beam polarization	P <sub>e</sub>	0.90
bunch population	N <sub>b</sub>	10 <sup>10</sup>
repetition rate	f <sub>rep</sub>	200 kHz
bunch length	σ <sub>z</sub>	30 μm
crossing angle	θ <sub>c</sub>	≥20 mrad
normalized horizontal emittance	γε <sub>x</sub>	5 μm
normalized vertical emittance	γε <sub>y</sub>	0.5 μm
horizontal IP beta function	β <sub>x</sub> <sup>*</sup>	5 mm
vertical IP beta function	β <sub>y</sub> <sup>*</sup>	0.1 mm
horizontal rms IP spot size	σ <sub>x</sub> <sup>*</sup>	400 nm
vertical rms IP spot size	σ <sub>y</sub> <sup>*</sup>	18 nm
horizontal rms e- CP spot size	σ <sub>x</sub> <sup>CP</sup>	400 nm
vertical rms laser CP spot size	σ <sub>y,laser</sub> <sup>CP</sup>	2800 nm
laser wavelength	λ	351 nm

laser pulse energy	$E_{\text{laser}}$	5 J
Rayleigh length	$Z_R$	0.3 mm
horizontal rms laser CP spot size	$\sigma_{x,\text{laser}}^{\text{CP}}$	2800 nm
vertical rms laser CP spot size	$\sigma_{y,\text{laser}}^{\text{CP}}$	2800 nm
longitudinal rms laser pulse length at CP	$\sigma_{z,\text{laser}}^{\text{CP}}$	0.15 mm
distance CP-IP	$L_{\text{CP-IP}}$	0.6 mm
$e^-e^-$ geometric luminosity	$L_{ee}$	$2 \times 10^{34} \text{ cm}^{-2} \text{ s}^{-1}$
$\gamma\text{-}\gamma$ luminosity (>125 GeV)	$L_{\gamma\gamma}$	$6 \times 10^{32} \text{ cm}^{-2} \text{ s}^{-1}$

Another recent proposal for a gamma-gamma Higgs factory, submitted to the European Strategy Group Open Symposium in Cracow, uses CLIC technology [xcvii]. There had also been an earlier proposal and study for a gamma-gamma Higgs factory “CLICHÉ” based on CLIC-1 [xcviii]. Yet another proposal has been presented during the ICFA Higgs Factory workshop 2012 at Fermilab [xcix].

Gamma-gamma Higgs factories realize collisions through Compton backscattering of laser (or FEL) photons off the high energy electron beams close to the interaction point. A Higgs factory has advantages compared to a positron-electron collision scheme, in that the electron beam energy required to produce a Higgs particle is lower (about 80 GeV instead of 120 GeV), and positrons are not required. Electron beam energies of 80 GeV and a high repetition rate are the basis of the Higgs gamma-gamma collider, and are within reach of present accelerator technology. At a beam energy of 80 GeV, the laser wavelength should be 300-400 nm. For efficient conversion the total energy of the Compton-scattering laser pulse should be a few joules, e.g., 1 TW peak power and 5 ps pulse length, implying 1 MW average power at 200-kHz repetition rate. Stacking laser pulses in a high-finesse optical cavity reduces the input laser power required by two orders of magnitude, to about 10 kW. An economic way to produce the required  $e^-$  energy is by means of a SC recirculating linac [xcvi]. Operating a recirculating linac with much higher electron current in energy-recovery mode would also, or further, decrease the needed laser power [c]. The Compton IR layout with integrated optical cavity and the production of the required photon beam using a laser or FEL need strong R&D, a large part of which could be studied at FACET-II.

FACET-II can perform several important tests for future gamma-gamma colliders. Specifically, FACET-II could study the realization of multiple collisions using a multi-mirror optical stacking cavity, and the associated laser systems. Two types of such cavities, built by LAL Orsay in France and U. Hiroshima in Japan are presently being tested at the KEK-ATF2, but only with very low repetition rate. Studies of efficiency, tuning schemes, and the photon-beam parameters will be important steps towards a high-energy gamma-gamma collider.

In addition, low energy gamma-gamma collisions could directly be realized at FACET-II. A possible test involves generating electron-positron pairs using two gamma-ray beams colliding at a small angle, on the order of tens of mrad. This would be the first pair creation test using photons.

The maximum cross-section is at  $E_{cm} \sim 1.4 \text{ MeV} \sim 1e-25 \text{ cm}^2$ .

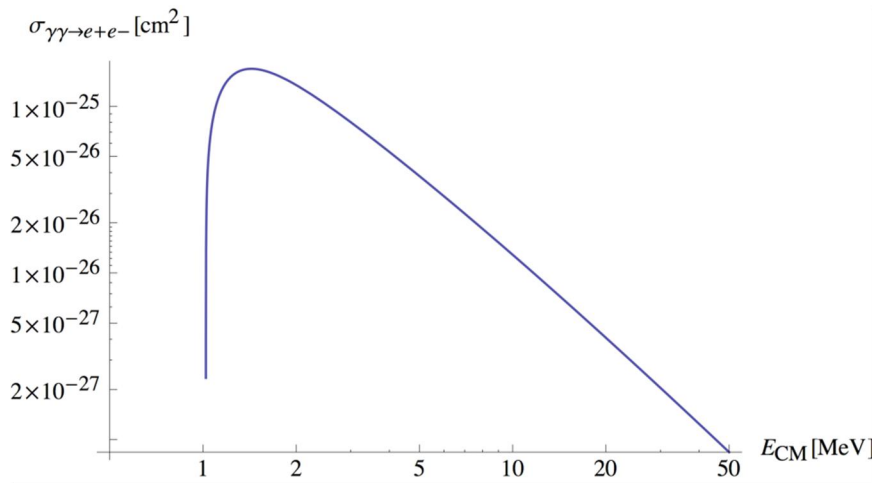


Figure 2-32 Figure 1. Pair creation cross section VS. C.M. energy of colliding gamma.

Therefore it is optimal to use a drive beam energy around 4 GeV and generate 30 MeV gammas using a CO<sub>2</sub> laser. In this case the C.M. energy, calculated as  $E_{cm} = 2E_g \sin \theta$ , comes to  $\sim 1.4 \text{ MeV}$ . Generated positrons and electrons will have close to 30 MeV energy in the laboratory system with an energy spread of 1.4 MeV.

The trajectories of the generated particles are defined by the magnet field of the last dipole. This will allow for a very practical detection system that can detect about 30 events per minute.

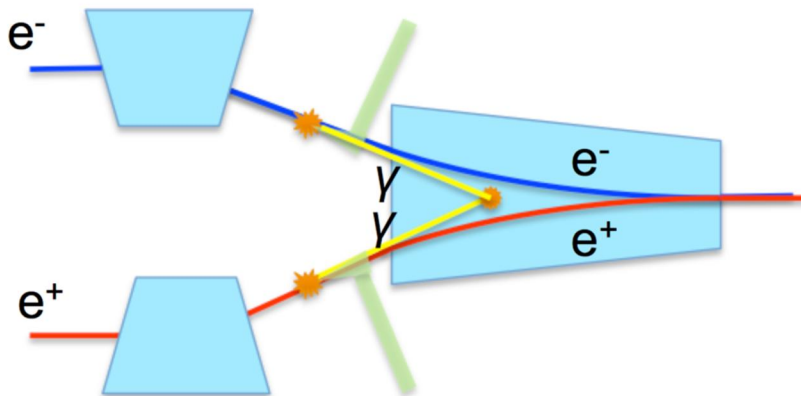


Figure 2-33: Possible layout for gamma-gamma collider using FACET/FACET-II "sail boat" chicane.

Another option is to generate a gamma-ray beam and a VUV beam from two consecutive electron bunches. A focusing mirror can then reflect helium VUV photons and cause them to collide with the gamma-ray head-on. There is potential of higher luminosity in this mode of operation as well as reaching energies needed for generating muon pairs. Also this scheme of self-generated gamma-rays could be of interest for a future gamma-gamma Higgs factory. The gamma-ray and VUV could be generated by an undulator, or possibly by an FEL process.

### 3.8 High intensity Positron Source studies using Gamma beam generated with Compton Beam scattering

The SLC positron source was developed in the early 1980s and successfully supported the physics needs for decades of operations. It still holds the record for highest positron flux capability of the order  $4 \cdot 10^{12}$  e<sup>+</sup>/sec. Demands for newly proposed collider facilities exceed capabilities of the SLC type positron source by a few orders of magnitude. There are number of proposals aimed at addressing this issue, yet there is no demonstrated solution that provides a positron source that can meet the needs of ILC, CLIC, LHeC, eRHIC, and other projects [ci, cii, ciii, civ]. ILC needs a positron source capable of  $3 \cdot 10^{14}$  e<sup>+</sup>/sec, and luminosity of LeHC will be limited with a source below  $4 \cdot 10^{16}$  e<sup>+</sup>/sec (see Table 2-4). The survival of the conversion target is ultimately the limiting factor. Use of novel targets (liquid metal jet target, crystal structure target, pellets) might be necessary to address the demand on the positron beam intensity for the next generation of colliders. The gamma beam capabilities at FACET-II will open unique opportunities to study and advance the ideas on novel positron sources. In this section, we will address the generation of the gamma beams that will be of interest for the testing of novel conversion targets [cv].

Table 2-4: Positron production at the SLC source compared with the needs of future projects

	SLC	CLIC (3 TeV)	ILC (RDR)	LHeC
energy	1.19 GeV	2.86 GeV	5 GeV	60 GeV
e <sup>+</sup> / bunch at IP	$40 \times 10^9$	$3.72 \times 10^9$	$20 \times 10^9$	$2 \times 10^9$
e <sup>+</sup> / bunch before DR inj.	$50 \times 10^9$	$7.6 \times 10^9$	$30 \times 10^9$	N/A
bunches / macropulse	1	312	2625	N/A
macropulse rep. rate	120	50	5	CW
bunches / second	120	15600	13125	$20 \times 10^6$
e <sup>+</sup> / second	$0.06 \times 10^{14}$	$1.1 \times 10^{14}$	$3.9 \times 10^{14}$	$400 \times 10^{14}$

Experimental programs require one of two types of gamma beams: quasi-mono-energetic photons beams or beams with a large energy spread. Optimization of the laser and electron beam parameters to achieve a narrower energy spread (and higher polarization) with angular collimation often results in many orders of flux reduction. The positron generation experiment requires maximizing gamma beam flux, possibly along with a high polarization. The laser and electron beam intensity and their focusing are pushed to the practical limits in this case.

There are many factors to consider when selecting the optimal energy of the gamma beam for positron generation. The energy dependence of the Bethe-Heitler  $e^-e^+$  pair creation process is shown in Figure 2-34.

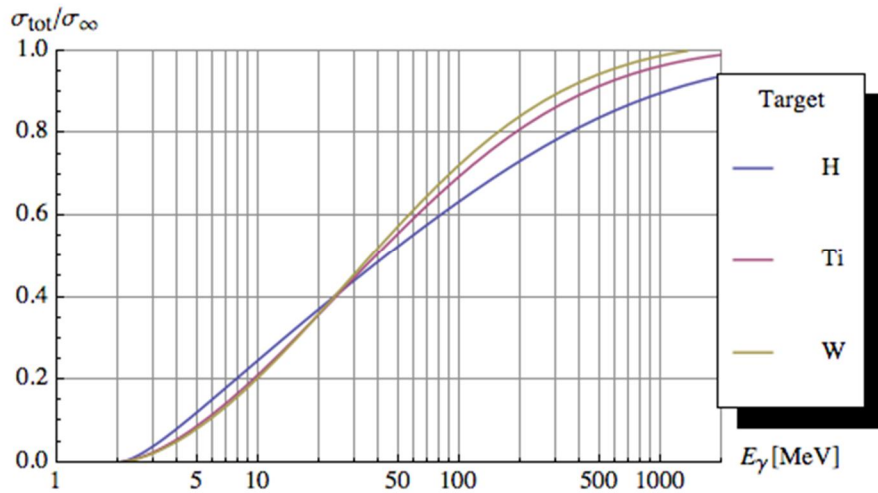


Figure 2-34: Energy dependence for the cross section of the Bethe-Heitler process  $\gamma \rightarrow e^-e^+$  plotted as ratio of cross-sections at given energy to one at extremely high  $E_\gamma$ :  $\sigma_{tot}/\sigma_\infty$ . The dependence is plotted for hydrogen, titanium and tungsten targets.

The energy dependence curve suggests that this process would benefit from a higher energy gamma beam. On the other hand, the longitudinal emittance of the captured beam is proportional to the energy of the generated positrons. The acceptance of the damping ring in practical designs thereby limits the energy of the gamma beam. Detailed optimization studies [ci] concluded a soft optimum in the range of 30-100 MeV.

The expected efficiency of converting polarized  $\gamma$ -photons into captured positrons is between 0.2 and 2%, depending on the energy of the gamma beam [6]. Therefore, every positron requires, as precursors, more than fifty  $\gamma$ -photons assembled in the beam format (time pattern) of the  $e^-e^+$  collider beams. There are different proposals to accumulate this  $\gamma$ -flux for collider applications. A lower intensity yet more concentrated gamma beam is proposed for the conversion studies at FACET-II.

The integral efficiency of the  $\gamma$ -production in the collision can be estimated from  $\frac{N_\gamma}{N_e} = \frac{N_\phi}{S} \sigma_c$ , where  $N_\gamma$ ,  $N_e$ , and  $N_\phi$  are the numbers of  $\gamma$ -rays, electrons, and laser photons, respectively,  $S$  is the cross-sectional area of the interacting beams,  $\sigma_c = \frac{8}{3} \pi r_e^2 = 6.652 \times 10^{-29} m^2$  is the Compton scattering cross-section, and  $r_e = \frac{e^2}{mc^2} = 2.818 \times 10^{-15} m$  is the classical electron radius. With 0.1 Joule of a CO<sub>2</sub>-laser beam focused to its practical limit of 25- $\mu m$  rms radius, the efficiency is estimated as  $N_\gamma/N_e=0.1$ . It is expected that electron beam will be focused to a size smaller than laser beam, at 7.4-GeV electron energy, for the generation of the 100 MeV gammas. A similar efficiency can be achieved in the case of a Ti: Sapphire laser beam of 1.0 Joule. With the Ti:Sapphire laser only a 2.1-GeV beam will be needed for the generation of 100 MeV gammas. The laser beam can be focused much more tightly in this case, but the interaction cross section will be dominated by the electron beam size at approximately the same 25 - $\mu m$  spot. It will become more challenging to design the IP optics for Ti:Sapphire laser beam due to the small divergence of this high energy laser. Generation of gamma beams with lower than 100MeV energy will be more efficient with a CO<sub>2</sub> laser beam. The advantages of CO<sub>2</sub> laser beam for this applications as well as its excellent match to the high-energy pulse linac at SLAC were discussed in more detail in [cv].

To complete the optimization of the laser parameters, such as the peak power  $P$ , pulse duration  $\tau$ , and the energy per pulse  $E$ , we note that to maintain the maximum efficiency of the laser and e-beam interactions, the laser focal spot should match the e-beam size, and its pulse length should be close to the Rayleigh length  $Z_R = \frac{2\pi\sigma^2}{\lambda}$ , where  $\sigma$  is the laser beam radius at the focal plane. For a Gaussian beam of radius 25  $\mu m$ , the Rayleigh  $Z_R \approx 0.3$  mm, and the optimum pulse length of the CO<sub>2</sub> laser is  $\sigma_\tau \cong 1$  ps.

The magnitude of the nonlinear Compton scattering is characterized by the normalized vector potential,  $a = \frac{e\sqrt{-(A_\mu A^\mu)}}{mc^2}$ , where  $e$  is the charge of the electron,  $A_\mu$  is the four-vector potential of the laser, and  $mc^2$  is the electron's rest energy. The parameter  $a$ , simply called "laser strength", can be re-written more conveniently as a function of the laser's wavelength  $\lambda$ , in  $\mu m$ , and intensity  $I$ , in  $W/cm^2$ . In this form  $a = 0.60 \times 10^{-9} \lambda I^{1/2}$ . The nonlinear Compton scattering approaches the linear process at  $a \geq 1$ , thereby putting an upper limit on the maximum laser intensity. The laser strength is not expected to exceed 0.3 for the proposed CO<sub>2</sub> laser beam parameters.

Summarizing this discussion on optimizing the IP for the Compton  $\gamma$ -source, we propose the set of parameters compiled in Table 2-5.

Table 2-5: CO<sub>2</sub> laser- and e-beam parameters at the Compton IP.

Parameter	Symbol	Value
-----------	--------	-------

Laser beam energy	$E_L$	0.1 J
Laser wavelength	$\lambda$	10.2 $\mu\text{m}$
Rayleigh length	$R_L$	0.3 mm
Laser beam length	$\sigma_t$	1 ps
Normalized vector potential	$a_0$	0.3
Electron beam size	$\sigma_e$	15-25 $\mu\text{m}$
Electron beam energy	$E_e$	4-7.4 GeV
Gamma beam energy	$E_\gamma$	30-100 MeV
$\gamma$ -ray production efficiency	$N_\gamma/N_e$	~0.1

A wide range of gamma beam energies, high peak intensities, and low divergence of the gamma beam (due to high energy and low geometrical emittance of the electron beam) make this source optimal for studying novel ideas for conversion targets.

Crystal and hybrid targets are examples of novel conversion targets. Either a gamma beam or the electron beam could be used to hit the test targets. Particles traversing at small angles along a single crystal axis experience the collective scattering force of many crystal atoms. The enormous fields inside the crystal can trap the particles along an axis or plane, a process called channeling. High-energy electrons are attracted by the positive nuclei and, therefore, can produce strongly enhanced coherent bremsstrahlung and pair production. These effects could be used in a positron production target. The target length can be shorter than for an amorphous material, which then yields a higher conversion coefficient and a lower emittance of the positron beam. This makes single crystals very interesting for positron production targets.

### 3.9 BIG - gamma-ray source at FACET-II

The BIG, based on the electron beam and lasers at FACET-II, will be a very versatile, nearly mono-energetic gamma-ray source for nuclear physics experiments. The high quality of the incoming electron beam will allow it to act as a collimator, turning BIG into a nearly mono-energetic gamma-ray beam.

We will assume that energy of the beam in FACET-II can be tuned from 1 GeV to 10 GeV. In combination with two lasers operating at 800 nm and 10  $\mu\text{m}$ , the BIG therefore has 1,000-fold tunability from about 2 MeV to 2 GeV. The high-energy reach can be increased to 5 GeV using the third harmonic of 800 nm laser, but with an accompanying 5-fold loss in the flux.

We will be able to switch lasers or select different harmonics to adjust gamma-ray energy in coarse steps, or change the electron beam energy to provide nearly continuous fine-tuning of the laser.

Table 2-6: Main e-beam and laser parameters for the BIG

Injectors	Beam	Energy [GeV]	$\epsilon_{NX} \times \epsilon_{NY}$ [ $\mu\text{m} \times \mu\text{m}$ ]	$\sigma_X \times \sigma_Y$ [ $\mu\text{m} \times \mu\text{m}$ ]	$\sigma_Z \times \Delta E/E$ [ $\mu\text{m} \times \%$ ]
Thermionic	3nC e <sup>-</sup>	10	30 x 3	20 x 20	40 x 1
	1.5nC e <sup>+</sup>	10	30 x 3	20 x 20	40 x 1
Photoinjector	20pC e <sup>-</sup>	10	0.1 x 0.1	1 x 1	2 x 1
	1nC e <sup>-</sup>	10	1 x 1	3 x 3	5 x 1
	6nC e <sup>-</sup>	10	5 x 5	10 x 10	20 x 1
	3nC e <sup>+</sup>	10	30 x 3	20 x 20	40 x 1
Witness photoinjector	0.1nC e <sup>-</sup>	0.1	1 x 1	50 x 50	20 x 0.1
Lasers	Energy / Power [Joule / TW]	Rep rate [Hz]	$\tau$ [fs]	$\lambda$ [ $\mu\text{m}$ ]	
Tl: Sapphire	1 / 30	10	30	0.8	
CO <sub>2</sub> laser	0.1 / 0.1	120	1000	10.2	
Gamma beams (Inverse Compton)	Energy [GeV]	Intensity	Rep rate [Hz]	$\sigma_X \times \sigma_Y$ [ $\mu\text{m} \times \mu\text{m}$ ]	$\sigma_Z$ [ $\mu\text{m}$ ]
Tl: Sapphire	1.8 GeV	10 <sup>10</sup>	10	5 x 5	10
CO <sub>2</sub> laser	150 MeV	10 <sup>10</sup>	120	5 x 5	10

The  $\gamma$ -ray beam

energy range comfortably covers the energy ranges of interest for users of H $\gamma$ S (TUNL, Duke University) and LEPS (Spring 8, Japan). Using two set of lasers (CO<sub>2</sub> and Ti: Sapphire) and electron beam energies from 1 GeV to 10 GeV, FACET can generate gamma rays with continuously tunable energy from 2 MeV to 1.9 GeV. This three orders of magnitude tunability is indeed unprecedented.

FACET can create gamma rays with unprecedented intensity – from 10<sup>10</sup> to 10<sup>11</sup> gammas per second. This intensity, in combination with the high brightness of the electron beam, allows us to collimate the gamma ray to a nearly mono-energetic beam with energy spread as low as 0.1%.

There is, however, a tradeoff between energy spread comes and flux: For example, a gamma-ray beam with 1% rms energy spread would have typical flux of 10<sup>8</sup> – 10<sup>9</sup> gammas per second, while increasing resolution to 0.1% will reduce the flux to 10<sup>7</sup> – 10<sup>8</sup> gammas per second. Exact numbers depend on specific choice of the gamma-ray energy, as shown in Figure 2-35.

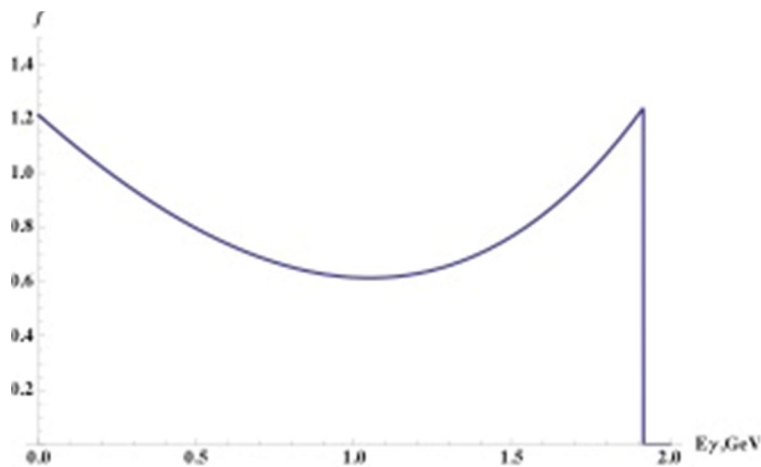
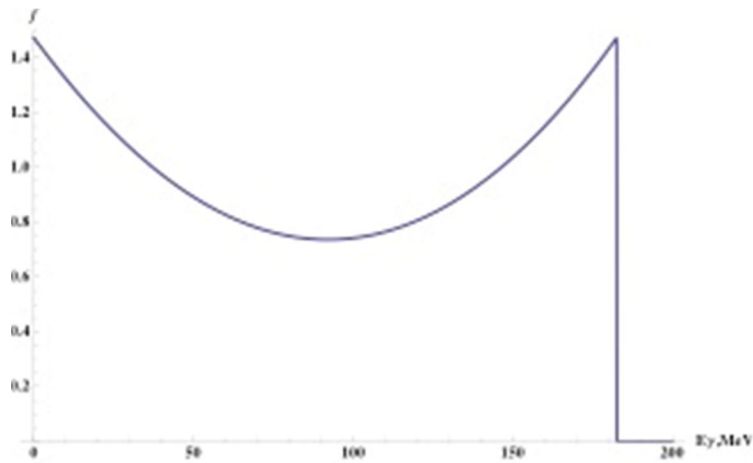


Figure 2-35: Normalized gamma-ray distribution as function of their energy for 10 GeV e-beam: top graph is for a CO<sub>2</sub> laser, bottom graph is for a Ti: Sapphire laser.

The polarization of the  $\gamma$ -rays can be controlled by that of the scattered laser beam, and can be linear (vertical or horizontal), circular (left or right) or elliptical. The degree of polarization depends on the gamma-ray energy: it is very close to 100% at low energies and is 97.7% for 1.9 GeV gamma rays.

Many experiments require a fine energy resolution, and an electron beam with very low emittance provides for such possibility. A simple geometrical collimation of the  $\gamma$ -ray beam can create a  $\gamma$ -ray energy spectra with FWHM below 0.1% (see Figure 2-36). Scanning the energy of the beam will allow us, for example, to de-convolve fine structure of the spin observable at the pion threshold.

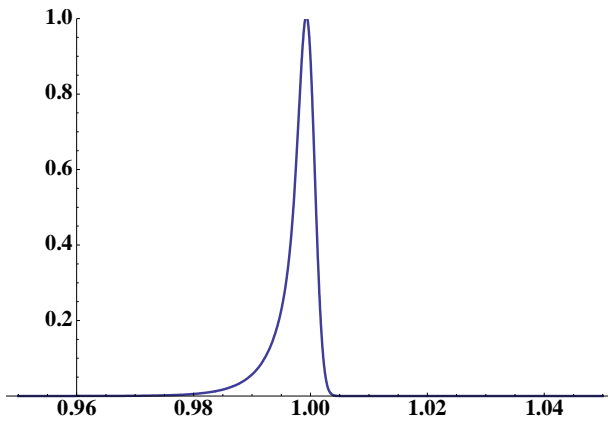


Figure 2-36: A narrow energy spectrum of BIG's collimated beam. Energy spectrum of 0.1% FWHM or better could be obtained at BIG.

Time structure of the gamma-ray bursts can be important for experiments. While pulsed structure with 100-120 Hz is a standard feature of BIG, the structure of each pulse can vary. The  $\gamma$ -rays can be delivered in one short picosecond duration burst, or can be distributed into as many as 1,000 ps bursts separated by 1 nanosecond.

### 3.10 Generating High-Brightness Muon Beams With High-Energy Gammas

Hadron colliders are impractical at very high energies because effective interaction energy scales with beam energy and luminosity must rise as energy squared. Further, the prevailing gluon-gluon background radiation makes it difficult to sort out events. Positron-electron colliders are constrained at TeV energies by bremsstrahlung radiation and also by cost because long linacs are required to avoid synchrotron radiation in the rings. A muon collider will have the same advantages in energy reach as a positron-electron collider, but without prohibitive beamstrahlung and synchrotron radiation.

High-brightness polarized muon ( $\mu^+\mu^-$ ) beams are generated through gamma conversion into pairs in the nuclei field. The dominant effect in the interaction of the high-energy photons with the solid target will be the production of electron-positron pairs. The low-phase space of the resulting muon beams adequately compensates for the small probability of generating a  $\mu^+\mu^-$  pair. The probability of a  $\mu^+\mu^-$  pair creation is suppressed approximately by a factor of  $\mu_0^2/\mu_e^2$ . However, FACET-II will be able to generate extremely powerful high-energy  $\gamma$  beams through Compton backscattering, making it possible to study high brightness muon beam production. Low intrinsic emittance from the direct production of the  $\mu^+\mu^-$  pairs makes this approach competitive with the currently considered production scheme, in which a high-power proton beam generates a pion shower, and the pions, in turn, decay into muons. Indirect muon production is orders-of-magnitude more efficient in terms of the number of the muons per incident beam power. Approximately 0.2% of the drive beam power is converted into the muon beams in case of proton drivers, and only 0.001% is converted with gamma drivers. The brightness of the resulting beam, however, is much lower with protons, so that very challenging

and complicated cooling schemes must be incorporated into the system. Therefore, using protons to create neutrinos may not be as cost-effective as some researchers believe. [cvi]

The interaction of few-GeV gamma rays with the solid target is dominated by their conversion into electron-positron pairs. At these energies, Compton scattering of the photon from the atomic electron is considerably smaller. We will consider the ratio of the  $\gamma \rightarrow \mu^- \mu^+$  to  $\gamma \rightarrow e^- e^+$  cross sections. One can split the Bethe-Heitler total cross-section, describing pair creation, into two parts: an asymptotic region at very high energies of the photon cross sections  $\sigma_\infty$ , and an energy dependent part at lower energy,  $\sigma(E_\gamma) = \sigma_{tot}/\sigma_\infty$  (Figure 2-34), that is in the range from 0 to 1. [lxxxviii] It shows moderate advantage of the light nuclear targets at the lower energy range, and low efficiency for the gamma energies near the muon pair creation threshold.

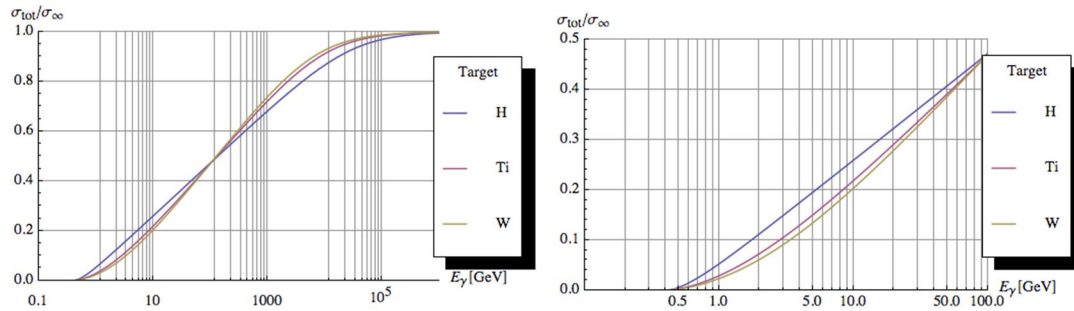


Figure 2-37: Energy dependence for the cross section of the Bethe-Heitler process  $\gamma \rightarrow \mu^+ \mu^-$  plotted as  $\sigma_{tot}/\sigma_\infty$ . The dependence is plotted for hydrogen, titanium and tungsten targets.

The energy-independent part can be written in the following form [lxxxviii]:  $\sigma_\infty = \left(\frac{7}{9}\right) 4\alpha Z^2 r_c^2 \log(W_\infty)$  where  $\alpha$  is the fine structure constant,  $Z$  is the atom charge,  $r_c$  is a classical-particle's radius,  $W_\infty \cong 136 \frac{m_{e,\mu}}{m_e}$  for hydrogen, and  $W_\infty \cong \frac{119}{A^{0.27}} \frac{m_{e,\mu}}{m_e}$  for the rest of the nuclei. The total cross section rises linearly in  $\log(E_\gamma)$  with the slope  $W_M \cong \left(\frac{1}{4}\right) \frac{1}{1.49 m_{e,\mu}}$  for hydrogen, and  $W_M \cong \left(\frac{1}{4}\right) \frac{1}{1.54 A^{0.27} m_{e,\mu}}$  for the rest of the nuclei. Therefore, the total cross-section is  $\sigma_{tot} \cong \left(\frac{28}{9}\right) \alpha Z^2 r_c^2 \log(1 + W_M E_\gamma)$ .

This derivation is valid for well above the threshold photon energy for the muon pair creation and below its saturation energies, i.e. where  $W_M E_{sat} < W_\infty$ . The gamma beams generated with Ti:Sapphire laser beam at FACET-II are within this range.

Now, the probability that the photon will create a  $\mu^+ \mu^-$  pair can be estimated as  $\frac{\sigma_{tot,\mu}}{\sigma_{tot,e}} \approx \left(\frac{1}{4}\right) \frac{m_e^2}{m_\mu^2}$  or between  $0.2 \times 10^{-5}$  and  $0.5 \times 10^{-5}$  (see Figure 2-38). Using the second or third harmonic of the Ti:Sapphire laser beam will result in a harder energy gammas (at lower beam intensity) and will improve muons pair cross section as well it will lower emittances. Some electrons and positrons will be scattered and will regenerate gamma photons with sufficient energy for  $\mu^+ \mu^-$  pair

production. This or other sources of correction to the assessment were not considered since they are not expected to change the result by more than tens of percents.

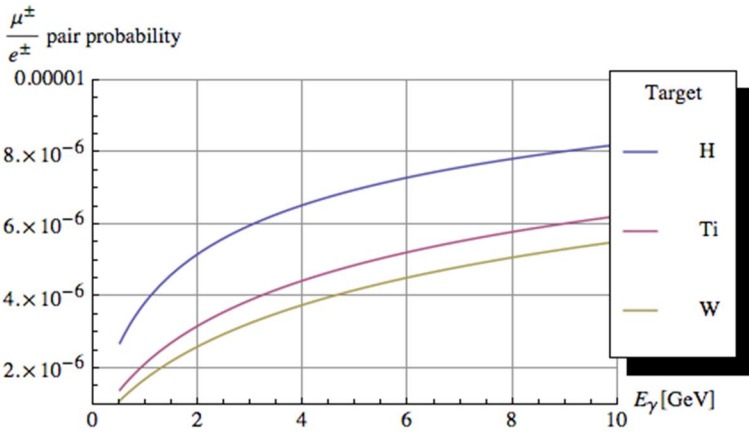


Figure 2-38: Probabilities of creating  $\mu^+\mu^-$  pairs as a function of the incident photon energy for hydrogen, titanium and tungsten targets are plotted.

Approximately 50% of the  $\mu^+$  and  $\mu^-$  beams will be generated with energies ranging from  $E_\gamma/2$  to  $E_\gamma$  when  $E_\gamma \gg 4m_\mu c^2$ . The duration of the  $\mu$ -beam will be similar to that of the  $\gamma$  beam, or drive electron-beam. The estimate of longitudinal emittance can be written in the form  $\varepsilon_{N\parallel} \cong c\tau_e \frac{\gamma_{max} - \gamma_{min}}{4}$ , where  $\gamma_\mu$ ,  $\gamma_{min}$ , and  $\gamma_{max}$ , are the mean, the minimum, and the maximum values for the captured  $\mu^+$  and  $\mu^-$  beams, and  $\tau_e$  is the duration of the electron bunch.

The generated muons have a divergence of  $1/\gamma_\mu$  and muon beam size at the exit of the target with length  $L_{target}$  will be dominated by the muons divergence and can be estimated as  $\sigma_{\mu min} \cong \frac{L_{target}}{2\gamma_\mu}$ . Therefore, the normalized transverse emittance can be assessed as  $\varepsilon_{N\perp} \cong \frac{L_{target}}{2\gamma_\mu}$ . The longitudinal and transverse normalized emittances of the  $\mu^+\mu^-$  beams produced with a high-intensity 2 GeV  $\gamma$  beam from the tungsten target which is one radiation length long are calculated as 150 and 50  $\mu\text{m}$ , respectively. For comparison, it is estimated [cvi] that the longitudinal and transverse normalized emittances of the captured muon beam produced with proton beams are 20 cm and 18 mm, respectively. Approximately one million muons are expected to be captured per second in the 120 Hz mode with abovementioned emittances. Immersing the target into a focusing field, thereby limiting the muon beam's size expansion during the gamma ray-beam interaction, can further reduce transverse emittances. Utilizing crystal targets for pair creation will allow channeling of the created muons therefore will result in even colder beams.

Availability of the muon beams with very low transverse emittances is crucial for studies of novel muon beam cooling and acceleration techniques in the crystal lattices and nanostructures [cvii, cviii] due to naturally low acceptance angles of such structures.

### 3.11 Laboratory Astrophysics at FACET

Ultrahigh-energy cosmic rays (UHECR) and photons have been observed, but their sources and production mechanisms in space are yet to be understood. Laboratory astrophysics experiments may contribute to the understanding of cosmic accelerators in two categories: 1) Calibration experiments for the testing and calibration of UHECR observational techniques, and 2) Dynamics experiments for the investigation of relativistic plasma dynamics to elucidate the underlying physics of cosmic acceleration.

Two calibration experiments have been carried out at the FFTB. The E-165 FLASH experiment helped shed light on the apparent discrepancies in the energy determinations of cosmic rays around  $10^{19}$  eV with precision measurements of air fluorescence yield in an electromagnetic shower. [cix] The T460 experiment demonstrated the principle of a novel detection technique for ultrahigh-energy cosmic neutrinos based on radio Cherenkov signals due to the Askaryan effect. [cx]

In principle FACET can provide high-energy-density particle beams at  $10^{16}$  J/m<sup>3</sup> for dynamics experiments, creating extreme relativistic plasmas in a regime relevant to cosmic acceleration studies and accessible in a terrestrial environment. A third category of lab-astro experiments involves using high intensity or high energy density particle and laser beams as a probe for fundamental physics. An example is the creation of Unruh radiation from a violently accelerated electron in a laser field due to interaction with quantum vacuum fluctuations, a process similar to Hawking radiation from the event horizon of a black hole. [cxi]

While the extreme astrophysical conditions can never be replicated in the laboratory, the challenge is to devise and perform lab-astro experiments that will uncover the physical principles involved that can be scaled up to understand these powerful astronomical sources. Relativistic particle outflows, commonly observed in astrophysical sources such as active galactic nuclei and gamma-ray bursts, are a key element in many models of cosmic acceleration. Their interaction with ambient plasmas is believed to give rise to particle acceleration producing the observed radiation spectrum. An understanding of their dynamics is thus crucial to the development of a theory of a cosmic accelerator. In particular, experiments seek to investigate how kinetic energy of the outflow is converted into plasma instabilities which in turn power particle acceleration and radiation.

A key difficulty is the need for overall charge-neutral beams (overlapping e<sup>+</sup> and e<sup>-</sup> beams) to mimic astrophysical outflows. At FACET, relativistic electron-positron plasmas in the form of directed “jets” could be created by showering high-energy-density electron beams onto a solid target, analogous to the e<sup>+</sup> e<sup>-</sup> pairs that come off the positron target. The dynamics of jet-plasma interaction can be investigated over a scale length of several collisionless skin-depths. In a collisionless plasma, the mean-free-path is long compared to the skin depth so the latter is the relevant scale. Laboratory results can be applied to astronomical collisionless plasmas and will provide important tests of simulations for magnetic filamentation, inductive, wakefield, and ponderomotive acceleration, synchrotron radiation spectra, jet-plasma instabilities, and jet propagation over long distances.

The 2001 Workshop on Laboratory Astrophysics [cxii], the 2003 Workshop on Quantum Aspects of Beam Physics [cxiii], the 2003 Orion Workshop [cxiv], and the 2006 SABER Workshop [cxv] all included presentations on lab astrophysics using particle beams. After the 2006 workshop, SLAC conducted a limited study of these beam-based lab-astro concepts. During the past decade, research teams around the world have instead developed astrophysics-relevant research utilizing high energy-density (HED) facilities such as intense lasers and z-pinchs [cxvi]. Research is underway in many areas, such as compressible hydrodynamic mixing, strong shock phenomena, radiation flow, radiative shocks and jets, complex opacities, equations of state, dust formation, super strong magnetic fields, and relativistic plasmas. We will not review these developments, so the reader is referred to the HEDLA Meetings, held every two years, for details. [cxvii]

We list the presentations from the Lab-Astro, Orion and SABER workshops that are relevant to possible lab-astro experiments in Table 2-7 through 2-9. Online workshop proceedings include further details [cxii, cxiv, cxv]. The Proceedings of the 2003 “Quantum Aspects of Beam Physics” workshop [cxiii] cover many of the same lab-astro topics, so we do not review it here. The titles in the tables clearly indicate the preponderance of “dynamics” experiments, especially those involving charged beams, neutral beams, and lasers, in some cases with background magnetic fields superimposed to mimic astrophysical environments such as shocks, particle jets, gamma-ray bursts, supernovas, and neutron stars. Calibration experiments are the next most represented, and these can be related to dynamics experiments when code validation is required to connect simulations, laboratory results, and astrophysical observations. Beam parameters for most experiments are usually not discussed in detail, although for jet-plasma and laser-induced shock/instability experiments there is some specific information in the slide presentations. Broadly speaking, the lab-astro experiments that might use SLAC’s relativistic electron-positron beams are often flexible with respect to beam energies, which simply change the time and length scales according to the Lorentz factor. The bunch densities are usually in the range  $10^{14}$  -  $10^{18}$  /cc, bunch lengths are in the range 10 - 1000  $\mu\text{m}$ , bunch diameters are of order 10 to 100  $\mu\text{m}$ , plasma lengths are about a meter, and background magnetic fields (usually solenoidal) vary from 1 to 104 Gauss depending on the experiment.

Table 2-7: Presentations related to possible experiments from 2001 Lab-Astro Workshop. [cxii]

Presenter	Title	Experiment Type
David Cline	Primordial Black Hole Induced Plasma Instability Expt.	Dynamics
Pierre Sokolsky	High Energy Shower Expt. for UHECR	Calibration
Jasper Kirkby	CLOUD Cosmic Ray Expt. on Climate Variation	Calibration
Pisin Chen	Plasma Wakefield Acceleration Expt. for UHECR	Dynamics

K. Nakajima	Laser Driven Dirac Acceleration for UHECR Expt.	Dynamics
A. Odian	Non-Askaryan Effect Expt.	Calibration
R. Rosner	Astro Fluid Dynamics Computer Code Validation Expt.	Calibration
S. Colgate	Magnetic Flux Transport and Acceleration Expt.	Dynamics
T. Kamae	Photon Collider for Cold $e + e -$ Plasma Expt.	Dynamics
M. Begelman	X-Ray Iron Spectroscopy and Polarization Expt.	Calibration
Johnny Ng	Relativistic $e + e -$ Plasma Expt.	Dynamics
T. Katsouleas	Beam-Plasma Interaction Induced Photon Burst Expt.	Dynamics
R. Blandford	Beam-Plasma Filamentation Instability Expt.	Dynamics
J. Scargle	Relativistic MHD Landau Damping Expt.	Dynamics

Table 2-8: Presentations related to possible experiments from Orion Workshop 2003. [cxiv]

Presenter	Title	Experiment Type
Pierre Sokolsky	Laboratory Particle Astrophysics	Calibration
Robert Bingham	Fundamental Physics using Atomic Beams and Lasers	Fundamental Physics
David Saltzberg	Neutrino Astrophysics and the Askaryan Effect	Calibration
Pierre Sokolsky	Ultra High Energy Cosmic Rays and the FLASH Expt.	Calibration
Kevin Reil	Alfven Wave Induced Wakefield Acceleration for UHECR	Dynamics
Richard Sydora	Nonlinear Alfven Wave Dynamics: Wave Steepening and Particle Acceleration	Dynamics
Johnny Ng	Cosmic Accelerators in the Laboratory	Dynamics
K. Nakajima	Intense $e+e-$ Pair Beam Production in Superstrong Laser-Matter Interactions for LabAstro Experiments	Dynamics
A. Yashin	Wave-Packet Approach to Unruh Effect	Fundamental Physics

Richard Klein	Creation of a Neutron Star on a Petawatt Laser	Dynamics
A. Spitkovsky	Electrodynamics of Magnetized Rotators	Dynamics
Robert Bingham	Similarities between e and v Beams in Plasmas	Dynamics
R. Paul Drake	Connecting Laboratory Experiments with Astrophysical Phenomena	Dynamics

Table 2-9: Presentations related to possible experiments from SABER Workshop 2006. [cxv]

Presenter	Title	Experiment Type
Pierre Sokolsky	Some Thoughts on the Importance of Accelerator Data for UHE Cosmic Ray Experiments	Calibration
Pisin Chen	ESTA: End Station Test of ANITA	Calibration
A. Spitkovsky	Pulsars as Laboratories of Relativistic Physics	Dynamics
Johnny Ng	Astro-Jet-Plasma Dynamics Experiment at SABER	Dynamics
Kevin Reil	Astrophysical Plasma Wakefield Accelerator	Dynamics
Bruce Remington	Science Outreach on NIF: Possibilities for Astrophysics Experiments	Dynamics, Calibration
Eduardo de Silva	Can GLAST Provide Hints on GRB Parameters?	Dynamics, Calibration
G. Barbiellini	Stochastic Wakefield Particle Acceleration in GRB	Dynamics

### 3.12 Measurements for the CLIC study at the FACET-II facility

The characteristics of the FACET-II facility at SLAC makes it an ideal test-bed for measurements of crucial importance for the CLIC study. Consequently the CLIC study is preparing a formal proposal for the approval of the following experiments to be performed at FACET-II:

- Experimental verification of the performance of system identification, feedback and on-line alignment algorithms for the linear collider and final-focus
- Direct measurement of the long-range transverse wakefields of industrialized CLIC main-linac accelerating structures
- Direct measurement of the transverse wakefields of linear collider final focus collimator geometries

More details of the experiments are presented in the following sections.

### 3.12.1 Verification of on-line system-identification, feedback and tuning algorithms

The performance of future linear colliders depends critically on beam-based alignment (BBA) and feedback systems. ILC and CLIC will routinely undergo dispersion-free steering (DFS) in the main linacs [cxviii, cxix]. In CLIC, an option for a parasitic on-line dispersion-free correction is being studied.

DFS is a beam-based alignment technique for steering the orbit and correcting the dispersion at the same time. The technique requires accelerating one or more test beams with different gradients to evaluate the dispersion. The steering is performed by minimizing the offset of the nominal beam in the beam position monitors (BPMs) and zeroing the difference between the test beam trajectories and the nominal trajectory. The experimental verification of the DFS algorithm is essential to prove its effectiveness and to prepare the commissioning of such machines.

Knowledge of the system model is crucial for developing effective beam-based algorithms. In the CLIC main linac for example, even small changes in the acceleration gradients, the phases, or the magnet strengths can significantly change the the system model. A reliable knowledge of such a system response is very important. We propose using an adaptive system identification algorithm that measures the system response matrix dynamically and automatically [cxx]. We propose to test such system identification procedures and beam-based alignment algorithms for linear colliders at FACET-II. Figure 2-39 shows the results of some simulations.

The very small emittances in linear colliders require fast correction of static and dynamic imperfections, e.g. misalignment and ground motion, through beam-based alignment algorithms and feedback. The effectiveness of such algorithms is, however, limited by the knowledge of the matrix representing the response of the beam trajectory to the action of the correctors. FACET-II, with its km-long linac accelerating both electrons and positrons to a relatively high final energy, and with micro-metric emittances, offers an ideal setup for testing beam-based alignment algorithms and the system identification algorithms. We believe that this experiment will be crucial to consolidate and perfect the procedures needed to commission and operate future linear colliders.

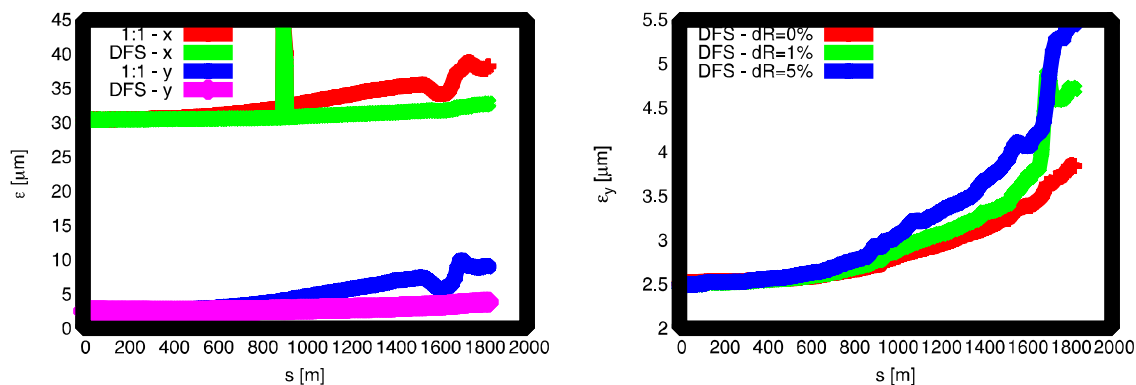


Figure 2-39: Emittance growth in the first 2 km of SLC linac, after BBA correction. Left-hand plot shows the horizontal and vertical emittance for 1:1 corrected and DFS corrected machines. The right-hand plot shows the

vertical emittance growth after DFS when the correction is computed using an imperfect model. Each curve is the average of 100 randomly misaligned machines.

During the first half of 2012 we have been able to perform the experiment at FACET. During this time we have installed our software on the FACET servers and performed several tests of system identification and beam-based alignment. The system identification and beam-based alignment algorithms have proven to be extremely successful, especially when dealing with orbit correction. We believe we can improve these results and test more advanced techniques such as emittance tuning bumps or dispersion bumps.

System identification results are shown in Figure 2-40. The response matrices shown in the figure were obtained automatically in about two hours of operation with no need for any human intervention, using our dedicated software.

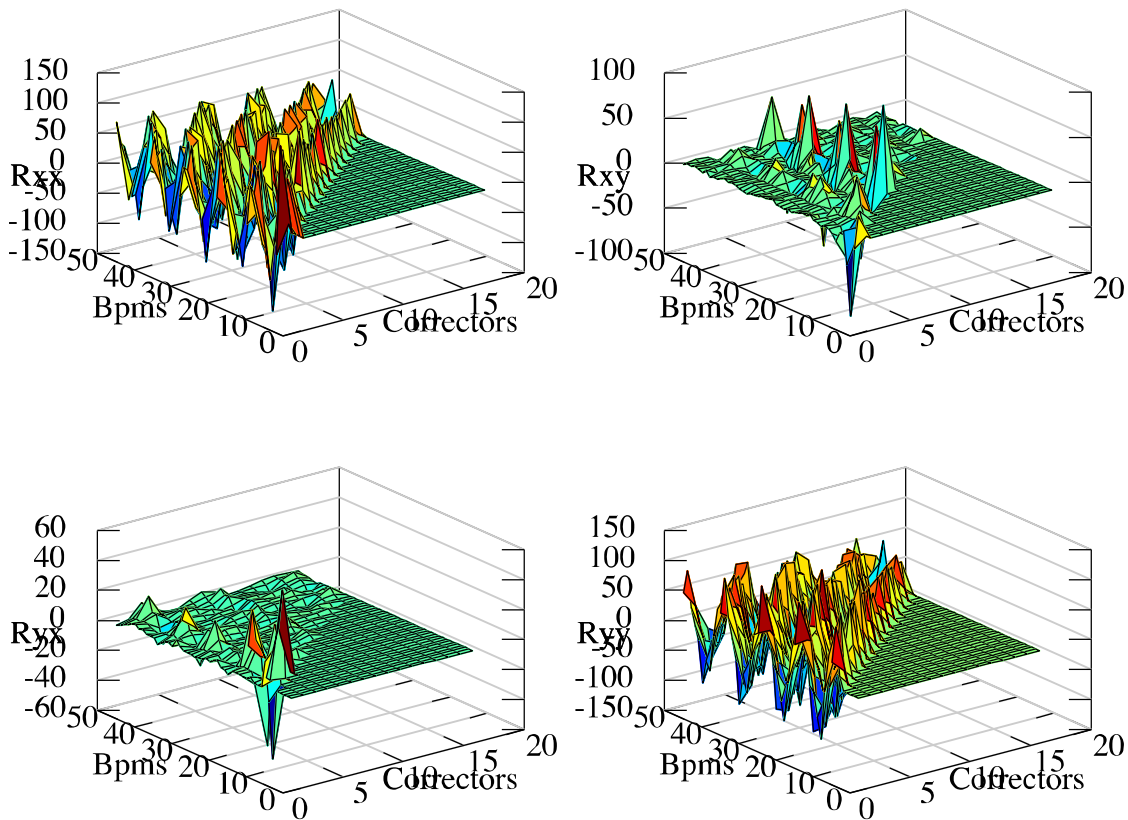


Figure 2-40: Result of the system identification algorithm during the run in June 2012. From top to bottom, left to right, the matrices  $R_{xx}$ ,  $R_{xy}$ ,  $R_{yx}$ , and  $R_{yy}$ .

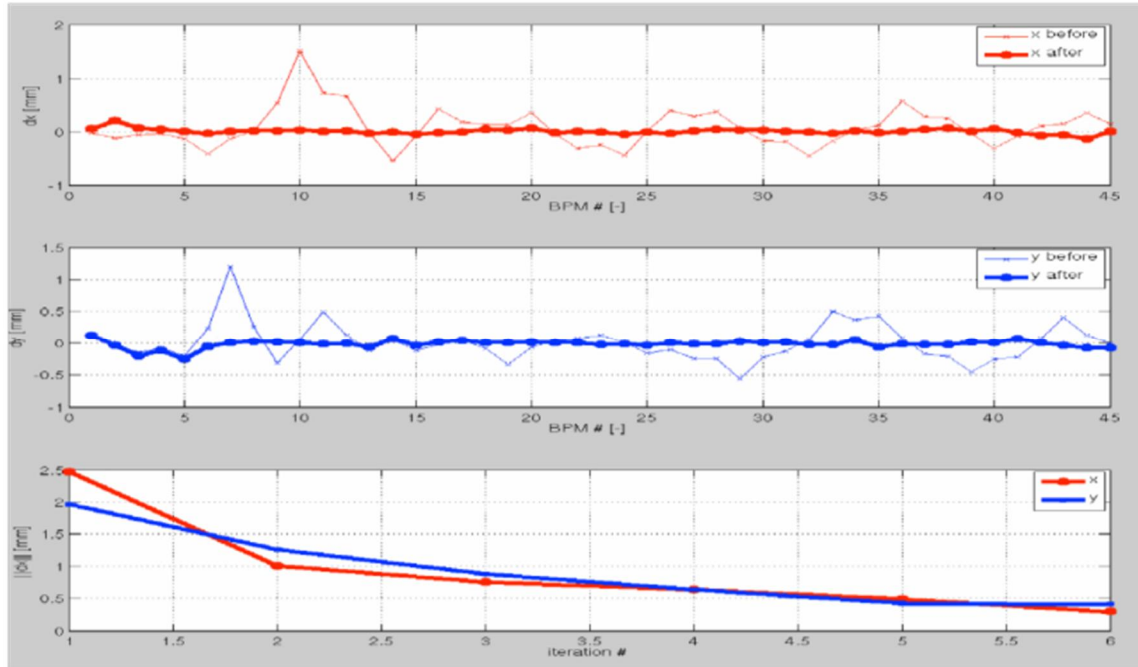


Figure 2-41: Result of the orbit correction algorithm during the run in June 2012. From top to bottom: the horizontal orbit, the vertical orbit, and the absolute error.

Example of results of global orbit correction are shown in Figure 2-41. An initial orbit, exhibiting an oscillation as large as about 1 mm, was steered to read zero on the BPMs, within the jitter of the machine. The orbit correction we implemented performed in an efficient and robust manner. The orbit correction software automatically performed the six iterations shown in figure in less than two minutes, with each iteration taking about 20 seconds.

### 3.12.2 Measurement of long-range transverse wakefields in industrialized accelerating structures

Manufacturing of the CLIC main linac accelerating structures will progress from the prototype phase to an industrial facility in a few years. Given the complexity of the manufacturing process, it will be crucial to suppress the long-range wakefields as effectively in the industrialized structure as in the test prototypes. Given the characteristics of its electron and positron beams, the FACET-II facility provides a unique opportunity to measure wakefield suppression.

The CLIC baseline accelerating structure is composed of a tapered chain of 26 damped cells with a double-feed coupler for the input and the output power [cxix]. See Figure 2-42 for a picture of a prototype. The damping suppresses the wakefields in order to reduce them to an acceptable value and to preserve small emittances during the accelerating process. It is implemented by four rectangular waveguides coupled to the main accelerating cells. The waveguides are terminated by inserting pieces of lossy dielectric loads inside. We expect to have strong long-range wakefield suppression, about a factor 50 in 6 RF cycles (15 cm). This allows us to minimize

the coupling of two consecutive bunches of the CLIC train. The simulated transverse wakefield is shown in Figure 2-43.



Figure 2-42: High-power test structure. The overall length is 30 cm.

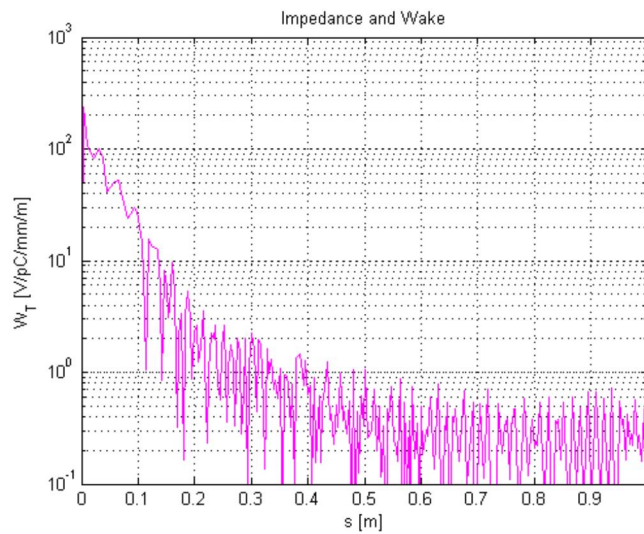


Figure 2-43: Simulated wakefields for the CLIC accelerating structure as a function of the distance from the driving bunch.

The x-band test structure setup will consist of six accelerating structures in a common vacuum tank. At this stage no power will be sent to the test structure and the double feed couplers will be terminated by the loads. The test structure will consist of clamped aluminum cells. We would need positrons to function as a driving bunch and electrons as a witness bunch to measure the kicks due to the drive bunch by varying the bunch separations in order to map wakefields.

We would like to measure the transverse wakefields of a fully-featured accelerating structure as a function of distance behind a driving bunch. The driving and the witness bunches must be separately positrons and electrons in order to separate trajectories and achieve sufficient resolution in the downstream beam position monitors (BPMs), which measure the deflecting angle. This angle is in inverse proportion to the energy of the witness bunch. The achievable resolution of the wakefield will depend on beam energy, driving bunch charge, beam offset and BPMs resolution. The absolute value of the wakefield can be increased by installing multiple structures. Bunch length should be ideally less than 1 mm in order to resolve the third dipole band which shows up a peak around 40 GHz in the real part of the impedance spectrum.

### 3.12.3 Measurement of collimator transverse wakefields

Another experiment to be performed at SLAC is the measurement of collimator wakefields. Collimator wakefields in the Beam Delivery System (BDS) of future linear colliders, such as the ILC and CLIC can be an important source of emittance growth and beam jitter amplification, consequently degrading the luminosity. For this reason it is vital to understand and measure such collimator wakefields both theoretically and experimentally. Single-bunch collimator wakefields have been measured in [cxxii, cxxiii, cxxiv, cxxv] with the aim of benchmarking theory, numerical calculations and experiments. Those studies revealed some discrepancies between the measurements and the theoretical models. Given the characteristics of such wakefields, a lower energy beam with short bunches is required. The perfect candidate for such measurements is the beam provided by the End Station Test Beam (ESTB) test facility at SLAC.

New measurements using ESTB at SLAC will help to understand the origin of the above-mentioned discrepancies. For a rigorous comparison between measurements, theoretical calculations and simulations, the precise measurement of the bunch length will be essential. We are especially interested in the regime of short bunches relevant for the CLIC studies. This experimental test uses several collimator prototypes with different materials and geometric design, with the system set up to provide bunches with longitudinal length as close as possible to the nominal CLIC bunch length. We will compare the measured wakefield kick factors with simulation and analytic calculation results.

## 3.13 FEL R&D or 'A particle beam physics research program at the FACET-II'

### 3.13.1 Introduction

Particle beam physics is at the core of the development of new instruments for the exploration of the properties and organization of matter at the sub-atomic, atomic and molecular scale with increasing space-time resolution. High energy accelerators, are the instruments that allowed the development of the standard model of elementary particles, and are now opening the exploration of atomic and molecular science with the resolution of angstroms and femtoseconds.

A strong and robust program of research in the physics of particle beams and their interaction with lasers and plasmas is critical as we continue to expand the capabilities of particle accelerators, while reducing their cost and size. The program must have a theoretical/numerical

simulations component and a strong experimental component to verify calculated expectations on a large scale. National laboratories such as SLAC have the facilities needed to carry out the research and are the natural medium for this activity. The program should also have a strong university component, essential for educating the new generation of scientists in this field. The university component can and should include some smaller “university scale” experiments as well. We can prove many concepts with experiments at existing, medium size, accelerator test facilities, such as the Accelerator test facility at Brookhaven National Laboratory or NLCTA at SLAC, using beam energies in the range of 50 to a few hundred MeV.

There is a large class of important, frontier experiments requiring electron beam energies larger than a few GeV. One such class of experiments is that of laser/plasma accelerators. Another class is the acceleration and manipulation of high brightness electron beams, including manipulation with lasers, used for synchrotron radiation sources and FELs, discussed in section 3.13.2.

In the following sections we describe several experiments. It is important to notice that while these frontier experiments may vary in their primary goal, the beam physics, the required instrumentation and the theoretical/numerical tools have much in common. There is a strong synergy between the these types of research and the facilities needed for experimental proof. The advances in laser/plasma accelerators, with the capability of producing accelerating fields of 1 GeV/m or larger, is an important step toward reducing the cost and size of hard x-rays FELs and advancing particle physics. The improved knowledge of how to transport high brightness beams while preserving their 6-dimensional phase space and measuring their characteristics will be extremely useful for advances in laser plasma accelerators and their applications.

There are four lines of research to improve the performance of existing FELs and open the way to the next generation of these photon sources:

- Quality and control of the electron bunch - the lasing medium and the 6-dimensional phase space distribution;
- Quality and control of the FEL photon pulses, including transverse and longitudinal coherence, peak power, and spectral power density;
- Special features important for experiments using the photon pulses, are tunability, synchronization, polarization control, intensity stability, pulse duration, and multicolor FELs;
- Maximization of the energy transfer from the electrons to the photon pulse. Increasing the number of coherent photons generated per electron.

### 3.13.2 Electron beam - brightness for next-generation FELs

The FEL lasing, its gain length and many other characteristics depend strongly on the electron brightness and 6-dimensional phase space distribution. The phase space distribution is determined by the electron source, the acceleration and compression process, and a variety of collective effects, including coherent synchrotron radiation, wake fields in the linac, longitudinal space charge effects and more. The present state of the art is good enough to power a SASE FEL down to a few Ångstrom wavelengths. However, the peak current is limited by CSR effects, and

the distribution is not ideal for the lasing process. A typical example of longitudinal distribution of the electron bunch at the LCLS undulator is shown in Figure 2-44.

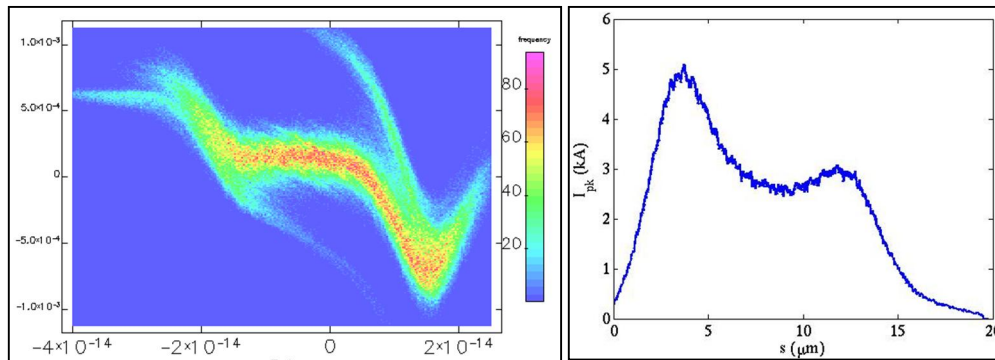


Figure 2-44: Start-to-end simulation of the longitudinal distribution of the LCLS electron bunch.

The current and energy spread change along the bunch, thus changing the local gain length, a situation similar to that of a conventional atomic laser where the density and temperature of the lasing medium change along its length. The less than ideal current and energy profile limit the transverse and longitudinal photon pulse coherence, and the effectiveness of seeding, self-seeding or iSASE. It also reduces the peak power obtainable when tapering the undulator.

Improving the 6-dimensional phase space distribution and making it nearer to the ideal condition for driving an FEL is a difficult task, requiring the development of new methods to: compress the beam to achieve the high current needed to drive an FEL, better control and possibly take advantage of collective instabilities, shape the beam temporal profile, and optimize the electron current generated by the gun. Improved higher resolution diagnostics to characterize high brightness, very short (femtosecond duration) electron and photon pulses, as well as hundreds of femtoseconds long bunches needed for very small radiation line width, are also a challenge and in need of continuous development. It will also need the development of higher resolution phase space diagnostic instrumentation

Examples of possible studies include, but are not limited to: shaping the temporal and spectral profile of the electron current from the gun to minimize linac wakefield effects, using velocity bunching in the injector to minimize downstream magnetic compression, introducing nonlinear elements in the bunch compressors. These experiments are time consuming and require the flexibility to modify critical components such as the electron gun, linac, compressor system, thus making it impossible to execute in a user facility FEL such as LCLS. Study and proof of techniques to reduce the RF jitter from the power sources is another crucial program as jitter in the RF amplitude and phase translates to electron beam energy jitter in the accelerator and a chirp in the photons.

### 3.13.3 SASE FELs and longitudinal coherence

Hard x-ray FELs now in operation operate in the SASE mode, the typical photon pulse line width is given by the FEL parameter,  $\rho$ , of about  $10^{-3}$ , and the temporal profile consists of spikes with length proportional to the cooperation length. Each spike has a transform limited line width, again on the order of  $\rho$ . Very short photon pulses of a few femtosecond duration, consisting of a few spikes, have been obtained at LCLS at SLAC by two methods: 1) reducing the electron bunch charge and compressing its duration to a few femtosecond; 2) filtering the electrons through a foil to spoil their emittance except for those in a very short part of the bunch.

The generation of very short photon pulses is one line of development for soft and hard x-ray FELs. However, the small number of lasing electrons limits the number of photons in a pulse. For larger bunch charges and longer photon pulses with many spikes, the longitudinal coherence is well above the transform limit.

Much attention and work has been dedicated to improving the longitudinal coherence for long bunches and reducing the line width to values between  $10^{-4}$  and  $10^{-5}$ . The methods proposed include seeding the electron beam with external lasers, and self-seeding. More recently an idea was proposed at SLAC to implement a corrugated pipe to induce strong longitudinal wakefields, which can be used to manipulate the chirp in the beam energy. [cxxvi] Calculations to prove this principle at lower energies and some experiments at about 60MeV to confirm the theory were conducted [cxxvii,cxxviii]. We need to conduct a full-scale demonstration using high brightness GeV beams with parameters similar to the beams at the entrance to the wiggler to validate the use of the technique on FEL accelerators. Another recent proposal, called the improved SASE (iSASE), is to insert electron delay lines between the undulator sections to discretely increase the photon/electron interaction instances within the bunch to increase the SASE gain [cxxix]. This experiment also requires a full scale experimental facility. An R&D program should include experimental assessments of the most promising methods, explore the capabilities of each technique and characterize their technology requirements.

For the studies of these techniques, in particular the external laser seeding (which requires imprinting an external energy modulation on the electron beam, which then causes the beam to bunch further and using the higher harmonics of the initial bunching) it is important to have a beam of a few GeV energy, similar to that required for soft x-ray FELs and high brightness beams. The preservation of the bunching from the seeding point to the radiating undulator and the study of nonlinear effects in the harmonic generation are important and can only be realistically studied with a beam energy not too far from that of the beam energy required for the FEL.

### 3.13.4 Polarization control, multicolor FELs, synchronization and other special features

A GeV class test facility is needed with enough space dedicated to the undulator systems to test methods of varying and controlling the photon polarization, generating prescribed multicolor

photon beams, and developing techniques to synchronize x-ray pulses with other laser pulses for pump-probe experiments down to the femtosecond level.

Multicolor pulses can be generated by using different undulators on the same electron beams or possibly with other techniques such as electron beam energy chirping by use of external lasers. The proposed facility offers the unique opportunity to utilize the beam generated by a laser/plasma accelerator to drive an FEL, possibly using undulators with a transverse magnetic field gradient to compensate for large energy spread in the electron beam generated by plasma accelerators. If successful this opportunity for a novel way to drive the FEL would have an important impact on the design of future coherent photon sources, reducing the cost and size of these facilities and making them available on a wider scale.

### 3.13.5 Terawatt peak power FELs

Increasing the peak power and reducing the pulse duration of the x-ray pulse can have an important impact on single shot imaging experiments, making possible the imaging of a single molecule. This goal can be achieved using tapered undulator if the longitudinal coherence of the photon pulse is increased with respect to the SASE case, reducing the line width to  $10^{-4}$  or better. The studies of the longitudinal coherence, and the related longitudinal phase space distribution are critical for this possibility.

An alternative to the tapered undulator approach is to use a high charge, long, energy chirped electron bunch to drive the FEL, generating a long photon pulse with a frequency chirp. The chirp could be of the order of 1% in energy and 2% in frequency. The photon pulse, initially in the few hundred femtosecond region, can then be compressed with a double grating system to a pulse length of about 10 fs, with a corresponding increase in peak power. The large frequency band can be useful in imaging, in particular to reduce the number of diffraction patterns needed for 3-dimensional sample reconstruction. The electron energy chirp can be further enhanced with specially designed vacuum pipe as wakefield generator, which can be tested on the FACET-II beamline as described in section Error! Reference source not found..

### 3.13.6 Seeding Methods

We present several schemes for seeding that should be pursued.. These schemes each have distinctive requirements and areas for concern, and may best be studied at dedicated test facilities. We also discuss issues can apply to any FEL scheme, seeded or otherwise, although some are more relevant or suited to certain design types than to others.

#### 3.13.6.1 Self-seeding

Self-seeding is a straightforward extension to SASE FELs that can ideally yield coherent output, or at the minimum a significantly reduced bandwidth and thus increased spectral brilliance. Researchers at SLAC have demonstrated a self seeding scenario [cxxx] At the beginning of 2012 the LCLS implemented hard x-ray self-seeding with a single diamond monochromator. This

scheme is currently limited to a pulse duration of the order of 10 fs. To produce x-rays with even narrower bandwidth, we can investigate different crystals and alternative self-seeding configurations, such as using two bunches.

For soft x-ray applications, R&D is focused on various monochromators that provide high resolving power, tunability, and small optical delay to reduce the electron chicane requirements. Soft x-ray self-seeding R&D efforts can be pursued at the LCLS as well. The main challenges are how to achieve tight synchronization, and how to improve the resolving power of the monochromator to yield a coherence length of 100s of fs (a bandwidth below 20 meV).

The Enhanced Self-Amplified Spontaneous Emission (ESASE) technique could resolve some of the synchronization issues by providing an alternative method to link the output to an external laser. It also provides an alternative method to changing the electron bunch length for controlling the pulse length and can be applied to generate short pulses, as described below. Cross-correlation between x-rays and experimental lasers is needed to provide the necessary time stamp.

R&D in this area has several goals. We need to improve soft x-ray monochromators by reducing bandwidth and increasing tunability, which implies R&D on optical systems. It is important to test optimal placement of monochromators, verify improved brilliance, and explore tapering. With ESASE, we can evaluate these techniques in combination and develop required laser cross-correlation technology. Most of these goals can be met at existing facilities or involve component R&D that do not need to be incorporated into a full FEL facility. However, since lower bandwidth monochromators deliver less power to the second stage of the FEL, the minimum power levels required for coherent output need to be experimentally observed. This does require a full FEL facility, although the scaling for the required power can be verified without achieving 1 nm wavelength.

#### *3.13.6.2 High Gain Harmonic Generation*

High Gain Harmonic Generation (HGHG) is a standard harmonic generation scheme and has recently been successfully implemented in the FERMI FEL operation down to 20 nm radiation wavelength. The expected effective harmonic conversion factor for a single stage HGHG is about 10. In order to go to shorter wavelengths, the concept of the "fresh bunch" cascaded HGHG has been proposed. The scheme can be sensitive to beam timing jitters and various errors can be accumulated through the cascading process.

R&D should focus on demonstrating cascaded HGHG at higher harmonic radiation wavelengths. This research can be carried out in SDUV in SINAP, SDL in BNL and FERMI FEL in Trieste.

While the HGHG operates in the nonlinear regime and does not require much FEL gain, the power radiated by the electron bunch is critical for the scheme. Thus, there are constraints on minimum current and maximum emittance for this scheme to work. While it would be preferable to observe HGHG reaching 1 nm output, a well-characterized FEL output one harmonic jump away from 1 nm, in the range of 5 to 10 nm, should be sufficient for R&D needs.

### *3.13.6.3 Echo Enabled Harmonic Generation*

Echo Enabled Harmonic Generation (EEHG) is a novel beam manipulation concept using two seeded lasers, and is currently under intense study in several laboratories. The scheme has the potential to go directly to a higher harmonic number well beyond a factor of 10. However, going beyond a factor of 100 (to reach soft x-rays from UV laser) presents tough challenges due to physical effects such as intrabeam scattering and incoherent and coherent synchrotron radiation, as well as practical effects such as tolerance, jitter, and imperfection of laser and electron beams. R&D should focus on better understanding and modeling of these physical and practical effects. The strictest requirements are on the second seed laser with tolerances that depend on the ratio  $\lambda_2/\lambda_{x\text{-ray}}$ . Demonstrations of EEHG beyond a factor of 10 as well as reaching shorter wavelengths are critical, and are planned at NLCTA at SLAC, SDUV in SINAP, SDL at BNL and FLASH at DESY.

EEHG involves purely external manipulations of the electron beam, with radiated power during the seeding stage actually being a deleterious effect. The manipulations themselves are very complex and produce a delicate phase space structure, so it is crucial to demonstrate bunching at the 1 nm wavelength. While FEL radiation and gain are helpful indicators of success, they could in theory be replaced by accurate slice diagnostics of the beam.

### *3.13.6.4 HHG (at-wavelength and cascaded)*

This direct seeding method uses a High Harmonic Generation (HHG) process in a noble gas to produce attosecond pulses with enough power at very short wavelengths to overcome incoherent shot noise. The broad bandwidth of HHG systems is not well matched to the FEL bandwidth, dropping the effective efficiency of the seeding process. Typical efficiencies for state-of-the-art systems are on the order of  $10^{-6}$  and fall significantly lower below 10 nm wavelength. Several optical elements are necessary to transport and focus the HHG source to the undulator entrance, causing further losses. As a result, power requirements for the HHG driver are daunting. Combining an Extreme Ultraviolet High Harmonic Generation (EUV HHG) source with a single-stage HHG or EEHG in a hybrid approach may enable us to reach soft x-rays of nm wavelengths. R&D can be carried out at FLASH, SPARC and elsewhere.

Key R&D efforts include improving total efficiency from the HHG drive laser to FEL output and optimizing transport of HHG output radiation. We can either reduce HHG bandwidth at a given high harmonic, or explore filtering of the HHG source. It is important to test FEL output beam quality both at the selected HHG target wavelength and at an x-ray harmonic.

Even more so than in the HHG scheme, radiation by the electron beam is a crucial aspect of HHG seeding. The seeding begins in the small-signal regime, requiring a large amount of FEL gain. Still, the FEL performance could be characterized in the 5 to 10 nm range and then extrapolated to a final harmonic jump to 1 nm. There might be some advantage in varying the tradeoff between bunch compression and energy spread in order to make the effect of HHG seeding on the beam more readily apparent.

#### *3.13.6.5 FEL efficiency and high peak power*

As electron beam power is a limiting factor, improving the efficiency of energy conversion from the electron beam to the radiation pulse is a major priority. This becomes especially important when applications require pulses of short duration with a large number of photons. Typical SASE FELs have an efficiency on the order of  $10^{-3}$ , which can be modestly increased through tapering. Simulations suggest seeded FELs can be tapered much more effectively with an order of magnitude improvement. After succeeding with the self-seeding experiment, LCLS can be the ideal place to carry out R&D with increased taper strength and additional undulators, potentially producing a TW-class FEL. High power may also allow one x-ray pulse to be split and delivered to several experimental stations, increasing the capacities of x-ray FELs.

#### *3.13.6.6 Harmonics and short wavelength optimization*

Nonlinear 3rd and 5th harmonics allow for radiation at significantly shorter wavelengths than what is practical at the fundamental resonant wavelength for a given electron beam energy. Typical measured power levels at LCLS and FLASH are 1% for the 3rd harmonic and 0.1% for the 5th harmonic, as a fraction of the fundamental power level. With a tapered undulator, simulations predict reaching a few percent of the power level in the fundamental on the 3<sup>rd</sup> harmonic under some conditions. This potential enhancement should be explored further. Harmonic afterburners that are not effective at the FEL gain can still produce enhanced radiation at short wavelengths if placed after the saturation when a subharmonic pulse has been reached.

#### *3.13.6.7 Polarization control*

Polarization control can be carried with an afterburner undulator, tuned to either the upstream wavelength or a harmonic, as described above. A pair of undulators in crossed geometry and a phase shifter in between is an alternative method, which may allow more rapid variation of polarization but with less control of stability. R&D can be carried out at FERMI@Elettra with APPLE undulators and is planned at LCLS with a DELTA undulator.

#### *3.13.6.8 Pulse duration and bandwidth*

Coherent pulses are desirable for many applications. Low-bandwidth pulses with transform-limited duration of hundreds of fs are also useful, but may require a post-FEL monochromator. In the opposite limit, attosecond pulses, especially synchronized as part of a pump-probe configuration, have many applications. Various techniques have been proposed to reduce the x-ray pulse length below a femtosecond. The spoiler foil has been successfully tested. Other promising techniques include: compressing few-pC electron bunches; ESASE or ESASE-like bunch manipulation; and variants of EEHG and HHG using a few-cycled seed laser. Methods for pulse shaping and control are also important goals.

### *3.13.6.9 Beam quality and consistency*

Jitter in the FEL output should be reduced as much as possible. In addition to designing for low jitter in timing, pulse energy, and wavelength, diagnostics for both electron beam and radiation fields and feedback control are important areas of R&D. Many applications require longitudinal and transverse coherence. While SASE typically offers ~80% transverse coherence, seeded beamlines may yield even better results. Laser-seeded FELs must contend with the multiplication of phase variations (e.g., frequency chirp) by the total harmonic jump.

### *3.13.6.10 Justification and priorities*

A full scale test facility is needed to test the most promising schemes explored and developed and experimentally demonstrated at various laboratories. Such a full scale demonstration is important prior to implementing the novel schemes at user facilities.

For hard x-rays, self-seeding is likely the only viable approach for seeding. For soft x-rays, EEHG is the best risk-reward scheme, and should be aggressively pursued. Self-seeding is also a very viable option with possibly a modest loss in capabilities. R&D on hard and soft x-rays is already being pursued at LCLS and should be expanded upon. HHG seeding and other short-wavelength sources to a large part depend on external developments in the field; however, the criteria for a good laser for seeding an FEL are distinct from those for atomic physics research, and thus some guided HHG development is desirable, especially for trains of pulses with narrow bandwidth at a given harmonic. Also, HHG seeding with a single pulse is a good candidate for producing an attosecond pulse. Other ideas for generating attosecond pulses, such as using short electron bunches or variations on the EEHG scheme, are important to pursue as well. Work on an HHG cascade is underway at FERMI@Elettra, and its requirements are essentially a subset of what is necessary for studying the EEHG scheme.

Improving the photon intensity is an important aspect to enhance the capabilities of a given FEL facility. The efforts will allow for more science to be done at a single FEL beam-line. A full FEL beamline with enough undulator to go past the conventional saturation point should be aggressively pursued for these studies. Optimization of FEL harmonics production can improve the photon energy reach and/or reduce the linac cost.

Polarization control requires a functioning FEL but does not require going to saturation, in fact it is expected not to work well at saturation. As improvements in undulator technology may solve this concern, this is a lower priority item. Again, it is less important to operate at 1 nm for these studies.

Synchronization, generating repeatable, high-quality electron beams, measuring sub-fs pulses accurately, and other diagnostics are important issues but do not require a functioning FEL to pursue. To study repeatability and uniformity of the electron beam, a priority item is to work with an at least 2 GeV and high beam quality electron beam which is compressed to the order of 1 kA current, and to use some combinations of laser heater, third harmonic cavity, and wakefield enhancement device in order to flatten the energy profile and damp small-scale instabilities. Other desirable R&D consists of studies of independent components which will be discussed in the section on diagnostics and control systems.

### 3.14 FACET-II THz Studies

The terahertz (THz) region of the electromagnetic spectrum represents a largely unexplored and untapped tool with respect to manipulating and controlling phases of matter using light. When we apply intense THz fields to samples we have the potential for conditioning or controlling matter, stimulating it with surgical precision, and exploring pathways to induce new phases not accessible via other means. An ultrashort single-cycle THz light pulse (see Figure 2-45) has a frequency that is resonant with the bonds that hold materials together ( $\sim 1\text{-}20$  THz) and is capable of biasing a material or device on time-scales of order 100 femtoseconds.

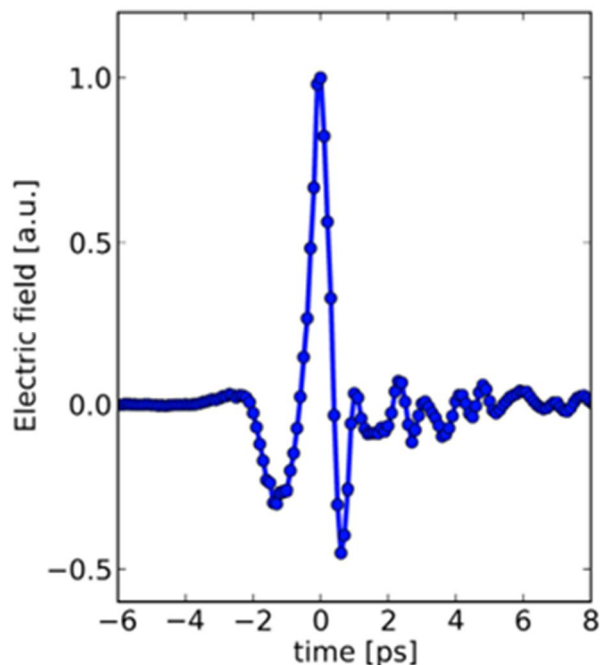


Figure 2-45: THz electric field temporal profile

The bonding strength of materials corresponds to energies of around 1 eV, with the spacing between atoms of a few Angstroms. The ratio of these numbers gives electric fields on the order of  $0.1 - 1 \text{ V/\AA}$  ( $10\text{-}100 \text{ MV/cm}$ ), which sets the scale of fields that are required in order to exert a non-perturbative influence on the structure of solids all-optically. These fields correspond to electromagnetic energy densities of 1 to 10 GPa, comparable to the pressures required to synthesize new phases of matter in diamond anvil cells.

There is a long history of using lasers and various nonlinear optical down-conversion techniques to generate single cycle THz light fields, and field strengths are now on the order of  $1 \text{ MV/cm}$ . While these approaches are being continuously improved, there is no clear pathway towards reaching the field strengths noted above in the frequency range of interest. [cxxxi] Accelerator-based sources, making use of the large electric and magnetic fields associated with a relativistic electron bunch, provide a means of reaching fields at the level of  $1 \text{ V/\AA}$ . Indeed, at  $0.35 \text{ nC}$  bunch charges, experiments at using the SLAC linear accelerator have demonstrated peak fields of around  $0.4 \text{ V/\AA}$  with higher fields possible. [cxxxi] Similar fields are possible at FACET now, with peak energies around 1 mJ. Recent experiments also using the SLAC linac have

demonstrated that these fields can be used for switching of magnetic materials. [cxxxiii, cxxxiv] Figure 2-46. shows a historical summary of the THz electric fields generated by both laser-based and accelerator-based sources.

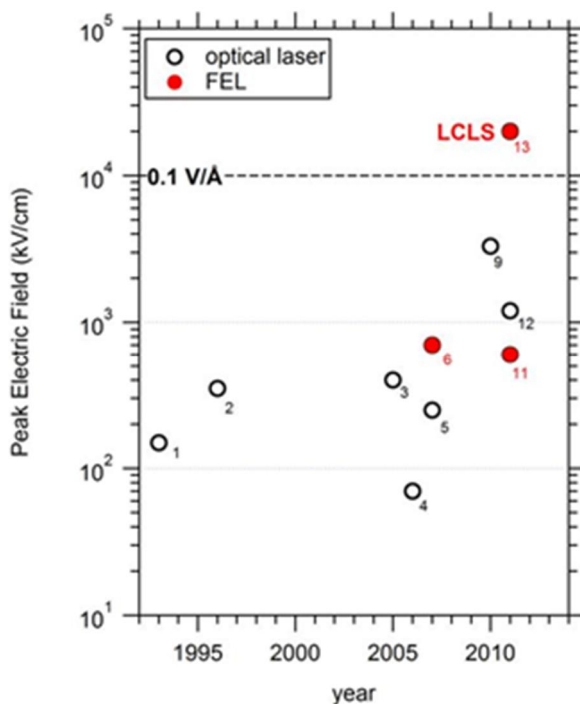


Figure 2-46: Historical summary of peak THz electric field, comparing laser-based and accelerator-based sources.

The interaction of THz fields in this parameter space with matter is only just beginning to be explored. The science case is broad, with opportunities spanning atomic and molecular to condensed phase systems. We described a few examples in the sections that follow.

### 3.14.1 THz manipulation of atoms in the solid state:

Whereas many nonlinear THz-driven responses associated with electron motion in materials have been observed [cxxxv, cxxxvi, cxxxvii, cxxxviii, cxxxix] over the last decade and more, studies in which these fields are used to directly manipulate atomic positions are in their infancy. In parallel with the magnetic switching studies, the electric field of single cycle THz fields can be used to manipulate and unravel the coupled structural and electronic degrees of freedom and the complex phase transitions that underlie the emergence of ferroelectricity and multiferroicity, in which the ferroelectric polarization is encoded through atomic displacements within the unit cell. Through vibrational excitation and all-optical application of intense single-cycle fields, [cxl] these measurements will enable discovery of means for programming these materials with light and controlling the microscopic pathways that the atoms and electrons follow along their potential energy surfaces, which in turn determine their functional properties. In recent experiments at the LCLS, [cxli] we have shown how large amplitude modulations in the internal electric fields within ferroelectric  $\text{PbTiO}_3$  nanolayers are reflected in atomic-scale motions within the unit cell, elucidating the first steps in the photovoltaic response of these materials. The THz fields generated by FACET-II may be used to directly

reorient or switch the polarization, or induce specified electrical, electromechanical, or structural responses, effectively guiding these systems along well-defined atomic-scale trajectories. We will be able to couple these THz fields with absolutely synchronized probe pulses also generated by the FACET-II electron beam.

### 3.14.2 THz manipulation of electrons and spins

Relativistic electron beams at FACET-II represent a truly unique source of intense half cycle electric and magnetic field pulses that are the closest analog to an electric switch operating at THz speeds. They enable novel forms of controlling the behavior of electrons and spins in future devices relevant for information technology. While transition-metal oxide electronics based on electric field driven metal-to-insulator phase transitions is one of the most promising avenues towards energy efficient field-effect transistors, [cxlii] switching the magnetization direction in ferromagnetic transition metals by electric fields alone, i.e. without dissipative electric currents, can be considered as the holy grail of energy efficient magnetic data storage. Both goals can be attacked using the unique x-ray and THz capabilities available at FACET-II.

Ongoing magnetic switching experiments at FACET demonstrate the feasibility of such an approach (Figure 2-47). The high-energy electron bunch traverses the magnetic sample with an in-plane easy axis, imprinting a figure-eight magnetic pattern that depends on the number of electrons in the bunch and the temporal length of the bunch. Before exposure to the beam the sample is uniformly magnetized in-plane. When using 140 fs long pulses a characteristic deviation from an ideal figure-eight pattern (observed for ps long pulses) occurs. This deviation is ascribed to the influence of the electric field as indicated by the simulation shown in the lower panel of the figure. Such experiments currently employ a post mortem analysis of the magnetic switching patterns.

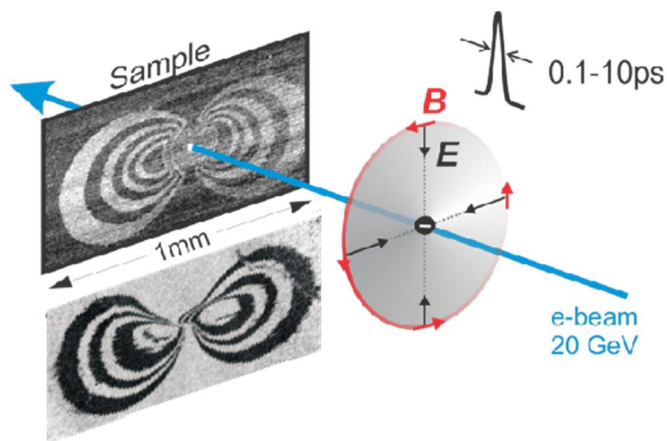


Figure 2-47: Schematic of the magnetic switching experiment using an ultrashort electron bunch surrounded by a magnetic and electric field. [cxxxiii]

The availability of femtosecond laser probe beams at FACET-II opens up radically new ways of probing transient electronic and magnetic states. It will enable us to study femtosecond electron dynamics in epitaxial transition metal oxide films undergoing an insulator-to-metal transition induced by THz electric-field pulses ( $\sim 0.1$ GV/m). [cxliii] Obtaining laser snapshots of

the evolving electronic structure in a single-shot fashion is essential to the fundamental understanding of pure Mott-Hubbard-like switching of electrical conductivity without dissipative lattice transformation.

Current methods often require repetitive measurements near the damage threshold [cxliii]. We need to go beyond that to understand the fundamental processes and develop new materials that can withstand the required electric fields. Such studies can also be extended to ferromagnetic metals, where even higher THz fields ( $>1\text{GV/m}$ ) can alter the electronic structure significantly, [cxxxiii] leading to novel forms of magnetization switching. Our final goal of such switching experiments is to determine the coherence time of THz electronic excitations driven by the intense electrical field pulses. While electronic dephasing and lifetimes have been studied in detail for the optical frequency region less is known for low-energy excitations in the THz spectral range. The unique availability of electron-positron bunch pairs with variable temporal spacing at FACET-II would finally open up the possibility to study the influence of electronic coherence in the time domain. Only for a coherent electronic motion would the subsequent positron bunch restore the initial electronic and spin configuration.

### 3.14.3 THz radiation to trigger surface chemical reactions

Many processes relevant to society, such as catalysis in chemical and energy production, the fabrication of computer chips, weathering and corrosion, the behavior of biomaterials and the fate of contaminants in the environment, rely on surface chemical reactions. . Catalytic reactions are driven thermally. These thermal excitations include phonons (substrate lattice vibration), frustrated vibrational motion of molecular adsorbates, and translational and rotational motion of molecular adsorbates (Figure 2-48A). When the excitation of these vibrations mediates the nuclear motion along the reaction coordinate, chemical reactions cause bonds to either break or form.

FACET-II provides opportunities to develop ways to stimulate chemical reactions on surfaces by triggering the motion of nuclei using THz radiation generated by an ultra short electron bunch. Assuming an electron pulse width of 100 fsec, broadband radiation is obtained with a high frequency cut-off at 10 THz, which matches the frustrated vibrational motions of adsorbed species on the surface. Both the frequency of THz radiation and the strong, directional electric field are of major interest. The coherent and broadband character of THz radiation from FACET-II generates a strong electric field,  $>1 \times 10^9 \text{ V/m}$  (or  $>0.1 \text{ V/\AA}$ ). The quasi half-cycle pulse character of the radiation corresponds to a strong ultrashort half-cycle unipolar pulse. We envision using this strong electric field to excite frustrated vibrational motions collectively to drive a chemical reaction (Figure 2-48B). [cxliv]

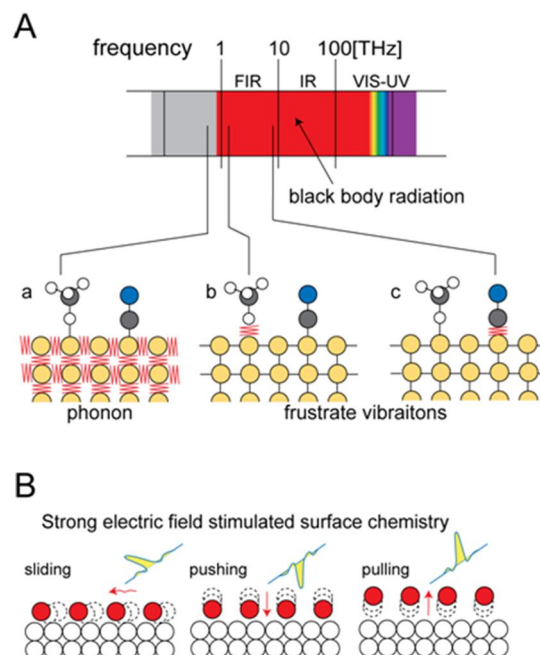


Figure 2-48: A) Excitation at surfaces: a) lattice vibration of the substrate (phonon), b) frustrated vibrational motion of the physisorbed (weakly adsorbed) species, c) frustrated vibrational motion of the chemisorbed (strongly adsorbed) species. The arrows indicate the maximum frequency of black body radiation at room temperature. B) Excitation of frustrated motions collectively using half cycle electric field pulse in different directions to the surface.

In addition to the field strengths and pulse shapes noted above, a key aspect of these studies involves generating synchronized optical or infrared probe pulses to probe the dynamics driven by the THz fields. These can be generated by a phase-locked laser or directly by the same transition radiation process that has been employed at FACET to generate coherent THz fields (Figure 2-49). Here the optical transition radiation can be separated by a dichroic mirror from the broadband THz fields and used as an absolutely synchronized probe pulse to record chemical dynamics. Nonlinear optical probes, for example, allow for direct access to the structural symmetries of a crystal and can be used as powerful probe of the underlying atomic-scale dynamics. We have carried out preliminary studies along these lines using the LCLS electron beam with high fields and observed dynamic processes at these high fields not previously observed (Figure 2-49).

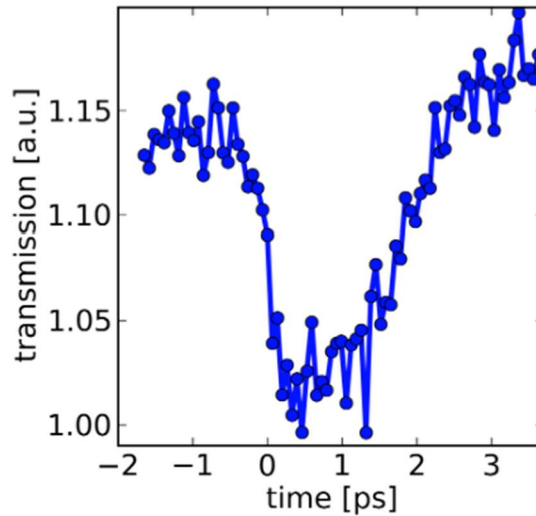
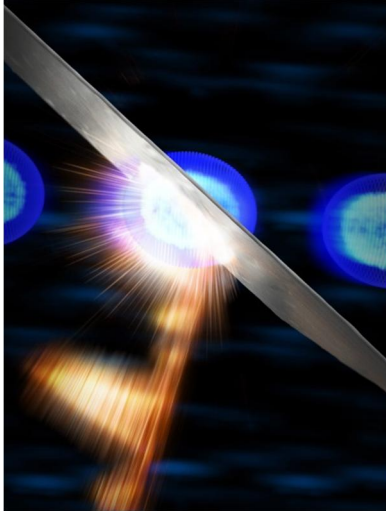


Figure 2-49: Schematic of coherent transition radiation process in which a femtosecond electron beam passes through a thin metallic foil in order to generate intense THz fields (left). First THz pump/optical probe studies of dynamics in GaAs in which pump and probe are simultaneously generated by the foil (right).

### 3.15 National-Security and Fundamental Topics with Intense Beams of Photons of Energy 5 MeV and Greater Produced by Inverse Compton Scattering

The DOE's National Nuclear Security Agency (NNSA) of the United States has instructed the nation's design laboratories to conduct full-system certification using a methodology called Science-based Stockpile Stewardship that is expressly absent any future full-scale test. In short, the Stewardship program must make the best scientific use of the cataloged data.

Were it possible, tests of nuclear weapons would include the confinement of the released energy (the yield) by a calorimeter, the temperature rise of which would provide a direct measure of the yield. Realistically, however, the yield is determined indirectly by a variety of other means. For example, the prompt yield is inferred from the output of gamma rays. [cxlv, cxlvi, cxlvii] Radiochemical analyses of the atomic and isotopic constituents remaining in the aftermath of the explosion provide another, independent evaluation of the yield. Both methods of yield inference hinge on extant knowledge of instrument calibrations and photonuclear cross sections. Today, while the data may be stored and static, these methods remain active topics in search of better information on which to base their estimations.

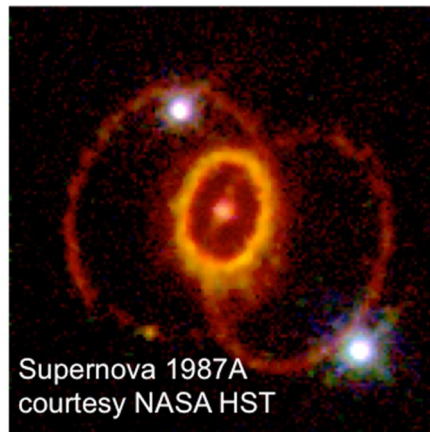


Figure 2-50: Supernovas – the fiery death of massive stars where heavy-element nucleosynthesis takes place – provide C, O and other elements of life.

Our proposal for national security missions entails the use of FACET-II for reducing uncertainty in models tangible to stockpile stewardship, for example, to improve our understanding of absolute energy output. Other topics relevant to national security and undertaken with a bright, quasi-monoenergetic source of gammas of  $\geq 5$  MeV in energy include predictive capability of material damage, fundamental nuclear physics, and radiography. More advanced, if ambitious, uses of FACET-II are also of interest to the NNSA. The generation of coherent gammas for the manipulation of nuclear transitions in analogy with the coherent excitation of electronic transitions is but one example. Below, we outline some of the research areas of interest as well as introduce topics for general consideration at FACET-II.

### 3.15.1 Calibration of United States Nuclear Test Gamma-Ray Detectors

This topic is of interest to science-based and predictive-capability Stockpile Stewardship programs at the LANL and LLNL. HFK detectors (high-frequency kintertium, the latter being a tungsten alloy) were used to measure gamma production from nuclear tests, and their data are archived. These detectors produced vital statistics that are recorded for significant events in United States Nuclear Test History, which ended in September 1992. Pulsed, spectrally-broad bremsstrahlung radiation produced at LINACS was used to calibrate the bandwidth response of HFK detectors. We remain far less certain, however, of the absolute energy calibration, or spectral response, of these detectors. To the extent that models carry uncertainties from this clouded aspect of archived data, a program in spectral calibration of HFK detectors becomes a matter of Stockpile Stewardship. For the calibration, we would chart the response of an HFK detector versus energy of an incident and reasonably monochromatic gamma beam. The gamma source at Duke University's H $\gamma$ S has the needed energy range but not enough flux. A gamma source at FACET-II, however, could deliver all the needed aspects of energy range, energy resolution, and flux.

### 3.15.2 Astrophysics and Stellar Nucleosynthesis

Nuclear reactions in stars take place at temperatures between  $10^3$  and  $10^5$  eV, but the corresponding reaction rates are rarely measured below 1 MeV in the laboratory. Most rates

used in stellar models thus come from severe extrapolations of the experimental data into the astrophysical-temperature regime. We offer as an example the lively controversy [cxlviii, cxlix] about the laboratory cross sections for  $^{12}\text{C}(\alpha, \gamma)^{16}\text{O}$  and consequences [ci] of their theoretical extrapolation to the low energies at which the reaction effectively operates. As for the nomenclature of the reaction, the parenthetical  $(\alpha, \gamma)$  and ordering of nuclei means that  $^{12}\text{C}$  is the target bombarded by an alpha particle, which on collision produces a  $\gamma$  and leaves  $^{16}\text{O}$ . The reaction affects the relative abundance of two atoms of which we are largely made, making it little wonder that the  $^{12}\text{C}(\alpha, \gamma)^{16}\text{O}$  problem is of paramount importance in nuclear astrophysics. Moreover, the ratio C/O following helium burning (of which  $^{12}\text{C}(\alpha, \gamma)^{16}\text{O}$  is a part) figures critically in the fate of massive stars, determining in some instances whether they collapse to black holes or neutron stars. The  $^{12}\text{C}(\alpha, \gamma)^{16}\text{O}$  cross section also appears in burning models and perhaps forensics of nuclear weapons.

Weller *et al.* at HI $\gamma$ S indicate that  $^{12}\text{C}(\alpha, \gamma)^{16}\text{O}$  cross sections are reported for energies no lower than 1.2 MeV and are in sufficient discord to make extrapolation to stellar-burning energies of 0.3 MeV treacherous. [cxlix] The *inverse* reaction,  $^{16}\text{O}(\gamma, \alpha)^{12}\text{C}$ , however can be examined at HI $\gamma$ S and the cross section for  $^{12}\text{C}(\alpha, \gamma)^{16}\text{O}$  obtained by detailed balance. Calculations by Weller *et al.* showed that the then present  $5 \times 10^7$   $\gamma$ /s flux of HI $\gamma$ S at  $E_\gamma \approx 10$  MeV in 2009 was sufficient to inspect  $^{12}\text{C}(\alpha, \gamma)^{16}\text{O}$  at the equivalent energy of 1.5 MeV. An expected brightness upgrade for HI $\gamma$ S to  $\sim 10^{11}$   $\gamma$ /s would push the equivalent energy far lower. Still greater fluxes, however, as might be produced at FACET-II, will be needed to measure the  $^{12}\text{C}(\alpha, \gamma)^{16}\text{O}$  cross sections accurately at the equivalent (incident alpha) energies of 300 keV and lower as relevant to nucleosynthesis in red giants (*cf.* Fig. 6 of Fowler [cxlviii]). In topics as diverse as stellar evolution, the nucleosynthetic origins of life's elements, and the outcome of silicon burning and the heavier elements that follow, much would be riding on such a foundational measurement.

Apart from  $^{12}\text{C}(\alpha, \gamma)^{16}\text{O}$ , there are numerous other reactions of importance in nucleosynthesis with still greater uncertainty. Weiss [cli] lists ten *p*-capture processes (proton-capture nucleosynthesis, such as  $^{27}\text{Al}(p, \gamma)^{28}\text{Si}$ ) for which the uncertainties at stellar temperatures range from factors of 2 to nearly 2000. Specific isotopes of Na, Mg, and Al figure in these processes and range widely in their calculated abundances, often turning an estimated metallicity of a star into a hazardous guess. As with the  $^{12}\text{C}(\alpha, \gamma)^{16}\text{O}$  reaction, a FACET-II beam of high flux could interrogate nine of these *p*-capture processes at relevant stellar temperatures using the inverse reaction and detailed balance. Doubtless other nucleosynthetic processes are in need of similar clarifications.

### 3.15.3 Nucleon Compton Scattering and Tests of QCD

Experimental work on photo-disintegration of few-body nuclei at energies below the pion threshold ( $<145$  MeV) probes the universal dynamics of nuclei (at low energies) and the effects specific to the nuclear force (at higher energies). With implications for the Gerasimov-Drell-Hearn Sum Rule, and their connections to quantum chromodynamics (QCD), such experiments are certain to stimulate collaborations between theorists and experimentalists, in particular toward understanding the way that QCD manifests itself in low-energy photon reactions. Weller *et al.* [cxlix] capably motivates this area of research in the context of HI $\gamma$ S and conveys its

excitement. We wish to call attention to the fact that H $\gamma$ S is the only facility within the United States active in this nuclear-science subfield, while China, Japan, and Europe have either built new inverse-Compton gamma sources or are about to, for entry into this and other fields of photonuclear physics. It is crucial, we believe, for FACET-II to complement or exceed the capacity of H $\gamma$ S in order for the U.S. to maintain an active international role in what appears to be the growing topical areas made possible by inverse-Compton gamma sources.

#### 3.15.4 Polarizing and Probing the Quantum Vacuum

The vacuum is not inert. Since the beginnings of quantum electrodynamics in the mid 1930s, it has long been predicted that the vacuum in special circumstances can be a nonlinear medium through which photons interact. Strong electromagnetic fields, for example, can convert the vacuum into a birefringent and dichroic dielectric medium. Intense laser pulses available today provide high intensities of  $10^{22}$ – $10^{24}$  W/cm<sup>2</sup> and associated strong electric fields of  $10^{12}$ – $10^{13}$  V/cm but are insufficient by themselves for us to witness vacuum polarization. The combination of intense lasers, a gamma photon source, and nuclear physics at FACET-II, however, could reveal the long-sought prediction of QED of elastic photon-photon interactions within the vacuum. We imagine that lasers capable of producing peak pulsed intensities of  $6 \times 10^{24}$  W/cm<sup>2</sup> are available. Propagating against this laser pulse in vacuum is a linearly-polarized gamma pulse of 10-MeV photons (generated by FACET-II). The net rotation of the beam that probes the vacuum polarization is proportional to the fluence of the intense laser pulse and the photon energy of the probe beam. The gamma energy of a probe beam can thus be a significant multiplier of rotation. Where the linear polarization of a visible-wavelength probe (<2 eV) would rotate <50 nanoradians when propagating against a  $6 \times 10^{24}$  W/cm<sup>2</sup> pulse in vacuo, the polarization of a 10-MeV beam rotates 0.25 rad (14 degrees). A probe-beam detector is necessary, and in this case involves a deuterium target. The known nuclear physics of the angular distribution of deuteron photodisintegration at 10 MeV can be used to deduce the polarization angle of the incident gammas. We offer this realizable experiment as but one example where extremes in energy and fields that exist in the separate disciplines of lasers and nuclear physics can be joined to bring about interesting and unique phenomena.

#### 3.15.5 Diffraction, Imaging, and Coherent Excitation

Nuclear-resonant diffraction is not a new topic [c] but needs to be re-examined for experimental use amid the coming generation of gamma sources produced by Compton laser-backscattering, as planned for FACET-II. Such sources of gammas are bright, quasi-monochromatic (energy resolution of  $\leq 1\%$ ), polarized, and tunable across the giant dipole resonances (GDRs) held by isotopes from tritium through transuranics. In analogy with visible optics, the GDRs have real and imaginary indices of refraction that can influence a diffraction pattern depending on the detuning of the gamma energy from resonance. Thus, complementary to x-ray diffraction and its sensitivity to electron density, nuclear diffraction of gammas would presumably have a tunable sensitivity to atomic constituents and positions. The gammas of Compton laser-backscattering are also expected to exhibit a partial spatial coherence, presenting the opportunity to image the structures of non-crystalline materials. Coherent diffractive imaging is applicable to spatially-coherent sources and is used, for example, at DESY and the LCLS in

connection with their programs in 2-D imaging (and 3-D reconstructions) of biological molecules illuminated by x-ray, FEL light. A program in imaging would take into account the issue of pair production within the examined material and the mitigation of this problem through the latest or foreseeable advances in gamma-beam imaging or geometries. The combination of today's high-intensity lasers with advanced high-current sources such as FACET-II can also be examined for ways to produce spatially- and temporally-coherent gammas, for entry into the topic of coherent-excitation of nuclear transitions.

- 
- i E. Adli et al SLAC-PUB-15426, [arXiv:1308.1145](https://arxiv.org/abs/1308.1145) (2013).
  - ii M.Tzoufras et al *Phys. Rev. Letts.* 101, 145002 (2008).
  - iii T. Katsouleas et al, *Phys. Rev. A* 33,2056 (1986)
  - iv Seryi et al *Proceedings of PAC* May 4-8, pp. 1-3 (2009).
  - v Huang et al *Phys Rev. Letts.* 99, 255001 (2007).
  - vi W. Lu et al (2012). Unpublished manuscript.
  - vii M. J. Hogan et al *New Journal of Physics* 12, 055030 (2010).
  - viii H.Suk et al *Phys. Rev. Letts.* 86, 1011 (2007).
  - ix C.Geddes et al *Phys Rev. Letts.* 100, 215004 (2008).
  - x J.Shaw et al (2012). Unpublished manuscript.
  - xi C.E. Clayton et al *Phys. Rev. Letts.* 105, 105003 (2010).
  - xii B.Hidding et al *Phys. Rev. Letts* 108, 035001, (2012).
  - xiii F. Li et al (2012). Unpublished manuscript.
  - xiv T. Katsouleas and M.J. Hogan, Proposal to SAREC committee (2012).
  - xv D. Johnson et al *Phys. Rev. Letts.* 97, 175003 (2006).
  - xvi A. Caldwell et al., *Nature Physics* 5, 363 (2009).
  - xvii N. Kumar et al., *Phys. Rev. Lett.* 104, 255003 (2010).
  - xviii B.E. Blue et al., *Phys. Rev. Lett.* 90, 214801 (2003).
  - xix M. J. Hogan et al., *Phys. Rev. Lett.* 90, 205002 (2003).
  - xx P. Muggli et al., *Phys. Rev. Lett.* 101, 055001 (2008).
  - xxi J. Vieira et al., *Phys. Plasmas* 19 *Nature Physics*, 063105 (2012).
  - xxii A. Caldwell et al., *Nature Physics* 5, 363 (2009).
  - xxiii. J. B. Rosenzweig, et al, *Nucl. Instrum. Method A* 593 39 (2008).
  - xxiv. R. Bonifacio, C. Pellegrini, and L. Narducci, *Opt. Commun.* 50, 373 (1984).

- 
- xxv. R. Bonifacio et al., *Phys. Rev. Lett.* 73, 70 (1994).
- xxvi Y. Ding, et al., *Phys. Rev. Lett.* 102, 254801 (2009).
- xxvii. M. J. Hogan et al., *Phys. Rev. Lett.* 95, 054802 (2005).
- xxviii. I. Blumenfeld, et al., *Nature*, 445 7129 (2007).
- xxix. J.B. Rosenzweig, N. Barov, M.C. Thompson, R.B.Yoder, *Phys. Rev. ST Accel. Beams* 7, 061302 (2004).
- xxx N. Barov, J.B. Rosenzweig, M.C. Thompson, R.B.Yoder, *Phys. Rev. ST Accel. Beams* 7, 061301 (2004).
- xxxi. J.B. Rosenzweig, B. Breizman, T. Katsouleas and J.J. Su, *Phys.Rev. A* 44, R6189 (1991).
- xxxii. D. L. Bruhwiler *et al.*, *Phys. Plasmas* 10, 2022 (2003)
- xxxiii. J. K. Lim, et al., *Phys. Rev. ST Accel. Beams* 8, 072401 (2005)
- xxxiv M. Borland, *Advanced Photon Source LS-287* (2000).
- xxxv D. Bauer and P. Mulser, *Phys. Rev. A* 59, 569 (1999).
- xxxvi Caolionn L. O'Connell, *Stanford PhD thesis* (2005).
- xxxvii Eric Mevel *et al.*, *Phys. Rev. Lett.* 70 406 (1993).
- xxxviii J.B. Rosenzweig, et al., *Nucl. Instr. and Methods A* doi:10.1016/j.nima.2011.01.073 (2011).
- xxxix. J.B. Rosenzweig, N. Barov, M.C. Thompson, R.B.Yoder, *Phys. Rev. ST Accel. Beams* 7, 061302 (2004)
- xl. N. Barov, J.B. Rosenzweig, M.C. Thompson, R.B.Yoder, *Phys. Rev. ST Accel. Beams* 7, 061301 (2004)
- xli. S. Lee, et al., *Phys. Rev. ST—Accel. Beams* 5, 011001 (2002).
- xlii. Tor O. Raubenheimer, in *11th Advanced Accelerator Concepts Workshop*, AIP Conf. Proc. 737, (AIP, New York, 2004), p. 86.
- xliii. "Single-shot coherent diffraction imaging of microbunched relativistic electron beams for free-electron laser applications," A. Marinelli, *et al*, to appear in *Phys. Rev. Lett.*
- xliv. J.B. Rosenzweig, A.M. Cook, A. Scott, M.C. Thompson, R. Yoder, *Phys. Rev. Lett* 95, 195002 (2005)
- xl . "The Quasi-nonlinear Regime of the Plasma Wakefield Accelerator", J.B. Rosenzweig, *et al.*, *Proceedings of Advanced Accelerator Concepts 2010*, Annapolis, Md, USA (AIP, 2010).
- xlvi. Plasma wakefields in the quasi-nonlinear regime: Experiments at ATF, J.B. Rosenzweig, *et al.*, to appear in *Proceedings of Advanced Accelerator Concepts 2012*.
- xlvii. P. Muggli, *et al.*, *Phys. Rev. Lett.*, 101, 054801 (2008)

- 
- xlvi N. Holtkamp, SAREC presentation, October 2012,  
<https://slacspace.slac.stanford.edu/sites/ard/facet/sarec12-2/Documents/Oct-2012-Presentations/FutureFACETTestFacilities-Holtkamp-SAR-Oct12.pptx>.
- xlvii F. Oshea et al., *PRSTAB* 13, 070702 (2010).
- lviii Richard Feynman, *Photon-Hadron Interactions*, Addison Wesley (1992).
- lix J. Ballam, *Phys. Rev. Lett.* 23, 498–501 (1969).
- lvi M. Gai, *Journal of Physics: Conference Series* 316, 012033 (2011).
- lvii A.M. Bernstein et al., *Annu. Rev. Nucl. Part. Sci.* 59, 115–44 (2009).
- lviii D. Choudhury, A. Nogga and D. Phillips, *Phys. Rev. Lett.* 98, 232303 (2007)
- lix K. Helbing, Proc. Third Int. Symp. On the GDH Sum Rule and its Extensions, Norfolk, USA, 28 (2004).
- lvi A. M. Sandorfi et al., *J Phys G*38, 053001 (2011).
- lvii Frank Close and Phillip R. Page, "Glueballs", *Scientific American*, 279: 5, 80 (1998).
- lviii D. Babusci, *Il Nuovo Cimento*. 103, N11, 1555 (1990).
- lix <https://str.llnl.gov/AprMay11/pdfs/4.11.3.pdf>
- lx [http://apc.fnal.gov/programs2/ASTA\\_TEMP/index.shtml](http://apc.fnal.gov/programs2/ASTA_TEMP/index.shtml).
- lxi Bern
- lxii E. Ydrefors, *Proc. 4th International Symposium on Neutrinos and Dark Matter in Nuclear Physics*, <http://web.ias.tokushima-u.ac.jp/physics/nucl/NDM12/NDM12.html>, (2012).
- lxiii J. Piekarewicz, *Phys. Rev. C* 83, 034319 (2011).
- lxiv D. Vretenar, et al., *Phys. Rev. C* 85, 044317 (2012).
- lxv J. Piekarewicz, et al., *Phys. Rev. C* 85, 041302 (2012).
- lxvi C. J. Horowitz, et al., *Phys. Rev. Lett* 86, 5647 (2001).
- lxvii E. Litvinova, et al., *Nucl. Phys. A* 823, 26 (2009).
- lxviii H. Utsunomiya, et al., *Phys. Rev. C* 84, 055805 (2011).
- lix F. Dönau, G. Rusev, R. Schwengner, A. R. Junghans, K. D. Schilling, and A. Wagner, *Phys. Rev. C* 76, 014317 (2007).
- lxx A. Krasznahorkay, "Triple-Humped Fission Barriers," *Handbook of Nuclear Chemistry*, Springer: Verlag, Berlin, 281 (2011).
- lxxi P. Thirolf and D. Habs, *Prog. Part. Nucl. Phys.* 49, 325 (2002).
- lxxii Yoichiro Nambu, Nobel Lecture: "Spontaneous symmetry breaking in particle physics," *Int. J. Mod.Phys. A*24, 2371 (2009).

- 
- lxxiii S. Weinberg, *Trans. N.Y. Academy of Science, Series II* 38 (I.I.Rabi Festschrift), 185 (1977).
- lxxiv N. Fettes and U.G.Meiner, *Nucl. Phys. A*693, 693 (2001).
- lxxv V. Baru et al., *Nucl. Phys. A* 872, 69(2011).
- lxxvi D. Gotta, *Lecture Notes in Physics* 745, 165 (2008).
- lxxvii Th. Strauch et al., *Eur.Phys.J. A*47, 88 (2011).
- lxxviii A.M. Bernstein, *Phys. Lett. B* 442, 20 (1998).
- lxxix B. Ananthanarayan, *Phys. Lett. B* 634, 391 (2006).
- lxxx A.M. Bernstein, et al. *Ann. Rev. Nucl. Part. Sci.* 59, 115 (2009).
- lxxxi V. Baru et al., *Nucl. Phys. A* 872, 69 (2011).
- lxxxii S.B. Gerasimov, *Sov. J. Nucl. Phys.* 2, 430 (1966).
- lxxxiii S.D. Drell and A.C. Hearn, *Phys. Rev. Lett.* 16, 908 (1966).
- lxxxiv M. Hosada and K. Yamamoto, *Prog. Theor. Phys.* 36, 426 (1966).
- lxxxv B. Sawatzky, Ph.D. dissertation, "A Measurement of the Neutron Asymmetry in near Threshold," University of Virginia (2005).
- lxxxvi D. Choudhury et al *Phys. Rev. Lett.* 98, 232303 (2007).
- lxxxvii Nath, et al, *Nucl. Phys. A* 194, 49 (1972).
- lxxxviii H. Bethe and W. Heitler, *Proc. Roy. Soc. Lond. A* 146, 83 (1934).
- lxxxix P. A. M. Guichon, M. Vanderhaeghen, *Phys. Rev. Lett.* 91, 142303 (2003).
- xc A. V. Afanasev, S. J. Brodsky, C. E. Carlson, Y. C. Chen and M. Vanderhaeghen, *Phys. Rev. D* 72, 013008 (2005).
- xci B. Aubert et al., *Phys. Rev. Lett.* 97, 112001 (2006).
- xcii J. Beringer et al., *Phys. Rev. D* 86, 010001 (2012).
- xciii R.Edwards et al., arXiv:1212.5236v1 (2012).
- xciv A.M. Sandorfi et al., *J Phys G*38, 053001 (2011).
- xcv T. Nakano et al., *Nuclear Physics A*629, 559 (1998).
- xcvi J. Ellis et al., "SAPPHiRE: a Small gamma-gamma Higgs Factory", arXiv:1208.2827 (2012).
- xcvii G. Unel et al., "A Higgs" Factory at the Greek-Turkish Border" (2012). Manuscript submitted for publication, ESPG.
- xcviii D. Asner et al., "Higgs physics with a gamma gamma collider based on CLIC I," *Eur. Phys.J. C* 28, 27 (2003).
- xcix T. Raubenheimer, "An SLC-Style Higgs Factory," ICFA Higgs Factory Workshop "HF2012", FNAL 14 November 2012.

- 
- c Y. Zhang, "Design Concept of a - Collider-Based Higgs Factory Driven by Energy Recovery Linacs," Jefferson Lab Technote JLAB-TN-12-053 (2012).
- ci "ILC Reference Design," <http://www.linearcollider.org/about/Publications/Reference-Design-Report>.
- cii *The Linear Collider Physics Resource Book for Snowmass* (2001). pp. 333-345; <http://www.slac.stanford.edu/grp/th/LCBook/positron.pdf>.
- ciii CERN Report 2004-005: Physics at the CLIC Multi-TeV Linear Collider, editors; M. Battaglia, A. de Roeck, J. R. Ellis, and D. Schulte, p. 208; ISBN: 92-9083-226-6 <http://cdsweb.cern.ch/search.py?recid=749219&ln=en>.
- civ F. Zimmermann et. al. , Positron Options for the Linac-Ring LHeC, IPAC'12, New Orleans.
- cv V. Yakimenko, I.V. Pogorelsky, Polarized gamma source based on Compton backscattering in a laser cavity, *Phys.Rev.ST Accel.Beams* 9, 091001 (2006).
- cvi J. S. Berg, et al. "A Cost-effective design for a neutrino factory," *Phys.Rev.ST Accel.Beams* 9, 011001 (2006).
- cvi ASTA proposal.
- cviii V. Biryukov, Chesnokov Yu, V. Kotov, "Crystal Channeling and Its Application at High Energy Accelerators" (Springer-Verlag, Berlin, Heidelberg, 1997).
- cix K. Reil et al, "Measurements of the Fluorescence Light Yield in Electromagnetic Showers", 22nd Texas Symposium On Relativistic Astrophysics, Dec. 13-17, 2004, Stanford, CA, SLAC-PUB-11068.
- cx D. Saltzberg et al., *Phys. Rev. Lett.* 86, 2802 (2001).
- cxii P. Chen and T. Tajima, *Phys. Rev. Lett.* 83, 256 (1999).
- cxii 2001 Workshop on Laboratory Astrophysics, WP-020, SLAC.
- cxiii 2003 Workshop on "Quantum Aspects of Beam Physics", Hiroshima, Japan, P. Chen and K. Reil, editors (World Scientific Publ., Singapore, 2004).
- cxiv Second Orion Workshop, WP-026, SLAC, 2003.  
<http://www.slac.stanford.edu/pubs/slacwps/slac-wp-026.html>
- cxv SABER Workshop, WP-070, SLAC, 2006.  
<http://www.slac.stanford.edu/pubs/slacwps/slac-wp-070.html>
- cxvi "HEDLA from 1996 to 2012", R. Paul Drake, abstract for HEDLA 2012.  
[http://hedla2012.sc.fsu.edu/hedla2012/website/data/program/talk/paul\\_drake\\_t.pdf](http://hedla2012.sc.fsu.edu/hedla2012/website/data/program/talk/paul_drake_t.pdf)
- cxvii HEDLA 2012 meeting. <http://www.hedla2012.org/>
- cxviii N. Phinney, N. Toge and N. Walker (ed.), "LC Reference Design Report Volume 3 - Accelerator", arXiv:0712.2361 [physics.acc-ph]

- 
- cxix Oh. Burrows et al., "ILPS Deliverable 2: Report on Luminosity Tuning and Control Strategies", EUROTeV- Report-2008-090.
- cxx J. Pfingstner et al., "An interleaved, model-supported system identification scheme for the particle accelerator CLIC", *Proceedings of the 49th IEEE Conference on Decision and Control* (2010).
- cxxi A. Grudiev et al. "Design of the CLIC main linac accelerating structure for the CLIC conceptual design report", *Proceedings of LINAC10*, Tsukuba, Japan (2010).
- cxxii P. Tenenbaum et al., "Direct measurement of the transverse wakefields of tapered collimators", *Phys. Rev. ST-AB* 10, 034401 (2007).
- cxxiii S. Molloy et al., "Measurements of the transverse wakefields due to varying collimator characteristics", *Proceedings of EPAC07*, Albuquerque, New Mexico, USA, FRPMS074 (2007).
- cxxiv J. L. Fernandez-Hernando et al., "Measurements of collimator wakefields at End Station A", *Proceedings of EPAC08*, Genoa, Italy, WEPP163 (2008).
- cxxv P. Tenenbaum et al., "Direct measurement of the resistive wakefield in tapered collimators", *Proceedings of EPAC04*, Lucerne, Switzerland (2004).
- cxxvi K. Bane and G. Stupakov, SLAC-PUB-14925 (2012).
- cxxvii Emma, NGLS, 2012.
- cxxviii S. Antipov, et. al. *Phys. Rev. Lett.* 108, 144801 (2012).
- cxxix <http://accelconf.web.cern.ch/accelconf/IPAC2013/papers/weodb101.pdf>
- cxx J. Amann et al *Nature Photonics* 6, 693–698 (2012).
- cxix Hirori, H., Doi, A., Blanchard, F. & Tanaka, K. "Single-cycle terahertz pulses with amplitudes exceeding 1 MV/cm generated by optical rectification in LiNbO<sub>3</sub>." *Appl. Phys. Lett.* 98, 091106 (2011).
- cxixii Daranciang, D. et al. "Single-cycle terahertz pulses with >0.2 V/Å field amplitudes via coherent transition radiation." *Appl. Phys. Lett.* 99, 141117 (2011).
- cxixiii Gamble, S. J. et al. "Electric field induced magnetic anisotropy in a ferromagnet." *Phys. Rev. Lett.* 102, 217201 (2009).
- cxixiv Tudosa, I. et al. "The ultimate speed of magnetic switching in granular recording media." *Nature* 428, 831–833 (2004).
- cxixv Wen, H., Wiczer, M. & Lindenberg, A. "Ultrafast electron cascades in semiconductors driven by intense femtosecond terahertz pulses." *Phys Rev B* 78, 125203 (2008).
- cxixvi Hirori, H. et al. "Extraordinary carrier multiplication gated by a picosecond electric field pulse." *Nature Communications* 2, 594–6 (2011).
- cxixvii Liu, M. et al. "Terahertz-field-induced insulator-to-metal transition in vanadium dioxide metamaterial." *Nature* 487, 345–348 (2012).

---

cxxxviii Gaal, P. *et al.* "Internal motions of a quasiparticle governing its ultrafast nonlinear response." *Nature* 450, 1210 (2007).

cxxxix Turchinovich, D., Hvam, J. & Hoffmann, M. "Self-phase modulation of a single-cycle terahertz pulse by nonlinear free-carrier response in a semiconductor." *Phys Rev B* 85, 201304 (2012).

cxl Qi, T., Shin, Y.-H., Yeh, K.-L., Nelson, K. & Rappe, A. "Collective Coherent Control: Synchronization of Polarization in Ferroelectric PbTiO<sub>3</sub> by Shaped THz Fields." *Phys Rev Lett* 102, 247603 (2009).

cxli Daranciang, D. *et al.* "Ultrafast Photovoltaic Response in Ferroelectric Nanolayers." *Phys Rev Lett* 108, 087601 (2012).

cxlii Zheng Yang, Changhyun Ko and Shriram Ramanathan, "Oxide Electronics Utilizing Ultrafast Metal-Insulator Transitions", *Annu. Rev. Mater. Res.* 41, 337 (2011).

cxliii M. Liu, *et al.*, "Terahertz-field-induced insulator-to-metal transition in vanadium dioxide metamaterial", *Nature* 487, 345 (2012).

cxliv H. Ogasawara, D. Nordlund, A. Nilsson, SLAC-PUB-11503 (2005).

cxlv Langenbrunner, J.R., Booker, J.M. Ross, T.J., Hemez, F.M. "Uncertainty Qualification: Estimating uncertainties due to Inference," *Uncertainty Quantification and Multiscale Materials Modeling, DOE conference*, El Dorado Hotel, Santa Fe, NM, June 13-15, 2011, Technical Report LA-UR-11-03366, Los Alamos National Laboratory, Los Alamos, New Mexico.

cxlvi Langenbrunner, J.R., Booker, J.M., Ross, T.J. Hemez, F.M. (2010b), "Evolving Desiderata for Validating Engineered-Physics Systems Without Full-scale Testing," *American Institute of Aeronautics and Astronautics, Proceedings 12<sup>th</sup> Non-Deterministic Approaches Conference*, Orlando, Florida, April 12-15, 2010, LA-UR-10-01494, LA-UR-10-02167.

cxlvii Langenbrunner, J.R., Booker, J.M., Ross, T.J. Hemez, F.M. (2010c), "Inference Uncertainty Quantification Instead of Full-scale Testing," *Proceedings, American Institute of Aeronautics and Astronautics, 49<sup>th</sup> AIAA/ASME/ ASCE/AHS/ASC Structures, Structural Dynamics, and Materials Conference and 10<sup>th</sup> AIAA Non-Deterministic Approaches Conference*, Schaumburg, Illinois, April 7-10, 2008; Technical Report LA-UR-08-1669, Los Alamos National Laboratory, Los Alamos, New Mexico.

cxlviii W. A. Fowler, "Experimental and Theoretical Nuclear Astrophysics; The Quest for the Origin of the Elements," in *Nobel Lectures, Physics 1981-1990*, Tore Frängsmyr, editor-in-charge, Gösta Ekspång, editor. World Scientific Publishing Co.: Singapore (1993).

cxlix H. R. Weller, M. W. Ahmed, H. Gao, W. Tornow, Y. K. Yu. M. Gai, and R. Miskimen, "Research Opportunites at the upgraded HIγS facility," *Prog. Part. Nucl. Phys.* 62, 257 (2009).

cl C. Tur, A. Heger, and S. M. Austin, "Dependence of s-process nucleosynthesis in massive stars on triple-alpha and <sup>12</sup>C(α, γ)<sup>16</sup>O reaction rate uncertainties," *Astrophys. J.* 702, 1068 (2009).

cli A. Weiss, "Stellar nucleosynthesis," *Phys. Scr. T133*, art. no. 014025 (2008).

---

clii D. A. O'Connor, "The theory of nuclear resonant diffraction of gamma rays by perfect crystals," J. Phys. C 1, 973 (1968).

# 4 Performance and Parameters

## 4.1. Introduction and Overview

The FACET-II electron system design uses a copy of the LCLS-I injector system installed in the existing off-axis bunker at Sector 10. The 135 MeV beam is injected into the linac and accelerated in Sectors 11-19 (the second kilometer of the SLAC linac) to the existing FACET experimental area in Sector 20. To achieve the required bunch length, the bunch compression is done in three stages: the first compression with a chicane in Sector 11; the second with a chicane in Sector 14; and the third in the W-chicane in Sector 20. Minor upgrades are foreseen for the existing experimental area in Sector 20. The accelerator requirements are described below.

The FACET-II positron system takes the beam from the existing positron target, capture section and return line and transports it to Sector 10. To match the 335 MeV energy of the damping ring, four sections of S-band acceleration (each 7 feet long) will be installed on the return line at Sector 14. Starting in Sector 11, a new beamline takes the positrons from the existing return line and injects them into a small damping ring in the Sector 10 Linac tunnel. The beam from the damping ring undergoes a 1<sup>st</sup> stage of bunch compression and is then injected into the Linac at the Bunch Compressor in Sector 11, BC1. The positrons have a 2<sup>nd</sup> stage of bunch compression in a 2<sup>nd</sup> arm of the Sector 14 chicane.

Sector 20 contains the final bunch compression stages for both the electron and positron beams. The beams are separated at the first bend magnet at the start of sector 20 and each travel through their own compression chicanes. The positron chicane has a path length 52.7mm longer than the electron chicane to position the positron beam 150um behind the electron (drive) beam for plasma acceleration experiments, swapping the temporal ordering of the 2 bunches.

### 4.1.1. Electron Requirements and Parameters

For the FACET-II experimental program, the electron beam must meet a specific set of requirements for electron transverse beam size at IP waist, peak current, energy, energy spread, and stability. These electron parameters are listed below in Table 4.1. Transverse rms values are from a Gaussian fit to the core of the distribution. A schematic layout of the accelerator is shown in Figure 4.1 with beam parameters listed at various points along the accelerator.

Table 4.1. Nominal electron beam parameters at the FACET IP and their operational ranges.

Parameter	Symbol	Unit	Nominal	Range
Final electron energy	$E_f$	GeV	10.0	4.0 – 13.7
Initial electron bunch charge	$Q_0$	nC	2	2 – 5
Final electron bunch charge	$Q_f$	nC	0.7	0.7 - 5
Pulse repetition rate	$f_{rep}$	Hz	30	1 - 30
Number of electron bunches per RF pulse	$N_b$	-	1	1 - 2
Electron transverse core beam size (x/y, rms)	$\sigma_x/\sigma_y$	$\mu\text{m}$	6/6	6-20/6-10

Final electron peak current	$I_{pk}$	kA	76	10-100
Final electron bunch length (rms)	$\sigma_z$	$\mu\text{m}$	1	1 - 20
Electron rms energy spread (rms)	$\sigma_E/E$	%	0.44	0.4 – 1.8
Max. avg. $e^-$ beam power (10 GeV, 5 nC, 1 bunch/pulse, 30 Hz)	$P_b$	kW	1.5	0.1 - 4.2
Dump design for avg. $e^-$ beam power	$P_D$	kW	5	-

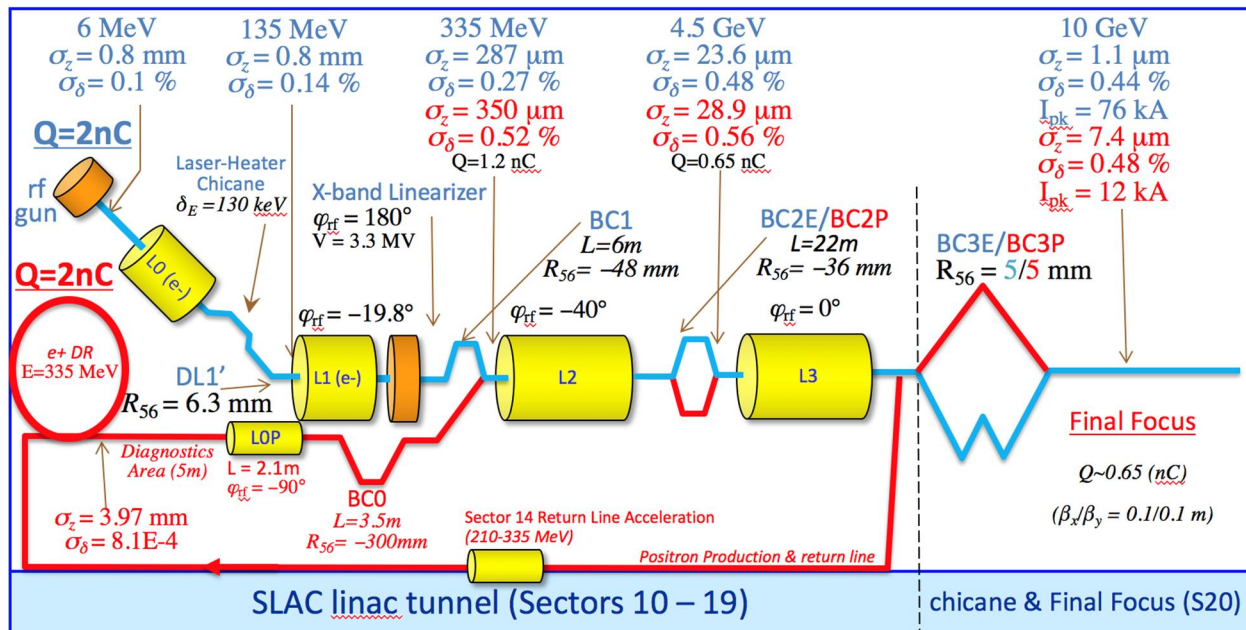


Figure 4.1. Schematic layout of FACET-II injector, linac, bunch compressors, and experimental area, with main parameters listed for operation. The blue sections depict the electron specific and common  $e^-/e^+$  areas. The red sections are for positrons.

#### 4.1.2. Positron Requirements and Parameters

For the FACET-II experimental program, the positron beam must meet a specific set of requirements for emittance, peak current, energy, energy spread, and stability. These parameters are listed below in Table 4.1. A schematic layout of the positron system is also shown in Figure 4.1 with beam parameters listed at various points along the accelerator.

Table 4.2. Nominal positron beam parameters at the FACET IP and their operational ranges.

Parameter	Symbol	Unit	Nominal	Range
Final positron energy	$E_f$	GeV	10	4 – 13.7
Initial positron bunch charge from DR	$Q_0$	nC	2	1 - 2

Final positron bunch charge at IP	$Q$	nC	0.6	0.6-2
Pulse repetition rate	$f_{rep}$	Hz	5	1 - 5
Number of positron bunches per RF pulse	$N_b$	-	1	1
Positron transverse core beam size (x/y, rms)	$\sigma_x/\sigma_y$	$\mu\text{m}$	10/7	10-25/7-10
Positron peak current	$I_{pk}$	kA	12	12 – 15
Positron bunch length (rms)	$\sigma_z$	$\mu\text{m}$	7	7 – 11
Positron rms energy spread	$\sigma_E/E$	%	0.5	0.5 – 1.5
Max. avg. $e^+$ beam power (10 GeV, 2nC, 5Hz,1 bunch/pulse)	$P_b$	W	100	5 – 140

#### 4.1.3. Positron Return Line Requirements and Parameters

The positron return line (PRL) is responsible for accelerating the positrons to 335 MeV and then transporting them (18" below the ceiling of the linac tunnel) to Sector 11, where they are matched and injected into the damping ring. To accomplish this, 4 new beamline sections are required. These accelerate the beam to 335 MeV, translate the beam horizontally 103" across the accelerator housing, then transport down vertically 74", and finally inject into the DR. This system takes the measured PRL beam parameters and existing optics and matches into the required optics at the DR injection point.

Table 4.3. Beam parameters for beamline section injecting into DR in Sectors 10 and 11.

Parameter	Symbol	Nominal	Min-Max	Unit
Beam Energy	$E_0$	335	-	MeV
Initial Transverse Emittance	$\gamma\epsilon_x / \gamma\epsilon_y$	2.0 / 2.0	-	mm.rad
Final Transverse Emittance	$\gamma\epsilon_x / \gamma\epsilon_y$	2.5 / 2.2	-	mm.rad
Initial Twiss	$\beta_x / \alpha_x$	0.352 / -0.040	-	m
<i>(At entrance to first horizontal dogleg bend)</i>	$\beta_y / \alpha_y$	12.918 / 4.082		
Final Twiss	$\beta_x / \alpha_x$	0.335 / 0.243	-	m
<i>(At exit of injection kicker)</i>	$\beta_y / \alpha_y$	8.813 / -0.555		
Initial Bunch Length (rms)	$\sigma_z$	3	-	mm
Final Bunch Length (rms)	$\sigma_z$	3	-	mm
Initial Energy Spread (rms)	$\sigma_E/E$	1.0	-	%
Final Energy Spread (rms)	$\sigma_E/E$	1.1	-	%
Initial Bunch Charge	$Q$	4		nC
Final Bunch Charge (in DR)	$Q$	2	1-2	nC

#### 4.1.4. Positron Damping Ring Requirements and Parameters

As the positron beam emerges from the target and reaches an energy of  $E=335$  MeV, it has a normalized emittance  $\gamma\epsilon$  of about 2.0 mm-rad. This emittance is three orders of magnitude larger than the electron beam out of the photo-injector. A damping ring is necessary to reduce the positron emittance to  $\mu\text{m-rad}$  level in a few milliseconds. For practical reasons, the ring is placed in sector 10 inside the existing linac tunnel. This implies that the diameter of the ring has to be smaller than 3 meters. This constraint dictates a compact design with minimal gaps between the magnets in the arcs.

Table 4.4. Main parameters of the positron damping ring

Parameter	Value
Energy, $E$ [MeV]	335.0
Circumference, $C$ [m]	20.15
Tune, $\nu_x, \nu_y, \nu_z$	4.586, 2.615, 0.0383
Natural emittance, $\epsilon_0$ [nm-rad]	7.28
Bunch length, $\sigma_{z0}$ [mm]	2.23
Energy spread, $\sigma_{\delta 0}$	$4.84 \cdot 10^{-4}$
Momentum compaction	$5.84 \cdot 10^{-2}$
Damping partition, $J_x, J_y, J_z$	1.97, 1.0, 1.03
Damping time, $\tau_x, \tau_y, \tau_z$ [ms]	15.9, 31.4, 30.6
Natural chromaticity, $\xi_{x0}, \xi_{y0}$	-5.99 -5.25
Energy loss per turn, $U_0$ [keV]	1.435
RF voltage, $V_{RF}$ [MV]	1.1
RF frequency, $f_{RF}$ [MHz]	714.0
Harmonic number	48

#### 4.1.5. Positron Extraction Line Requirements and Parameters

The positron extraction line starts at the entrance to the DR extraction kicker on the final extraction turn and ends at the positron injection point into the main linac in the final bend of the BC1 electron bunch compressor. In order to match with the electron compression scheme, this system must also compress the bunch length by a factor of  $\sim 10$ . These tasks are achieved with 4 sub-systems, a vertical dog-leg to extract from the damping ring, a diagnostics section, an initial stage of bunch compression (BC0) and a horizontal dog-leg to inject into the last magnet of the first Linac bunch compressor (BC1).

This system is matched given the damping ring beam parameters at the extraction point and provides the required positron (and electron) matching conditions at the insertion point into the main FACET-II beamline.

Table 4.5. Beam parameters for positron extraction and compression system from the entrance of the DR extraction kicker on extraction turn to injection into the main linac in the final bend of the electron BC1 chicane bend.

Parameter	Symbol	Value	Range	Unit
Beam Energy	$E_0$	335		MeV
Initial Transverse Emittance	$\gamma\epsilon_x / \gamma\epsilon_y$	5.9 / 5.9	5.24-5.9	$\mu\text{m}\cdot\text{rad}$
Final Transverse Emittance	$\gamma\epsilon_x / \gamma\epsilon_y$	6.5 / 5.9		$\mu\text{m}\cdot\text{rad}$
Initial Twiss	$\beta_x / \alpha_x$	2.0 / 0		m
	$\beta_y / \alpha_y$	5.0 / 0		
Final Twiss	$\beta_x / \alpha_x$	6.362 / -2.567		m
	$\beta_y / \alpha_y$	16.866 / -4.067		
Initial Bunch Length (rms)	$\sigma_z$	4	3.5-4	mm
Final Bunch Length (rms)	$\sigma_z$	0.350		mm
Final E-z chirp	$\alpha_z$	0.389		
Initial Energy Spread	$\sigma_E/E$	0.11		%

Final Energy Spread	$\sigma_E/E$	1.53		%
Initial Bunch Charge (rms)	Q	2	1-2	nC
Final Bunch Charge (rms)	Q	1.2	1-2	nC
BCO Collimator Aperture	A	4.5	2-10	mm

#### 4.1.6. Sector 20 Chicane Requirements and Parameters

The sector 20 system is designed to deliver high peak-current (>10kA) at the IP area with  $\sim 10\mu\text{m}$ , or less, transverse beam sizes simultaneously for both incoming electron and positron beams. The optics match is highly constrained and must satisfy specific requirements for both electron and positron optical systems simultaneously. These are described in detail in Chapter 9.

Table 4.6: Beam parameters for sector 20 chicanes and final focus system for electron and positron beams.

Parameter	Symbol	Value	Unit
Beam Energy	$E_0$ (e+)	10.0	GeV
	$E_0$ (e-)	10.0	
Initial Transverse Emittance	$\nu\epsilon_x / \nu\epsilon_y$ (e+)	6.3 / 5.9	$\mu\text{m}\cdot\text{rad}$
	$\nu\epsilon_x / \nu\epsilon_y$ (e-)	3.3 / 3.3	
Final Transverse Emittance	$\nu\epsilon_x / \nu\epsilon_y$ (e+)	35 / 6.4	$\mu\text{m}\cdot\text{rad}$
	$\nu\epsilon_x / \nu\epsilon_y$ (e-)	8.2 / 5.1	
Initial Twiss	$\beta_x / \alpha_x$ (e-)	2.423 / -0.027	m
	$\beta_y / \alpha_y$ (e-)	5.098 / 0.133	m
Final Twiss (IP)	$\beta_x / \alpha_x$ (e-)	0.1 / 0	m
	$\beta_y / \alpha_y$ (e-)	0.1 / 0	m
Initial Bunch Length / peak Current	$\sigma_z / I_{pk}$ (e+)	28.9 / 3.1	$\mu\text{m} / \text{kA}$
	$\sigma_z / I_{pk}$ (e-)	23.5 / 3.8	
Final Bunch Length / peak Current	$\sigma_z / I_{pk}$ (e+)	7.6 / 12.1	$\mu\text{m} / \text{kA}$
	$\sigma_z / I_{pk}$ (e-)	1.1 / 75.5	
rms relative Energy Spread	$\sigma_E/E$ (e+)	0.48	%
	$\sigma_E/E$ (e-)	0.44	
rms Transverse Core Size at IP Waist	$\sigma_x / \sigma_y$ (e+)	10.1 / 7.3	$\mu\text{m}$
	$\sigma_x / \sigma_y$ (e-)	5.5 / 5.9	
Bunch Charge	Q (e+)	0.6	nC
	Q (e-)	0.7	nC
Chicane compression coef.	$R_{56}$ (e+)	5	mm
	$R_{56}$ (e-)	5	mm

---

# 5 Electron Injector

---

---

## Technical Synopsis

*In order to achieve the scientific goals of the experimental program at FACET-II, a high electron peak current with small transverse core beam size at the experimental IP waist,  $\sim 10\mu\text{m}$ , and a small longitudinal emittance are required. FACET-II will operate with an electron energy up to 10 GeV. The most challenging parameters are for the plasma wakefield acceleration (PWFA) experiments which benefit from peak currents in excess of 10 kA. The RF photocathode gun and injection system is similar to that used in LCLS. This injector is capable of producing up to 5 nC in a bunch length of  $< 5.4\text{ ps}$ , corresponding to a peak current of  $> 120\text{ A}$  with a transverse emittance of  $< 5\mu\text{m}$ . This implies a required compression ratio in excess of 100 to achieve the desired beam characteristics at the IP waist in sector 20. The acceleration and compression is done in the 2<sup>nd</sup> kilometer of the SLAC linac in 3 compression stages.*

*The capabilities of FACET-II vary in a non-trivial way depending on the choice of initial charge from the RF gun. The baseline design is for a 2nC electron bunch charge from the electron gun, operating together with a 2nC positron bunch from the positron damping ring once positrons have been reestablished. To demonstrate design flexibility and characterize the extremes of the possible parameter space, a second configuration option is considered in chapter 10 corresponding to a 5 nC pulse from the electron gun. The conceptual design here represents a parameter set to demonstrate the highest deliverable peak currents to the sector 20 user area which adhere to the various parameter constraints dictated by later operational requirements. This design is limited by the requirements of the positron bunch which has a larger initial longitudinal emittance. For single sign particle operation, the compression scheme can be tailored more towards higher electron-only peak current if desired.*

*6D tracking simulations have been made to model the beam transport through the FACET-II complex including the non-linear compression and final beam focus processes. The simulations include the effects of longitudinal and transverse wakefields in the 1km linac as well as incoherent and coherent synchrotron radiation effects in the various bending magnets. Longitudinal space charge effects are also simulated throughout the beam transport. Simulations have also been made which calculate emittance dilution in the linac due to transverse wakefields and anomalous momentum dispersion, each of which arises with component misalignments. These simulations include realistic correction techniques and successfully demonstrate the level of transverse emittance preservation required. Diagnostics, correction techniques, and feedback systems have also been incorporated into the design. For phase-III operations, the electron bunch is preceded by a positron bunch separated by one half an s-band RF wavelength ( $\sim 5\text{cm}$ ). The coupling of trajectory errors through transverse wakefields of this two-bunch system are also included in the tracking simulations.*

---

---

## 5.1 Accelerator - Introduction and Overview

The FACET-II electron system design uses a copy of the LCLS-I injector system installed in the existing off-axis bunker at Sector 10. The 135 MeV beam is injected into the linac and accelerated in Sectors 11-19 (the second kilometer of the SLAC linac) to the existing FACET experimental area in Sector 20. To achieve the required bunch length, the bunch compression is done in three stages: the first compression with a chicane in Sector 11; the second with a chicane in Sector 14; and the third in the W-chicane in Sector 20. Minor upgrades are foreseen for the existing experimental area in Sector 20. The accelerator requirements are described below.

### 5.1.1 Accelerator Requirements and Parameters

For the FACET-II experimental program, the electron beam must meet a specific set of requirements for electron transverse beam size at IP waist, peak current, energy, energy spread, and stability. These electron parameters are listed below in Table 5.1. Transverse rms values are from a Gaussian fit to the core of the distribution. A schematic layout of the accelerator is also shown in Figure 5.1 with beam parameters listed at various points along the accelerator. The electron beam optics from cathode to the dump in Sector 20 is also plotted in Figure 5.2.

Table 5.1. Nominal electron beam parameters at the FACET IP and their operational ranges.

Parameter	Symbol	Unit	Nominal	Range
Final electron energy	$E_f$	GeV	10.0	4.0 – 13.7
Initial electron bunch charge	$Q_0$	nC	2	2 - 5
Final electron bunch charge	$Q_f$	nC	0.7	0.7 - 5
Pulse repetition rate	$f_{rep}$	Hz	30	1 - 30
Number of electron bunches per RF pulse	$N_b$	-	1	1 - 2
Electron transverse core beam size (x/y, rms)	$\sigma_x/\sigma_y$	$\mu\text{m}$	6/6	6-16/6-9
Final electron peak current	$I_{pk}$	kA	76	10-130
Final electron bunch length (rms)	$\sigma_z$	$\mu\text{m}$	1	1 - 11
Final electron rms energy spread (rms)	$\sigma_E/E$	%	0.44	0.4 – 1.8
Max. avg. $e^-$ beam power (10 GeV, 5 nC, 1 bunch/pulse, 30 Hz)	$P_b$	kW	1.5	0.1 - 4.2
Dump design for avg. $e^-$ beam power	$P_D$	kW	5	-

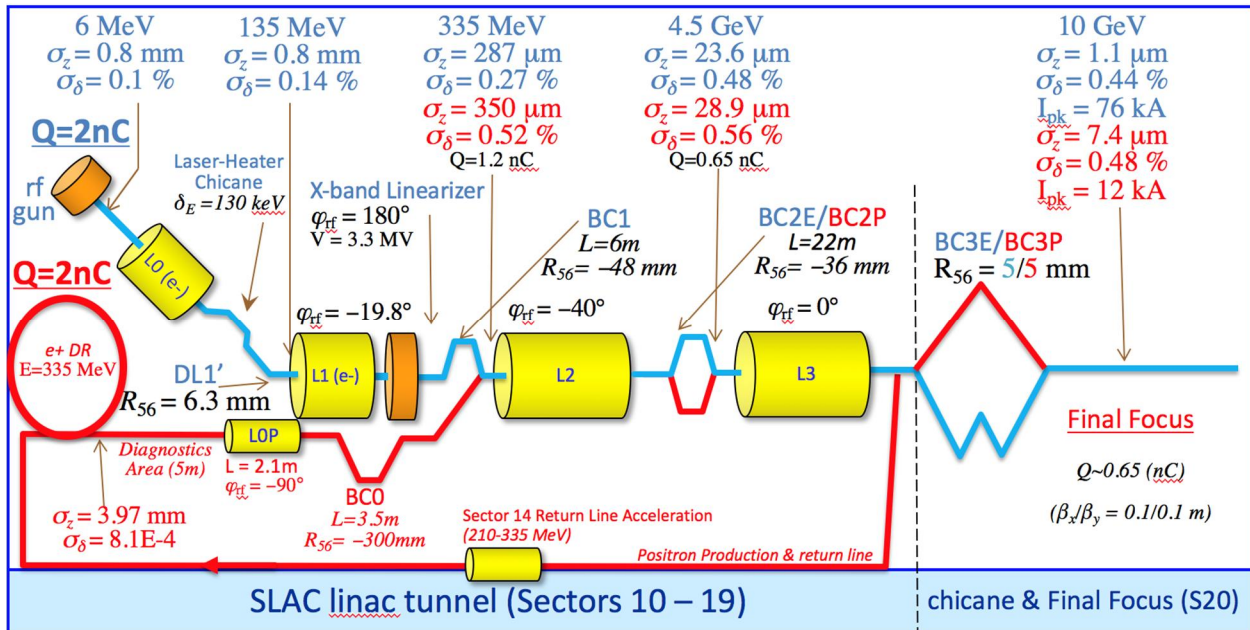


Figure 5.1. Schematic layout of FACET-II injector, linac, bunch compressors, and experimental area, with main parameters listed for operation. The blue sections depict the electron specific and common e-/e+ areas. The red sections are for positrons.

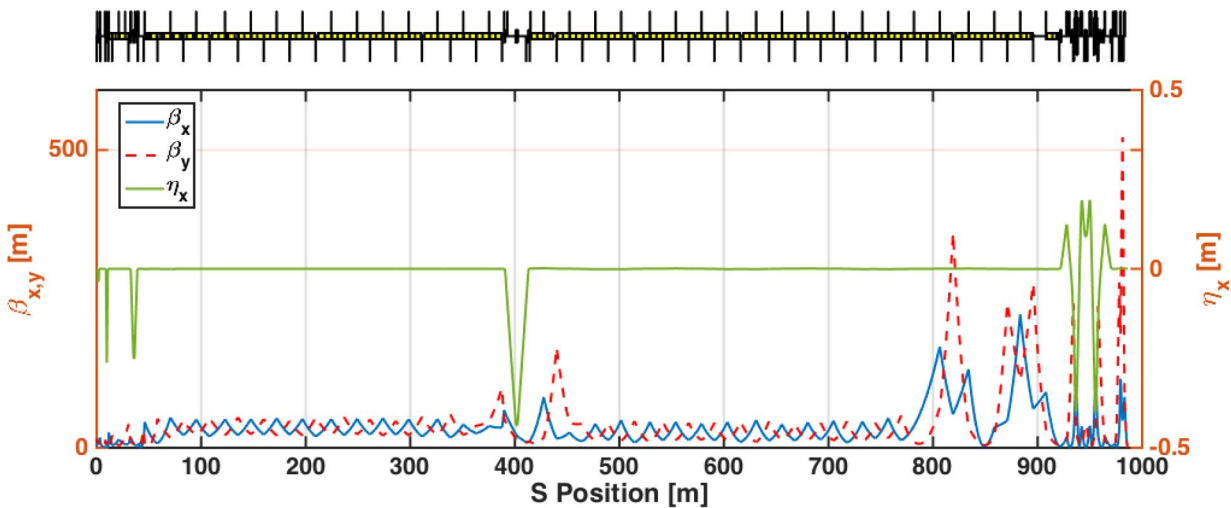


Figure 5.2. Linac electron optics from the exit of L0 (135 MeV point) to the IP waist in sector 20. BC1 is at  $s \approx 30\text{ m}$ , BC2 is at  $s \approx 390\text{ m}$ , FACET W-chicane is at  $s \approx 920\text{ m}$ .

## 5.1.2 Accelerator Layout

The FACET-II accelerator layout will occupy the second kilometer of the SLAC S-band linac (2.856 GHz), from sector 11 through 20, in order to generate up to a 10 GeV electron beam at 1-30 Hz.

A single bunch of electrons is generated at a 1-30 Hz repetition rate in an S-band (2.856 GHz) RF photocathode gun (see "RF gun" in Figure 5.1) by exciting a copper cathode with Ultra-Violet (UV) laser

---

light from a high-power drive laser system located in the linac gallery above the existing Sector 10 off-axis injector vault. The electrons are then accelerated to 6 MeV in the gun where the transverse emittance is formed by choosing an appropriate UV laser spot size on the cathode (1.76 mm diameter for 2 nC) and using a strong focusing solenoid magnet immediately after the gun.

Further acceleration in the injector vault (see "Linac-0" in Figure 5.1) takes the beam energy up to 135 MeV where it is horizontally deflected by 35 degrees into the main SLAC linac at the start of Sector 11 (see "DL1" in Figure 5.1). The beam is then accelerated 15° off of the RF crest where an electron energy chirp (time-energy correlation) is generated (see "Linac-1" in Figure 5.1). The energy chirp is linearized using an X-band (11.424 GHz = 4×2.856 GHz) RF accelerating section (see "Linac-X" in Figure 5.1) to slightly decelerate the beam ( $\Delta E = -24$  MeV). A 6-m long, four-dipole magnetic chicane at 335 MeV (see "BC1" in Figure 5.1) compresses the bunch length from 800  $\mu\text{m}$  to 290  $\mu\text{m}$ . More off-crest acceleration follows (see "Linac-2" in Figure 5.1) to 4.5 GeV where a second chicane (see "BC2" in Figure 5.1) compresses the bunch length to a 46  $\mu\text{m}$  length. The last accelerator section (see "Linac-3" in Figure 5.1) accelerates at the RF crest phase up to 10 GeV. The bunch is over-compressed in BC2 with the wakefield chirp delivered in Linac-3 further enhancing the chirp to rotate the beam in E-z phase-space to the correct orientation to allow for the final (+ve  $R_{56}$ ) compression stage in sector 20. The final compression stage is then performed by the existing FACET W-chicane system in sector 20 (see Chapter 9) which compresses the beam to a bunch length of down to 1  $\mu\text{m}$ , corresponding to a peak current of up to 70 kA (at a final bunch charge of 1 nC including design collimation in the bunch compressors to suppress non-linear tails). A final focus system comprising of 5 families of quadrupole magnets forms a small-beta waist of  $\beta^* = 0.1\text{m}$  in both transverse planes at one of several possible user areas in the beam IP waist experimental region. This allows core beam sizes of  $<10$   $\mu\text{m}$  rms to be delivered to experiments.

The electron beam is finally directed onto the dump at the end of Sector 20 through 3 quadrupoles and a vertical bend to provide high energy bandwidth energy spectrometry to the user community, as used during FACET operations.

## 5.2 Drive Laser

The injector drive laser serves two purposes in the FACET-II injector: The UV output is used to illuminate the copper cathode producing the electrons for acceleration and the Infra-Red (IR) output is used in the laser heater (Sections 5.2.2 and 5.3.3.3). A copper cathode has been demonstrated to produce very good thermal emittance levels, long lifetimes (>2 years in LCLS-I at <250 pC/bunch), and does not require extreme vacuum pressure control ( $\sim 10^{-9}$  Torr), but it also can have a fairly low quantum efficiency (QE) from between  $2.4 \times 10^{-5}$  (early LCLS-I) to  $1.2 \times 10^{-4}$  (recent LCLS-I for UV light at 253 nm). The lower range of QE requires an ultra-violet (UV) laser pulse energy of 400  $\mu\text{J}$  on the cathode for a 2 nC electron bunch. The drive laser is of the same design as has been demonstrated at LCLS-I for several years [1]. In LCLS-I the entire system has been very reliable with up-time >98%. The drive laser system is composed of the following components:

- The laser, which produces the UV beam for electron generation and the IR beam for the heater.
- The gun transport system, which conditions the UV beam to meet the required spatial and temporal parameters, and projects the beam onto the cathode at near normal incidence.
- The heater transport, which conditions the IR beam to meet the required spatial and temporal parameters and launches the beam through the heater undulator.

- Diagnostics that allow all relevant beam parameters to be measured at the appropriate places in the system, integrated with feedback loops for pointing stability.
- The laser hall that provides the environmental conditions required by the laser, which serves to limit the exposure to laser hazards and includes a laser safety system that meets SLAC, DOE, OSHA, and ANSI laser safety standards.

### 5.2.1 Drive Laser Specifications

As is the case in LCLS-I, the drive laser itself will be based on chirped pulse amplification (CPA) in Ti:sapphire followed by harmonic conversion to the required UV wavelength. In this case we begin with a mode-locked Ti:sapphire oscillator that generates a 68-MHz train of nano-Joule level pulses in the 750-780 nm wavelength range. The 68-MHz repetition rate is important because it is commensurate with the RF timing systems of the SLAC linac, allowing the laser oscillator to be synchronized to the linac. Because these pulses are roughly 30 fs in duration the time-bandwidth limited spectral width is roughly 30 nm. In CPA systems, this large spectral width is exploited to stretch the pulse to a width of  $>150$  ps by passing the pulses through a device with significant group velocity dispersion. This stretcher expands the pulses temporally so that they can be amplified to higher energy without the risk of damaging the amplifier components. After the pulses are amplified to the desired energy, they can be compressed back to the 30-fs level in a device with group velocity dispersion that cancels that of the stretcher.

The laser consists of commercially available laser hardware with minor modifications to meet our specific needs. In the case of the laser oscillator, there are at least two companies that can provide an oscillator (Figure 5.3) that meets the FACET-II requirements. Between the LCLS-I injector and the NEH experimental laser systems, SLAC is currently operating several of these oscillators from both companies and has worked with both companies to make the required modifications.

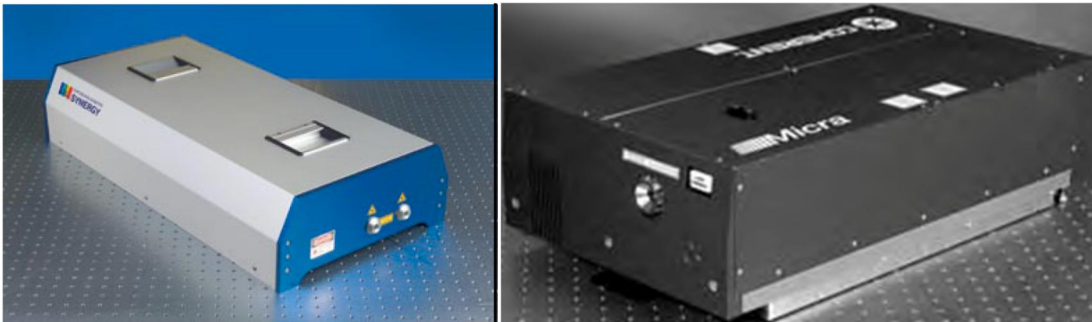


Figure 5.3. Commercially available mode-locked oscillators that meet FACET-II requirements.

The stretcher, amplifiers, and compressor used in LCLS-I are also commercially available devices with minor modifications. In all cases, the first stage of amplification is performed in a regenerative amplifier (regen) based on Ti:sapphire pumped by frequency doubled Nd:YAG or Nd:YLF and running at 30 Hz repetition rate. The regenerative amplifier provides very high gain in a compact space, raising the pulse energy from nJ to mJ. We are currently using regens from two different companies (Figure 5.4) with SLAC modifications to force the amplifier to operate at the desired wavelength. Following the regen, one or more multi-pass Ti:sapphire amplifiers will be used to increase the pulse energy to the required level. We currently operate multi-pass amplifiers from commercial companies as well as SLAC designed units.



Figure 5.4. An example of a commercial regenerative amplifier (regen).

After amplification to the desired energy and compression to the desired pulse width, the 760-nm pulse is frequency doubled and then tripled to 253 nm. The final output parameters required are shown in Table 5.2.

Table 5.2. Parameters of the UV drive laser system ("nominal" 2 nC bunch charge).

Parameter	Symbol	Unit	Nominal	Range
Operating wavelength (for Cu cathode)	$\lambda_{UV}$	nm	253	253-266
Pulse repetition rate	$f_{rep}$	Hz	30	1-30
Number of laser pulses per RF pulse	$N_b$	-	1	1-2
Nominal pulse energy on cathode	$U$	$\mu\text{J}$	100	100-1000
Laser spot diameter on cathode (FWHM)	$d$	mm	1.76	0.5-5.0
Pulse length (FWHM)	$\Delta t$	ps	3.2	2-10
Longitudinal pulse shape	-	-	Gaussian	-
Transverse pulse shape	-	-	cut Gaussian	-
Spatial homogeneity on cathode (peak-to-peak)	-	%	<15	-
Longitudinal homogeneity on cathode (peak-to-peak)	-	%	<10	-
Optical energy jitter (in UV, rms)	-	%	<2	-
Laser-to-RF phase jitter (rms)	-	ps	<0.2	-
Laser rms position jitter on cathode / rms spot size	-	%	<3	-

Once laser pulses are produced with these parameters, they leave the laser and move into the transport system. The transport system consists of three primary parts: The upstairs beam conditioning and transport, the transport tube down to the injector vault (evacuated for most of the distance), and the gun laser transport in the vault. Drawings of the optical components upstairs and in the vault are shown in Figure 5.5 and Figure 5.6.

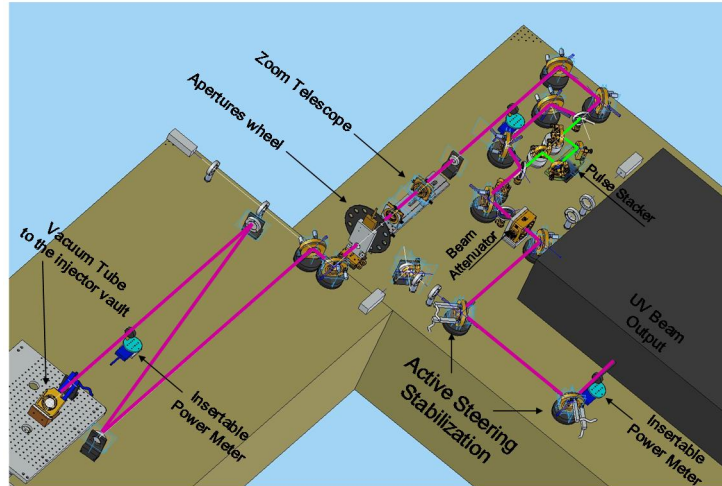


Figure 5.5. Upstairs laser beam conditioning and transport.

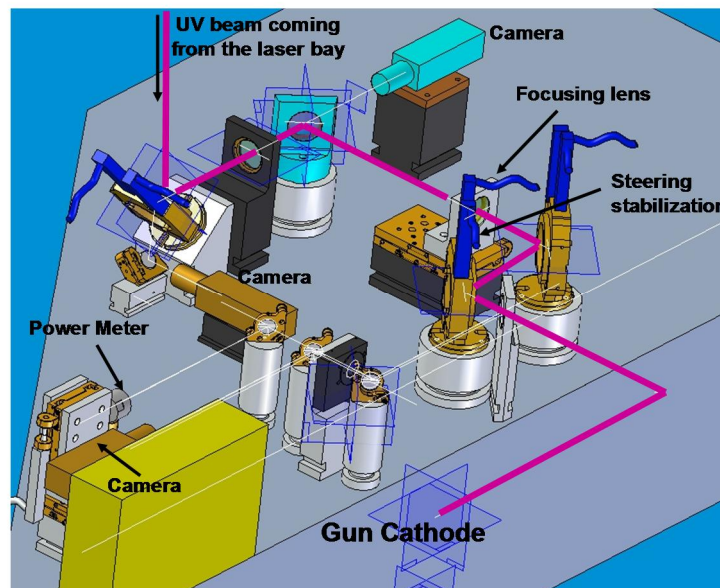


Figure 5.6. Laser transport system in the vault.

Upstairs, the beam is first propagated through a beam pointing stabilization system consisting of two cameras and two motorized mirrors. After that the beam passes through a waveplate and polarizer that allows the laser pulse energy to be controlled in a feedback loop that measures the charge produced from the gun. The pulses can then be sent into a pulse stacker that allows for more temporal control or multi-bunch production. The beam diameter is then adjusted in a zoom telescope before being spatially clipped on one of twelve apertures that allow production of a more uniform, flat-top spatial distribution. This aperture is then relay imaged through the transport pipes, to the vault transport optics where the image is reformed on the photocathode. Before reaching the cathode a fraction of the pulse is sampled for another pointing stabilization system, an energy measurement, and an equivalent plane imaging system that allows the spatial profile on the cathode to be monitored on the Virtual Cathode Camera (VCC). The spatial profile for LCLS-I as seen on the VCC is shown in Figure 5.7.

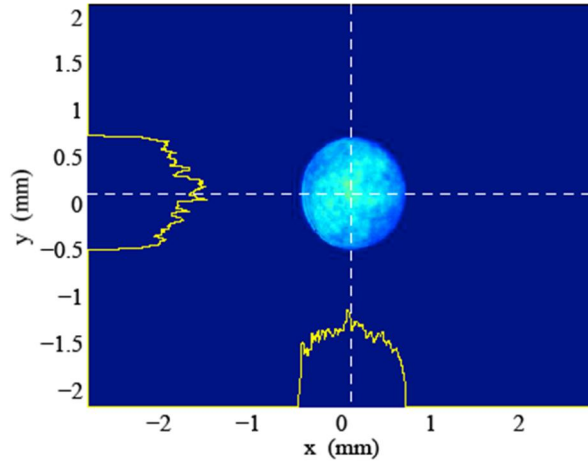


Figure 5.7. Spatial profile on cathode as recorded by Virtual Cathode Camera in LCLS-I. Yellow curves are “line-out” traces showing the instantaneous distribution along that line.

## 5.2.2 Multiple Bunch Operation

In order to operate FACET-II with both electron and positron bunches simultaneously, a second laser system will be required to provide a second electron bunch in the photoinjector. This laser system will be comprised of an amplifier chain seeded by a later pulse from the same oscillator as the primary laser system, and a separate third harmonic generation (THG) stage coupled to the same spatial shaping optics and beam transport as the output of the primary laser. The amplifier and THG will be identical to those of the primary laser. An optical delay line will be used to independently control the phase of the second laser pulse relative to the RF.

## 5.2.3 Laser Heater

The laser heater [1] has been performing well in LCLS-I for at least 7 years now [2]. The IR beam used for the heater (Section 5.3.3.3) is extracted from the drive laser as the spent beam which is left over after the frequency tripler crystal; therefore it is well synchronized to the electron beam. The requirements for the laser in the heater system are listed in Table 5.3.

Table 5.3. IR laser parameters of the laser-heater system for FACET-II.

Parameter	Symbol	Unit	Nominal	Range
Maximum IR pulse energy in the undulator	$u$	$\mu\text{J}$	200	0-4000
IR wavelength	$\lambda_{IR}$	nm	760	760-800
Max. IR pulse rate	$f_{rep}$	Hz	30	1-30
IR beam size at center of the undulator (rms)	$\sigma_{x,y}$	$\mu\text{m}$	400	200-600
IR pulse length in undulator (FWHM)	$\Delta\tau_{FWHM}$	ps	12	10-20
Laser beam Rayleigh range	$LR$	cm	50	42-1600
Laser pulse energy in the undulator	$P_E$	$\mu\text{J}$	50	0-1500
Laser power in undulator	$P_L$	MW	1.0	0-17
Laser rms beam size in undulator	$\sigma_{L-x,y}$	mm	0.4	0.4-0.55

Position stability of IR beam in und. (rms)	$\Delta x/\sigma_x$	%	<20	-
Timing stability of IR beam in und. (rms)	$\Delta t/\Delta\tau_{FWHM}$	%	<30	-



Figure 5.8. (Left) Optical bench attached to the ceiling of the LCLS vault and relay imaging lens and tube that transports the beam to the heater. (Right) Laser heater optical table with diagnostics and controls.

IR light for the laser heater is taken from the residual IR that comes out of the tripler. Because the tripler efficiency is roughly 10%, we have roughly 10 times the UV energy (>10 mJ) left in the IR which is more than the required amount shown in Table 5.3. The IR is sent through a parallel grating pulse stretcher to produce the required temporal width and is then relay imaged first to an optical bench that is attached to the ceiling (see Figure 5.8) in the vault and then to the heater interaction region. There are pointing stability lock loops and diagnostics included as part of this optical transport system.

#### 5.2.4 Laser Room

The laser room serves several purposes. It provides a stable clean environment for the laser. It also serves to limit access to the laser hazard zone and provides the infrastructure for the Laser Safety System (LSS). The laser room is at ground level above the injector vault and the UV and IR beams are transported through 10-meter long vacuum pipes that are installed in a penetration to the injector tunnel (see Figure 5.9).

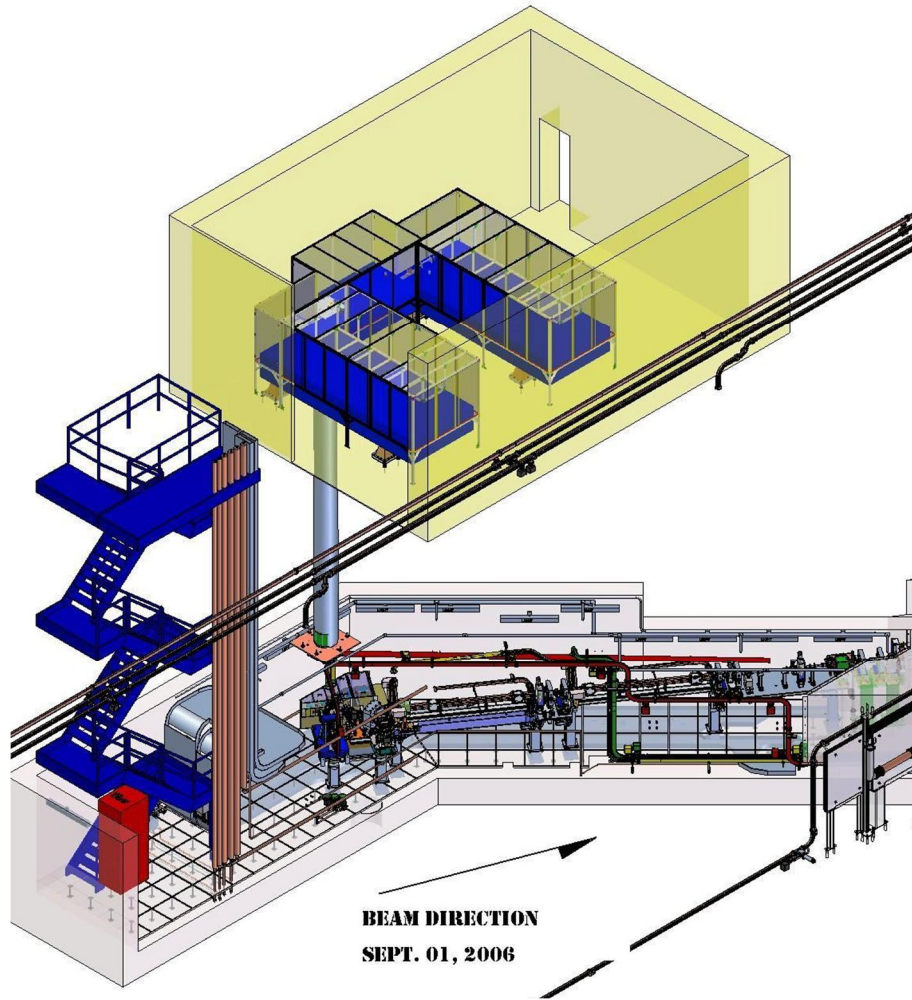


Figure 5.9. Laser room above the LCLS injector vault. Silver pipe is UV transport to laser bench attached to ceiling. Red pipe is IR transport to heater.

The laser room is designed to provide a temperature stability of better than  $\pm 1^\circ\text{F}$  at a humidity of  $50\% \pm 10\%$ . The conditioned air is filtered by High Efficiency Particulate Air (HEPA) filters, providing a clean environment for the laser system. The LSS controls the operational state as well as entry and exit to and from the room. If there are interlock faults, the LSS will insert the required shutters or turn off lasers as described in the facility Standard Operating Procedure (SOP).

### 5.2.5 Laser Controls

FACET-II can utilize both currently supported controls components used throughout the facility, or systems under development as part of ongoing projects, given the similarity between the FACET-II electron injector and LCLS-I injector systems. Generally, these components fall into two categories, either OEM equipment which is vendor supplied and usually has specified controls interfaces, or SLAC-designed components which therefore have SLAC-maintained controls interfaces and structures.

The first category of components that will be used in the FACET-II injector include many of the optical components necessary for commissioning and maintaining operation of the laser generation and transport. Examples of such components include power meters, translation stages and motion control

systems, shutters and cameras. In many cases, these are readily available from common vendors, and have well defined controls interfaces for which SLAC controls groups have already deployed support.

Examples within this first category of components are camera systems and motor control systems. Ongoing development programs at SLAC are working on high-rate, high-survivability camera systems that will mitigate some of the failure modes we've encountered maintaining camera systems on LCLS-I. Motion control systems have also been susceptible to failure when placed within the accelerator housings, necessary due to OEM equipment design. However, SLAC has active programs to address these requirements, such that we can move sensitive motion control hardware outside of the accelerator housing, increasing supportability and reducing aggregate system cost. Further, where possible, controls hardware in general will be installed outside the injector vault.

Some specific controls additions in this first category which are not available in the LCLS-I injector systems will be considered for FACET-II, due to experience commissioning and operating LCLS-I systems. First, remote monitoring of laser cooling systems will be implemented as available. Second, as available and depending on stability requirements, the laser delay stage for two pulse operation (see section 5.2.2) may be motorized for remote control.

The second category of components include those systems developed entirely at SLAC. A specific example of this category are the SLAC Laser Timing Module System (LTMS), which controls laser pulse timing. These components typically have well-delineated controls interfaces necessitating only software support to integrate with the existing accelerator systems. The LTMS system interfaces with accelerator LLRF systems and the accelerator timing system at large. FACET-II will use existing EVR/EVG style systems as used in LCLS-I and some FACET-I systems, so little development work will be needed for the LTMS system and analog/digital signal processing systems. There is little design or implementation risk, and the system is well understood.

Much of the FACET-II laser system and controls will look much like the LCLS-I injector laser systems. FACET-II will benefit from the operational experience with LCLS-I.

### 5.3 Electron Gun and Injector

The FACET-II performance relies critically on the electron gun and injector beam quality. The electron beam requirements from the gun and injector are listed in Table 5.4. The performance of the LCLS-I gun and injector is described in Ref. [1].

Table 5.4. Electron beam requirements from the electron gun and injector (before L1-linac).

Parameter	Symbol	Unit	Nominal	Range
Electron bunch charge	$Q_0$	nC	2	2 - 5
Pulse repetition rate	$f_{rep}$	Hz	30	1 - 30
Electron energy after injector (before L1-linac)	$E_0$	MeV	135	120 - 150
Number of electron bunches per RF pulse	$N_b$	-	1	1 - 2
Electron transverse, rms, normalized, emittance	$\gamma\epsilon_{x,y}$	$\mu\text{m}$	3.2	3.2 - 4.3
Electron longitudinal, rms, normalized emittance (un-heated)	$\gamma\epsilon_z$	mm	0.2	0.2 - 1.5
Electron peak current (before BC1)	$I_{pk}$	A	270	270-314
Electron rms bunch length ((before BC1)	$\sigma_z$	mm	0.8	0.8 - 1.6

Electron rms energy spread	$\sigma_{E/E}$	%	0.11	0.11 – 0.35
RMS transverse stability (norm. to rms spot size)	$x_{rms}/\sigma_x$	%	<4	-
RMS energy stability (norm. to rms spot size)	$E_{rms}/E_0$	%	<0.1	-
RMS relative bunch charge stability	$\Delta Q_{rms}/Q_0$	%	<2	-
RMS bunch arrival time stability (before BC1)	$\Delta t_{rms}$	ps	<0.3	-

### 5.3.1 Electron Gun Design and Performance

The performance of the existing gun in LCLS-I has been outstanding owing to a careful design [3]. The FACET-II injector will use the same gun design, which has been proven to meet all requirements. Figure 5.10

The gun is a 1.6-cell normal conducting copper structure at S-band RF frequency (2.856 GHz) with dual feed RF input and copper cathode supported on the back-plane of the half cell. The gun fields are fully rotationally symmetric by incorporating dual feed (to eliminate dipole fields) and a racetrack geometry (to cancel quadrupole fields induced by the dual feed) for the full cell into which the RF is coupled. The RF gun parameters are listed in Table 5.5.

The entire Gun-To-Linac (GTL) beamline from the gun exit to the entrance of the first linac section has been designed to mitigate wakefields. This includes tapering of the beam tube through the gun solenoid, the vacuum valve after the gun solenoid, all bellows, diagnostics, and the vacuum chamber for the gun-spectrometer magnet. The beamline is pumped through longitudinal slots to minimize the wakes.

The LCLS-I gun has produced exceptional transverse normalized emittance levels of  $0.4 \mu\text{m}$  at a 250-pC bunch charge with a reasonably uniform spatial UV (253 nm) laser transverse distribution (1.2-mm diameter) on the photocathode and a Gaussian temporal laser pulse with 3-4-ps FWHM at up to 120 Hz (~35 A peak current). The RF field on the cathode is set at 115 MV/m producing a 6.0-MeV electron beam at the gun exit. The cathode quantum efficiency has been  $1.2 \times 10^{-4}$  with a 30-deg laser phase w.r.t. the gun RF zero-crossing.

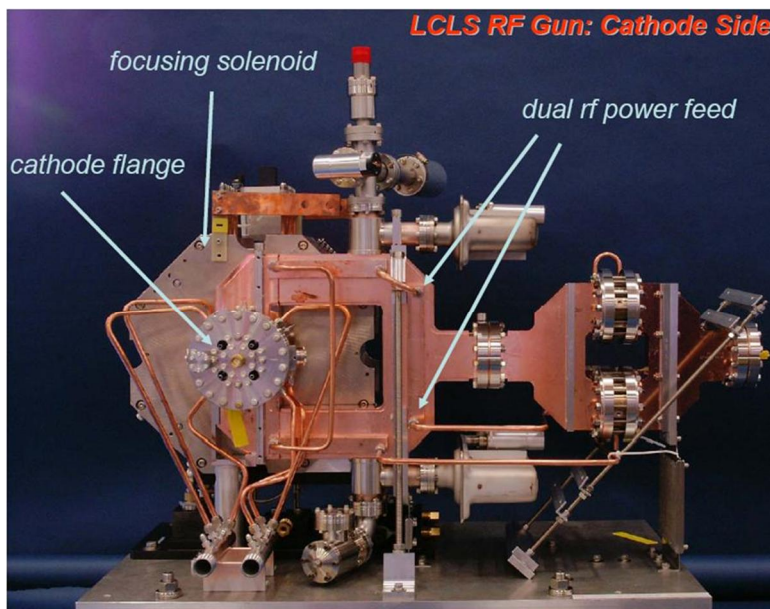


Figure 5.10. The LCLS-I RF photocathode gun seen from the cathode side.

Table 5.5. RF photocathode electron gun parameters for FACET-II.

Parameter	Symbol	Unit	Nominal	Range
Cathode material	-	-	Cu	-
Minimum useable diameter of cathode	$d_u$	mm	12	-
Expected cathode quantum efficiency (at 253 nm UV)	$QE$	$10^{-4}$	1.2	1 - 1.5
Peak RF field (2856 MHz)	$E_{pk}$	MV/m	120	100 - 130
Electron energy after gun	$E_0$	MeV	6.0	5.5 - 6.2
Electron energy spread, rms (before heater)	$\sigma_E$	keV	~1	0.1 - 5
RF repetition rate	$f_{rep}$	Hz	30	1 - 30
RF pulse duration (one bunch per RF pulse)	$\Delta t_{RF}$	$\mu s$	1.3	1 - 3
Peak RF power	$P_{RF}$	MW	10	7 - 12
Number of cells	$N_c$	-	1.6	-
Length of gun	$L_{gun}$	m	0.17	-

### 5.3.2 Photocathode

The main area of gun improvement is the copper photocathode. At LCLS, the cathode has only been changed once in period of more than 3 years and the present cathode has been operating reasonably well for several years. Operation of the LCLS-I gun originally showed a slow degradation of the quantum efficiency due to surface contamination but this process has been successfully reversed with laser cleaning since 2011.

### 5.3.3 Electron Injector

The electron injector optics, from cathode through the Dog Leg (DL1) system, is shown in Figure 5.11 with the laser heater undulator gap and chicane at their nominal setting (strong vertical focusing from each of these components). A layout of the LCLS-I injector vault is also shown in Figure 5.12, with the FACET-II layout almost identical.

The LCLS-I injector has performed quite well, as described in [Error! Bookmark not defined.], and consists of the drive laser, the RF photocathode gun, two 3-m long S-band RF accelerating structures, the laser heater system, a transverse RF deflecting cavity, and a 35-deg bend system (DL1) to bring the beam into the main SLAC linac. In addition, a gun spectrometer is located immediately after the gun and can be switched on when needed, and a 135-MeV spectrometer is located adjacent to the DL1 bend system, which can also be switched on easily. These allow high resolution energy and energy spread measurements at these key locations. The gun accelerates the electrons to 6 MeV, while the two S-band structures accelerate to 63 MeV (first section, L0a, 19 MV/m) and then to 135 MeV (second section, L0b, 24 MV/m). Several YAG and OTR screens, and optional wire-scanners, are available, in conjunction with the transverse RF deflector, to measure projected emittance, absolute bunch length, projected energy

spread, and final energy chirp. The system has performed quite well and will be a nearly identical copy for FACET-II. Beam diagnostics for the FACET-II injector, and beyond, are described in Section 5.4.

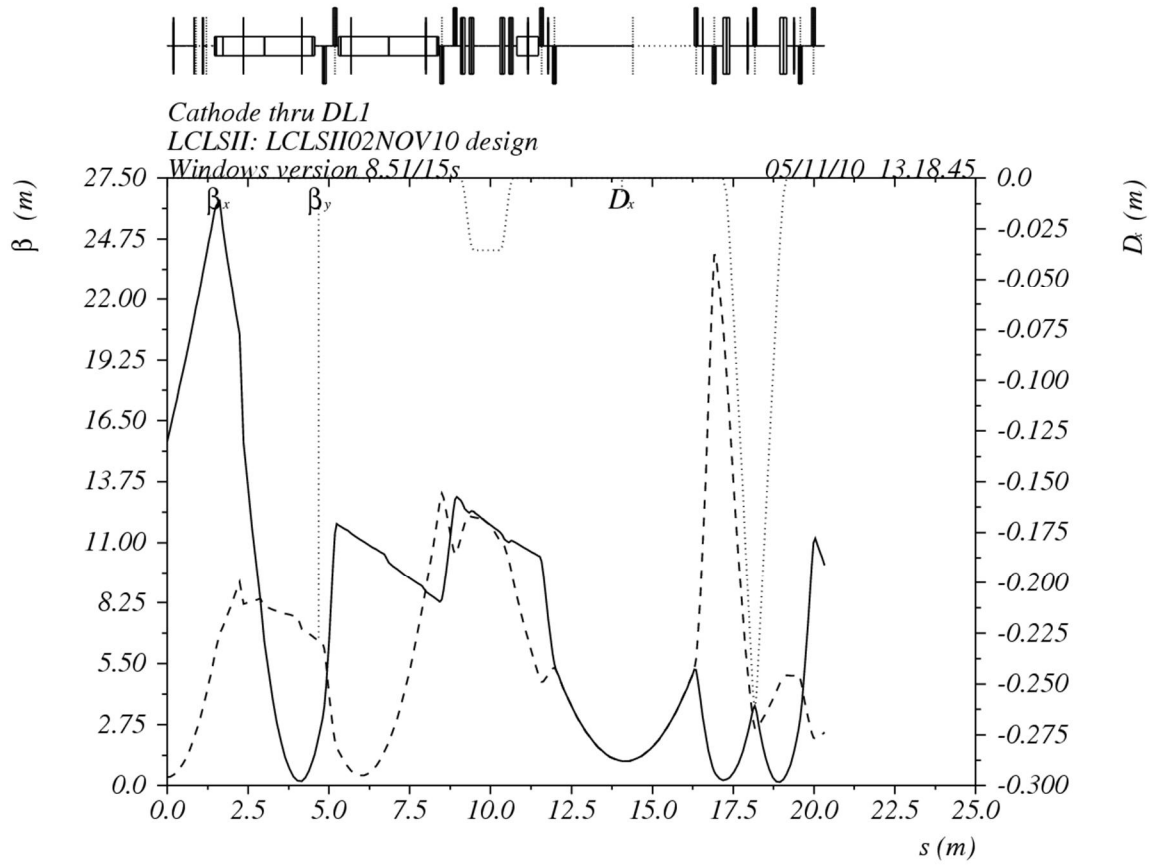


Figure 5.11. The electron injector optics and layout from cathode through the DL1 dog-leg system (with heater chicane ON and laser-heater undulator at its nominal gap of 34 mm).

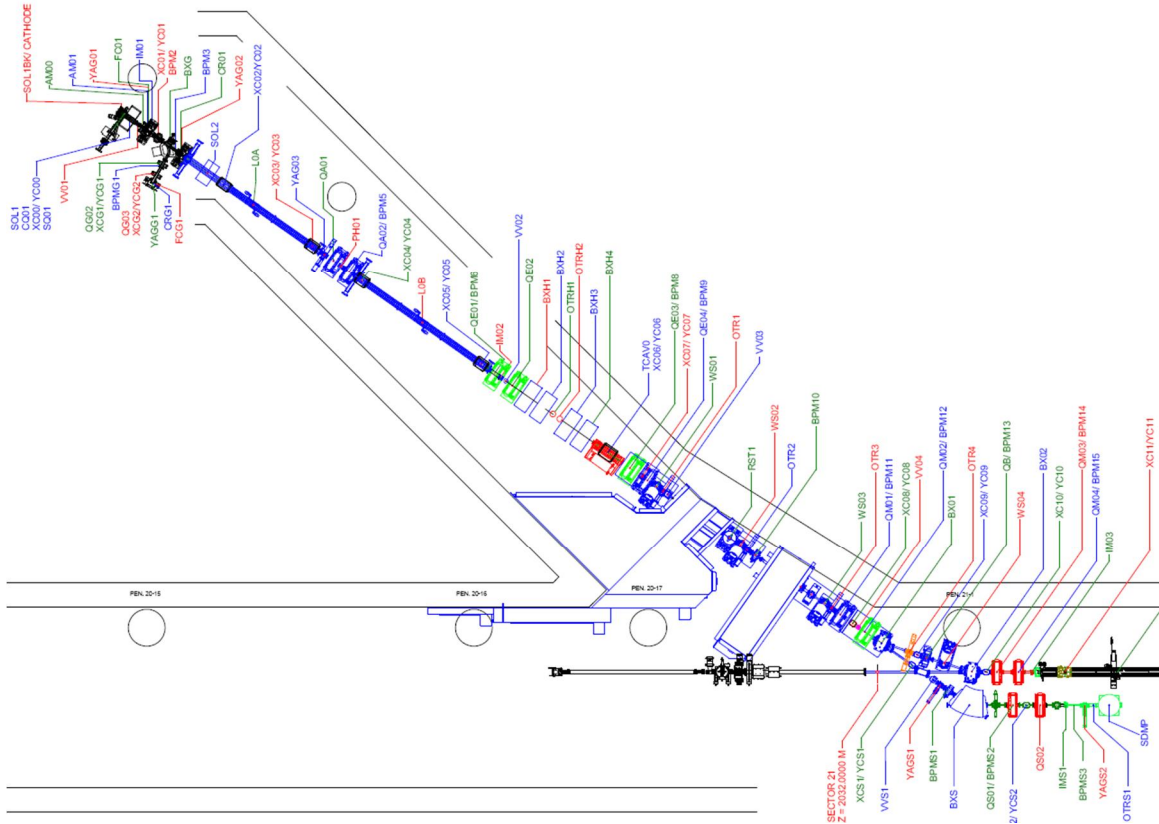


Figure 5.12. Layout of the LCLS-I injector vault, which is nearly identical to the FACET-II layout.

### 5.3.3.1 Transverse Projected Emittance Measurements

A simulation was performed, using *Impact-T* [4], of the evolution of the transverse injector emittance and beam sizes of a 2 nC beam up to an electron energy of 135 MeV. The calculated evolution of beam sizes and transverse emittance is given in Figure 5.13, the electron energy along the injector is shown in Figure 5.15 and the tracked longitudinal phase-space at the exit of linac-0 is shown in Figure 5.14.

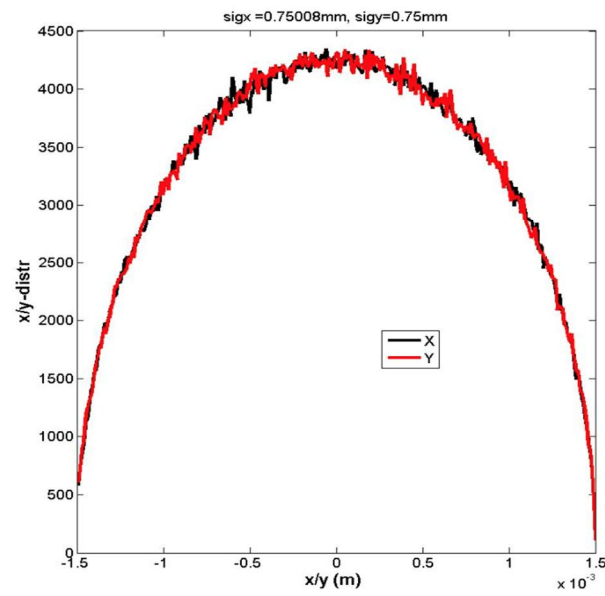
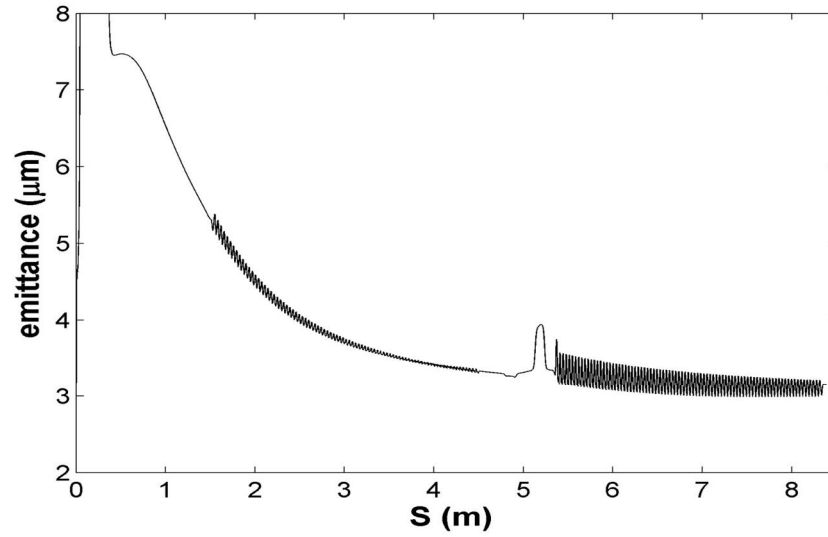


Figure 5.13. Simulated beam emittance evolution through the injector, from cathode up to exit of LOB RF structure at 135 MeV (top), transverse beam distribution at LOB exit (bottom).

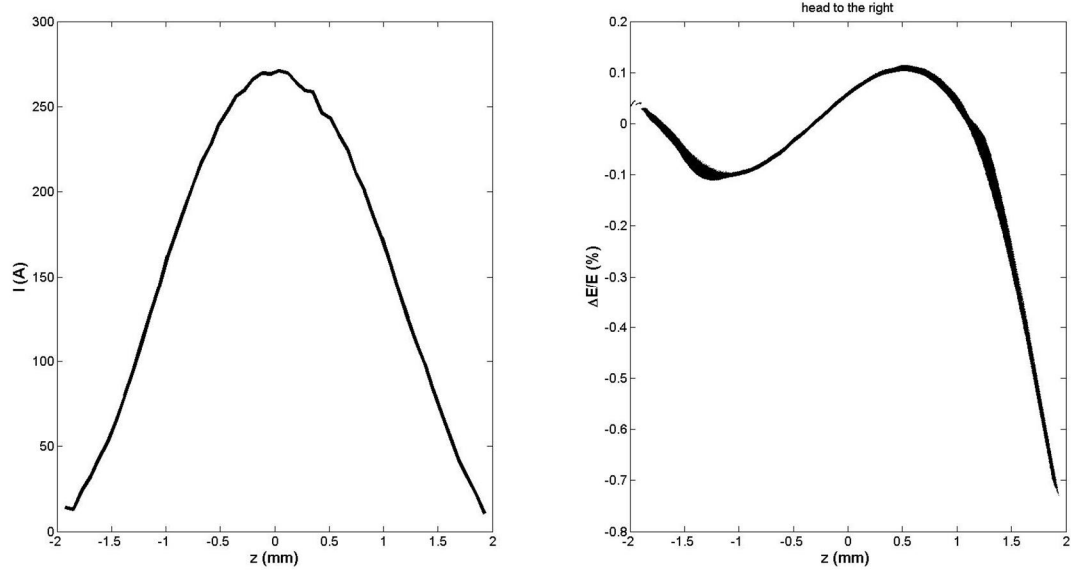


Figure 5.14: Longitudinal and transverse profiles from ImpactT simulated tracking of electron beam through to end of L0 (135MeV).

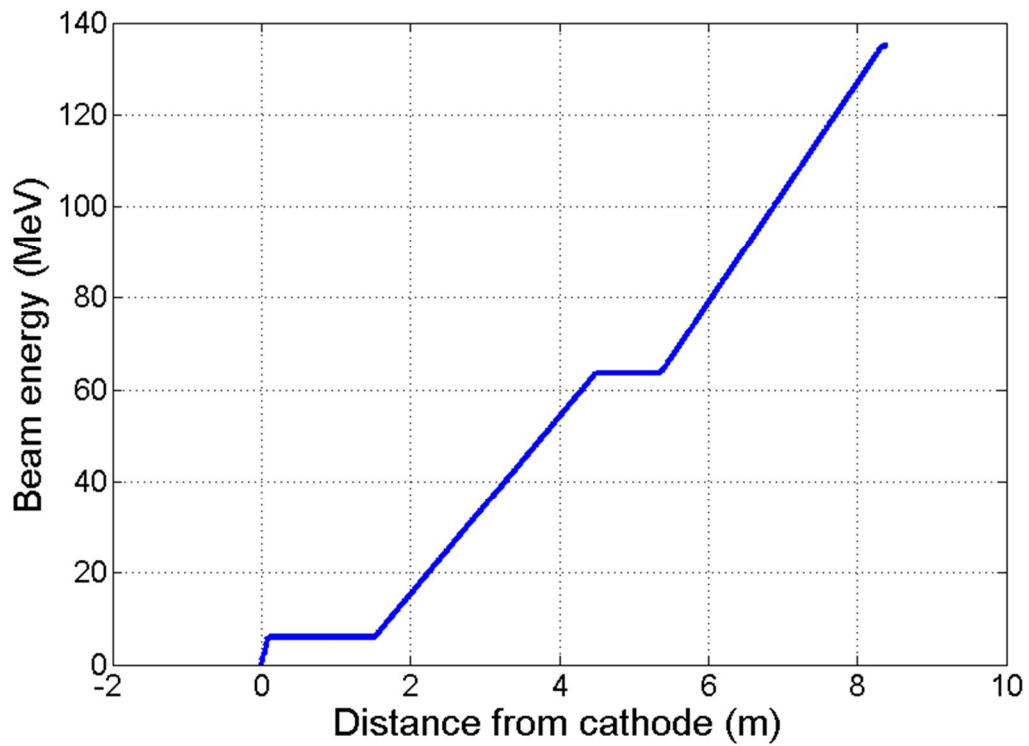


Figure 5.15. Electron energy from cathode to end of L0b accelerator section at 135 MeV.

### 5.3.3.2 6-MeV Spectrometer

A dipole magnet is located just downstream of the RF gun and can be switched on in order to measure the absolute energy and energy spread from the gun using a YAG screen. The energy measurement is used to calibrate the gun RF amplitude read-back in units of MV. The magnetic fields of the spectrometer bend (85°) are precisely measured prior to installation and the magnet includes a small trim coil so that its field can be reliably zeroed for normal operations (spectrometer off). A YAG screen and Faraday cup are located at the end of this short spectrometer (see Figure 5.16).

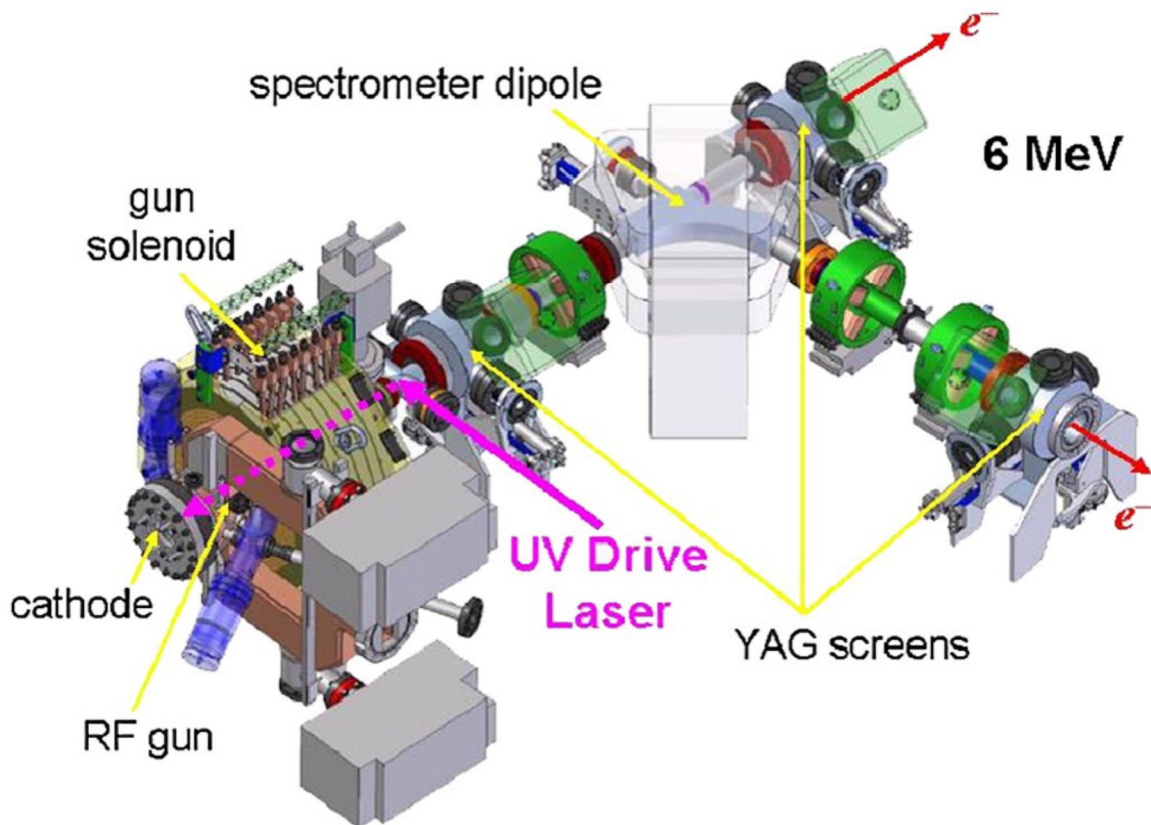


Figure 5.16. The gun and gun-to-linac (GTL) transport, including spectrometer, YAG screens, and solenoid. The drive laser actually enters on the opposite side. None of the green quadrupole magnets will be installed since they are unnecessary.

### 5.3.3.3 Laser Heater System

The injector system will incorporate a laser/electron beam heater system (an inverse free electron laser) in order to generate an increased intrinsic energy spread in the electron beam [2]. This produces damping in the bunch compressor chicane which suppresses the micro-bunching instabilities driven by Coherent Synchrotron Radiation (CSR) in the bunch compressors, and Longitudinal Space Charge (LSC) forces in the linac. The heater system is located just downstream of the LOB accelerator section at 135 MeV in the off-axis LCLS injector housing (see Figure 5.17).

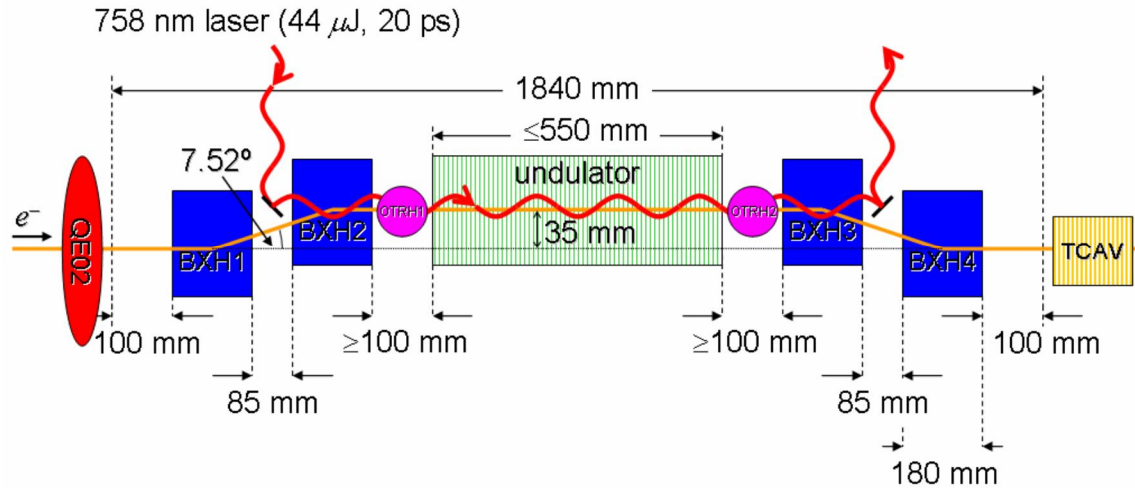


Figure 5.17. The laser-heater system in a weak chicane with co-propagating laser beam. The blue squares represent chicane magnets and the green rectangle represents the 9-period undulator.

Two OTR screens with photo-diodes are included to aid in achieving spatial and temporal overlap of the co-propagating laser and electron beams. Dimensions and laser power are approximate.

The electron beam (3 ps long) propagates collinearly with the Ti:sapphire laser pulse (~10 ps long, 760 nm wavelength) through a 55-cm long, 9-period, adjustable gap, planar, permanent magnet undulator located within a magnetic chicane. The laser-electron interaction modulates the electron energy along its bunch length with a period equal to that of the laser (760 nm). The chicane provides convenient injection of the laser beam and, more importantly, an effective time-smearing of the energy-modulation due to the path length dependence (through the last two chicane bends) on each electron's horizontal angle in the undulator (finite transverse emittance). This smearing erases all time-structure on the bunch and produces an effective 'thermal' local energy spread [2]. A 20-MW laser power (400 μJ in 20 ps), and system parameters given in Table 5.6, will produce a 130-keV rms local energy spread, rather than the very small level expected from the RF gun. The heated energy spread of 130 keV is small enough to have a minimal impact on the available peak current deliverable at 10 GeV, but large enough to considerably Landau damp beam instabilities in the accelerator helping to mitigate transverse beam quality degradation due to CSR and LSC effects. The heater's system parameters are listed in Table 5.6, while its laser parameters are above in Table 5.3. The laser heater electron optics functions are shown in Figure 5.18.

Table 5.6. Laser-heater electron beam, chicane, and undulator parameters for FACET-II.

Parameter	Symbol	Unit	Nominal	Range
Electron energy	$E$	MeV	135	135
Electron bunch length (FWHM)	$\Delta t$	ps	7	7-12
Electron transverse beam size (rms)	$\sigma_{x,y}$	mm	0.35	0.35-0.53
Undulator period	$\lambda_u$	cm	5.4	-
Undulator parameter	$K$	-	1.385	1.047-2.229
Undulator minimum gap	$g$	mm	34	25-100

Number of undulator periods	$N_u$	-	9	-
Chicane magnet eff. length	$L_B$	m	0.18	-
Bend angle of each chicane magnet	$\theta$	deg	7.52	0-7.52
Beam offset in chicane center	$ \eta_x $	mm	35	0-35
Required spatial overlap of laser and $e$ -beam	$ \Delta x  =  \Delta y $	mm	<0.2	-
Total rms energy spread induced	$\sigma_E$	keV	130	0-130

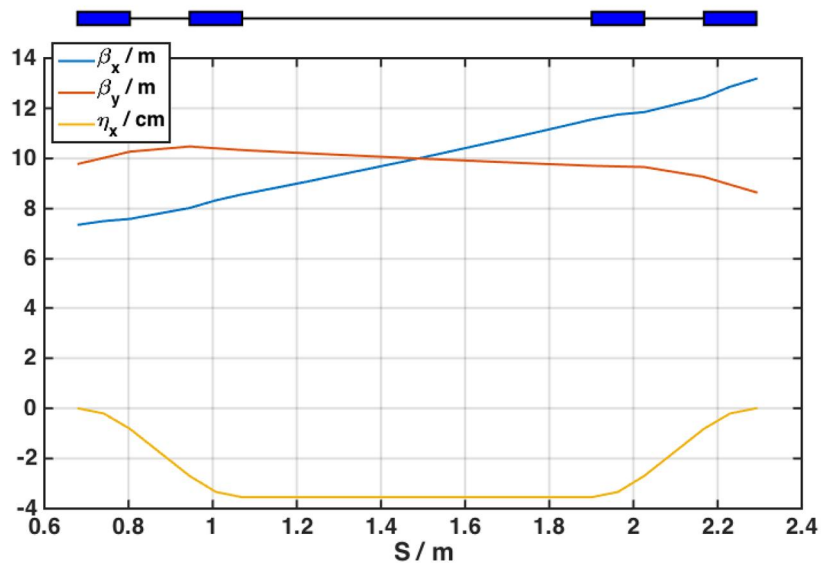


Figure 5.18. The laser heater electron optics in the FACET-II injector at 135 MeV.

#### 5.3.3.4 Linac Injector Horizontal Bend System (DL1)

The function of the low-energy 'Dog-Leg' (DL1) is to transport 135-MeV electrons from the new injector into the existing SLAC linac. DL1 is designed as a simple transport line, its design requirements are:

- Provide a horizontal beamline deflection of  $35^\circ$  over a short distance,
- Should not alter the bunch length (*i.e.*, should be nearly isochronous),
- Should introduce no significant transverse emittance dilution,
- Should provide a dispersive section for energy and energy spread measurement.

A simple system that satisfies these conditions is composed of two dipole magnets of equal strength with a quadrupole lens located between them to produce a linear achromat. The dipoles are rectangular bends. A profile monitor based on Optical Transition Radiation (OTR) and a BPM at the high dispersion point will provide energy and energy spread measurements.

Table 5.7. Parameters of the linac injector horizontal bend system (DL1).

Parameter	Symbol	Unit	Value
Beam energy	$E_{DL1}$	MeV	135
Total horizontal deflection (sum of 2 bends)	$\theta$	deg	35
RMS bunch length	$\sigma_z$	mm	0.8-1.6
RMS energy spread throughout beamline (at 135 MeV)	$\sigma_\delta$	%	0.7-2.0
Momentum compaction	$R_{56}$	mm	6.3
Second order momentum compaction	$T_{566}$	mm	140
Length of each of two dipole magnets	$L_B$	m	0.20
Bend angle of each dipole	$ \theta_B $	deg	17.5
Magnetic field of each dipole	$ B $	kG	6.9
Maximum horizontal dispersion	$ \eta _{\max}$	mm	263

The momentum compaction,  $R_{56}$ , of such a system for ultra-relativistic electrons and small angles is

$$R_{56} \approx \frac{1}{3} \theta_B^2 L_B, \quad (1)$$

where  $\theta_B$  and  $L_B$  are the bend angle and length of each dipole, respectively. A 1.3-meter long beamline with two  $17.5^\circ$  bends provides the required deflection and the 20-cm long dipoles produce an  $R_{56}$  of 6.3 mm (opposite sign of a chicane). Therefore, an electron which is off energy by 1% will move axially by only  $60 \mu\text{m}$ , which is small compared to the 0.8-1.6 mm rms bunch length. The effect of the second order momentum compaction,  $T_{566}$ , is even less. Nevertheless, the non-zero  $R_{56}$  value and the second order term of  $T_{566} \approx 0.14$  m has been taken into account throughout the design and stability optimization, and in the 2D and 6D particle tracking.

### 5.3.3.5 Injector Vacuum Systems

The pressure requirements for the FACET-II gun/injector vacuum systems are listed in Table 5.8. To maintain a differential pumping regime with a vacuum gradient that is lowest away from the gun, an additional ion pump (with respect to LCLS-I) will be located immediately downstream of the RF gun at the location that was occupied by a YAG screen, which is not often used in LCLS-I. The RGA originally installed on the gun in LCLS-I will be installed at this location. A fast DAQ system will be implemented to allow detailed tracking of vacuum events. The LCLS-I injector was upgraded with such a system in 2010.

Table 5.8. Injector vacuum system pressure requirements.

<b>LCLS-1 equivalent</b>	<b>Unit</b>	<b>Value</b>
Waveguides	Torr	$<1 \times 10^{-8}$
Gun	Torr	$<5 \times 10^{-10}$
GTL	Torr	$<5 \times 10^{-9}$
L0A/B	Torr	$<5 \times 10^{-9}$

## 5.4 Instrumentation, Diagnostics, Feedback, and Collimation

Critical to the preservation of the transverse emittance and the generation of a low-energy spread electron bunch are the precise measurement techniques and correction schemes used to initially commission and maintain the machine. The FACET-II injector has diagnostics located after each functional area of the injector, with correction schemes built into the design. All of the injector diagnostics will be controlled and read out via EPICS-based hardware and software developed for LCLS.

### 5.4.1 Beam Position Monitors (BPMs)

The FACET-II injector has 12 beam position monitors (BPMs) distributed along the injector with one in or near each quadrupole focusing magnet, as well as at high-dispersion regions for measurement and control of beam energy. The BPMs are stripline type with 5-10 micron resolution. Three toroids for precise measurement of beam charge are located after the gun, after L0 accelerating structures, and after the injection dogleg bend. Four additional BPMs and two additional toroids are located in the gun and injector spectrometer diagnostic lines.

### 5.4.2 Electron Beam Profile Monitors (Screens and Wire Scanners)

Ten intercepting electron beam screens and four wire-scanners are used throughout the injector to measure the transverse beam size. The screens are mostly Yttrium Aluminum Garnet (YAG) and Optical Transition Radiation (OTR) foils inserted into the beam path by pneumatic actuators. These allow measurement and tuning of the transverse beam distribution, as well as longitudinal tuning in conjunction with the transverse deflecting cavity. YAG screens are located in each of the gun and injector spectrometer lines as energy spread diagnostics. Two additional OTR screens are located in the laser heater chicane to set the transverse spatial overlap between the electron beam and heater laser. Four wire scanners upstream of the injection dogleg allow for non-invasive beam size measurements to be made.

### 5.4.3 Transverse Emittance Diagnostics

Located between the L0 accelerating section and the DL1 dogleg is a drift space spanning the radiation shield wall separating the injector vault from the linac accelerator housing. This drift space contains three OTR screens and wire scanners (OTR1-OTR3, WS01-WS03) which allows non-invasive emittance measurements to be made during normal machine operation, or can also be made using a 'quadrupole-scan' technique, taking advantage of the nominal beam waist on the center profile monitor, OTR2.

Table 5.9. Transverse emittance measurement stations along FACET-II ( $\gamma\epsilon_{x,y} \sim 4\text{-}5 \mu\text{m}$ ).

Location	Station Name	Energy (GeV)	$\sigma_x$ (mm)	$\sigma_y$ (mm)	No. of Prof. Monitors	Existing
Following L0	ED0	0.135	0.6-0.9	0.07-0.08	3	No
Following BC1	ED1	0.335	0.2-0.5	0.2	3	No
At the end of Linac-2	L2-ED	4.5	0.3-0.4	0.05-0.08	4	No
At the end of Linac-3	L3-ED	10.0	0.03-0.1	0.05	1	Yes
At the IP	IP-ED	10.0	0.01-0.02	0.005-0.01	3	Yes

#### 5.4.4 Bunch Length Diagnostics

The peak current delivered to the experimental user area in sector 20 is a critical parameter. It is determined by both the charge and the final bunch length and non-trivially dependent on the specific compression configuration employed by the various compression stages. To setup the compression, the bunch length and distribution needs to be measured and corrected before injection into the linac.

In the injector, the bunch length range of interest is approximately 1.6-0.8 mm rms (12-6 psec FWHM). A relative bunch length monitor based on a diode measuring power radiated from the electron beam through a ceramic gap in the beam pipe has been successfully used at FACET in Sector 2. This system provides pulse-by-pulse non-invasive bunch length measurement and will be moved to the FACET-II injector, but as it provides only a relative bunch length will need external calibration from a transverse deflecting cavity.

##### 5.4.4.1 Transverse RF Deflectors

A very simple technique to measure the very short electron bunch is to use a transverse RF deflecting cavity. This idea has been used in the past [5], [6] and has been quite successful at the LCLS-I and also in sector 20 during FACET-I operations. The high frequency time variation of the deflecting field is used to 'pitch' the electron bunch, while the resulting transverse beam width is measured on a simple profile monitor. This is a reliable, single-shot measure of the absolute bunch length. The technique is completely analogous to a streak camera, but with much better potential resolution down to about 10 fs rms, depending on the energy and vertical emittance. Detailed studies have been made of this technique [7], including wakefield and chromatic effects, and beam measurements have also been made at LCLS-I and FACET-I [8], [9]. A design for a 0.55-meter long S-band RF deflecting structure is available at SLAC and is now used in the LCLS-I injector. A cut-away view of the S-band traveling-wave rf-deflector is shown in Figure 5.19. A new deflecting structure of this design will need to be fabricate.

The bunch length,  $\sigma_z$ , can be calculated from knowledge of the deflecting voltage,  $V_0$ , the RF wavelength,  $\lambda_{rf}$ , and the beam energy at the screen,  $E_s$ .

$$\sigma_z \approx \frac{\lambda_{rf}}{2\pi} \frac{E_s}{|eV_0 \sin \Delta\psi \cos \varphi|} \sqrt{\frac{\sigma_y^2 - \sigma_{y0}^2}{\beta_d \beta_s}} \quad (2)$$

Included here is the product of  $(\beta_o\beta_s)^{1/2}\sin(\Delta\psi)$ , which is the (measurable) vertical transfer matrix element from angle-to-position and deflector-to-screen. Finally,  $\varphi$  is the RF phase of the deflector ( $\varphi = 0$  at zero-crossing) and  $\sigma_y$  and  $\sigma_{y0}$  are the measured vertical beam sizes with RF on and off, respectively. The voltage of the deflector is easily calibrated using simple BPM measurements as a function of RF phase. The RF deflecting structure (55 cm long) will be located in the injector at 135 MeV, as in the LCLS-I, providing  $<0.1$  ps resolution of the 5 ps long bunch there (see Figure 5.20).

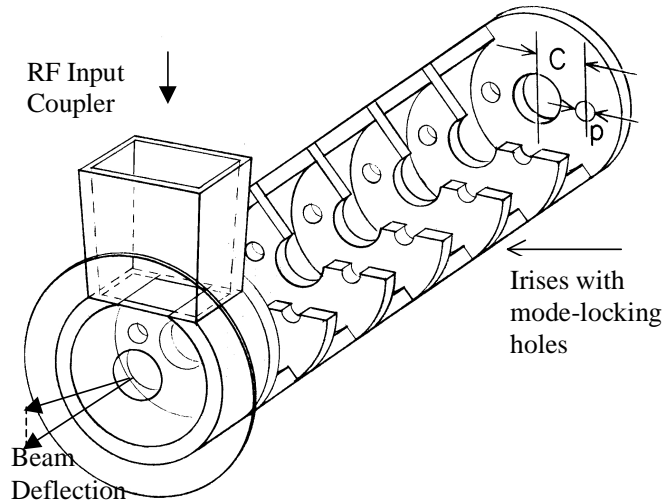


Figure 5.19. Schematic of a SLAC S-band transverse deflecting structure. The kick is vertical here.

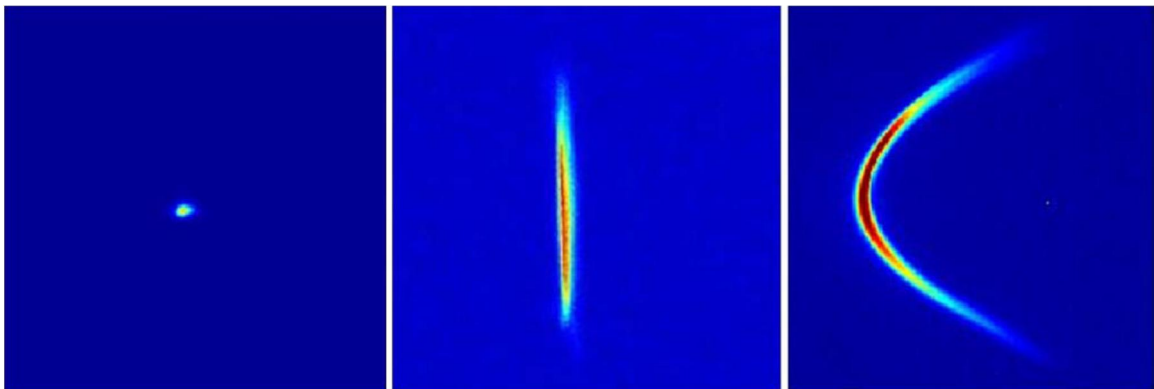


Figure 5.20. OTR image with RF deflector "OFF" (left) and "ON" (middle), to measure slice emittance. YAG screen after a bend (right) with deflector ON, reveals longitudinal phase space directly on the screen. The horizontal axis ( $\pm 4$  mm) is the horizontal beam coordinate in the left two plots, but it becomes relative energy in the right plot ( $\pm 0.8\%$ ). The vertical axis ( $\pm 4$  mm) is the vertical beam coordinate in the far left plot, but it becomes time in the two right plots ( $\pm 8$  ps).

---

## 5.4.5 Beam Energy Spread Diagnostics

The electron energy spread is typically measured using a profile monitor at a location with large momentum dispersion and small beta function. Several locations have been designed into the FACET-II optics in order to enable this measurement. The key locations are after the gun at 6 MeV where a spectrometer magnet can be switched on; in the DL1 dog-leg system at 135 MeV (35 deg bend from injector into the linac) and the 135-MeV spectrometer which is an off-axis diagnostic with high resolution.

### 5.4.5.1 DL1 Energy Spread Diagnostics

The energy spread measurement in DL1 is made with one of two possible profile monitors (a retractable OTR screen or a wire-scanner) located between the two dipoles of DL1 at the point where the horizontal dispersion function reaches a value of  $|\eta_x| \approx 154$  mm (OTR) or 166 mm (wire) with a horizontal beta function of  $\beta_x \approx 1.4$  m. For the nominal emittance and nominal energy spread of  $\sigma_\delta = 0.7$ -2.0 % at 135 MeV, the betatron beam size is 160  $\mu\text{m}$  rms, but the dispersive size is 1120-3200  $\mu\text{m}$ . This produces a high resolution energy spread measurement. The statistical error depends on the profile monitor and should be 5–10%. A more accurate measurement of this same energy spread is available in the 135-MeV spectrometer, which can be switched on or off at any time (see below).

### 5.4.5.2 135-MeV Spectrometry

The energy spread measurement in the 135-MeV spectrometer is made with a profile monitors (a retractable YAG screen) located after the 35-deg BXS bend magnet where the horizontal dispersion function reaches a value of  $|\eta_x| \approx 887$  mm with a horizontal beta function of  $\beta_x \approx 0.13$  m. For the nominal emittance and nominal energy spread of  $\sigma_\delta \approx 0.07\%$  at 135 MeV, the betatron beam size is 17  $\mu\text{m}$ , but the dispersive size is 444  $\mu\text{m}$ . This produces no significant systematic energy spread measurement error. The statistical error depends on the profile monitor and should be 5–10%.

## 5.4.6 Trajectory Feedback Systems

Trajectory feedback systems will be placed at the exit of the gun and in the injector. As at the SLC [10], and as utilized during FACET-I operations, these systems will each be composed of approximately ten BPMs which record both  $x$  and  $y$  positions, preceded by a set of two horizontal and two vertical fast dipole corrector magnets controlled by a microprocessor based feedback system.

In order to control transverse orbit variations to better than  $1/10^{\text{th}}$  of the beam size, the individual one-pulse BPM resolution for the various 10-BPM feedback systems described above needs to be  $<10$   $\mu\text{m}$  rms. Trajectory variations which occur at frequencies below  $\sim 5$  Hz will be stabilized. Faster variations cannot be damped significantly and will need to be identified at the source. In addition, a bunch charge feedback loop will maintain the bunch charge by reading a toroid and controlling the UV laser energy per pulse with a waveplate.

Transverse vibrations of quadrupole magnets will generate orbit variations, which if fast enough will not be damped by feedback systems. Tolerance calculations indicate that uncorrelated random vibrations of all FACET-II quadrupoles must be at the level of  $< 100$  nm rms, to hold the rms beam stability at  $< 10\%$  of the rms beam size there. Measurements in the SLC indicate that existing linac magnet vibrations are  $< 250$  nm [11] with the highest frequency content at 59 Hz and 10 Hz driven by cooling water.

## 5.4.7 Energy and Bunch Length Feedback Systems

---

Energy feedback systems will be placed in the bending region (DL1). A single BPM or group of BPMs placed at a high dispersion point will be used to determine energy variations, and upstream RF will be used to stabilize the energy.

## 5.5 References

---

1. R. Akre *et al.*, Phys. Rev ST – Accel. Beams 11, 030703 (2008).
2. Z. Huang *et al.*, Phys. Rev ST – Accel. Beams 13, 020703 (2010).
3. D. H. Dowell *et al.*, *The Development of the Linac Coherent Light Source RF Gun*, <http://www-bd.fnal.gov/icfabd/Newsletter46.pdf>.
4. J. Qiang *et al.*, Phys. Rev. ST Accel. Beams 9, 044204 (2006).
5. G. A. Loew, O. H. Altenmueller, *Design and Applications of R.F. Deflecting Structures at SLAC*, PUB-135, Aug. 1965.
6. R.H. Miller, R.F. Koontz, D.D. Tsang, *The SLAC Injector*, *IEEE Trans. Nucl. Sci.*, June 1965, p. 804-8.
7. P. Emma, J. Frisch, and P. Krejcik, *A Transverse RF Deflecting Structure for Bunch Length and Phase Space Diagnostics*, LCLS-TN-00-12, August 2000.
8. P. Emma, *et al.*, *Bunch Length Measurements Using a Transverse RF Deflecting Structure in the SLAC Linac*, Proceedings of the 2002 European Particle Accelerator Conference, Paris, France, June 3-7, 2002.
9. V. A. Dolgashev *et al.*, Design and application of multimegawatt X-band deflectors for femtosecond electron beam diagnostics, Phys. Rev. ST Accel. Beams 17, 102801 (2014)
10. T. Himel *et al.*, *Adaptive Cascaded Beam-Based Feedback at the SLC*, Proceedings of the 1993 Part. Accel. Conf., Washington, DC, 1993.
11. J. L. Turner *et al.*, *Vibration Studies of the Stanford Linear Accelerator*, Proceedings of the 1995 Part. Accel. Conf., Dallas, TX, 1995.

---

# 6 Bunch Compressors and Linac

---

## Technical Synopsis

*In order to achieve the scientific goals of the experimental program at FACET-II, a high peak current bunch with small transverse core beam size at the experimental IP waist, of order  $10\mu\text{m}$ , and small longitudinal emittance is required. FACET-II will operate with electron and positron bunches at an energy of up to 10 GeV. The most challenging parameters for the design of the bunch compression scheme are given by the plasma wakefield acceleration (PWFA) experiments which benefit from peak currents in excess of 10 kA. The RF photocathode gun and injection system are capable of producing up to 5 nC in a bunch length of  $<5.4$  ps (rms), corresponding to a peak current of  $>120$  A (before compression) with a transverse emittance of  $<5\mu\text{m}$ . This implies a required compression ratio of about 100 to achieve the desired beam characteristics at the IP waist in Sector 20.*

*Both electrons and positrons undergo three stages of bunch compression, the first two stages in Linac Sectors 11 and 14 and the final compression stage in Sector 20. The Sector 20 chicanes are described in Chapter 9. For positron operation, positrons produced in sector 19 are returned to the beginning of the linac in a ceiling-mounted transfer line and injected into a damping ring in Sector 10 at an energy of 335 MeV. The initial stage of positron compression takes place in the transfer line from the damping ring before injection into the main linac in the final bend of BC1 (in Sector 11). The design of the compression scheme addresses the most challenging option which requires the positron beam to be co-accelerated along with the electron beam through the main linac, separated by  $\sim 5\text{cm}$ , i.e.  $\frac{1}{2}$  of an S-band RF bucket. This requires a common RF chirp and BC2 compression configuration for both electron and positron bunches. Hence, the configuration of the linac-based compression scheme must take into account the compression requirements of both particle species simultaneously. The details of the positron systems are mainly described in chapters 8 and 9.*

*The capabilities of FACET-II vary in a non-trivial way depending on the choice of initial charge from the RF gun. The baseline design is for a 2nC electron bunch charge from the electron gun eventually operating together with a 2nC positron bunch from the positron damping ring. A possible future upgrade configuration option with a 5 nC bunch from the electron gun together with a 1nC positron bunch is described in Chapter 10. The conceptual design here represents a parameter set to demonstrate the highest deliverable peak currents to the Sector 20 user area within the various parameter constraints of operation with both electrons and positrons. This design is limited by the requirements of the positron bunch which has the larger initial longitudinal emittance, and greater sensitivity to CSR effects in the final compression stage. The compression scheme can be tailored more towards higher electron-only peak current if desired.*

*The bunch compression is accomplished by a series of magnetic chicanes arranged and located such that non-linearities in the compression and acceleration process (longitudinal wakefields, RF curvature, and second order momentum compaction) are all approximately compensated. A short section of X-band deceleration (3.3 MeV, 11.424 GHz) ahead of the first compressor is used to linearize the compression for the electron beam. The goal for the linac design is to a) achieve design peak current requirements for both positron and electron bunches, b) cancel the correlated energy spread after the final compression and c) minimize sensitivities to RF phase and amplitude variations and also to bunch charge variations. The electron energy at the first compressor is 335 MeV. This choice avoids space charge effects, while the bunch compression is still early enough in the linac to ease the effects of transverse wakefields. In the*

---

first compressor (BC1), the electron bunch length is reduced from 0.8 mm to 287  $\mu\text{m}$  (rms). For operation with positrons, the positron beam is injected into the linac in the final BC1 bend. The injection energy of 335 MeV is also convenient for the design of the compact positron damping ring. The bunch length of the positrons, upon extraction from the damping ring, is 4 mm (rms). To match well into the linac compression scheme, an additional bunch compressor (2.1m S-band RF section and 4-bend chicane) is included in the damping ring-to-linac beamline section. The positron bunch length is compressed to 308  $\mu\text{m}$  (rms) before being injected into the shared linac through a horizontal dogleg section

The second compressor (BC2 in Sector 14) produces a 23.6/28.9  $\mu\text{m}$  rms bunch length for electrons/positrons. The energy of the second compressor, 4.5 GeV, is chosen as a balance between the conflicting requirements of longitudinal emittance dilution due to synchrotron radiation, and the need to cancel the final correlated energy spread when including the final compression stage in sector 20. The design of the compressors is dominated by the need to reduce Coherent Synchrotron Radiation (CSR) effects, which are most pronounced for short bunches. The most significant effect of CSR is to generate a time-dependent energy variation along the bunch. Designs utilizing relatively weak chicanes and larger initial correlated energy spreads for the various compression stages help control the effect CSR has on transverse emittance dilution. Additionally, adjustable collimators in the center of BC1 and BC2 are used to cut high-energy, non-linear tails and also allow for fine-tuning the positron and electron bunch populations to help with balancing relative beam-loading energy losses in the linacs. The final compression stage in sector 20 using the BC3E and BC3P chicanes at 10 GeV is described in Chapter 9.

6D tracking simulations have been made to model the beam transport through the FACET-II complex, including the non-linear compression and final beam focus process. The simulations include the effects of longitudinal wakefields in the 1km linac as well as incoherent and coherent synchrotron radiation effects in the various bending magnets. Longitudinal space charge effects are also simulated throughout the beam transport. Simulations have also been made which calculate emittance dilution in the linac due to transverse wakefields and anomalous momentum dispersion, each of which arises from a variety of considered error sources such as component misalignment and magnetic field errors. Diagnostics, correction techniques, and feedback systems have also been incorporated into the design. For operation with positrons, the electron bunch is preceded by a positron bunch separated by  $\frac{1}{2}$  an S-band RF wavelength (5.25 cm). The coupling of trajectory errors through transverse wakefields in the two-bunch system required for simultaneous operation with both electrons and positrons is also included in the tracking simulations.

---

---

## 6.1 Main FACET-II Linac

The main linac of FACET-II (sectors 11-20) is designed to accelerate the electron beam to 10 GeV using about 850 meters of S-band (2.856 GHz) radio frequency (RF) traveling-wave accelerating structures. The main linac for the FACET-II electron system (as in LCLS-I) is segmented into three separate sections, as shown in Figure 6.1.

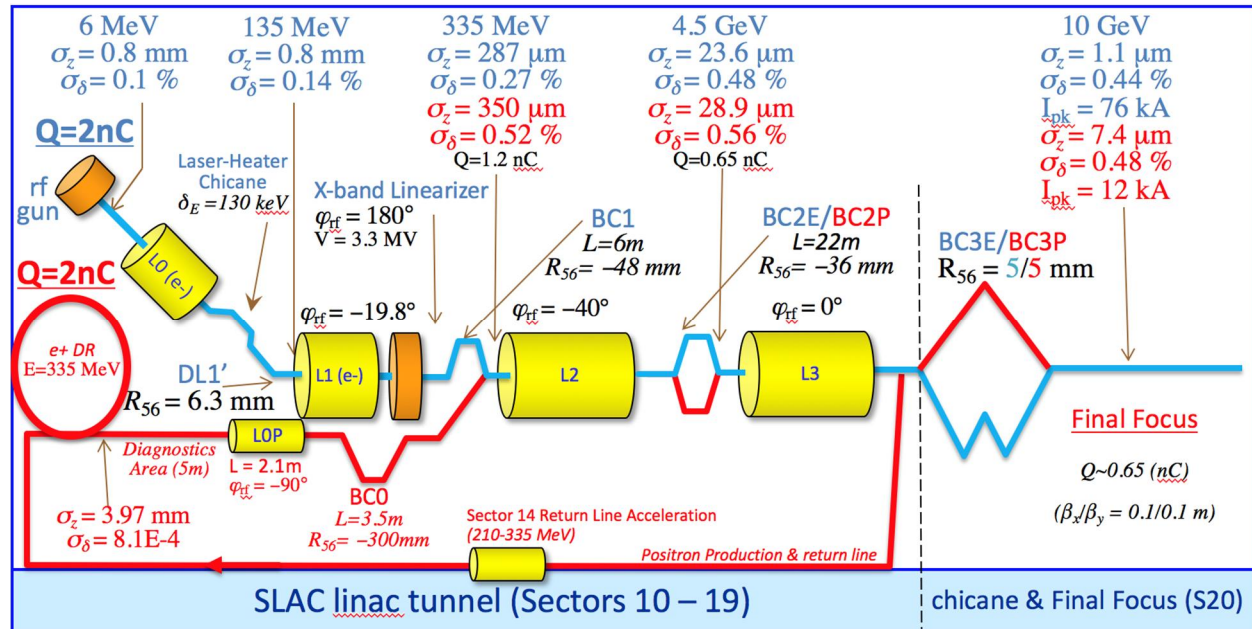


Figure 6.1. Schematic layout of FACET-II injector, linac, bunch compressors, and experimental area, with main parameters listed for operation. The blue sections depict the electron specific and common e-/e+ areas. The red sections are for positrons.

The first acceleration section after the injector is the L1-linac (L1) composed of three 3-m long S-band accelerating structures in each of RF sections 11\_1 and 11\_2 and one X-band 4<sup>th</sup> harmonic accelerating structure just prior to the Bunch Compressor 1 (BC1) chicane. Here the bunch is accelerated off the RF crest (-19.8 deg S-band) up to 335 MeV and then compressed partially in the BC1 chicane. The X-band RF section decelerates the beam by 3.3 MeV and is used to linearize the energy chirp prior to BC1. The L2-linac (~326 m) follows the BC1 chicane and also accelerates off crest (-40 deg S-band) up to 4.5 GeV where the Bunch Compressor 2 (BC2) chicane executes the next stage of bunch length compression. Beyond BC2 is the L3-linac (582 m), which accelerates on crest to an energy of 10 GeV. To avoid excessive energy spread, the sector 20 chicanes are designed with opposite sign  $R_{56}$  compression parameters (compared to the earlier chicanes) to compress most effectively in conjunction with the wakefield chirp imposed by L3. The positron beam on extraction from the damping ring requires an additional compression stage (BC0) provided by a 4-bend chicane and a 2.1m s-band RF section (PLO) operating 90-degrees off crest.

For simultaneous delivery of both sign bunches, the positron beam is co-accelerated within the same RF half-wavelength as the electron beam through L2 and L3. The electron and positron beams have different initial longitudinal emittances, and also experience different wakefield-induced energy chirps in L2 and L3 due to different bunch charges and/or different bunch lengths. Each bunch type must

---

receive the same off-crest RF configuration in L2 and L3 leaving the following free design-time parameters to configure the compression for simultaneous high peak-current operation:

- L1 RF phase and BC1 chicane  $R_{56}$  to adjust chirp and compression configuration for electron injection through BC1. The  $R_{56}$  setting of BC1 is assumed to be static after construction.
- PLO RF phase and BC0  $R_{56}$  setting to adjust chirp and compression configuration for positron injection into L2. The BC0  $R_{56}$  setting is assumed to be static after construction.
- BC2  $R_{56}$  setting is assumed to be symmetric across electron and positron paths of the chicane (BC2E/BC2P) (equal bend angles in the shared first and last chicane bends). Changing the initial bunch charge and/or collimation setup if operational changes in final bunch charge are required will require changes to the BC2 bend angles post-construction to adjust the BC2  $R_{56}$  for optimal compression.
- BC3E and BC3P have independently controllable  $R_{56}$  settings (both at design time and during operation) achieved through matching quadrupole magnets inside each chicane. The  $R_{56}$  parameters can be adjusted (independently for BC3E and BC3P) from approximately -10 to +10 mm.
- Adjustable collimators in BC0, BC1 and BC2E/P are independently controllable for the electron and positron beams. This allows high energy-spread, non-linear tails in the beam distributions, necessary due to the required high-compression ratios, to be clipped and for the relative charges in L2 and L3 to be controlled. The clipping of high-energy tails in the bunch compressors improves the transverse emittance delivered to users in Sector 20 without considerably reducing the delivered peak current. Due to different initial longitudinal properties of the electron and positron beams, they experience different levels of wakefield-induced energy loss in the linacs which cannot be compensated using the RF system due to the fact that the two bunch types share the same RF accelerating wave. To fine-tune the energies through the bunch compression stages, the charge profile is independently controlled both at source and using the collimation stages.

The transverse optics in the various linac sections are designed to minimize transverse wakefield effects and also to loosen magnet alignment tolerances. This is done at the design stage by selection of the phase-advance per linac cell independently for the three linac sections, again taking into consideration both the electron and positron beam dynamics.

### 6.1.1 Linac Energy Management

With two bunch compressor chicanes to be located within the 850 meters of main linac, and the RF phase to be set significantly off crest ( $-19.8^\circ$  in L1 and  $-40^\circ$  in L2), the recommended layout of the accelerating sections is summarized here, including spare klystrons in each long linac section (L2 and L3) suggested. There is one spare klystron in L2 with the RF 40-deg off crest, and 2 klystrons are reserved for BC2 energy feedback control. With the BC1 energy as  $E_1$ , we can show the BC2 energy,  $E_2$ , and the max final linac energy,  $E_3$ , as

$$E_2 = E_1 + N_{k2}\Delta E_k \cos \varphi_2 + N_{f2}\Delta E_k \cos \varphi_{2f} \quad (1)$$

$$E_3 = E_2 + N_{k3}\Delta E_k \cos \varphi_3 + N_{f3}\Delta E_k \cos \varphi_{3f} \quad (2)$$

where  $\Delta E_k$  is the average energy gain of each klystron (taken as 231 MeV or 19 MV/m average gradient),  $N_{k2}$  as the number of powered klystrons in L2 at an RF phase of  $\varphi_2$ ,  $N_{f2}$  as the number of powered energy-feedback klystrons in L2 at a phase of  $\varphi_{2f}$ ,  $N_{k3}$  as the number of powered klystrons in L3 at an RF phase of  $\varphi_3$ , and  $N_{f3}$  as the number of powered energy-feedback klystrons in L3 at a phase of  $\varphi_{3f}$ . Choosing  $E_1 = 0.335$  GeV,  $E_2 = 4.5$  GeV,  $E_3 = 10.0$  GeV, and also choosing  $N_{f2} = 2$ ,  $\varphi_{2f} \approx 60^\circ$ , and  $\varphi_3 = 0$ , and  $N_{f3} = 6$  and  $\varphi_{3f} \approx 60^\circ$  we find that  $N_{k2} = 23$  and  $N_{k3} = 21$ . Adding in a spare klystron per linac section, accounting for the feedback klystrons, and reserving an RF station in each section for use by a transverse cavity for bunch length diagnostics, then the total number of required klystrons in L2 is 27, and 29 in L3. BC1 is placed in the location of the 11-3 and 11-4 RF structures, with BC2 taking over the space of 14-7 and 14-8. RF station 19-7 is used, as for FACET, for extracting the beam into the positron production line and stations 11-4 and 15-1 are used for TCAV installations for bunch length measurements. There are 10 additional klystrons in L3, which would allow for a final energy up to 13.7 GeV if all available RF stations in L3 were to be used. The expected linac layout is shown in Figure 6.2.

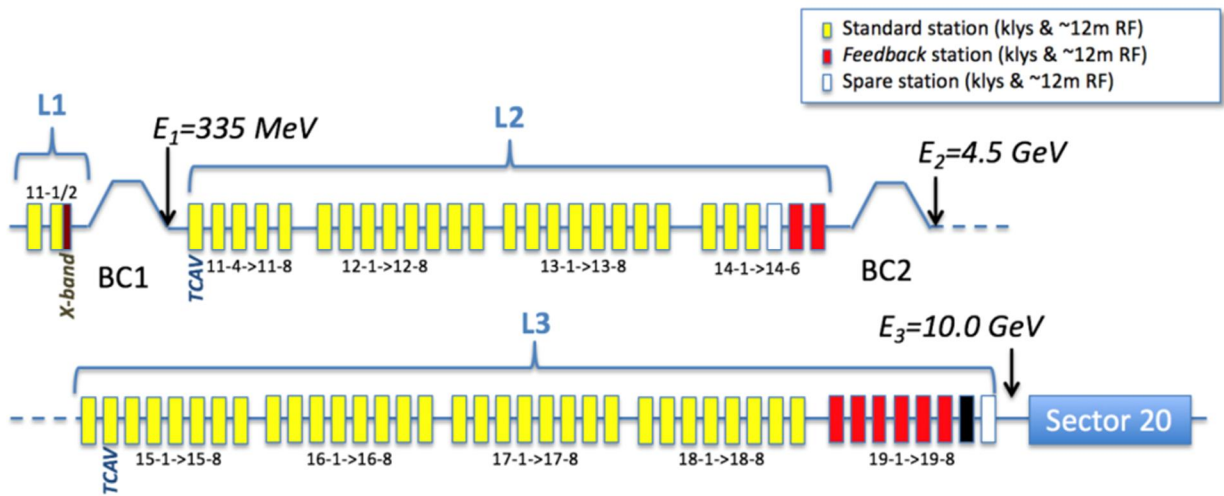


Figure 6.2. Linac klystron distribution showing sectors 11 through 20, where each box represents one klystron (typically 12 meters of accelerator with 231 MeV energy gain on crest).

The yellow boxes are typical stations usually with four 3-m RF sections, the red boxes are energy-feedback stations, the white boxes are spare stations reserved for when failures arise, and the brown station at 11-2 is the X-band RF station used to linearize the longitudinal phase space of the electron beam. The black colored box indicates the removed section in 19-7 used for extraction of the positron-generating “scavenger” pulse.

Table lists, for each FACET-II linac section, the total number of klystrons potentially available,  $N_{klys}$ , the number of klystrons held in reserve,  $N_{res}$ , the largest off-crest RF phase,  $\varphi_i$ , the on-crest average energy gain per klystron,  $\Delta E_k$ , the beam loading energy loss (+ CSR energy loss in bunch compressors) for  $Q = 2$  nC initial charge,  $\Delta E_B$ , the nominal initial and final energy,  $E_i$  &  $E_{nom}$ , of that section, and the maximum energy,  $E_{max}$ . For L2 and L3 two numbers are presented for electron and positron beams respectively. The nominal charge,  $Q$  in each section (again for electron and positrons in L2 and L3) is shown. The charge of each beam is differentially collimated using moveable collimator jaws in each bunch compressor.

Table 6.1. Energy management parameters for the four main linac sections. L2 and L3 parameters show 2 numbers for electrons, positrons respectively. The beam loading energy losses indicated here include the few MeV energy-loss due to CSR in the bunch compressors.

Linac	$N_{klys}$	$N_{res}$	$\varphi_i$ [deg]	$\Delta E_k$ [MeV]	$\Delta E_B$ [MeV]	$E_i$ [GeV]	$E_{nom}$ [GeV]	$E_{max}$ [GeV]	$Q$ [nC]
L1	1	0	-19.8	102	3.1	0.135	0.338	0.44	2.0
LX	1	0	-180	-3.3	5	0.338	0.335	0.44	2.0
L2	26	1	-40	160	33,33	0.335	4.50	4.55	1.2,1.2
L3	38	1	0	145	46,46	4.50	10.0	13.7	0.6,0.7

### 6.1.2 Linac Optics

The electron optics in the various linac sections are designed to minimize transverse wakefield effects and also to loosen magnet and RF structure alignment tolerances. Each section, with its different bunch length and energy spread values, has a different optimal configuration. Additionally, the beta functions are manipulated to be small and close to waist locations at the exit of each BC1 and BC2 bunch compressor in both dimensions. For the optics in sectors 18 and 19, the beta functions must be kept small in both planes as the beam enters the sector-20 bunch compressors, and they must also be matched into the positron production beamline optics. This minimizes the impact of CSR induced emittance growth for both electron and positron beams. The optics functions of the L1, L2, and L3 linac sections are plotted in Figure 6.3, Figure 6.4 and Figure 6.5, respectively.

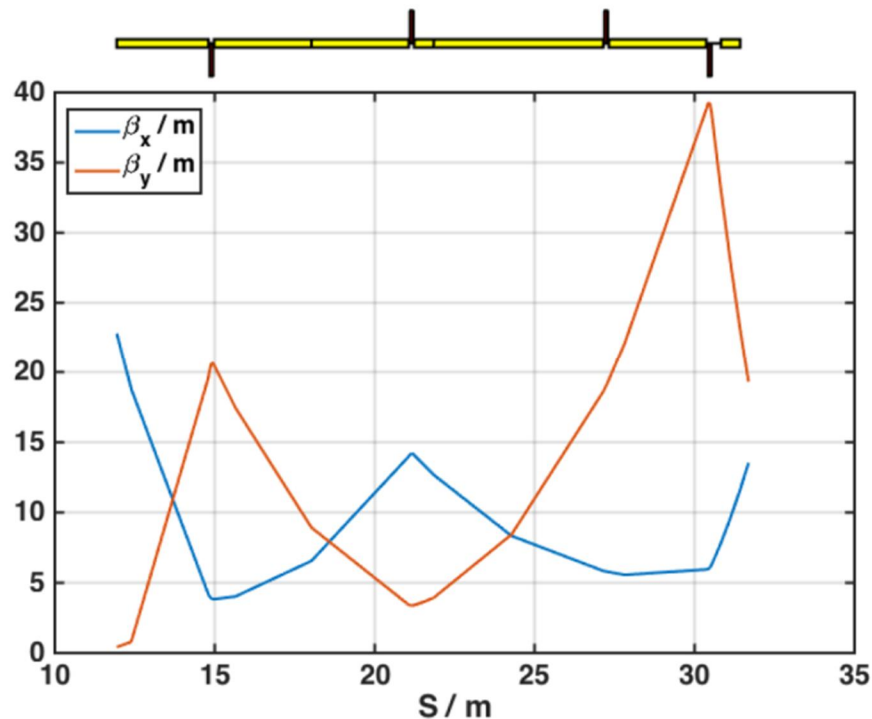


Figure 6.3. The optics functions of the L1-linac (11-1 and 11-2).

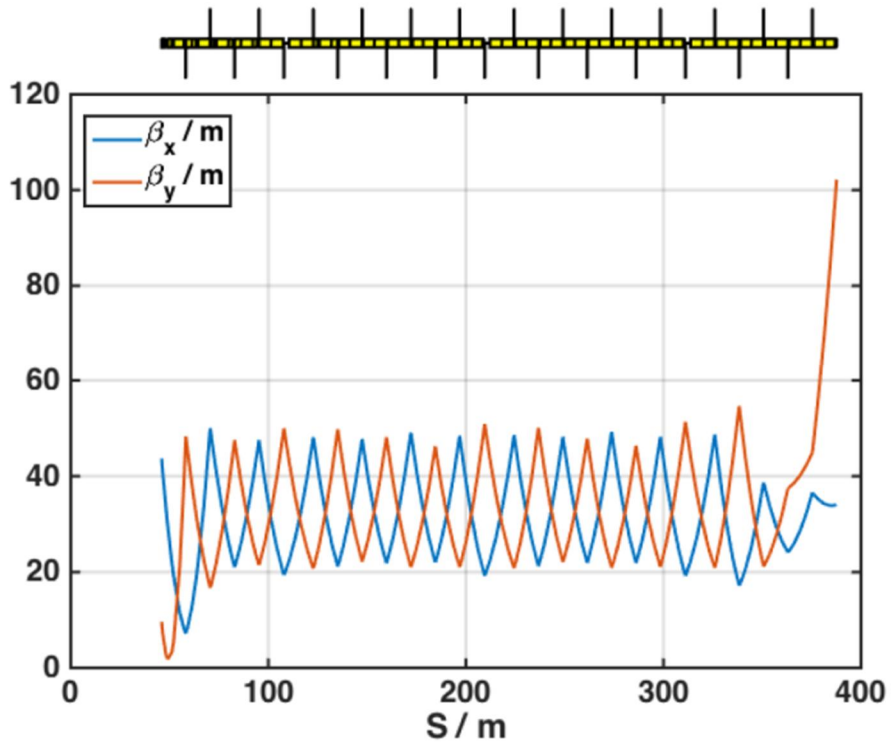


Figure 6.4. The optics functions of the L2-linac from 11-2 to 14-6, with a phase advance per FODO cell of 70 degrees.

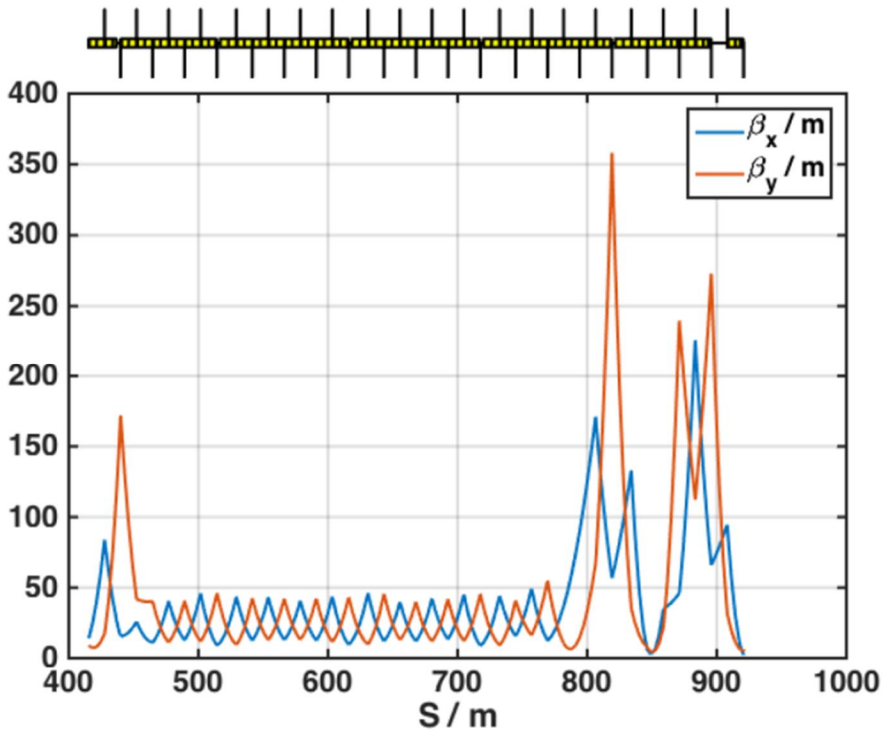


Figure 6.5. The optics functions of the L3-linac from 15-1 to 19-8, with a phase advance per FODO cell of 67 degrees.

---

### 6.1.3 Linac Modifications and Installation Issues

The SLAC linac between sectors 11 through 19 must be modified to install the main components of FACET-II, especially considering the new bunch compressor chicanes. A list of the linac beamline modifications follows:

- The 11-1b and 11-2b RF 10-foot sections must be replaced with 9.4-foot sections in order to insert a quadrupole magnet after each RF section in the L1-linac (there has never been an 11-1a RF section in the linac and this will continue).
- All four of the 11-3a, b, c, and d 10-foot RF sections need to be removed to install the new BC1 compressor chicane and its associated beam diagnostics.
- The 11-3 RF modulator will be modified and used to power the new X-band RF section (L1X) using an X-band klystron. The L1X structure takes the place of the slot currently occupied by 11-2d.
- The 11-4 klystron and modulator are reserved for use by an 8-foot S-band TCAV section to be located in one of the 11-4 accelerating sections. The remaining three 11-4 sections are not used, but if an additional klystron can be supplied to the secondary slot in 11-4 then these 3 sections can be used to provide additional energy overhead for the L2 acceleration section.
- The four 10-foot RF sections at 13-8d, 14-2d, 14-4d, and 14-6d will each be replaced by a 9.4-foot section in order to install four new wire scanners.
- All eight of the 14-7a, b, c, d and 14-8a, b, c, d 10-foot RF sections will be removed to install the new BC2 compressor chicane.
- The 15-2d 10-foot RF section will be removed in order to make room for another 8-foot S-band TCAV transverse RF deflector.
- Four 10-foot RF sections at 19-8d, 19-6d, 19-4d, and 19-2d will each be replaced by a 9.4-foot section in order to install four new wire scanners.

### 6.2 Bunch Compression

In order to achieve the bunch density required for the PWFAs experiments, the final electron bunch must be compressed in length to several thousand amperes of peak current. The bunch compression system must meet several basic requirements as follows:

- To improve stability and to avoid significant space charge forces, two separate and independently adjustable stages of bunch compression should be included. These are in addition to the existing final compression stage in sector 20 which also provides additional non-linearity correction and diagnostic functionality.
- The two new electron compression stages (BC1 and BC2E) should be based on a four-dipole magnetic chicane, which is simple and achromatic to all orders.
- The first compressor should be located as far upstream as possible, but at high enough energy to avoid space charge effects after compression. An additional constraint on the energy of BC1 is given by the requirement to inject the positron beam at the final chicane bend, the energy of the damping ring should be as high as possible to maximize the quality of the damped positron beam (given other space constraints imposed on the ring design).

- The second compressor should be located as far upstream as possible, but at high enough energy to avoid space charge effects, and also located so that the remnant energy chirp after compression is fully cancelled by the longitudinal wakefield of the post-BC2 linac plus the sector 20 bunch compressor. There must also be enough remaining accelerating structures to reach the desired 10 GeV Sector 20 beam energy. BC2 is shared for both e- and e+ beams (shared first and last bend magnets, independent symmetrically placed middle two bends). To keep the chicane simple, the compression design presented here assumes a symmetric arrangement with equal  $R_{56}$  compression coefficients for both beams.

Bunch compression in FACET-II is closely based both on the successful design of LCLS-I and on the experience operating FACET. The compression is accomplished by the standard method where a linear energy chirp (energy correlation along the bunch) is generated by accelerating at an RF phase,  $\varphi$ , which is a few tens of degrees away from the RF crest. With the correct sign of correlation (*i.e.*,  $\varphi < 0$  for chicane compressors), the head of the bunch (low energy particles) will travel a longer distance within a given bunch compressor's magnetic optics, while the tail of the bunch (high energy particles) will travel a shorter path, effectively compressing the bunch length. For compression of the electron bunch, there are two standard 4-bend chicane compressors in the linac. The bunch is set to 'over-compression' in the second, where compression proceeds beyond the minimum bunch length. Then the wakefield-induced energy chirp in L3 is made to add to the remnant chirp in the right way to fully compress in the sector 20 W-chicane. Unlike the negative  $R_{56}$  of the simple 4-bend chicanes (defined for a coordinate system with bunch head at  $z < 0$ ), the W-chicane has a more complex arrangement of magnets and is made to have a positive  $R_{56}$  which can be varied across the range -0-10mm and is nominally set to +5mm.

The compression factor is encompassed in its  $R_{56}$  value, where each electron is delayed or advanced by its energy deviation with respect to the reference particle (design energy). If the relative energy deviation is expressed as  $\delta (= \Delta E/E_0)$ , then the electron delay (or advance) is written as

$$\Delta z = R_{56} \delta . \quad (3)$$

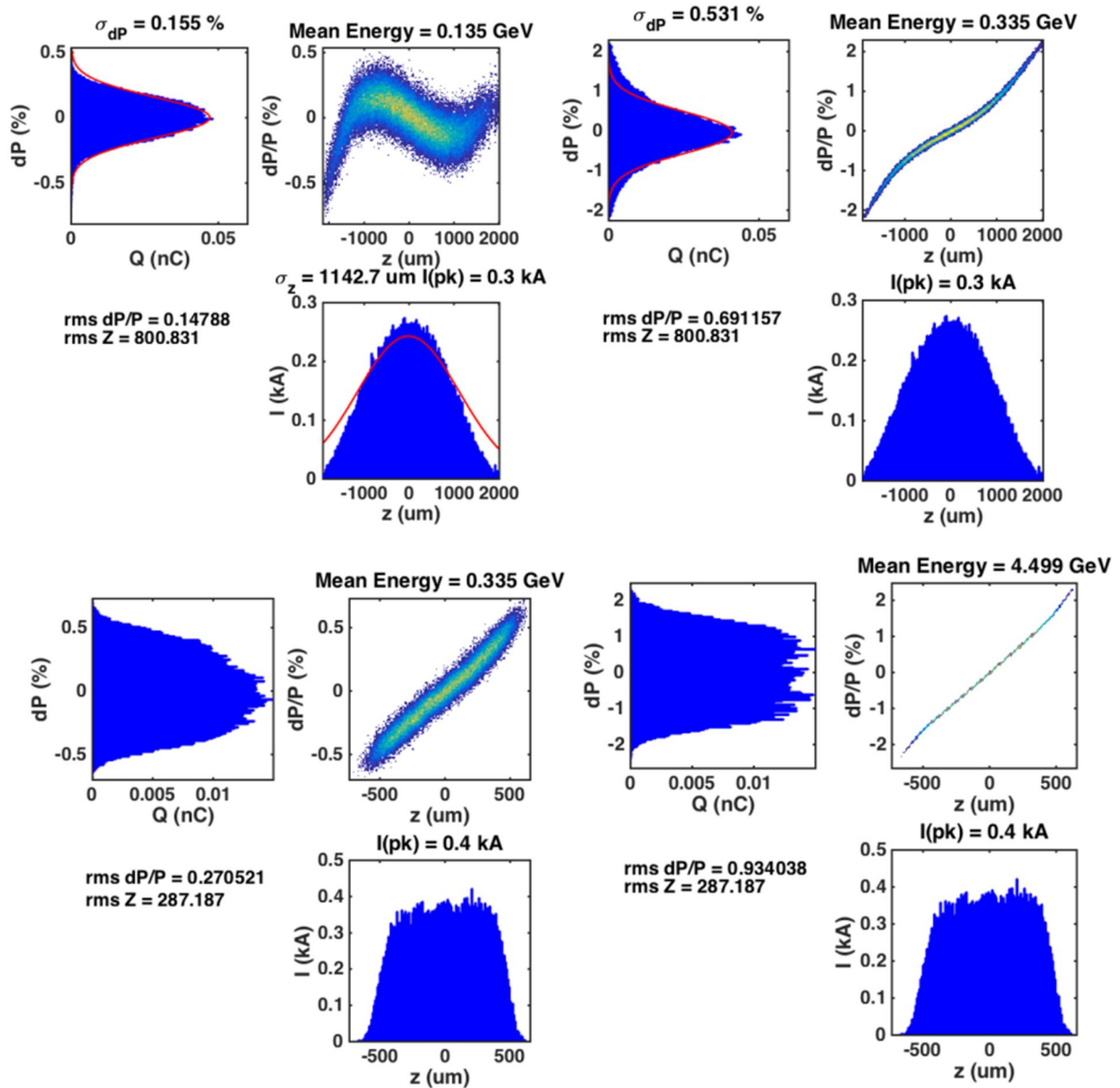
The  $R_{56}$  coefficient for simple 4-bend chicanes (BC1 and BC2) is related to the chicane strength through the following formula

$$R_{56} \approx -2\theta^2 \left( \Delta L + \frac{2}{3} L_B \right) , \quad (4)$$

where  $\theta (<< 1)$  is the bend angle of each dipole magnet,  $\Delta L$  is the drift distance between 1<sup>st</sup> and 2<sup>nd</sup> (and 3<sup>rd</sup> and 4<sup>th</sup>) dipoles, and  $L_B$  is the magnetic length of each magnet. The more complex arrangement of magnets in the sector 20 requires optics matching software, such as MAD8, to compute the  $R_{56}$  of that system, along with the other matching requirements for that sector.

Longitudinal phase-space from a 6D particle tracking simulation of the FACET-II compression process (using *Lucretia* [1]) is shown in Figure 6.6 for the electron bunch and Figure 6.7 for the positron bunch (see Section 56.16.6 for full 6D tracking results and further explanation of the tracking simulation performed). Longitudinal wakefields of the SLAC S-band accelerating structures are included in addition to a simulation of the ISR and CSR effects in the bends of the bunch compressors. In the shown plots,  $z$  shows the local projected time coordinate of the macro particles (negative  $z$  particles are at the head of the bunch),  $dP$  is the relative deviation of the particle energy away from the mean energy of the bunch.

Bunch lengths and energy spreads are presented for both Gaussian fits to the distributions where appropriate and rms quantities are also shown.



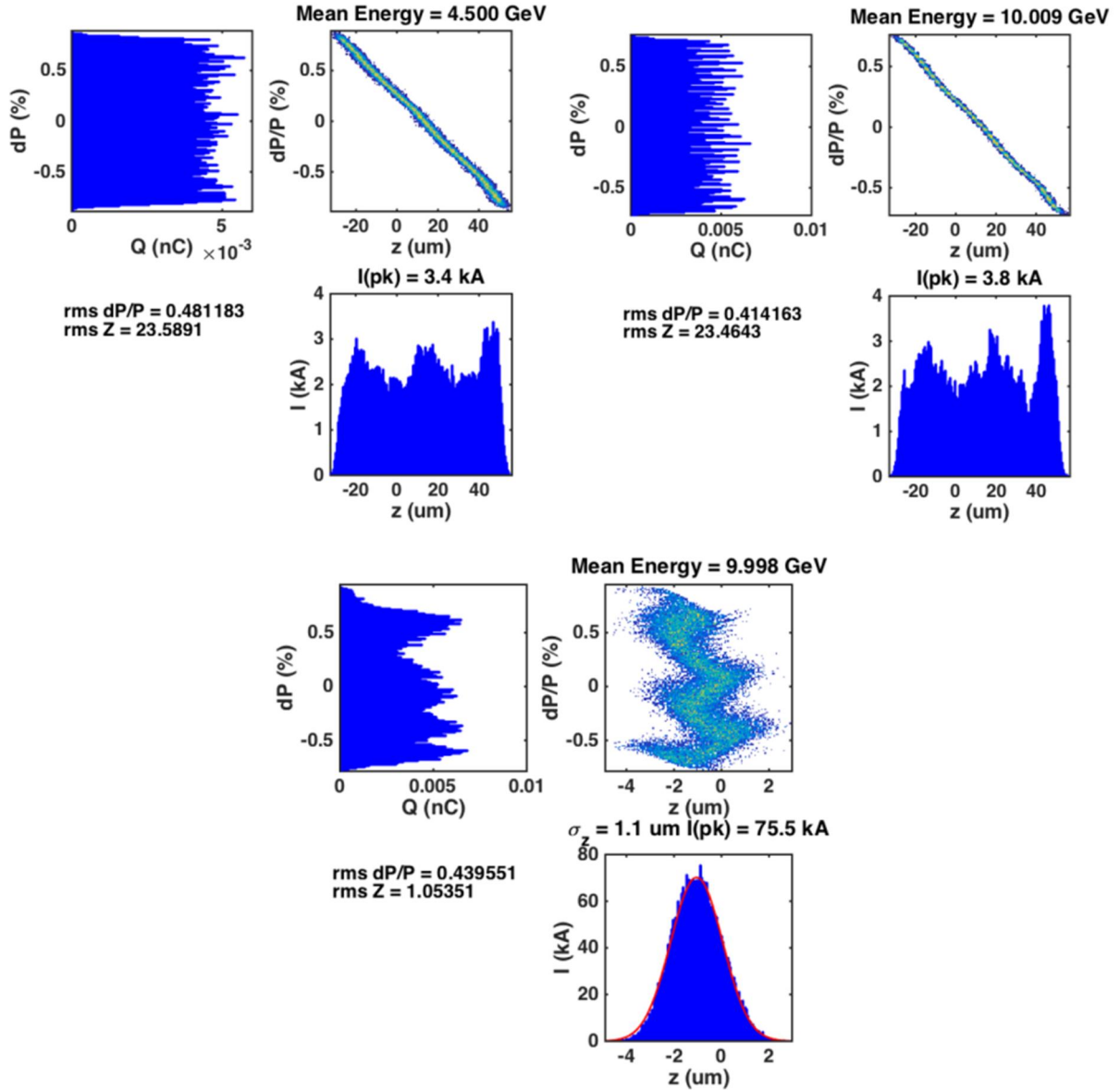
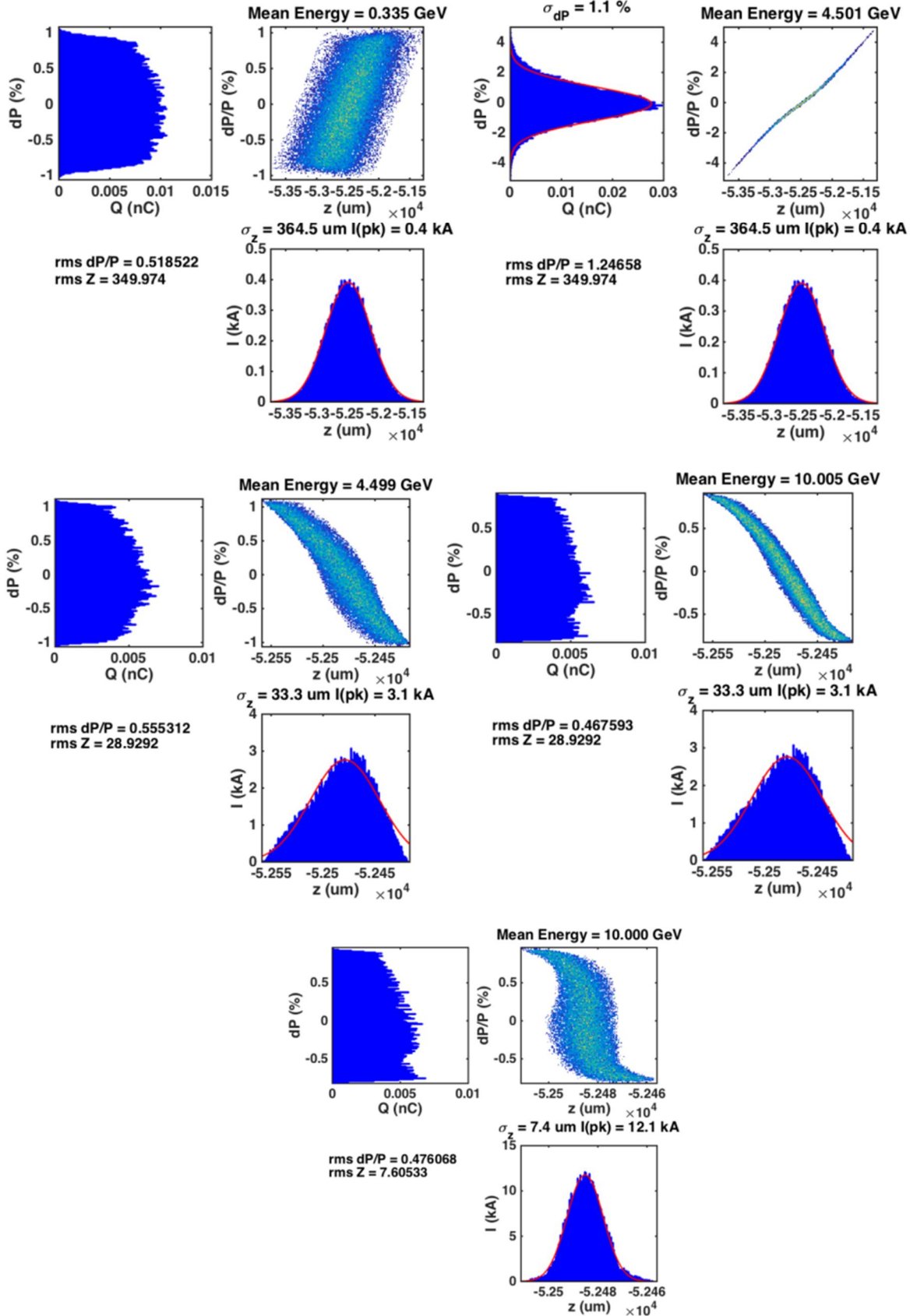


Figure 6.6. Tracking simulation of the electron bunch compression process. Sigma numbers displayed above plots indicate the widths of fitted Gaussians where appropriate, the rms quantities from the distributions are shown in the text in the lower-left quadrant of each plot. Charge is 2.0 nC up to BC1 where it is collimated to 1.2 nC and down to 0.7 nC in BC2.

Details pertaining to Figure 6.6: starting at the end of the L0b section at 135 MeV (top row, left), before the BC1 compression chicane at 335 MeV (top row, right), after the BC1 compression chicane at 335 MeV (2<sup>nd</sup> row, left), before BC2 at 4.5 GeV (2<sup>nd</sup> row, right), after BC2 at 4.5 GeV (3<sup>rd</sup> row, left), at the start of the BC3E chicane in Sector 20 at 10 GeV (3<sup>rd</sup> row, right) and at the IP experimental waist at 10 GeV (bottom row).



---

Figure 6.7: Tracking simulation of the positron bunch compression process. Sigma numbers displayed above plots indicate the widths of fitted Gaussians where appropriate, the rms quantities from the distributions are shown in the text in the lower-left quadrant of each plot. Charge is 2.0 nC up to BC0 where it is collimated to 1.2 nC and down to 0.6 nC in BC2

Details pertaining to Figure : starting at the end of the BC1 section where the positrons are injected into the main L2 linac section along with the electron bunch at 335 MeV (top row, left), before the BC2P compression chicane at 4.5 GeV (top row, right), after the BC2P compression chicane at 4.5 GeV (2<sup>nd</sup> row, left), before BC3P at 10 GeV (2<sup>nd</sup> row, right), at the IP experimental waist location in Sector 20 (3<sup>rd</sup> row).

### 6.2.1 Stability Requirements and System Sensitivities

The final level of bunch compression and transverse beam quality in 3 dimensions is quite sensitive to RF phase and amplitude variations in the different sections of the machine. The simulated final beam spot sizes for delivery to users in the Sector 20 IP region have been studied using particle tracking (with *Lucretia*) while varying many of the system parameters (see Section 6.7 for further details of the tracking simulations). Table 6.2 lists the various parameters (mostly phase and amplitude of each major linac section), plus the bunch charge, drive-laser timing, magnet vibration, and bunch compressor settings. The value listed for each jitter property is either from a tolerance specification elsewhere (e.g. laser timing fluctuation from LCLS requirements and operation experience) or directly measured (magnet vibrations) or motivated from past experience operating FACET. Table 6.2b shows the impact of all these jitter properties on the delivered beam to experiments at the Sector 20 IP waist. The Monte Carlo simulations performed using 100 random seeds for the jitter parameters yield results with non-Gaussian distributions. Hence the results shown in Table 6.2b do not well describe the particular distributions of errors. Figures 6.8 – 6.11 below depict the numerical distributions from the simulations, both for the total set of jitter properties and also with the parameters individually applied so the major contributions can be identified. These are statistical “box plots”: for each box, the red line indicates the median value for the distribution, the blue “box” shows the 25<sup>th</sup> and 75<sup>th</sup> percentiles and the dotted line “whiskers” show the range of the distribution. Where there are red crosses included, these are considered outliers (if they are larger than  $q3 + w(q3 - q1)$  or smaller than  $q1 - w(q3 - q1)$ , where  $q1$  and  $q3$  are the 25th and 75th percentiles, respectively, and  $w$  is 1.5 meaning that the outliers correspond to approximately  $\pm 2.7\sigma$  if the distribution were Gaussian).

The jitter properties mostly contributing to the observable errors are vertical laser spot jitter, laser timing fluctuations and L1 S-band phase and amplitude jitter for the electrons, and BC3P magnetic field jitter for the positrons. Note that the BC0 field jitter tolerance is tighter than those of the other chicanes due to the strength of BC0: with a jitter value of  $10^{-4}$ , both the positron and electron (through orbit jitter transference via transverse wakefields in L2 and L3) performance becomes intolerably bad. The actual BC0 field stability tolerance is somewhere between the quoted  $10^{-5}$  and  $10^{-4}$  and will be more precisely determined after the CD1 design phase. The sensitivity of the vertical electron beam size to the laser spot position jitter is largely due to the transverse wakefields in the L1X X-band linearizer structure. Although still within the required  $10 \mu\text{m}$ , if desired the sensitivity due to this property can be reduced by either choosing to use a C-band cavity for the linearizer function or by re-optimizing the optical functions in L1 to lower the beta functions in the L1X structure (e.g. by relocating the structure further upstream in the L1 section). Sensitivity due to L1 S-band RF phase and amplitude was expected and has been an area of concentrated effort for the operation of LCLS. Also during FACET-II operations, special attention needs to be applied to this RF system to achieve the required tolerances. With the exception

of the horizontal positron beam size, all other required IP parameters can be achieved with the listed jitter property tolerances (<10 $\mu$ m transverse and longitudinal spot sizes, >10kA peak currents). In the case of the positron horizontal spot size the particular sensitivity to the magnet field fluctuations in BC3P have been noted. Further study will be applied to this area in the post CD-1 design phase to identify the specific magnets which we are sensitive to and to specify targeted tolerances for these magnets to reduce the sensitivity in this region to acceptable levels.

Table 6.2. Jitter properties studied and estimated achievable values.

<b>Property</b>	<b>Value</b>
Source Charge Fluctuation	1% (e-) 2% (e+)
Source Position Fluctuation	0.05 sigma (e-) 0.2 sigma (e+)
Initial Electron Laser Timing Error	200 fs
L1X Phase Jitter	0.25 degX
L1 Phase Jitter	0.1 degS
L2/L3 Phase Jitter	0.25 degS
L0P Phase Jitter	0.1 degS
L1X Amplitude Jitter	0.25 %
L1 Amplitude Jitter	0.1 %
L2/L3/L0P Amplitude Jitter	0.25 %
BC0 Magnet Strength Jitter	1e-5 dB/B
BC1/BC2/BC3 Magnet Strength Jitter	1e-4 dB/B
L1/L2/L3/S20/PEC Magnet Vibration (x/y)	1.5/0.5 $\mu$ m

Table 6.2b: Simulated range of delivered beam parameters at Sector 20 IP waist with all error parameters specified in Table 6.2 applied. Each entry shows mean and rms spread of results from a 100 seed Monte Carlo simulation. Note that the actual distributions are not actually Gaussian, see presented data in Figures 6.8-6.11 for error distributions and breakdown of errors into independent sources.

<b>IP Parameter</b>	<b>Electron Bunch</b>		<b>Positron Bunch</b>	
	<i>Design</i>	<i>With Errors</i>	<i>Design</i>	<i>With Errors</i>
$\sigma_x$ ( $\mu$ m)	8.5	7.9 +/- 3.1	9.0	13.7 +/- 5.4
$\sigma_y$ ( $\mu$ m)	6.9	7.6 +/- 1.9	6.0	7.4 +/- 0.3
$\sigma_z$ ( $\mu$ m)	1.1	3.5 +/- 2.2	7.4	7.4 +/- 0.9
$I_{pk}$ (kA)	76	37 +/- 20	12	11.7 +/- 1.8

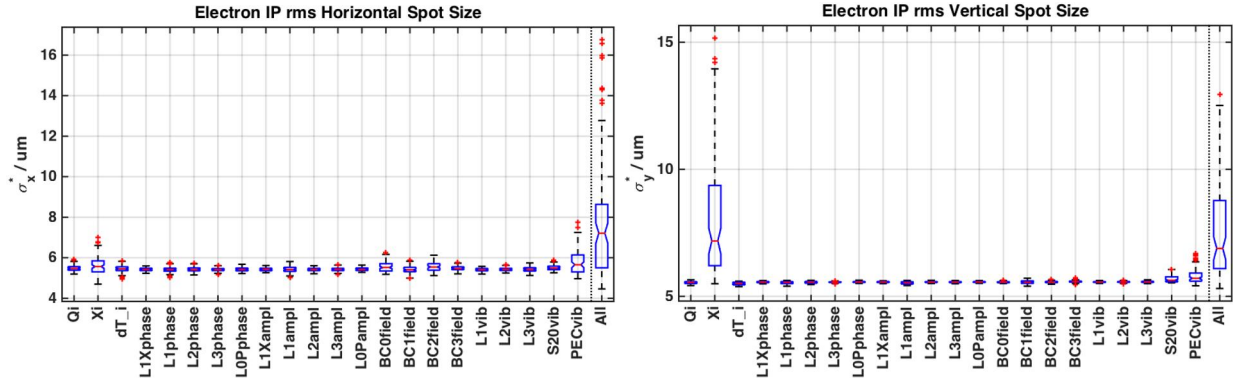


Figure 6.8: Box plots showing distributions for jitter simulation studies for properties shown in Table 6.2. Effect on electron horizontal and vertical spot sizes at the IP waist in Sector 20 are shown.

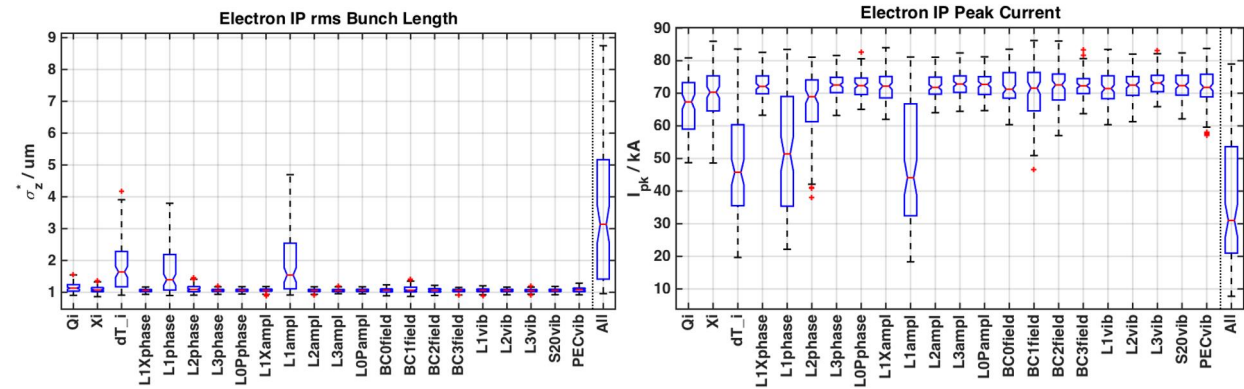


Figure 6.9: Box plots showing distributions for jitter simulation studies for properties shown in Table 6.2. Effect on electron bunch length and peak current at the IP waist in Sector 20 are shown.

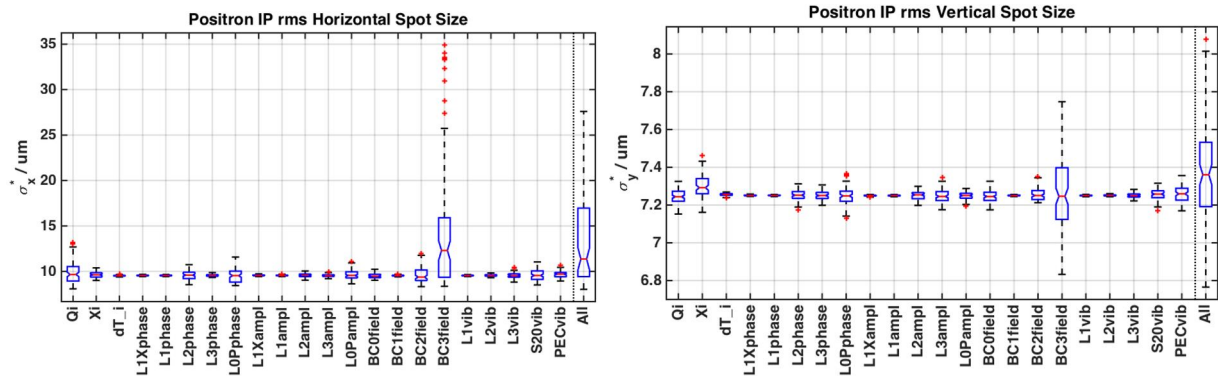


Figure 6.10: Box plots showing distributions for jitter simulation studies for properties shown in Table 6.2. Effect on positron horizontal and vertical spot size at the IP waist in Sector 20 are shown.

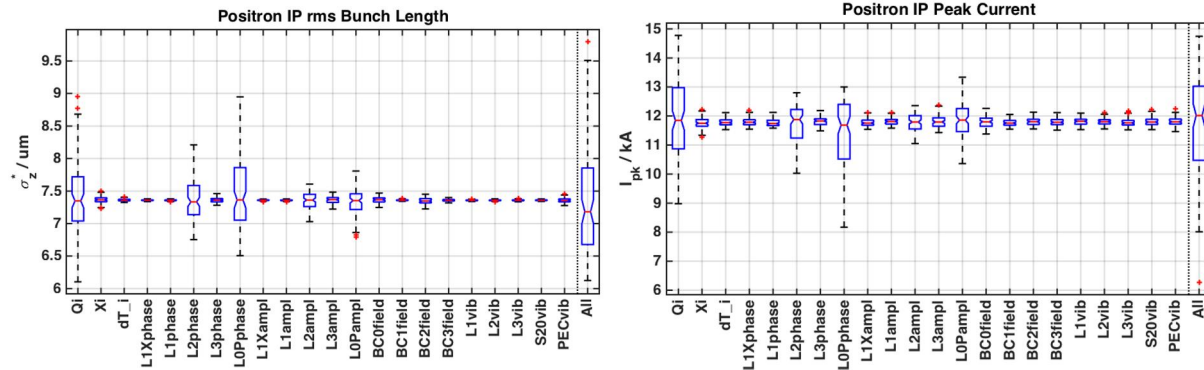


Figure 6.11: Box plots showing distributions for jitter simulation studies for properties shown in Table 6.2. Effect on positron bunch length and peak current at the IP waist in Sector 20 are shown.

## 6.3 The First Electron Bunch Compressor (BC1)

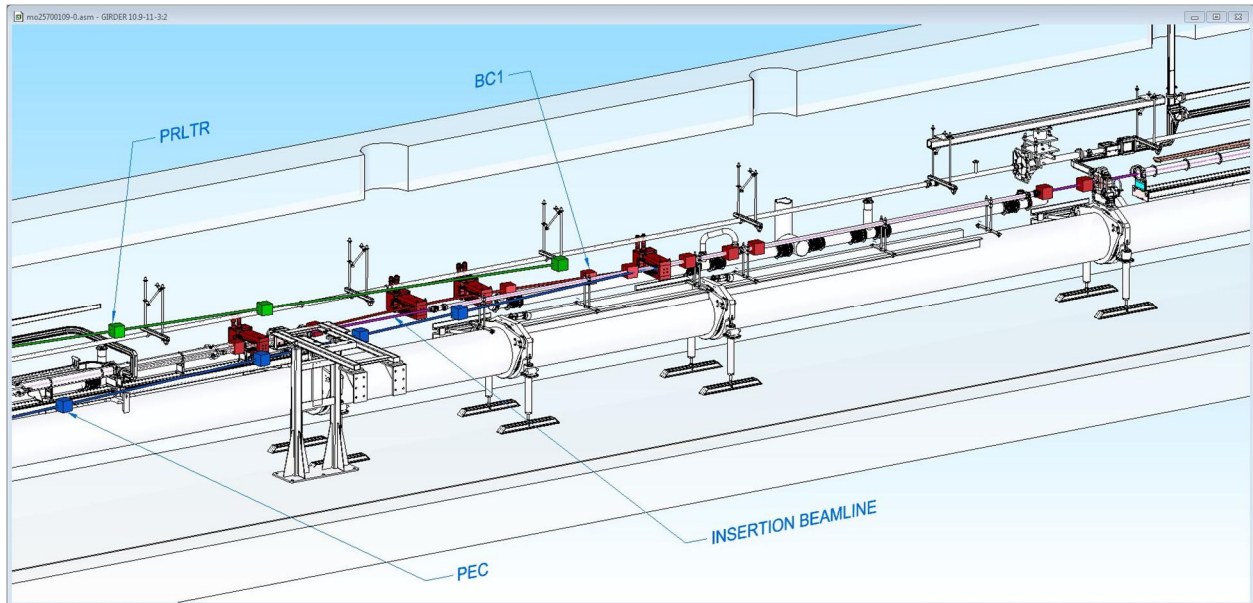


Figure 6.12: Sector 11 region of linac showing BC1 bunch compressor magnet locations.

### 6.3.1 Overview

The BC1 compressor is a symmetric chicane with 4 rectangular bend magnets, dispersion tweaking quadrupole magnets and a skew-quadrupole magnet in the chicane dispersive region. It serves as the first-stage bunch length compression for the electron beam and as a location to merge in the positron beam. The BC1 compressor forms part of the integrated compression system as one of a total of 6 compression systems employed for the electron and positron beam transport systems. Six quadrupole magnets before and after the chicane are included in this system for matching purposes from the L1 linac section into L2. The chicane is designed to provide an R56 of -40 mm. Information regarding the positron injection system is provided in Chapter 7. The positron beam is injected into the main linac in the shared final bend magnet of this chicane as can be seen in Figure 6.12 and 6.13. An adjustable collimator (rectangular with independent control of each of two jaws), located in the central region of the chicane, provides for the capability to selectively remove non-linear energy tails which improves the final peak current performance. A wire scanner and screen also placed in the central chicane region to provide energy spread diagnostics. Also, a BPM in this location provides information for the energy feedback system.

### 6.3.2 Beam Parameters for BC1

These are the nominal design beam parameters of the BC1 subsystem for operations with 2nC source charge for electron and positron operations.

Table 6.3: Beam parameters for the BC1 subsystem for the electron beam between the end of the L1 linac section to the beginning of the L2 linac section as depicted in Figure 6.12. See Section 6.7 for details of the beam tracking simulation.

Parameter	Symbol	Value	Unit
Beam Energy	$E$	335	MeV
Initial Proj. Transverse Emittance	$\gamma\epsilon_x / \gamma\epsilon_y$	3.5 / 3.2	$\mu\text{m}\cdot\text{rad}$
Final Proj. Transverse Emittance	$\gamma\epsilon_x / \gamma\epsilon_y$	3.2 / 3.2	$\mu\text{m}\cdot\text{rad}$
Initial Twiss	$\beta_x / \alpha_x$	17.527 / 2.231	m
	$\beta_y / \alpha_y$	11.734 / 0.907	
Final Twiss	$\beta_x / \alpha_x$	2.93 / -0.014	m
	$\beta_y / \alpha_y$	2.93 / -0.050	
Initial Bunch Length / peak Current	$\sigma_z \text{ rms} / I_{pk}$	801 / 0.3	$\mu\text{m} / \text{kA}$
Final Bunch Length / peak Current	$\sigma_z \text{ rms} / I_{pk}$	287 / 0.4	$\mu\text{m} / \text{kA}$
Initial Energy Spread	$\sigma_E/E \text{ rms}$	0.69	%
Final Energy Spread	$\sigma_E/E \text{ rms}$	0.27	%
Initial Bunch Charge	$Q$	2	nC
Final Bunch Charge	$Q$	1.2	nC
Collimator half-aperture	$A$	4.5	mm

### 6.3.3 Layout and Optics Design

The optics of BC1 is designed to match the outgoing electron and positron parameters from the L1 linac section into the L2 linac section. The final bend of the bunch compressor also serves as the injection point of the positron beam. The beta functions are matched to a low value in both planes in the final bend to minimize CSR effects for both the electron and positron bunches.

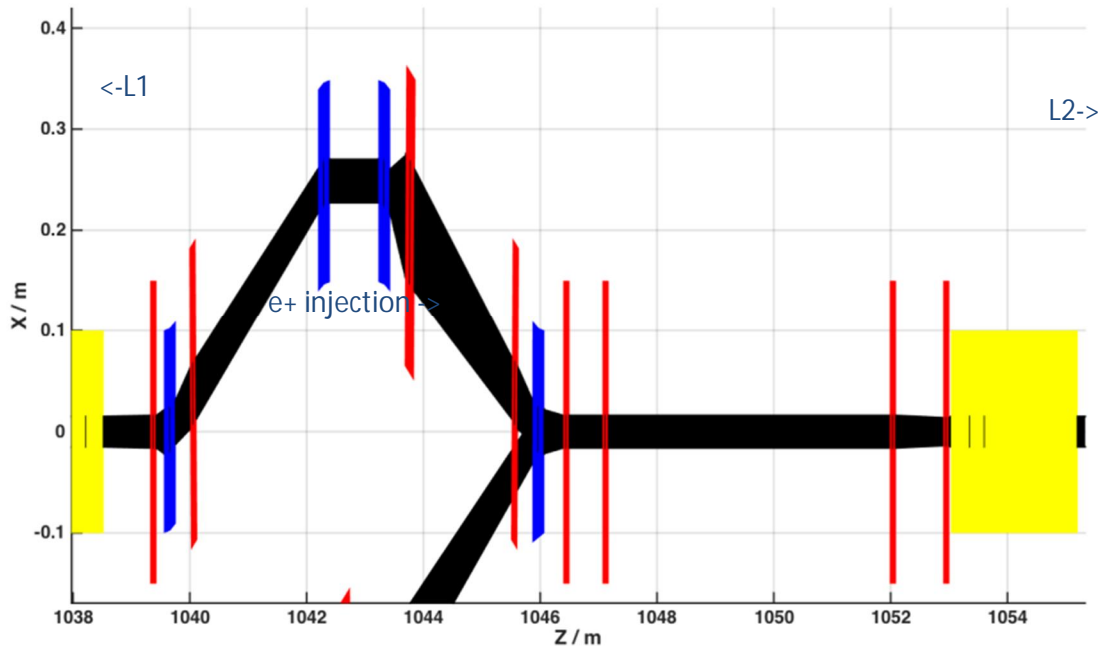


Figure 6.13: Plan layout view of BC1 system and transport optics. Yellow indicates RF, blue dipoles, red quadrupoles (with skew quad in chicane). Coordinate system is relative to SLC linac (x/y) and SLC z-reference.

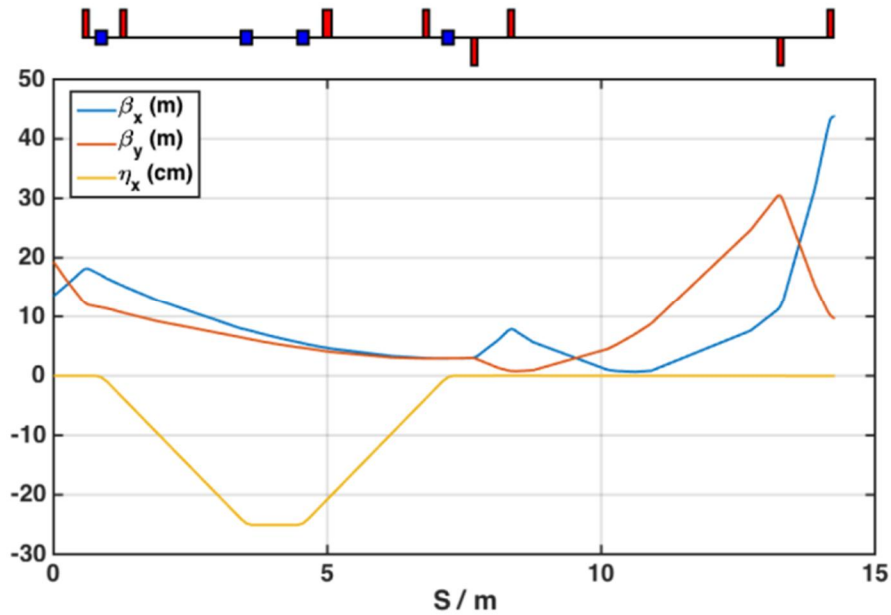


Figure 6.14: Twiss parameters across the BC1 compression system for the electron beam.

### 6.3.4 Electron Beam Dynamics

See Section 6.7 for further explanations of the beam tracking simulation and Figure 6.6 for the longitudinal phase space calculations across this subsystem. Figure 6.15 below shows 10X the tracked beam size through the system overlaid on top of the apertures to demonstrate adequate beam clearance.

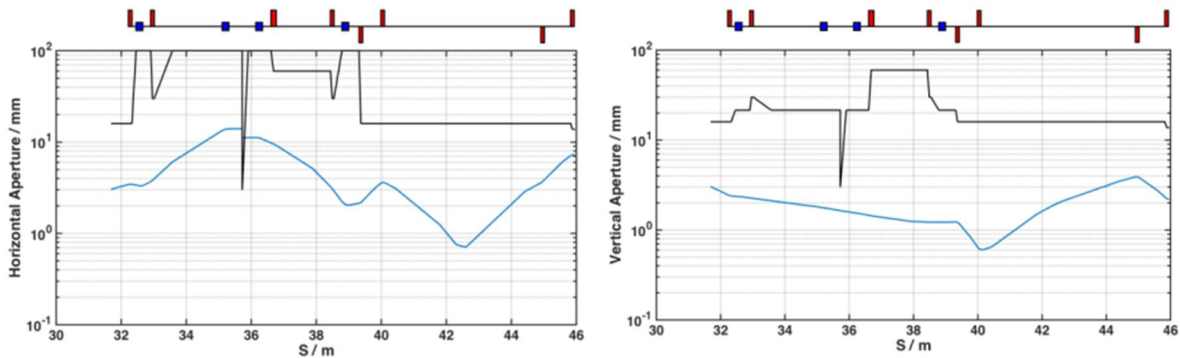


Figure 6.15: Required horizontal (left) and vertical (right) magnet apertures, over the full BC1 section for electrons, from tracked rms beam sizes. The blue curves are defined as 10X tracked rms beam size at element locations. Black curve shows design magnet and collimator apertures.

### 6.3.5 Magnets

The BC1 section consists of 8 quadrupole magnets of 4 engineering types and 4 dipole magnets of 2 types (the final bend is shared with the positron ring-to-linac section). The bend magnets are standard chicane-style bends (rectangular bend magnets, with no yaw angle with respect to the reference trajectory).

### 6.3.5.1 Quadrupoles

Table 6.4: Quadrupole magnet parameters for BC1.

Deck Name	Engineering Type	Effective Length / m	Design Int. Strength / T	Max. Int. Strength /  T	Design Pole Tip Field /  T	Max Pole Tip Field /  T	Aperture (radius) / m	Beam Energy / MeV
QM11B	A	0.108	0.410	0.5	0.061	0.074	0.016	335.0
CQ11B	B	0.108	0.000	0.5	0.000	0.139	0.030	335.0
SQ13B	C (Skew)	0.16	0.000	0.5	0.000	0.188	0.060	335.0
CQ12B	B	0.108	0.000	0.5	0.000	0.139	0.030	335.0
QM12B	B	0.108	-0.983	1.5	0.146	0.222	0.016	335.0
QM13B	B	0.108	1.144	1.5	0.170	0.222	0.016	335.0
QM14B	B	0.108	-0.764	1.5	0.113	0.222	0.016	335.0
Q11401	D	0.1068	0.668	0.75	0.086	0.097	0.014	335.0

### 6.3.5.2 Dipoles

Table 6.5: Dipole magnet parameters for BC1 (at 335 MeV).

Deck Name	Engineering Type	Effective Length / m	Bend Angle / radians	Bend Plane	Design Int. Strength / T.m	Max. Int. Strength /  T.m	Design Pole Tip Field / T	Max Pole Tip Field /  T	Aperture (radius) / m
BX11B	A	0.2035	-0.094	X	-0.104	0.12	0.5134	0.590	0.0215
BX12B	A	0.2035	0.094	X	0.104	0.12	0.5141	0.590	0.0215
BX13B	A	0.2035	0.094	X	0.104	0.12	0.5150	0.590	0.0215
BX14B	B	0.2035	-0.094	X	-0.104	0.12	0.5158	0.590	0.0215

## 6.4 BC2 - Bunch Compression System for e<sup>-</sup> and e<sup>+</sup> in LI14

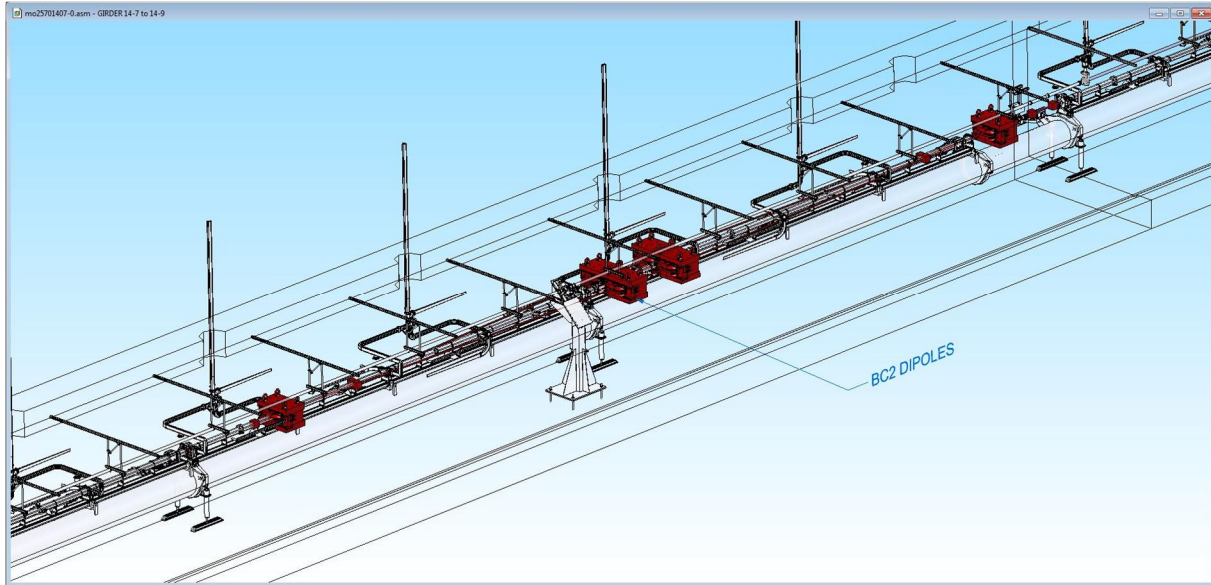


Figure 6.16: Sector 14 region of linac showing magnet locations for BC2E and BC2P chicanes.

### 6.4.1 Overview

The BC2E/P compressor is a symmetric chicane comprising 6 rectangular bend magnets (4 for each e<sup>-</sup>/e<sup>+</sup> beamline), for the purpose of bunch length compression of the electron and positron beams. The first and last bends are common to e<sup>-</sup> and e<sup>+</sup> beams, with a symmetric arrangement for the central 2 bends, providing equal  $R_{56}$  terms for both beams with equal energy. A pair of quads before and after the chicane are included in this system for matching purposes. Each chicane (for e<sup>-</sup> and e<sup>+</sup>) contains an adjustable collimator to cut the high-energy tail portion of the compressed beam for beam quality control and energy matching (linac wake loading) purposes. The internal edge angles of the first and last bend magnets and CQ quadrupoles are used as free parameters during the matching process to form an x $\leftrightarrow$ y betatron exchange transfer matrix to match both electron and positron optics simultaneously. Without this adjustment, a beta mismatch of order 10% exists between e<sup>-</sup> and e<sup>+</sup> beams due to the vertical focusing in the bend magnets. A wire scanner and screen are also placed near the center of the chicane to provide beam energy spread diagnostics. Also a BPM is placed in this region to provide information for the beam energy feedback system.

### 6.4.2 Beam Parameters in BC2E and BC2P

The optics are designed to match the outgoing electron and positron parameters from the L2 linac section into the L3 linac section. This is performed using a pair of quadrupole magnets before and after the chicane in conjunction to the first and last few quadrupoles in L2 & L3. The magnitude of the beta functions at the exit of the final BX24 bend magnet are kept to a minimum to suppress CSR effects. Also the internal edge angles of BX21 and BX24 are set along with small tweaks of CQ quadrupoles to produce an optimal x $\leftrightarrow$ y betatron transform matrix ( $M_x(e^-) = M_y(e^+)$ ;  $M_y(e^-) = M_x(e^+)$ ) between electron and positron arms. Although not perfect, this is achievable with a BMAG mismatch parameter <1% for both particle types which is well within normal operational working accuracy for the optical matching. The dispersion must also be completely closed at the exit of the system.

Table 6.6: Beam parameters across the BC2E and BC2P subsystems for  $e^-$  and  $e^+$  bunches. Bunch length from fitted asymmetric Gaussian to tracked z-distributions. See section 6.7 for details of beam tracking simulation.

Parameter	Symbol	Value	Unit
Beam Energy	$E$ ( $e^+$ / $e^-$ )	4.5 / 4.5	GeV
Initial Transverse Emittance	$\nu\epsilon_x / \nu\epsilon_y$ ( $e^+$ )	7.0 / 5.8	$\mu\text{m}\cdot\text{rad}$
	$\nu\epsilon_x / \nu\epsilon_y$ ( $e^-$ )	3.6 / 3.2	
Final Transverse Emittance	$\nu\epsilon_x / \nu\epsilon_y$ ( $e^+$ )	6.0 / 5.8	$\mu\text{m}\cdot\text{rad}$
	$\nu\epsilon_x / \nu\epsilon_y$ ( $e^-$ )	3.3 / 3.2	
Initial Twiss ( $e^+$ )	$\beta_x / \alpha_x$	61.303 / 2.229	m
	$\beta_y / \alpha_y$	47.575 / 2.088	
Final Twiss ( $e^+$ )	$\beta_x / \alpha_x$	9.388 / -0.119	m
	$\beta_y / \alpha_y$	10.527 / -0.539	
Initial rms Bunch Length / peak Current	$\sigma_z / I_{pk}$ ( $e^+$ )	350 / 0.4	$\mu\text{m} / \text{kA}$
	$\sigma_z / I_{pk}$ ( $e^-$ )	287 / 0.4	
Final rms Bunch Length / peak Current	$\sigma_z / I_{pk}$ ( $e^+$ )	28.9 / 3.1	$\mu\text{m} / \text{kA}$
	$\sigma_z / I_{pk}$ ( $e^-$ )	23.6 / 3.4	
Initial rms Energy Spread	$\sigma_E/E$ ( $e^+$ )	1.1	%
	$\sigma_E/E$ ( $e^-$ )	1.0	
Final rms Energy Spread	$\sigma_E/E$ ( $e^+$ )	0.5	%
	$\sigma_E/E$ ( $e^-$ )	0.9	
Initial Bunch Charge	$Q$ ( $e^+$ )	1.2	nC
	$Q$ ( $e^-$ )	1.2	
Final Bunch Charge	$Q$ ( $e^+$ )	0.6	nC
	$Q$ ( $e^-$ )	0.7	
Collimator half-aperture	$A$ ( $e^+$ )	4.5	mm
	$A$ ( $e^-$ )	3.6	

### 6.4.3 Layout and Optics Design in BC2

BC2E and BC2P are symmetric bend chicanes with equal R56 for the electron and positron portions of the chicanes. The bend angles are 41.92 mrad and each of BC2E and BC2P provides a compression  $R_{56} = -36\text{mm}$ . For higher charge operation where CSR effects become even more pronounced in BC2 a smaller bend angle may be required for optimal emittance preservation, it is assumed that under these circumstances the chicane geometry will have to be changed, but this is not expected to be a routine procedure. Figure 6.16 and Figure 6.17 below show a schematic layout of the section and the details of the edge angle requirements for the outer bend magnets. In addition to the collimator in the center of the chicanes, it is also required to have a screen for energy spread measurements and a BPM for input to the beam energy feedback system. Figure 6.19 shows the twiss parameters through each of BC2E and BC2P.

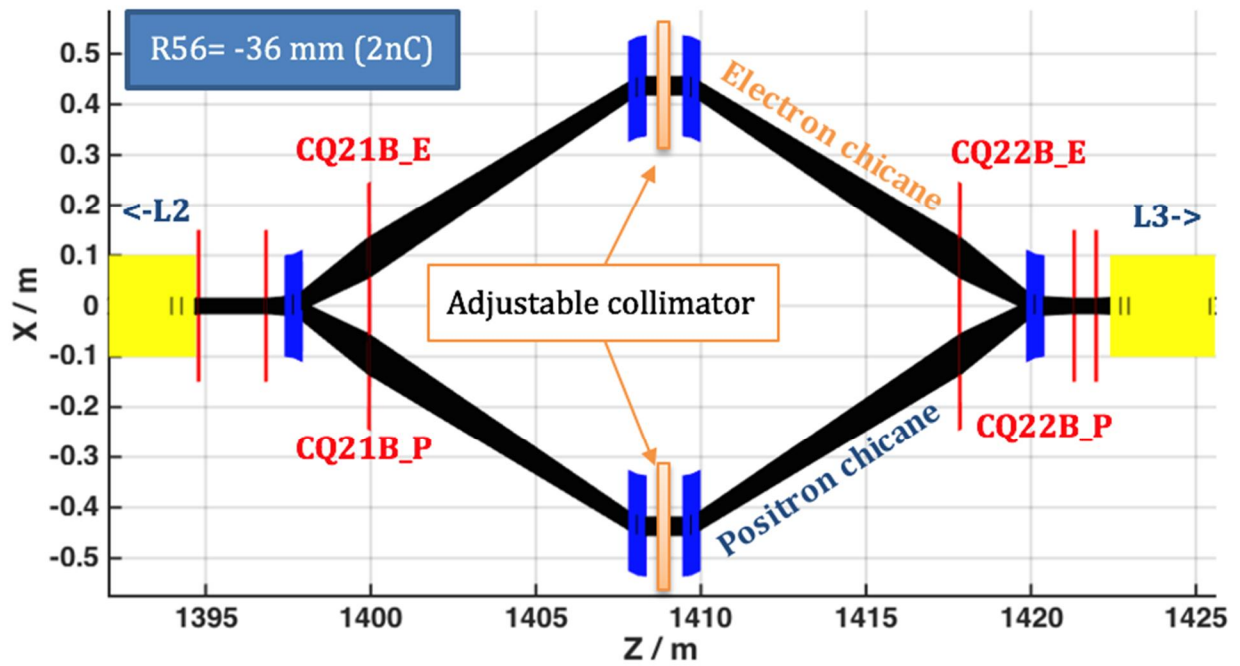


Figure 6.17: Plan layout view of BC2E and BC2P chicanes. Yellow indicates RF, blue dipoles, red quadrupoles. Co-ordinate system is relative to SLC linac (x/y) and SLC z-reference.

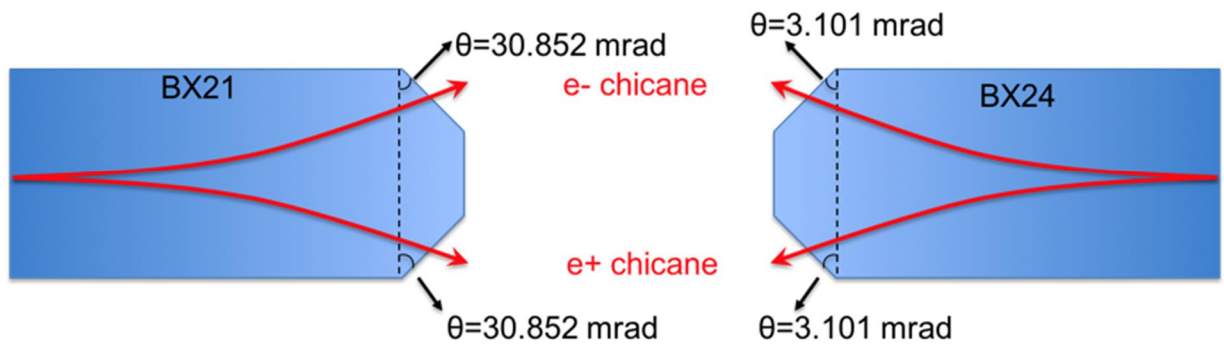


Figure 6.18: Design edge angles for first and last chicane bend magnets.

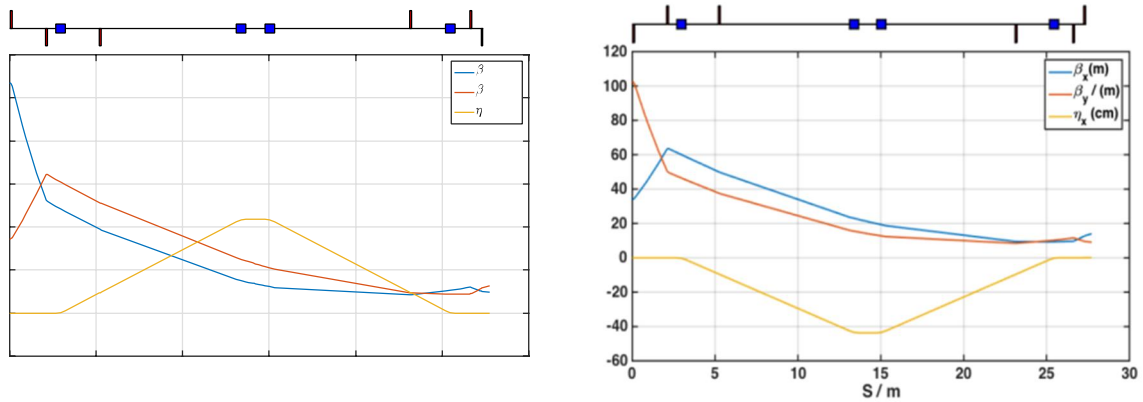


Figure 6.19: Twiss parameters across BC2 system for the positron beam (left) and the electron beam (right).

#### 6.4.4 Beam Dynamics in BC2 for e+ and e-

See Section 6.7 for explanation of beam tracking simulation and Figure 6.6 and 6.7 for the longitudinal phase space calculations for e+ and e- beams across this subsystem. Figure 6.20 below shows 10X the tracked beam size through the system overlaid on top of the apertures to demonstrate adequate beam clearance.

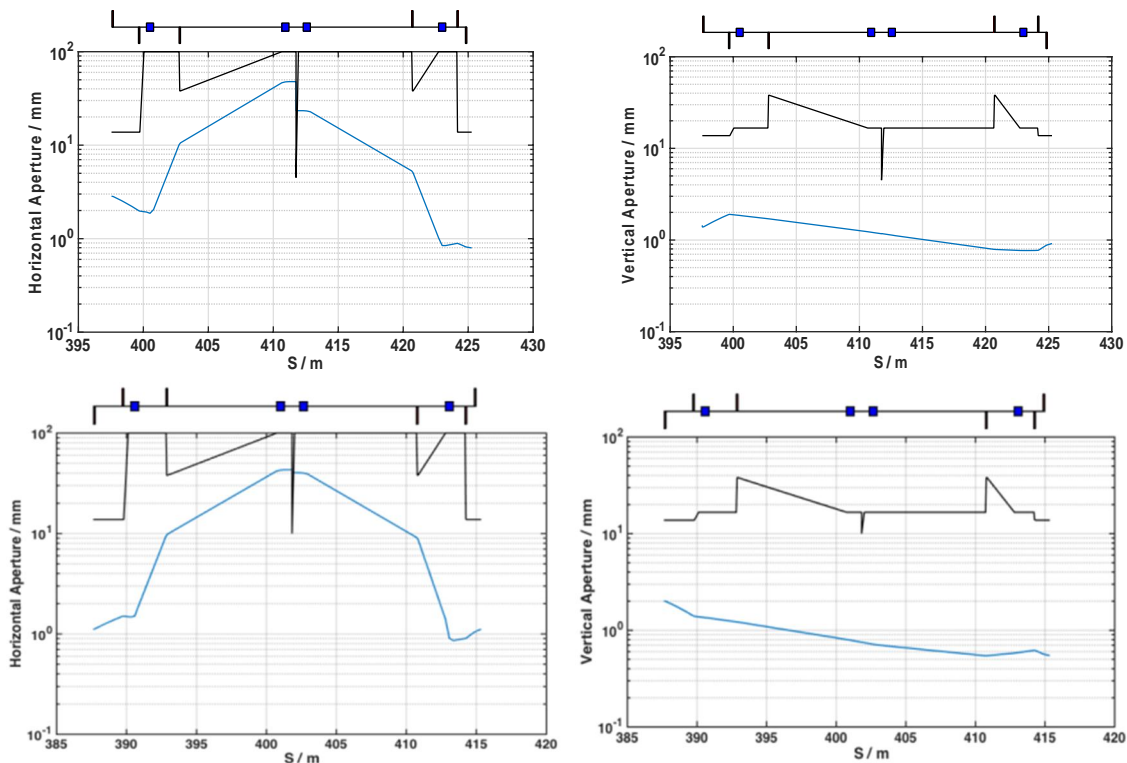


Figure 6.20: Required horizontal (left) and vertical (right) magnet apertures in BC2 from tracked rms beam sizes (10X tracked beam sizes shown by blue curve). The black curves show design magnet apertures. Top row is for the positron beam design; bottom row is for the electron beam.

## 6.4.5 BC2 Magnets

The BC2 compressor section consists of 8 quadrupole magnets of 2 engineering types and 6 dipole magnets of 3 types. The outer bends are shared between electron and positron beams and have specially designed interior edge angles, the central bends are normal chicane-style rectangular bends.

### 6.4.5.1 Quadrupoles

Table 6.7: Quadrupole magnets for BC2, required new and existing.

Deck Name	Engineering Type	Effective Length / m	Design Int. Strength / T	Max. Int. Strength /  T	Design Pole Tip Field /  T	Max Pole Tip Field /  T	Aperture (radius) / m
Q14701	A	0.1068	2.661	5.500	0.343	0.710	0.014
QM21B	A	0.1068	-2.533	5.500	0.327	0.710	0.014
CQ21B_E	B	0.108	0.000	3.000	0.000	1.056	0.038
CQ22B_E	B	0.108	0.000	3.000	0.000	1.056	0.038
QM22B	A	0.1068	2.970	5.500	0.383	0.710	0.014
Q14901	A	0.1068	-1.343	5.500	0.173	0.710	0.014
CQ21B_P	B	0.108	0.000	3.000	0.000	1.056	0.038
CQ22B_P	B	0.108	0.000	3.000	0.000	1.056	0.038

### 6.4.5.2 Dipoles

Table 6.8: Dipole magnet parameters in BC2. BX21B and BX24B are shared between e- and e+ beams. Edge angles follow MAD8 convention and define edge angle with respect to trajectory of beam.

Deck Name	Engineering Type	Effective Length / m	Bend Angle /  mrad	Design Int. Strength /  T.m	Max. Int. Strength /  T.m	Design Pole Tip Field / T	Max Pole Tip Field /  T	Aper. radius / m	E1 Edge Ang. / mrad	E2 Edge Angle / mrad
BX21B	A	0.54913	41.92	0.62932	0.6500	1.1460	1.1837	0.0167	0	11.50909
BX22B_E	B	0.54913	41.92	0.62932	0.6500	1.1460	1.1837	0.0167	41.92	0
BX23B_E	B	0.54913	41.92	0.62928	0.6500	1.1460	1.1837	0.0167	0	41.92
BX24B	C	0.54913	41.92	0.62922	0.6500	1.1459	1.1837	0.0167	20.96	0
BX22B_P	B	0.54913	41.92	0.62932	0.6500	1.1460	1.1837	0.0167	41.92	0
BX23B_P	B	0.54913	41.92	0.62928	0.6500	1.1460	1.1837	0.0167	0	41.92

---

## 6.5 Sector 20 Chicanes (BC3E and BC3P) and Final Focus Systems

### 6.5.1 Overview

Sector 20 contains the final bunch compression stages for both the electron and positron beams, the existing W-chicane system for the electrons (BC3E) and the positron sailboat chicane (BC3P) are both described in Chapter 9. The beams are separated at the first B1 bend magnet at the start of sector 20 before each travels through their own compression chicanes. Both Sector 20 chicanes have a positive  $R_{56}$  between 0-10mm (design=5mm), providing the final stage of bunch compression while also providing other measurement and corrective functions before delivery of each beam to the experimental IP area. The layout of BC3E is unchanged from the FACET experiment and will be operated in a similar way.

## 6.6 Radio Frequency (RF) Systems

The RF system for FACET-II has several performance requirements as follows:

- The high-power RF system must make use of the existing linac RF stations in an efficient and convenient configuration.
- The RF system needs to provide adjustable phase and amplitude for each main linac section (*i.e.*, Gun, L0a, L0b, TCAV0, L1, LX, TCAV1, L2, TCAV3, L3, XTCAV\_E, XTCAV\_P).
- The phase and amplitude stability must meet the requirements described in this chapter.
- Several transverse RF deflectors are included in order to measure the electron bunch length at various locations.

LCLS-I has been successfully delivering beam to users since October 2009 with the stability and availability of the RF systems meeting all requirements. With this clear success, the RF systems for FACET-II will be modeled following the design and experience of LCLS-I.

The installed complement of S-band (2.856 GHz) klystrons in the SLAC linac, from Sector 10 through Sector 19, is capable of accelerating the FACET-II beam to at least the required energy of 10.0 GeV (for both e- and e+). In addition to setting the electron beam energy, precise control of RF phase and amplitude is required to manipulate the longitudinal phase space of the beam to produce the desired short bunch in Sector 20. Specifically, the linac RF is used to introduce an energy-time correlation along the bunch for compression, and to compensate for longitudinal wakefields generated by the accelerating structures. This process is supplemented with an additional, higher-harmonic X-band (11.424 GHz) accelerating structure installed just upstream of the first bunch compressor. The success of the bunch compression and wakefield compensation schemes require very tight tolerances for phase and amplitude control of the linac. Methods used in LCLS-I to achieve this will be duplicated for FACET-II.

### 6.5.1 The RF System Stability Tolerances

The RF system stability tolerances specify the pulse-to-pulse rms variations that are acceptable in linac phase and amplitude, while still maintaining the desired peak current and energy at the FACET IP. These pulse-to-pulse random variations cannot be corrected by feedback and therefore place upper limits on the phase and amplitude noise level of individual components, such as klystrons. Longer timescale drifts, ranging from several seconds to several days, will be corrected by feedback systems. Beam-based diagnostics of relative bunch length and relative energy will be used to provide feedback for the RF phase and amplitude to control variations slower than ~0.5 Hz.

Although beam-based feedback will be the final mechanism to stabilize RF phase and amplitude, there are several reasons for keeping the low-level RF distribution system as stable as possible. Some development work on feedback tuning algorithms is to be expected before subsystems can be cascaded together. Any extension in the duration over which the beam remains stable and within tolerance makes the task of tuning easier, both during the period of commissioning the accelerator and subsequent operation. The detailed RF stability tolerances are listed in Table 6.2.

### 6.5.2 Radio Frequency (RF) Distribution in the SLAC Main Linac

The RF master signal will be generated by a stress compensated cut quartz crystal located at Sector 10, which is 50m up-stream of the FACET-II injector. The RF from the crystal oscillator is multiplied up to 476 MHz and distributed along the final 2/3 of the 3-km linac on an air dielectric rigid coax referred to as the Main Drive Line (MDL). The timing system fiducial, which is locked to the 8.5-MHz damping ring revolution frequency, and the 360-Hz harmonic of the power lines is also distributed down the MDL. A coupler will be added in Sector 11 to pick off some of the 476-MHz and generate the RF frequencies required for FACET-II.

The SLAC linac is divided into 30 sectors, of which FACET-II will utilize sectors 10 through 19. The RF distribution for two adjacent, nominal sectors is shown in Figure 6.21, showing how the RF power is derived for each sector and distributed to each of the eight klystrons (typical) in the sector.

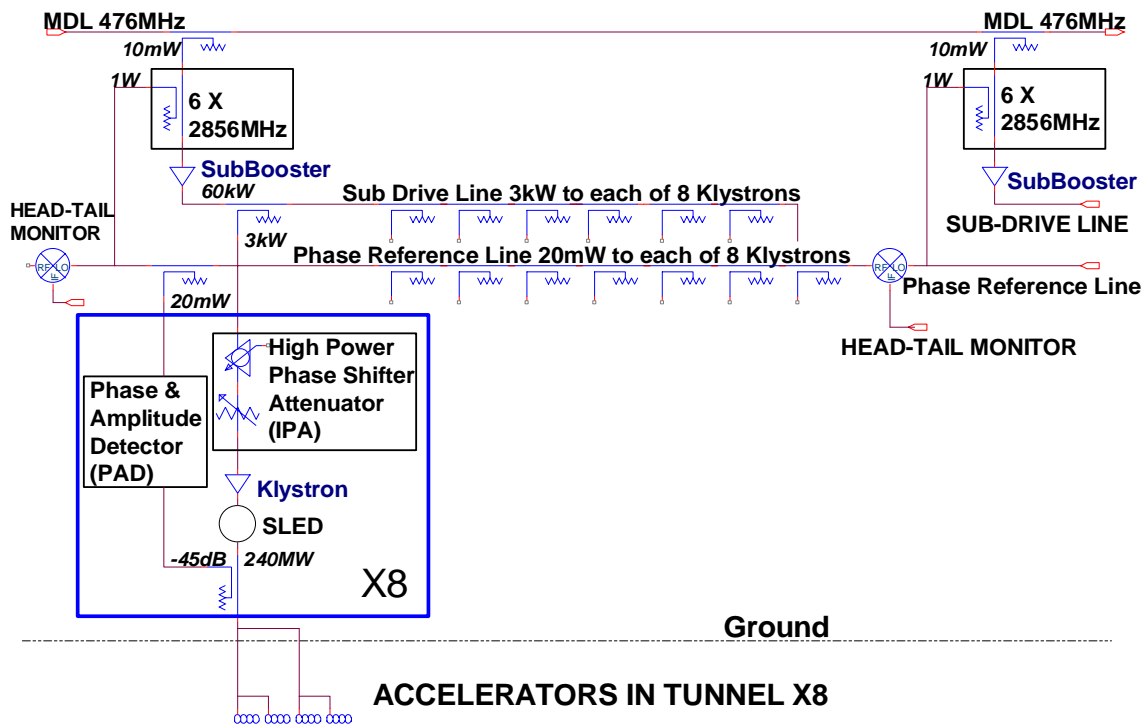


Figure 6.21. Schematic of two adjacent, nominal linac sectors showing distribution of RF power to the 8 klystrons per sector.

At each sector boundary a  $\times 6$ -multiplier is coupled to the MDL and provides 2856-MHz power for the sector phase reference line and the sub-booster klystron. The sub-booster klystron produces 60 kW of pulsed RF power to drive the Sub-Drive Line (SDL). The SDL and the Phase Reference Line (PRL) run the length of one sector (101.6 m) and are temperature stabilized over most of their length. The SDL

provides 3 kW of RF power to each klystron and the PRL provides 20 mW of RF power to the Phase and Amplitude Detector (PAD).

After the injector, when the beam enters the linac it passes through an S-band (2.856 GHz) accelerator and then an X-band (11.424 GHz) accelerator. The RF stability and phase relationship between these sections is critical to stable operation of FACET-II. Since these stations are centrally located, as with their counterparts in LCLS-I, a temperature stabilized enclosure will be built in the linac gallery at the end of Sector 10 to route temperature sensitive RF cables from the tunnel which measure phase and amplitude of the RF devices. This enclosure is referred to as the "RF Hut". The routing of sensitive measurement cables and the area layout is shown in Figure 6.22.

RF cables will be run in the tunnel to Sector 14, where an RF phasing cavity, a second transverse deflector, and the L2 energy feedback klystrons will be located. Another cable will route the RF reference from Sector 14 to Sector 19 and 20, where another phasing cavity and L3 feedback klystrons will be located.

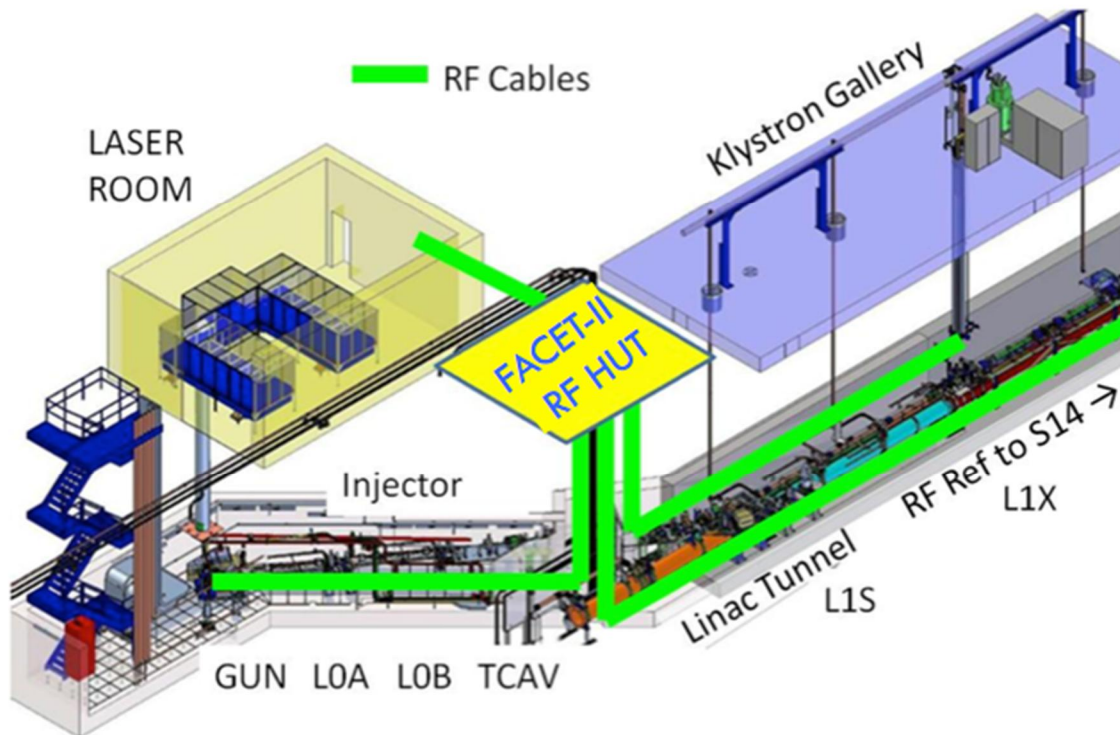


Figure 6.22. Layout of the injector area with the new temperature stabilized FACET-II "RF Hut" at the end of Sector 10, the laser room, and the routing of temperature sensitive RF cables.

### 6.5.3 Improvements to the RF Control System

A low noise RF control system is required to meet FACET-II specifications for jitter and drift. The RF control system will be modeled after LCLS-I, in that it will go on top of the existing linac system. This will add a tighter control of phase and amplitude for individual klystrons in the injector and for feedback klystrons in L2 and L3. The majority of the klystrons in L2 and L3 will use existing linac controls and not require any changes.

---

### *6.5.3.1 L2 and L3 RF Distribution and Control*

In LCLS-I, a separate phase reference line is used to control the phases of the klystrons in L2. This phase reference line feeds four sectors and has a Phase and Amplitude Controller (PAC) which is used to adjust the overall L2 phase based on beam measurements. In FACET-II the L2 phase reference line will need to control klystrons in four sectors, as in LCLS-I. Sectors 11, 12, 13, and a portion of the klystrons in Sector 14 will need to be controlled by the L2 phase reference line. Three amplitude feedback klystrons will be used in Sector 14. These feedback klystrons will require solid-state sub-boosters (SSSBs), PADs and PACs.

The L3-linac in FACET-II will need to have separate control from the MDL, since the MDL also drives L3 in LCLS-I. To achieve this control, PACs will be placed at the drops from the MDL for Sectors 15 to 20. PACs and SSSBs will be installed in Sector 19 for each klystron so individual klystrons in this sector can be used for the final energy feedback.

### *6.5.3.2 Sub-Boosters*

The present linac uses one klystron sub-booster per sector to provide 60 kW of drive power divided into 8 klystrons. Low power phase control is therefore only done at the input side to the sub-booster klystron and hence changes the phase of all 8 klystrons. The high power mechanical phase shifters on the individual klystrons are only capable of coarser,  $0.125^\circ$  steps. Also they were not designed for pulse-to-pulse operation, typically making only a few tens of phase corrections per day in the present linac operation.

The three klystrons in the injector, the L1-linac klystron, the three feedback control klystrons in L2 and the twelve feedback control klystrons in L3, as well as the special X-band and RF deflector klystrons, will require individual sub-boosters. This allows PACs to be used at each individual klystron, on the input side to its sub-booster, to enable the necessary pulse-to-pulse phase control with fine resolution. FACET-II will then require a total of 21 solid state sub-boosters.

### *6.5.3.3 Phase and Amplitude Detectors and Control Units*

The Phase and Amplitude Detectors (PADs) designed and built for LCLS-I are capable of measuring phase variations down to  $<30$  fs ( $<0.03$  degS) as shown in the plot for phase jitter on the LCLS-I Gun in Figure 6.21.

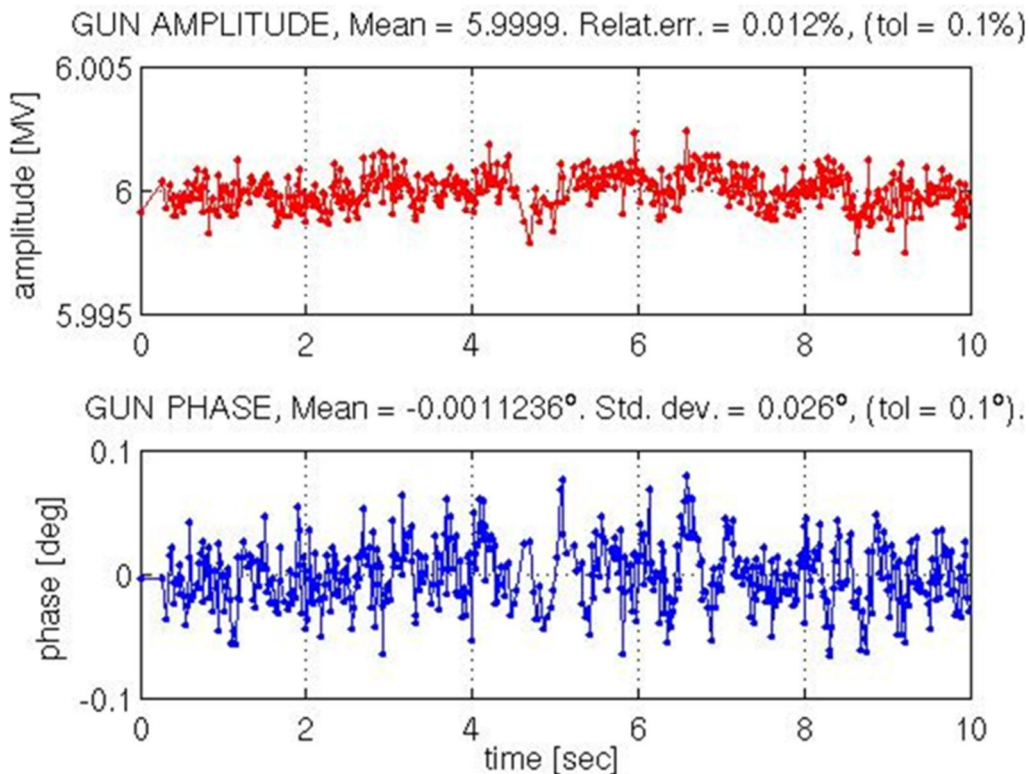


Figure 6.23. LCLS-I gun RF phase and amplitude jitter measurements over 10 seconds at 60 Hz.

The PADs use low noise RF and Local Oscillator signals to down-mix the RF to 25.5 MHz. The RF is then digitized at a 102-MHz sample rate and digitally down-mixed to baseband. The signals are integrated over the portion of the RF pulse of interest and made available as EPICS Process Variables (PVs) on TCP/IP Ethernet. A second Ethernet, User Datagram Protocol (UDP), port sends out data at beam rate for feedback and Beam Synchronous Acquisition (BSA). Matlab programs are used to read and analyze the PVs. There will be 35 total RF PADs used for FACET-II.

The LCLS Phase and Amplitude Controllers (PACs) use high speed Diamond Anvil Cells (DACs) to put out a waveform that is up-converted to the RF frequency. FACET-II will use similar type electronics to control the phase and amplitude of the RF system. Both the drive laser at the gun and the spare drive laser will have their own PACs. There will be 33 PACs at all klystrons, sectors, and lasers that require control.

#### 6.5.3.4 Timing System

The present linac timing system is based on 360-Hz fiducials superimposed on the 476-MHz RF that is distributed along the 2-mile linac. LCLS-I uses an Event Generator (EVG) which reads beam code information over a serial link and superimposes the beam code information and a 119-MHz clock on a 2.38-GHz high speed serial link. This high speed serial link is then distributed to Event Receivers (EVRs). This EVR based timing system will be used to supply FACET-II with triggers that are locked to the Linac RF.

#### 6.5.3.5 Beam Diagnostics

Pulse-to-pulse measurements of relative bunch length after each bunch compressor will be available for feedback control of the RF phase. These will be (are) based on CSR detectors (pyro-electron thermal

detectors). The bunch length monitors will be calibrated against the absolute bunch length measurement using the RF deflecting cavities (see Section 6.8).

Direct measurement of the beam phase with respect to the linac RF is desirable from the point of view of feedback control. However, the thermal sources of phase drift that need to be compensated in the RF distribution systems are equally likely to disturb the phase measurement at the 0.1 deg S-band level required here. A technique of measuring the phase of the beam-induced signal in the accelerating structures relative to the RF drive has been studied. One accelerating structure per klystron in a typical linac station is equipped with an output coupler on its load, where such measurements can be made. This may be a suitable technique for long-term phase control at the sub 1 deg S-band level in the L2 and L3-linacs. This measurement requires a dynamic range of over 120 dB and has been done using the configuration shown in Figure 6.24. By using two channels of Analog to Digital Converter (ADC), one channel with a 60-dB attenuator to measure the RF and the other channel with a limiter to protect the ADC that will handle 1 kW of RF input power from the klystron, to measure the 0.5 mW of beam induced RF, we achieved 120 dB of dynamic range. The 1-kW RF and 0.5-mW beam signal from the output of the accelerator structure is split into two paths. One path has a 60-dB attenuator and the other path has a limiter. The 60-dB attenuator gives 1 mW of power from the RF. The limiter limits the RF to 13 mW to protect the circuits and allows 0.25 mW of beam power to pass. This has been tested on LCLS-I with very good results.

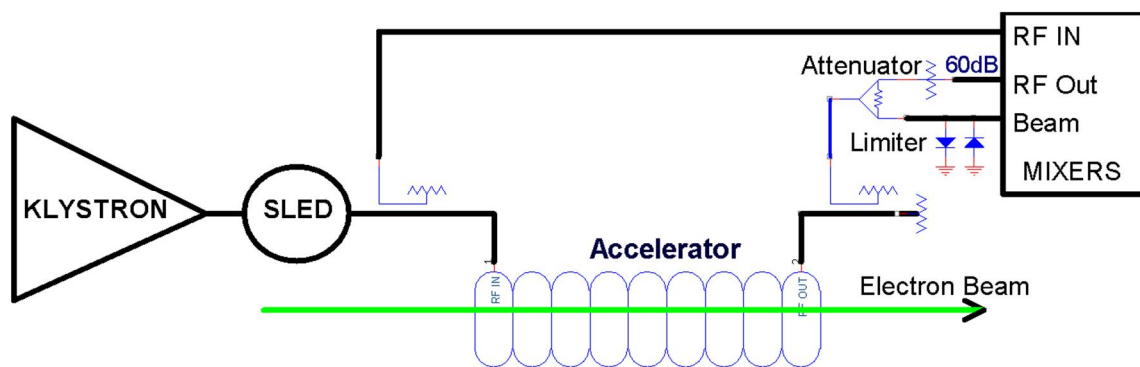


Figure 6.24. Beam and RF phase measurement from output of an accelerator structure.

#### 6.5.4 Layout and Performance of the Present SLAC Linac RF

FACET-II will use klystrons 11-1 to 19-8 in the linac. The injector area, RF Gun, L0a, L0b, TCAV0, L1S and L1X, will be done similar to LCLS-I with 11-1 and 11-2 stations providing for L1S (operating 19.8 degrees off crest) and L1X. The L2-linac (operating 40 degrees off crest) will consist of 29 klystrons from 11-4 to 14-6. 11-3 is removed to make room for the BC1 compressor, 11-4 station is used for an S-band transverse deflecting cavity and 11-6 is kept as a spare, 11-4 and 11-5 are used as energy feedback stations and are operating nominally +/- 60 degrees off crest. The L3-linac (accelerating on crest) will consist of 39 klystrons from 15-1 to 19-8, with a deflecting cavity in 15-1, 19-8 as a spare and 19-1 through 19-6 operating as energy feedback stations (operating nominally +/- 60 degrees off crest). 14-7 and 14-8 are removed to make room for the BC2 compressor chicane system and 19-7 is empty for use by the scavenger beam extraction system to generate positrons as at FACET.

The FACET-II gun will be driven from klystron 10-6. The SLED cavity will be removed and enough waveguide, more than 600 ns, will be installed to provide isolation in time for the klystron from the

reflected power of the standing wave gun. This method provides better isolation than a circulator and requires no sulfur hexafluoride gas.

L0a will be driven from klystron 10-7 and L0b will be driven from klystron 10-8. Both of these stations will have the SLED cavities removed and waveguide will be routed to the structures in the off axis injector bunker. These two 3-m long structures will be SLAC type structures modified with dual feed inputs, but single outputs (as in LCLS-I). Inputs and outputs of the structures will have Bethe hole couplers and new high power loads with vacuum ion pumps directly on each load.

The TCAV0 transverse deflector in the injector will be driven with klystron 10-5 using a high power 10 dB coupler to drop the power level to 0.5 MW. The SLED cavity will be removed from this station. Both input and output of the structure will have Bethe hole couplers and the output will have a new high power load.

Two of the three L1S structures (11-1b and 11-1c) will be shortened to 9.4 feet so quadrupole magnets can be placed between them. The L1S station will have the SLED cavity remain as is. Bethe hole couplers will be added to the input of the 11-1b section and to the outputs of all the sections. New high power loads will be installed at the outputs of the three structures with vacuum ion pumps directly on each load.

The X-Band station will be placed at klystron station 11-2. The station will be a copy of the 21-2 LCLS-I X-Band station with about 20 MV of peak RF available. All high power S-Band components at 11-2, including the four 3-m long structures will be removed to make room for BC1.

Table 6.9 gives the no-load energy gain (in MeV) of the klystrons in the L2 and L3-linacs. Nominal FACET-II operational energy is 10.0 GeV.

Table 6.9. Unloaded energy gain (MeV) of each klystron in L2 and L3.

	Sector	1	2	3	4	5	6	7	8
<b>L1/L2</b>	11	103	103	--	TCAV	163	150	163	175
	12	175	163	175	175	175	175	175	175
	13	175	175	175	175	175	175	175	175
	14	175	175	175	115	115	SPARE	--	--
<b>L3</b>	15	TCAV	138	162	162	162	162	162	162
	16	162	162	162	162	162	162	162	162
	17	162	162	162	162	162	162	162	162
	18	162	162	162	162	162	162	162	162
	19	91	91	91	85	91	91	--	SPARE

---

## 6.7 Particle Tracking

Particle tracking studies have been performed throughout the injector, accelerator, and sector 20 compression and final focus by stringing together results from *Impact* (injector) and *Lucretia* [2] (linac & Sector 20). Included in the tracking are longitudinal and transverse wakefields, Coherent Synchrotron Radiation (CSR), Incoherent Synchrotron Radiation (ISR), and up to 3<sup>rd</sup>-order optics (*e.g.*, chromatic effects). 3D space charge forces are only included in the *Impact* run up to 135 MeV at the exit of L0, with output particles transferred to *Lucretia*. *Lucretia* does include a model of longitudinal space-charge forces for completeness, although the observed effects are negligible. The results from the tracking simulation ( $10^6$  macro-particles simulating the particle bunch) are shown earlier in this chapter in the relevant sections. Results from the *Impact* tracking can be seen in chapter 5.

The electron beam tracking is first performed through to the end of BC1. The positron beam is tracked from the design parameters at the extraction point of the positron damping ring, through the positron ring to linac beam optics including the BC0 compressor, to the common injection point at the exit of BC1. Both electron and positron macro-particle bunch definitions are then merged with the appropriate  $\frac{1}{2}$  s-band wavelength (5.25cm) separation and tracked through L2, BC2 and L3. This allows the simulation to properly treat the transverse wake deflection imparted on the electron beam by the positron beam in the accelerating structures. Each bunch is then tracked through BC3E and BC3P, through the common final focus system in Sector 20 to the common interaction point in the experimental area.

Results from particle tracking are summarized in Table 6.10 below, the beam optics for electron and positron beam lines are shown in Figure 6.25 and Figure 6.26 and the energy profile is shown in Figure 6.27. The tracked longitudinal phase space for electron and positron beams are shown in Figure 6.6 and Figure 6.7. The final tracked transverse beam profiles for electrons and positrons at the experimental IP location are shown in Figure 6.28. All components are error free for these tracking simulations (*e.g.*, perfect alignment). Due to energy loss due to synchrotron radiation in the bunch compressors, there are steering and dispersive “errors” by design. During operation, these are taken care of by the routine steering and dispersion correction systems. For design tracking purposes here, the orbit and dispersive “errors” are numerically subtracted after each bunch compression stage to mimic these operational corrections and derive the expected performance for the machine. These fixed corrections are stored and used during tolerance calculations which apply additional errors (*e.g.* RF phase and amplitude errors) so the impact of those errors is properly treated.

Collimators within the BC0, BC1 and BC2 bunch compression chicanes are used to selectively collimate the high and low energy offset tails of the beam. Figures 6.29 and 6.30 below show how the transverse and longitudinal beam sizes at the experimental IP waist vary as a function of final beam charge (initial beam charge is 2nC) for the positron and electron beam. The beam charge is varied by symmetrically adjusting the bunch compressor collimators. Treating each beam independently it can be seen that there is an optimal collimator setting in each case in terms of maximum achievable peak current: around 1.5 nC for electrons and 1.7 nC for positrons. Due to increasing energy spread generating larger aberrations through BC3E, BC3P and the final focus, and also due to CSR effects (which become more pronounced for larger peak currents and shorter bunch lengths), the horizontal spot size at the IP is also strongly correlated to the final bunch charge. The collimation is determined by the positron beam which is most sensitive to the bunch charge. The configuration presented here and elsewhere in this CDR report corresponds to an electron bunch charge of just over 0.6 nC which meets the requirements of  $< 10 \times 10 \times 10$   $\mu\text{m}$  bunch dimensions at the experimental IP, and the requirement of  $> 10$  kA peak current, whilst leaving a small overhead for operational errors etc. The electron collimation is then set to provide

a similar final electron bunch charge which tracks to the same final energy when taking into account beam loading in the linacs. The electron bunch in this configuration also meets the required final bunch parameters. In principal, an additional 50% peak current is achievable if the chromatic aberrations and CSR effects can be further mitigated (mainly in BC3P) to suppress the horizontal beam spot size growth. Further studies will be carried out to optimize the Sector 20 optics with this in mind. e.g. the principal of CSR-matching will be applied.

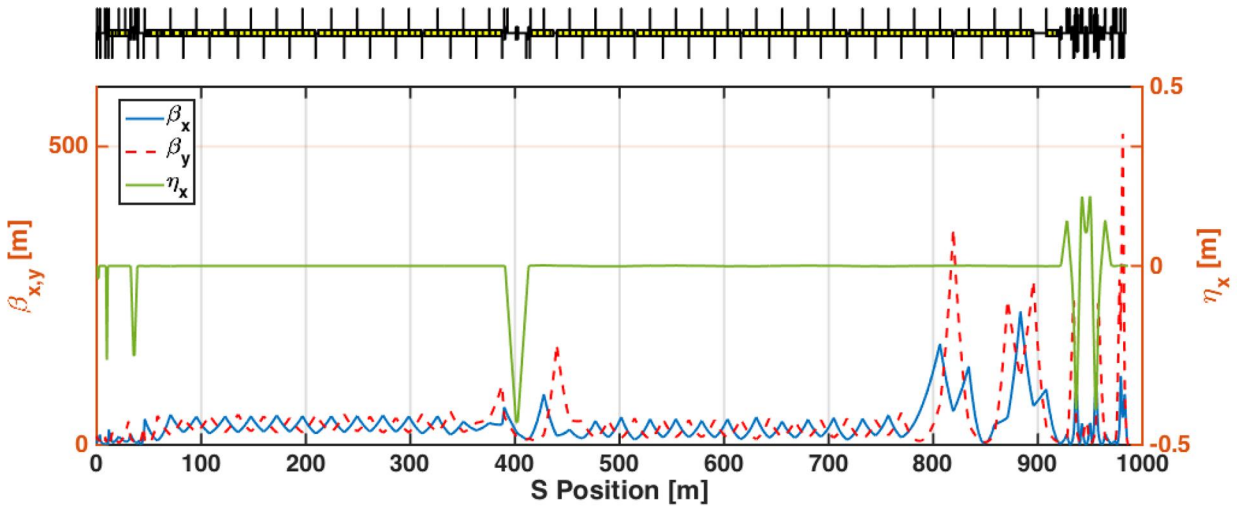


Figure 6.25: Electron optics across entire FACET-II (using *Lucretia*), from exit of L0 (at 135 MeV) to the start of the experimental IP area.

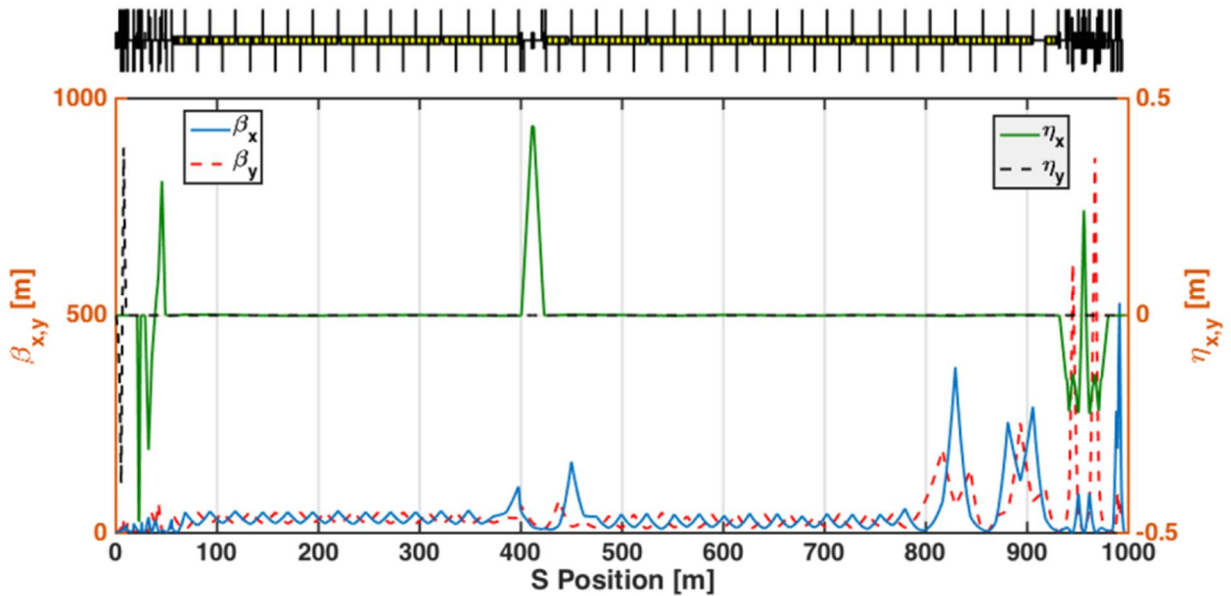


Figure 6.26: Positron optics across entire FACET-II (using *Lucretia*), from exit of positron damping ring (at 335 MeV) to the start of the experimental IP area.

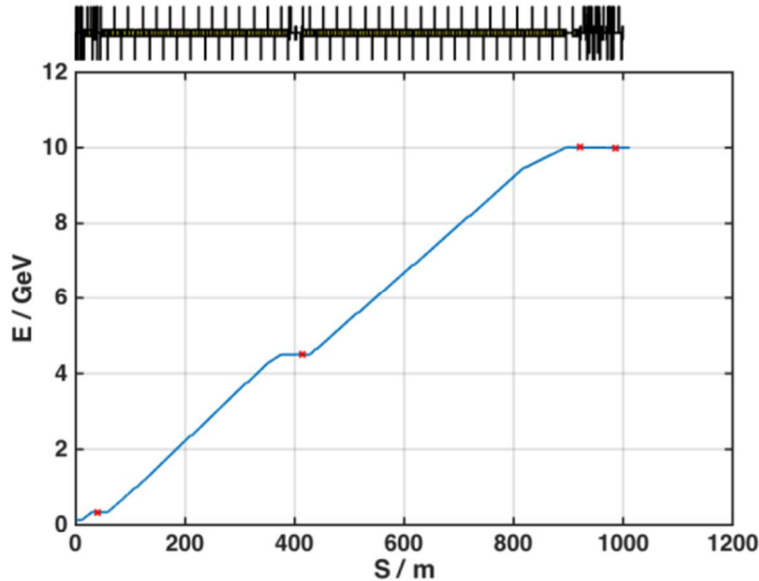


Figure 6.27: Energy profile through FACET-II electron beamlines. Computed energy profile in blue with tracked energy marked as red crosses after each compression stage.

The following list describes the various effects which are included in the particle tracking.

- $10^6$  macro particles representing a 2 nC electron bunch was tracked using *ImpactT*, which includes 3D space charge forces, up to the exit of the LO accelerator section at 135 MeV. The initial temporal profile, with a 0.8-mm rms duration, is shown in Figure 5.16.
- First to third-order optics of dipole, quadrupole, sextupole, and sinusoidal RF fields.
- Longitudinal and transverse wakefields of the SLAC S-band RF accelerating structures with 321.8 meters of structures between BC1 and BC2, and 471.0 meters after BC2.
- CSR applied to all bends and downstream drift spaces using the 1D line-charge model in *Lucretia*, which includes transient fields but ignores the transverse beam dimensions (typically not of major impact).
- ISR applied to all bends, which impacts the energy spread and beam emittance, although by insignificant levels.
- A simulation of longitudinal space charge impedance effects is applied in the *Lucretia* tracking model, although the effect is negligible.
- An increased slice energy spread (130 keV rms) at 135 MeV is produced by the laser heater system. This reduces instabilities due to micro-bunching through CSR and LSC.
- Collimation of the beam in BC0, BC1 and BC2 bunch compressor collimation sections.

Table 6.10: Beam tracking simulation results for electron and positron beams from exit of L0 @ 135 MeV (electrons) and exit of damping ring (positrons) to experimental IP waist. Bunch length and energy spread quantities are rms values.

Beamline Section (end)	$\nu_{\epsilon_x}$ ( $\mu\text{m}\cdot\text{rad}$ )	$\nu_{\epsilon_y}$ ( $\mu\text{m}\cdot\text{rad}$ )	$\sigma_z$ ( $\mu\text{m}$ )	$\sigma_E/E$ (%)	E (GeV)	Q (nC)
L0 (e-)	3.4	3.2	803	0.15	0.135	2.0
L1 (e-)	3.5	3.5	801	0.69	0.135	2.0
BC1 (e-)	3.2	3.2	285	0.27	0.335	1.2
BC1 (e+)	6.5	5.9	350	0.52	0.335	1.2
L2 (e-)	3.6	3.2	285	0.93	4.5	1.2
L2 (e+)	7.0	5.8	350	1.2	4.5	1.2
BC2E (e-)	3.3	3.2	23	0.48	4.5	0.7
BC2P (e+)	6.0	5.8	29	0.55	4.5	0.6
L3 (e-)	3.3	3.3	23	0.41	10.0	0.7
L3 (e+)	6.3	5.9	29	0.47	10.0	0.6
S20 IP (e-)	8.2	5.1	1	0.43	10.0	0.7
S20 IP (e+)	35.0	6.4	8	0.48	10.0	0.6

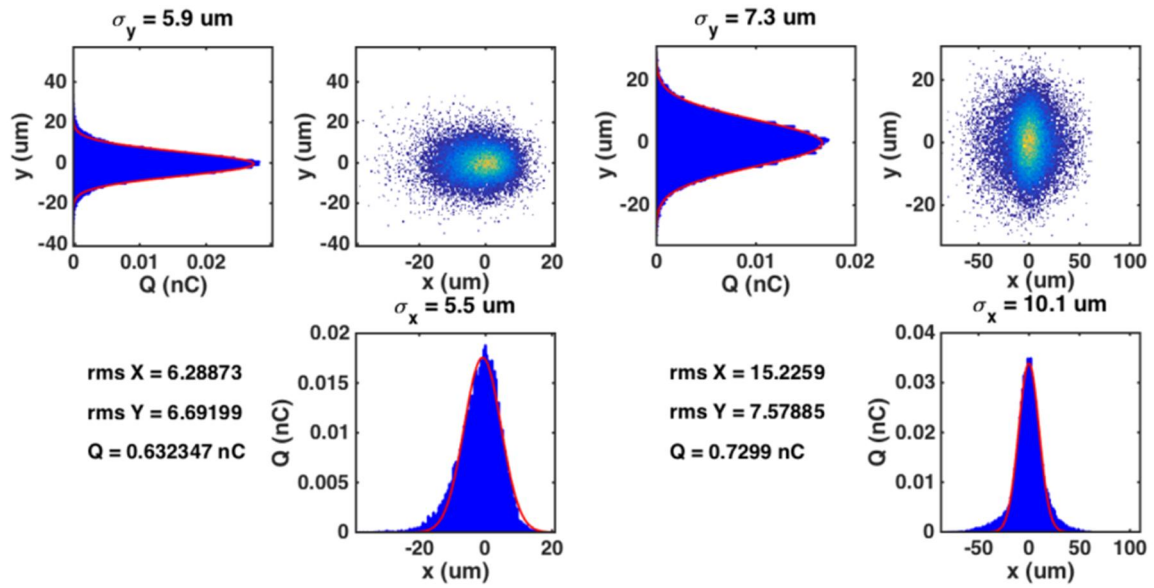


Figure 6.28: Tracked beam particles for electron (left) and positron (right) beams at the experimental IP waist in Sector 20, transverse beam dimensions shown.

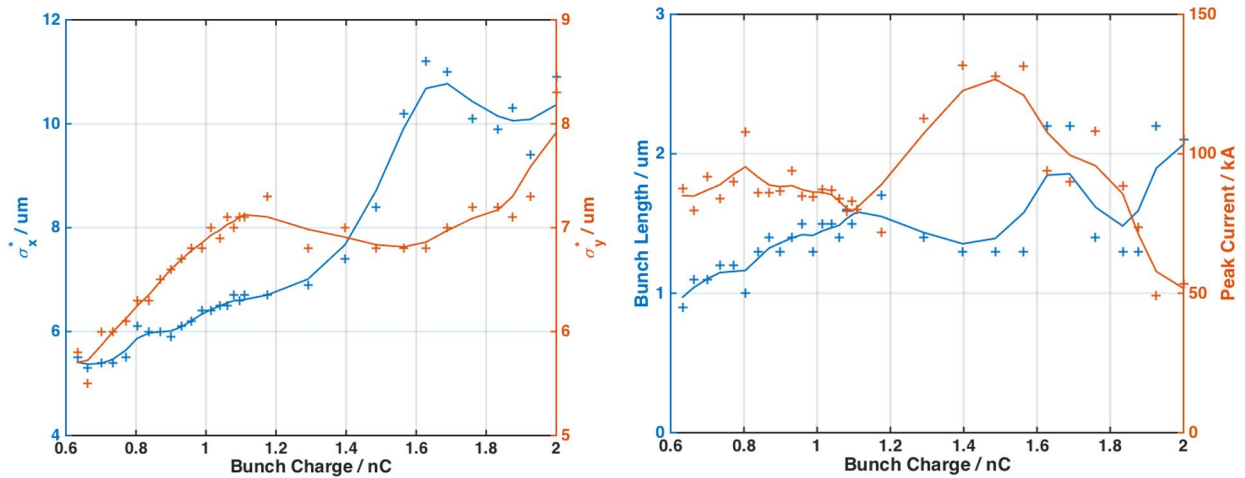


Figure 6.29: Transverse and longitudinal bunch sizes at Sector 20 waist for Electrons as a function of bunch charge. Lines are smoothed data values. Bunch charge is varied using BC1 and BC2 collimators.

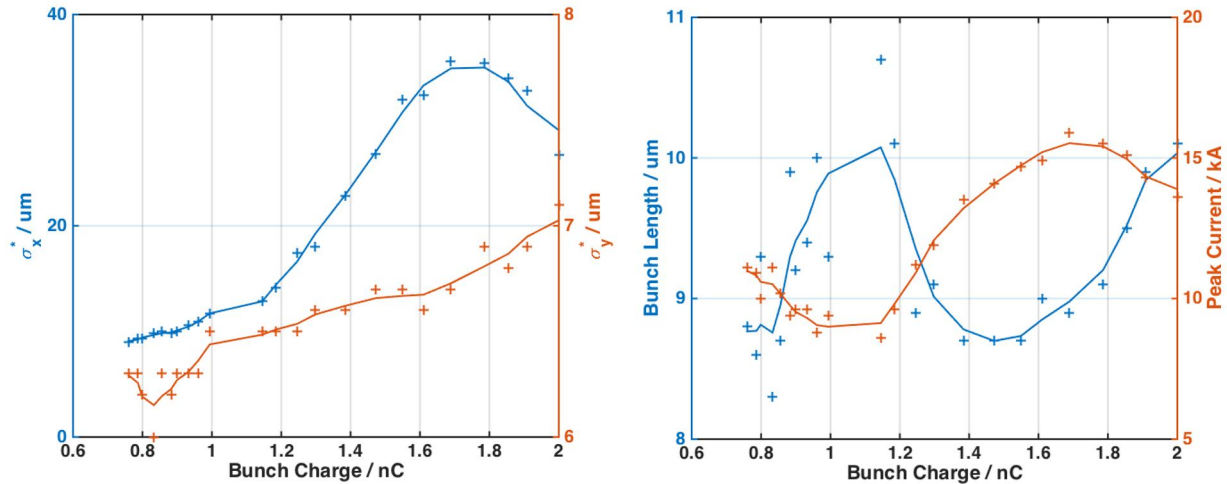


Figure 6.30: Transverse and longitudinal bunch sizes at Sector 20 waist for Positrons as a function of bunch charge. Lines are smoothed data values. Bunch charge is varied using BC0 and BC2 collimators.

## 6.8 Instrumentation, Diagnostics, Feedback, and Collimation

Careful measurement and correction of the transverse and longitudinal beam parameters are critical for preservation of beam emittance and the production of high peak current, small transverse beam sizes at the experimental IP. Diagnostic devices are distributed all over the FACET-II linac in order to provide precise measurements for use both during initial commissioning and regular operation. An overview of these diagnostics is shown in Figure 6.31.

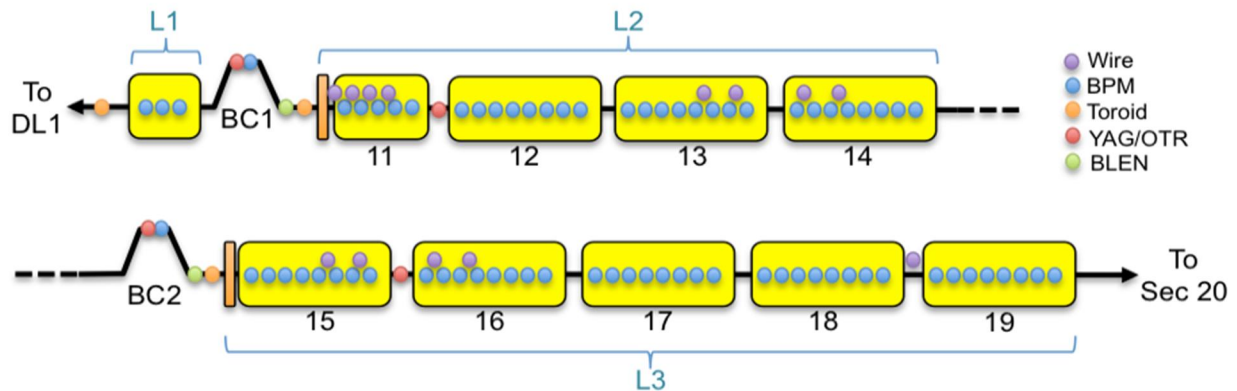


Figure 6.31. Beam instrumentation in the FACET-II linac and bunch compressors. For clarity, the e+ sides of the bunch compressor chicanes are omitted; the diagnostics are symmetric with the e- sides.

### 6.7.1 Beam Position Monitors and Toroid Charge Monitors

Beam position monitors (BPMs) measure the transverse beam centroid and are a primary tuning and monitoring diagnostic. Approximately 80 in total are distributed along the FACET-II linac from the beginning of L1 to the end of Sector 19, with one located in each focusing quadrupole magnet. These BPMs are of the stripline type, with 5-10 micron resolution of beam position. Additionally, large

---

horizontal aperture BPMs will be located at high-dispersion points in the center of BC1 and BC2 to provide precise measurement of beam energy. The existing linac BPMs will be read out via the legacy SLC control system, while the new BPMs in the bunch compressors will have EPICS interface. A suite of existing software interfaces allow for sharing pulse-by-pulse measurements between control systems.

The existing BPMs will be capable of providing beam position readings for  $e^-$  and  $e^+$  beams during phase I and phase II of FACET-II, when those bunches are accelerated on different machine pulses separated by milliseconds. In phase III, the co-accelerated bunches are separated in time by only half an S-band wavelength, or roughly 150 ps. Coupling of the two bunches through long-range wakefield and beam loading effects potentially alter the beam energy and trajectory significantly. In this scenario, the existing stripline BPM design lacks the GHz bandwidth necessary to resolve the two bunches distinctly. Energy differences between the  $e^-$  and  $e^+$  bunches can still be discerned and corrected in the bunch compressors, as the two beams split and travel down separate arms of the chicane, allowing standard stripline BPMs to be used on each side. However, trajectory effects in the shared linac BPMs will be masked. A conceptual design for a high-bandwidth C-band RF BPM exists, which could be installed in each of the instrumentation sections after every linac sector, in order to provide some direct measurement of the effects of co-acceleration.

Toroid charge monitors provide precise, externally calibrated measurement of the total beam charge. In addition to this direct diagnostic purpose, they are used for monitoring beam losses along the linac as interlocks to prevent damage to the various components. There are three toroids in the linac, at the beginning of L1, L2, and L3 respectively.

### *6.7.2 Electron Beam Profile Monitors*

Profile monitors (screens) and wire scanners are located throughout the accelerator to measure the transverse beam size and distribution. The screens function via either the emission of optical transition radiation (OTR) from the surface of thin metallic foils which the beam passes through, or by scintillation from cerium-doped yttrium aluminum garnet (YAG) crystals which emit visible light upon the absorption of high-energy particles. Several older phosphorescent screens also remain in use, primarily as a monitoring tool. Experience at LCLS has proven the OTR screens after BC1 suffer from degraded utility due to the effects of coherent OTR (COTR); thus the downstream screens will be of the YAG variety.

In the FACET-II linac, profile monitors are mainly used as longitudinal phase space diagnostics. YAG screens for measurement of electron beam energy spectrum will be installed just upstream of the center of BC1 and BC2. YAG screens for use with the transverse RF cavities after each bunch compressor will also be installed at the 11-9 and 15-9 instrumentation girders to provide measurement of the longitudinal beam distribution.

### *6.7.3 Wire Scanners and Transverse Emittance Diagnostics*

Wire scanners providing direct and robust measurement of the beam profile sampled over many consecutive pulses remain the workhorse tool for measuring and tuning transverse emittance, both at LCLS and at FACET. In the FACET-II linac there are 3 emittance diagnostic stations, each of which comprises 4 wire scanners located with optimal phase advance to provide complete measurement of the transverse beam phase space. In general, 4 wire scanners are planned for each emittance measurement station for redundancy and accurate fitting of the transverse phase space ellipse.

Three of the four existing SLC-style wire scanners located in sector 11 will be left in place. The wire scanner at 11-3d will be moved to the drift space after the existing 7-foot accelerator structure at 11-7d. Four 10-foot accelerator sections in sectors 13/14 will be replaced by 9.4-foot sections in order to make

space for new 4-inch wire scanners of a design currently in use in the FACET IP area. Similar modifications will be made in sectors 15/16 (see section 6.1.3). Additionally, the existing single wire scanner at the 18-9 girder will be left in place to allow for quadrupole-scan emittance measurements. An optional upgrade would be to install three additional wires in sector 19. These four emittance diagnostic stations allow for measurement and correction of transverse emittance and optical mismatch at the entrance and exit of L2 and L3, respectively.

Table 6.1. Transverse emittance measurement stations along the FACET-II linac ( $\gamma\epsilon_{x,y} = 6 \mu\text{m}$ ).

Location	Station Name	Energy (GeV)	$\sigma_x$ ( $\mu\text{m}$ )	$\sigma_y$ ( $\mu\text{m}$ )	No. of Prof. Monitors	Existing
Following BC1	ED1 (Sec 11)	0.335	145-215	113-215	4	Yes
At the end of Linac-2	L2-ED (Sec 13)	3.1-4.0	37-68	40-67	4	No
Following BC2	ED2 (Sec 15)	4.5	35-57	38-56	4	No
At the end of Linac-3	L3-ED (Sec 18)	9.0	67	85	1	Yes

### 6.7.4 Bunch Length Diagnostics

The proposed bunch compression scheme's strong sensitivity to RF drift and jitter, as described in section 6.2, requires precise measurement and control of the longitudinal bunch length and charge distribution. Each compression stage has bundled with it a pair of bunch length diagnostics, which are used in tandem to set up and maintain the desired longitudinal profile.

In the FACET-II linac the bunch lengths vary from  $\sim 400 \mu\text{m}$  rms to  $\sim 20 \mu\text{m}$  rms (4 ps to 200 fs FWHM). Transverse RF deflectors have been used at LCLS and FACET across this range and provide excellent resolution of the beam's temporal structure. These measurements are invasive, however. Non-invasive bunch length monitors using coherent dipole edge radiation allow for beam-based feedback and bunch length stabilization.

The transverse RF deflecting cavities have already been described in detail in the previous chapter, Section 5.4.4.1.

One such RF deflecting structure will be placed downstream of each of the BC1 and BC2 chicanes at 250 MeV and 4.5 GeV respectively. These will be located at the 11-4a and 15-2d locations, where existing 10-foot accelerating structures will need to be removed and replaced by newly fabricated 2.44-meter deflecting structures. The corresponding screens will be located at the 11-9 and 15-9 instrumentation drift sections where space is available

#### 6.7.4.1 Bunch Length Monitors

For pulse-by-pulse monitoring and feedback stabilization, non-invasive measurement of peak current will be done by bunch length monitors (BLMs) which use the coherent diffraction or "edge" radiation emitted from the downstream face of the final bend magnet in each bunch compressor. The power in the coherent radiation is very sensitive to the bunch length. An annular mirror reflects the radiation into a pyro-electric detector that is read out with a "pizza-box" type digitizer. This style of bunch length monitor provides only a relative measure of the peak current and must be calibrated with its companion TCAV. There are two such BLMs in the FACET-II linac, located just after each bunch compressor.

---

### 6.7.5 *Beam Energy Spread Diagnostics*

The electron energy spread is typically measured using a profile monitor at a location with large momentum dispersion and small beta function. Several locations have been designed into the FACET-II optics in order to enable this measurement. The key locations are in the first bunch compressor, BC1, and the second bunch compressor, BC2. Each of these locations will be equipped to allow adequate energy spread measurements along the FACET-II accelerator as described below. The location of the transverse deflecting cavities after each bunch compressor precludes the ability to measure sliced energy spread at the profile monitors in the chicanes.

#### 6.7.4.2 *BC1 Energy Spread Diagnostics*

The energy-spread after the first compressor, BC1, is made with a profile monitor (a retractable OTR screen which is not greatly compromised by COTR) located in the center of the chicane at a point where the horizontal dispersion function is  $\eta_x \approx 250$  mm and the horizontal beta function converges towards a minimum of  $\beta_x \approx 6.8$  m. For the nominal emittance and nominal energy spread of  $\sigma_\delta \approx 0.5\%$  at 250 MeV, the betatron beam size is  $90 \mu\text{m}$ , but the dispersive size is 1.3 mm. This produces a systematic error in the energy-spread measurement of  $<1\%$ .

#### 6.7.4.3 *BC2 Energy Spread Diagnostics*

The energy-spread after the second compressor, BC2, is also made with a single profile monitor (a retractable YAG screen to avoid the COTR effects) located in the center of the second chicane at a point where the horizontal dispersion function is  $\eta_x \approx 367$  mm and the beta function converges towards a minimum of  $\beta_x \approx 26$  m. For the nominal emittance and nominal energy spread of  $\sigma_\delta \approx 1.1\%$  at 4.5 GeV, the betatron beam size is  $42 \mu\text{m}$ , but the dispersive size is 4 mm. This produces no significant systematic error in the energy-spread measurement. The collimator jaws in BC2, upstream of the profile monitor, can be used to select energy bands for diagnostic purposes.

### 6.7.6 *Trajectory Feedback Systems*

Trajectory feedback systems will be placed at the entrance of the L2-linac and the L3-linac. As at the SLC [3], these systems will each be composed of approximately ten BPMs which record both  $x$  and  $y$  positions, preceded by a set of two horizontal and two vertical fast dipole corrector magnets controlled by a software based feedback system.

In order to control transverse orbit variations to better than  $1/10^{\text{th}}$  of the beam size, the individual one-pulse BPM resolution for the various 10-BPM feedback systems described above needs to be  $<10 \mu\text{m}$  rms. Trajectory variations which occur at frequencies below  $\sim 1$  Hz will be stabilized. Faster variations cannot be damped significantly and will need to be identified at the source.

Transverse vibrations of quadrupole magnets will generate orbit variations, which if fast enough will not be damped by feedback systems. Tolerance calculations indicate that uncorrelated random vibrations of all FACET-II quadrupoles must be at the level of  $<100$  nm rms, to hold the rms beam stability at  $<10\%$  of the rms beam size there. Measurements in the SLC indicate that existing linac magnet vibrations are  $<250$  nm [4] with the highest frequency content at 59 Hz and 10 Hz driven by cooling water. These observed vibrations will need to be improved about a factor of two to achieve stability goals. At lower energies most of the new quadrupole magnets are air-cooled and have looser vibration tolerances.

### 6.7.7 *Energy and Bunch Length Feedback Systems*

---

Energy feedback systems will be placed in each bending region (BC1 and BC2). A single BPM placed at a high dispersion point will be used to determine energy variations, and the corresponding bunch length monitor will be used to determine variations in bunch length. In BC1, the phase and amplitude of L1S will be used to stabilize the energy and bunch length. In BC2, the L2 reference phase will be adjusted to modulate the bunch length, while vernier control of two klystron phases will maintain the beam energy. These operations are to be carried out by a software feedback similar in design to the 6×6 feedback loop system that has already been fully tested and operational at LCLS-I. Modifications to this design will be required to add energy and bunch length states for both electron and positron beams, making it an “8x8” feedback, as energy feedback for the injector, positron injector and Sector 20 will be split out and handled by separate dedicated feedback loops.

## References

---

1. K. Bane, P. Emma, Proc. of the 2005 Part. Accel. Conf., Knoxville, TN, May 16-20, 2005.
2. <http://www.slac.stanford.edu/accel/ilc/codes/Lucretia/>
3. T. Himel et al., *Adaptive Cascaded Beam-Based Feedback at the SLC*, Proceedings of the 1993 Part. Accel. Conf., Washington, DC, 1993.
4. J. L. Turner et al., *Vibration Studies of the Stanford Linear Accelerator*, Proceedings of the 1995 Part. Accel. Conf., Dallas, TX, 1995.

# 7 Experimental Area and Infrastructure

---

---

## Technical Synopsis

*In addition to construction of the FACET-II injector and bunch compressors, several modifications are needed in the Linac infrastructure before electron beams can be restored. A concrete shielding wall must be constructed in Sector 10 to separate the LCLS-II and FACET-II sections of the Linac tunnel. This allows access to the LCLS-II tunnel while there is beam in the FACET-II area. It does not permit access to the FACET-II area during LCLS-II beam operation. In addition to the wall, the Personnel Protection System (PPS) for the two areas must be separated to allow independent access. A separate PPS zone with Controlled Access will be created in Sector 20 to facilitate efficient entry to that region. Other infrastructure tasks include modifications to the control system network to restore the legacy control system post LCLS-II modifications in the first 10 sectors and a new Beam Containment System for the injector and chicanes.*

---

---

## 7.1 Introduction and Overview

In addition to construction of the FACET-II injector and bunch compressors, several modifications are needed in the Linac infrastructure before electron beams can be restored. A concrete shielding wall must be constructed in Sector 10 to separate the LCLS-II and FACET-II sections of the Linac tunnel. This allows access to the LCLS-II tunnel while there is beam in the FACET-II area. It does not permit access to the FACET-II area during LCLS-II beam operation. In addition to the wall, a Personnel Protection System (PPS) enclosure that covers sectors 10 through to 20 would need to be established. The PPS zone that contains the experimenter area (sectors 19 and 20) will be upgraded to have Controlled Access to facilitate efficient entry to that region. Other infrastructure tasks include modifications to the control system network to restore the legacy control system post LCLS-II modifications in the first 10 sectors and a new Beam Containment System for the injector and chicanes.

Modifications to the Experimental Area extend beyond the FACET II project with future upgrades through Accelerator Improvement Projects described in Chapter 10.

## 7.2 Sector 10 Shielding Wall

A shielding wall will be constructed to isolate FACET-II from LCLS-II in Sector 10. This allows beam operation in the FACET-II area independent of LCLS-II operational status. However, access to the FACET-II area is not allowed while LCLS-II is in operation.

### 7.2.1 Sector 10 Layout

The shielding wall is a solid wall starting around  $Z = 969\text{m}$  in the Accelerator Housing, downstream of Penetration 10-9 at Sector 10. It will be designed to allow personnel to access upstream (LCLS-II) whilst FACET-II beam is in operation.

The wall will be solid except for three penetrations to accommodate (1) LCLS-II dog-leg, (2) accelerator cooling water return pipe and (3) a plugged penetration that can be used for line of sight between alignment monuments on each side of the shield wall.

LCLS-II will remove the existing alignment light pipe from S0 to S10-7 or 10-8. The new starting location of the light pipe will be  $Z = 993\text{m}$ , and Metrology will have a camera at 992m for use with this alignment system when needed for FACET-II and LCLS-I.

The LCLS-II dog-leg passes through the shield wall and a 2" diameter hole will accommodate this pipe. There are LCLS-II beamline components in the area (corrector magnets, diagnostics and collimators) however there are 7.9 m between LCLS-II components within which the wall can be located.

Penetration 10-10 is not required by either FACET-II or LCLS-II and may be blocked by the shield wall.

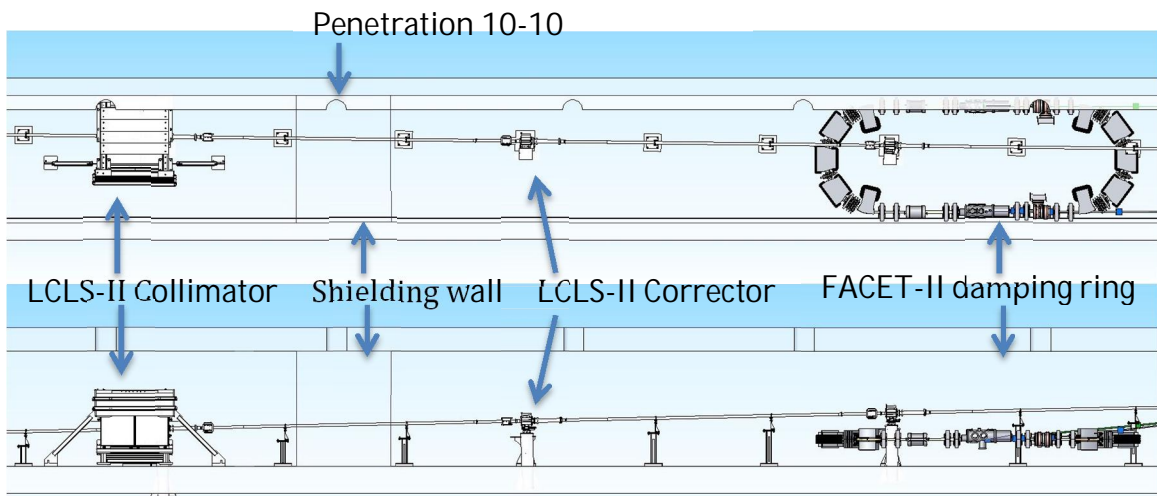


Figure 7.1. A conceptual drawing of Sector 10 shows a potential location for the sector 10 shielding wall (top: plan view, bottom: elevation view). The LCLS-II dogleg components (collimator, correctors) are shown. The beam pipe passes through the shielding wall. The FACET-II damping ring is the closest FACET-II component to the shielding wall. The shielding wall is depicted as 2.5 m thick with stands immediately upstream and downstream to support the LCLS-II beam pipe.

### 7.2.2 Shield Wall Requirements

The shield wall material and thickness is set by the physics requirements from Radiation Physics (RP) to meet ionizing radiation dose criteria for personnel to be present upstream of the wall during FACET-II beam operation. RP perform calculations with FLUKA Monte Carlo Code based on assumptions on beam losses to estimate the dose rate on the upstream side of a modelled shield wall. The radiation physics studies cover multiple cases: the normal operations case, the worst possible missteer case and the Maximum Credible Incident (MCI) case. Each beam loss scenario dictates a minimal width for the shield wall which must be simultaneously satisfied.

The largest contribution to the dose, and hence the driver for the radiological requirement on the thickness of the wall, is positron beam loss upon injection into the damping ring. The positron beam (3.5 W beam power) at this point is directed west, towards the shielding wall. Other radiation sources from the damping ring and positron return line include beam-interruptive diagnostics in the positron return line (PRLTR) and extraction line (PEC) (Fig.7.2). In addition, there will be a vacuum valve each at the point where the positron beam is extracted from and injected into the damping ring to isolate the damping ring vacuum from the linac vacuum. Apertures are expected to be narrow in the damping ring also contributing to a small degree of beam loss. Contributions from the eastward travelling electrons also need to be considered.

Traditionally, a mixture of material is used for a shield wall. Photon field attenuation is achieved with a high-Z material such as iron or lead which is then followed by a moderating material such as concrete with the addition of a material to capture thermal neutrons (e.g. borated polyethylene).

Using concrete only, the estimated thickness of the sector 10 shield wall, based on preliminary calculations, is of order 300 cm. The space available in sector 10 is greater than this and such a wall would not constitute an issue. A combination of materials, however, would satisfy requirements in shorter distance. Preliminary estimates show 175 cm of concrete and 15 cm of iron can also satisfy requirements (Fig.7.3) for both expected operational losses and full beam loss in the missteer case. The final shield wall design can be optimized by what is the lowest cost of construction and the simplest design.

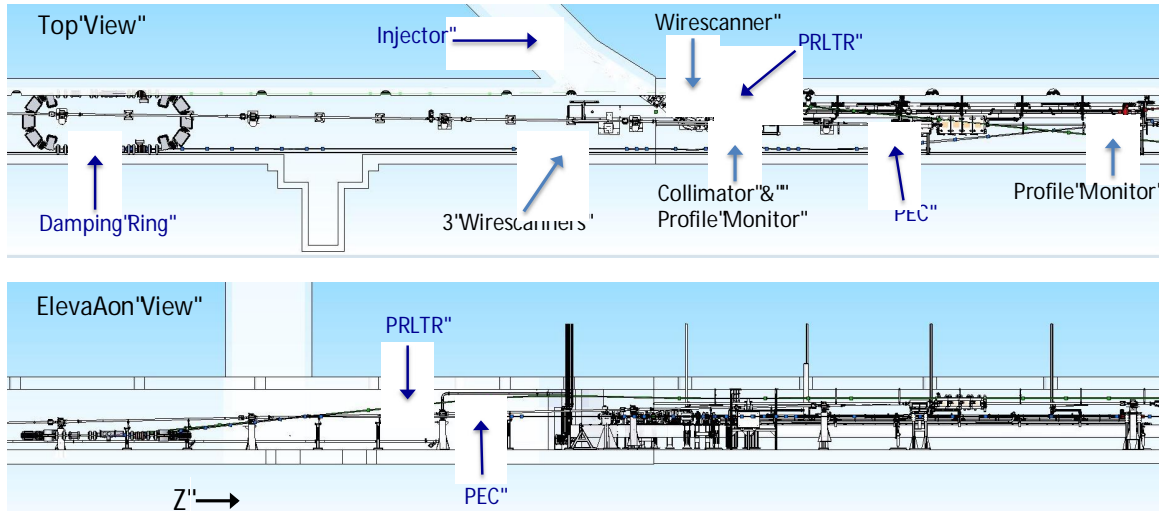


Figure 7.2. A preliminary layout of the damping ring, Positron Extraction and Compression (PEC), and Positron Return Line to Damping Ring (PRLTR) showing potential locations for beam-interruptive diagnostics.

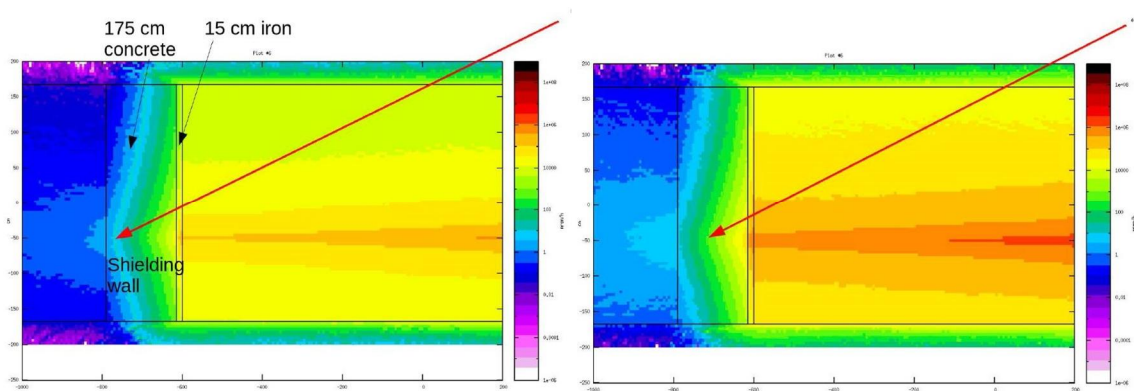


Figure 7.3. Preliminary calculations for dose rates due to expected positron beam losses (left) and full positron beam loss (right). The calculations were done with FLUKA Monte Carlo code. The shield wall was modeled as 15 cm iron with 175 cm concrete and was shown to satisfy the criteria for personnel to be downstream of the shield wall in both cases. The red arrow shows the contour for the dose rate criterion that must be contained within the wall for the criterion to be met.

## 7.3 *Experimental Area*

### 7.3.1 Overview

The FACET II Facility is designed to support a wide range of user experiments. The experimental area in Sector 20 needs to be upgraded to more efficiently support these different users. A major constraint is that the LCLS-II bypass beamline runs through the same section of tunnel. Since there is no access during LCLS-II operation, the time available for setting up experiments will be much more limited than for FACET. This makes it critical that experiments can be installed and commissioned as efficiently as possible. It is also important to have multiple experiments ready to use beam time in the event that the scheduled experiment encounters a problem.

FACET-II faces additional challenges because most of the experiments have not been and cannot be performed elsewhere. While this can lead to unexpected results and break-through science, these high risk (but high reward) experiments need considerable time to commission new hardware and hone methods to perform the experiment. This makes it difficult to predict the amount of beam time an experiment will require and makes it necessary that the experimental area be configured to flexibly support multiple concurrent experiments.

The changes foreseen for beyond the FACET II project include a differential pumping scheme, laser upgrades, data acquisition at increased repetition rate, new diagnostics, additional beamline for the installation of more concurrent experiments and a witness bunch injector. Many of these upgrades are presented in detail in Chapter 10. There is also the possibility to add a new experiment station as the lower energy of FACET-II permits the use of smaller magnets which could free up additional beamline space.

In addition to hardware modifications, we plan to improve the user preparation for the experiments. Apparatus will be installed and commissioned prior to scheduling the full experiment's beam time. There will be a framework for experimenters to collaborate with existing users on techniques, to benefit from common hardware development and beam time experience and to participate in beam time of other experiments to learn the tools hands-on. Wherever possible, users will be given the opportunity to gain experience in how to perform their experiment at other facilities with more accessibility (such as ESTB at SLAC).

### 7.3.2 LCLS-II transport line

The LCLS-II beam is transported from sector 10 through the rest of the Linac tunnel to the undulator hall in the former PEP-II high energy bypass line. This beam pipe already exists in most of the Linac including through the sector 20 shield wall separating FACET from LCLS.

There are minor changes necessary to the FACET dump shielding to accommodate the LCLS-II transport line but there are not major concerns with its physical installation.

## 7.4 Personnel Protection and other Safety Systems

### 7.4.1 Overview

Two independent systems — the Personnel Protection Systems (PPS) and the Beam Containment System (BCS) — protect people from accidental exposure to high power beams and radiation. A third system, the Machine Protection System (MPS), is used to protect accelerator equipment. These systems exist for the present LCLS and FACET but will be altered to accommodate the new configuration of beamlines. A high-level overview showing these systems is given in Figure 7.4.

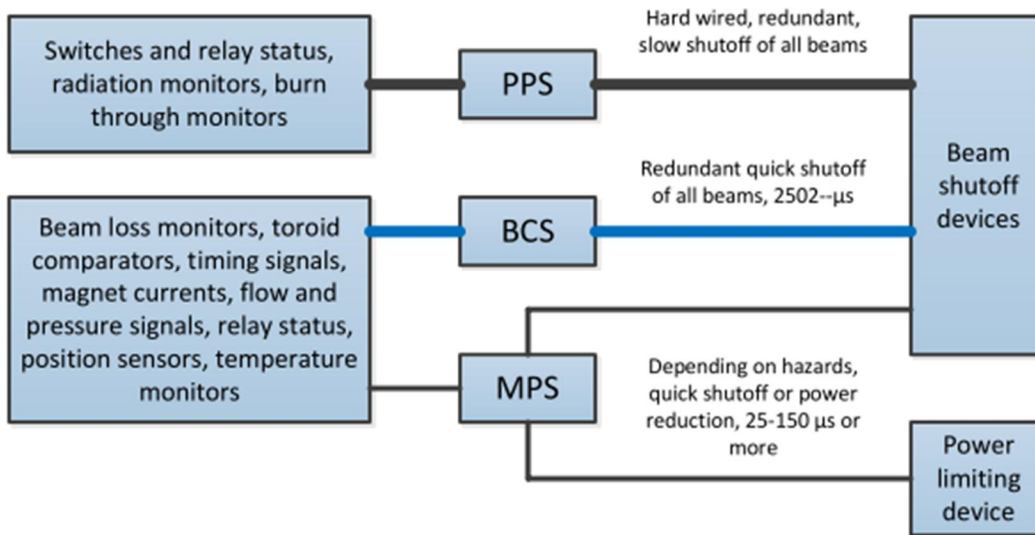


Figure 7.4. Overview of Controls for Safety Systems.

Safety systems must respond to two main types of hazards. One occurs when beams go astray. Such beams can quickly damage equipment, and they can produce intense radiation fields that are not adequately shielded, thus endangering people outside the radiation area. The other type of hazard occurs when the beam power runs away. In this type of event, the beam may damage a dump and also produce more radiation than the shielding can safely attenuate. The necessary response time and action to be performed depend on the specific safety system and hazard.

Table 7.1. Response Time Requirements for the Safety Systems for Controls

System	Response Time	Type of Response
PPS	$\leq 5$ s	Shut off all beams and the high power RF system
BCS	$\leq 100$ $\mu$ s	Shut off all beams
MPS	$\approx 150$ $\mu$ s	Limit beam power

Required response times and actions to be performed for the safety systems related to controls are given in Table 7.1. The response time is the time between when an event occurs and the

time a response is performed by the appropriate devices. In the case of the PPS and BCS system, the response is to turn off all beams. In the MPS case, depending on the location and severity, the response may be to reduce the beam power by dropping back to a less powerful beam mode, or turning off the beam in the most sensitive cases.

The required response time for the PPS system is relatively slow since it deals with access control. The time it takes a person to traverse the shortest distance from outside the accelerator enclosure, through the maze or shaft, to a point where the dose is not meaningfully shielded is estimated to be around 5 seconds.

The BCS system has to deal with the cases where a device malfunctions and excessive beam power is striking some aperture in the accelerator. In these situations, there could be excessive levels of radiation or the targeted location could be damaged by the highly concentrated thermal load, and the beam must be turned off quickly.

In the MPS case, the response varies depending on the MPS fault and the components at risk. Where the hazard is radiation damage, speed is not an issue, but proper integration or averaging of the radiation levels is needed. Devices which require the fastest response time are those that might be exposed to misdirected beams, such as vacuum chambers, septa, or halo collimators.

The existing FACET Personnel Protection System (PPS) includes the Linac from Sector 0 to 20, the damping rings and the positron vault. This needs to be modified to remove Sector 0 to 9 and the damping rings. The new FACET-II PPS zone will include only the region of the Linac between the new Sector 10 shielding wall and the existing Sector 20 shielding wall, in addition to the positron vault and the new injector vault in Sector 10. To facilitate access to the FACET-II experimental area, the Sector 19-20 PPS zone will be upgraded to allow controlled access.

The Beam Containment System (BCS) and Machine Protection System (MPS) will also require modifications to accommodate construction of LCLS-II in Sector 0 to 9. Many systems currently terminate in Sector 0 and these terminations will need to be relocated to Sector 10. Additional devices requiring Beam Containment Systems include the injector and the two bunch compressors in Sector 11 and 14.

#### 7.4.2 FACET-II Personnel Protection System

To remove the LCLS-II part of the Linac from the existing FACET PPS requires modifications to the hard-wired PPS connections in Building 3. The conduit and racks for the Sector 10 PPS is located in the Sector 10 alcove.

In addition to restoring the integrity of the PPS system for the FACET region, changes in the global logic are required. The FACET-II PPS must communicate with the LCLS-II PPS to ensure that LCLS-II beam is prevented unless FACET-II is in No Access. This is similar to the existing communication with the LCLS-I PPS system where FACET beam is prevented unless LCLS-I is in No Access. See Fig. 7.5, 7.6, 7.7 and 7.8 for minimal access states across the multiple accelerator programs. There may also be other hazards that are monitored and integrating with the PPS system such as ozone and residual radiation monitors.

Sector 10 and 11 are a single PPS “sector pair” and is configured as a unit that can be searched and secured. Sector 10 will be divided between the two programs LCLS-II and FACET-II with a solid wall delineating a new boundary mid-way in sector 10. Reconfiguration of this pair is therefore needed with the establishment of a “sector 10.5 and 11” PPS zone.

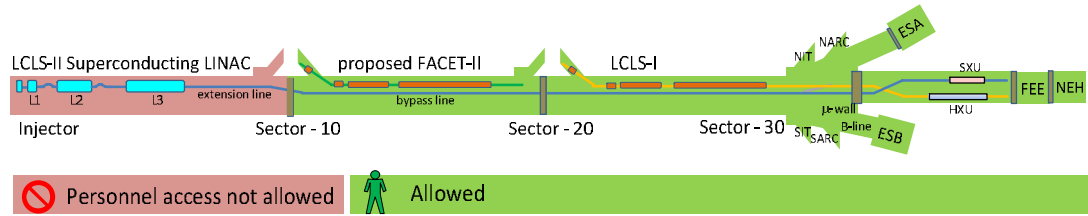


Figure 7.5: Minimal access state during LCLS II gun commissioning. This is a temporary mode for commissioning only. Access downstream of sector 10 is permitted.

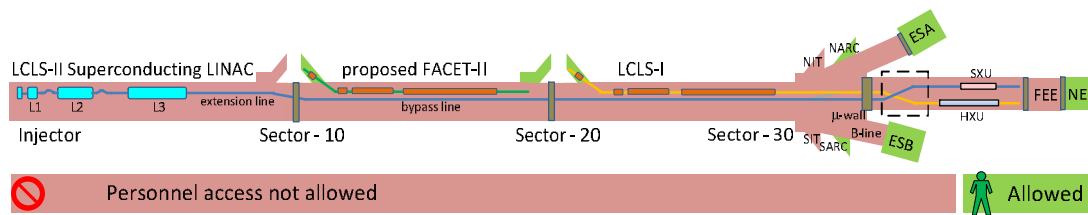


Figure 7.6: Minimal access state for LCLS II operation. No access is permitted to FACET-II if LCLS-II is operating. Sector 10 (FACET-II) and sector 20 (LCLS-I) injector vaults and the Sector 20 positron vault are likely to be accessible during LCLS-II operation based on preliminary radiological studies.

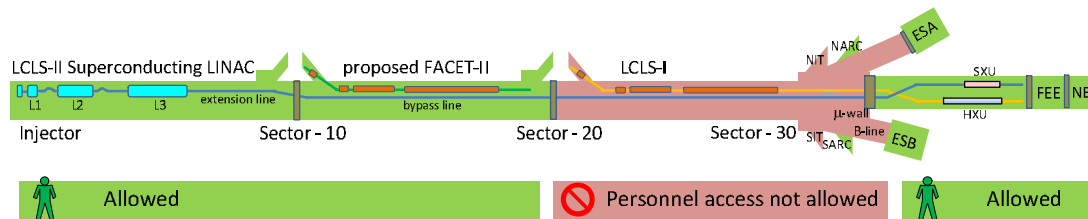


Figure 7.7: Minimal access state for LCLS I operation. FACET II can be in access conditions if LCLS-II is not operating regardless of LCLS-I operations.

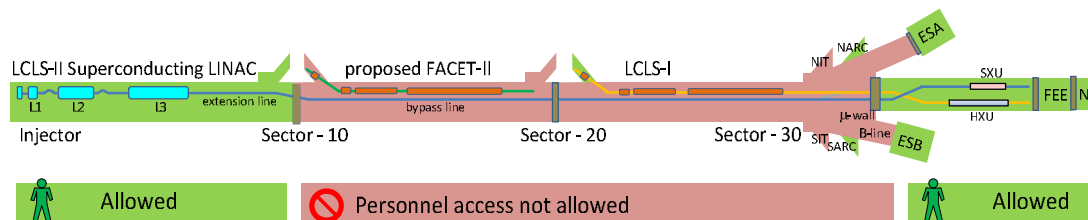


Figure 7.8: Minimal access state for FACET-II electron operations. LCLS-II can be in access due to the shield wall at sector 10. LCLS-I linac must be in no access.

### 7.4.3 Sector 20 PPS Zone

The existing PPS zone in Sector 19-20 will be upgraded to allow Controlled Access in addition to the current No Access and Permitted Access states. This requires the installation of two key

banks near the PPS door at the top of the Sector 19 stairs and appropriate modifications to the Sector pair PPS logic. Similar modifications are planned for the LCLS Sector pairs from Sector 21 to 30 and the system has already been designed and costs estimated. This will be a single Controlled Access area with no special logic for the gates at the ends of the region. Any breach of an end gate will drop the region to permitted Access and require a search.

#### 7.4.4 Beam Containment System

The Beam Containment System (BCS) is a safety system that keeps potentially dangerous accelerator beams within their prescribed channels and within allowed power limits, and hence prevents the generation of excessive level of radiation within occupied areas. The BCS also protects the integrity of safety-related beam line components. It performs this function by monitoring beam power and beam loss, and shutting beams down if a limit is exceeded.

The FACET Beam Containment System (BCS) must be modified to include only Sectors 10 to 20, the positron vault and the new Sector 10 injector and tune-up dump. In addition, the BCS for the existing chicane in Sector 10 will be relocated to the new BC2 in Sector 14 and a similar system installed for BC1 in Sector 11. In stage 2 of the project, additional BCS will be required for the new positron damping ring and its injection and extraction lines. The existing BCS in Sector 20 should be adequate when the second arm of the chicane is installed.

Ideally, the BCS should minimize the mutual interference across the FACET-II and LCLS-II programs by providing targeted shutoffs. Alternatively, a BCS fault anywhere could shut off both beams.

##### Shutoff Mechanisms:

Beam shut-off mechanisms comprise a key component in the BCS. There shall be three independent shut-off mechanisms for FACET-II, which mirrors the requirements of LCLS-I as recommended in the SLAC Radiation Safety Systems Technical Basis Document:

A dedicated BCS Laser Safety Shutter (LSS) will stop laser light from striking the RF Gun cathode, stopping the production of beam. This shutter will be situated as close to the production point of laser light as practicable.

The BCS will move the Gun from an accelerate time to a standby time. This will permit the gun to operate in order to maintain a constant duty factor and temperature.

RF timing signals will be rendered non-synchronous so that no beam or dark current can be accelerated.

Four independent shutoff paths variously drive these shutoff mechanisms.

##### BCS Sensors:

1. Protection Ion Chamber (PIC): Typically situated on or near the mechanical device that is to be protected.
2. Long Ion Chamber (LION): These are typically installed along the inside walls of the accelerator housings where shielding is inadequate.
3. Flow Switch: These are installed in cooling water systems for dumps, collimators, and slits.

4. Pressure Switch: These are installed in PIC and LION gas systems.
5. Microswitch: These are used to confirm the correct position of mechanical beam line components, such as stoppers.
6. Current Transducer: Used to monitor current in magnet power supply.
7. Toroid: These are current transformers that produce an output proportional to beam current.

#### 7.4.5 Machine Protection System

The role of the machine protection system (MPS) is to turn off the electron beam or limit the average power by lowering the repetition rate of the beam when a fault is detected. This measure is not a life safety system [see descriptions of Beam Containment System (BCS) and Personnel Protection System (PPS)], but is designed to prevent excessive losses of the electron beam, which would otherwise cause damage to sensitive machine components.

The existing FACET Machine Protection System (MPS) receives input from many different devices, such as vacuum valves, beam charge monitors, beam loss monitors, protection ion chambers, and beam position monitors. Based on the severity of the input signals, the MPS may either rate limit or completely shut off the beam. LCLS-II construction will necessitate relocating the tone loop receiver from sector 0 alcove to sector 10 alcove and reconfiguring the existing MPS system to remove offline hardware.

New MPS devices are only expected in the injector which will be an independent installation of hardware following mature LCLS-I designs.

MPS faults, whether from legacy devices or the new injector vault installation, will shut off the FACET-II electron beam using the same mechanisms as BCS faults.

### 7.5 *Control System Recovery*

#### 7.5.1 Overview

LCLS's dependence on the SLC control system was reduced through a linac upgrade project and is now able to operate without the legacy control system. FACET, NLCTA and ESTB programs are still dependent on the legacy control system.

Most installations in the FACET-II project will use the EPICS-based control system that is standard across LCLS. However, unmodified systems in the linac continue to use the legacy SLC control system.

The mixing of SLC and EPICS solutions throughout FACET-II will necessitate integrated displays, for example with BPMs.

To restore the legacy control system post demolition in the first ten sectors, hardware needs to be relocated from sector 0 and cables need to be cut and re-terminated at sector 10.

# 8 Positron Systems

---

---

## Technical Synopsis

*In order to achieve the scientific goals of the experimental program at FACET-II, a high positron peak current with small transverse and longitudinal emittance is required. FACET-II will operate with a positron energy up to 10 GeV. The most challenging parameters are for the plasma wakefield acceleration (PWFA) experiments which require a peak current of at least 2.0 kA. The positrons are produced by sending an electron bunch onto the existing positron target and capture section in Sector 19. The positron bunch is transported back to Sector 11 in the existing Positron Return Line. A new beamline that starts in Sector 11 takes the positrons from the Return Line and injects them into a new Damping Ring in the Sector 10 Linac tunnel. The energy of the beam from the positron production system is 210 MeV and the Damping Ring energy is 335 MeV, so 125 MeV of energy must be provided by S-band accelerating structures to be located in Sector 14. The accelerating structures will replace a section of the existing return line.*

*The positron beam into the damping ring has a very large transverse emittance that must be reduced by three orders of magnitude in a few milliseconds. Because the damping ring is located in the existing Linac tunnel, the diameter of the ring must be smaller than 3 meters. This constraint dictates a compact design with minimal gaps between the magnets in the arcs. The large injected beam size also dictates that the acceptance of the ring be large enough to accommodate on-axis injection. The proposed design incorporates many aspects of recent developments for diffraction-limited light sources. The beam energy is chosen to be 335 MeV which is as high as possible given the space constraints.*

*Given the compact dimensions, the magnet design for the damping ring arcs is particularly challenging. As proposed, the three dipole magnets in each arc cell are wound on a single block of steel, the arc quadrupoles have a very compact and innovative design, and the arc sextupoles are very thin permanent magnets. Conceptual designs for these magnets are described in Section 8.3.6. The straight sections contain both the injection, the extraction and the RF cavities. Vacuum requirements are not particularly challenging.*

*A second new positron beamline in Sector 10 takes the beam from the damping ring extraction point, performs a 1<sup>st</sup> stage of bunch compression and injects it into the last dipole magnet of the 1<sup>st</sup> electron bunch compressor (BC1) in Sector 11. All of the components of the injection and extraction lines are conventional. Once the positrons are injected into the Linac, they are accelerated to 10 GeV in Linac sections 2 and 3. The second stage of bunch compression is performed in a second arm of the bunch compressor in Sector 14 (BC2) and the 3<sup>rd</sup> stage in a second arm of the chicane in Sector 20, which is described in Chapter 9. They are focused to a transverse size of about 10 microns at the FACET Interaction Point and dumped at the end of Sector 20.*

*Simulations have been performed to demonstrate the performance of the transport lines and damping ring. Collective effects have been estimated analytically and appear to be controllable. It should be noted that this stage of the project is at the level of maturity of a Conceptual Design and has not yet had engineering designs of many of the support systems like power supplies, controls and vacuum.*

## 8.1 Positron System - Introduction and Overview

The FACET-II positron system design takes the beam from the existing positron target, capture section and return line, transporting it backwards to Sector 10. To match the 335 MeV energy of the damping ring, four sections of S-band acceleration (each 7 feet long and with ~20MV/m gradient) will be installed in Sector 14 of the return line. Starting in Sector 11, a new beamline brings the positrons from the existing return line and injects them into a small damping ring in the Sector 10 Linac tunnel. The beam from the damping ring undergoes a 1<sup>st</sup> stage of bunch compression and is then injected into the Linac at the Bunch Compressor in Sector 11, BC1. One constraint on the positron beamlines and damping ring is the path of the LCLS-II bypass line which has a dogleg section through Sector 10.

### 8.1.1 Requirements and Parameters

For the FACET-II experimental program, the positron beam must meet a specific set of requirements for emittance, peak current, energy, energy spread, and stability. These parameters are listed below in Table 8.1. A schematic layout of the positron system is also shown in Error! Reference source not found. with beam parameters listed at various points along the accelerator. The positron beam optics from the target to the reinjection point in Sector 11 is plotted in Figure 8.2. The design collimator settings of the beam are chosen to maximize the delivered peak beam current whilst keeping the transverse spot size at the experimental IP location below 10  $\mu\text{m}$ .

Table 8.1. Nominal positron beam parameters at the FACET IP and their operational ranges.

Parameter	Symbol	Unit	Nominal	Range
Final positron energy	$E_f$	GeV	10	4 – 13.7
Initial bunch charge from PDR	$Q_0$	nC	2	1 - 2
Final bunch charge at IP	$Q$	nC	0.6	0.6-2
Pulse repetition rate	$f_{rep}$	Hz	5	1 - 5
Number of bunches per RF pulse	$N_b$	-	1	1
Transverse core beam size (x/y, rms)	$\sigma_x/\sigma_y$	$\mu\text{m}$	10/7	10-35/7-10
Peak current	$I_{pk}$	kA	12	12 – 15.5
Bunch length (rms)	$\sigma_z$	$\mu\text{m}$	7	7 – 11
rms energy spread	$\sigma_E/E$	%	0.5	0.5 – 1.5
Max. avg. $e^+$ beam power (10 GeV, 2 nC, 5 Hz, 1 bunch/pulse)	$P_b$	W	100	6 – 100

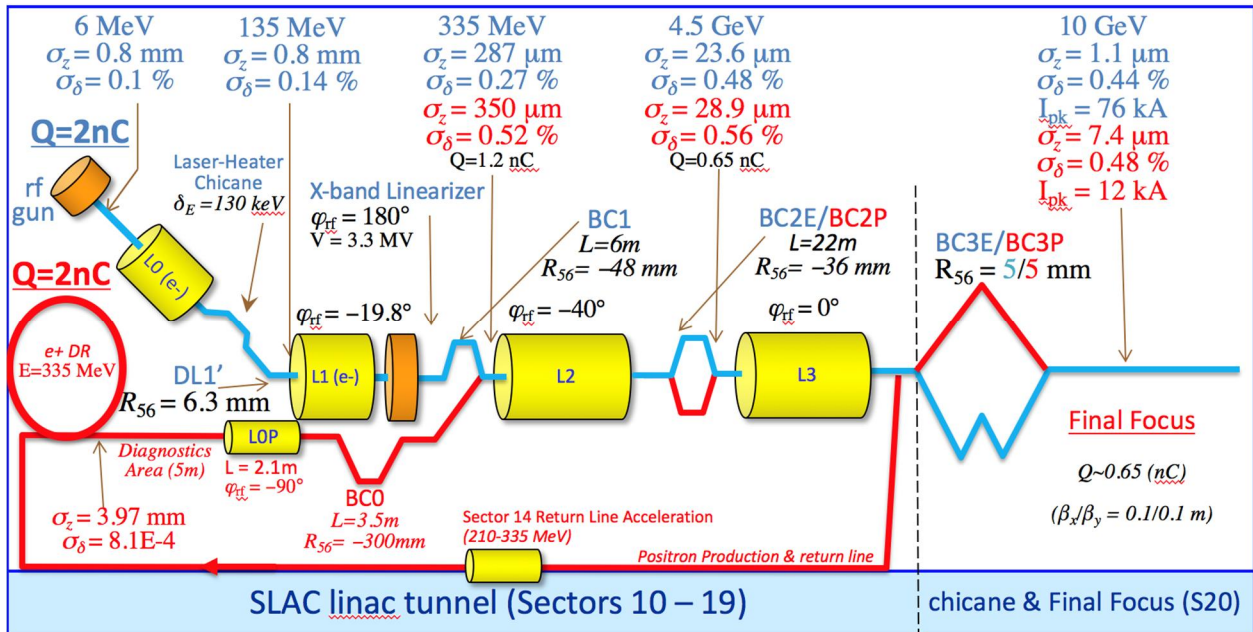


Figure 8.1. Schematic layout of FACET-II injector, linac, bunch compressors, and experimental area, with main parameters listed for operation. The blue sections depict the electron specific and common  $e^-/e^+$  areas. The red sections are for positrons.

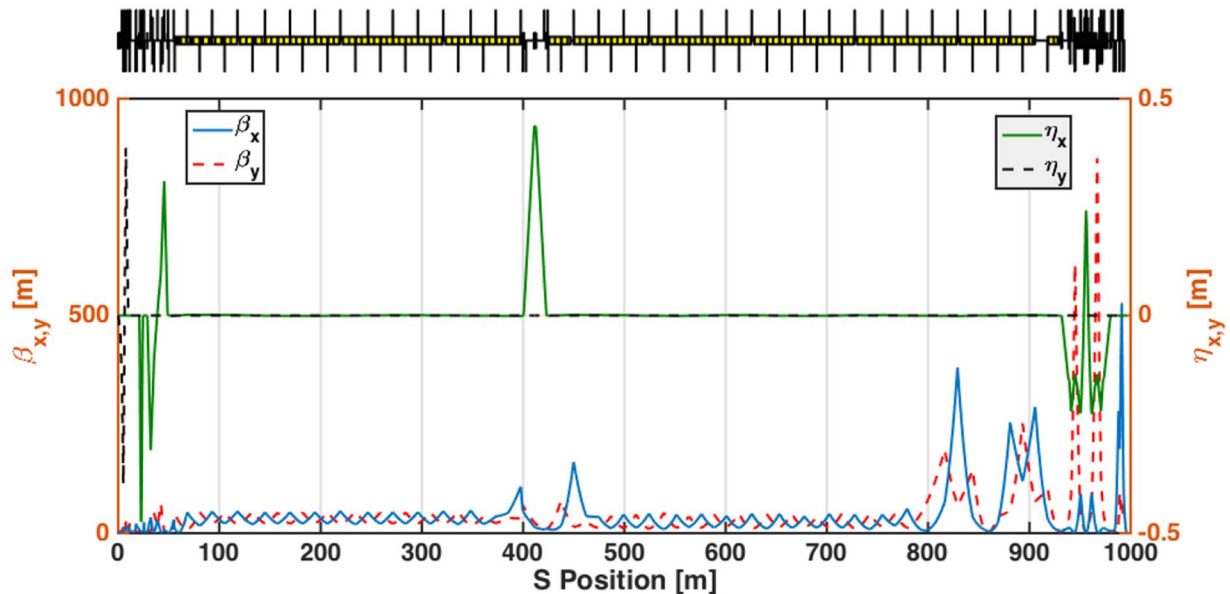


Figure 8.2a : Positron optics from exit of positron damping ring (at 335 MeV) to the start of the experimental IP area. The positrons are injected into the existing Linac at the last bend magnet of BC1. There are three stages of bunch compression: BC0 in the extraction line; a second arm of BC2 in Sector 14; and the new "sailboat chicane" in Sector 20.

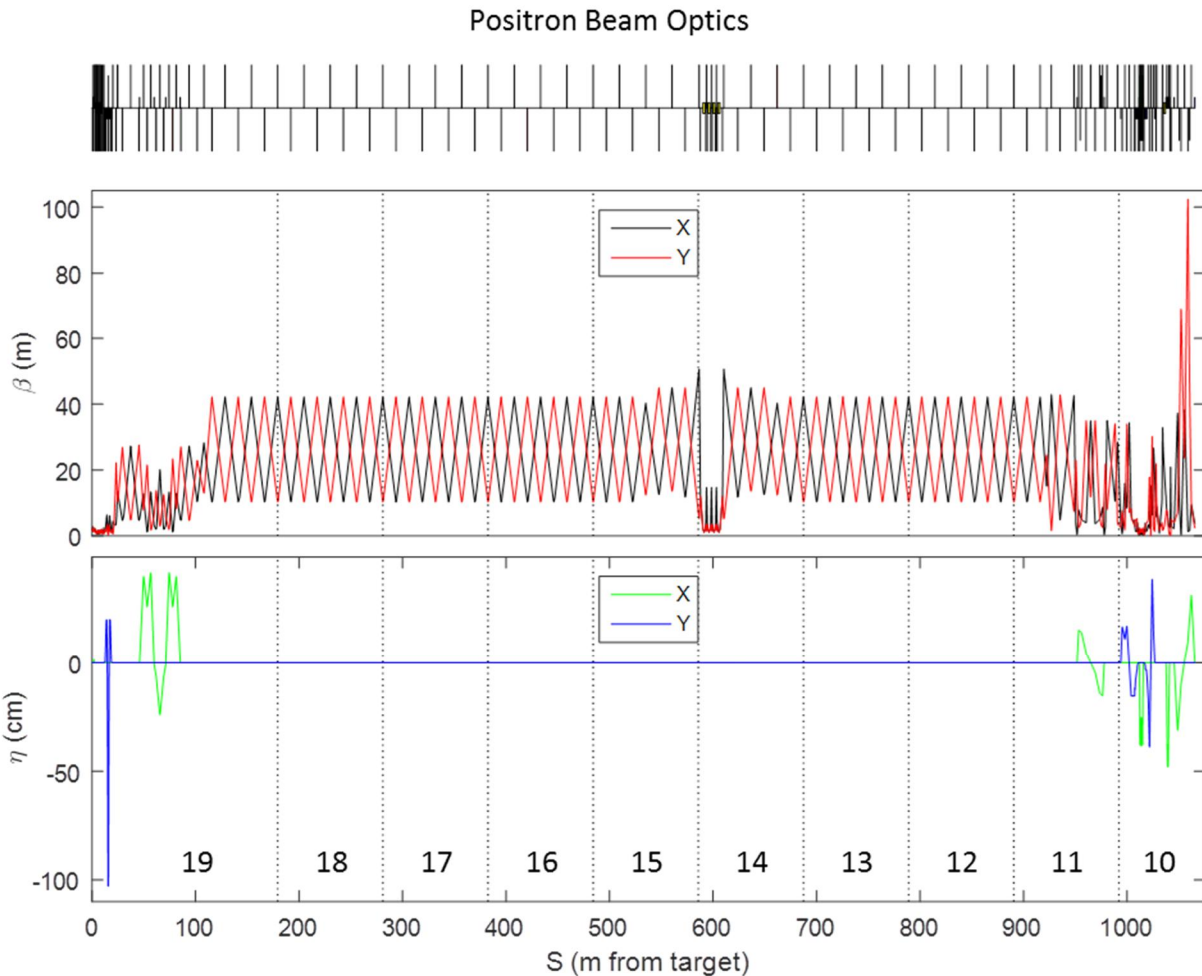


Figure 8.2b. Positron beam optics from the target to the reinjection point in Sector 11. Sector numbers are indicated at the bottom. Note that the dispersion ( $\eta$ ) is shown in cm. This includes the existing capture section, the return line with new accelerating structures in Sector 14, the new damping ring and the new injection and extraction lines in Sector 10.

### 8.1.2 Brief Description of the Positron System

A single bunch of positrons is generated at a 5-Hz repetition rate from a 10 GeV electron bunch impinging on an existing rotating WRe target in Sector 19. The positrons are captured in the flux concentrator and capture section and accelerated to 210 MeV. They are injected into the Positron Return Line (PRL) and transported back to Sector 10 where a new injection line brings them into a new damping ring (DR). The energy of the damping ring is 335 MeV so there will be 125 MeV of S-band acceleration installed in Sector 14 of the existing return line. A new extraction line takes the beam from the damping ring, performs the first stage of bunch compression and injects it into the main linac at the last magnet of the BC1 chicane in Sector 11.

### 8.1.3 Positron Yield

The positron source in Sector 19 was originally constructed for the SLC. In SLC operation, a 6.5nC electron beam at 33 GeV had a yield of approximately 4.4 positrons per incident electron after the 210

MeV capture section. However, the ultimate yield through the system, defined by the number of positrons exiting the damping ring per incident electron, was roughly 1:1. For FACET operation, a 20.35 GeV electron beam with 3.2nC has a measured yield at 200 MeV of 2.5:1 positrons per incident electron. In spite of the roughly 60% reduction in yield from the target, the yield of positrons from the damping ring remains approximately 1:1 after optimization through the rest of the positron return line. For FACET-II, the incident electron beam energy is only 10 GeV. However, given the experience with positron operation in FACET, it is predicted that the final system yield should be no worse than 0.5:1. To verify this assumption, machine studies are planned during the Spring 2016 FACET run to test the full system yield with 10 GeV incident electrons on the positron target.

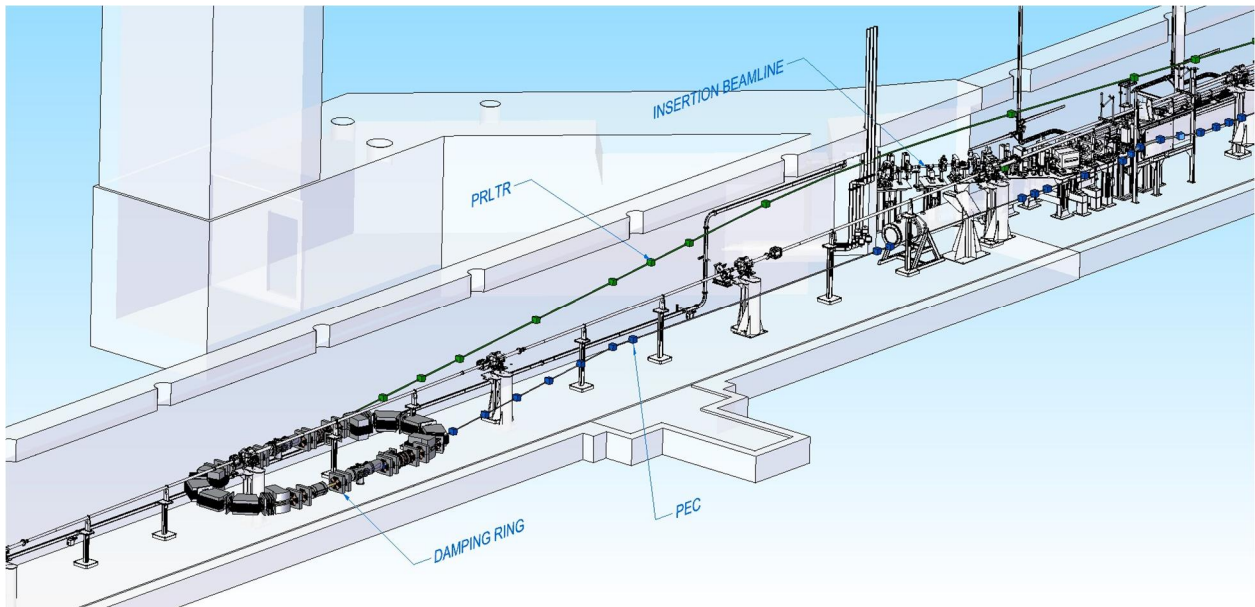
The expected positron yield can be approximated as a function of the scavenger electron beam energy area density per pulse and rms radius incident on the positron target and the damping ring physical acceptance:

$$N^+ \sim \epsilon \sigma \rho [1],$$

where,

$$\rho = \frac{N^- E^-}{\pi \sigma^2}$$

Comparing expected running conditions at FACET-II with FACET: to maintain a similar positron flux from the target while keeping the same level of energy area density (so as to not increase the risk of damaging the positron target) the rms radius of the incident electron beam should be reduced by  $\frac{\sigma}{\sigma_0} \sim 0.79$  for 4 (vs. 3.2) nC charge and 10 (vs. 20) GeV. To achieve the required 0.5:1 positron to incident electron ratio this implies a minimum relative positron damping ring (PDR) injection acceptance of  $\frac{\epsilon}{\epsilon_0} \sim 0.63$  compared to FACET.



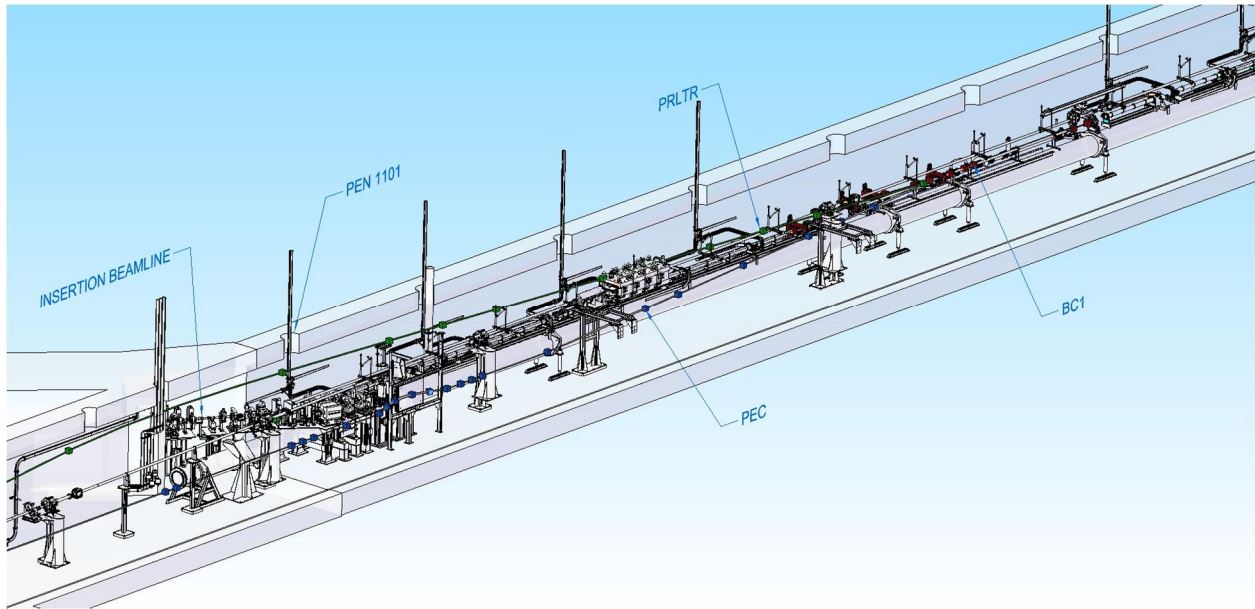


Figure 8.3. Layout of positron damping ring and injection and extraction lines in the Sector 10 tunnel. (This layout is being revised for the current design described in this text. The damping ring has been moved upstream in Sector 10 and the new magnet designs fit correctly in the tunnel. The figure is included here as evidence that all beamlines fit in a 3D layout.)

## 8.2 PRLTR – Positron Return Line to Damping Ring

### 8.2.1 Overview

This beamline section is responsible for accelerating the positrons to 335 MeV and transporting them to Sector 11 through the existing Positron Return Line (PRL), which is 18" below the ceiling of the linac tunnel. The positrons are matched and injected into the damping ring (PDR) in a new beamline in Sector 10. To accomplish this, four new beamline sections are specified below and shown in Figures 8.4, 8.5, 8.6 and 8.7. These are required to accelerate the beam to 335 MeV, translate the beam horizontally 103" across the accelerator housing, then down vertically 74", and finally into the new PDR.

#### 8.2.1.1. Acceleration in Sector 14

Four 7-foot S-band accelerating structures accelerate the positron beam in the return line on crest from 210 MeV to 335 MeV. Each structure, fed 25% of the power of a standard klystron, is capable of providing up to ~42 MeV (19.7 MeV/m). This maintains a comfortable 25% energy overhead. RF station 14-8, made available due to the installation of BC2 at the end of Sector 14, will be used to power these four new structures. The PRL consists of 25.4 m long FODO cells (4 cells per sector) with a phase advance per cell of 75° in both planes, and with  $\beta$ -function peaks of ~42 m. Because of the large emittance of the positron beam, the PRL quadrupoles have 4.625" diameters. The S-band accelerating structure, on the other hand, has a 0.75" iris diameter (minimum aperture in structure). In order to squeeze the positrons through the structures, a quadrupole doublet is first used to step the PRL  $\beta$ -functions down to ~2 m at the entrance to the first structure. The structures are then separated by quadrupole triplets which maintain the small beam size. After acceleration the process is reversed with another quadrupole doublet and matched back into the PRL optics. This section replaces a single PRL FODO cell. Figure 8.4 shows this rms beam size in greater detail. Table 8.3 lists the quadrupole magnet parameters.

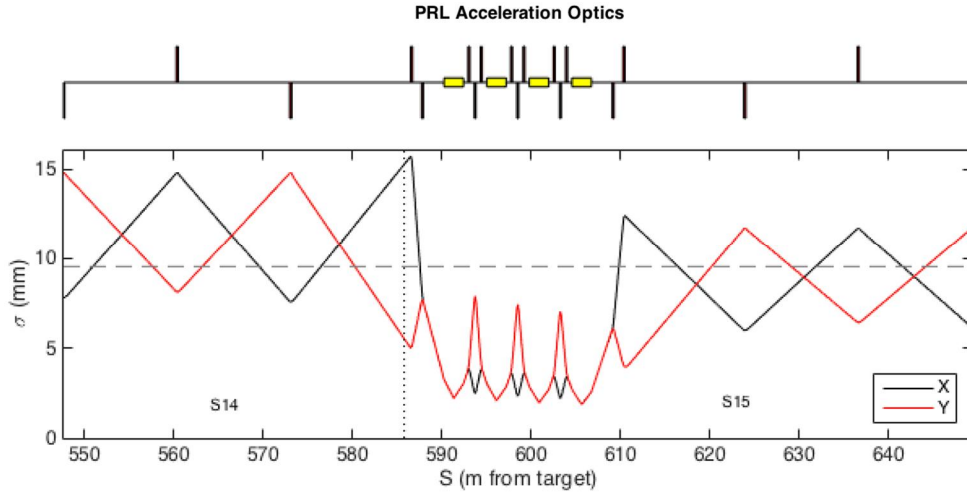


Figure 8.4. Positron acceleration optics in Sector 14. The accelerator iris radius is indicated with a faint gray dashed line. The indicated rms beam sizes are  $\sqrt{\epsilon\beta}$ .

### 8.2.1.2. Horizontal dogleg

In Sector 11, six quadrupole magnets are provided to match the beam from the PRL FODO lattice into the horizontal dogleg. A pair of rectangular bending magnets (bend angle = 100 mrad), 7 quadrupoles and 2 chromatic correction sextupoles translate the beam 103" horizontally across the accelerator housing in a z length of 86'. The downstream end of the dogleg is placed so as not to interfere with the LCLS-II BRB2 bend magnet installation. Figure 8.5 shows the optics of the PRL match and the horizontal dogleg.

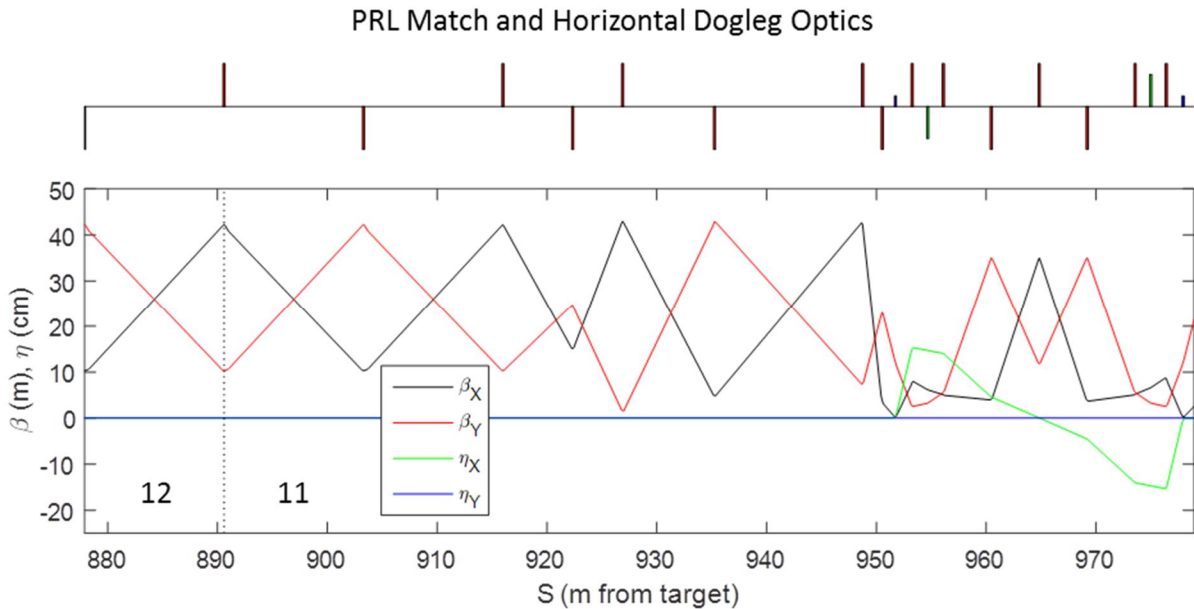


Figure 8.5. PRL match and Horizontal Dogleg optics in Sector 11. Note that the dispersion ( $\eta$ ) is shown in cm.

### 8.2.1.3. Vertical inflector

Four quadrupoles are used to match the beam from the horizontal dogleg into the vertical inflector. The angle of the inflector is set by the PDR injection trajectory at 125 mrad. A rectangular bending magnet (bend angle = 125 mrad), 5 quadrupoles and 2 chromatic correction sextupoles comprise the initial part of the inflector. The final components of the inflector, including the PDR septum and kicker, are described below. The inflector translates the beam from the PRL at a height of 36" above the Linac beamline into the PDR at a height of 38" below the Linac beamline in a length of 56'. Figure 8.6 shows the optics of the match and the vertical inflector, including PDR injection.

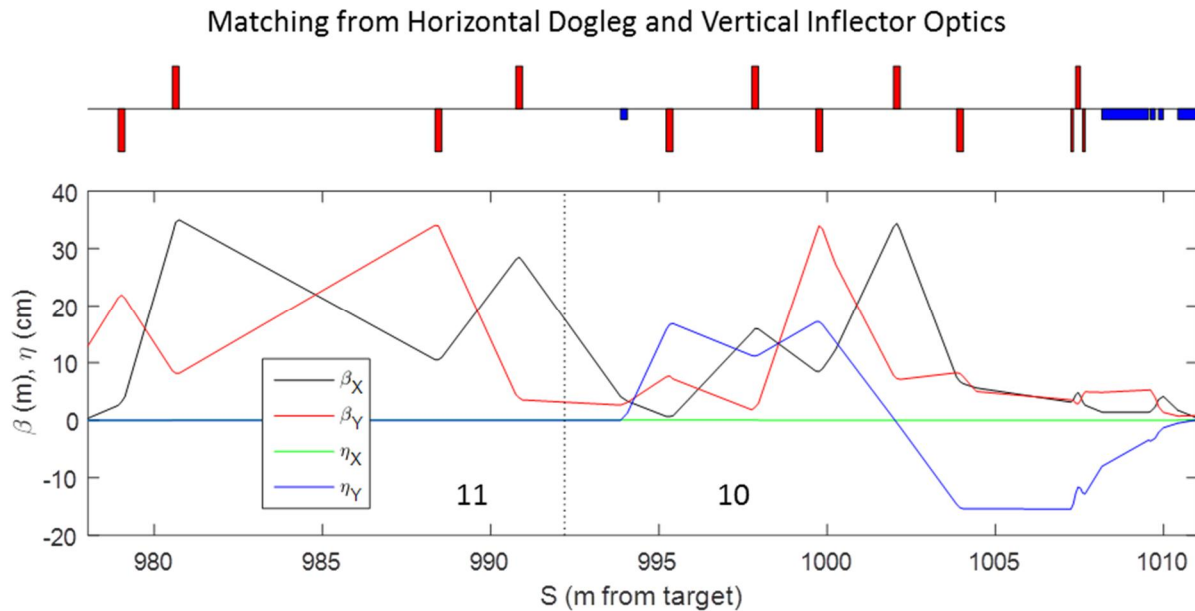


Figure 8.6. Match from the dogleg and Vertical Inflector optics in Sector 10. Note that the dispersion ( $\eta$ ) is shown in cm, and that the sextupoles are not shown.

#### 8.2.1.4. Damping Ring Injection

The final magnet in the initial part of the inflector is kept at least 3.5" back from the PDR footprint. As the positrons approach the PDR injection straight section vertically, they must first clear the edge of one of the PDR RF cavities, 9.5" above the plane of the ring. A 2.8 m drift allows the beam to pass above some PDR magnets and the RF cavity. Then, a compact triplet of permanent magnet quadrupoles<sup>1</sup> (total length = 42 cm) matches the Twiss  $\alpha$  and  $\eta$  of the injecting beam to the PDR optics. The triplet is installed above the space in the PDR between the RF cavity and the adjacent QFI quadrupole. The PDR QFI and QDI quadrupoles near the upstream face of the injection septum (vertical bend) will be of a narrow frame "Collins" design (full yoke height of  $\leq 200$  mm), allowing the injecting beam to pass above them, outside of their yokes. The beam then enters the injection septum (angle = 123 mrad) at a height of 116 mm above the plane of the PDR, passes off-axis through the (large) bores of the PDR QDI and QFI quadrupoles near the downstream face of the injection septum, and finally is kicked vertically onto the PDR centerline by the injection kicker (angle = 17.5 mrad). Figure 8.7 shows this injection scheme.

<sup>1</sup> Permanent magnet quadrupoles have previously been fabricated for the SLC damping rings with 5 kG/cm gradient and 5" outer diameter. The maximum required gradient proposed for this FACET-II section is 2.8 kG/cm.

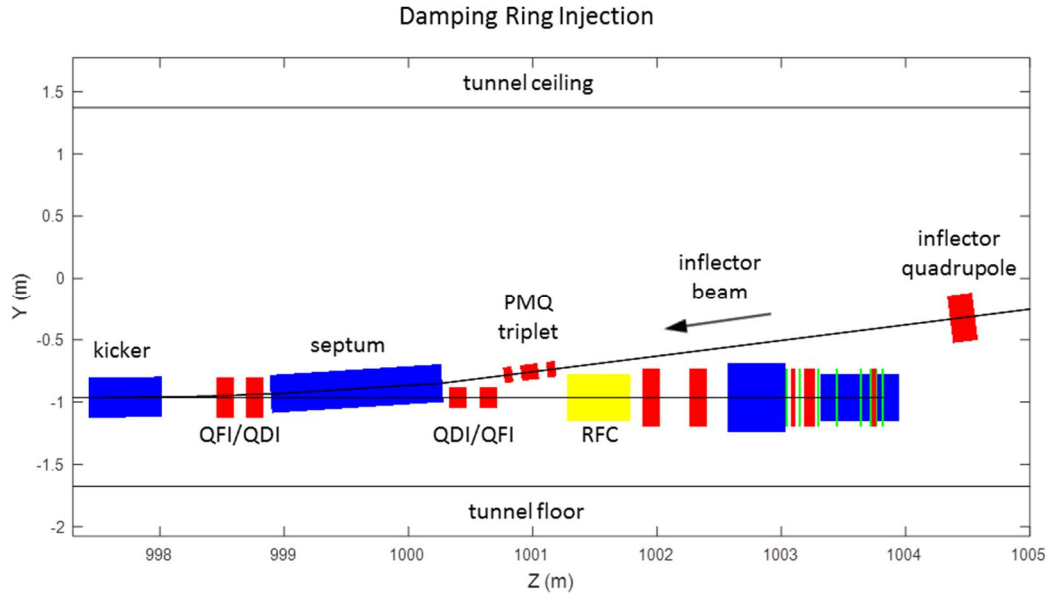


Figure 8.7. Vertical injection into the Damping Ring. RFC is the RF cavity and PMQ are permanent magnet quadrupoles.

#### 8.2.1.5. Septa and kickers

The Damping Ring injection septum will be a current-sheet device, modeled after the existing SLC e+ Damping Ring injection septum, which deflects the injecting beam vertically by a total of 123 mrad; the assumed magnetic length of the septum is 1.38 m. The normalized (invariant) emittances of the injecting e+ beam are  $\nu\epsilon_{x/y} = 2$  mm-rad; the matched beta functions of the Damping Ring optics at the ends of the septum are  $\beta_{x/y} = 1.390/5.291$  m. At 335 MeV, the beam size is  $\sigma_{x/y} = 2.059/4.018$  mm. The clear aperture for both the injecting beam and the Damping Ring beam should be approximately 1" high by 0.5" wide in order to accept  $\pm 3\sigma$  of the injecting beam. The blade of the septum is assumed to be 4 mm thick. The injecting channel of the septum is assumed to follow the injection trajectory, so that the injecting beam is always in the center of the aperture. Figure 8.8 shows the proposed septum geometry at the kicker (downstream) end of the septum. The extraction septum will be identical to the injection septum.

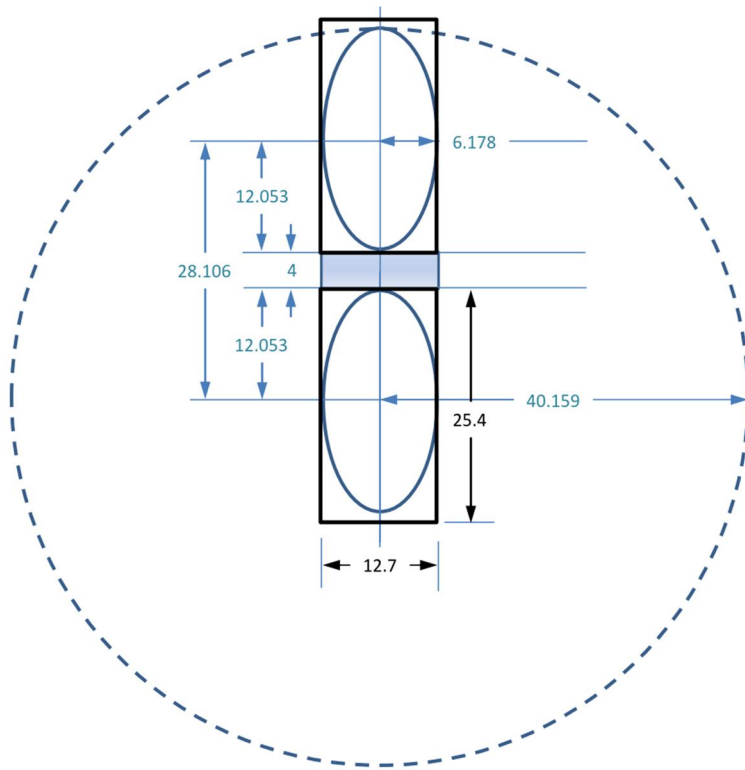


Figure 8.8. Injection septum geometry (kicker end); drawing is to scale, and all dimensions are in mm. The beam ellipses (blue) show  $\pm 3\sigma$  of the injected beam, matched to the nominal e+ Damping Ring optics at this point. The black rectangles show the septum apertures. The blue shaded region shows the septum blade. The blue dashed circle represents the bore of the Damping Ring QFI and QDI quadrupoles between the septum and kicker.

For the injection kicker, we will reuse the existing SLC e+ Damping Ring kicker, rotated to kick vertically. Looking at injection in reverse, the kicker must generate 28.106 mm of vertical offset at the entrance to the septum in order to allow  $\pm 3\sigma$  on both sides of the septum blade. Given the present FACET-II e+ Damping Ring optics, this implies a kick angle of 17.5 mrad; the magnetic length of the kicker is 0.59 m. The existing SLC Damping Ring kicker angle is 6.35 mrad at 1.19 GeV ... at 335 MeV this angle would be 22.5 mrad. The kicker has a 20 mm bore, which is adequate for  $\pm 3\sigma$  of the injected beam plus the vertical trajectory offset at the downstream end of the kicker (8.3 mm). Figure (8B) shows the injecting and Damping Ring beam in the injection area, with the  $\pm 3\sigma$  beam envelopes shown. The extraction kicker will be identical to the injection kicker.

The QFI and QDI quadrupoles between the kicker and septum (QDI being closest to the septum) must have a bore that allows for  $9\sigma$  of the injected beam plus the septum blade thickness, centered on the Damping Ring orbit ... 40.159 mm radius, or 3.162" bore.

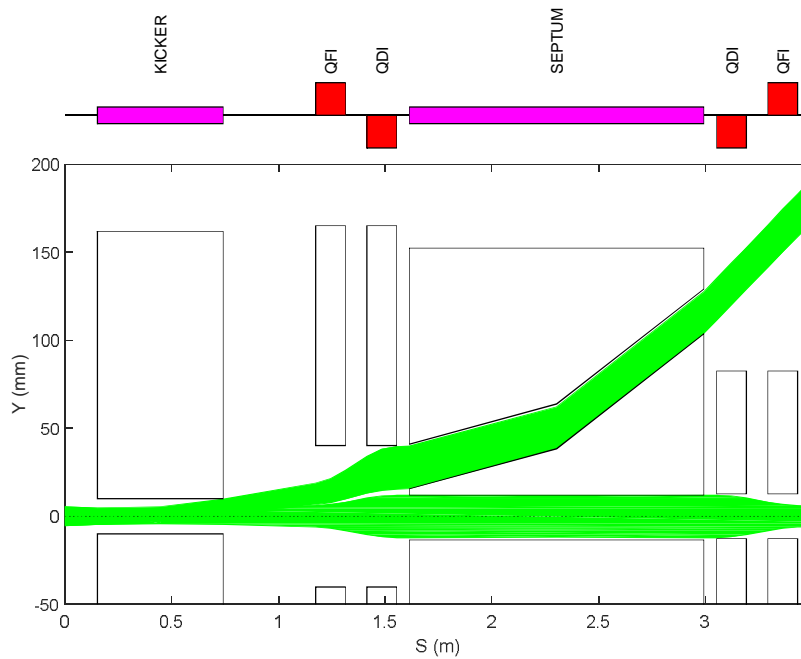


Figure 8.9: PDR injection. Beam injects vertically (from right to left in this Figure).  $\pm 3\sigma$  envelopes of injecting and 1<sup>st</sup> turn beams are shown in green. Kicker and septum apertures are shown. Apertures of large-bore quadrupoles ( $S < S_{\text{septum}}$ ), and apertures and yokes of narrow-frame quadrupoles ( $S > S_{\text{septum}}$ ) are included.

## 8.2.2 Beam Parameters

This system is designed given the measured PRL beam parameters and existing optics and matches into the required optics at the PDR injection point. A 4 nC “scavenger” electron pulse is generated in the linac specifically for positron production. For FACET operations at 20 GeV, a 1:1 ratio between scavenger electron beam charge and extracted positron beam (from positron damping ring) was routinely achieved. For operations at FACET-II at 10 GeV, a pessimistic assumption is made here where the final positron yield is reduced by a relative factor of 2 compared with FACET operations (see 8.1.3).

Table 8.2. Beam parameters for beamline section injecting into PDR in Sectors 10 and 11.

Parameter	Symbol	Unit	Nominal	Range
Beam Energy	$E$	MeV	335	-
Initial Transverse Emittance	$\gamma\epsilon_x / \gamma\epsilon_y$	mm.rad	2.0 / 2.0	-
Final Transverse Emittance	$\gamma\epsilon_x / \gamma\epsilon_y$	mm.rad	2.5 / 2.2	-
Initial Twiss (At entrance to first horizontal dogleg bend)	$\beta_x / \alpha_x$ $\beta_y / \alpha_y$	m	0.352 / -0.040 12.918 / 4.082	-
Final Twiss (At exit of injection kicker)	$\beta_x / \alpha_x$ $\beta_y / \alpha_y$	m	0.335 / 0.243 8.813 / -0.555	-
Initial Bunch Length (rms)	$\sigma_z$	mm	3	-
Final Bunch Length (rms)	$\sigma_z$	mm	3	-

Initial Energy Spread (rms)	$\sigma_E/E$	%	1.0	-
Final Energy Spread (rms)	$\sigma_E/E$	%	1.1	-
Initial Bunch Charge	Q		4	
Final Bunch Charge (in PDR)	Q		2	1-2

### 8.2.3 Beam Dynamics

Using a 6D tracking code (Lucretia), a 1M macro-particle representation of the positron bunch is tracked through the lattice. Figure 8.10 shows the tracked projected transverse emittance through the PRL and injection into the PDR. Some chromatic emittance growth (~5%) is present as the beta functions are shrunk to fit the beam within the S-band structure iris apertures, and also within the two doglegs as the beam is injected into the PDR (<20%). Optimization of the chromatic emittance growth in this final section using sextupole magnets is envisioned before construction. Chromatic emittance dilution through the accelerating structure can also be optimized by adjusting the beta functions (quadrupole strengths) between horizontal and vertical dimensions in the focusing triplets depending on required final emittance estimates after optimizing the dogleg systems. Figure 8.11 shows the longitudinal and transverse phase space of the tracked beam at injection into the PDR.

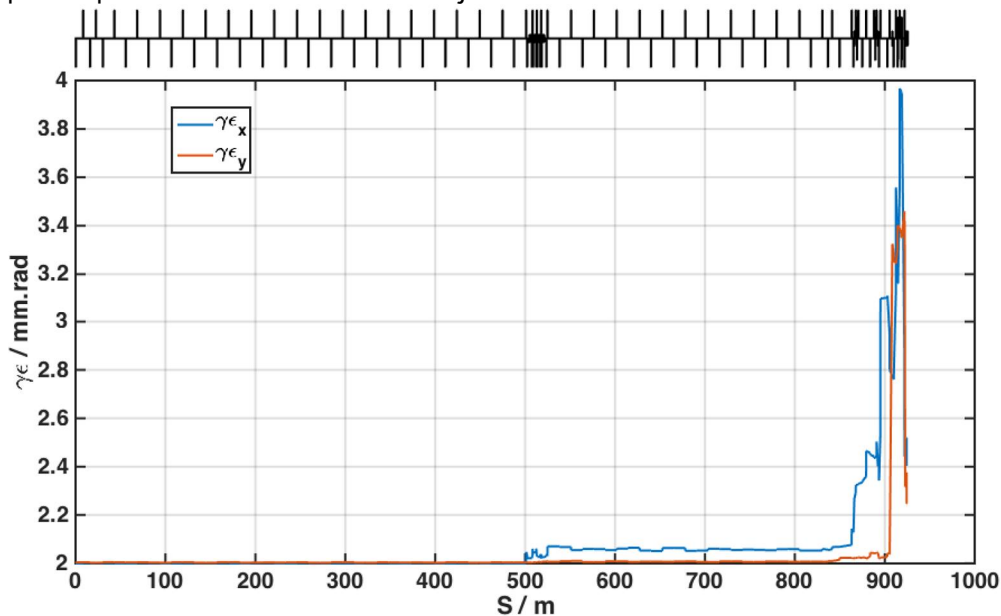


Figure 8.10. Transverse emittance of tracked beam through PRL and double dogleg injection into positron damping ring.

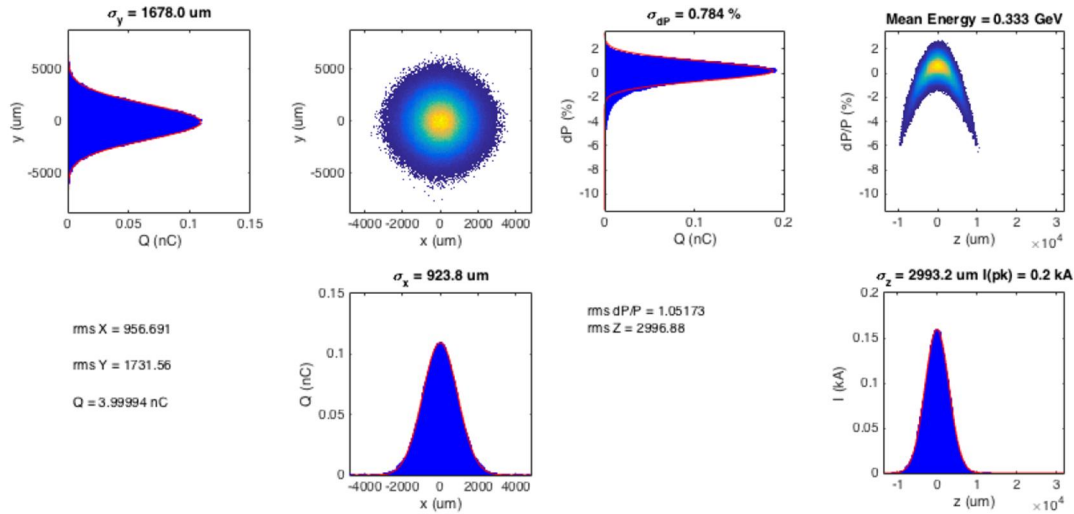


Figure 8.11. Transverse and longitudinal phase-space of tracked macro-particle bunch at the PDR injection point.

## 8.2.4 Magnets

The special optics in Sector 14 requires 13 new quadrupole magnets of 3 engineering types. The remainder of the system downstream of the PRL consists of 25 quadrupole magnets of 3 engineering types; 4 sextupole magnets of 2 engineering types; 3 dipole magnets of 1 type.

### 8.2.4.1 Quadrupoles

Table 8.3. Quadrupole magnet parameters for new magnets in Sector 14

Deck Name	Engineering Type / subsection	Effective Length / m	Design Int. Gradient / T	Max.   Int. Gradient / T	Design Pole Tip Field / T	Max  Pole Tip Field / T	Aperture (radius) / mm	Beam Energy / MeV
QLTRA1	A	0.211	0.3307	1	0.0998	0.30	63.691	210
QLTRA2	B	0.2	-0.4031	3	-0.1284	0.96	63.691	210
QT11	C	0.2	-0.8606	3	-0.1384	0.48	32.169	241.25
QT12	C	0.2	1.2615	3	0.2029	0.48	32.169	241.25
QT13	C	0.2	-0.8606	3	-0.1384	0.48	32.169	241.25
QT21	C	0.2	-0.9721	3	-0.1564	0.48	32.169	272.5
QT22	C	0.2	1.4249	3	0.2292	0.48	32.169	272.5
QT23	C	0.2	-0.9721	3	-0.1564	0.48	32.169	272.5
QT31	C	0.2	-1.0836	3	-0.1743	0.48	32.169	303.75
QT32	C	0.2	1.5883	3	0.2555	0.48	32.169	303.75
QT33	C	0.2	-1.0836	3	-0.1743	0.48	32.169	303.75
QLTRA3	B	0.2	-0.6431	3	-0.2048	0.96	63.691	335
QLTRA4	A	0.211	0.5276	1	0.1592	0.30	63.691	335

Table 8.4. Quadrupole magnet parameters for the Sector 10-11 systems.

Deck Name	Engineering Type / subsection	Effective Length / m	Design Int. Gradient / T	Max. Int. Gradient / T	Design Pole Tip Field / T	Max Pole Tip Field /  T	Aperture (radius) / mm
QLTRM1	D	0.2	0.1292	1	0.0380	0.29	58.737
QLTRM2	D	0.2	-0.2758	1	-0.0810	0.29	58.737
QLTRM3	D	0.2	0.2023	1	0.0594	0.29	58.737
QLTRM4	D	0.2	-0.1988	1	-0.0584	0.29	58.737
QLTRM5	D	0.2	0.5266	1	0.1547	0.29	58.737
QLTRM6	D	0.2	-0.5546	1	-0.1629	0.29	58.737
QLTRH6	E	0.2	0.7822	2	0.1258	0.32	32.169
QLTRH5	E	0.2	0.1370	2	0.0220	0.32	32.169
QLTRH4	D	0.2	-0.2740	1	-0.0805	0.29	58.737
QLTRH3	D	0.2	0.3570	1	0.1049	0.29	58.737
QLTRH2	D	0.2	-0.2740	1	-0.0805	0.29	58.737
QLTRH1	E	0.2	0.1370	2	0.0220	0.32	32.169
QLTRH0	E	0.2	0.7822	2	0.1258	0.32	32.169
QLTRD4	D	0.2	-0.5646	1	-0.1658	0.29	58.737
QLTRD3	D	0.2	0.5732	1	0.1683	0.29	58.737
QLTRD2	D	0.2	-0.4016	1	-0.1179	0.29	58.737
QLTRD1	D	0.2	0.4329	1	0.1271	0.29	58.737
QLTRV5	E	0.2	-1.0095	2	-0.1624	0.32	32.169
QLTRV4	D	0.2	0.5756	1	0.1690	0.29	58.737
QLTRV3	D	0.2	-0.7282	1	-0.2139	0.29	58.737
QLTRV2	D	0.2	0.6048	1	0.1776	0.29	58.737
QLTRV1	E	0.2	-0.5885	2	-0.0947	0.64	32.169
PMQ3	F	0.07	-1.9031	4	-0.6995	1.47	25.730
PMQ2	F	0.14	3.6053	4	0.6626	0.74	25.730
PMQ1	F	0.07	-1.9031	4	-0.6995	1.47	25.730

### 8.2.4.2 Sextupoles

It is assumed that each sextupole is mounted on a remotely controllable motion stage, capable of +/- 2mm motion in x/y with 5 $\mu$ m precision. The final sextupole strengths are still being optimized.

Table 8.4. Sextupole magnet parameters for the Sector10-11 systems

Deck Name	Engineering Type / subsection	Effective Length / m	Design Int. Strength / T.m <sup>-1</sup>	Max. Int. Strength /  T.m <sup>-1</sup>	Design Pole Tip Field / T	Max Pole Tip Field /  T	Aperture (radius) / mm
SLTRH2	G	0.2	-11.500	20	-0.575	1.0	100
SLTRH1	G	0.2	-0.036	20	-0.002	1.0	100
SLTRV2	G	0.2	0.420	20	0.021	1.0	100
SLTRV1	H	0.2	0.050	10	0.005	0.98	140

### 8.2.4.3 Dipoles

Table 8.5. Dipole magnet parameters

Deck Name	Engineering Type / subsection	Effective Length / m	Design Int. Field / T.m	Max. Int. Field/T.m	Design Pole Tip Field / T	Max Pole Tip Field / T	Aperture (radius) / mm
BPRLTR1	I	0.203	0.1117	0.2	0.5499	0.98	30.4
BPRLTR2	I	0.203	-0.1117	0.2	-0.5499	0.98	30.4
BPRLTR3	I	0.203	0.1398	0.2	0.6879	0.98	30.4

## 8.3 Positron Damping Ring

### 8.3.1 Introduction

As the positron beam emerges from the target and reaches an energy of E=335 MeV, it has a normalized transverse emittance  $\gamma\epsilon$  of 2.5/2.2 mm-rad in the horizontal and vertical planes, respectively. This emittance is three orders of magnitude larger than the electron beam out of the photo-injector. A damping ring is necessary to reduce the positron x and y emittance values to  $\mu$ m-rad level in a few milliseconds. For practical reasons, the ring is placed in sector 10 inside the existing linac tunnel. This implies that the diameter of the ring has to be smaller than 3 meters. This constraint dictates a compact design with minimal gaps between the magnets in the arcs.

Given a large injected beam size, the acceptance of the ring has to be large enough to accommodate an on-axis injection. Here, accumulation is not necessary because only a single bunch is to be damped in the ring at a given time. To provide adequate intensity for the experiment, a charge of 1-2 nC is required per positron bunch. The bunched beam has to be collectively stable as its emittance decreases in the ring. Moreover, the extracted emittance will include growth due to intra-beam scattering (IBS) during storage.

Table 8.6. Main parameters of the positron damping ring

Parameter	Value
Energy, $E$ [MeV]	335.0
Circumference, $C$ [m]	20.15
Tune, $\nu_x, \nu_y, \nu_z$	4.586, 2.615, 0.0383
Normalized emittance, $\gamma\epsilon_0$ [ $\mu\text{m-rad}$ ]	7.28
Bunch length, $\sigma_{z0}$ [mm]	2.23
Energy spread, $\sigma_{\delta 0}$	$4.84 \cdot 10^{-4}$
Momentum compaction	$5.84 \cdot 10^{-2}$
Damping partition, $J_x, J_y, J_z$	1.97, 1.0, 1.03
Damping time, $\tau_x, \tau_y, \tau_z$ [ms]	15.9, 31.4, 30.6
Natural chromaticity, $\xi_{x0}, \xi_{y0}$	-5.99 -5.25
Energy loss per turn, $U_0$ [keV]	1.435
RF voltage, $V_{RF}$ [MV]	1.1
RF frequency, $f_{RF}$ [MHz]	714.0
Harmonic number	48

The fractional tunes are results of the phase advances required for emittance and the constraints of magnetic field. Although above a half integer tunes are not preferred from a point view of instability driven by resistive-wall impedance, our estimate shows that the growth rate is much slower than the radiation damping rate. Moreover, the fractional tunes above half integer were successfully used PEP-II and KEKB.

Separation of horizontal and vertical emittance will be discussed in a later section that deals with the intra-beam scattering (IBS). The final emittance including the IBS scattering seems adequate based on the simulation from the ring to the final focusing system.

Since the energy spread is small, wigglers can be added to reduce the damping time and emittance. However, the wigglers have to be superconducting because the field of the bending magnet is already high at 1.44 Tesla. A meter of space will be reserved for wigglers in a future upgrade.

### 8.3.2 Lattice Design

In general, the choice of the beam energy in damping rings is a balancing act. On one hand, it should be higher to damp more quickly and also to mitigate the IBS effects. On the other hand, a higher energy requires a stronger magnetic field or a larger ring. In this design, the minimum energy is determined by the existing target at 200 MeV. Given the fixed size of the ring, the highest possible energy,  $E=335$  MeV, has been chosen to reduce the IBS growth of the beam emittance.

Given the beam energy  $E = \sqrt{m^2c^4 + c^2p^2}$  the magnetic rigidity of the ring is given by

$$B\rho = \frac{p}{e}$$

where  $m$ ,  $e$  are the mass and charge of the positron respectively,  $p$  the design momentum.

$B\rho \approx 0.335 \times 10/2.998 \approx 1.12$  T-m. Taking the dipole field  $B=1.44$  T, the bending radius is  $\rho = 0.777$  m. So the packing factor of the dipole magnets in the arcs is  $0.777m/1.4m \approx 55\%$ . The denominator (1.4m radius) is derived from the size of the tunnel. Here, some space has been left for the transverse dimension of the components such as RF cavities. Since these parameters are taken from the design lattice, it is not surprising to see that the packing factor is consistent with the layout of the cell shown in Fig. 8.11. As can be seen from the figure, the packing factor cannot be increased further because the space is needed for quadrupoles, sextupoles, and gaps between the magnets.

### 8.3.2.1 Scaling

Starting with these ideas about the bending dipoles and geometry of the ring, the damping times are largely determined. For example, the horizontal damping time is given by,

$$\tau_x = \frac{2\gamma C mc^2}{cJ_x U_0}$$

where  $C$  is the circumference of ring,  $J_x$  the horizontal damping partition number, and  $U_0$  the energy loss per turn,

$$U_0 = \frac{2r_e mc^2 \gamma^4}{3} I_2$$

with  $I_2$  a radiation integral,

$$I_2 = \oint \frac{ds}{\rho^2}$$

and  $r_e$  the classical radius of the electron. It is worth mentioning that the damping times increase rapidly as the energy is reduced.

It is well known [2] that an equilibrium (bend plane) emittance,  $\epsilon_x$ , is a result of the balancing acts between quantum excitation and radiation damping. It can be written in terms of the radiation integrals,

$$\epsilon_x = C_q \frac{\gamma^2 I_5}{J_x I_2},$$

with

$$C_q = \frac{55}{32\sqrt{3}} \frac{\hbar}{mc}, I_5 = \oint \frac{\mathcal{H}_x}{\rho^3} ds,$$

where

$$\mathcal{H}_x = \beta_x \eta_x'^2 + 2\alpha_x \eta_x \eta_x' + \gamma_x \eta_x^2,$$

$\eta_x, \eta'_x$  are the horizontal dispersion and its slope  $\beta_x, \alpha_x, \gamma_x$ , the horizontal Courant-Snyder parameters.

For a simple ring with identical arc cells, the emittance can be computed and written as,

$$\epsilon_x = C_q \gamma^2 \phi^3 \frac{F_c}{J_x},$$

where the parameter  $F_c$  depends only on the structure of the cell,  $\phi = 2\pi/N_c$  is the bending angle per cell, and  $N_c$  the number of cells. For a minimal emittance, it is therefore desired to have a large  $N_c$  and cell with a small  $F_c$  value.

For FODO cells with equal phase advances,  $\mu_x = \mu_y = \mu$ , there is an analytical expression for  $I_5$ . Knowing  $I_5$ , one can easily derive the parameter  $F_c$ ,

$$F_c^{FODO} = \frac{1 - \frac{3}{4} \sin^2 \frac{\mu}{2} + \frac{1}{60} \sin^4 \frac{\mu}{2}}{4 \sin^2 \frac{\mu}{2} \sin \mu},$$

which is plotted as a function of  $\mu$  in Fig. 8.10. Although there is a minimum  $F_c^{min} = 0.15381$  at  $\mu = 2.39062$ , the rate of reduction decreases significantly beyond  $\pi/2$ . For all practical purposes of emittance reduction, it is not so efficient to choose a phase advance larger than  $\pi/2$ . For a typical value,  $F_c^{FODO}(\pi/2) = 151/480$ .

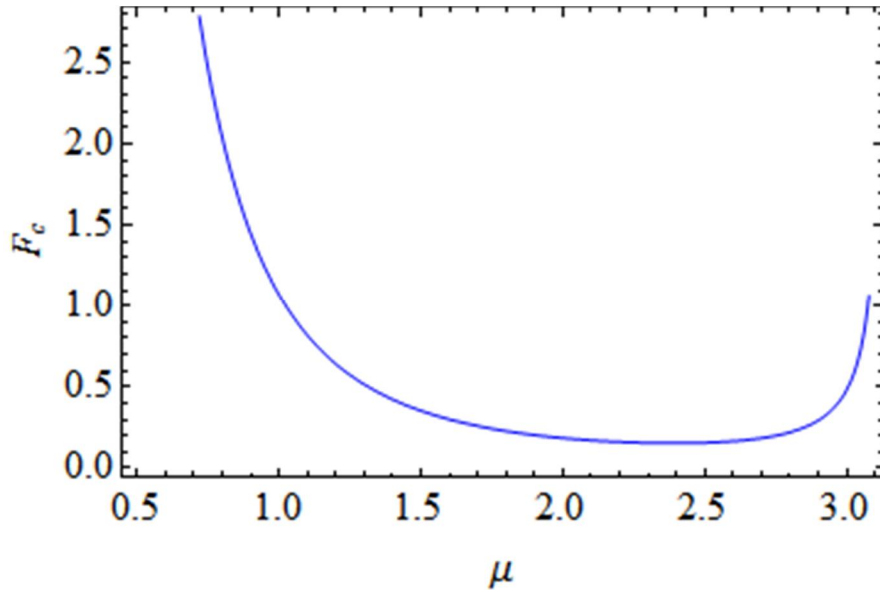


Figure 8.12. The emittance scaling parameter  $F_c$  a function of phase advance  $\mu$  (radians) per FODO cell.

For more efficient reduction of the emittance, the theoretical minimum emittance (TME) cell has been known [3] to yield the lowest possible emittance corresponding to the minimum value of  $F_c$ :

$$F_c^{(TME)} = \frac{1}{12\sqrt{15}}$$

This, however, requires very strong focusing which may limit dynamic aperture; hence in practical designs the TME lattice is usually set to a higher  $F_c$  value. These TME-type cells are widely used in damping rings [4,5] for linear colliders. Unfortunately, they require too much space between the magnets, especially quadrupoles. Given the size of the tunnel, there cannot be any large spaces between the magnets in the arcs; otherwise the dipole field will be too high as estimated previously. Another way to reduce the damping time and to achieve smaller emittance is using a wiggler. However, the wigglers have to be superconducting because the field of the bending magnet is already quite high at 1.44 T. Extra space should be reserved for wigglers as a future upgrade.

### 8.3.2.2 Cell

An alternative is a FB cell using a combined function dipole magnet with a defocusing gradient, which lowers the horizontal beta functions and dispersion inside the dipole to minimize the emittance. Moreover, it generates a high horizontal damping partition number  $J_x$  for a further reduction of emittance. This design was widely used in the multi-bend achromat cell in the next generation light sources such as MAX-IV [6] and ESRF-II [7].

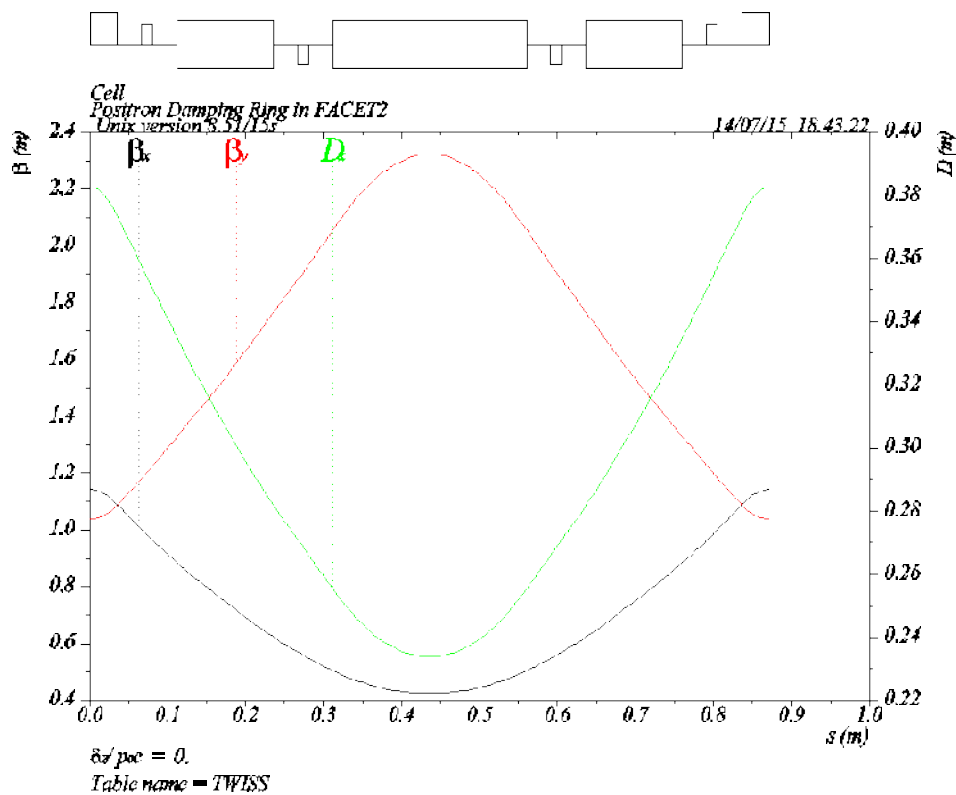


Figure 8.13. Lattice functions of the nominal cell with a combined function dipole at the center.

This type of cell is chosen for its compactness. The optics functions of the nominal cell are plotted in Fig. 8.13. Here, the dipole is segmented into three pieces so that defocusing sextupoles can be placed some distance away from the focusing sextupoles to make them more orthogonal and therefore more

effective for chromatic compensation. Moreover, the defocusing gradient is removed from the two short dipoles near the focusing quadrupole because they are not so effective and not necessary.

The phase advance values of the cell are  $\mu_x = 78.92^\circ$  and  $\mu_y = 31.38^\circ$  in the horizontal and vertical planes, respectively. Although the phase advances values are modest, the strength of the focusing quadrupole and the gradient in the dipole are quite strong because of the short length of the cell. Its scaling parameter  $F_c$  can be estimated using the equation above, provided  $\mu$  is identified as the horizontal phase advance. So for the same reason as for the FODO cell, the choice of the phase advances are reasonable and efficient.

### 8.3.2.3 Dispersion Suppressor

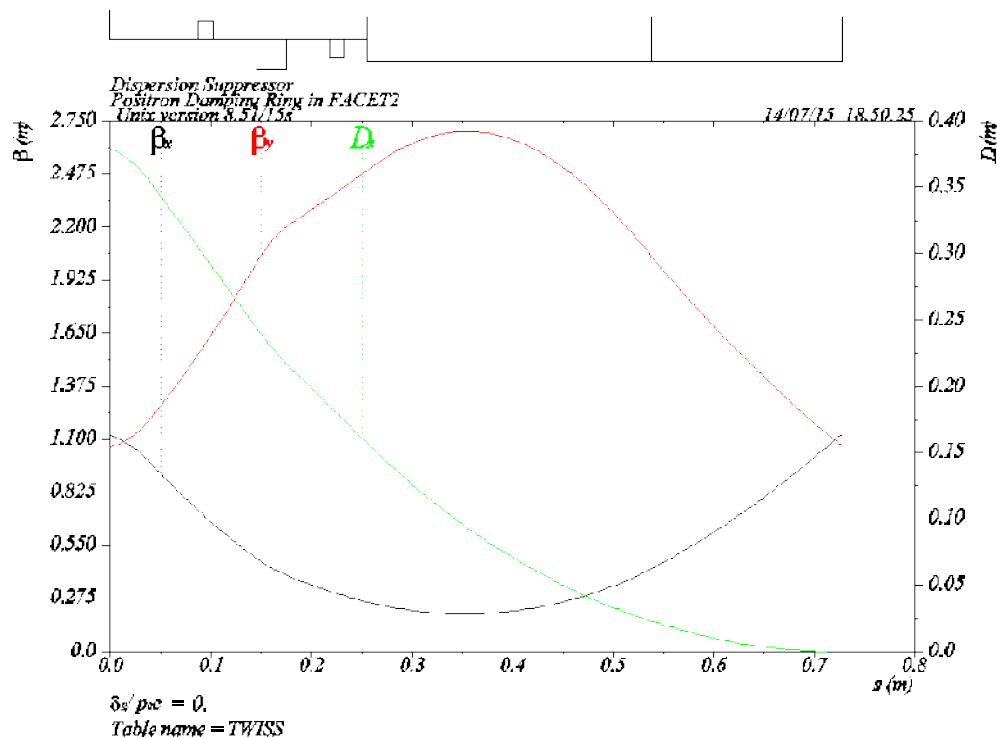


Figure 8.14. Lattice functions of the dispersion suppressor.

The dispersion in the arc has to be reduced to zero by a dispersion suppressor, such as shown in Fig. 8.14 as the beam enters the straight. Leaking dispersion into the straights is not an option because of the tight aperture in the RF cavities. The bending radius of the dipoles in the dispersion suppressors are the same as those in the regular cells. The total bending angle is 95% of that in a regular cell. The first segment of the suppressor dipole is a combined function magnet. The gradient is necessary to control the vertical beta function to a reasonable value at the exit. The value of the gradient is set the same as in the gradient dipole in the regular cell to simplify the engineering effort. A pair of quadrupoles are used to adjust the dispersion and its slope to zero at the exit.

### 8.3.2.4 Straight Sections

The straight sections contain the injection and extraction systems. Since they are dispersion free, they are also good regions in which to place RF cavities. The injection and extraction are vertical because of the limitation in the horizontal tunnel size. The injection and extraction beamlines are placed on opposite sides of the ring. The optics that meets these requirements are shown in Fig. 8.15 as a part of the entire ring.

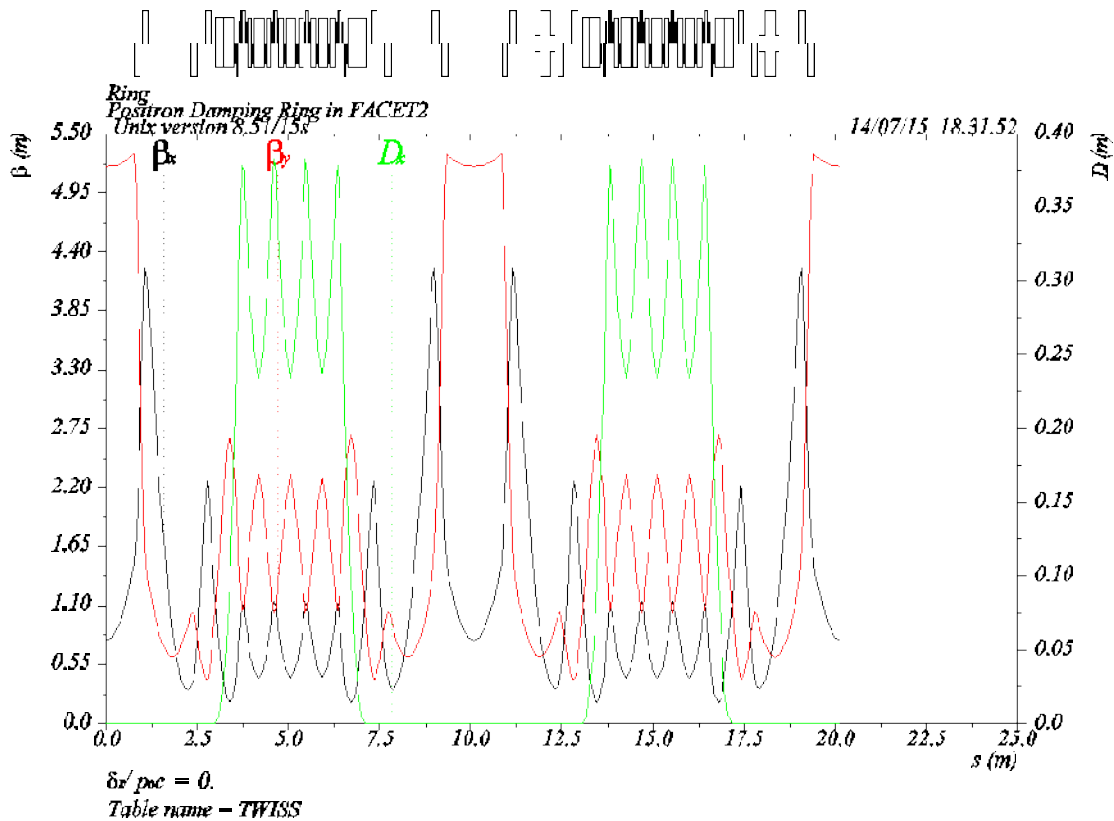


Figure 8.15. Lattice functions of the positron damping ring in FACET2.

The large vertical beta function at the middle of the straight is designed to enlarge the acceptance at the septum as the beam is injected into the ring. A vertical kicker is placed at a position about  $90^\circ$  down stream to guide the injected beam onto the designed orbit. The large beta function is also helpful to reduce the strength of the kicker. The extraction is merely the reverse of the injection process. Because of the phase relation between the septum and kicker, the phase advance in one side of the straight is fixed. For the tune adjustment, there can be a slightly different optics in the other side of the straight. The straights are designed to be reasonably short so that the damping times are adequately fast. Some space will be reserved for wigglers as a future upgrade.

### 8.3.2.5 Ring

In addition to the dispersion suppressors at the end of the arcs, it is desirable to have more cells in the arcs to reach lower emittance. To make this scheme work, more and stronger quadrupoles are required as the number of cells increases. As a result, there is not enough space left between the magnets. To

leave adequate room for the ends of the physical magnets, there are only three regular cells per arc. The arcs as designed are shown in Fig. 8.15. Each arc can be seen as a “5-bend” achromat.

The lattice is matched using the computer program MAD [8]. The main parameters of the ring are tabulated in Table 8.6.

For full coupling (set with tunes of  $\nu_x - \nu_y = 2$ ), the natural emittance values are  $\epsilon_{x0} = \epsilon_{y0} = 5.43$  nm-rad, and the normalized emittance  $\gamma\epsilon = 3.64$   $\mu\text{m-rad}$ , which is three orders of magnitude smaller than that of the injected beam. The growth from IBS, covered in a later section, is not yet included. The existing RF system is the same as that used in the damping rings constructed for the SLC. Therefore the RF parameters are fixed for the design. The betatron tunes are chosen after many iterations of maximizing the dynamic aperture of the ring.

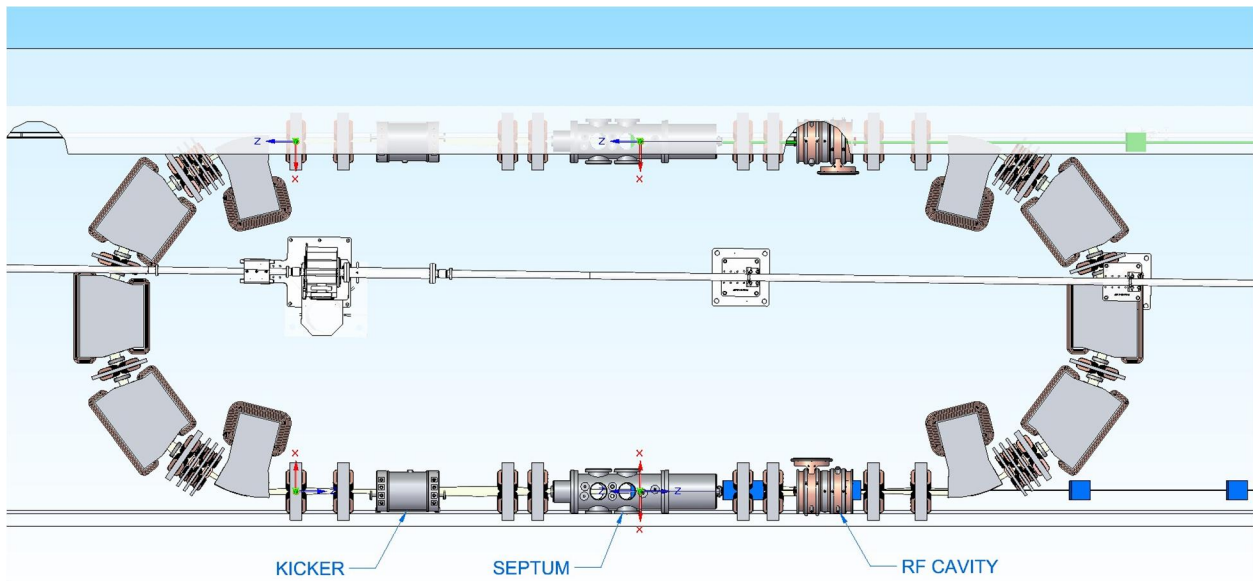


Figure 8.16. Schematic of the positron damping ring for FACET-II. Yellow surface shows 10X stored beam size.

### 8.3.3 Beam Dynamics

A low emittance lattice is characterized by very small beta functions and dispersion, achieved with many quadrupoles and resulting in a very large natural chromaticity. To correct the chromaticity, the chromatic sextupole magnets become extremely strong as the dispersion gets smaller and smaller. The nonlinear effects generated by such strong sextupoles result in a severe reduction of the dynamic aperture. An efficient minimization of these nonlinearities becomes essential for a successful design of storage rings.

The sextupole scheme consists of two families of sextupole magnets. The focusing sextupoles are placed near the focusing quadrupoles while the defocusing ones reside near the combined function dipoles. The two families are sufficiently separated so that they are more orthogonal and therefore their strengths are reduced accordingly. If necessary, sextupoles in the dispersion suppressors can be used as additional families to further optimize the high-order chromaticity.

### 8.3.3.1 Normal Form Analysis

Table 8.7. Nonlinear chromaticities and tune shifts due to betatron amplitudes in the damping ring.

Derivatives of tunes	Values
$\partial v_{x,y} / \partial \delta$	+0.5, +0.5
$\partial^2 v_{x,y} / \partial \delta^2$	+16.3, +25.6
$\partial^3 v_{x,y} / \partial \delta^3$	-279.0, -1734.6
$\partial v_x / \partial J_x [m^{-1}]$	+49.2
$\partial v_{x,y} / \partial J_{y,x} [m^{-1}]$	-78.6
$\partial v_y / \partial J_y [m^{-1}]$	+213.1

To assess the nonlinearity in the ring, a Taylor map is first extracted using a differential algebra technique [9] and then the normal form [10] is analyzed for the high-order chromaticities and the tune shifts of the ring. The computation is carried out using LEGO [11]. The result is tabulated in Table 8.7 with the sextupoles at their nominal values, setting the linear chromaticities at a half unit. Clearly, the chromaticities are well corrected with two families of sextupoles. The nonlinear tune shifts are very modest, largely because of not much accumulation in the small ring. This analysis shows that the beam footprint in the tune space is small, so it can easily avoid nonlinear resonances.

### 8.3.3.1 Dynamic Aperture

For efficient injection, it is important to design a lattice that has a sufficiently large dynamic aperture. The dynamic aperture is obtained from particle tracking simulations that include synchrotron oscillations using LEGO [10]. The calculations included on- and off-momentum particles without any machine errors. The dynamic apertures with various momentums are shown in Fig. 8.17 with sextupoles set at their nominal values. As one can see from the figures, the aperture is between 8 to 15 sigma of the injected beam, which has a normalized emittance of 2.5/2/2 mm-rad in the horizontal and vertical planes respectively. The momentum aperture is larger than 3%, which is three times as large as the energy spread of the injected beam.

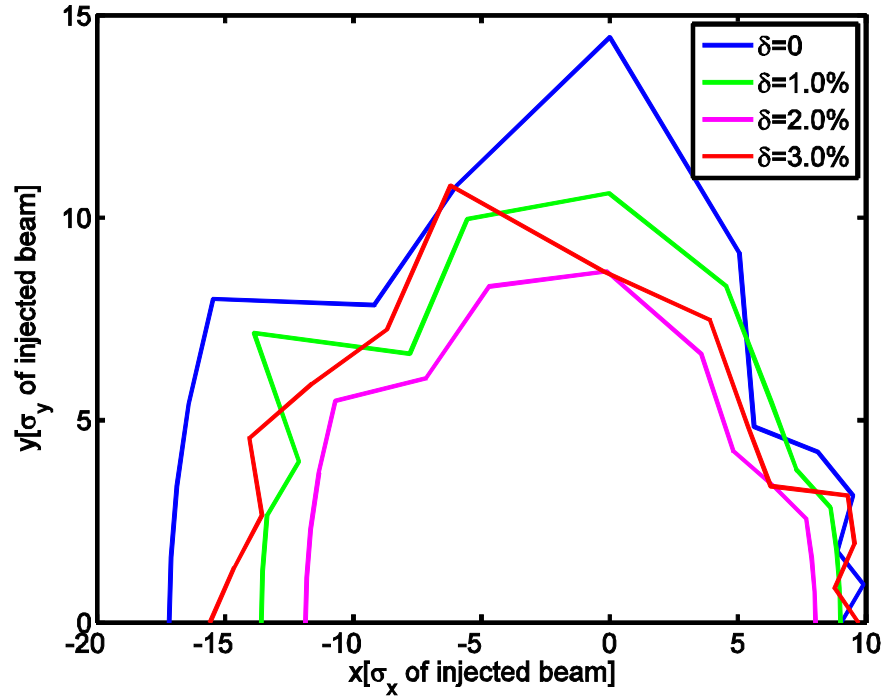


Figure 8.17. Dynamic aperture of the ideal lattice at various momentum deviations.

### 8.3.3.2 Round Beam

A round beam is required not only for the plasma acceleration experiment but also as a means to mitigate the IBS growth in emittance of the positron beam while it undergoes radiation damping in the ring. The ring will operate on the linear coupling resonance  $\nu_x - \nu_y = 2$  to achieve a round beam in the damping ring. The design tunes in Table 8.6 have been chosen to be close to the resonance condition. In addition, small coupling excitation, driven by a vertical orbit through the sextupoles, is necessary. This process of generating a round beam is being simulated.

### 8.3.3.3 Magnetic Tolerances

The magnet multipole tolerance is defined relative to the field component normalized at a reference radius  $r$ :

$$\frac{\Delta B_n}{B_N} = \frac{(N-1)! B^{(n-1)'}}{(n-1)! B^{(N-1)'}} r^{n-N}, B^{(n-1)'}, = \frac{\partial^{n-1} B}{\partial^{n-1} x}$$

where  $N$  equals 1 represents dipole,  $N$  equals 2 represents quadrupole and  $n$  is the index of the harmonics for the magnetic errors. The measurements of dipole and quadrupole multipole field components from PEP II HER ring are shown in Table 8.8. The multipole components of permanent sextupole at reference radius 15 mm is shown in Fig. 8.40. These sets of magnetic multipole errors are applied to the damping ring. The dynamic apertures with multipole magnet errors of ten random seeds are shown in Figure 8.18. After applying the magnet multipole errors the dynamic aperture shrinks but is still larger than 12 sigma of the injected beam size of on momentum particles. If the magnet aperture is smaller than what is used at PEP II then the multipole field error shown in Table 8.8 may be increased and the dynamic aperture will be reduced further. The linear fringe field is included in the simulation.

Nonlinear ones have to be studied once we have engineering designs of the magnets. Finally, the fringe fields should be measured and verified, and then used in future simulations.

Table 8.8. Systematic and rms normalized multipole errors.

Multipole errors of dipole at radius 30 mm						
multipole type	$\frac{\Delta B_3}{B_1}$	$\frac{\Delta B_4}{B_1}$	$\frac{\Delta B_5}{B_1}$	$\frac{\Delta B_6}{B_1}$		
systematic	1.0e-5					
rms	3.2e-5	3.2e-5	6.4e-5	8.2e-5		
Multipole errors of quadrupole at radius 44.9 mm						
multipole type	$\frac{\Delta B_3}{B_2}$	$\frac{\Delta B_4}{B_2}$	$\frac{\Delta B_5}{B_2}$	$\frac{\Delta B_6}{B_2}$	$\frac{\Delta B_{10}}{B_2}$	$\frac{\Delta B_{14}}{B_2}$
systematic	1.03e-3	5.6e-4	4.8e-4	2.37e-3	-3.10e-3	-2.63e-3
rms	5.6e-4	4.5e-4	1.9e-4	1.7e-4	1.8e-4	7.0e-7

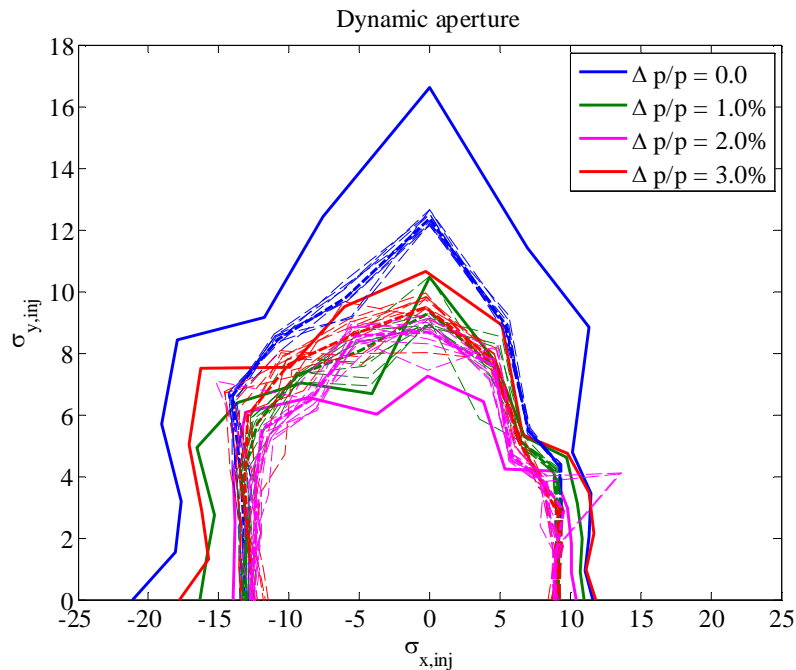


Figure 8.18. Dynamic aperture tracking with magnet multipole field errors. Total of 10 sets of random errors are simulated. The solid line is the aperture without multipole errors and the dashed line is the dynamic aperture with multipole field errors of different random seeds. The thick dashed line is the average dynamic aperture of 10 random seeds.

### 8.3.3.4 Alignment Tolerances and Correction System

The schematic layout of the orbit correction scheme is shown in Figure 8.19. There are 14 horizontal correctors (HCOR), 14 vertical correctors (VCOR) and 22 H/V beam position monitors (BPM) in the

correction scheme. Quadrupole displacement, dipole field error and dipole rotation are the sources of errors that cause a closed orbit. The closed orbit is generated according to the closed orbit formula:

$$\Delta x, y_{co} = \frac{\sqrt{\beta_{x,y}}}{2 \sin(\pi\nu_{x,y})} \sum_i \sqrt{\beta_{(x,y),i}} \cos([\phi_{(x,y),i} - \phi_{(x,y)}] - \pi\nu_{x,y}) \Delta\Theta_{(x,y),i}$$

where  $\Delta\Theta$  is the effective kick due to different error sources. For a dipole field error,  $\Delta\Theta_x = \frac{\Delta B_1}{B_1} \theta_{bend}$ , for a dipole rotation,  $\Delta\Theta_{x,y} = \Delta\phi_{rot} \theta_{bend}$ , and for a quadrupole displacement,  $\Delta\Theta_{x,y} = \Delta x, y k_1 |_{quad}$ , where  $\theta_{bend}$  is the bending angle of the dipole,  $\phi_{rot}$  rot is the rotation angle of dipole,  $k_1 = \frac{B'_2}{B_1 \rho}$ . The alignment errors of the damping ring are shown in Table 8.9. The field errors are shown in Table 8.10. Dynamic aperture with alignment errors, field errors and multipole field errors of 10 seeds with corrections are shown in Figure 8.20. The corrections include linear chromaticity, orbit, beta beat, coupling and vertical dispersion. The blue solid line in Fig. 8.20 is the dynamic aperture without errors. The dashed line is dynamic aperture with errors and with corrections. The red solid line is the average dynamic aperture of 10 seeds after correction. The dynamic aperture with errors after corrections gives sufficient aperture for injection. The closed orbits of 10 random seeds after correction are shown in Figure 8.19. The corrector strengths are shown in Figure 8.20. The horizontal orbit can be corrected to less than 100  $\mu\text{m}$  and the vertical orbit to less than 200  $\mu\text{m}$ . The corrector strength is less than 1 mrad.

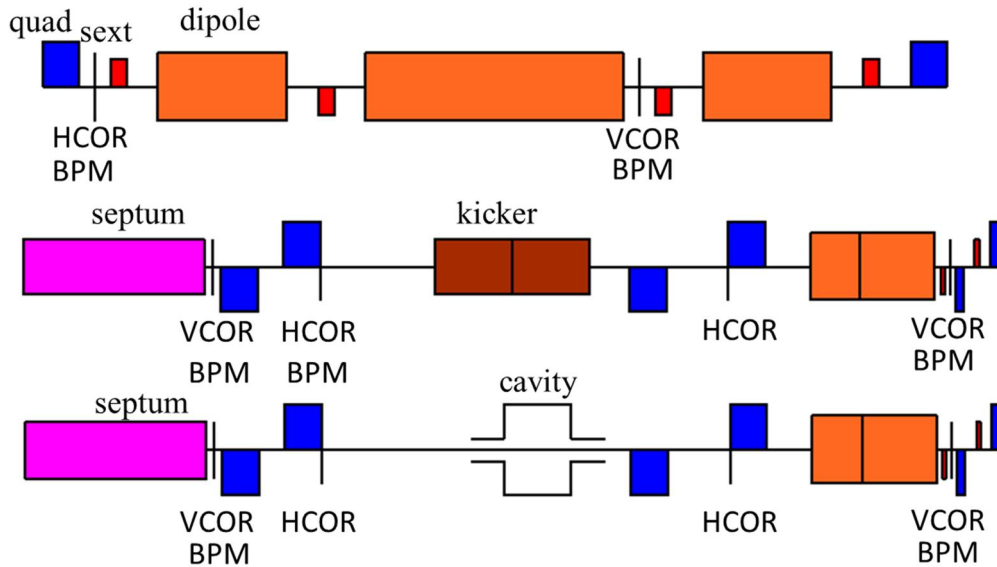


Figure 8.19. Schematic layout of the orbit correction scheme. The correction scheme includes: 14 horizontal correctors, 14 vertical correctors and 22 H/V position monitors. The first beamline is the FODO cell, the second beamline is downstream of the injection septum (the reverse order applies to upstream of the extraction septum); the third beamline is downstream of the extraction septum (the reverse order applies to upstream of the injection septum).

**Table 8.9. Alignment errors**

	$\Delta x$ ( $\mu\text{m}$ )	$\Delta y$ ( $\mu\text{m}$ )	$\Delta\phi$ ( $\mu\text{rad}$ )
Dipole	50	50	100
Quadrupole	50	50	100
Sextupole	50	50	100

**Table 8.10. Field errors**

$\Delta B_1/B_1$	1.0e-3
$\Delta B_2/B_2$	1.4e-3
$\Delta B_3/B_3$	1.0e-3

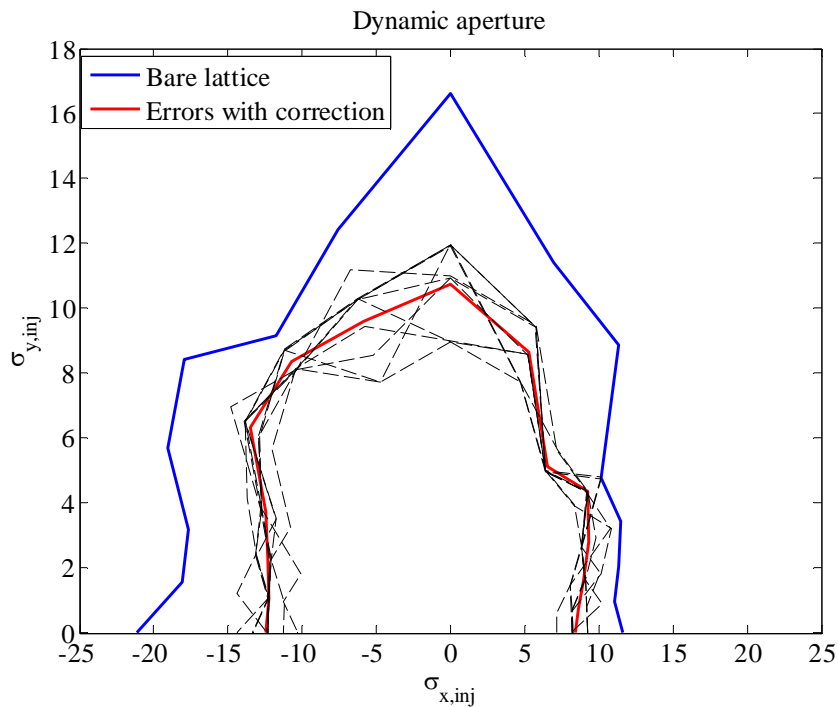


Figure 8.20. Dynamic aperture tracking with alignment errors, field errors and magnet multipole field errors. Total of 10 sets of random errors are simulated. The blue solid line is the dynamic aperture without errors. The dashed line is the dynamic aperture with errors and with corrections. The corrections include linear chromaticity, orbit, beta beat, coupling and vertical dispersion. The red solid line is the average dynamic aperture after correction. The dynamic aperture with errors and after corrections gives sufficient aperture for injection.

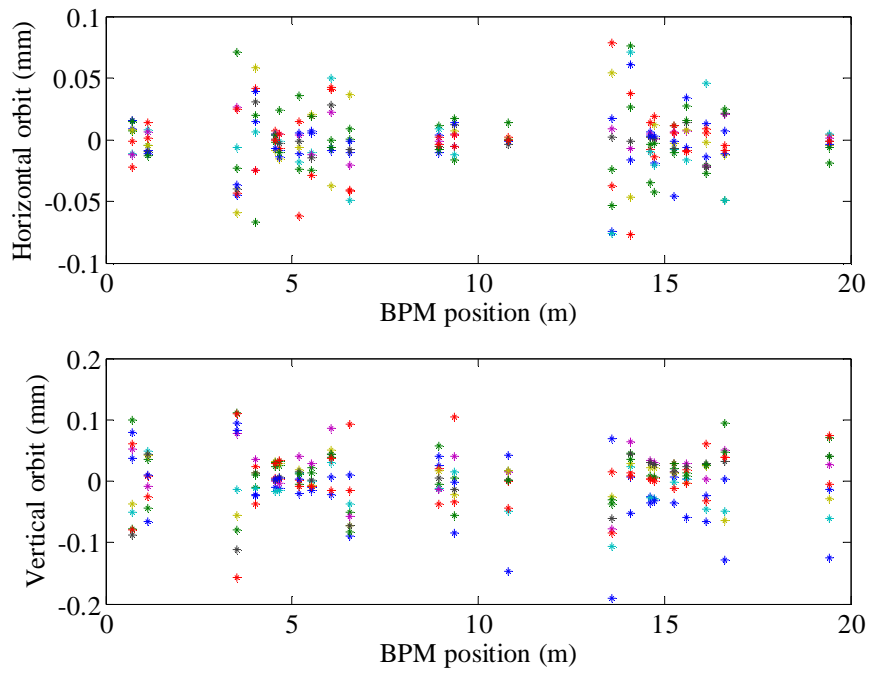


Figure 8.21. Closed orbits of 10 sets of random errors after correction.

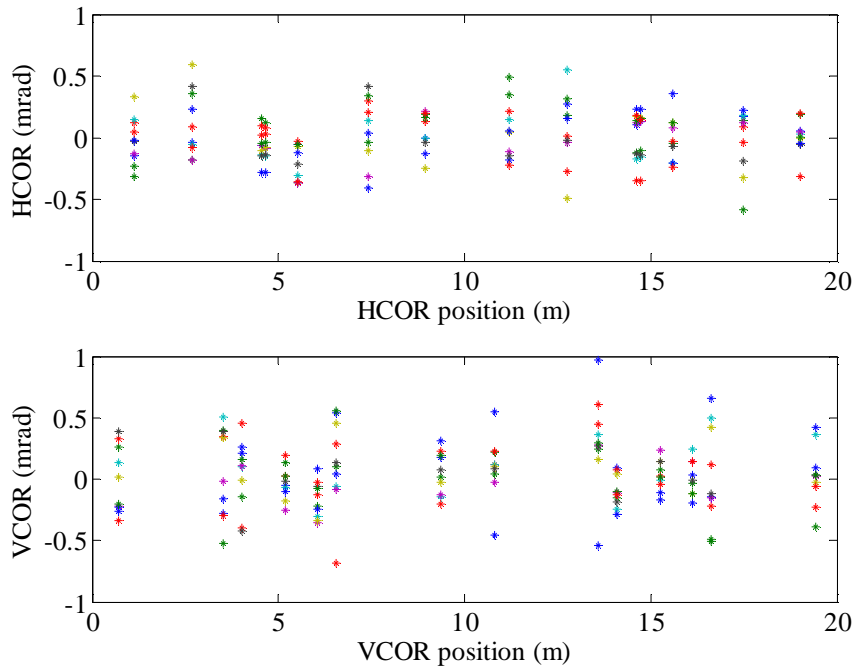


Figure 8.22. Corrector strengths of orbit corrections of 10 sets of random errors.

### 8.3.4 Intra-beam Scattering

Intra-beam scattering describes multiple Coulomb scattering that leads to growth in emittance and energy spread in electron machines, whereas the Touschek effect concerns large single Coulomb scattering events where energy transfer from transverse to longitudinal planes leads to particle loss. In low emittance storage rings both effects are important.

To obtain round beams in a storage ring will likely entail the use of coupling or vertical dispersion. But for simplicity here, for the purpose of IBS calculations, the vertical emittance is assumed to be primarily generated by the coupling, and the effects of the vertical dispersion can be ignored. Then the vertical emittance is proportional to the horizontal emittance

$$\epsilon_x = \frac{\epsilon}{1+\kappa} \text{ and } \epsilon_y = \frac{\kappa\epsilon}{1+\kappa},$$

with  $\kappa$  being the coupling constant between 0 and 1 and  $\epsilon = \epsilon_x + \epsilon_y$  being the sum emittance at finite current with IBS. The nominal (no IBS) horizontal and vertical emittances are given by  $\epsilon_{x0} = \epsilon_0/(1 + \kappa)$  and  $\epsilon_{y0} = \kappa\epsilon_0/(1 + \kappa)$  where  $\epsilon_0$  is the natural emittance at zero current and its value is given in Table 8.6.

It can be shown that the steady-state values of the emittance and energy spread are given by,

$$\epsilon = \frac{\epsilon_0}{1-\tau_x^*/T_x} \text{ and } \sigma_\delta^2 = \frac{\sigma_{\delta 0}^2}{1-\tau_z/T_p},$$

where  $\tau_x^* = \tau_x/(1 + \kappa\tau_x/\tau_y)$ . The quantities  $\tau_x, \tau_y, \tau_z$  signify the radiation damping times in  $x, y, z$  respectively and  $\sigma_{\delta 0}$  the energy spread without the IBS growth. Their values can be found in Table 8.6.  $1/T_x, 1/T_{xp}$  gives the IBS growth rate in amplitude.

For the damping ring growth rates the Bjorken-Mtingwa formulation [12] is used, using the Nagaitsev [13] algorithm for efficient calculation. Given the growth rates, the steady-state  $\epsilon$  and  $\sigma_\delta$  are obtained by solving the equations for  $\epsilon$  and  $\sigma_\delta$  simultaneously. Since the growth rates depend on the beam emittances, energy spread, and bunch length, the equations are solved by iteration using Newton's method.

For the IBS calculations for the damping using lattice parameters found in Table 8.8, it is assumed that the nominal current is below the threshold of the microwave instability and that potential well bunch lengthening is not significant (so that  $\sigma_z = \sigma_{z0}\sigma_\delta/\sigma_{\delta 0}$ ). The vertical emittance is given by coupling with  $\kappa = 1$  and the beam is round.

The steady-state emittances,  $\epsilon_x, \epsilon_y$  and energy spread  $\sigma_\delta$  are calculated as a function of bunch charge. The results are summarized in Figure 8.23. There is a substantial increase in the emittances and energy spread. With 2 nC bunch charge, there is about a factor of two increase.

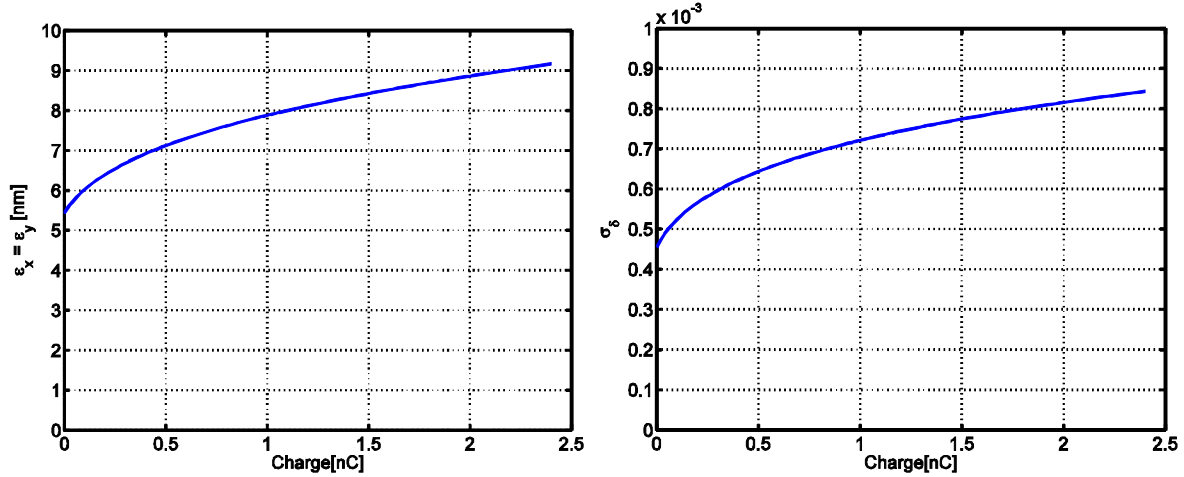


Figure 8.23. Equilibrium emittances (left) and energy spread (right) as a function of bunch charge.

### 8.3.5 Impedance and collective instabilities

An impedance model is required for calculations on longitudinal and transverse instability thresholds and on growth rates. Without a detailed engineering design of the vacuum chamber and its components, it is only possible to focus on a few generic types of impedance, such as the longitudinal impedance generated by coherent synchrotron radiation (CSR) and resistive-wall impedance. Here three instabilities are briefly addressed: (i) the single-bunch microwave instability driven by CSR, (ii) the single-bunch transverse mode coupling instability (TMCI) due to the resistance in the walls, and (iii) the multi-turn transverse instability driven by the wall resistance. Detailed study needs to be carried out with simulations in future as the ring components are designed.

#### 8.3.5.1 Microwave Instability due to CSR

Here the microwave threshold is estimated only due to one contributor to the impedance, shielded CSR. In the model used for the calculations the beam is assumed to be moving in a circle of radius  $\rho$  (in the plane  $y=0$ ) between two parallel plates at locations  $y=\pm h$ . In normalized units the threshold current  $S^{th}$  is given as a function of shielding parameter  $\Pi$  by [14]

$$S^{th} = 0.50 + 0.12\Pi$$

with

$$S = \frac{r_e N_b \rho^{1/3}}{2\pi v_s \gamma \sigma_{\delta 0} \sigma_{z0}^{4/3}}, \quad \Pi = \frac{\sigma_{z0} \rho^{1/2}}{h^{3/2}}$$

with  $N_b$  being the number of electrons per bunch and  $v_s$  being the synchrotron tune. Here  $S^{th}$  is the threshold current beyond which the energy spread of the beam starts to increase.

The vacuum chamber in the arcs is round with radius of  $r = 2$  cm and bending radius  $\rho = 0.777$  m; for these calculations  $h = r$ . With these assumptions, the effect with shielding is not significant: with  $\Pi = 0.695$ , the threshold bunch population  $N_b^{th} = 4.81 \times 10^9$ , and the threshold bunch charge 0.77 nC, which is much lower than the design bunch charge of 2 nC.

Realistically, the bunch will be lengthened by the IBS scattering about 74% with 2 nC charge based on the estimate in Section 8.3.4. Using the longer bunch length and the larger energy spread generated from the IBS scattering, the threshold increases to 2.8 nC, which is significantly higher than the design value.

### 8.3.5.2 Transverse Single Bunch Instability

In most light sources with regions of small-aperture vacuum chambers, the resistive wall is the dominant contribution to the transverse single-bunch instability. The kick factor (the average kick experienced over a bunch) for a Gaussian bunch passing through a round, resistive beam pipe is given by

$$\kappa_y = (0.723) \frac{c}{\pi^{3/2} r^3} \sqrt{\frac{Z_0}{\sigma_z \sigma_c}}$$

with  $r$  the radius of the pipe,  $Z_0=377 \Omega$ ,  $\sigma_z$  the bunch length, and  $\sigma_c$  the conductivity of the beam pipe. The single bunch threshold current is given by [15]

$$I_b^{th} \approx 0.7 \frac{4\pi c v_s (E/e)}{C} \frac{1}{\sum_i l_i \beta_{y,i} \kappa_{y,i}}$$

with  $C$  the circumference of the ring. The equation above allows for several region types in the ring, each of total length  $l$ , beta function  $\beta_y$ , and kick factor  $\kappa_y$ .

Taking the conductivity of Al to be  $3.5 \cdot 10^7 \Omega^{-1} \text{ m}^{-1}$  and  $\beta_y = 5 \text{ m}$ , the threshold current is  $I_b^{th} = 49 \text{ A}$ , comfortably above the nominal current  $I_b = 28.6 \text{ mA}$ .

### 8.3.5.3 Multi-Turn Transverse Instability

Aside from HOM, the resistive wall impedance is often the dominant contributor to the transverse coupled bunch instability in storage rings. Assuming only this source of impedance, the growth rate of the instability can be estimated as [16]

$$\Gamma = \frac{c(I_b/I_A)}{4\gamma \sqrt{C(1 - [v_y])}} \langle \beta A \rangle$$

where

$$\langle \beta A \rangle = \frac{4}{\sqrt{\pi Z_0}} \sum_i \frac{l_i \beta_{y,i}}{r_i^3 \sqrt{\sigma_{c,i}}}$$

$[v_y]$  being the fractional part of the vertical tune and  $I_A = ec/r_e \approx 17045 \text{ A}$ , the Alfven current. Here the beam pipe is again assumed to be round with radius  $r$ .

For the growth rate calculation, the same vacuum chamber is assumed and the total growth rate  $\Gamma = 16.68 \text{ s}^{-1}$ , which is much slower than the radiation damping rate.

### 8.3.6 Magnets

#### 8.3.6.1 Overview

The FACET-II damping ring magnet parameters are summarized in Table 8.11, assuming  $E_e = 335 \text{ MeV}$ ,  $B\rho = 1.117 \text{ T}\cdot\text{m}$ , On-axis dipole field ( $B_0$ ) = 1.44 T, Dipole bend radius ( $\rho$ ) = 0.775 m.

The magnet yoke length = magnetic length ( $L_m$ ) – magnet gap size ( $2g$ ) (an approximation), and the following magnet parameter formulas are assumed:

NI/pole (ampere-turns) for dipoles =  $B_0g/\mu_0$ ,  $g$  = half gap

NI/pole (A-t) for quadrupoles =  $B'R^2/2\mu_0$ , where  $B'$  = quadrupole gradient (T/m) and  $R$  = bore radius

NI/pole (A-t) for sextupoles =  $B''R^3/6\mu_0$ , where  $B''$  = sextupole gradient ( $\text{T/m}^2$ ) and  $R$  = bore radius

Pole-tip field (T) for gradient dipoles =  $B_0 + B'x$ , where  $B'$  is the gradient and  $x$  is the horizontal distance from the on-axis magnet center

Pole-tip field (T) for quadrupoles =  $B'R$

Pole-tip field (T) for sextupoles =  $B''R^2/2$

The gradient dipole pole equation is given by

$$y = \pm g/(1 + x/X_0), \text{ where } g \text{ is the on-axis magnet half gap and } X_0 = B_0/B'.$$

A concept for the magnet layout for one of the two damping ring arcs is depicted in Figure 8.24. The SF/PM and SD/PM sextupoles in the figure are permanent magnet sextupoles and are discussed in Section 8.3.6.6.

Table 8.11. FACET-II damping ring electromagnet parameters (approximate).

(B = dipole, Q = quadrupole, S = sextupole)

Magnet	Qty	Magnetic length (m)	Half gap/bore radius (cm)	Bend angle (deg)	Field (T, beam axis)	Max pole tip field (T)	Gradient (T/m, $\text{T/m}^2$ )	NI/pole (A-t, 95% efficiency)	Power (kW @ 55°C)
BC	6	0.249	2.2	18.4	1.44	1.85	-10.156	26537	8.0 per BE-BC-BE block
BE	12	0.1245	2.2	9.2	1.44	1.44	-	26537	
BMH	4	0.283	2.2	20.9	1.44	1.85	-10.156	26537	7.2 per BMH-BME block
BME	4	0.189	2.2	13.9	1.44	1.44	-	26537	
QFCH	4	0.07	2.2	-	-	1.06	48.22	9775	1.3
QF2H	4	0.09	2.2	-	-	1.14	51.90	10520	1.7
QDDS	4	0.03	2.2	-	-	0.64	-28.88	5854	0.7
QFI	4	0.14	2.2	-	-	0.47	21.21	4300	0.4
QDI	4	0.14	2.2	-	-	0.37	-16.62	3370	0.3
QFI1	4	0.14	2.2	-	-	0.59	26.82	5440	0.6
QDI1	4	0.14	2.2	-	-	0.42	-18.98	3850	0.3
SF	4	0.015	2.2	-	-	0.63	2589.3	3849	0.4
SD	4	0.015	2.2	-	-	0.76	-3122.2	4641	0.6

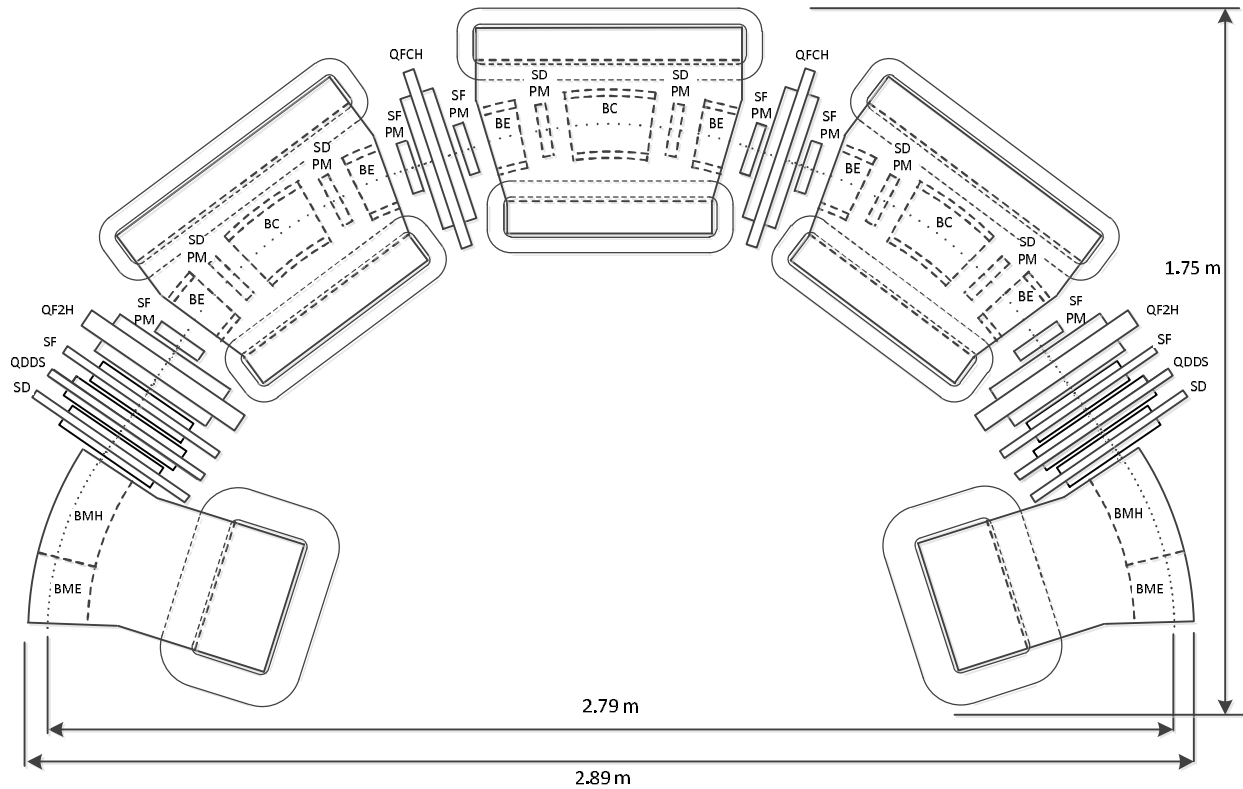


Figure 8.24. Concept for layout of magnets in one arc of the FACET-II damping ring.

As seen in Fig 8.24, the damping ring lattice is very compact and has some magnet design issues. It is proposed that closely spaced dipoles be machined from a common block of high quality magnet steel (e.g. ARMCO grade 4), with the concept shown from the top in Fig 8.24. Where it might be possible to extend this common block-machining to include adjacent quadrupoles, as has been done, for example, for the MAX-III and MAX-IV storage rings [6], the difference in vertical dimensions for the dipoles and quadrupoles make this less than desirable. The dipoles would have to be substantially larger in that dimension to match the quadrupoles, resulting in a large increase in dipole block weight.

As seen in Figure 8.25, a significant design challenge is the very close spacing of quadrupoles and sextupoles adjacent to the BMH/BME magnet blocks. These magnets must be physically short in the longitudinal dimension, significantly shorter than the magnet length defined by fringe fields, which overlap. Whether the necessary magnetic parameters can actually be reached with these short closely-spaced magnets will need to be determined by 3D magnetic modeling in the future.

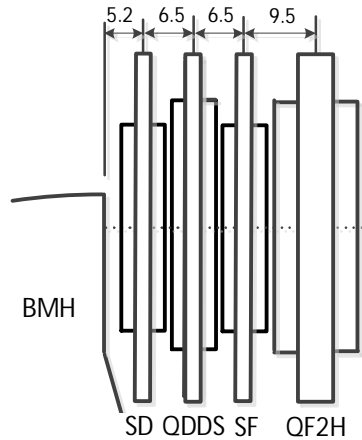


Figure 8.25. Close spacing between quadrupoles (QF2H, QDDS), sextupoles (SD, SF) and nearby dipole (BMH), with overlapping magnetic lengths determined by fringe fields. Dimensions are centimeters.

### 8.3.6.2 BE-BC-BE Dipole Block

The top view of the BE-BC-BE magnet block concept dimensions is shown in Figure 8.26. End pole shaping is not included in this conceptual depiction. The back-leg sections are shown as rectangular for simplicity of machining and coil shape. It is assumed the three poles in this block would be machined with  $\sim \pm 10\text{-}\mu\text{m}$  precision.

In principle the magnet poles can be shaped to ensure proper field properties for the three dipoles (i.e. 1.44-T on-axis field strength and sufficient good field region). Future magnetic analysis will determine if this can be accomplished, or if three separate blocks will be needed. In addition, trim windings can be installed on one or more of the poles for relative adjustment and horizontal orbit correction.

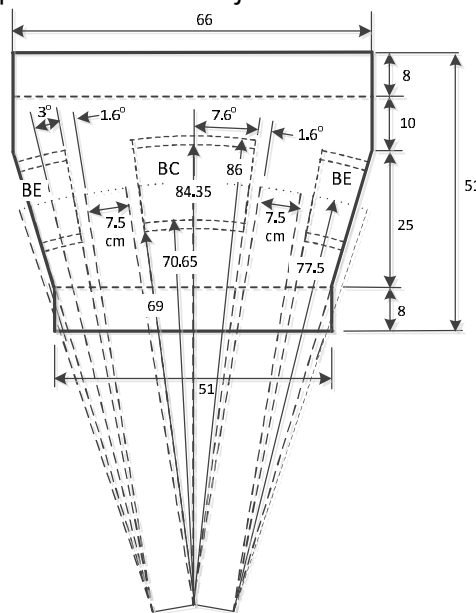


Figure 8.26. BE-BC-BE dipole magnet block showing only pole bases (curved dashed lines) for BC and BE. Magnetic length for each dipole is assumed to extend one half-gap (2.2 cm) beyond each pole edge, corresponding to a  $1.6^\circ$  bend angle beyond each edge. Dimensions are centimeters unless noted.



innermost conductor layer. Given the 26537 A-turns needed per pole, with 80 turns per pole, the dipole current would be ~332 A. With a conducting cooling hole diameter of ~4.5 mm, the conductor would have ~65 mm<sup>2</sup> cross-sectional area and the current density would be ~5.1 A/mm<sup>2</sup>.

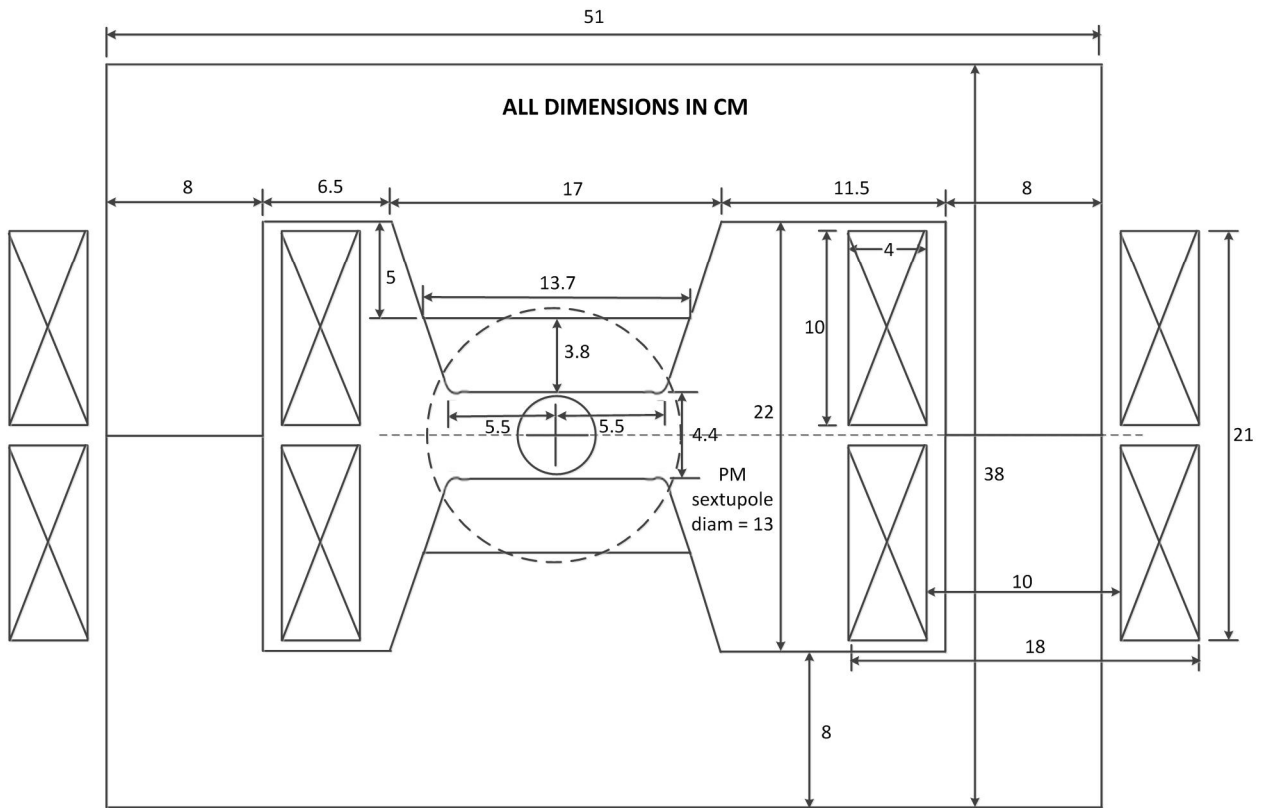


Figure 8.28. BE dipole concept. The dipole face module is normal magnet steel. Top- and back-leg widths are conservatively large and might be reduced. Coil dimensions define an envelope, not necessarily actual conductor dimensions. Not shown are trim windings on the poles. Dimensions are in centimeters.

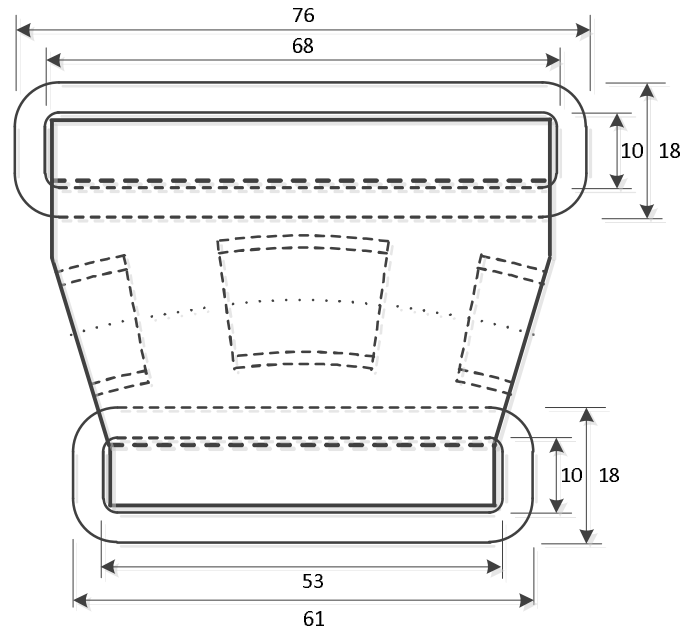


Figure 8.29. BE-BC-BE coil envelopes. Dimensions are in centimeters.

### 8.3.6.3 BMH-BME Magnet Block

The top view of the BMH-BME magnet block concept dimensions is shown in Figure 8.30. This magnet must be a C-magnet in order for the diameter of the lattice arc (Fig. 8.24) not to exceed the ~3-m-wide space constraint. End pole shaping is not included in this conceptual depiction. Each pole is divided into two sections: 60% of the magnetic length is the BMH gradient pole (Figure 8.30), and 40% of the magnetic length is the BME pure dipole (Figure 8.31). In principle the magnet poles can be shaped to ensure proper field properties for the two dipoles (i.e. 1.44-T on-axis field strength and sufficient good field region). The back-leg section is shown as rectangular for simplicity of machining and coil shape. The back-leg is retracted sufficiently far from the poles to avoid physical conflict with the nearby sextupole and quadrupole (Fig. 8.24). It is assumed the poles in this block would be machined with  $\sim \pm 10\text{-}\mu\text{m}$  precision. As with BC and BE, the top- and back-leg widths are conservatively large.

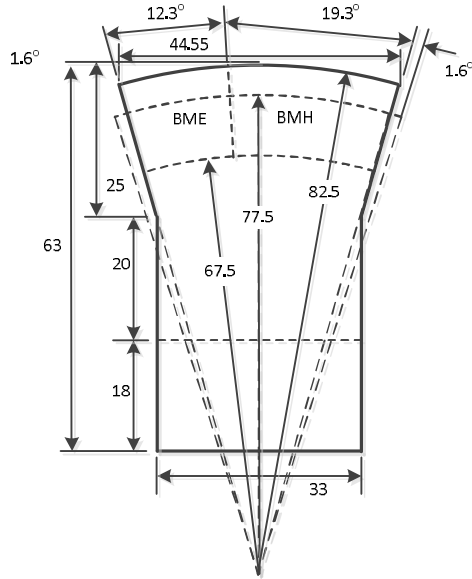


Figure 8.30. BMH-BME dipole magnet block showing only pole bases (curved dashed lines). Magnetic length for each dipole is assumed to extend one half-gap (2.2 cm) beyond each pole edge, corresponding to a  $1.6^\circ$  bend angle beyond each edge. Dimensions are centimeters unless noted.

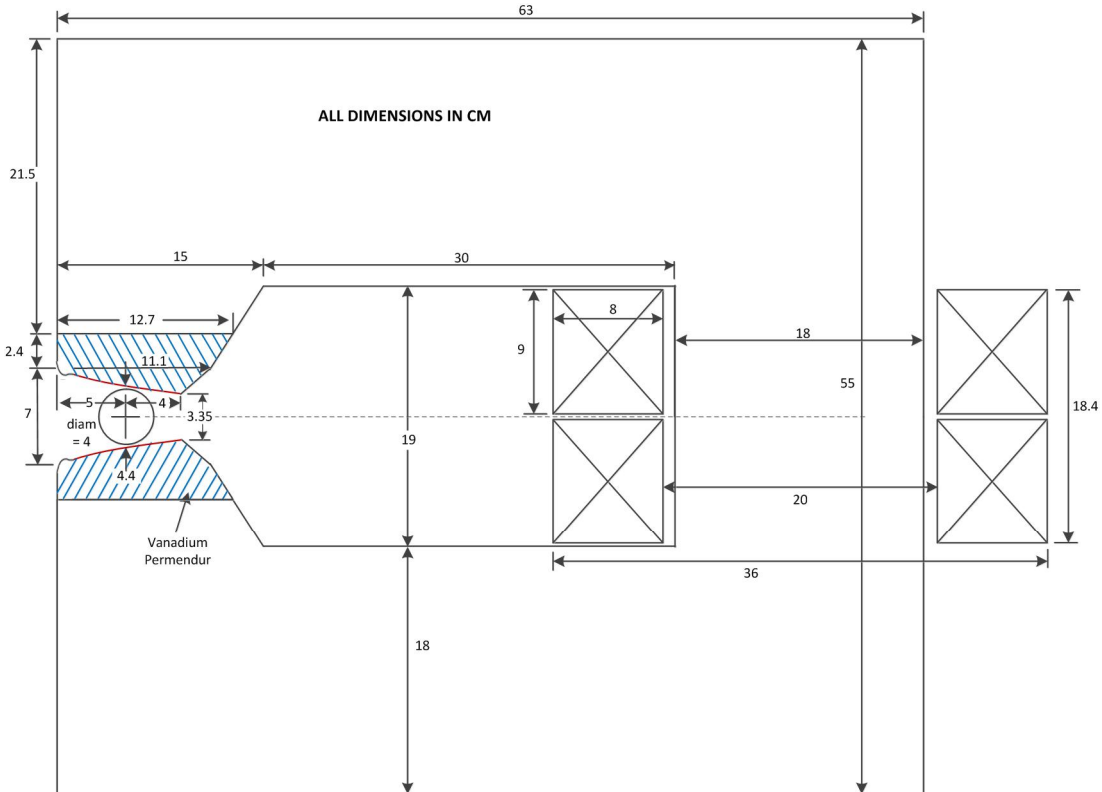


Figure 8.31. BMH gradient dipole concept. The pole face module (shaded) is shown as being all Vanadium Permendur, although this material is only really needed in the area to the right of the beam centerline where fields are  $> \sim 1.55$  T. Top- and back-leg widths are conservatively large and might be reduced. Coil dimensions define an envelope, not necessarily actual conductor dimensions. Dimensions are in centimeters.

The notional cross-section envelopes for coils for the BMH-BME dipole block are shown in Figs. 8.31 and 8.32 and the top view is shown in Figure 8.33. With a conductor size of  $\sim 0.9 \text{ cm} \times 0.9 \text{ cm}$ , each coil could have  $8 \times 10 = 80$  turns and the coil cross-section could be a bit less than the envelope. Given the 26537 A-turns needed per pole the dipole current would be  $\sim 332 \text{ A}$ . With a conducting cooling hole diameter of  $\sim 4.5 \text{ mm}$ , the conductor would have  $\sim 65 \text{ mm}^2$  cross-sectional area and the current density would be  $\sim 5.1 \text{ A/mm}^2$ . Each coil may have to be comprised of two  $8 \times 5$ -turn coil pancakes, each having its own cooling circuit.

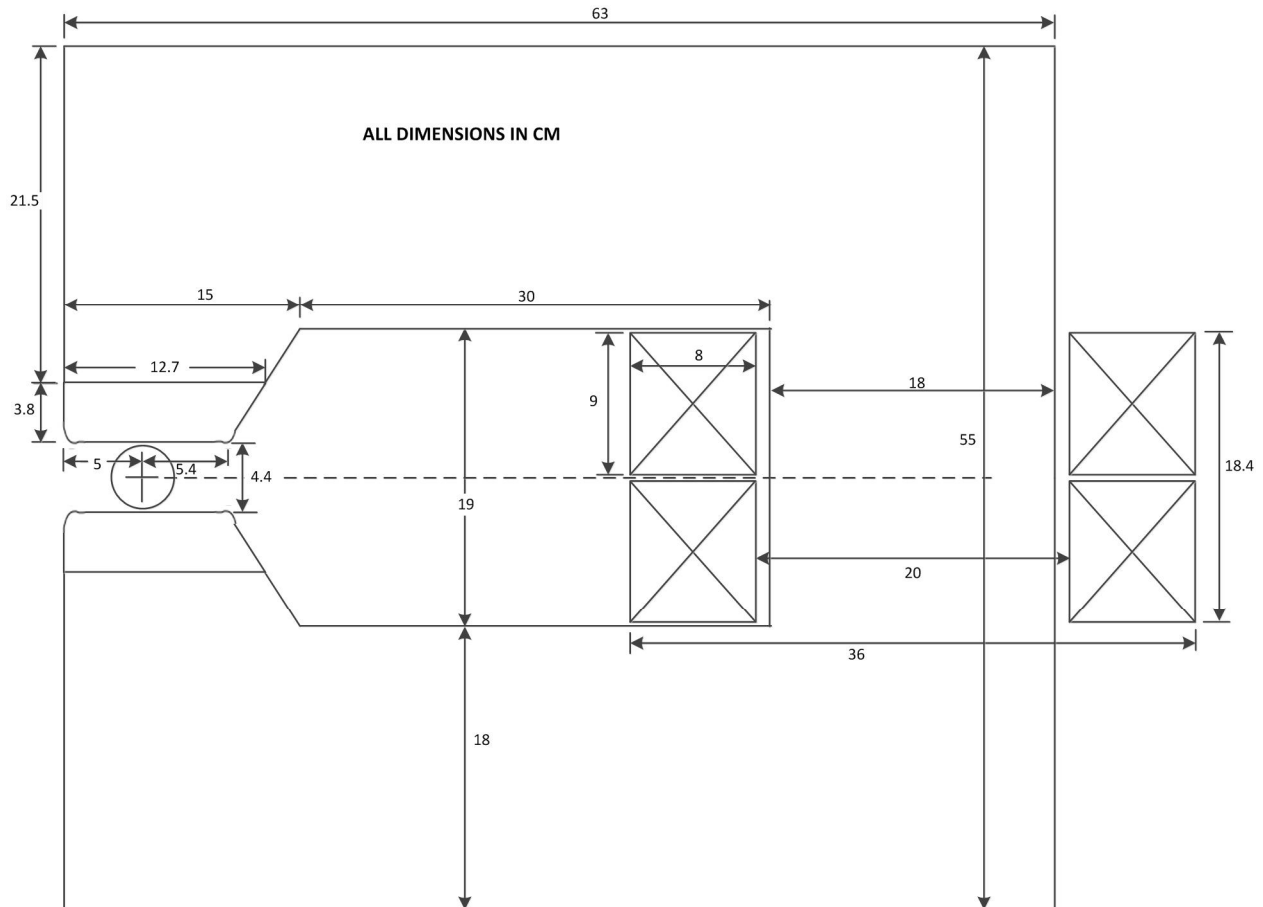


Figure 8.32. BME dipole concept. The dipole face module is normal magnet steel. Top- and back-leg widths are conservatively large and might be reduced. Coil dimensions define an envelope, not necessarily actual conductor dimensions. Dimensions are in centimeters.

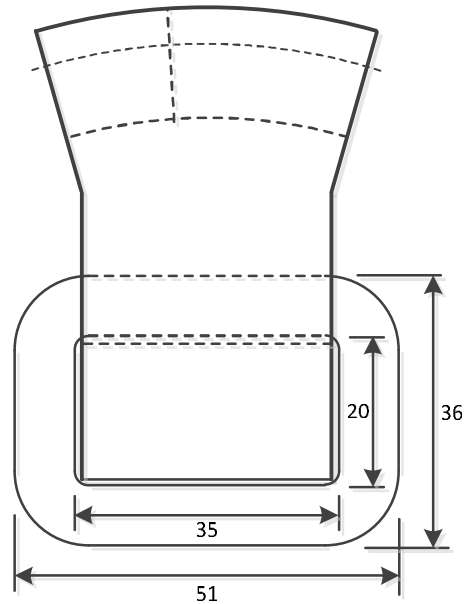


Figure 8.33. BMH-BME coil envelope. Dimensions are in centimeters.

#### 8.3.6.4 Quadrupoles

The notional cross-section for damping ring quadrupoles is shown in Figure 8.34, and the side view of their dimensional envelopes is shown in Figure 8.32. No pole shaping is included in these sketches. The magnet frame must have four sections, or the poles must be removable, to permit coil installation. Trim coils on the back-legs provide the capability for horizontal and vertical dipole orbit correction. As indicated in Fig. 8.23, the spacing between quadrupoles and adjacent magnets is very tight, so there is a premium on minimizing the width of the coils so that these magnets will not collide. The spacing is particularly tight between QDDS and the adjacent SF and SD sextupoles in the dispersion suppressor sections (Fig. 8.25). An alternative quadrupole design concept is shown in Figure 8.36 that has coil packs retracted from the beam axis to enable the coils of an adjacent sextupole to fit in between should mechanical constraints require such a solution.

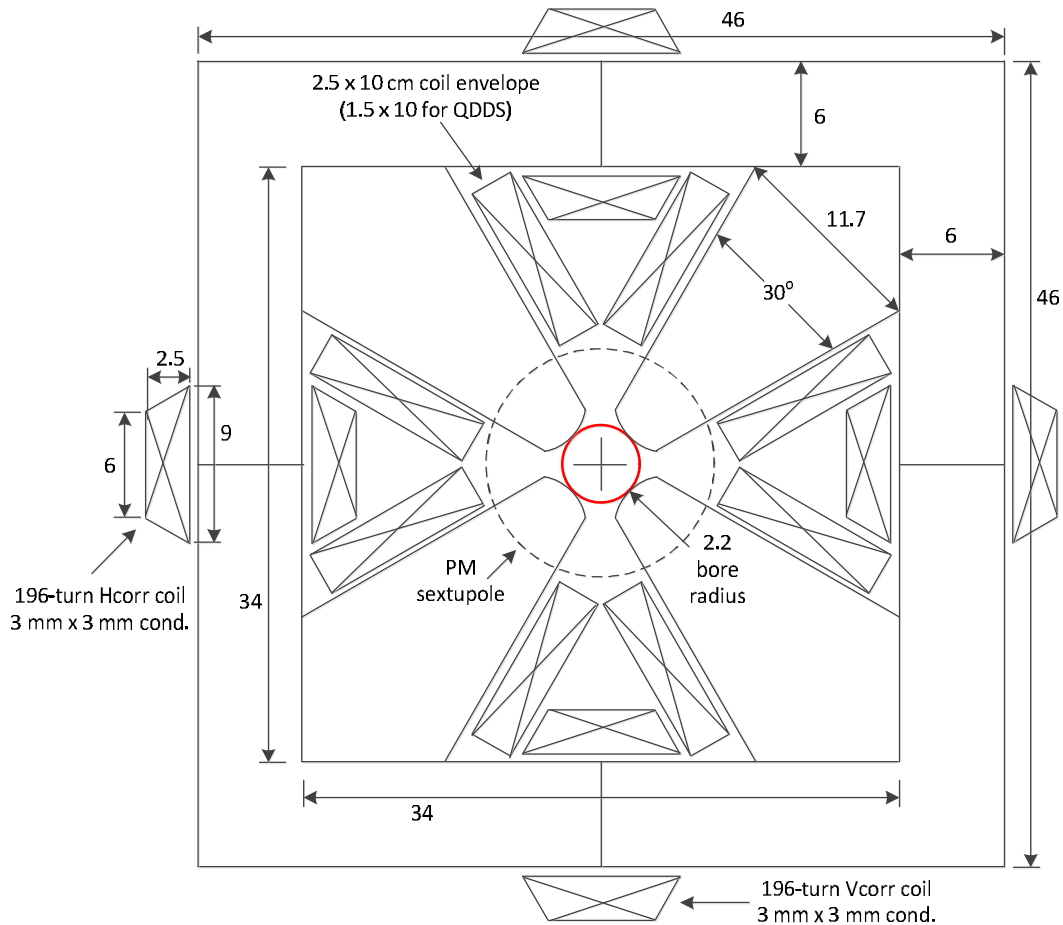


Figure 8.34. Quadrupole cross-section design concept. Dimensions are in centimeters unless otherwise noted.

Given the simple estimate that magnetic length for these quadrupoles is the core length plus an additional bore diameter length (4.4 cm), it is noted that the magnetic length for the short QDDS exceeds the 3-cm length specified in Table 8.11. The core length for this magnet has been chosen to be 2 cm to provide mechanical strength for the 46-cm-tall by 46-cm-wide core. The magnetic length is thus estimated to be 6.4 cm, about twice the specified value. The integrated strength for this magnet can still meet the lattice specification by reducing the operating gradient by a factor of about two. It is noted that the actual magnetic length for QDDS and all magnets will be more accurately estimated with future 3D magnetic modeling that accounts for the complete magnetic environment of the lattice. The notional 2.5 cm x 10 cm cross-section envelope for the quadrupole coils would accommodate 100 (5 x 20) turns per pole of ~5 mm x 5 mm conductor. Assuming a 3-mm diameter cooling hole, this conductor would have 17.9 mm<sup>2</sup> cross-sectional area. For the strongest quadrupole (QF2H) requiring 10520 A-t per pole, the operating current would be ~105 A and the current density would be 5.9 A/mm<sup>2</sup>. The QDDS quadrupole is relatively weak, so a thinner 1.5 cm x 10 cm coil would have 60 (3 x 20) turns per pole and, operating at 98 A, would have a conductor current density of 6.1 A/mm<sup>2</sup>. The trapezoidal corrector trim coils use 196 turns of 3 mm x 3 mm solid conductor in 8 layers and provide 15 mrad or more orbit deflection at 25 A, depending on the length of the quadrupole.

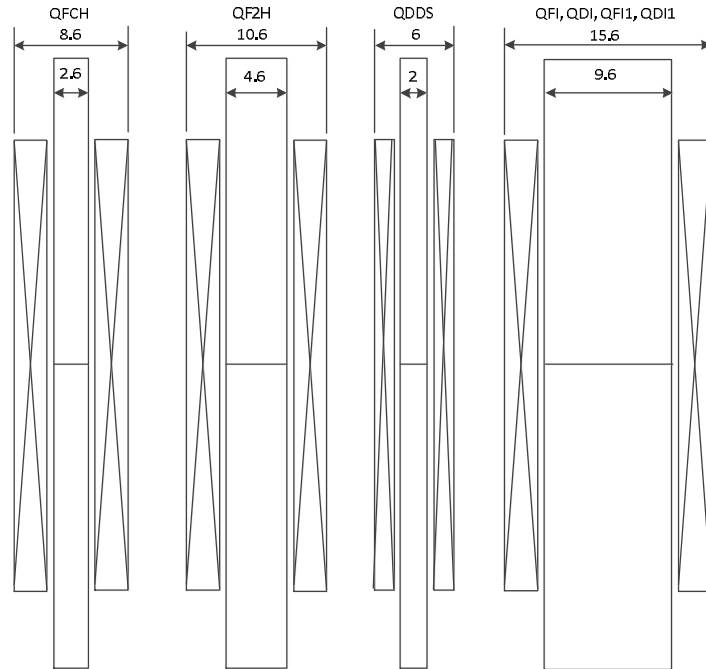


Figure 8.35. Side view of dimensional envelopes for damping ring quadrupole design concepts. Dimensions are in cm.

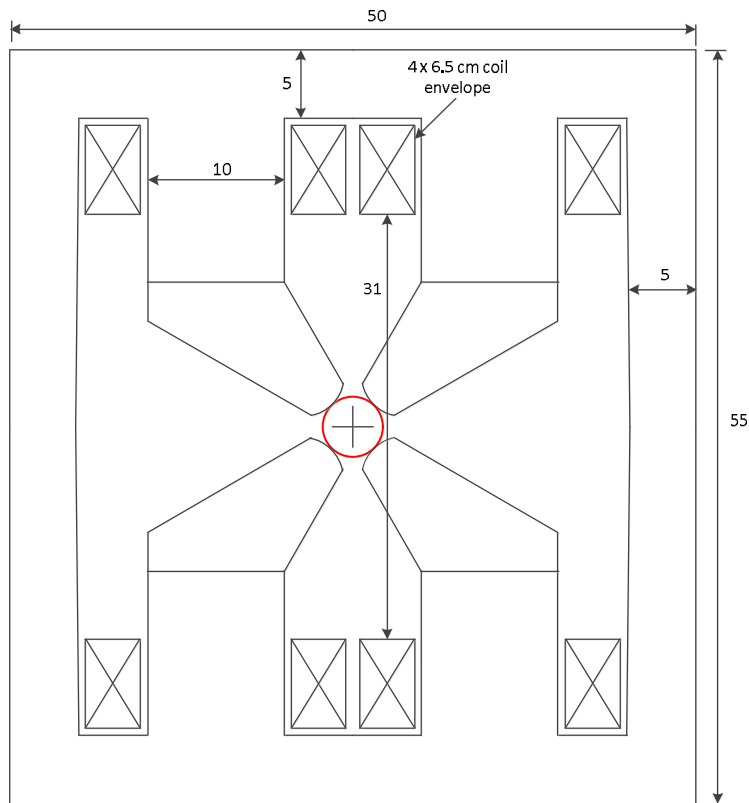


Figure 8.36. An alternative quadrupole design concept with coils retracted from the beam axis to enable adjacent sextupole coils to fit in between. Dimensions are in cm.

### 8.3.6.5 Electromagnet Sextupoles

A notional design concept for damping ring electromagnet sextupoles is shown in Figure 8.37, and a possible simplified core geometry is shown in Figure 8.38. The width and height of the core has been adjusted to match the quadrupole cores. Actual core geometries will be determined with more detailed engineering. No pole shaping is included in these sketches. As discussed in Section 8.3.7.4, the spacing between these sextupoles and adjacent magnets is very tight (Fig. 8.25), so there is a premium on minimizing the width of the coils so that these magnets will not collide. The alternate quadrupole design in Fig. 8.36 would accommodate wider sextupole coil packs. The core must be sectioned, or the poles be removable, to permit coil installation.

As for the QDDS quadrupole, the magnetic length of these sextupoles exceeds the 1.5-cm specification in Table 8.11 due to the extended fringe fields. Like QDDS, the core length for this magnet has been chosen to be 2 cm to provide mechanical strength for the 46-cm-tall by 46-cm-wide core. The magnetic length is thus estimated to be 6.4 cm, about four times the specified value. In principle the integrated strength for these magnets can still meet the lattice specification by reducing the operating gradients. The actual magnetic length, and thus the required operating gradients, for the sextupoles will be more accurately estimated with future 3D magnetic modeling that accounts for the complete magnetic environment of the lattice.

The 1.5 cm x 8 cm cross-section envelope for the sextupole coils would accommodate 48 (3 x 16) turns per pole of ~5 mm x 5 mm conductor. Assuming a 3-mm diameter cooling hole, this conductor would have 17.9 mm<sup>2</sup> cross-sectional area. For the strongest sextupole requiring 4641 A-t per pole, the operating current would be ~97 A and the current density would be 5.4 A/mm<sup>2</sup>. Given that the magnetic length will be longer than specified in Table 8.11, the operating gradient and required ampere-turns per pole will most likely be less than these values.

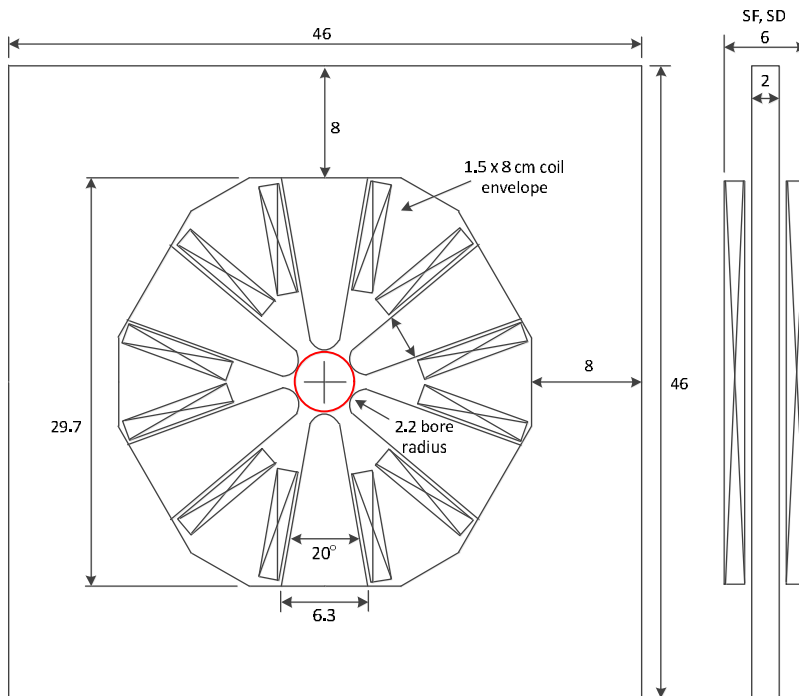


Figure 8.37. Sextupole design concept. Dimensions are in cm unless otherwise noted.

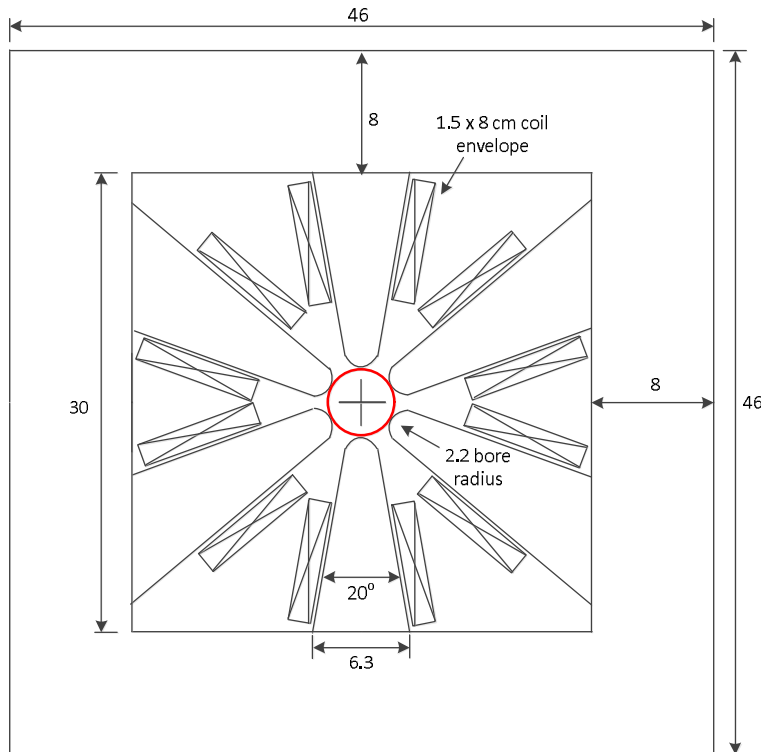


Figure 8.38. Alternative sextupole design concept having simplified core geometry. Actual core geometry will be determined by detailed design. Dimensions are in cm unless otherwise noted.

### 8.3.6.6 Permanent Magnet Sextupoles

The design of the arc lattice calls for a total of 32 sextupoles, 16 in each half arc. The magnetic length of these magnets in the design is 1.5 cm. Space is very precious in the arcs of the damping ring (DR), hence permanent magnet (PM) sextupoles are proposed. The present damping rings use PM sextupoles due to the lack of space in the ring. For the new damping ring, a Halbach style PM design [17,18] is used. A hybrid design does not work here because the sextupole magnets need to be iron-free designs since they are essentially inside the dipole and quadrupole fringe fields. The magnet consists of 12 blocks of magnetic material arranged in a circle. There are two types of blocks with different magnetization angles. The inner radius is 25 mm and the outer radius is 60 mm. The magnet Z length is 25 mm. This length is longer than the design magnetic length but there are no coils for these magnets so the 1 cm of extra length is not an issue. Using the formulas in Refs. [17] and [18], a program has been used to construct an ensemble of magnets with a spread of errors in block position and angle, block magnetization strength and angle, and accounting for the gaps between blocks as well as the finite  $\mu$  of the material. This allows an estimate of the harmonic content of these sextupole magnets based on a realistic set of construction errors. Figure 8.39 is a picture of the block positions and magnetization angles for a sextupole magnet. In this design, the blocks are oriented so that only two unique magnetized blocks are needed.

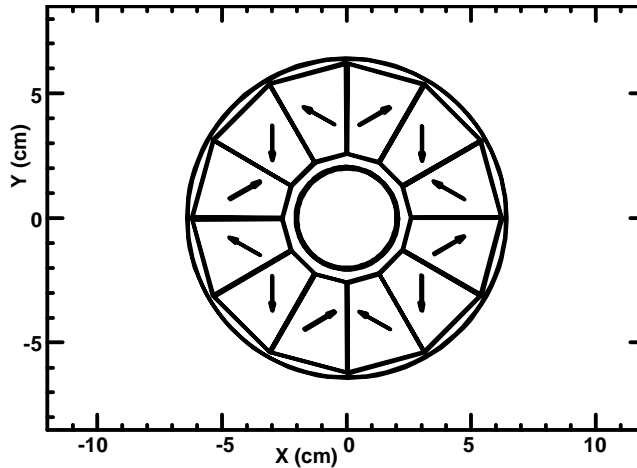


Figure 8.39. A permanent magnet design for the sextupoles in the FACET-II damping ring. There are a total of 12 blocks and two types of blocks.

Table 8.12: Parameter list for the PM sextupoles.

Inner Radius (R1) (cm)	2.5
Outer Radius (R2) (cm)	6.0
Remnant Field (T)	1.05
Relative $\mu$	1.05
Reference Radius (cm)	1.5

Table 8.13. List of errors for each block. The error distribution is uniform over each range.

Radial thickness (R2-R1)	$\pm 51 \mu\text{m}$
Radial placement	$\pm 51 \mu\text{m}$
Remnant Field strength	$\pm 1.9\%$
Remnant Field angle	$\pm 0.75 \text{ deg}$
$\phi$ thickness	$\pm 51 \mu\text{m}$
$\phi$ Placement	$\pm 0.31 \text{ deg}$ ( $\pm 135 \mu\text{m}$ @R1)

The use of 12 blocks reduces the ideal field strength of the magnet by 0.811 due to the finite block size and the fixed magnetization angle throughout each block. The modeling assumes  $\text{Sm}_2\text{Co}_{17}$  type material which has a very high intrinsic coercive force (in excess of 18 kOe). Based on the above dimensions and error distributions, the following average harmonic content is estimated for an ensemble of 100 magnets.

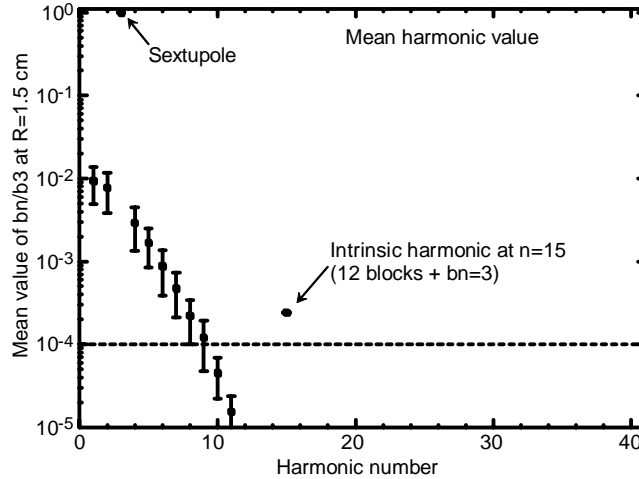


Figure 8.38. The average harmonic content of 100 magnets using the above dimensions and error distributions. The reference radius is 1.5 cm. Note: there is an intrinsic harmonic at  $n=15$  (12 blocks +  $n=3$ ). However, this extra harmonic is quite small.

As one can see from Fig. 8.37, there is space between the magnet material and the beam pipe which is drawn in as a 4cm inner diameter pipe with a 0.5 mm wall. If necessary, (to get more strength) the inner radius can be decreased to as little as 22 mm. However, the harmonics will increase slightly. Fig 8.39 is a plot of the harmonic content of the magnet if the inner radius is decreased to 22 mm. The magnet strength increases from 1639 to 2216  $\text{kg/m}^2$  a +35% increase.

A suggested procedure for assembly which follows the procedure developed for the PEP-II PMs is described here [19]. The outer casing can be made from a stress-free Al tube where the inside is wire EDM cut to make flat surfaces that are used to glue the blocks into position. There will be side forces on the blocks already glued into position as the final blocks are moved into position and glued. The already glued blocks can be temporarily restrained while the last blocks are being glued to the casing. Then a

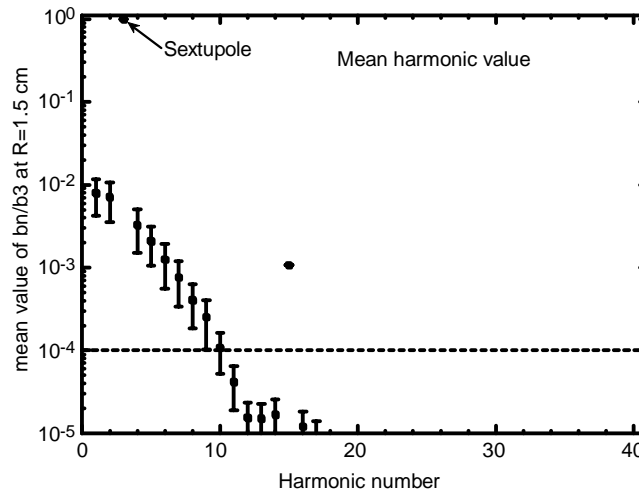


Figure 8.39. Harmonic content of a magnet with an inner radius of 2.2 cm. One can see that the higher harmonics have increased but they probably are still small enough to not be an issue. The magnet strength has significantly increased (+35%).

slow setting epoxy is used to glue all of the blocks together. The outer casing would be in two halves with a split at the boundary between two blocks which allows for installation around a beam pipe.

It is assumed that each sextupole is mounted on a motion stage, capable of +/- 2mm motion in x/y with 5um precision.

### 8.3.7 RF System

#### 8.3.8 Overview

The RF system for the positron damping ring is designed for 1.1MV of accelerating gap voltage to be provided by two RF cavities, one each in the injection and extraction straights.

#### 8.3.9 Klystron

The two cavities will be powered by a 714MHz klystron from the current damping rings. The HVPS and klystron will be moved from the South Damping Ring and installed in the klystron gallery in Sector 10. Waveguide will be run down penetration 10-13 and power split on the ceiling of the tunnel to the two cavities.

#### 8.3.10 Cavities

The two cavities will be recovered from the South Damping Ring and installed in the straight sections near the septa.

#### 8.3.11 LLRF

The low-level RF and feedback system from the current damping ring will be adapted to use the new global clock. New PLC logic will be developed to interface to EPICS.

#### 8.3.12 Vacuum System

##### 8.3.8.1. Arcs

The design of the positron damping ring arc lattice has a dense set of magnets. There is little room for vacuum pumping. The design considered here has lumped pump options for the damping ring vacuum. A program called VACCALC [20] is used to compute the pressure profile under various pumping schemes. The beam pipe in the arc is a 4 cm diameter pipe which has reasonable conductance. The length of the arc is about 4.1 m. The first case considered has lumped pumps at either end of the arc. Figure 8.40 shows the pressure profile around the arc. This assumes a thermal outgassing rate of 0.1 nTorr (l/s)/cm<sup>2</sup>. The pump speeds at the ends of the arc are 100 l/s.

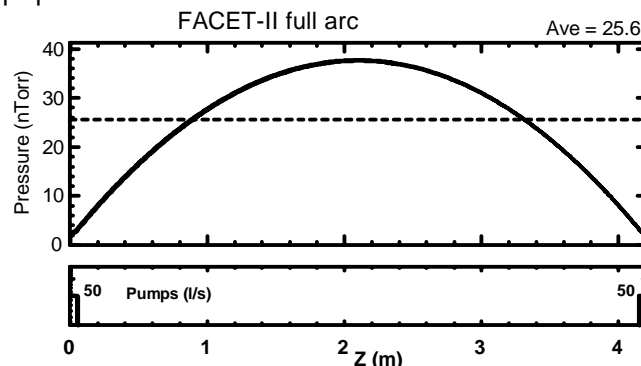


Figure 8.40. Plot of the arc vacuum with pumping only at the ends of the arc. The average pressure is about 26 nTorr.

To improve the pressure profile a vacuum pipe stub (4 cm dia. 10 cm long) is added to the center of the arc chamber and a pump attached to the end of the stub. Fig. 8.41 shows the pressure profile of the first half of the arc (the other half is a mirror image). The pump speeds of the three pumps in this model are 50 l/s. Increasing the pump speed will lower the pressure.

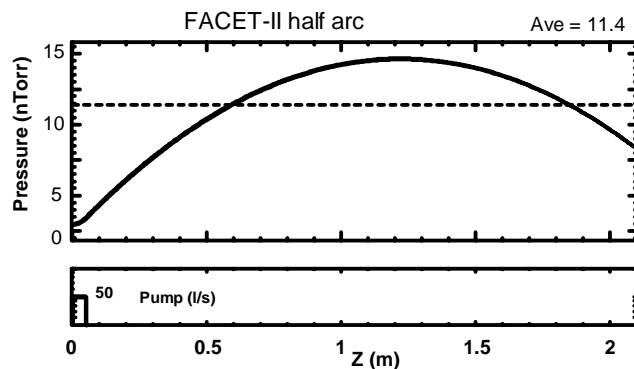


Figure 8.41. Pressure profile of one half of the arc when a pump is added to the center point of the arc with a 10 cm pipe stub to the pump. The average pressure is 11.4 nTorr.

One more improvement was tried where pumps were added to the arc at the 1/3 and 2/3 points. The results are summarized below in Table 8.14. The table also includes runs with higher pump speeds.

Table 8.14. Results from various vacuum pumping scenarios for the arcs of the positron damping ring.

Case	Description	Ave press nTorr
1	2 end pumps only (100 l/s) (Fig 1)	25.6
2	2 end + 1 center (50 l/s) (Fig. 2)	11.4 11.4
3	2 end (100 l/s) + 1 at 1/3 & 2/3 pts (50 l/s)	5.8 7.5 5.8
4	2 end (100 l/s) + 1 at 1/3 & 2/3 pts (100 l/s)	5.2 6.7 5.2
5	2 end + 1 center (100 l/s)	9.4 9.4

In summary, an average pressure of 6 nTorr in the arc chambers can be achieved if 100 l/s pumps are placed at each end of the arc and at the 1/3 and 2/3 points. The pumps inside the arc are attached with a 10 cm long 4cm diameter pipe stub. This calculation does not presently account for an RF screen that might need to be placed at the junction to the main arc beam pipe. Such a screen will reduce the

conductance to the pump located at the end of the stub. The pressure in the arc chamber will rise slightly but the effect should be less than 10%.

### 8.3.8.2. Straights

Next the pumping needed for the straights is considered. The RF expert [21] argues that anything less than 100 nTorr is OK for the RF cavity. However, the kicker structures for the damping ring need a pressure that is less than 6 nTorr [22]. The following pumping scheme was developed based on the kicker requirements. Most of the beam pipe in the straight sections has a 5cm diameter, the same size as the current damping rings. However, the region between the septum and the kicker has a larger beam pipe diameter due to the larger size of the beam in this region and due to the orbit of the kicked beam. The diameter of the pipe between the septum and the kicker is 8 cm at the septum and through the quadrupole doublet. Then the pipe narrows down to a 3 cm diameter at the kicker. Also, in order to account for the extra surfaces that are inside the septum chamber, the thermal outgassing value for this pipe segment has been doubled to 0.2 nTorr (l/s)/cm<sup>2</sup>. The present septum magnet has a 440 l/s pump mounted at the center of the chamber and that pump will be located in the same place in the new damping ring. Figure 8.42 shows the pressure profile where 100 l/s pumps are installed upstream and downstream of the kicker segment and upstream and downstream of the RF cavity. This assumes no RF processing for the cavity. Processing should scrub the surfaces and hence the cavity vacuum should be lower than this estimate. There is also a 440 l/s pump in the center of the septum chamber as mentioned above. These pumps are all in addition to the previously mentioned arc pumps. The average pressure of the straight is just over 5 nTorr. The pressure at the kicker is about 4 nTorr and the pressure at the RF cavity is 10.5 nTorr.

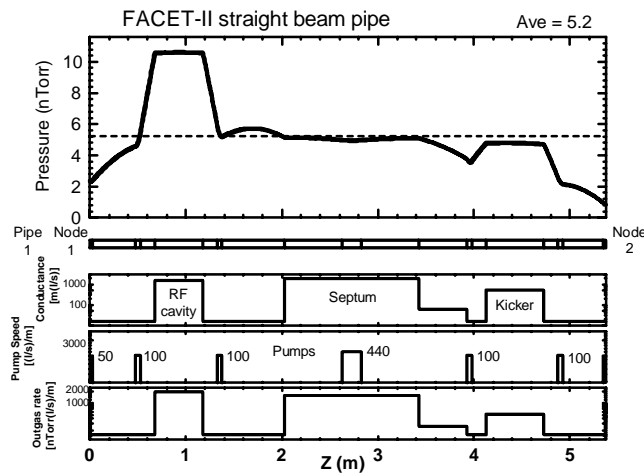


Figure 8.42. Pressure profile of the PDR straight section. There are 2 100 l/s pumps on either side of the kicker and RF cavity. There is also a 440 l/s pump at the middle of the septum chamber.

For case 3 in Table 8.14, the total number of pumps for the positron damping ring is 18. There are 16 100 l/s pumps and two 440 l/s pumps. The overall average base pressure for the entire ring is then about 5-6 nTorr.

### 8.3.13 Synchrotron Radiation

The beam energy of the damping ring is low (335 MeV). The bend field in the arc magnets is 1.44 T. The standard formula for synchrotron radiation gives a critical energy value of 108 eV. The ring circumference is 20.154 m. The go-around frequency is 14.885 MHz. The beam current for a bunch

charge of  $2 \times 10^{10} e^+$  is 48 mA. This gives a synchrotron radiation power from the bends of 0.14186 W per cm of bending magnet length. The total length of the bending magnets in one arc is 244 cm so the total SR power is 34.6 W for each ring arc. This power is essentially spread all around the arc beam pipe which is 4.1 m long. So power per unit length is 8.4 W/m. This is a small number and can be considered to be negligible except that one may want to add an occasional cooling tube to portions of the arc chamber to absorb the small power incident from the synchrotron radiation. The number of photons hitting the beam pipe surface is  $1.3 \times 10^{19}$  /s half of which have an energy below 10 eV. Nevertheless there are probably enough photons to start to “scrub” the beam pipe so some initial commissioning time will likely be needed to let the SR photons “clean up” the beam pipe inner surface.

## 8.4 Positron Extraction and Compression

### 8.4.1 Overview

The Positron Extraction and Compression system(PEC) starts at the entrance of the PDR extraction kicker on the final extraction turn and ends at the positron injection point into the main linac in the final bend of the BC1 electron bunch compressor. In order to match with the electron compression scheme, this system must also compress the bunch length by a factor of ~10. Figure 8.43 gives a schematic of the PEC beamline. These tasks are achieved with the following four sub-systems:

#### *8.4.1.1 Vertical dogleg extraction from damping ring.*

With a linear footprint of ~10 m, the dogleg extracts the beam from the damping ring at an angle of 114.6mrad and raises the beam from the damping ring height by 96.4 cm to match the Linac beam height. Five quadrupole magnets provide beta matching whilst keeping the vertical dispersion reasonably small (max ~40 cm). The extraction angle is given by requirements to cleanly extract the beam from the PDR, and the optical match is an optimal balance between keeping reasonably sized beta functions and keeping the dispersion function from becoming too large. The energy spread is small upon extraction from the damping ring (<0.1%) so chromatic aberrations are not a problem in this section.

#### *8.4.1.2 Diagnostics section.*

A 5 m diagnostics section is provided with a beam waist in the center for emittance measurement. Four OTR profile measurement devices will be placed across the diagnostic waist to provide fast emittance measurements and monitoring and provide matching data to correct betatron errors from the PDR.

#### *8.4.1.3 Bunch compression (BC0).*

A 2.1 m S-band accelerating cavity section, operating at a design RF voltage of 16.91 MV is operated at the RF zero-crossing to provide an energy chirp to the positron bunch. The bunch length is compressed across a 4-bend (360 mrad per bend) chicane providing  $R_{56} = -300$  mm (BC0). Two “dispersion-tweaker” quadrupole magnets are provided within the chicane for dispersion correction control. An adjustable gap collimator is located in the center section of the chicane, half-aperture=4.5 mm, which reduces longitudinal non-linearities in the high-dispersion bunch tails helping control the quality of the longitudinal bunch profile throughout the machine and maximizing the delivered peak positron beam current. Although the 4-bend chicane is shown in a horizontal arrangement here (Figure 8.43), we would most likely prefer to perform the final installation in a vertical dimension to maximize available floor space adjacent to the main main beam line in the accelerator tunnel.

#### *8.4.1.4 Horizontal dogleg injection.*

In a z-length of 20m, this horizontal dogleg injects the positron beam into the main FACET-II beamline at a horizontal angle of 94 mrad, matching the BC1 bend angle. The final BC1 bend magnet is shared with the electron beam. The positron bunch is injected  $\frac{1}{2}$  of an S-band wavelength (5.25 cm) in front of the electron beam for co-acceleration through the linac. Five quadrupole magnets provide beta function matching into the main beamline and maintain a manageable horizontal dispersion function given the required injection angle (94 mrad) and beam energy spread. After the energy chirp is added, the higher energy spread beam (compared with the vertical dogleg) requires chromatic aberration control, which is achieved by using 2 sextupole magnets in dispersive regions of the dogleg.

### 8.4.2 Beam Parameters

This system is matched, given the damping ring beam parameters at the extraction point, and provides the required positron (and electron) matching conditions at the insertion point into the main FACET-II beamline. The matched twiss parameters are shown below in Figure 8.45.

Table 8.15. Beam parameters for positron extraction and compression system from the entrance of the PDR extraction kicker on extraction turn, to injection into the main linac in the final bend of the electron BC1 chicane bend. Initial parameters include beam dynamics calculations performed for the damping ring (e.g. IBS growth of emittance as shown in Figure 8.21).

Parameter	Symbol	Value	Range	Unit
Beam Energy	$E_0$	335		MeV
Initial Transverse Emittance	$\gamma\epsilon_x / \gamma\epsilon_y$	5.9 / 5.9	5.24-5.9	$\mu\text{m}\cdot\text{rad}$
Final Transverse Emittance	$\gamma\epsilon_x / \gamma\epsilon_y$	6.5 / 5.9		$\mu\text{m}\cdot\text{rad}$
Initial Twiss	$\beta_x / \alpha_x$ $\beta_y / \alpha_y$	2.0 / 0 5.0 / 0		m
Final Twiss	$\beta_x / \alpha_x$ $\beta_y / \alpha_y$	6.362 / -2.567 16.866 / -4.067		m
Initial rms Bunch Length	$\sigma_z$	4	3.5-4	mm
Final rms Bunch Length	$\sigma_z$	0.350		mm
Final E-z chirp	$\alpha_z$	0.389		
Initial rms Energy Spread	$\sigma_E/E$	0.11		%
Final rms Energy Spread	$\sigma_E/E$	0.52		%
Initial Bunch Charge	Q	2	1-2	nC
Final Bunch Charge	Q	1.2	1-2	nC
BC0 Collimator Aperture	A	4.5	2-10	mm

### 8.4.3 Layout and Optics Design

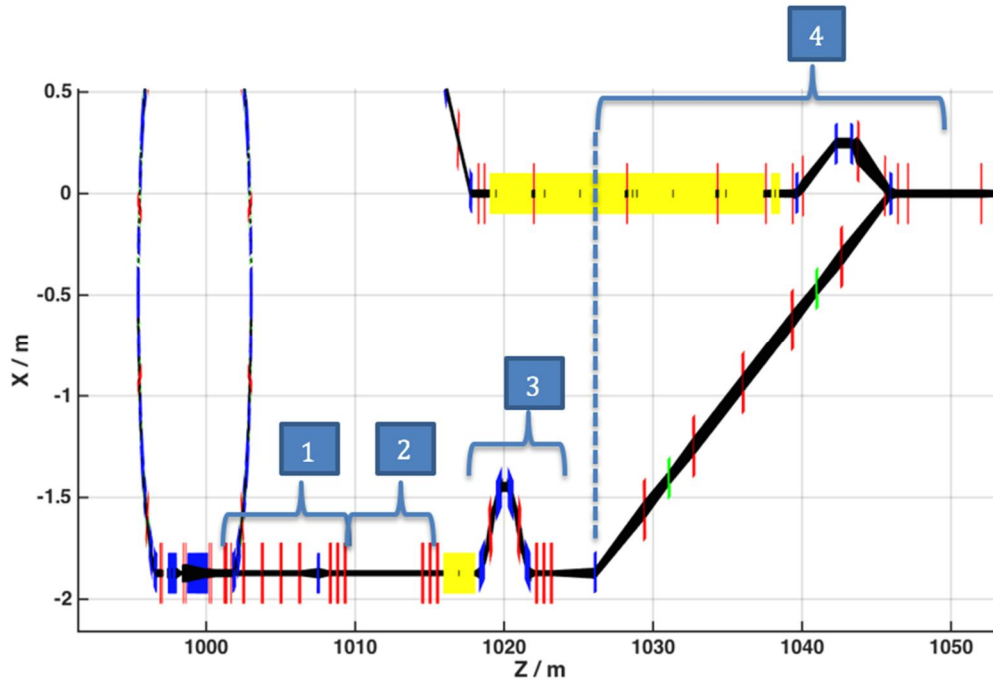


Figure 8.43. Plan layout view of Positron Extraction System (PEC). Yellow indicates RF, blue dipoles, red quadrupoles, green sextupoles. Coordinate system is relative to SLC linac (x/y) and SLC z-reference. The numbered subsections refer to the Sections 8.4.1.1 to 8.4.1.4.

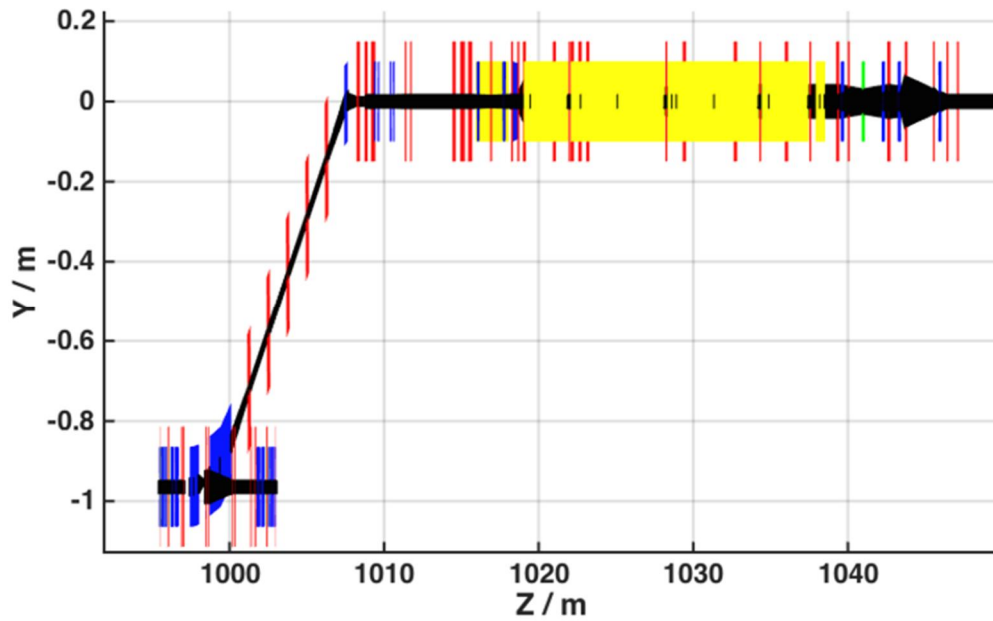


Figure 8.44. Elevation view of PEC system area. Yellow indicates RF, blue dipoles, red quadrupoles, green sextupoles. Coordinate system is relative to SLC linac (x/y) and SLC z-reference.

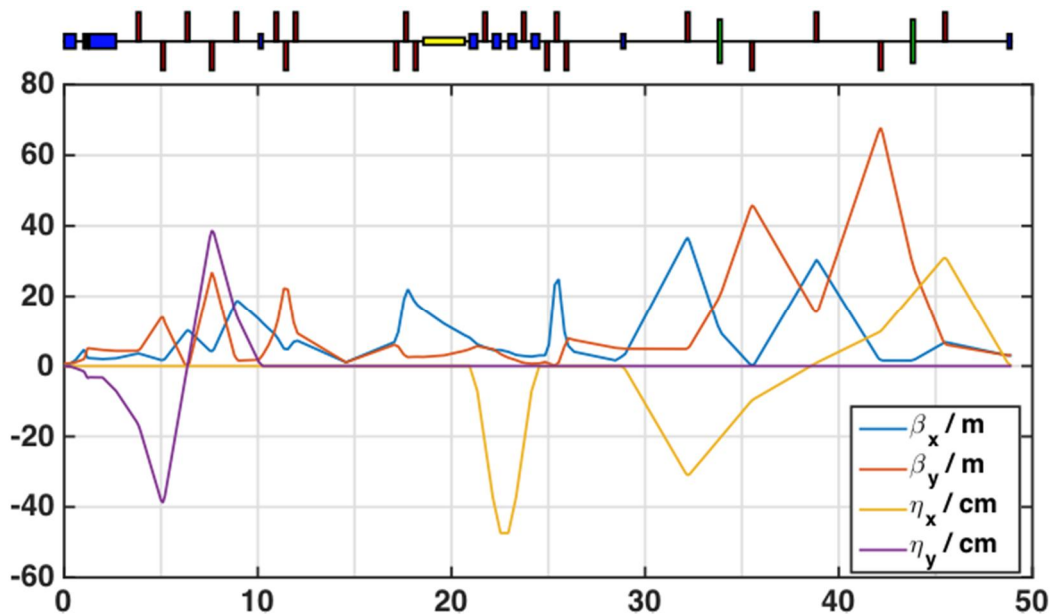


Figure 8.45. Twiss parameters across PEC system.

#### 8.4.4 Beam Dynamics

Using a 6D tracking code (*Lucretia*), a 100K macro-particle representation of the positron bunch is tracked through the lattice including ISR, CSR and LSC effects as well as wakefield effects in the cavity. The final tracked longitudinal and transverse phase space of the positron beam after BC1 is shown in Figure 8.46. The sextupole magnets were set to minimize transverse emittance growth through the final horizontal dogleg due to chromaticity and second-order dispersion. The emittance growth is controlled to ~10% (>100% without sextupole magnets).

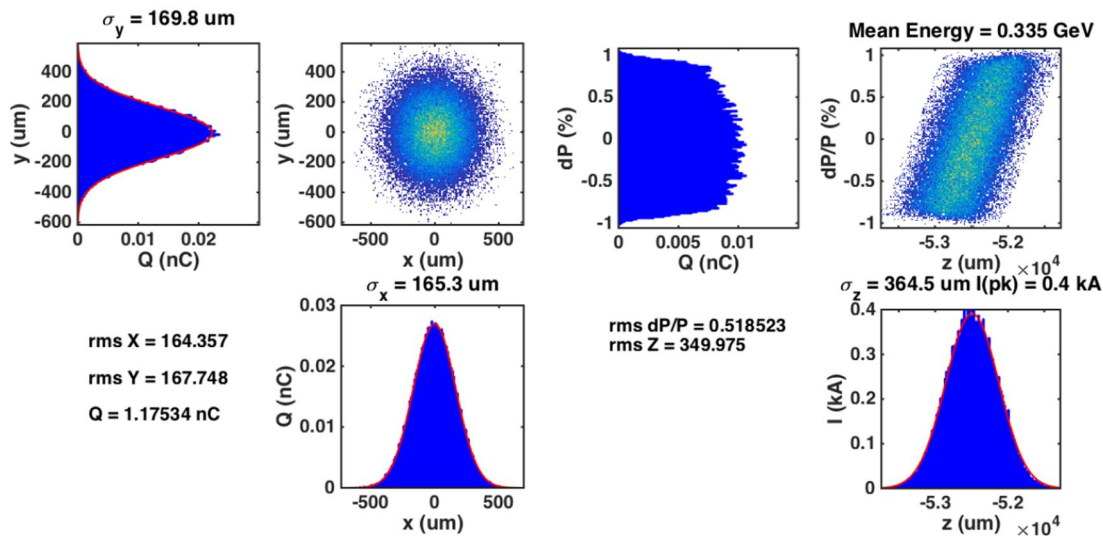


Figure 8.46. Transverse and longitudinal phase-space of tracked macro-particle bunch at exit of BC1 final bend. Note the collimation of the original 2 nC beam to 1.2 nC using the 4.5 mm aperture collimator in BC0.

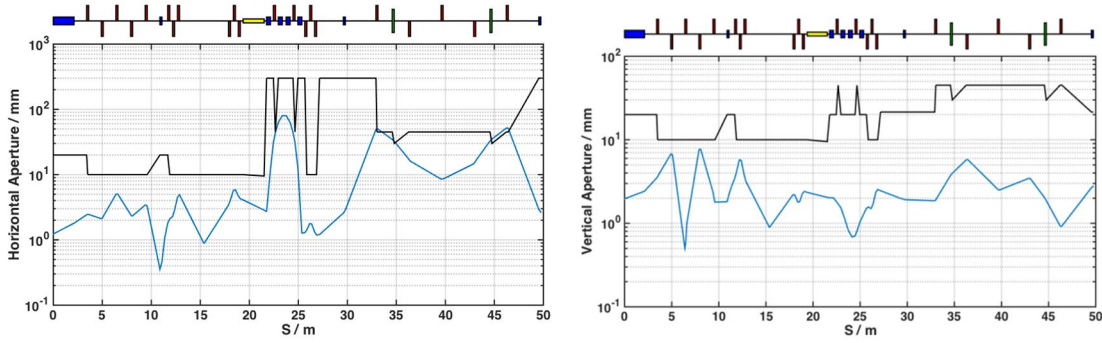


Figure 8.47. Required minimum horizontal and vertical magnet apertures (black) compared to tracked X10 rms beam sizes (blue). Shown is the tracked beam envelope without collimation.

### 8.4.5 Magnets & RF

The PEC section consists of 21 quadrupole magnets of 2 engineering types; 2 sextupole magnets of the same type; 7 dipole magnets of 2 types (one of which is shared with the BC1 system). One S-band structure for providing bunch compression energy chirp.

## 8.4.6 Quadrupoles

Table 8.16. Quadrupole magnet parameters.

Deck Name	Engineering Type / subsection	Effective Length / m	Design Int. Strength / T	Max. Int. Strength / T	Design Pole Tip Field / T	Max Pole Tip Field /  T	Aperture (radius) / m
QPEC1	A	0.2	0.3764	5	0.0188	0.25000	0.01
QPEC2	A	0.2	-1.1837	5	0.0592	0.25000	0.01
QPEC3	A	0.2	0.9000	5	0.0450	0.25000	0.01
QPEC4	A	0.2	-1.3320	5	0.0666	0.25000	0.01
QPEC5	A	0.2	1.0671	5	0.0534	0.25000	0.01
QPEC6	A	0.2	1.0045	5	0.0502	0.25000	0.01
QPEC7	A	0.2	-2.1609	5	0.1080	0.25000	0.01
QPEC8	A	0.2	1.6467	5	0.0823	0.25000	0.01
QPEC11	A	0.2	-1.1307	5	0.0565	0.25000	0.01
QPEC12	A	0.2	1.7400	5	0.0870	0.25000	0.01
QPEC13	A	0.2	-0.8282	5	0.0414	0.25000	0.01
QPEC9	B	0.2	0.0000	1	0.0000	0.22500	0.045
QPEC10	B	0.2	0.0000	1	0.0000	0.22500	0.045
QPEC14	A	0.2	-0.7746	5	0.0387	0.25000	0.01
QPEC15	A	0.2	1.6782	5	0.0839	0.25000	0.01
QPEC16	A	0.2	-1.1107	5	0.0555	0.25000	0.01
QPEC17	B	0.2	0.5797	1	0.1304	0.22500	0.045
QPEC18	B	0.2	-0.4256	1	0.0958	0.22500	0.045
QPEC19	B	0.2	0.5628	1	0.1266	0.22500	0.045
QPEC20	B	0.2	-0.4256	1	0.0958	0.22500	0.045
QPEC21	B	0.2	0.5797	1	0.1304	0.22500	0.045

### 8.4.7 Sextupoles

It is assumed that each sextupole is mounted on a remotely controllable motion stage, capable of +/- 2mm motion in x/y with 5um precision.

Table 8.17. Sextupole magnet parameters.

Deck Name	Engineering Type / subsection	Effective Length / m	Design Int. Strength / T.m <sup>-1</sup>	Max. Int. Strength /  T.m <sup>-1</sup>	Design Pole Tip Field / T	Max Pole Tip Field /  T	Aperture (radius) / m
SPEC1	A	0.2	-11.833	100	0.05325	0.45000	0.03
SPEC2	A	0.2	10.785	100	0.04853	0.45000	0.03

### 8.4.8 Dipoles

Table 8.18. Dipole magnet parameters.

Deck Name	Engineering Type / subsection	Effective Length / m	Design Int. Strength / T.m	Max. Int. Strength /  T.m	Design Pole Tip Field / T	Max Pole Tip Field /  T	Aperture (radius) / m
BPEC2	A	0.2	0.11174	0.5	0.5587	2.500	0.02
BPEC3	B	0.4	-0.40228	0.5	1.0057	1.250	0.02
BPEC4	B	0.4	0.40228	0.5	1.0057	1.250	0.02
BPEC5	B	0.4	0.40228	0.5	1.0057	1.250	0.02
BPEC6	B	0.4	-0.40228	0.5	1.0057	1.250	0.02
BPEC7	A	0.2	-0.10504	0.2	0.5157	1.000	0.02
BPEC8	A	0.2	0.10504	0.2	0.5157	1.000	0.02

### 8.4.9 RF

Table 8.19. RF structure parameters. Phase is with respect to on-crest acceleration (phase > 0 is defined as early with respect to synchronous particle). Voltage is un-loaded cavity gain.

Deck Name	Freq. / MHz	Length / m	V / MV	Phase / deg	Aperture / m
LPEC1	2856	2.1336	16.91	-90	0.0095

## 8.5 Instrumentation, Diagnostics and Feedback

A standard suite of linac/transport line diagnostics will be installed in each of the functional areas of the positron system. The function of these devices – BPMs, toroids, profile monitors, bunch length monitors – is described in detail in Section 6.8 (Linac Diagnostics). In general, BPMs will be refurbished stripline BPMs retrieved from Sector 0-10, except for in the damping ring itself, where the tight conditions and aperture considerations make button-style pickups necessary.

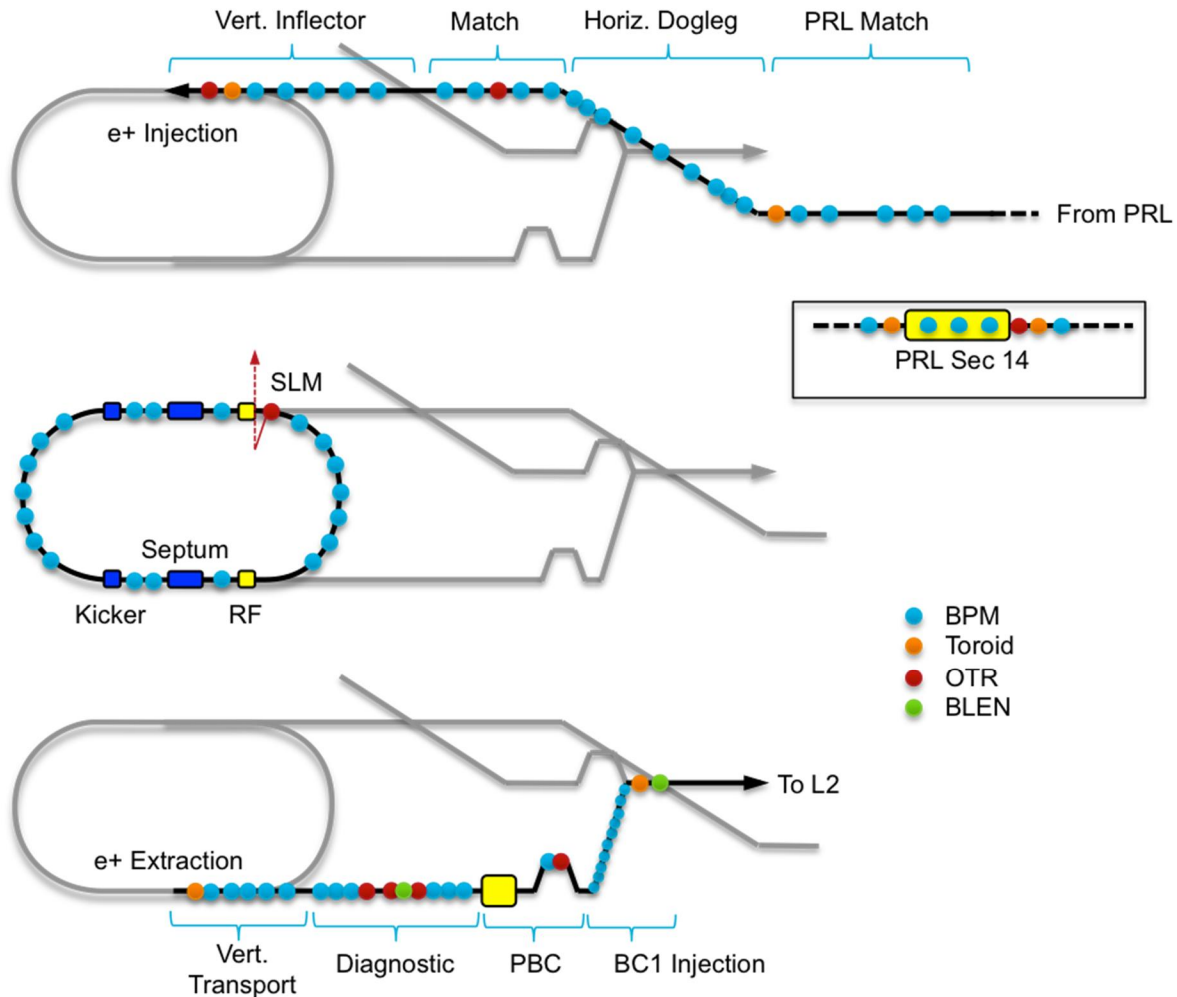


Figure 8.48. Overview of positron system diagnostics. Top: PRL and PDR injection; inset: accelerator structures from Sector 14; middle: damping ring; bottom: PDR extraction and PEC system. Yellow boxes indicate RF cavities or structures. Locations of diagnostics are approximate only.

Toroids and ceramic gap monitors will be salvaged as well; YAG and OTR screens will receive all new hardware modeled after the diagnostics in use at FACET. OTR screens are chosen over wire scanners for beam profile measurements as the repetition rate for positrons is only 5 Hz. COTR production in these screens is not expected to be significant at the low peak currents before the linac. With the exception of the BPMs and toroids in the positron return line, EPICS controls and infrastructure will be used for all new installations.

Table 8.20 – Counts of standard diagnostics for positron system.

New Devices	PRL	PRL	PDR	PEC
BPM	5	23	22	22
Toroid	2	1	0	2
OTR/YAG	1	2	0	4
BLEN	0	0	0	2

### 8.5.1 PRL Diagnostics

The existing BPMs in the PRL will be retained as-is and used via the legacy controls. The exception is at Sector 14, at the 125 MeV acceleration section, where 5 additional BPMs will be installed. One will be added in each of the new upstream/downstream doublet quadrupoles and one in each of the triplets between the accelerator structures in order to center the beam in the small aperture of the disk-loaded waveguide. An insertable OTR profile monitor just upstream of the first accelerating structure will allow quad-scan measurement and correction of any incoming beta mismatch which could compromise the beam size and lead to losses. Toroids upstream and downstream of the accelerator structure will be used to monitor for beam loss.

The line connecting the PRL to the PDR has 14 BPMs in the horizontal dogleg and 9 in the vertical inflector; these will be refurbished stripline BPMs read out through new EPICS processors. An OTR profile monitor will be located in the FODO transport between the horizontal and vertical sections for quad-scan emittance measurement. Just upstream of the permanent magnet quadrupole (PMQ) triplet is a toroid for charge monitoring and another OTR screen for energy spread measurement and tuning.

### 8.5.2 Damping Ring Diagnostics

Twenty-two BPMs are located in the damping ring as near as possible to the sextupole magnets, as space constraints due to the close proximity of magnet yokes and coils limit the BPM placement. Button-type pickups, rather than striplines, will be used to conserve aperture for the injected beam. Bandwidth limitations of the standard LCLS linac processors cause the signal to ring on a time scale of 2-3 revolutions of the stored damping ring beam. The necessary modifications to the BPM electronics to allow measurement of single turns is an area that requires further study.

Measurement of the betatron and synchrotron tunes will be done by splitting the signal from selected BPM pickups at high-beta (or high-dispersion for  $v_s$ ) locations into a networked spectrum analyzer which will be relocated from the existing NDR to Sector 10.

A synchrotron light monitor will be installed just after the final bend magnets at the beginning of the extraction straight. This consists of an in-vacuum mirror which reflects the visible portion of the synchrotron radiation spectrum through a quartz vacuum window towards the ring center. This synchrotron light will then be collected by a lens system and transported in an optical transport tube up a linac penetration to the laser prep room located adjacent to the injector laser room on the north side of the Klystron Gallery. Imaging this beam into a standard gated camera allows study of the transverse stability and damping during the store. Further, splitting the light into an optical streak camera allows for measurement of the longitudinal damping and extracted bunch length. A simplified schematic is shown in Figure 8.49.

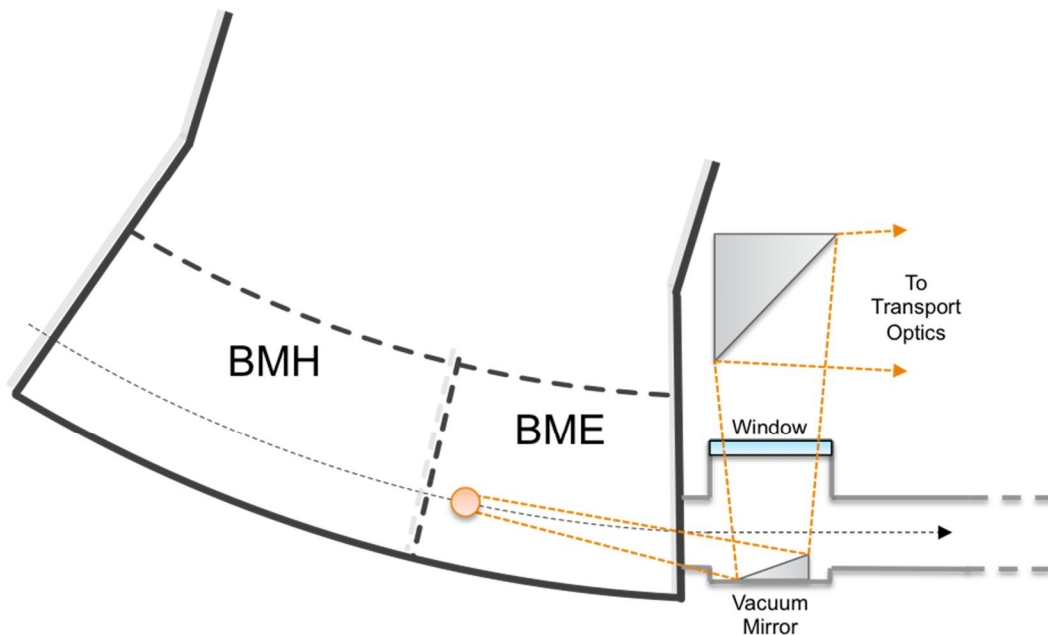


Figure 8.49. Location of synchrotron light monitor window at arc/straight boundary.

### 8.5.3 PEC Diagnostics

The PEC has 22 BPMs in total: 5 in the vertical extraction transport quads, 6 in the quadrupole triplets upstream and downstream of the diagnostic section, 1 for energy measurement at the center of the bunch compressor, and 10 in the horizontal dogleg into BC1 (8 in each quad plus 2 in each sextupole). Toroids for measuring the beam charge are located directly after the ring extraction and downstream of the compressor chicane. Like in the injection line, these BPMs and toroids will be refurbished from existing linac hardware and read out with new EPICS controls.

The 5-meter diagnostic drift section contains 3 OTR screens spaced symmetrically about the beam waist, allowing for fast multi-screen measurements of the extracted beam emittance. Another OTR screen at the midpoint of the bunch compressor will be installed for energy spread measurements and setting the adjustable collimator jaws. Ceramic gap bunch length monitors will be located upstream and downstream of the bunch compressor, allowing monitoring of the incoming and outgoing bunch lengths. These bunch length monitors will be calibrated with the TCAV1 transverse deflector located just after BC1 (See Chapter 6).

### 8.5.4 Feedback Systems

To correct for slow diurnally-driven drift, four-corrector ( $x$ ,  $x'$ ,  $y$ ,  $y'$ ) steering feedback loops modeled after the SLC design will be implemented at the end of the PRL, just after PDR extraction, and just before BC1 injection. If necessary, the trajectory in the ring may be stabilized by iterative application of a standard steering algorithm such as SVD or 1-to-1 over a several-minute time scale.

Energy feedback for the westbound positron beam will monitor the dispersive orbit in the vertical inflector at the end of the PRL line and vary the amplitude of the 14-8 klystron. For the extracted beam,

the energy and bunch length monitoring in the PEC chicane will feed into a "2x2" feedback that adjusts the phase and amplitude of the 2.1-m compressor klystron in a coupled fashion. This will have identical function to the BC1 – L1S feedback system for the electron beam.

These feedbacks will be implemented in the same fashion as at FACET, typically Matlab or python scripts reading inputs and writing outputs over EPICS channel access. The high-performance dedicated feedback networking used at LCLS is not applicable due to the relatively slow 5 Hz repetition rate.

- 
- 1 "A possible design for the NLC e+ source", H. Braun et. Al., EPAC 1992
  - 2 M. Sands, "The physics of electron storage rings, an introduction," SLAC Report No. SLAC 121, 1970.
  - 3 L.C. Teng, Fermilab Report No. TM-1269, 1984.
  - 4 Paul Emma and Tor Raubenheimer, "Systematic approach to damping ring design," Phys. Rev. ST, Accel. Beams, **4**, 021001 (2001).
  - 5 F. Antoniou and Y. Papaphilippou, "Analytical considerations for linear and nonlinear optimization of the theoretical minimum emittance cells: Application to the Compact Linear Collider predamping rings," Phys. Rev. ST, Accel. Beams, **17**, 064002 (2014).
  - 6 S.C. Leemann, et al., "Beam dynamics and expected performance of Sweden's new storage-ring light source: MAX-IV," Phys. Rev. ST, Accel. Beams, **12**, 120701 (2009).
  - 7 J-L. Revol, et al., "ESRF Upgrade Phase II Status," Proceedings of IPAC2014, MOPRO055, Dresden, Germany, (2014).
  - 8 H. Grote and F.C. Iselin, "The MAD Program (Methodical Accelerator Design) Version 8.15," CERN/SL/90-13 (AP), (1990).
  - 9 M. Berz, "Differential Algebra Description of Beam Dynamics to Very High Order," Part. Accel. **24**, 109 (1989).
  - 10 E. Forest, M. Berz, and J. Irwin, "Normal Form Methods for Complicated Periodic Systems: A Complete Solution Using Differential Algebra and Lie Operators," Part. Accel. **24** 91 (1989).
  - 11 Y. Cai, M. Donald, J. Irwin, Y. Yan, "LEGO: A Modular Accelerator Design Code," SLAC-PUB-7642, August (1997).
  - 12 J.D. Bjorken and S.K. Mtingwa, "Intrabeam Scattering," Part. Accel. **13**, 115 (1983).
  - 13 S. Nagaitsev, "Intrabeam scattering formulas for fast numerical evaluation," Phys. Rev. ST, Accel. Beams, **8**, 064403 (2005).
  - 14 K. Bane, Y. Cai, and G. Stupakov, "Threshold studies of the microwave instability in electron storage rings," Phys. Rev. ST, Accel. Beams, **13**, 104402 (2010).
  - 15 S. Krinsky, Brookhaven Report No. 75019-2005-IR, (2005).
  - 16 A. Wolski (et al.), LBNL Report No. 59449, (2006).
  - 17 Halbach, K., "[Physical and Optical Properties of Rare Earth Cobalt Magnets](#)" Nucl. Inst. and Methods 187, pp. 109-117 (1981).
  - 18 Halbach, K., "[Perturbation effects in segmented rare earth cobalt multipole magnets](#)", Nucl. Inst. and Methods 198, pp. 213-215 (1982)
  - 19 Sullivan, M., et al., "[Results from a Prototype Permanent Magnet Dipole-Quadrupole Hybrid for the PEP-II B-Factory](#)", Proceedings of PAC97, pp. 3330-3332, (1997), (SLAC-PUB 7562 ).
  - 20 Sullivan, M., "A Method for Calculating Pressure Profiles in Vacuum Pipes" SLAC-PEP-II-AP-NOTE-6-94, Mar 1994. 8pp.
  - 21 Private conversation with David Steele
  - 22 The present vacuum limit for the kicker structure in the damping ring is 6 nTorr.

# 9 Final Bunch Compression and Final Focus

---

## Technical Synopsis

*In order to achieve the scientific goals of the experimental program at FACET-II, it is necessary to bring both the electron and positron bunches to the FACET Interaction Point (IP) on the same pulse within about  $100\ \mu\text{m}$ . The chicanes in Sector 20 provide the 3<sup>rd</sup> and final stage of bunch compression for both bunches. The existing W chicane can compress and transport either type of particle, depending on the polarity of the magnets. When both chicanes are implemented, it will serve as the electron chicane so it is referred to as BC3E (3<sup>rd</sup> bunch compressor for electrons). BC3E compresses the beam to final high peak-currents  $>10\ \text{kA}$  and demagnifies the transverse spot sizes to  $\sim 10\ \mu\text{m}$  at selectable locations in the experimental region.*

*In order to bring both types of particle to the experiments on the same pulse, the positron bunch is co-accelerated through the main linac with the electron bunch, which follows the positrons by  $\sim 5\text{cm}$ , i.e.  $\frac{1}{2}$  of an S-band RF bucket. The 3<sup>rd</sup> stage of compression for positrons requires a second arm of the chicane in Sector 20 (BC3P -3<sup>rd</sup> bunch compressor for positrons). The positron chicane has a path length which is  $5.27\ \text{cm}$  longer than the electron chicane, reversing the order of the bunches when they arrive at the IP. The positron (witness) bunch arrives at the experimental plasma acceleration chamber  $\sim 215\ \mu\text{m}$  behind the driving electron beam. A pair of short 4-bend adjustable chicanes in each half of BC3P provide for fine adjustments to the electron-positron longitudinal spacing at the IP ( $\pm 100\ \mu\text{m}$ ).*

*Both chicanes share the first and last bend magnets. Sextupole magnets placed in dispersive locations of each main sector 20 chicane also control chromaticity and second-order dispersion caused by the chicanes and the final focus magnets.*

*Simulations have been made which calculate emittance dilution in the chicanes due to anomalous momentum dispersion as well as higher-order aberrations, each of which arises with component misalignments. Diagnostics, correction techniques, and feedback systems have also been incorporated into the design.*

---

## 9.1 Overview

Sector 20 contains the final bunch compression stages for both the electron and positron bunches. The bunches are co-accelerated in the main linac with the electrons following the positrons by ~5cm, i.e.  $\frac{1}{2}$  of an S-band RF bucket. The two bunches are separated horizontally at the first B1 bend magnet at the start of sector 20 and each travel through their own compression chicanes (see Fig. 9.1). In order to invert the order of the bunches for the plasma acceleration experiments, the positron chicane (BC3P) has a path length 5.27 cm longer than the electron chicane (BC3E). Each chicane has quadrupole magnets included to generate a positive  $R_{56}$  (defined for a beam coordinate system with the bunch head at  $z < 0$ ), providing the final stage of bunch compression for each beam. The chicanes also provide other measurement and corrective functions before delivery of the beam to the experimental IP area. The layout of the W-chicane (BC3E) is unchanged from the FACET experiment and it will be operated in the same way.

Sextupole magnets are included in each chicane, which provide chromatic and second-order dispersion correction targeted at the experimental waist location to minimize the focused transverse spot sizes. Transverse mover systems under the sextupoles also provide  $x$  and  $y$  dispersion correction and waist adjustment control.

A vertical wiggler section is included in each horizontal chicane (3 vertical bend magnets) to generate a vertical synchrotron radiation stripe for energy profile measurements.

An X-band (11.424 GHz) transverse, deflecting mode cavity in BC3E can measure the fully compressed bunch length. There will be a second identical structure in the second half of BC3P to perform the same function for the positron bunch. This second deflecting mode structure will be driven from the same Sector 20 X-band klystron as used for the existing electron cavity.

Operational control over the relative temporal position of the electron and positron bunches as they enter the plasma channel is required over the range  $\pm 6\sigma_z$ . A pair of 4-bend path-length adjustment chicanes are included into each half of the positron chicane which can provide up to  $\pm 100\mu\text{m}$  of  $\Delta z$  between drive and witness bunches ( $>10\sigma_z$  depending on machine configuration).

The FACET final focus system includes 8 quadrupole magnets for final demagnification of the beam to form the small-beta waist used by experiments. This system of magnets is shared by both electron and positron beams and is adjusted in order to provide equal beta-functions at the waist to accommodate the dissimilar beta functions from the 2 chicanes at the common chicane exit bend magnet. To provide the additional matching capability, an additional pair of power supplies is needed to independently power 2 extra magnets in the QFF2 and QFF4 magnet strings. The final focus system must accommodate the requirements of multiple users at different locations in the experimental region and thus maintains the flexibility of the system used at FACET to deliver different waist sizes to different  $z$ -locations along the experimental table.

Finally, the spectrometer after the experimental region consists of a vertical bend magnet and three quadrupoles. This is the same system used during FACET operation.

## 9.2 Beam Parameters

The sector 20 optics is designed to deliver high peak-current (>10kA) at the experimental area with ~10 $\mu$ m rms, or less, transverse beam sizes simultaneously for both incoming electron and positron beams. The optics match is highly constrained and must satisfy specific requirements for both electron and positron optical systems simultaneously:

- Chicane compression ratios set in the middle of their operating range for maximum flexibility when commissioning the beamline ( $R_{56} = +5\text{mm}$ ).
- Symmetry conditions maintained across each chicane to ensure co-located waist locations and beta functions for  $e^-$  and  $e^+$  beams at the waist location.
- Minimal beta functions through chicane, which past experience at FACET has shown to be highly desirable for stable operation. The optics going back into Sector 18 is manipulated to help with this and the following match requirements.
- Minimal CSR effects. The horizontal beta functions in the final bend magnet are matched to be small in both planes with a waist close to the final bend exits which helps to mitigate CSR growth effects in both electron and positron beams.
- Closed dispersion at exit of chicanes.
- Correct horizontal and vertical chromaticity at the waist.
- Minimal second-order horizontal dispersion.
- Sextupole-mover based multi-knobs for dispersion and waist control.
- Final transverse spot-sizes <10  $\mu$ m rms at the waist. A beta function of 10 cm is chosen to allow for beam aberrations from orbit and optical errors, non-perfect cancellation of both chromaticity and second-order dispersion and some CSR-induced horizontal beam size growth for high peak-charge operation.

Table 9.1 below shows some of the pertinent beam parameters for this beamline section. Note that the final beam phase space is considerably non-Gaussian in shape due to both CSR and non-perfect cancellation of both second order dispersion and chromaticity at the IP waist location. The calculated beam sizes are from Gaussian fits to the core of the beam at the IP waist which is typically the most informative measure of interest to FACET experimenters.

Table 9.1: Beam parameters for electron and positron beams in sector 20 chicanes and final focus system. Initial parameters are at the entrance to the first common bend magnet of the BC3E and BC3P chicanes, final parameters are quoted at the default IP waist location at the entrance to the E200 experiment plasma volume.

Parameter	Symbol	Value	Unit
Beam Energy	$E_0$ (e+)	10.0	GeV
	$E_0$ (e-)	10.0	
Initial Transverse Emittance	$\gamma\epsilon_x / \gamma\epsilon_y$ (e+)	6.3 / 5.9	$\mu\text{m}\cdot\text{rad}$
	$\gamma\epsilon_x / \gamma\epsilon_y$ (e-)	3.3 / 3.3	
Final Transverse Emittance	$\gamma\epsilon_x / \gamma\epsilon_y$ (e+)	35 / 6.4	$\mu\text{m}\cdot\text{rad}$
	$\gamma\epsilon_x / \gamma\epsilon_y$ (e-)	8.2 / 5.1	
Initial Twiss	$\beta_x / \alpha_x$ (e-)	2.423 / -0.027	m
	$\beta_y / \alpha_y$ (e-)	5.098 / 0.133	m

Final Twiss (IP)	$\beta_x / \alpha_x$ (e-)	0.1 / 0	m
	$\beta_y / \alpha_y$ (e-)	0.1 / 0	m
Initial Bunch Length / peak Current	$\sigma_z / I_{pk}$ (e+)	28.9 / 3.1	$\mu\text{m} / \text{kA}$
	$\sigma_z / I_{pk}$ (e-)	23.5 / 3.8	
Final Bunch Length / peak Current	$\sigma_z / I_{pk}$ (e+)	7.6 / 12.1	$\mu\text{m} / \text{kA}$
	$\sigma_z / I_{pk}$ (e-)	1.1 / 75.5	
rms relative Energy Spread	$\sigma_E/E$ (e+)	0.48	%
	$\sigma_E/E$ (e-)	0.44	
rms Transverse Core Size at IP Waist	$\sigma_x / \sigma_y$ (e+)	10.1 / 7.3	$\mu\text{m}$
	$\sigma_x / \sigma_y$ (e-)	5.5 / 5.9	
Bunch Charge	Q (e+)	0.6	nC
	Q (e-)	0.7	nC
Chicane compression coef.	$R_{56}$ (e+)	5	mm
	$R_{56}$ (e-)	5	mm

### 9.3 Layout and Optics Design

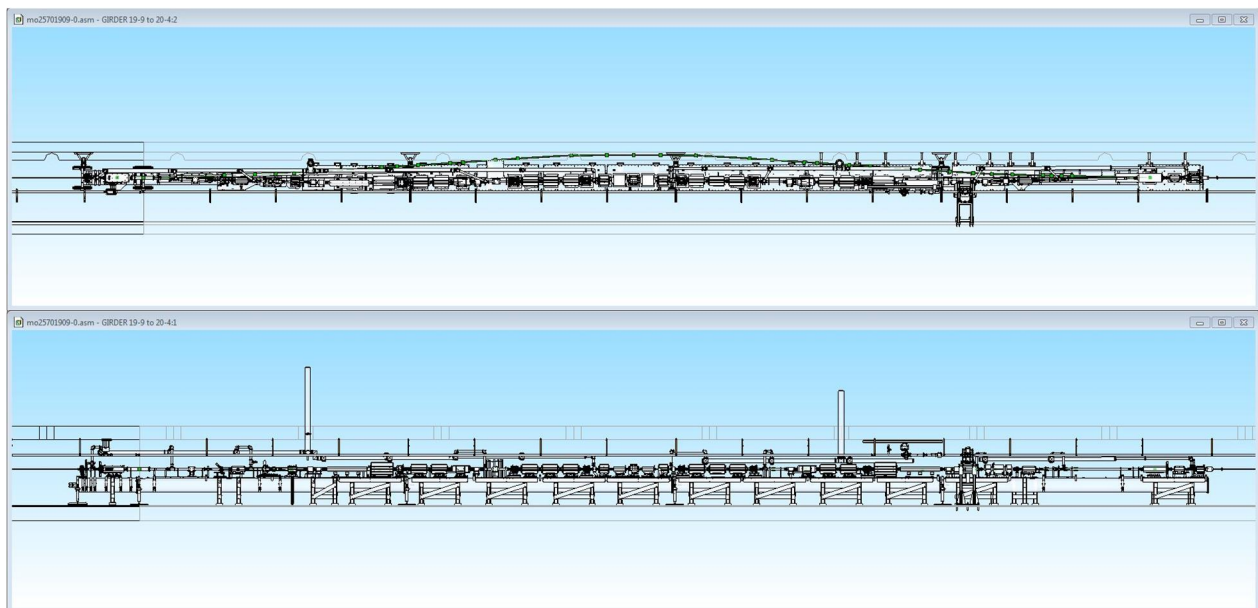


Figure 9.1: Layout of Sector 20 BC3E and BC3P (new) chicane magnets.

Figure 9.2 shows a schematic layout of Sector 20 including BC3E, BC3P, the final focus optics, experimental area and vertical energy spectrometer. The positron chicane is new and the other magnets and associated diagnostics are existing from the FACET User Facility. Figure 9.2 shows the optics functions for both the existing electron system and the new positron BC3P chicane and final focus. Note beta functions are kept small at the exit of the chicanes in both planes to help to minimize CSR effects. Although only the horizontal function needs to be kept small for this purpose, both planes are matched in order to handle both electron and positron beams simultaneously. The beta functions in the body of

each chicane are kept as small as possible while maintaining compatibility with the required dispersion functions to generate a positive  $R_{56}$  and the need to set the entrance/exit parameters to the chicanes.

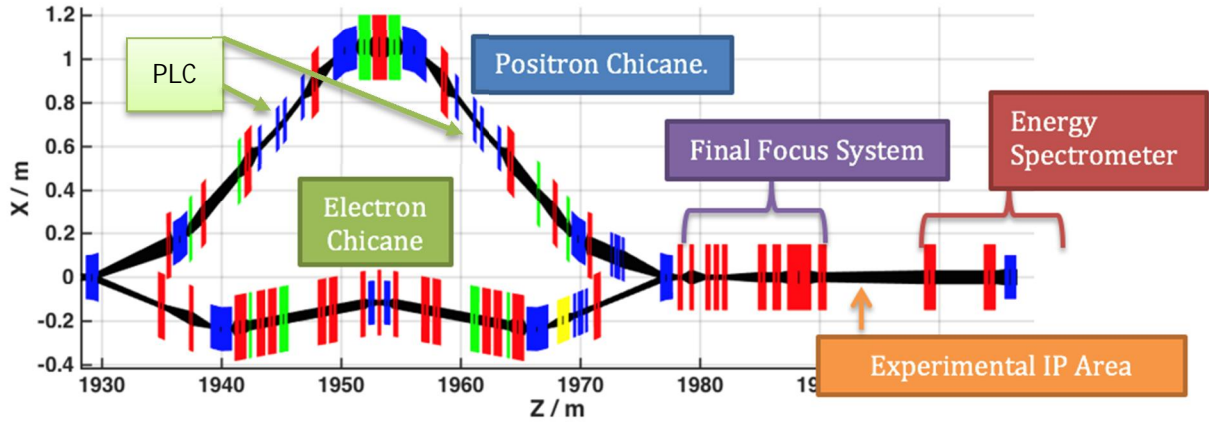


Figure 9.2: Plan layout view of sector 20 magnets, including e- and e+ horizontal chicanes, final focus and vertical energy spectrometer. Yellow indicates x-band RF TCAV, blue dipoles, red quadrupoles, green sextupoles. Co-ordinate system is relative to SLC linac (x) and SLC z-reference. The “PLC” label indicates the locations of the 2 path-length adjustment chicanes.

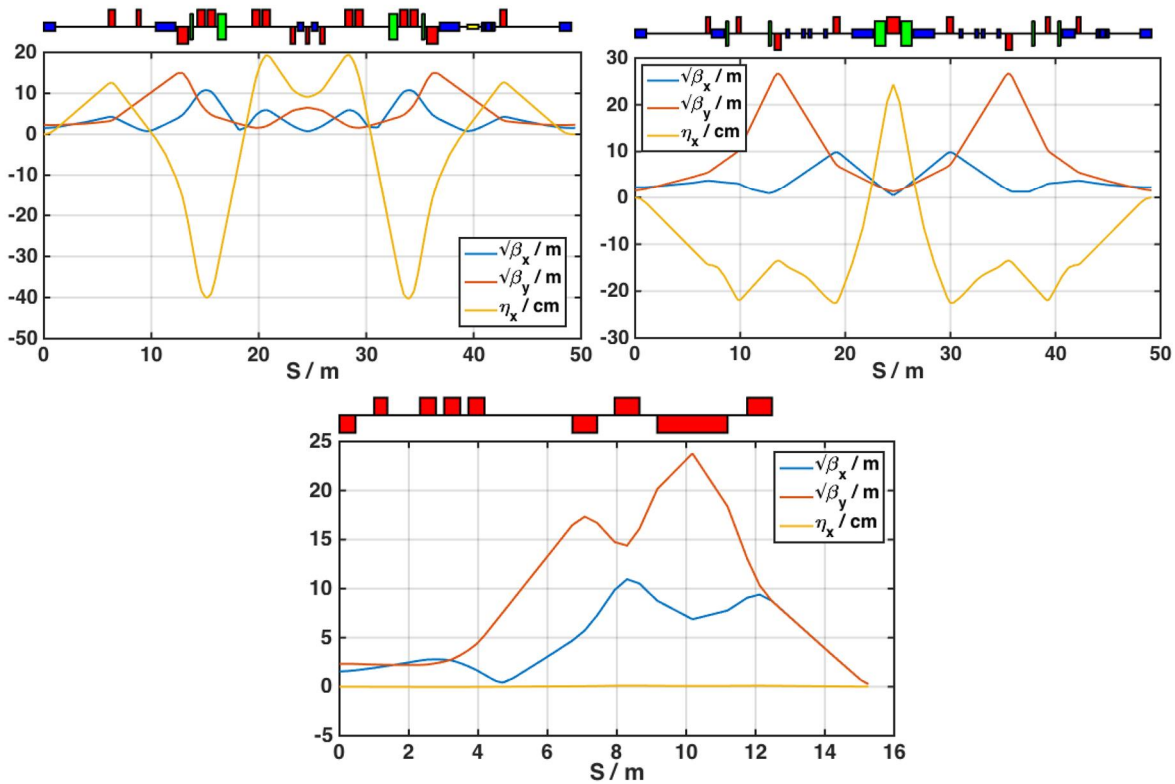


Figure 9.3: Twiss parameters across sector 20 electron and positron systems, including final focus. IP waist is at location of plasma chamber experiment. Top plot, left, shows BC3E electron chicane, top plot, right, shows for BC3P positron chicane. The bottom plot follows on immediately from the BC3E/P optics and shows the final focus system for the electron beam ( $x$  and  $y$  beta functions are reversed for

positron beam), where the IP is on the far right of the plot. The first and last bend magnets of each chicane are shared for the positron and electron beams.

## 9.4 Beam Dynamics

Using a 6D tracking code (*Lucretia*), a 1M macro-particle representation of the electron bunch is tracked through the entire FACET-II machine lattice including ISR, CSR and longitudinal space charge (LSC) effects as well as wakefield effects in the linac cavities. See Section 6.7 for more details of the beam tracking simulation. The longitudinal beam profiles at the end of L3 before BC3E/P and at the experimental IP are shown in Figure 9.4. The focused transverse beam profiles at the experimental IP waist are shown in

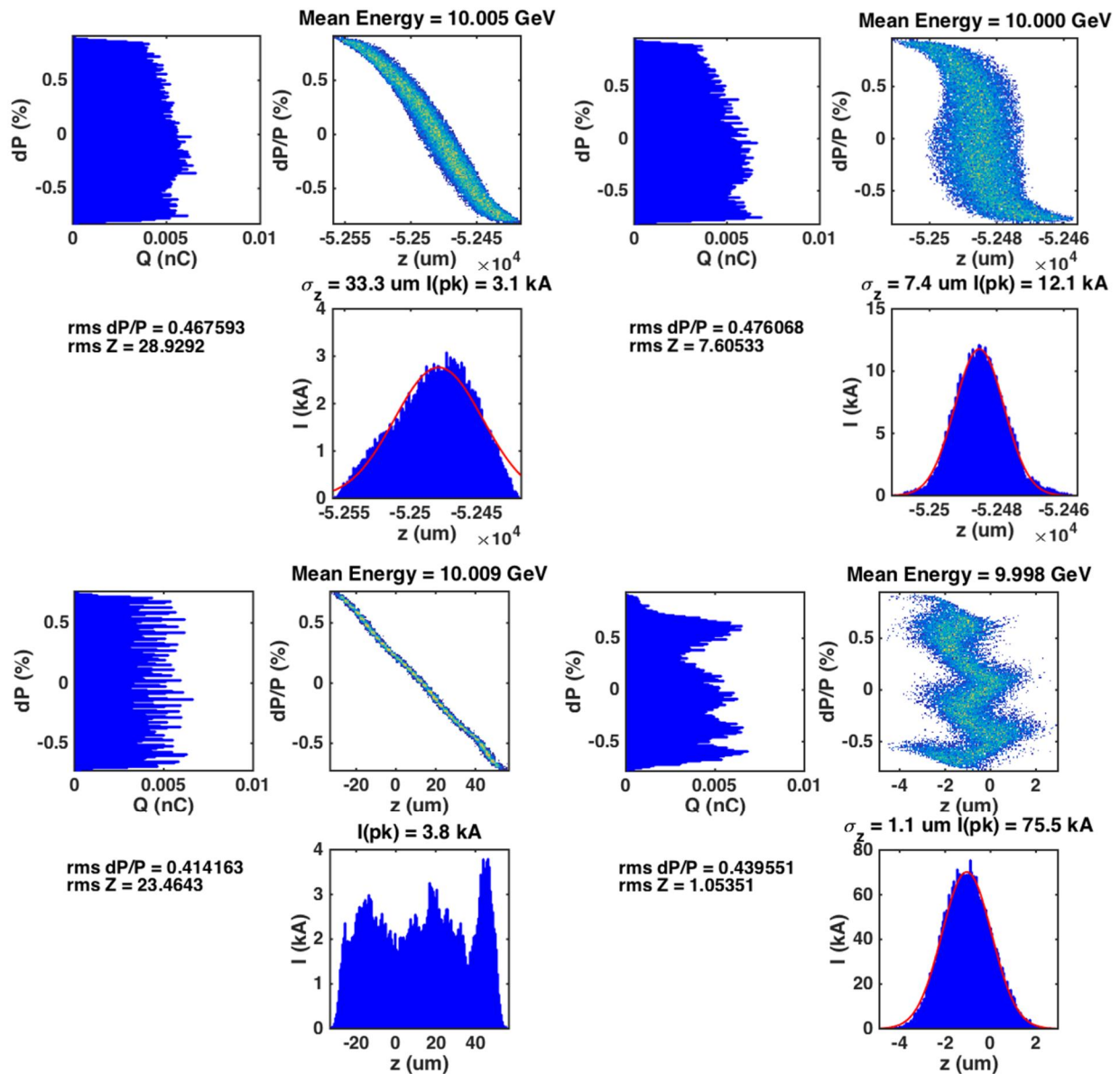


Figure 9.4: Longitudinal phase space before (left) and after (right) BC3P/E chicanes. Positron beam tracking results shown on the top row, electron tracking results on the bottom.

Figure 9.5. The beam tracking simulation in these cases is error-free. The final beam charge is chosen by adjusting the collimation apertures in the BC0, BC1 and BC2E/P chicanes which also reduces non-linear high-energy spread tails in the beam distributions. For higher charge in Sector 20, the BC3P chicane proves to be the limiting system. Increasing the final beam charge up to the full initial 2 nC only provides very modest increases in peak positron current at the IP (to a maximum of ~14 kA). At higher charge, CSR significantly degrades the horizontal emittance, giving a minimum horizontal spot size at the IP of >20 $\mu\text{m}$  rms. The parameters as presented are chosen for maximum peak current while preserving the final horizontal IP spot size at 10 $\mu\text{m}$  rms. The electron beam is less affected by CSR in BC3E. However, for simultaneous operation with both beams in the linac, to facilitate matching of both beam energies entering Sector 20 the electron beam is collimated to match the positron beam loading profile. With just the electron beam present, final peak electron currents of >100 kA are in principal possible.

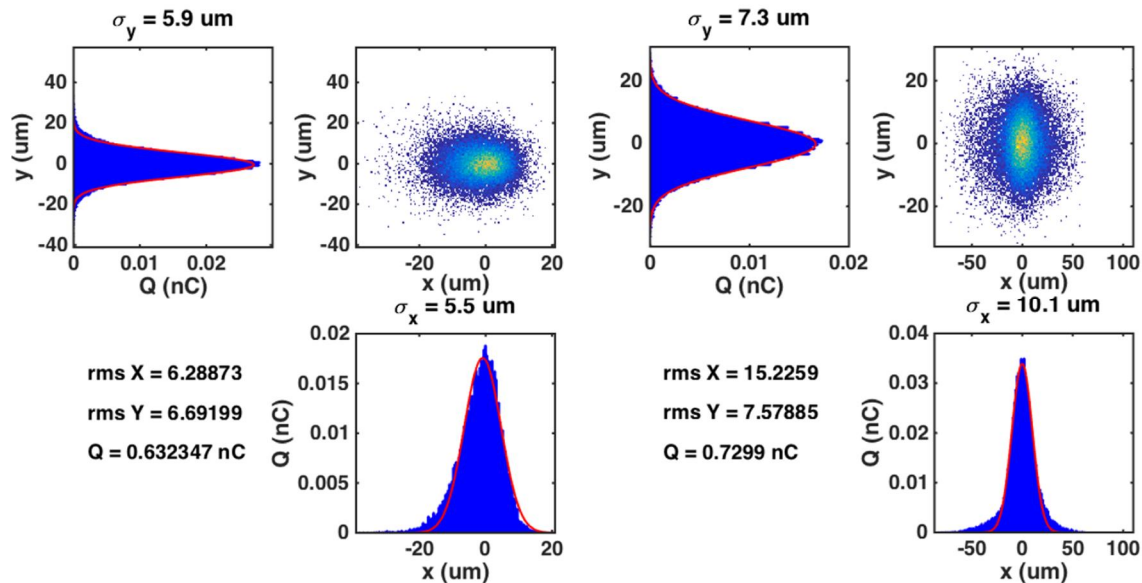


Figure 9.5: Transverse phase space at IP waist location after final focus. Positron bunch is shown on the left, electron bunch on the right.

The final focus and spectrometer systems are identical to those currently in use at FACET. The beam dynamics requirements for these systems are looser than the current system due to the lower relative energy spreads of the electron and positron beams in FACET-II. The only small change required for FACET-II operation is to allow the quadrupole pairs of Q1FF and Q4FF to have independently controllable power supplies. This is due to a greater required matching flexibility imposed by the desire to have round beams (equal beta functions) at the IP unlike at FACET which had a large transverse emittance ratio.

Figure 9.6 shows the beam stay clear requirements for Sector 20, defined as 10X the tracked rms spot sizes through BC3E/P and the final focus optics. The existing (BC3E) and proposed (BC3P) magnet apertures are also shown. The corresponding magnet parameters are presented in Section 9.7.

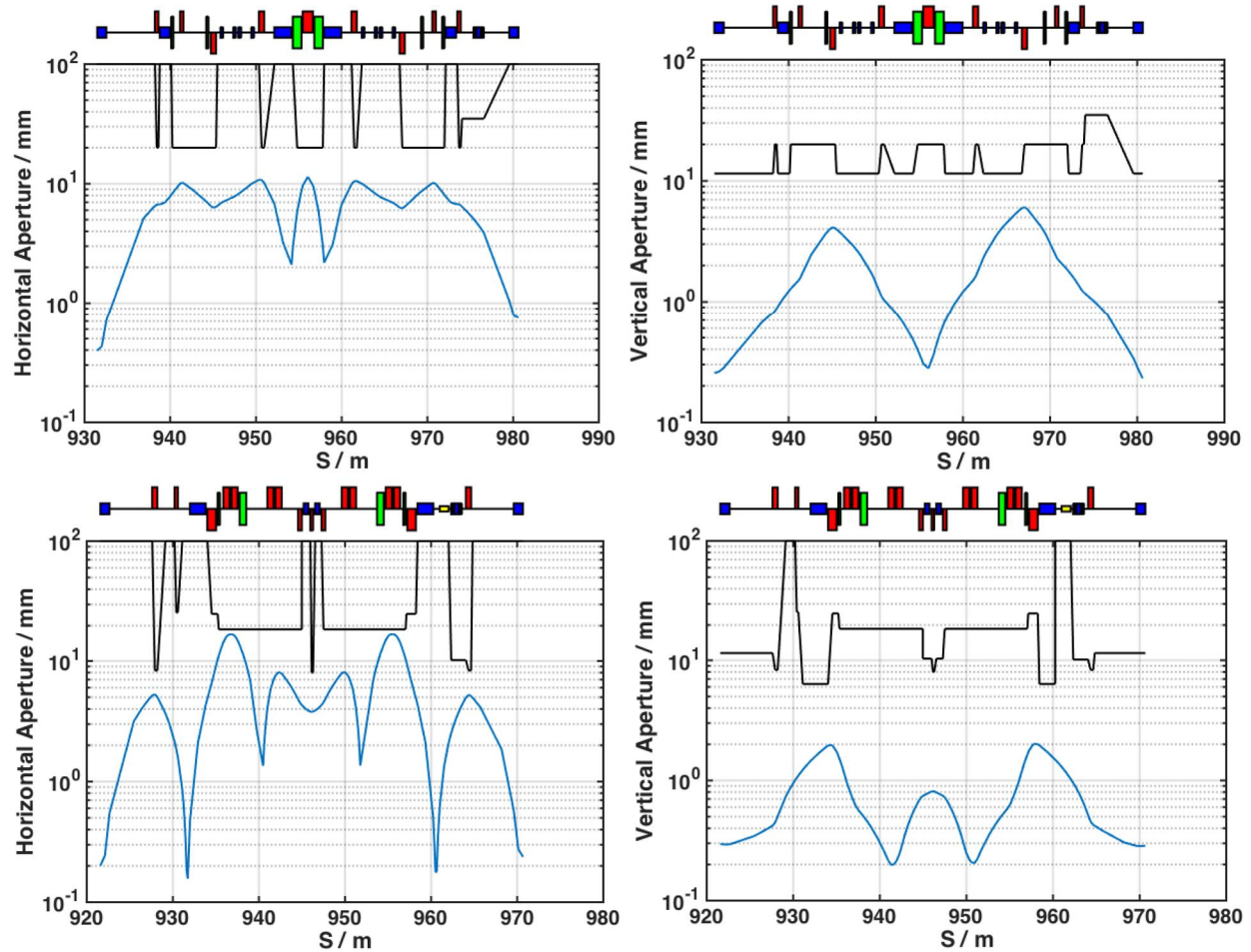


Figure 9.6: Horizontal (left column) and vertical (right column) magnet apertures (black line) and 10X tracked rms beam sizes (blue curves) through BC3E and BC3P and the final focus optics. Black curve shows design magnet apertures. Top plots for positron chicane & FFS, bottom plots for electron chicane and FFS.

## 9.5 Path-length Tuning Chicanes

Two 4-bend horizontal chicane systems (bend length=30cm, total length=3.9m each, distance between first and second pair of bends in each chicane=1.2m) in each half of the positron chicane provide path length adjustability between electron and positron bunches of  $\pm 100\mu\text{m}$  ( $>10 \sigma_z$  depending on charge and compression configuration). The default chicane configuration provides half the total path-length adjustment range. The rest of the main positron chicane is configured to deliver the design 52.7mm path length difference between electron and positron bunch to compensate for the  $\frac{1}{2}$  S-band bucket spacing in the linac. This provides for a nominal  $215\mu\text{m}$  longitudinal separation between electron and positron bunches at the IP.

To minimize the impact on the total positron system  $R_{56}$ , the distance between the central bends in the path length adjustment chicanes was minimized as a fraction of these chicane lengths.

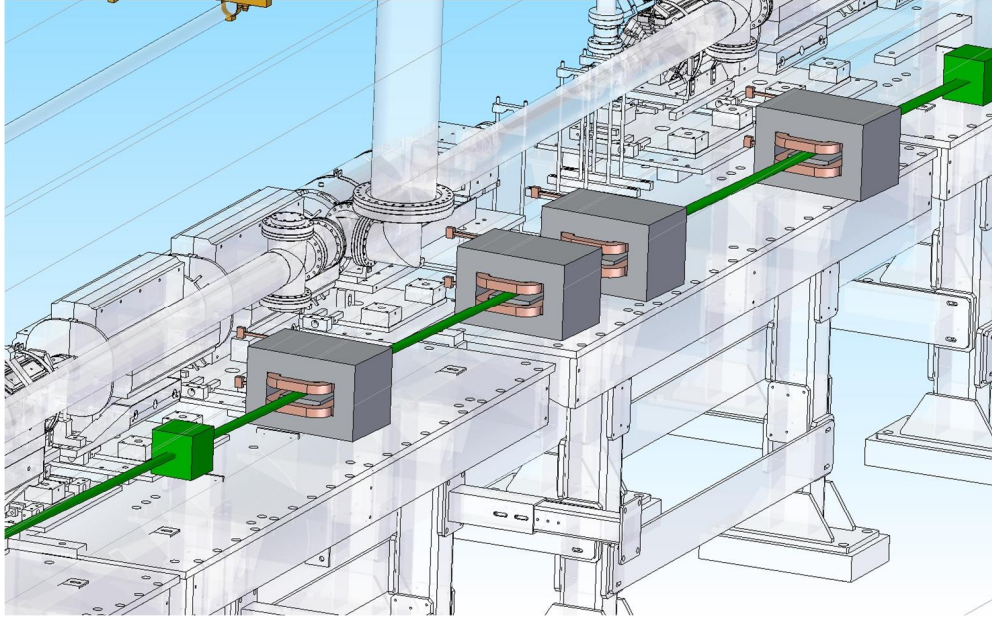


Figure 9.7: CAD drawing of downstream section of Sector 20 BC3P chicane showing second path length adjustment mini-chicane bend magnets.

Table 9.1: Operating parameters of path-length adjustment chicane system. The BMAGY parameter shown is the betatron mismatch caused by edge focusing effects from the chicane bends.

Bend angle / mrad	$\Delta S$ (path length change) / $\mu\text{m}$	$\Delta R_{56}$ / mm	$\Delta \text{BMAGY}$ / %	Change in horizontal beam position in central chicane bends / mm
0	-100	-0.23	-1.3	-9.7
6.45	0	0	0	0
9.14	+100	+0.23	+1.3	+4.0

## 9.6 New Magnets

### 9.6.1 BC3P Chicane

Construction of the new BC3P chicane requires 9 quadrupole magnets of 3 engineering types; 6 sextupole magnets of two engineering types; 17 dipole magnets of 5 types (two of which already exist and are shared with the electron W-chicane system).

#### 9.6.1.1 Quadrupoles

Table 9.3: Quadrupole magnet parameters at 10 GeV.

Deck Name	Engineering Type	Effective Length / m	Design Int. Gradient / T	Max. Int. Gradient /  T	Design Pole Tip Field /  T	Max Pole Tip Field /  T	Aperture (radius) / m

Q1PL	A	0.4	5.569	15	0.278	0.75000	0.02
Q2PL	A	0.4	9.943	15	0.497	0.75000	0.02
Q3PL	B	0.6	-10.436	20	0.348	0.66667	0.02
Q4PL	B	0.6	11.631	20	0.388	0.66667	0.02
Q5P	C	1.2	35.965	50	0.599	0.83333	0.02
Q4PR	B	0.6	11.629	20	0.388	0.66667	0.02
Q3PR	B	0.6	-10.433	20	0.348	0.66667	0.02
Q2PR	A	0.4	9.941	15	0.497	0.75000	0.02
Q1PR	A	0.4	5.567	15	0.278	0.75000	0.02

### 9.6.1.2 Sextupoles

Each sextupole is mounted on a remotely controllable motion stage, capable of +/- 2mm motion in x/y with 5 $\mu$ m precision.

Table 9.4: Sextupole magnet parameters at 10 GeV.

Deck Name	Engineering Type	Effective Length / m	Design Int. Field / T.m <sup>-1</sup>	Max. Int. Field /  T.m <sup>-1</sup>	Design Pole Tip Field / T	Max Pole Tip Field /  T	Aperture (radius) / m
S1PL	A	0.25	-301.002	320	0.2408	0.512	0.02
S2PL	A	0.25	187.001	320	0.1496	0.512	0.02
S3PL	B	1	289.329	1500	0.0579	0.600	0.02
S3PR	B	1	289.329	1500	0.0579	0.600	0.02
S2PR	A	0.25	187.001	320	0.1496	0.512	0.02
S1PR	A	0.25	-301.002	320	0.2408	0.512	0.02

### 9.6.1.3 Dipoles

Table 9.5: Dipole magnet parameters at 10 GeV. All are rectangular type dipole magnets. B1LP and B1RP are shared with B3E chicane first and last bend magnets.

Deck Name	Engineering Type	Effective Length / m	Bend Angle / radians	Bend Plane	Design Int. Field / T.m	Max. Int. Field /  T.m	Design Pole Tip Field / T	Max Pole Tip Field /  T	Aperture (radius) / m
B1LP	A	1.063	-0.0226	X	-0.754	0.8	0.709	0.7525	0.0115
B2LP	B	1.2	-0.0418	X	-1.393	1.45	1.161	1.2083	0.0115
BPA1L	C	0.3	0.0065	X	0.215	0.3	0.717	0.9999	0.0115

BPA2L	C	0.3	-0.0065	X	-0.215	0.3	0.717	0.9999	0.0115
BPA3L	C	0.3	-0.0065	X	-0.215	0.3	0.717	0.9999	0.0115
BPA4L	C	0.3	0.0065	X	0.215	0.3	0.717	0.9999	0.0115
B3LP	D	2.0	0.0643	X	2.147	2.2	1.073	1.1000	0.0115
B3RP	D	2.0	0.0643	X	2.147	2.2	1.073	1.1000	0.0115
BPA1R	C	0.3	0.0065	X	0.215	0.3	0.717	0.9999	0.0115
BPA2R	C	0.3	-0.0065	X	-0.215	0.3	0.717	0.9999	0.0115
BPA3R	C	0.3	-0.0065	X	-0.215	0.3	0.717	0.9999	0.0115
BPA4R	C	0.3	0.0065	X	0.215	0.3	0.717	0.9999	0.0115
B2RP	B	1.2	-0.0418	X	-1.393	1.45	1.161	1.2083	0.0115
WIGP1	E	0.244	-0.0025	Y	-0.083	0.2	0.342	0.8196	0.035
WIGP2	E	0.488	0.005	Y	0.167	0.2	0.342	0.4098	0.035
WIGP3	E	0.244	-0.0025	Y	-0.083	0.2	0.342	0.8196	0.035
B1RP	A	1.063	-0.0226	X	-0.754	0.8	0.709	0.7525	0.0115

### 9.6.2 Electron Chicane

This system remains as used in FACET. Two quadrupoles will be removed (Q3EL\_2 and Q3ER\_1) due to lower beam energy operation in FACET-II. Four sextupole magnets (S3EL\_1, S3EL\_2, S3ER\_1, S3ER\_2) will also be removed and re-purposed in other FACET-II subsystems. Operational experience showed these to have negligible impact on aberration control.

### 9.6.3 Final Focus System

The final focus system, as used in FACET operations, consists of an existing, installed set of 8 quadrupole magnets. Two of the existing magnet strings (OFF2 and OFF4) will be separated and powered separately to facilitate equal beta function matching for the IP. This is possible due to the lower final energy compared with FACET operations.

### 9.6.4 Energy spectrometer

A single vertical bend magnet and three quadrupole magnets, as installed and used during FACET operations will be maintained.

## 9.7 Instrumentation, Diagnostics and Feedback

The existing FACET electron beam diagnostics located in the BC3E chicane and experimental area will be retained and used as they currently are in FACET, with the following modifications:

- Two additional stripline BPMs will be added to the final focus system in the new QFF2 and QFF4 magnets.
- Three wire scanners spanning the IP waist will be installed interspersed with the experimental chambers and associated diagnostics. With the removal of the upstream beryllium window and installation of differential pumping described in Chapter 10, meaningful three-wire

measurements of beam emittance can be made across the IP waist in the absence of scattering media.

- In the IP area, the five existing insertable profile monitors (USOTR, IPOTR1, IPOTR2, IP2A, IP2B) will remain in place, providing final beam profile measurement at various Z locations across the experimental area. As is the case in FACET, it is expected that evolving experimental needs will require these shared diagnostics to be reconfigured frequently.

The significantly higher 3D charge density of the FACET-II  $e^-$  beam may compromise the performance and lifetime of intercepting beam diagnostics such as wire scanners, OTR and YAG screens in the IP area. At peak current of  $\sim 20$  kA in FACET, the highly focused electron beam has regularly burned through OTR foils and wires over several hundreds of pulses; the mechanism of this damage is hypothesized to be localized heating due to current flow driven by the radial electric field. At 75 kA these effects are expected to be greatly compounded. A number of mitigation schemes have been developed for FACET including multi-wire scanners, multi-screen profile monitors, and software-controlled MPS to enforce safe configurations for inserting diagnostics.

Between the FFS and the dump, diagnostics will be shared by  $e^-$  and  $e^+$  pulses traveling along the same beamline in Phase-III. The 215- $\mu\text{m}$  separation between the two pulses means they cannot be independently resolved by most of the existing single-bunch diagnostics in use such as BPMs, profile monitors, wire scanners, and toroids. Interlacing separate electron and positron pulses will allow for independent tuning of the two beams up to the entrance of the final focus. Measurement techniques in use at FACET for characterizing the two-bunch electron beam generated by insertion of the notch collimator will be adapted for the coupled  $e^+/e^-$  beam at FACET-II.

These concerns are not applicable in the BC3E and BC3P arms of the sailboat chicane, where the two beams diverge and follow separate paths before recombining in B3E-R. Hence, a standard suite of diagnostics is described in the following sections for BC3P. These diagnostics are designed to provide a symmetric complement of  $e^+$  measurements to go with the existing  $e^-$  diagnostics in BC3E.

### 9.7.1 Beam Position Monitors and Beam Current Monitors in BC3P

Nineteen new stripline BPMs will be installed in BC3P: one in each quadrupole and sextupole magnet (15), one downstream of B1LP and one upstream of B1RP for measurement of beam energy, and one in the center of each 4-bend path length chicane. Trajectory control in BC3 to an accuracy of  $< 100$  microns in the sextupole magnets is required for correction of dispersion and other aberrations to achieve transverse spot sizes of  $< 10$  microns. Toroids for  $e^+$  beam current and loss monitoring will be installed at the entrance and exit of the BC3P chicane.

### 9.7.2 Energy Spread and Bunch Length Diagnostics in BC3P

Diagnostics for characterization and tuning of the longitudinal phase space will be copied from the existing FACET diagnostics where applicable. A primary measurement of the energy spread will be at the entrance of the BC3 systems where existing phosphor screens with analog video cameras will be upgraded with digital cameras to enable quantitative measurements of energy spread.

Additionally, a 3-bend vertical wiggler will be installed after Q1P-R, at the exit of the positron chicane. The synchrotron radiation stripe generated from this wiggler will be imaged on an off-axis

YAG screen several meters downstream, identical in function to the SYAG diagnostic currently in use (see Figure 9.8). This provides a non-invasive measurement of the energy spectrum.

A second X-band transverse deflector identical to the existing XTCAV will also be installed near this location in BC3P, with its corresponding screen located in the IP area. The available RF voltage and transport optics of the existing system allow for resolution of bunch lengths down to 20  $\mu\text{m}$ .

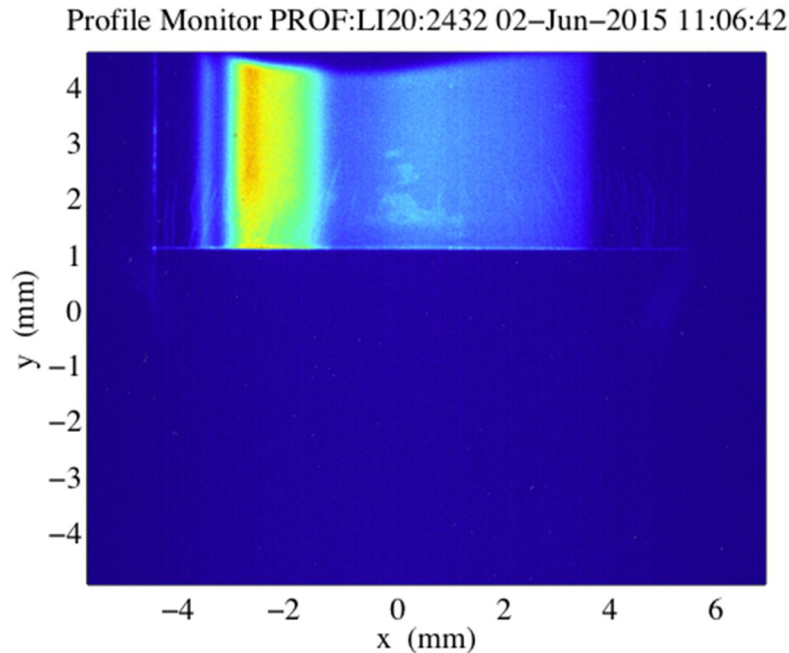


Figure 9.8. Vertical synchrotron radiation stripe imaged on an off-axis YAG crystal. The horizontal axis is energy, thus vertical projection of the stripe provides a measurement of the  $\sim 3\%$  full-width energy spread.

### 9.7.3 Feedback

Several Matlab-based software loops for control of  $e^-$  energy and TCAV phase have been in use at FACET and will be retained for the FACET-II  $e^-$  beam. The existing energy feedback monitors the electron beam energy through BPM readings at the positron source extraction point in Sector 19-7 and adjusts RF phase shifters in Sectors 17 and 18 to regulate beam energy at extraction, and subsequently in Sector 20. Regulation of the positron energy will require a different approach, as there is no off-axis positron dump. The positron energy can be extracted from a fit to the BPM readings in BC3P relative to a reference orbit. Though abandoned for the sake of operational simplicity, a similar feedback was in use for  $e^-$  in BC3E for several years.

# 10 Future Upgrades

---

---

## Technical Synopsis

*To support the full breadth of the experimental program outlined in Chapter 3, several additions or upgrades will be required to expand future capabilities. These are described briefly in this chapter. They could be funded as Accelerator Improvement Projects during the operation of the FACET-II facility, but they are also available as possible scope additions should project funds be available.*

*The Plasma Wakefield Acceleration experimental program could eventually desire a higher charge electron bunch than provided in the baseline configuration. As one possible implementation, the linac and bunch compression have been designed to be compatible with a 1nC/5nC configuration of the positron /electron beams respectively. The 1nC/5nC configuration has a large imbalance in the wakefield loading in the linac between electron and positron bunches as well as CSR effects.*

*This upgrade represents a highly “pushed” parameter set to demonstrate the highest deliverable peak currents to the Sector 20 user area. This requires pushing the limits of the bunch compressor systems while operating the beams with high energy spread which leads to highly non-Gaussian beam distributions in all 6 degrees of freedom. This leads to standard statistical measures of beam quality such as emittance being a poor choice for describing the desirable beam characteristics. Typically, where projected beam sizes are referred to in the text, this refers to a Gaussian fit to the core of the projection which de-weights smaller charge distributions at high relative offsets.*

*6D tracking simulations have been made to model the beam transport through the FACET-II complex similar to those discussed in earlier chapters.*

*Other upgrades are described briefly. 1) installation of a witness injector to provide an independent bunch to sample the plasma wakefields. This allows complete freedom to tailor the drive bunch shape for maximum transfer efficiency. 2) installation of a differential pumping system to isolate the vacuum in the experimental region from the Linac vacuum. This provides flexibility with the plasma chamber experiments and avoids the need for beryllium windows. 3) installation of a Compton source for a variety of proposed experiments. 4) operation of Compton sources in the Sector 20 chicanes to form a photon-photon collider in the final bend of BC3E & BC3P.*

---

---

## 10.1 Future Upgrades - Introduction and Overview

This section describes possible future upgrades to enhance the capabilities of the FACET-II facility. The Plasma Wakefield Acceleration experimental program could eventually desire a higher charge electron bunch than provided in the baseline configuration. To support this, the linac and bunch compression have been designed to be compatible with a 1nC/5nC configuration of the positron /electron beams respectively.

Other upgrades are described briefly. 1) installation of a witness injector to provide an independent bunch to sample the plasma wakefields. This allows complete freedom to tailor the drive bunch shape for maximum transfer efficiency. 2) installation of a differential pumping system to isolate the vacuum in the experimental region from the Linac vacuum. This provides flexibility with the plasma chamber experiments and avoids the need for beryllium windows. 3) installation of a Compton source for a variety of proposed experiments. 4) Operation of Compton sources in the Sector 20 chicanes to form a photon-photon collider in the final bend of BC3E & BC3P.

## 10.2 High electron charge operation mode

### 10.2.1 Accelerator Requirements and Parameters

For the FACET-II experimental program, the electron beam must meet a specific set of requirements for the electron transverse and longitudinal beam sizes at the experimental IP waist locations as well as requirements for peak current, energy, energy spread, and stability. These electron parameters are listed in Table 5.1 which shows both the design parameters and the ranges expected. The high charge option discussed here corresponds to the 5 nC parameters included in the ranges shown. Positron parameters are listed in Table 8.1. Nominal initial bunch charge operation for positrons is 2 nC out of the damping ring, here a pessimistic assumption of 1 nC extracted from the damping ring is made. This presents the most pushed configuration for the linac imaginable, a 5 nC electron bunch co-accelerated along with a 1 nC positron bunch. A schematic layout of the accelerator for the high electron charge configuration is shown in Figure 10.1 below with beam parameters listed at various points along the accelerator. The electron beam optics from cathode to the dump in Sector 20 for the electron and positron beam is shown in Figure 6.26.

No collimation is applied in BC0, BC1 or BC2 for the tracking studies presented below. The corresponding calculated apertures are then a worst-case which should be considered safe for all planned FACET-II operation modes.

Section 6.7 reviews the particle tracking environment similar to that applied to this asymmetric charge case. There are differences between the parameters studied in the previous chapters and those simulated here. For asymmetric charges, there is considerable difference in beam loading between the electron and positron bunches, as summarized in Table 10.1. To equalize the energy between the two bunches, a set of 2<sup>nd</sup> or 4<sup>th</sup> harmonic accelerating structures are required which accelerate the electron bunches (1/2 s-band wavelength behind the positron bunch in L2 and L3) while decelerating the positrons by a total of +/- 207 MeV. Due to the increased wakefield chirp imparted to the electron bunch in L3, the L2 S-band structures are operated with maximum chirp (while still achieving 4.5 GeV beam energy at BC2) so as to achieve optimal compression after BC3E. This requires sacrificing both the spare RF station and the 2 feedback RF stations. This may not be practical; and the configuration outlined here may need revisiting later if the 5 nC option is needed.

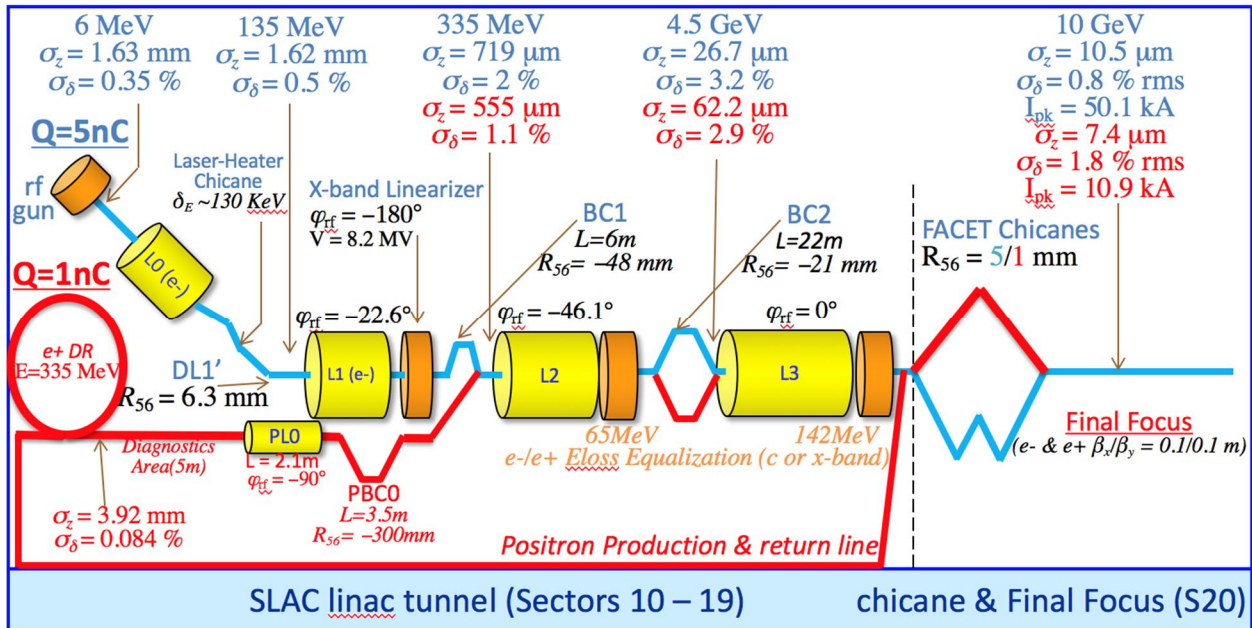


Figure 10.1. Schematic layout of FACET-II injector, linac, bunch compressors, and experimental area, with main parameters listed for operation. The blue sections depict the electron specific and common e-/e+ areas. Configuration is for the 1/5nC (e+/e-) charge option.

Table 10.1: Energy loss for electron and positron bunches in linac sections L2 and L3 due to beam loading, and in BC2/BC3 due to ISR/CSR energy loss. Required total c or x-band RF gradient to balance the electron and positron beam energies is also shown.

E Loss Section	Positron E Loss / MeV	Electron E Loss / MeV	$V_{x\text{-band}} / \text{MV}$
L2 + BC2	26.2	155.7	64.75
L3 + FACET	53.5	337.0	141.75

### 10.2.2 Bunch Compressor 1 (BC1) in Sector 11

The layout of BC1 is identical as that described in Section 6.3. The tracked longitudinal beam phase space with the 1/5 nC configuration can be seen in Figure 10.5 below. The BC1 apertures and 10X tracked beam sizes are shown in Figure 10.2.

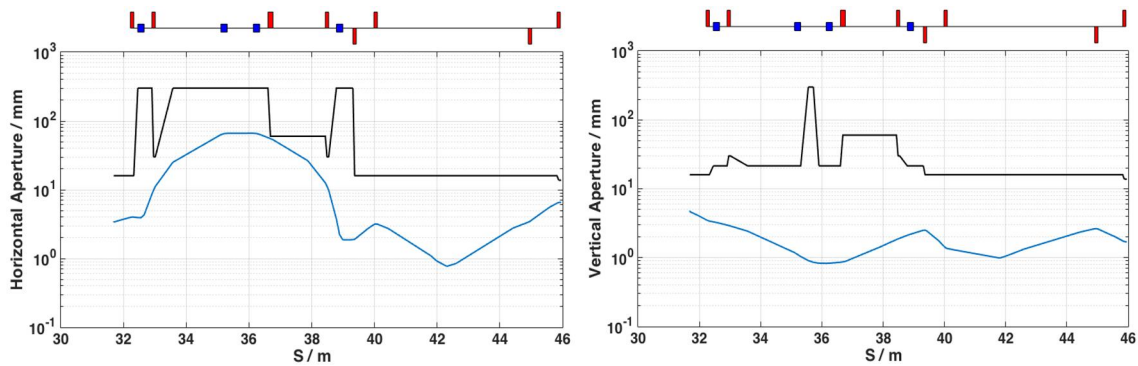


Figure 10.2: Horizontal and vertical magnet apertures from tracked rms beam sizes. Black curve shows design magnet apertures; blue curve shows 10X tracked rms transverse beam sizes.

### 10.2.3 Bunch Compressor 2 in Sector 1

The layout of BC2E and BC2P is identical as that described in Section 6.4. The electron and positron tracked longitudinal phase space is shown below in Figure 10.5. The tracked beam size and required apertures are shown in Figure 10.3.

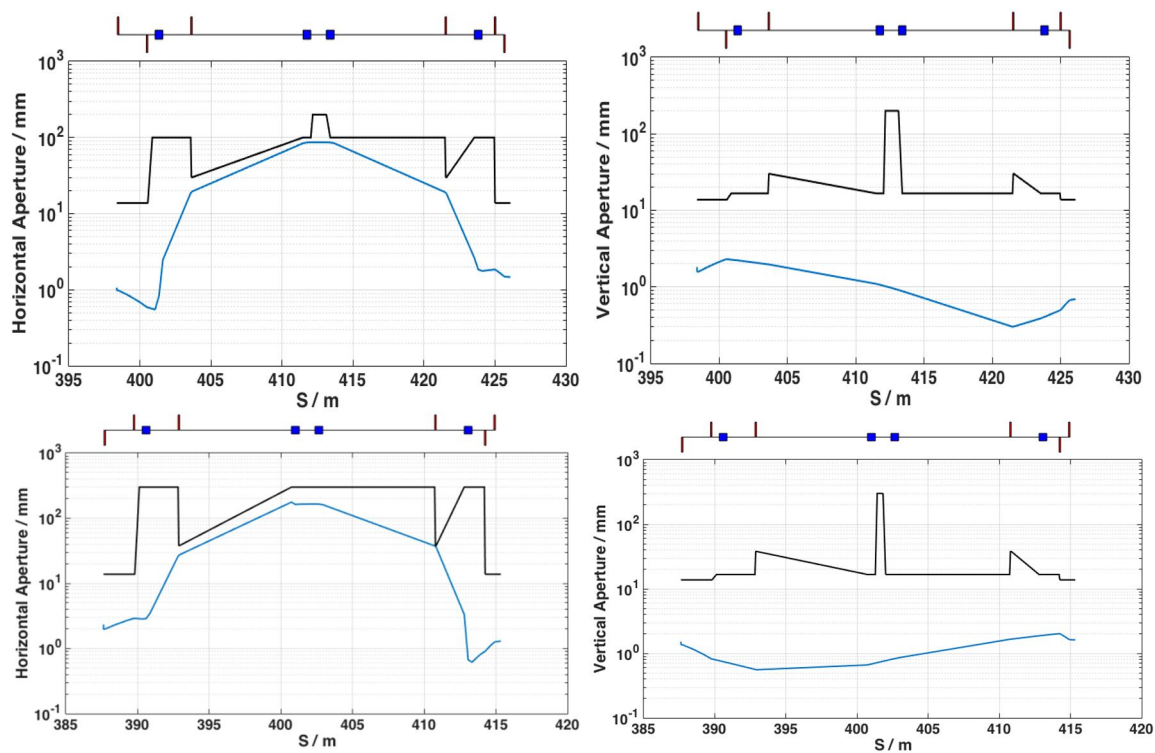


Figure 10.3: Horizontal and vertical magnet apertures from tracked rms beam sizes. Black curve shows design magnet apertures; blue curve shows 10X tracked rms transverse beam sizes. Top row is for the positron beam design; bottom row is for the electron beam.

## 10.2.4 Sector 20

Sector 20 is described for both the positrons and electrons in Chapter 9. The layout is the same here, the final tracked longitudinal and transverse phase spaces of the electron and positron beams at the experimental IP waist location are shown in Figure 10.6 and 10.7 below. Beamline apertures and tracked transverse beam sizes are shown in Figure 10.4. As can be seen, the 10X beam sigma envelope encroaches on some of the horizontal beam apertures in this high charge configuration. Careful beam orbit control is required and some beam loss (as experienced at FACET) may be experienced in this region.

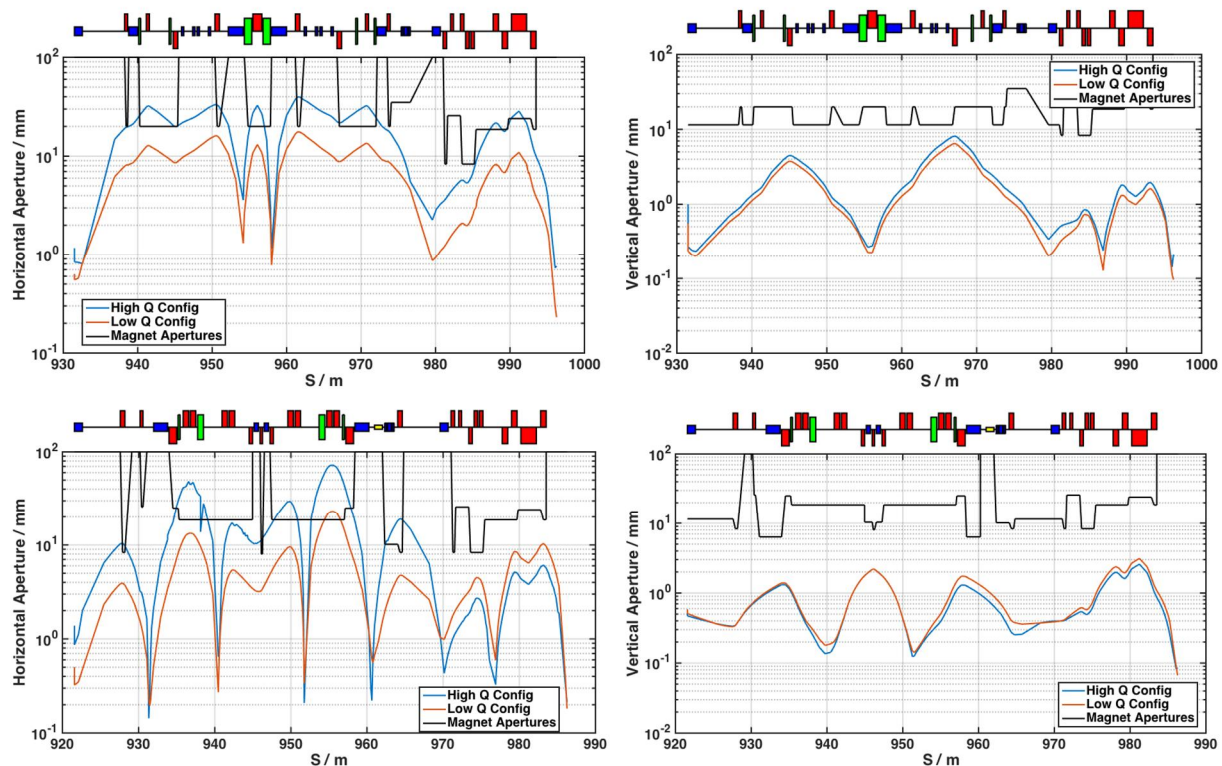


Figure 10.4: Beamline apertures in Sector 20 and 10X tracked transverse beam sizes. Top plots are for BC3P and the positron beam, bottom plots are for BC3E and the electron beam. The "High Q config" refers to the 1/5 nC (e+/e- beam) configuration, the "Low Q config" refers to the 2/2 nC configuration.

## 10.2.5 Particle Tracking

Figure 10.5 shows the longitudinal configuration of the electron and positron bunches as they are tracked through FACET-II from gun or damping ring extraction through to the IP waist location in Sector 20. Figures 10.7 and 10.8 show the longitudinal and transverse phase space for electron and positron bunches at the IP waist in detail. Note the longitudinal configuration is constrained by having to successfully transport and compress both electron and positron beams simultaneously. Due to the larger initial longitudinal emittance of the positron beam, the positron transport is the most challenging. If just the electron beam is required, an alternate L2 and L3 phase configuration makes it possible to deliver beams with >100 kA peak current.

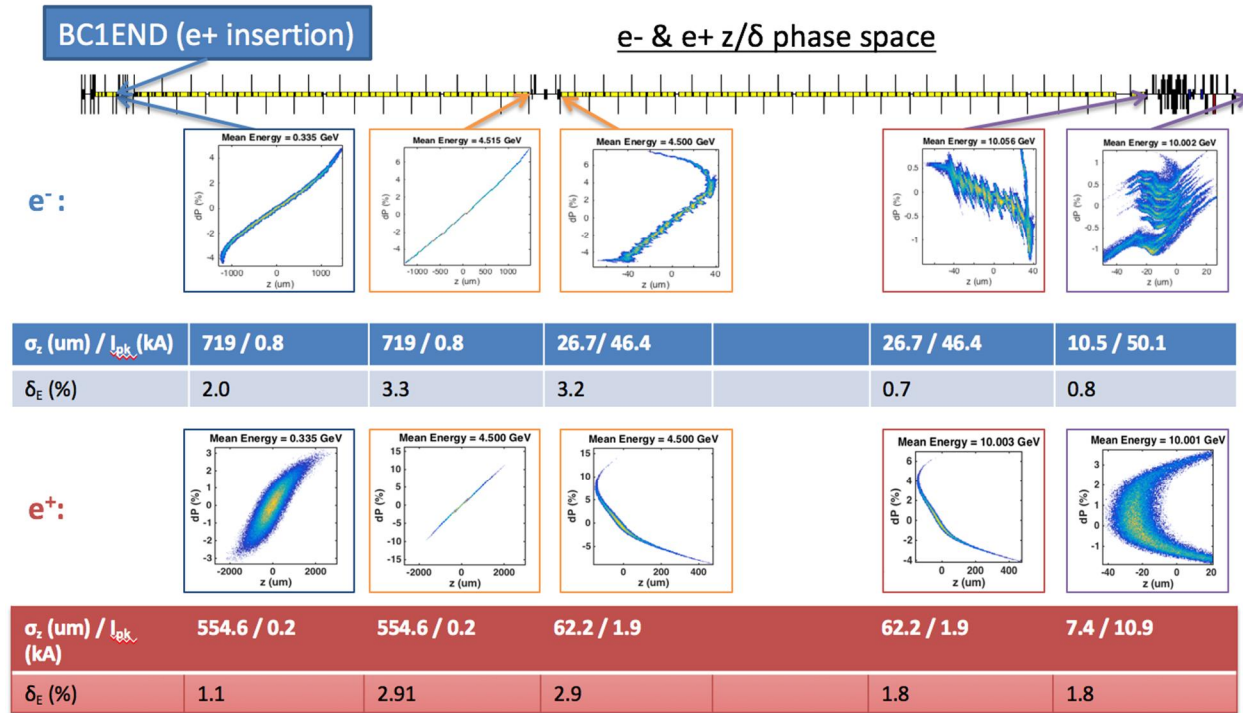


Figure 10.5: Longitudinal phase space of electron (top) and positron (bottom) beam as it is transported through L2, L3 and BC3 plus the final focus system to the experimental IP waist location in Sector 20. Also shown are the bunch length, peak current and relative energy spread after BC1, before and after BC2 and before and after BC3.

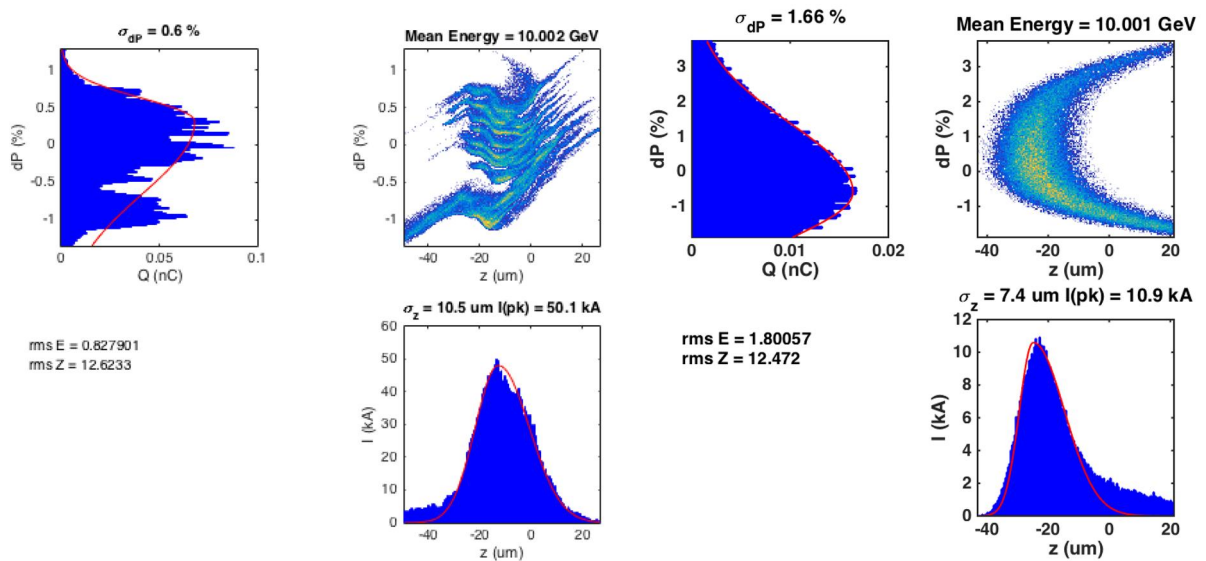


Figure 10.6: Longitudinal phase space of the electron beam (left) and the positron beam (right) at the Sector 20 experimental IP waist location.

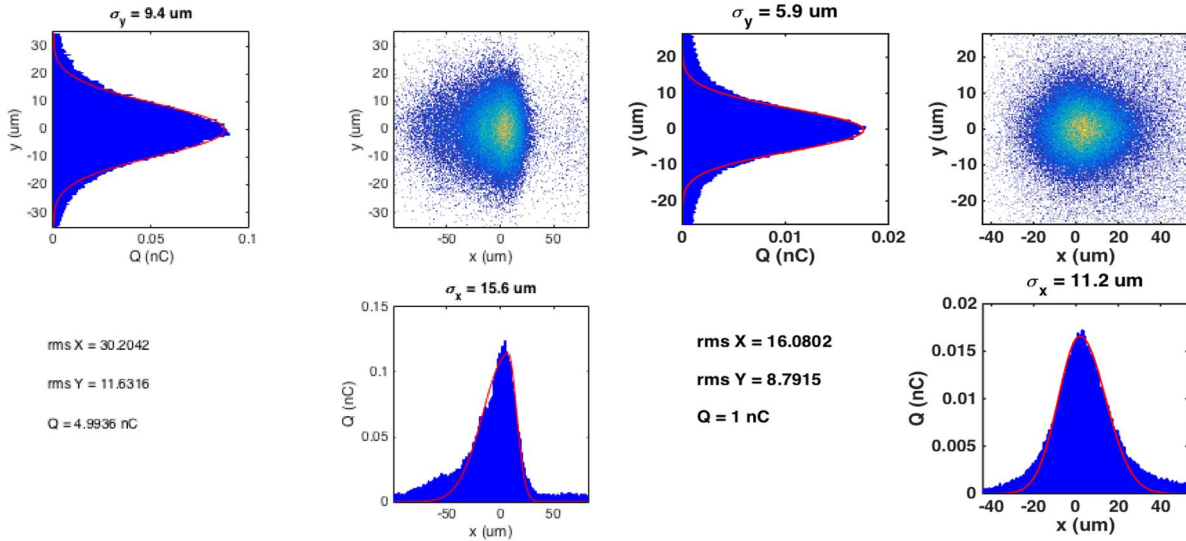


Figure 10.7: Transverse phase space of the electron (left) and positron (right) bunches at the Sector 20 experimental IP waist location.

### 10.3 Witness Bunch Injector

The addition of an independent witness bunch injector close to the experimental area will be a powerful tool for the plasma wakefield and dielectric wakefield programs, allowing independent control of the drive and witness bunch parameters (for example, current and energy profiles and bunch separation). The witness bunch injector will use a laser (the witness drive laser) to generate a high quality electron beam from a photocathode located inside a high field RF gun.

The witness drive laser includes a Coherent Astrella laser and a tripler to generate the 266 nm pulse for photoelectron production from a copper cathode. If needed, a multipass amplifier can be used to increase the pulse energy and electron yield. The laser system would be located in the existing FACET laser room which would be modified to house both this new laser and the FACET laser for plasma formation. An additional evacuated transport line would bring the laser a distance of approximately 50 m from the laser room to the photocathode.

The RF photocathode gun would be located in the sector 20 housing. The electrons from the gun output are accelerated to 100 MeV with two 3 meter long S-band structures.

The electron bunch needs to be compressed to meet requirements for wakefield experiments. The two accelerating sections also provide the chirp for subsequent bunch compression. The bunch is then compressed in a dogleg and injected co-linear into the main 10 GeV beamline.

Focusing of the witness bunch is provided by a final electromagnet doublet and permanent magnet quadrupole triplet located within the experimental area, The distance between the final triplet and the focus will be approximately 0.5 m. Wakefield experiments need to position their medium (whether plasma or dielectric) at the focus. The coexistence of the focusing magnets and the experiment can be achieved with a large vacuum chamber that can accommodate both the magnets and experimental apparatus. The FACET experimental area currently has two such large chambers and can reconfigure the beamline to position these at this location.

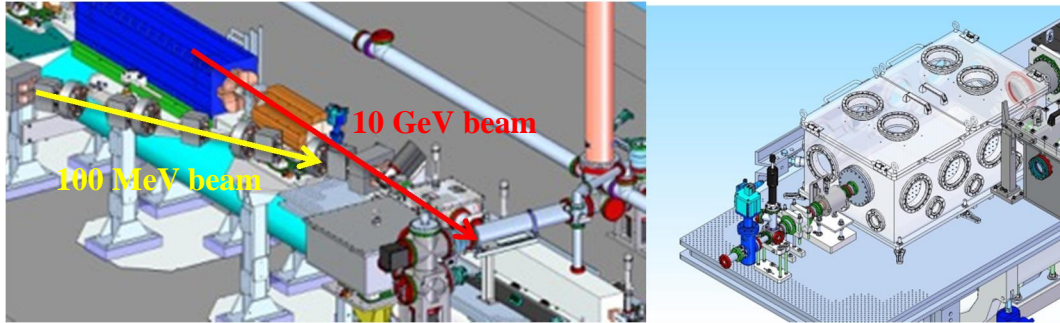


Figure 10.8. Dogleg and focusing magnets for independently injected witness bunch. The final triplet is optimally 25 cm from the focus and can occupy the same vacuum chamber as is used for laser optomechanics (right).

The design work to be completed includes locating the RF injector, subsequent accelerating sections and the dogleg magnets in such a way that still permits access to the experimental area. The optics need to be designed in coordination with the design of the experimental apparatus to make them compatible with the plasma source (lithium or hydrogen). The system needs to be tied into the Personnel Protection System and Beam Containment System.

#### 10.4.1 Zeroth-Order Design

Below is presented a zeroth-order design of a system which has a performance approaching what is desired for the witness bunch injector. Ideally a factor  $\sim 3$  more in peak current would be preferred for the final design. The specifics of the integration within the Sector 20 main beamline environment: the physical placement, the arrangement of final focus magnets and integration into the Sector 20 experimental area etc. will need further design iterations to meet the specific user requirements outlined above.

##### 10.3.1.1 Overview

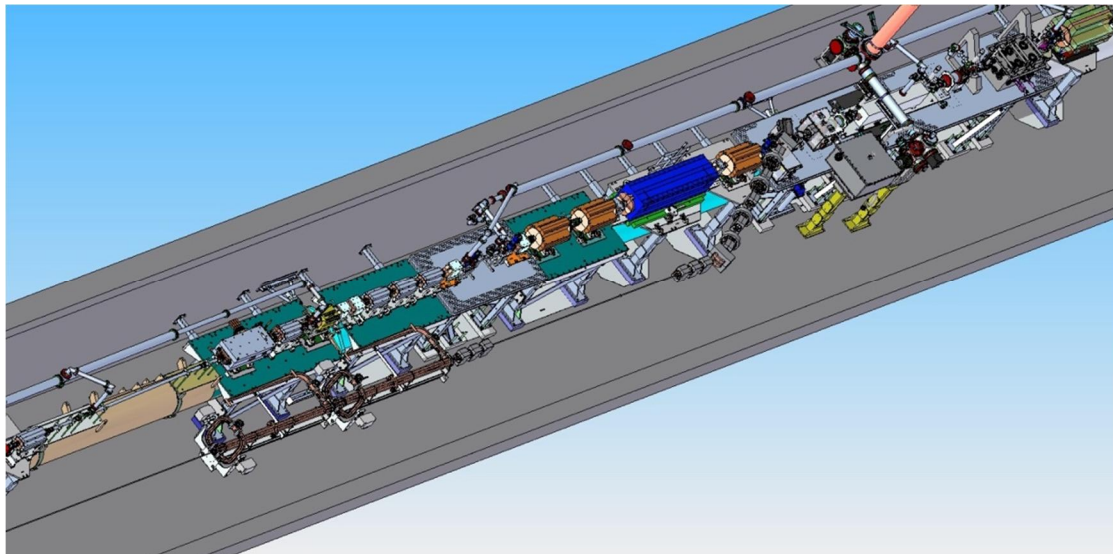


Figure 10.9: Example integration layout of witness bunch injector components into Sector 20. The gun (not shown) and injector RF are placed to the aisle side of the last BC3 bend, the diagnostics line runs alongside the main beam final focus optics, the horizontal dogleg injects the beam after the last QFF6 final focus magnet and is focused into the E200 plasma chamber with an insertable permanent magnet final triplet set of quads.

The key parameters and features of the witness bunch injector system are shown in Table 10.2 below. The example source parameters used in this design are presented in Table 10.3. The gun portion of the injector is not directly modeled here. The compressed beam must be directly injected into the main beamline, a short distance (~100-200  $\mu\text{m}$ ) following the main 10 GeV FACET-II “drive” beam. Hence the beam must be injected after the last main final focus quadrupole magnet (QFF6).

Table 10.2: Key parameters and features of the witness bunch injector design

Parameter	Symbol	Value
Drive Beam Energy	$E_d$	10.0 GeV
Witness Bunch Final Energy	$E_w$	100 MeV
rms Transverse Final Spot Size	$\sigma_x / \sigma_y$	< 10 / 10 $\mu\text{m}$
rms Longitudinal Final Bunch Length	$\sigma_z$	< 10 $\mu\text{m}$
Final Bunch Charge	$Q_f$	100 pC
Final Peak Current	$I_{pk}$	3,000 A
Final Beta Functions	$\beta_x / \beta_y$	5 x 5 mm
System Length	s	18 m
Injection Bend Angle	$\Phi$	25.78 degrees

Table 10.3: Electron Source Parameters for witness bunch injector.

Parameter	Symbol	Value
Initial Bunch Charge	$Q_i$	350 pC
Normalized Transverse emittance	$\gamma\epsilon_x / \gamma\epsilon_y$	1 / 1 $\mu\text{m}\cdot\text{rad}$
FWHM Bunch Length	$\Delta t_b$	1.0 ps
Peak Bunch Current	$I_{pk}$	300 A

The layout of the system is shown in the schematic in Figure 10.10, with a CAD implementation shown in Figure 10.9. The system consists of two ten-foot SLC S-band accelerating structures which are each operated at an unloaded accelerating gradient of 57.3 MV and at a phase 30.24 degrees of S-band off crest to provide the required chirp to longitudinally compress the bunch. A pair of quadrupole triplets then form a 5 m length beam diagnostics section and match the beam optics into the horizontal dogleg. The horizontal dogleg consists of a pair of bend magnets, five quadrupoles and four chromatic correction sextupoles. A quadrupole doublet immediately following the second bend magnet is shared with the drive beam, and a (removable) triplet of permanent magnet quadrupoles perform the focusing of the witness bunch just upstream of the E200 experimental plasma acceleration chamber. The  $L^*$  is designed (drift space downstream of final triplet quad to common (with drive beam) focus waist) to be 25 cm.

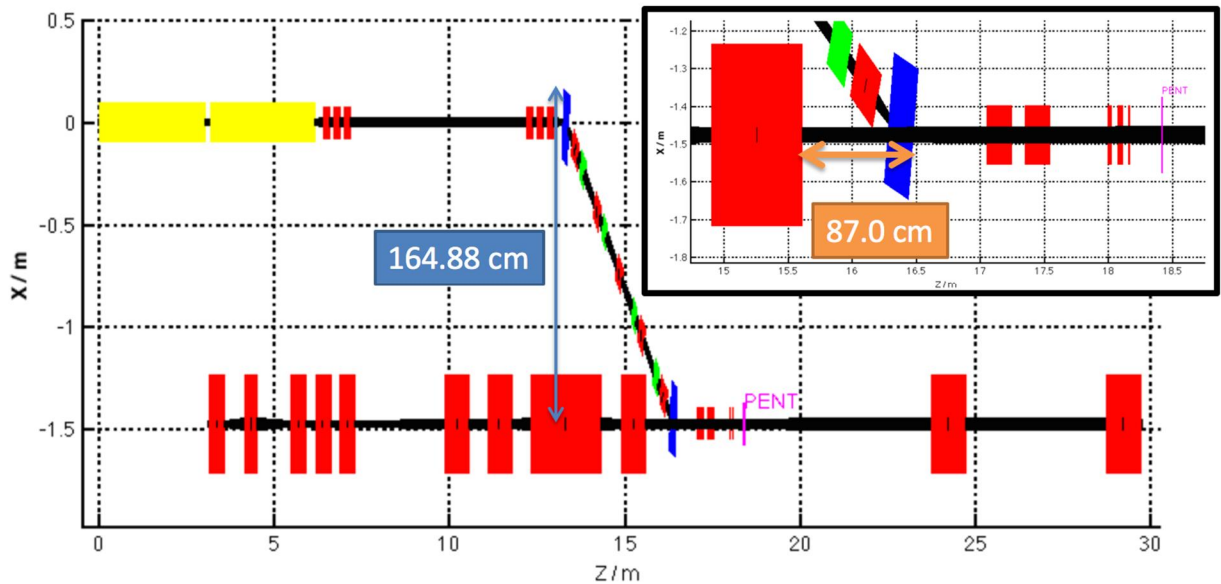


Figure 10.10: Schematic of witness bunch injector components and implementation into FACET-II drive beam line in Sector 20. "PENT" shows the entrance location to the E200 experimental plasma acceleration chamber. Yellow boxes show S-band RF structure, red shows quadrupole magnets, blue are bend magnets and green are sextupoles. The black line shows the required stay-clear aperture.

### 10.3.1.2 Optics Design

The design for the witness bunch injector meets the parameter requirements set out in Table 10.2 in a compact layout which can fit alongside the main FACET-II beamline in Sector 20 and injects the bunch directly behind the drive bunch. A simple dogleg design fulfills these requirements. Using a bend angle of about 26 degrees, the witness bunch can be brought into the main beam line immediately downstream of the last final focus magnet (QFF6) leaving room to focus the beam before the E200 plasma chamber. This choice of bend angle allows for enough magnet elements to be included into the dogleg to generate a substantial compression factor ( $R_{56}=13.6$  mm) and control the optics parameters through the dogleg while fitting horizontally within the confines of the SLC tunnel.

Figure 10.11 shows the design optics functions for the witness bunch injector system. A diagnostics waist is included upstream of the dogleg to provide emittance diagnostics and matching capabilities. A moveable jaw collimator located where the high dispersion to beta ratio is high (as shown with the dashed line in Figure 10.11) allows for fine-grained control over the longitudinal bunch profile. Four sextupole magnets at dispersive locations within the dogleg compensate for chromatic aberrations and second-order dispersion inherent in the design. If placed on mover systems, they can also be used to provide correction of errant dispersion, coupling or waist shifts at the IP focus. Longitudinal compression of the beam is achieved by running the two S-band RF structures off crest by  $\sim 30$  degrees which provides an energy chirp to the bunches so that they then compress in  $z$  as they travel through the dogleg. A doublet of quadrupole magnets and a final permanent magnet quadrupole triplet just before the E200 plasma chamber entrance provide the final focusing of the witness bunch. These can be shared with the main drive beam, because the upstream optics seen only by the drive beam can be matched to take these comparatively weak quadrupole fields into account. The witness bunch final focus provides beta functions at the waist of 5 mm, which for an expected  $1 \mu\text{m}\cdot\text{rad}$  normalized emittance should

produce a 5  $\mu\text{m}$  transverse beam size. This allows for a factor 2 additional beam size growth due to uncorrected errors while still meeting the requirements set out in Table 10.2.

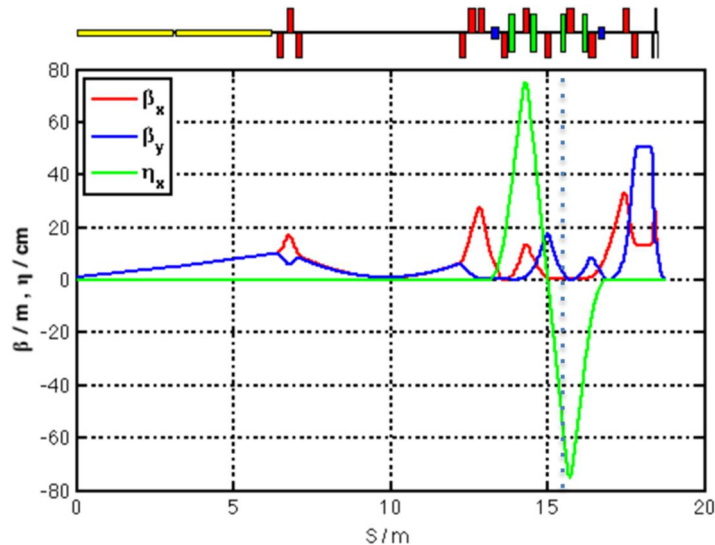


Figure 10.11 Twiss parameters for witness bunch injector design showing RF acceleration to 100 MeV, diagnostics waist, horizontal dog leg injection into main beamline and final focus doublet and triplet system. The beam waist in the E200 plasma chamber is the right-most point on the figure. The dashed line shows the location of the moveable jaw collimator within the dogleg.

### 10.3.1.3 Particle Tracking

Using a 6D tracking code (*Lucretia*), a 1M macro-particle representation of the beam was tracked through the design optics including the effects of ISR and CSR, but not space-charge. Figure 10.12 shows the beam clearance for the planned magnets as a function of their aperture sizes. As can be seen, the limiting apertures are in the horizontal in the high dispersion regions of the dogleg. Here the aperture is restricted to about  $\pm 5$  sigma. In these key locations, wider aperture magnets may be required.

Figure 10.13 shows the tracked beam at the IP waist location within the plasma volume (no attempt is made here to model the interaction with the plasma) where the required parameters are met. The jaw collimators within the dogleg were set to  $\pm 2\text{mm}$  to limit the non-linear high energy-spread tails to achieve this profile.

To estimate the maximum longitudinal contrast of the delivered beam, the core of the beam was cut with one jaw of the collimator and an asymmetric Gaussian function fitted to the beam at the IP waist. A minimum resolvable length scale of about 1.9  $\mu\text{m}$  rms looks feasible (see Figure 10.14).

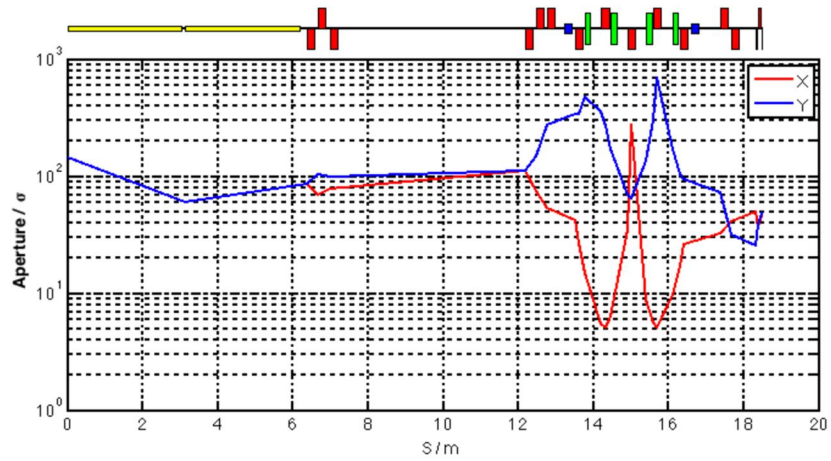


Figure 10.12: Beam clearance calculation from tracked beam through witness bunch injector optics. Lines show aperture widths of beamline elements as a factor of rms transverse beam sizes at those locations.

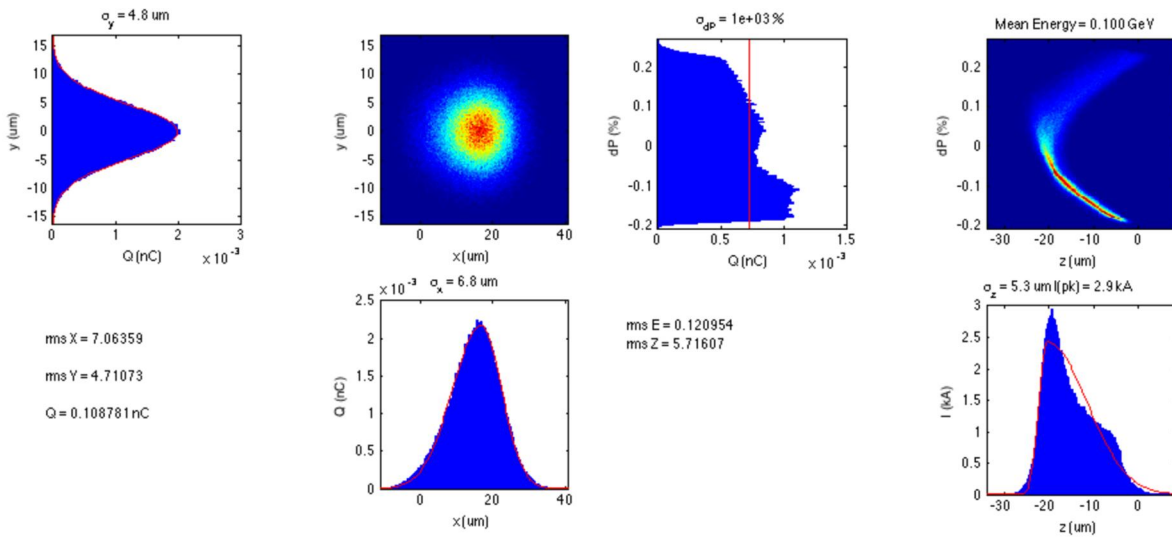


Figure 10.13: Tracked transverse and longitudinal phase space of witness bunch at IP focus point. Collimator jaws are set to +/- 2mm.

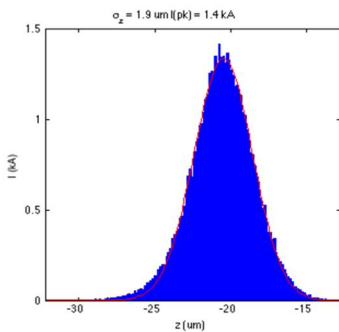


Figure 10.14: Longitudinal contrast- the longitudinal profile of the beam at the IP waist with one jaw collimator cutting into central core region of the beam. Shown is an asymmetric Gaussian fit to the longitudinal distribution.

### 10.3.1.4 Magnets

This design for the witness bunch injector requires 13 quadrupole magnets, one permanent magnet quadrupole triplet installation, 2 rectangular bends and 4 sextupoles. Most of the required magnets could come from the existing positron system in Sector 1 which will be decommissioned during the construction of LCLS-II. The magnet requirements are given in Table 10.6, with some further magnet details shown in Figures 10.15 through 10.18 and Tables 10.4 and 10.5. An example design for the final permanent quadrupole magnet was provided by an external vendor (see example in Figure 10.18).

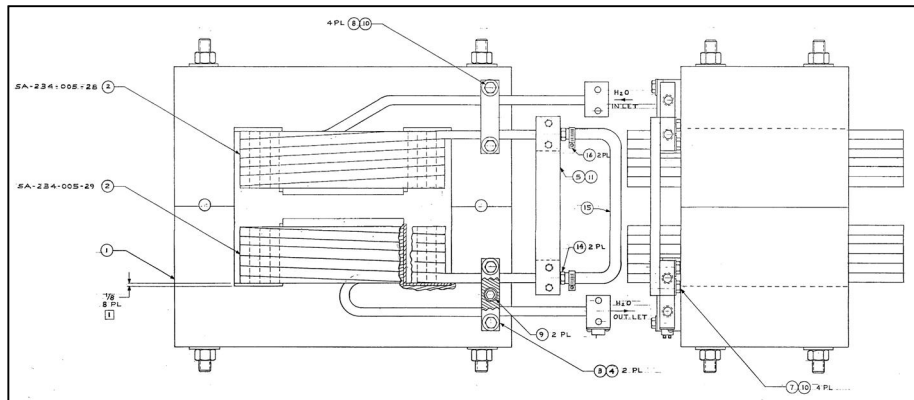


Figure 10.15: SLC "5D7.1" style bend magnet used in Sector 1 positron re-injection section.

Table 10.4: Parameters of selected existing bend magnets for use in witness bunch injector design.

Parameter	Value
Effective Length	0.2032 m
Design Bend Angle @ 200 MeV	12 deg
Half-Aperture	0.0133 m
Width	0.3556 m
Height	0.292 m
Max Integrated Strength @ I=290A	1.5 kG.m

Table 10.5: Parameters of selected existing quadrupole magnets for use in witness bunch injector design.

Parameter	Value
Effective Length	0.197 m
Half-Aperture	0.0192 m
Width	0.1588 m
Height	0.292 m
Max Integrated Strength @ I=90A	31 kG

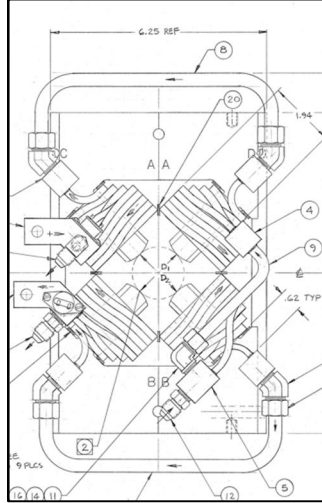
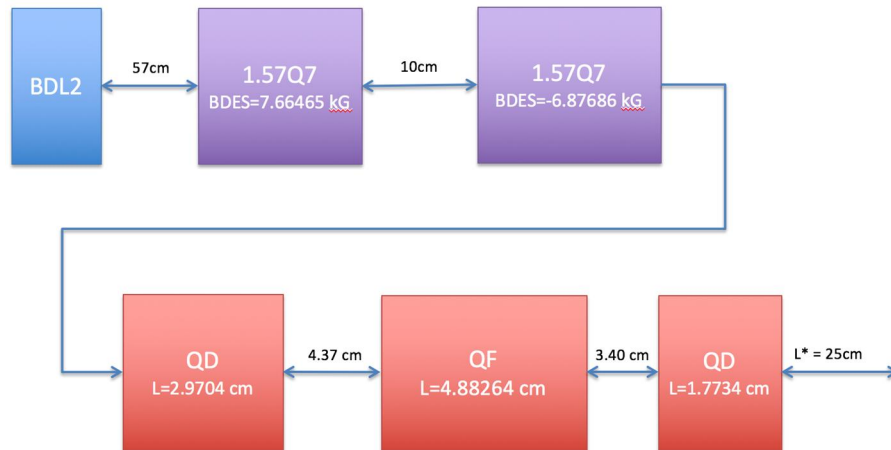


Figure 10.16: SLC "1.57Q7" style quadrupole magnet used in Sector 1 positron re-injection section.

Table 10.6: Magnet properties for witness bunch injector design.

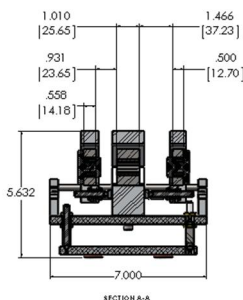
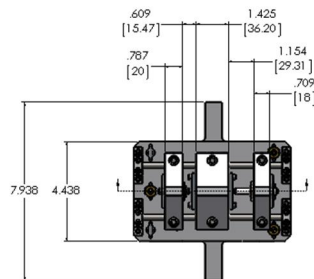
ELEMENT	Eng_Name	L_EFF	APER	Integrated_Field_Gradient_GL	SLAC Drawing #
		m	m	kG	
QWBM1	1.57Q7	0.197	0.038354	-3.499954304	SA-902-708-54
QWBM2	1.57Q7	0.197	0.038354	6.644913243	SA-902-708-54
QWBM3	1.57Q7	0.197	0.038354	-3.499954304	SA-902-708-54
QWBM4	1.57Q7	0.197	0.038354	-5.929464018	SA-902-708-54
QWBM5	1.57Q7	0.197	0.038354	1.199656258	SA-902-708-54
QWBM6	1.57Q7	0.197	0.038354	7.345447701	SA-902-708-54
BXWBDL1	5D7.1	0.2032	0.02667	1.5	SA-234-005-26
QWBDL1	1.57Q7	0.197	0.038354	-11.39898197	SA-902-708-54
SWBDL1	1.625SX3.53	0.1	0.041275	6.50E+02	SA-235-037-30
QWBDL2	1.57Q7	0.197	0.038354	9.669975057	SA-902-708-54
SWBDL2	1.625SX3.53	0.1	0.041275	79.99895551	SA-235-037-30
QWBDL3	1.57Q7	0.197	0.038354	-8.999882494	SA-902-708-54
SWBDL3	1.625SX3.53	0.1	0.041275	79.99895551	SA-235-037-30
QWBDL4	1.57Q7	0.197	0.038354	9.669975057	SA-902-708-54
SWBDL4	1.625SX3.53	0.1	0.041275	6.50E+02	SA-235-037-30
QWBDL5	1.57Q7	0.197	0.038354	-11.39898197	SA-902-708-54
BXWBDL2	5D7.1	0.2032	0.02667	1.5	SA-234-005-26
QWBFF1	1.57Q7	0.197	0.038354	7.661553482	SA-902-708-54
QWBFF2	1.57Q7	0.197	0.038354	-6.87604884	SA-902-708-54
QWBFF3	PMQ	0.029704	0.0254	-19.69349488	
QWBFF4	PMQ	0.048826	0.0254	32.37121536	

QWBFF5	PMQ	0.01773	0.0254	-11.75483653
--------	-----	---------	--------	--------------



- PM triplet quads = 663 kG/m

Figure 10.17: Schematic of design and placement of witness bunch injector final focus doublet and triplet quadrupole magnets.



NAME	GRADIENTS (T/m)
PMQ1	66.3
PMQ2	-66.3
PMQ3	66.3
PMQ4	66.3
PMQ5	-66.3
PMQ6	66.3

Figure 10.18: Vendor-sourced permanent quadrupole magnet triplet example.

## 10.4 Differential Pumping

The beam parameters for FACET-II force a new solution for isolating experimental vacuum from the main linac vacuum. To date, thin, low Z vacuum tight windows have been used (typically 50  $\mu\text{m}$  beryllium) to isolate the vacuum of the experimental systems (which by necessity include materials not suitable for the ultra-high vacuum systems needed in accelerating structures) from the linac. The windows need to be replaced every few months as part of general maintenance as sublimation from the powerful electron beams reduces the thickness and eventually leads to hole formation. Temporary mitigations include a series of vacuum windows on valves so there is redundancy if one gets damaged. The full solution of differential pumping reduces the down time of replacing these windows and also improves the quality of the beam that is delivered to the experiments as the beam does not get scattered by solid material.

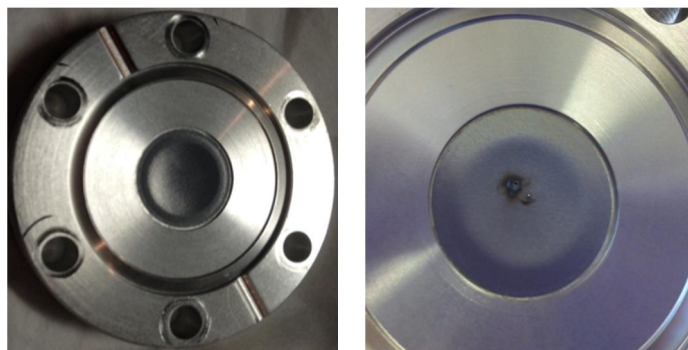


Figure 10.19: Left: New beryllium window, unused. Right: This beryllium window was used in the FACET beamline. Discoloration surrounds a microscopic hole.

Differential pumping has been designed for the XTES SXR gas attenuator, part of the LCLS-II project. The requirements for this instrument are similar to those needed for the FACET-II experiments and a similar design will be used. The XTES SXR differential pumping design has undergone Preliminary Design Review.

The principal function of the gas attenuator for LCLS-II is to provide variable attenuation to the FEL beam. They will use argon or nitrogen gas with variable pressure between 0.1 Torr and 50 Torr. Experiments at FACET have to date used between 1 Torr and 40 Torr of gas species such as hydrogen, helium, neon and argon. The gas is ionized with a high power laser or by the beam to form plasma for plasma wakefield experiments or it is used as a buffer to contain a column of alkali metal vapor.

The major components of the differential pumping for XTES SXR are shown in Fig.10.20. The differential pumping is symmetric about the center of the gas cell. For FACET-II, ultra-high vacuum requirements exist upstream of the gas cell but not downstream and aperture requirements for the beam passage are larger downstream so a symmetric design is not needed.

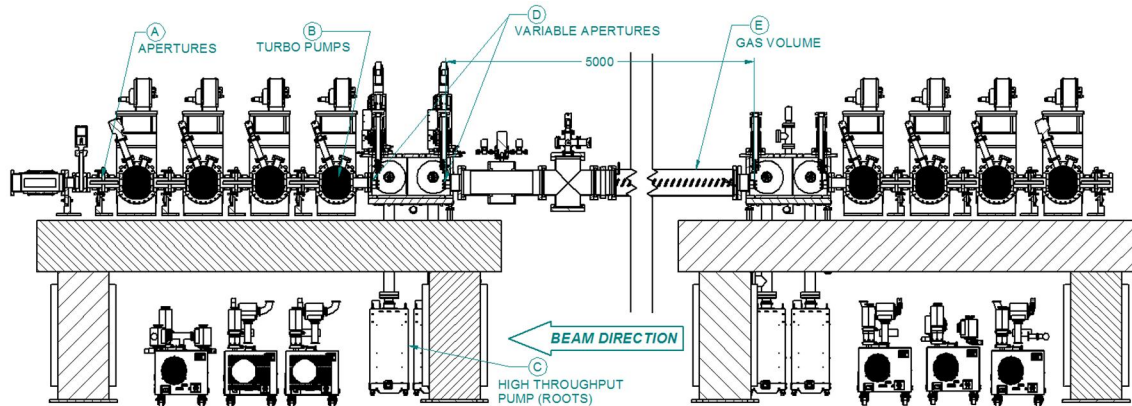


Figure 10.20 Differential pumping design for the XTES Gas Attenuator for LCLS II. The requirements for the differential pumping are close to those needed for FACET experiments.

On SXR, the two highest pressure apertures are variable apertures and at the lower pressures, fixed tubes. The variable apertures (labeled D in Fig. 10.20 and shown in detail in Fig.10.21) are required to satisfy the variable “beam stay clear” for different x-ray energies and variable gas cell pressure. FACET-II will take advantage of variable apertures to most efficiently reduce viscous or transitional gas flow to the differential pumping system. The aperture can also be moved to the beam position remotely making alignment tolerances in installation less of an issue. The smallest aperture in the SXR design is 4 mm (pressure is approximately 10 Torr of nitrogen gas for effective attenuation of 1.2 keV x-rays). Further from the gas volume, in the molecular flow regime, tubes (labeled A) are better at limiting flow than thin plate apertures and are approximately 12 mm in diameter in the SXR model.

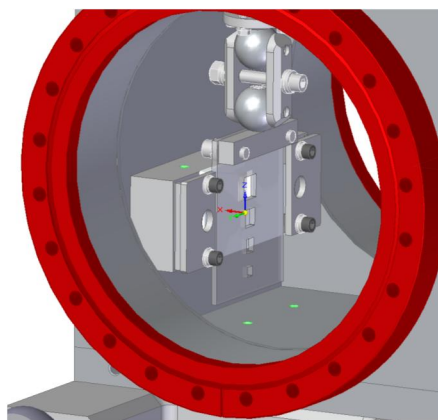


Figure 10.21 Variable aperture plate concept for XTES SXR.

The first stage of pumping will be high throughput pumps (>70 Torr //s) such as roots type pumps (labeled C). Attention needs to be paid to the first turbomolecular pump (labeled B in Fig.10.20). With increased pressure in the gas cell and the increase in the gas flow that follows, the first turbo is the most affected. The roots pumps that precede them can pump up to atmospheric pressure, but most turbos see an exponential degradation in speed when pressures are above  $10^{-3}$  Torr. The first turbo needs high throughput at high pressures (in the range  $10^{-2}$  to  $10^{-1}$  Torr) and will need to be carefully selected. If all turbos however are the same type, this reduces operations costs by saving money with the number of spare units and in maintaining systems. After the differential pumping stages, the final pressure is  $10^{-9}$  Torr, matching requirements for operating RF cavities.

The pressure management of the gas volume will be handled with capacitance manometers and a feedback system with a variable aperture valve on the gas input.

The XTES SXR design manages the decrease from approximately 50 Torr to  $10^{-9}$  Torr in 5 meters. FACET-II can afford to use more beamline for the differential pumping system. On the up-beam side, there are 20 meters between the final RF structure and the start of the gas cell. This beamline will however be shared with magnets that are part of the sector 20 final focus.

Turbo pumps similar to those needed for this installation are commonly used in FACET for the vacuum systems in the experimental area and are reliable in the FACET environment.

## 10.5 Compton Source

Compton experiments collide electrons on photons. FACET can provide both using existing infrastructure but to reach the required luminosity, the FACET laser needs to be upgraded in energy. Additional flash lamp YAG pump lasers (SAGAs) will be purchased and integrated as part of the FACET II project but run at low voltage so as to provide overhead for laser delivery, ensuring that the energy delivered to experiments remains nominal.

To run the SAGAs at their peak output and increase the energy of the FACET laser to 1 J at the delivery point, existing optics need to be replaced with larger ones.

The Compton Source experiments are statistical and benefit hugely from increased repetition rate. Current repetition rate of the FACET laser system is 10 Hz. This can be upgraded to 20 Hz by temporally interleaving two 10 Hz pulses. This requires an additional three SAGAs. Installation in the FACET laser room can be achieved by stacking the SAGAs vertically.

Theoretically, FACET II can operate an electron beam at 120 Hz. To upgrade the laser to 120 Hz involves the construction of a new laser facility and is not captured in this preliminary description. If 20 Hz SAGAs become available commercially, this project would also cover the upgrade of all FACET SAGAs to 20 Hz operation providing 40 Hz laser repetition rate after temporally interleaving the SAGAs.

## 10.6 Photon-Photon Collider Option

### 10.6.1 Overview

Section 3.7 proposes a gamma beam program that provides a test of pair creation by colliding Compton photons generated in the final sections of BC3E and BC3P. Given the geometry imposed by the final bend angles in BC3 (22.6 mrad), an optimal beam energy for this option is 4 GeV, where 30 MeV Compton photons collide inside the final BC3 bend magnet with a center of mass energy close to the maximum pair production cross-section at ~1.4 MeV.

Figure 10.22 below shows a sketch outlining a possible configuration for the laser interaction with the electron and positron beams in the second part of the BC3E and BC3P chicanes. A laser waist is formed as close as possible to the upstream face of the bend magnet (0.4m is assumed here) where it interacts with the electron/positron bunch. Compton photons collide at a point 0.93 m downstream within the bend magnet.

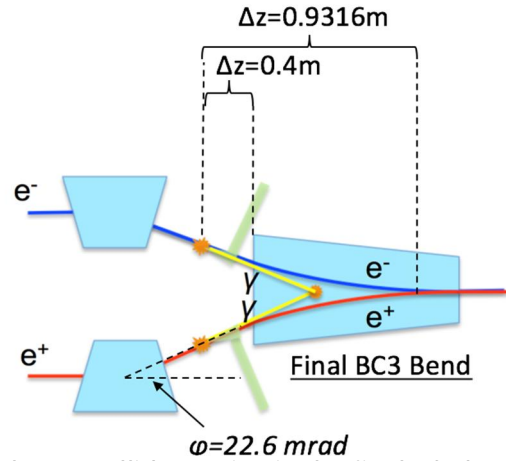


Figure 10.22: Sketch of photon-photon collider option in the final BC3 bend magnet.

### 10.6.2 Laser Parameters

The laser parameters at the interaction point with the electron/positron beam upstream of the final BC3 bend magnet are shown in Table 10.7.

Table 10.7: Parameters of CO<sub>2</sub> laser at waist location 0.4 m upstream of final BC3 bend magnet.

Parameter	Symbol	Value
Beam Energy / pulse	$E_l$	0.3 J
Wavelength	$\lambda_l$	10.2 $\mu\text{m}$
Rayleigh Length	-	300 $\mu\text{m}$
Beam Length	$\sigma_{z,l}$	300 $\mu\text{m}$
Beam Radius	$\sigma_l$	25 $\mu\text{m}$

### 10.6.3 Linac Configuration

The compression configuration for the FACET-II linac for 4 GeV beam energy operations in Sector 20 is summarized in Figure 10.23 below. For this configuration, the energy of the BC2 chicanes are lowered to 2.0 GeV, while the compression setting ( $R_{56}$ ) is the same as for nominal FACET-II operation. The beam is fully compressed by the end of L3 with a bunch length below 300  $\mu\text{m}$  and final energy spread below 0.1%. Beam tracking is performed as described in Section 6.7. Figures 10.24 and 10.25 show the tracked longitudinal and transverse beam phase space for the electron and positron bunch entering Sector 20. As the beam is fully compressed, without an energy chirp entering Sector 20, the  $R_{56}$  of the BC3E and BC3P chicanes is not a design parameter, see Section 10.6.9 below for details of the BC3 chicane design.

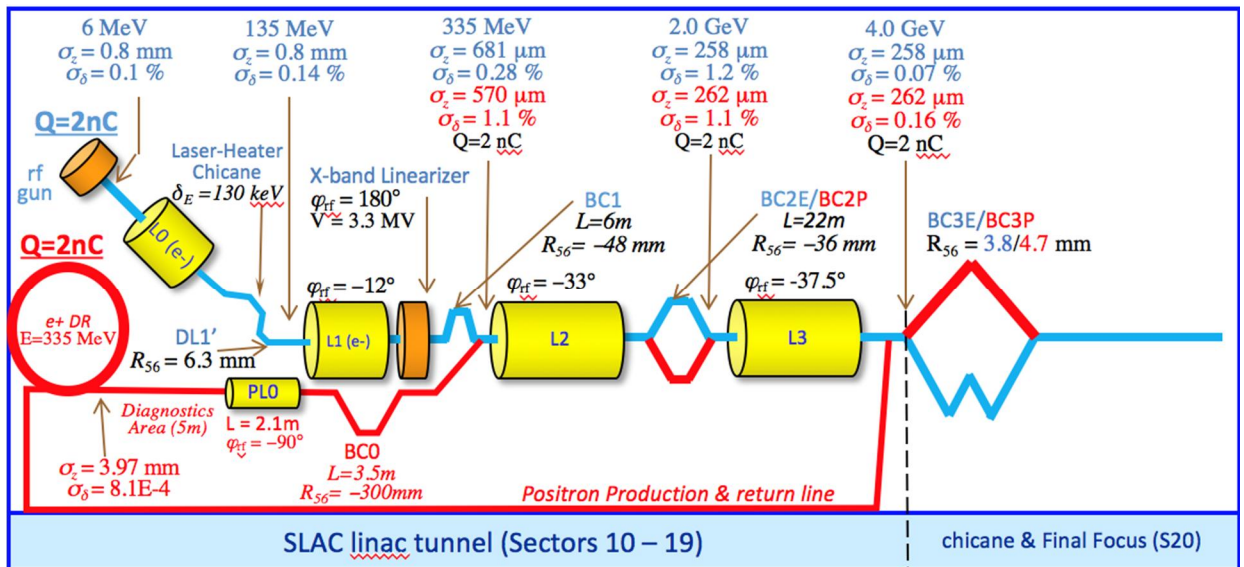


Figure 10.23: FACET-II configuration and longitudinal beam parameters for Photon-Photon collisions in Sector 20.

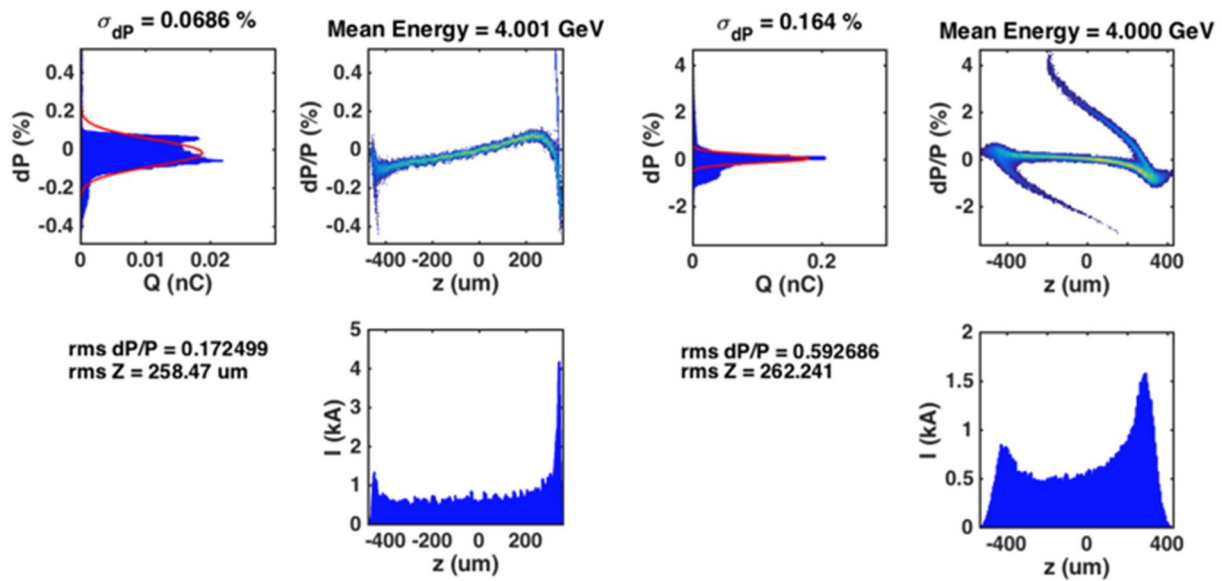


Figure 10.24: Longitudinal phase space of beam tracked to entrance of Sector 20. The 2 nC electron beam is shown to the left and the 2 nC positron beam on the right.

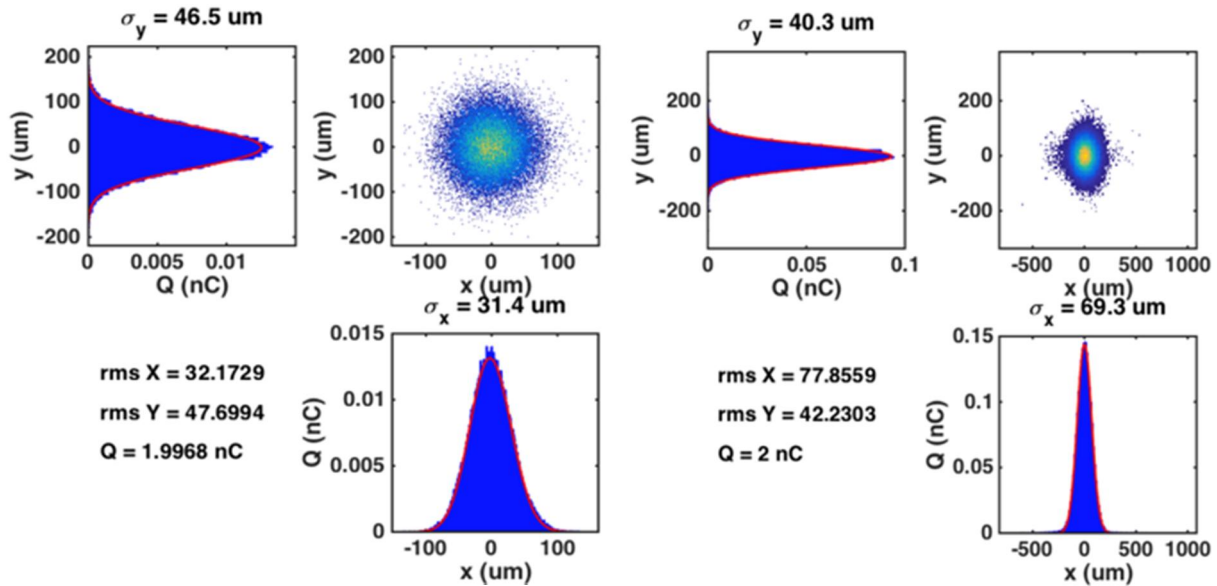


Figure 10.25: Transverse phase space of beam tracked to entrance of Sector 20. The 2 nC electron beam is shown to the left and the 2 nC positron beam on the right.

#### 10.6.4 BC3E & BC3P Configuration

The BC3E and BC3P chicanes are re-matched to maximize both the Compton photon production rate at the laser waist location 40 cm upstream of the final bend and the gamma-gamma luminosity at the collision point within the bend. The following match conditions are imposed while constraining the beam size to remain within the chicane magnet apertures at the 10-sigma level:

- Electron and positron transverse spot sizes at the Compton waists consistent with laser waist sizes at those locations (25  $\mu\text{m}$ ).
- Electron and positron transverse spot size at projected photon collision point within final bend small compared to projected photon waist size at that location (119  $\mu\text{m}$ ).
- Photon waist size at collision point given by  $(1/\gamma)*L$ , where  $\gamma$  is the relativistic factor of the particle beams and L is the drift distance to the collision point in the final bend magnet (0.93 m).
- Horizontal momentum dispersion of electron and positron beams canceled at Compton laser waist location.

Figures 10.26 and 10.27 below show the re-matched optics for BC3E and BC3P. To keep the changes to the normal operating system to a minimum, only the magnets within Sector 20 are adjusted. The matching solution here assumes that all magnets within the BC3E and BC3P chicanes have independently controllable power supplies. The beam spot sizes at the Compton laser interaction waist and the photon beam size at the collision point are shown in Table 10.8. Figures 10.28 and 10.29 show the magnet apertures in the two bunch compressor chicanes and the 10 sigma tracked beam envelope. The calculated beam clearance is considered generally acceptable, with one tight spot around the BC2ER bend in the vertical plane. This is however compatible with current operating FACET conditions.

Table 10.8: Electron/positron beam sizes at interaction waist with Compton laser source and projected photon beam sizes at gamma collision point in final bend magnet.

rms Transverse Beam Size	Electron		Positron	
	<i>Beam @ Laser Waist</i>	<i>γ IP</i>	<i>Beam @ Laser Waist</i>	<i>γ IP</i>
$\sigma_x^*$	8.8 μm	130 μm	43.0 μm	131 μm
$\sigma_y^*$	21.6 μm	123 μm	22.0 μm	133 μm

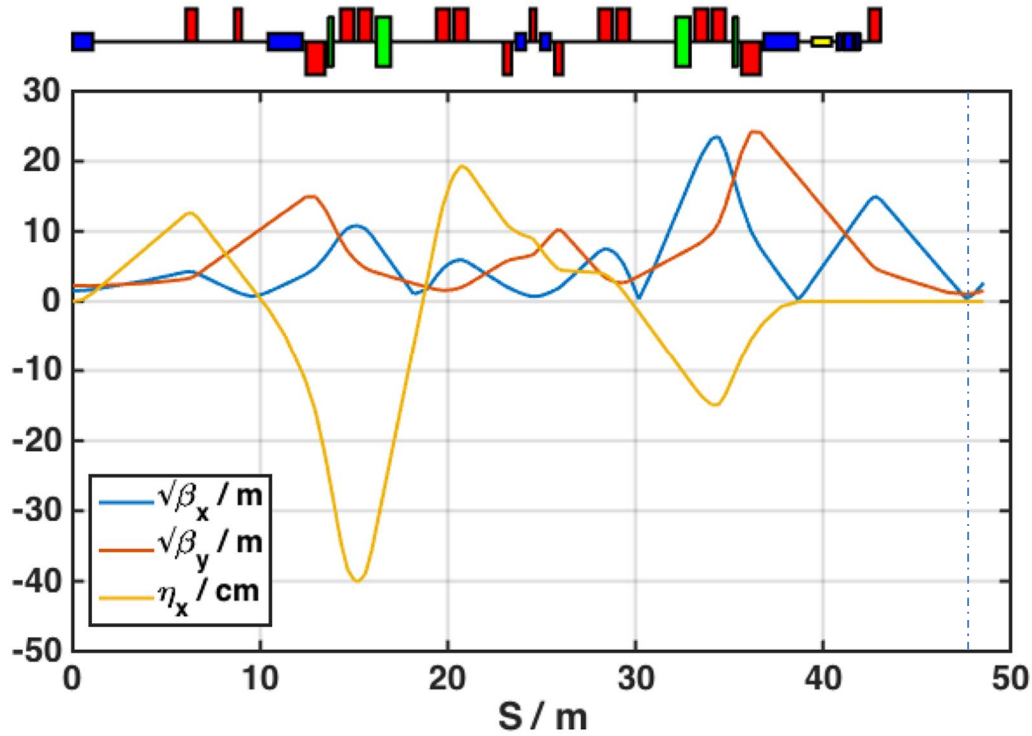


Figure 10.26: Optics functions for BC3E chicane (electron beam) for gamma-gamma collider configuration. Dashed line shows Compton laser waist location.

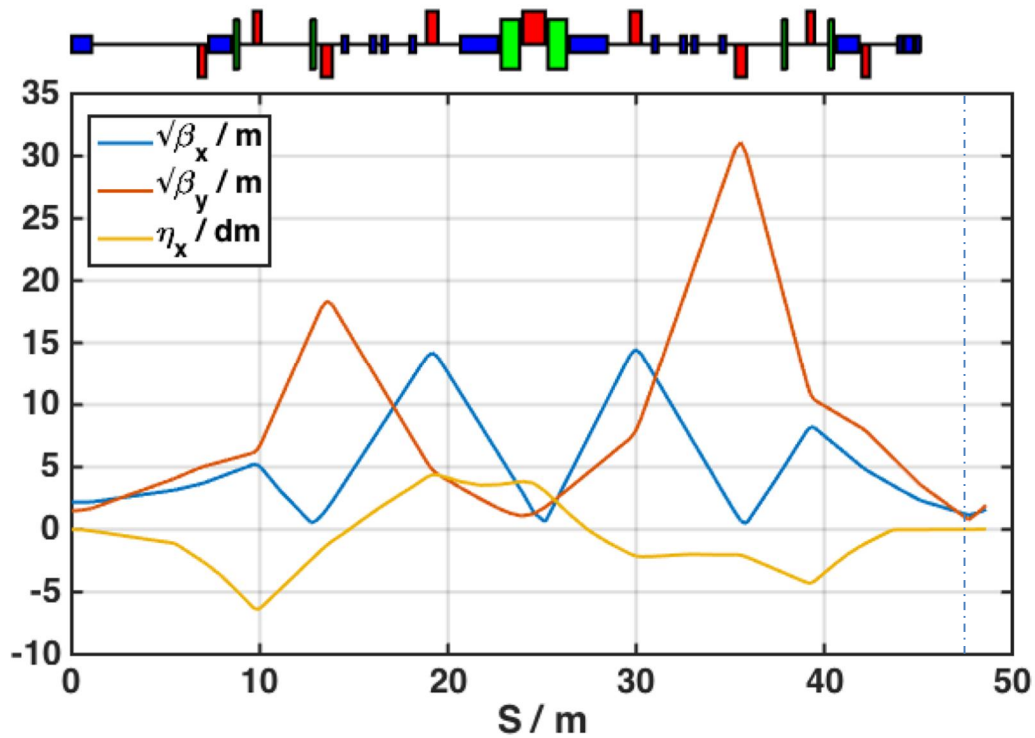


Figure 10.27: Optics functions for BC3P chicane (positron beam) for gamma-gamma collider configuration. Dashed line shows Compton laser waist location

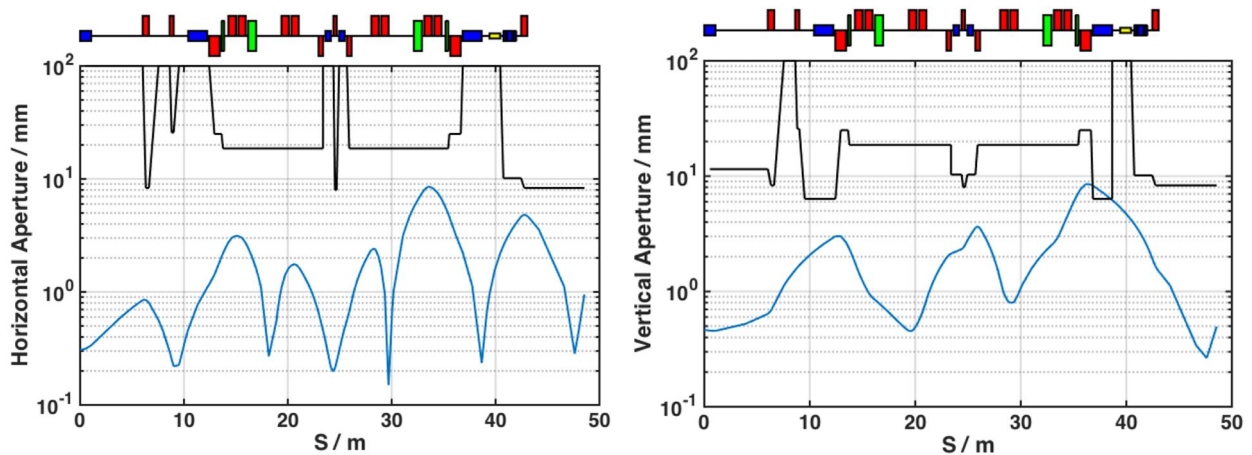


Figure 10.28: Horizontal and vertical beam apertures in BC3E (black line) and 10X tracked transverse beam envelope (blue curve). For BC3E (electrons).

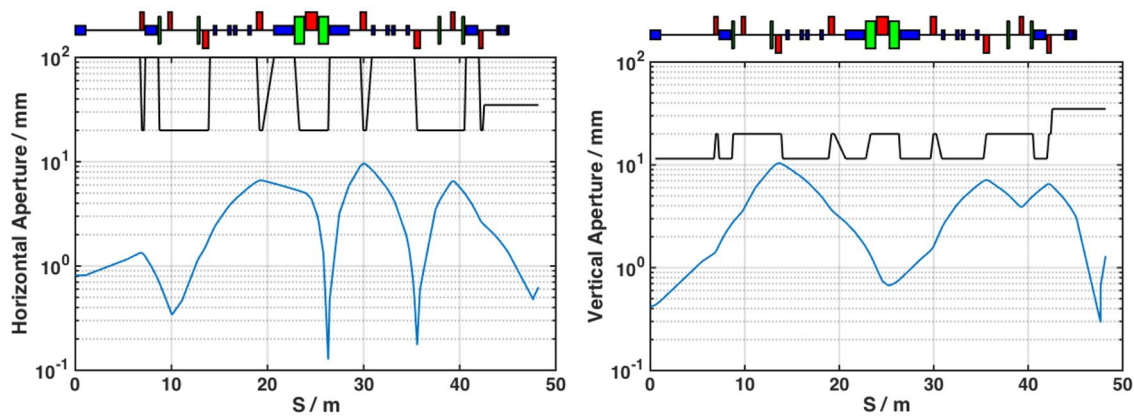


Figure 10.29: Horizontal and vertical beam apertures in BC3E (black line) and 10X tracked transverse beam envelope (blue curve). For BC3P (positrons).

### 10.6.5 Final Focus and Spectrometer Configuration

The only requirements for the downstream final focus and spectrometer magnets is that the beam remain contained within existing apertures and extract cleanly to the dump. The optical functions are shown in Figure 10.30 and the 10 sigma beam envelope and magnet apertures are shown in figures 10.31 and 10.32 which shows adequate beam clearance.

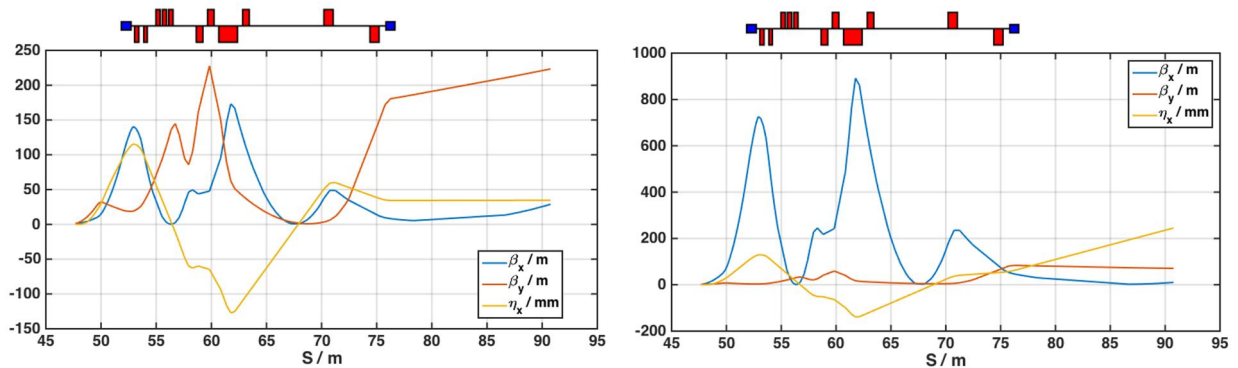


Figure 10.30: Optics functions for the final focus and spectrometer section following the BC3E and BC3P chicanes. Positrons are shown on the left and electrons on the right.

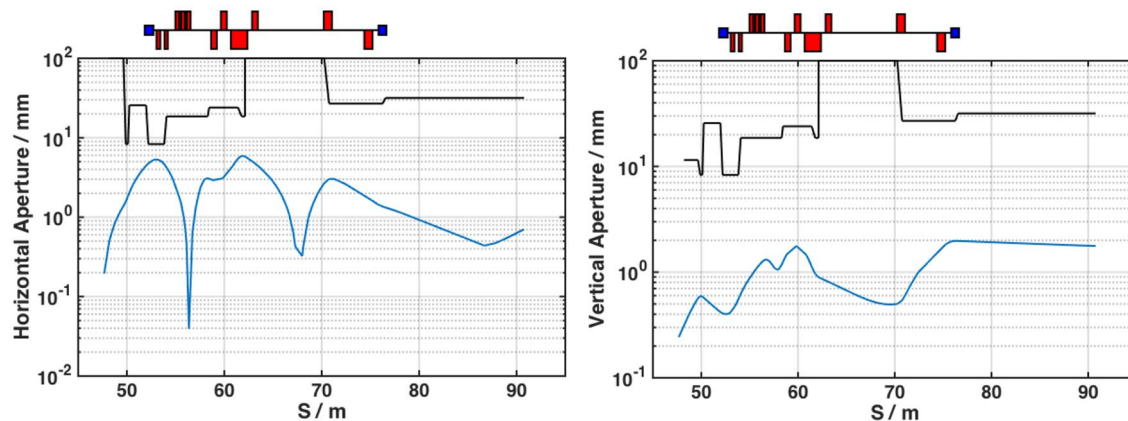


Figure 10.31: Electron beam 10 sigma beam envelope (blue) and final focus and spectrometer apertures (black). Horizontal dimension shown on the left, vertical shown on the right.

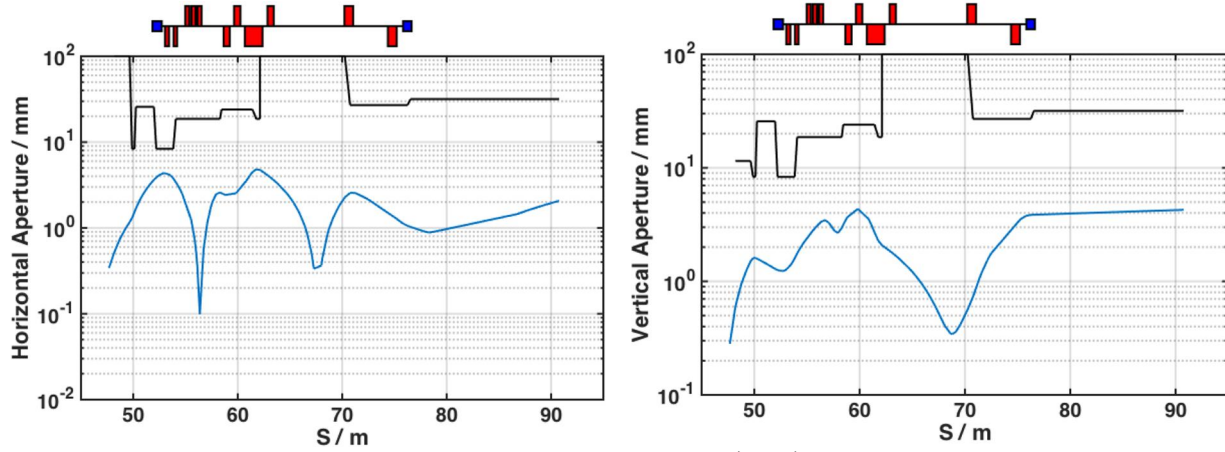


Figure 10.32: Positron beam 10 sigma beam envelope (blue) and final focus and spectrometer apertures (black). Horizontal dimension shown on the left, vertical shown on the right.

### 10.6.6 Photon-Photon Collision Luminosity and Expected Pair Production Rate

Using the proposed design and beam and laser parameters, the expected Compton photon luminosity per pulse is given by,

$$\mathcal{L}_\gamma = \frac{N_e N_\gamma^l}{2\pi \sqrt{(\sigma_x^2 + \sigma_l^2)(\sigma_y^2 + \sigma_l^2)}}$$

where,  $N_e$  and  $N_\gamma^l$  are the number of electrons (or  $N_p$  positrons) and number of laser photons per pulse, respectively.  $\sigma_{x,y}$  are the transverse beam spot sizes at the laser interaction waist of the electrons or positrons, and  $\sigma_l$  is the transverse spot size of the laser beam at the interaction point given in Table 10.2.

The number of laser photons per pulse is given by,

$$N_\gamma^l = \frac{E_l}{(h \cdot c) / \lambda_l}$$

with  $E_l$  the laser energy per pulse and  $\lambda_l$  the laser wavelength given in Table 10.2.

The number of Compton photons generated per pulse (for each of the electron and positron source beams) is then given by the product of the calculated luminosity from above with the Compton cross section, which at these energies is closely approximated by the Thomson scattering cross section ( $\sigma_T = 6.65E-29 \text{ m}^2$ ):

$$N_\gamma = \mathcal{L}_\gamma \sigma_c$$

The expected gamma-gamma collision luminosity is then given by:

$$L_{\gamma\gamma} = \frac{N_\gamma^e N_\gamma^p f_{rep}}{2\pi \sqrt{(\sigma_{x,e}^2 + \sigma_{x,p}^2)(\sigma_{y,e}^2 + \sigma_{y,p}^2)}} \cdot R_L$$

where  $N_\gamma$  is the above calculated Compton photon rate (for electrons (e) and positrons (p)),  $f_{rep}$  is the machine repetition rate of 5 Hz,  $\sigma$  values represent the projected Compton photon transverse beam sizes at the collision point determined by the divergence of the electron/positron beams at the laser interaction waist and the opening angle of the photon radiation cone.  $R_L$  is a modification factor applied to the luminosity to account for the angle between the colliding photon beams given by:

$$R_L = \left[ 1 + \left( \frac{\sigma_z}{\sigma_x} \tan \phi \right)^2 \right]^{-1/2},$$

for the values shown in Table 10.3 the expected gamma-gamma luminosity is calculated to be  $\sim 7 \times 10^{21} \text{ cm}^{-2} \cdot \text{s}^{-1}$ . Given a pair creation cross section of  $\sim 10^{-25} \text{ cm}^2$  for the 30 MeV photons (see Section 3.7), this implies a pair production rate of  $\sim 7 \times 10^4 \text{ s}^{-1}$ , or about one  $e^+e^-$  pair every 24 minutes.

The principal limitations to the pair production rate are given by the positron horizontal spot size at the laser waist and the distance of the Compton source to the gamma interaction point. The laser waist optimal location will be further studied in future and can be considerably closer to the final bend magnet (also a shorter bend magnet may be used). Then the gamma spot size might be reduced by as much as half. By adding additional parameters to the optics matching (e.g. by changing the incoming matching from the linac and/or trading off some dispersion control), the positron horizontal beam size could be reduced to close to the electron horizontal beam size. Combined with running at the highest electron bunch charges as outlined earlier in this chapter, these changes could increase the pair production rate by as much as a factor 10 ( $\sim$  one pair every 2.5 minutes).